STABILITY OF PRECAST PRESTRESSED CONCRETE BRIDGE GIRDERS CONSIDERING IMPERFECTIONS AND THERMAL EFFECTS

A Dissertation
Presented to
The Academic Faculty

by

Jonathan B. Hurff

In Partial Fulfillment
of the Requirements for the Degree
Doctor of Philosophy in the
School of Civil and Environmental Engineering

Georgia Institute of Technology
August 2010

STABILITY OF PRECAST PRESTRESSED CONCRETE BRIDGE GIRDERS CONSIDERING IMPERFECTIONS AND THERMAL EFFECTS

Approved by:

Dr. Lawrence F. Kahn, Advisor
School of Civil and Environmental
Engineering
Georgia Institute of Technology

Dr. Abdul-Hamid Zureick
School of Civil and Environmental
Engineering
Georgia Institute of Technology

Dr. Kenneth M. Will
School of Civil and Environmental
Engineering
Georgia Institute of Technology

Dr. Donald W. White
School of Civil and Environmental
Engineering
Georgia Institute of Technology

Dr. T. Russell Gentry
College of Architecture
Georgia Institute of Technology

Date Approved: June 30, 2010

ACKNOWLEDGEMENTS

TABLE OF CONTENTS

LIST OF TABLES

LIST OF FIGURES

LIST OF SYMBOLS AND ABBREVIATIONS

A	Term accounting for effect of load height on buckling load
A_{cp}	Area enclosed by outside perimeter of concrete cross-section
A_f	Final string length for the bottom horizontal string potentiometer
A_g	Gross area of concrete
A_o	Area enclosed by centerline of longitudinal reinforcing steel
A_{px}	Corrected experimental lateral displacement at the bottom of the cross-section
A_{py}	Corrected experimental vertical displacement at the bottom of the cross-section
A_R	Geometric relationship that considers load height (Rafla, 1973)
A_s	Area of mild steel reinforcement
A_t	Area of individual steel reinforcing bar in reinforcing tie
A_z	Gross cross-sectional area of bearing pad in vertical direction
A_0	Initial string length for the bottom horizontal string potentiometer
B	Weak axis flexural stiffness (EI_y)
B_f	Final string length for the top horizontal string potentiometer
B_r	Reduced weak axis flexural stiffness accounting for imperfections
B_0	Initial string length for the top horizontal string potentiometer
C	Torsional stiffness (GJ)
C_b	Moment gradient coefficient
C_f	Final string length for the top vertical string potentiometer
C_I	Warping stiffness (EC_w)
C_P	Prestressing force torsional stiffness effect

C_s	Torsional stiffness from steel reinforcing ties
C_ω	Warping constant
C_0	Initial string length for the vertical string potentiometer
C^*	Effective torsional stiffness
E	Elastic modulus
E_{bp}	Elastic modulus of bearing pad
E_c	Concrete modulus of elasticity
E_{hw}	Modified modulus of elasticity from Hansell and Winter (1959)
E_r	Reduced modulus of elasticity
E_s	Steel modulus of elasticity
E_{sec}	Secant modulus of elasticity
E_{tan}	Tangent modulus of elasticity
G	Shear modulus
G_{bp}	Shear modulus of elasticity of bearing pad
G_c	Concrete shear modulus
G_c'	Modified concrete shear modulus
G_s	Steel modulus of elasticity
H	Total height of bearing pad
I	Moment of inertia
I_b	Moment of inertia of bottom flange about its strong axis
I_{eff}	Effective moment of inertia
I_{gx}	Gross moment of inertia about the x-axis
I_{gy}	Gross moment of inertia about the y-axis

I_p	Polar moment of inertia
I_{Ry}	Cracked moment of inertia about y-axis
I_{sy}	Moment of inertia of individual longitudinal steel reinforcing bar
I_t	Moment of inertia of top flange about its strong axis
I_x	Major axis moment of inertia
I_y	Minor axis moment of inertia
I_{yc}	Weak-axis moment of inertia of compression zone
$I_{y\,eff}$	Effective moment of inertia about y-axis
I_1	Moment of inertia of top longitudinal reinforcing steel
I_2	Moment of inertia of bottom longitudinal reinforcing steel
J	Torsion constant
J_{eff}	Effective torsion constant
J_g	Gross torsion constant
J_R	Cracking torsion constant
K_θ	Rotational spring constant of support
$[K]$	Stiffness matrix
L	Length of the girder
L_{bp}	Length of bearing pad
L_2*	Second-order work of the system
M	Moment of the external forces and self-weight with reference to shear center
M_a	Applied moment at midspan
M_b	Critical buckling moment
$M_{b\,elastic}$	Elastic critical buckling moment

M_R	Cracking moment of cross-section
M_u	Ultimate flexural moment capacity of cross-section
M_{wb}	Moment from weight of beam
M_{wd}	Moment from weight of deck
M_0	Applied end moment
N	Lateral restoring force
P	Applied concentrated load
P_b	Critical prestressing force
P_{ps}	Prestressing force
$\{P\}$	Incremental load vector
S	Shape factor of bearing pad
T_R	Cracking torque
U	Total change in potential energy of system
U_b	Change in potential energy due to the beam self-weight
U_d	Change in potential energy due to the deck load
U_p	Change in potential energy due to prestressing force
V	Total strain energy
V_1	Strain energy from longitudinal stresses
V_2	Strain energy from shearing stresses
W	Work of elastic system
W_b	Girder self-weight per unit length
W_{bp}	Width of bearing pad
W_d	Weight of deck per unit length

Z	Property of girder cross-section; zero if symmetric about x-axis $$2y_0 I_x - \int_A y(x^2 + y^2)dA$$
$\bar{a}$	Load height above shear center
b	Breadth of cross-section
b_i	Effective width of cross-section (Rafla, 1973)
b_s	Lateral distance between longitudinal steel reinforcing bars
b_{tf}	Breadth of top flange
b_1	Breadth of area enclosed by steel reinforcing ties
c	Depth of neutral axis
c_a	Overturning moment arm
c_b	Depth of neutral axis of balanced section
c_r	Resisting moment arm
c_u	Depth of neutral axis at ultimate load
c_1	Depth of neutral axis of angled flexural member
d	Effective depth of cross-section
d_1	Depth of area enclosed by steel reinforcing ties
d_b	Diameter of steel reinforcing bar
d_e	Depth of individual fiber from angled neutral axis
d_f	Distance between centerline of top and bottom flange
d_n	Distance of angled neutral axis from extreme fiber
d'	Distance between top and bottom longitudinal reinforcing steel
$\bar{e}$	Idealistic compression strut imperfection
e	Prestressing strand eccentricity from centroidal axis

e_i	Eccentricity of girder center of gravity
e_o	Out-of-plane eccentricity of top of beam
e_u	Out-of-plane eccentricity of bottom of beam
e_x	Individual strand eccentricity from x-axis
e_y	Individual strand eccentricity from y-axis
f_c'	Concrete compressive strength
f_{pc}	Compressive stress in concrete at centroid of cross-section
h	Height of cross-section
h_{eq}	Equivalent height of cross-section for calculating corrected experimental displacements of initially rotated cross-sections and cross-sections with flanges
h_{ri}	Thickness of individual layer of elastomer
k_{rx}	Rotational stiffness of bearing pad about the x-axis
k_{ry}	Rotational stiffness of bearing pad about the y-axis
k_z	Vertical stiffness of bearing pad
m_0	Equivalent load eccentricity (Mann, 1976)
p	Pitch of steel reinforcing ties
p_{cp}	Outside perimeter of concrete cross-section
p_0	Perimeter of centerline of longitudinal reinforcing steel
r	Height where beam weight causes neutral equilibrium of beam (radius of stability)
u	Lateral deflection
u_0	Initial lateral deflection
$\{u\}$	Incremental displacement and rotation vector
v	Vertical deflection

w	Difference between top and bottom flange width
w_b	Critical uniform load
x	Coordinate axis along centroidal axis of girder
y	Coordinate axis perpendicular to centroidal axis of girder (lateral)
y_{cg}	Height of center of gravity above roll axis
y_n	Orthogonal distance from centroidal axis to angled neutral axis at the x-coordinate location of the individual fiber
y_0	Distance to shear center from centroidal axis
z	Coordinate axis along centroidal axis of girder with origin at end
z_{cg}	Lateral deflection of center of gravity of deflected beam
z_{cgo}	Lateral deflection of c.g. of beam if entire dead load applied laterally
z_d	Internal moment arm between compression zone and steel reinforcing
α	Angle of support before deformations
β_T	Parameter based on ratio d/b (Timoshenko and Goodier, 1951)
β_x	Section property $\dfrac{1}{I_y}\left(\int_A x^3 dA + \int_A xy^2 dA\right)$
β_y	Section property $\dfrac{1}{I_x}\left(\int_A y^3 dA + \int_A x^2 y dA\right)$
β_0	Initial rotation
γ	Parameter based on ratio d_1/b_1 (Cowen, 1953)
Γ	Warping constant for unequal flanges $\Gamma = \dfrac{d_f^2 I_t I_b}{I_b + I_t}$
δ_0	Initial lateral deflection at midspan
Δ_r	Factor reducing the buckling moment due to initial sweep

ε	Longitudinal strain
ε_c	Extreme compression fiber strain
$\varepsilon_{zz}^{(2)}$	Second-order strain
θ	Roll axis of beam with respect to vertical axis
θ_{eq}	Equivalent rotation of cross-section for calculating corrected experimental displacements of cross-sections with flanges
θ_{NA}	Angle of neutral axis
θ_0	Initial rotation at midspan
Θ_r	Factor reducing the buckling moment due to initial rotation
μ	Rigidity multiplier (1.2 for under-reinforced and 0.8 for over-reinforced)
ν	Poisson's ratio
ξ	Factor controlling depth of neutral axis (Rafla, 1969)
φ	Neutral axis angle
ρ_l	Longitudinal reinforcing steel reinforcement ratio
ρ_t	Transverse reinforcing steel reinforcement ratio
σ_c	Extreme compression fiber stress
σ_z	Longitudinal stress
ψ	0 for $c_u \le c_b$ (under-reinforced beam); 1 for $c_u > c_b$ (over-reinforced beam)
AASHTO	American Association of State Highway and Transportation Officials
LVDT	Linear Variable Displacement Transducer
PCI	Precast/Prestressed Concrete Institute

SUMMARY

An experimental and analytical study was performed to determine the stability behavior of prestressed concrete beams. Two stability phenomenons were investigated: (1) lateral-torsional buckling and (2) rollover. An emphasis was placed on the effects of initial imperfections on the stability behavior; the effect elastomeric bearing pads and support rotational stiffness was investigated. The experimental study consisted of testing six 40-in. (1016 mm) deep, 4-in. (102 mm) wide, 32-ft. (9.75 m) long rectangular prestressed concrete beams with varying prestressing force and prestressing strand eccentricity and testing one 100-ft. (30.5 m) long PCI BT-54 bridge girder. Elastic and nonlinear analyses were performed on the seven test specimens, on a hypothetical rectangular beam with a series of varying initial imperfections and a PCI BT-72 with varying imperfections.

The first set of experiments was performed on the six rectangular beams. The beams were designed to fail by lateral-torsional buckling. The results showed that the prestressing strands did not restrain the beams from buckling out-of-plane or destabilize the beam like in the case of a beam-column. The beams buckled after flexural cracking had occurred and did so at a load much less than what elastic lateral-torsional buckling theory predicted. Initial imperfections were shown to decrease the inelastic lateral-torsional buckling load due to a rotated neutral axis, additional torsion on the cross-section and progressive rotation that led to a larger component of flexure about the weak-axis (P-delta effect).

A material and geometric nonlinear, incremental load analysis was performed on the six rectangular beams. The nonlinear analyses matched the experimental load versus lateral displacement and load versus rotation behavior, and the analysis predicted the experimental maximum load within an error of 2%.

The nonlinear analysis was extrapolated to several different initial imperfection conditions to parametrically study the effect of initial lateral displacement and initial rotation on the inelastic lateral-torsional buckling load. A simplified expression for lateral-torsional stability of beams with initial imperfections was developed based on an elastic stability expression (Goodier, 1941 and 1942). The data from the parametric study were used to develop reduction parameters for both initial sweep and initial rotation.

The first experiment with the PCI BT-54 was a study on the deformation of the girder due to solar radiation. Solar radiation on the top and side of the girder, wind speed, internal strain, air temperature, internal temperature and surface temperature were recorded to determine additional sweep or rotation in the girder due to non-uniform heating. The research showed that the initial sweep of the 101-ft. (30.8 m) PCI BT-54 girder increased up to 40% due to the effect of solar radiation on the girder, an additional sweep of 0.0515-in. (1.31 mm) per 10-ft. (3.05 m) of girder length. However, only 0.000212 radians of additional rotation was developed due to the non-uniform heating of the girder.

The PCI BT-54 was tested under midspan point load to examine its rollover behavior. For the stability experiment, full torsional restraint was not provided at the

supports. Instead, torsional restraint was only provided by the couple created by the bottom flange and the elastomeric bearing pads. The load versus lateral displacement and load versus rotation response corresponded well with the prediction from the nonlinear incremental analysis that included a bearing pad model. A rollover failure occurred well before an inelastic lateral-torsional buckling mode was anticipated. In fact, the girder never cracked during the testing. The nonlinear incremental analysis did not predict the rollover failure because of assumptions made in the elastomeric bearing pad model. Imperfect bearing conditions were not modeled and nonlinear bearing stiffness behavior at large rotations was most likely inaccurate. The rollover methodology proposed by Mast (1993) predicted the rollover limit state very well.

From the research, it was apparent that rollover is the controlling stability phenomenon for prestressed concrete bridge girders. The nonlinear lateral-torsional stability failure is unlikely because prestressed concrete bridge girders are designed to not crack under self-weight alone. Therefore, the inelastic lateral-torsional buckling simplified equation initial imperfection reduction parameters do not apply to bridge girders. Instead, the elastic lateral-torsional buckling predictions should be used. However, the elastic lateral-torsional buckling loads were found to be greater than the rollover limit for girders with no end support lateral bracing.

CHAPTER 1

INTRODUCTION

1.1 Introduction

The spans of precast prestressed concrete bridge girders have become longer to provide more economical and safer transportation structures. Increases in concrete strength, strand diameter and manufacturing processes have enabled lengthening of girders. As the spans have increased, so has the depth of the girders which in turn have increased the slenderness of the girders. Slenderness in a beam or girder would increase the likelihood that a stability failure would occur. Stability failures could pose a danger to construction personnel due to the sudden nature in which a stability failure would occur. Furthermore, stability failures of prestressed concrete girders during construction would cause a detrimental economic impact due to the costs associated with the failure of the girder, the ensuing construction delays, damage to construction equipment and potential closures to highways over which the bridge was being constructed.

The collapse of 150 ft. (45.7 m) long, 90-in. (2.3 m) deep, precast prestressed concrete bridge girders in Pennsylvania in the fall of 2004, depicted in Figures 1.1 and 1.2, resonated the need to understand the behavior of such girders, particularly with respect to their stability. Mr. Brian Thompson, Pennsylvania Assistant State Bridge Engineer, suspected that additional sweep (lateral deformations) could have occurred due to the sun heating one side of the girder and causing the girder to bow. Additional sweep in the girders would have increased the possibility of a stability failure because eccentricity of the gravity load would apply torsion to these girders.

Figure 1.1 - Stability failure of 90 in. (2.3 m) deep precast prestressed concrete girders on I-80 in Pennsylvania (Zureick, Kahn and Will, 2005)

Figure 1.2 - Stability failure of precast prestressed concrete girders on I-80 in Pennsylvania (Zureick, Kahn and Will, 2005)

More recently in the summer of 2007, during the construction of the Red Mountain Freeway near Power Road in Mesa, Arizona, nine girders collapsed, as shown in Figure 1.3. The Arizona Department of Transportation hired CTLGroup to investigate the collapse. The investigation by the CTLGroup (Oesterle et al., 2007) concluded that the collapse probably was due to lateral instability of one girder which caused a progressive collapse of the adjacent eight girders. Oesterle et al. (2007) believed several factors caused the instability including "bearing eccentricity, initial sweep, thermal sweep, creep sweep, and support slope in both the transverse and longitudinal directions."

Figure 1.3 – Stability failure of AASHTO Type V bridge girders in Arizona (Oesterle et al., 2007)

Investigating the effect of girder sweep and eccentricity is of utmost importance due to the potential for a decrease in lateral stability caused by the imperfections. There are several causes of accidental eccentricity in precast prestressed concrete girders such

as imperfections during fabrication, eccentricity of prestressing strands in the girder, cracking and permanent deformations from handling and transportation of the girder and lastly, the eccentricity caused by solar radiation heating the girder on one side, only. Additionally, bearing support conditions can also adversely affect the stability of bridge girders. Therefore, understanding the stability behavior of precast prestressed bridge girders including reasonable magnitudes of girder and support imperfections and their affect on stability behavior are paramount in ensuring safety during erection of such girders.

1.1.1 Problem Definition

Understanding the stability of precast prestressed bridge girders would require the consideration of two different stability phenomenons that could have been the cause of the collapse of the aforementioned bridge girders in Pennsylvania and Arizona. The first of the potential causes essentially would be a rollover failure of the girder. A rollover failure in this case would be where the girder as a whole tips over since there were no physical restraints to prevent this from occurring. When the girder was placed, the girder was expected to stay in place simply by using its self-weight. However, if the girder's self-weight was off-center at all, an overturning moment would have been created that would try to tip the girder over if it became larger than the resisting moment.

There could be several causes of overturning moment. The first possible cause would be the eccentricity effect from imperfections during fabrication, eccentricity of prestressing strands in the girder, cracking and permanent deformations from handling and transportation of the girder and the eccentricity caused by solar radiation

4

inconsistently heating the girder. If the girder had an initial out-of-straightness there would be an overturning moment created that would be a function of the self-weight of the girder and the initial lateral deformation of the girder which could be generalized as:

$$\int_0^L W_b(x) \cdot e_i(x) dx \qquad (1.1)$$

where:

$W_b(x)$ = girder self-weight as it varies along the girder length

$e_i(x)$ = eccentricity of girder center of gravity as it varies along the girder length

L = length of the girder

The effect of the eccentricity induced overturning moment in Equation 1.1 would be amplified by considering that the girder was not rigid. The initial imperfections in the girder included rotation; therefore, a component of the self-weight load of the girder would act about the weak-axis of the girder causing the girder to both deform and rotate more. The additional deformation and rotation would add to the overturning moment which in turn would cause the girder to deform and rotate more, and so on. Mathematically it would become an iterative process until the system converged to equilibrium, or becomes unstable.

Overturning moment could also be created due to the support conditions. The bearing pads on which the girders rest may not have provided a level surface. If the bearing pad had a lateral slope, the girder would have had an initial rotation at the ends of

the girder which would have caused an overturning moment. Furthermore, many bridges have used elastomeric bearing pads, including the Red Mountain Freeway Bridge in Arizona (Oesterle et al., 2007). Elastomeric bearing pads would have had the capacity to deform under load. As the overturning moment increased, more of the load would be transferred from one corner of the bottom of the girder into the bearing pad as illustrated in Figure 1.4. Due to the load concentration on one side of the bearing pad, the bearing pad would deform more on that side further increasing the slope of the bearing, and once again it would become an iterative process until equilibrium was met.
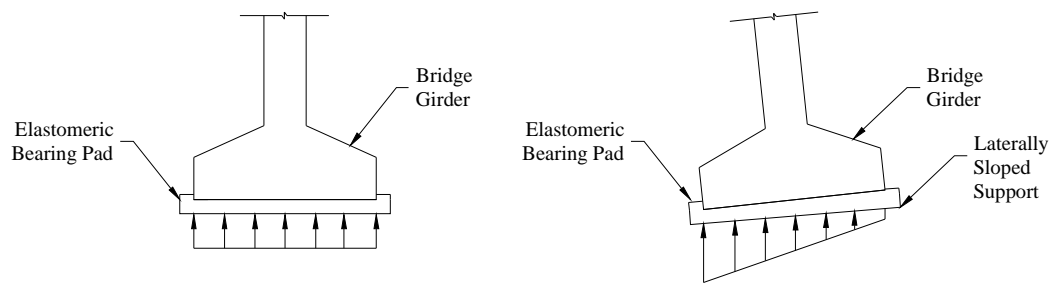
Figure 1.4 - Elastomeric bearing pad deformation and load condition for the perfect case and for the laterally sloped support case

The second possible stability phenomenon that could have caused the bridge girders to collapse in Pennsylvania was lateral-torsional buckling. Elastic lateral-torsional buckling was a topic that had been researched extensively for steel, timber and polymer composite beams due to the susceptibility to lateral-torsional buckling for typical beam cross-sections which used these materials. Most formulae on the subject could be traced back to the original development by Timoshenko (1905) and expanded by Goodier (1941, 1942) and reported by Timoshenko and Gere (1988); however, Chen and

Lui (1987) included the equations for many loading and support condition cases. The generalized case for a simply-supported elastic I-section subjected to strong-axis flexure was:

$$M_b = \frac{C_b \pi}{L} \sqrt{EI \cdot GJ \left[1 + \frac{\pi^2 E C_\omega}{L^2 GJ} \right]} \tag{1.2}$$

where:

M_b	=	buckling moment
C_b	=	moment gradient coefficient
E	=	elastic modulus
I	=	moment of inertia
G	=	shear modulus
J	=	torsion constant
C_w	=	warping constant

Additionally, effects of load height were discussed in Trahair (1993), and depending on the properties of the beam, the load height could significantly affect the critical load. The critical load was most affected in the case of shorter beams with a high modulus of elasticity, large warping constant and a low torsional stiffness.

Other cases that were important to consider included the simplified case of a thin rectangular beam in which the warping constant was zero; Equation 1.2 could thus be modified accordingly. Furthermore, Kirby and Nethercot (1979) gave one possible

approximate solution for the case where the in-plane deflection would have an effect on the critical load as:

$$M_b = \frac{C_b \pi}{L} \sqrt{\frac{EI_y \cdot GJ}{1 - \left(\dfrac{I_y}{I_x}\right)} \left[1 + \frac{\pi^2 EC_\omega}{L^2 GJ}\right]} \qquad (1.3)$$

where:

I_x =   strong-axis moment of inertia

I_y =   weak-axis moment of inertia

The use of Equations 1.2 and 1.3 for analyzing reinforced and prestressed concrete beams would result in extremely non-conservative results. In fact, an engineer would be hard-pressed to conceive of a reinforced or prestressed concrete cross-section that resembles anything that could be put to practical use where Equations 1.2 and 1.3 would result in a critical buckling load less than the flexural ultimate load of the cross-section. The reason for this is that the flanges of the girders and the relatively large web thicknesses create cross-section properties that are too large to cause stability concern. The possibility for a lateral-torsional buckling failure in a reinforced concrete or prestressed concrete girder lies in the fact that Equations 1.2 and 1.3 were for elastic cross-sections and would not compensate for the nonlinear behavior, including cracking, of reinforced or prestressed concrete beams.

Lateral-torsional buckling equations for a prestressed concrete beam would need to consider the nonlinear material properties of concrete when the compression zone of the concrete has been stressed significantly, or else the equations would be unconservative. Furthermore, during loading, the concrete in the tensile zone would crack and reduce the flexural and torsional rigidities. Prestressed concrete beams would involve additional complications to the analysis that differ from reinforced concrete beams. The addition of the steel prestressing strands would add a compressive stress to the cross-section as well as a bending stress component if the strands were eccentric. A prestressing force in the beam would pose additional questions about the behavior. Would the prestressing force act as an axial load like in a beam-column, would the fact that the strands are embedded in the concrete create a restraint to lateral deformation since the strands would want to resist being deflected out-of-plane, or would there be no effect and the behavior would be the same as reinforced concrete?

Initial imperfections and imperfections due to solar radiation were suspect during the collapse of the bridge girders in Pennsylvania and Arizona; therefore, the analytical model would need to represent the realistic imperfections of a bridge girder. In theory, the elastic buckling load for an imperfect beam would approach the same load as a perfect one; however, there would no bifurcation point in an imperfect beam. Increased lateral deformations would occur immediately upon loading, and substantial deformation would occur at a load less than that of the critical load. For an elastic beam with a constant end moment applied, Chen and Lui (1987) derived the equations for the lateral deflection and rotation given by Equations 1.4 and 1.5, respectively. The analysis was based on an initial lateral deflection and rotation given by Equations 1.6 and 1.7.

$$u = \left[\frac{1}{1 - (M_0/M_b)} \right] \delta_0 \ sin \frac{\pi z}{L} \qquad (1.4)$$

$$\beta = \left[\frac{1}{1 - (M_0/M_b)} \right] \theta_0 \ sin \frac{\pi z}{L} \qquad (1.5)$$

$$u_0 = \delta_0 \ sin \frac{\pi z}{L} \qquad (1.6)$$

$$\beta_0 = \theta_0 \ sin \frac{\pi z}{L} \qquad (1.7)$$

where:

u	=	lateral deflection
M_0	=	applied end moment
δ_0	=	initial lateral displacement at midspan
z	=	coordinate axis along centroidal axis of girder with origin at end
θ_0	=	initial rotation at midspan
u_0	=	initial lateral deflection
β_0	=	initial rotation

Equations 1.4 and 1.5 were for an elastic beam; however, the equations would need to be altered to consider the complexities of concrete. Furthermore, deformations in a reinforced or prestressed concrete beam would usually be associated with cracking of the beam which would reduce the stiffness and consequently reduce the critical buckling load as well. More discussion on the elastic behavior including initial imperfections was included in Bleich (1952) and Trahair et al (2001).

To accurately analyze a precast prestressed bridge girder with respect to lateral-torsional buckling, an analytical equation or method would need to consider the nonlinear behavior of concrete, the effect of prestressing force, and the effect of initial imperfections. Within the category of initial imperfections, fabrication error would already be limited by code, and, therefore, maximum imperfections could be predicted; however, the additional imperfections due to sloped bearings, creep sweep and solar radiation would need to be quantified so that they could be considered. Currently, these issues are not considered in the design of precast prestressed bridge girders.

The PCI Bridge Design Manual (2003) addresses the lateral stability of prestressed concrete bridge girders for two cases: (1) when the girder is hanging from a lifting device and (2) when the girder is resting on flexible supports (specifically referring to the case of the girder being transported). The PCI Bridge Design Manual (2003) provides an explicit procedure to determining the safety against instability for those two cases which were based on Mast (1989) with respect to a hanging girder and Mast (1993) with respect to a girder in transit. However, the PCI Bridge Design Manual (2003) does not provide methods or recommendations for prestressed girders in their erected position. There is an attempt to stress in the PCI Bridge Design Manual (2003) the danger of unbraced girders in their erected state when supported by elastomeric bearing pads due to the highly nonlinear behavior of the bearing pad, particularly when the bearing reaction leaves the confines of the bearing pad's kern.

There are several construction tolerances specified by the Precast Prestressed Concrete Institute. The PCI Bridge Design Manual (2003) specifies that the flatness of the support is limited to a 1/16 in. (1.6 mm) tolerance as shown in Figure 1.5 and a sweep

tolerance of 1/8 in. (3.2 mm) per 10 ft. (3 m) of girder length. Additionally, the PCI

Tolerance Manual for Precast Prestressed Concrete Construction (2000) limits the

centerline of the bottom of the girder to $\pm$ 1 in. (25.4 mm) relative to the centerline of the

elastomeric bearing pad as shown in Figure 1.6.
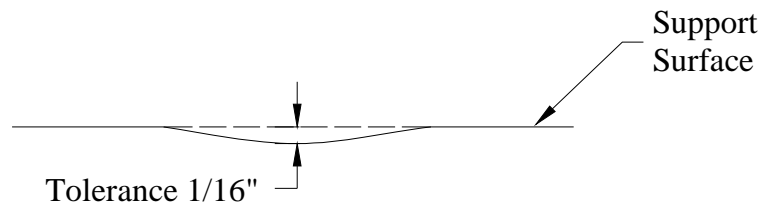
Figure 1.5 – Support flatness tolerance
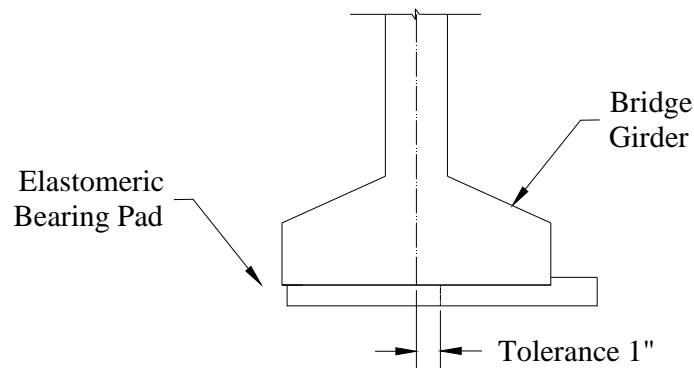
Figure 1.6 – Offset of girder and bearing pad centerline tolerance

The AASHTO LRFD Bridge Design Specifications (2007) and AASHTO LRFD

Bridge Construction Specifications (2004) do not limit construction tolerances in any

way as a direct result of stability considerations. The AASHTO LRFD Bridge

Construction Specifications (2004) stipulates in Section 8.13.6 that "the contractor shall

be responsible for the safety of precast members during all stages of construction." It is apparent that the governing design codes lack sufficient guidance on the subject of stability of precast prestressed bridge girders. Approaches from Mast (1993) were applied by Oesterle et al. (2007); however, it is unknown if that is accurate or even conservative for the case of a girder in its erected position. Furthermore, it is unknown if the girders that collapsed in Pennsylvania and Arizona were due to a rollover failure or a lateral-torsional buckling mechanism.

Rollover behavior as well as lateral-torsional behavior of precast prestressed bridge girders needs to be understood to ensure the safety of the placement of such girders. Furthermore, to fully understand the limits of the behavior, the flexural and torsional rigidities need to be accurately considered while also considering the maximum girder imperfections that can occur in practice, particularly with regards to the unknown sweep from solar radiation.

1.2 Scope

The research addressed several of the deficiencies in knowledge, as well as the lack of verification in current analytical techniques with respect to the lateral-torsional buckling of precast prestressed concrete bridge girders and the rollover of prestressed concrete bridge girders. This broad objective was split into several smaller objectives. The first objective was to quantify the magnitude of additional sweep that could occur due to solar radiation. The study on girder deformations due to solar radiation was not intended to be an extensive study, but instead, an investigation into the possibility of solar radiation causing non-negligible geometric imperfections. The second objective was to

13

perform a series of lateral-torsional buckling experiments on prestressed beams to determine the effect of the prestressing force on their stability. Additionally, a validation of the existing analytical techniques was performed and proved the need for a better analytical approach; therefore, both a calculation intensive analytical approach and a simplified equation were developed to predict the lateral-torsional buckling behavior of prestressed concrete flexural members. Lastly, the rollover behavior and the effect of the bearing pad on rollover were investigated by an experiment on a PCI BT-54 bridge girder. An emphasis was placed on the magnitudes of the initial imperfections and the effect the initial imperfections had on the stability of the girders.

All of the experimental work was performed on seven beam specimens. The first six specimens were rectangular prestressed concrete beams. The beams had a length of 32 ft. (9.75 m), a width of 4 in. (10.2 cm) and a height of 40 in. (102 cm). The seventh specimen was a 101 ft. (30.8 m) PCI BT-54 bridge girder. The BT-54 was prestressed with 40 – 0.6 in. diameter prestressing strands with each strand having a jacking force of 43,943 lbs. (195.47 kN). The details of the seven test specimens are described in Chapter 2.

The six rectangular test specimens were used in a lateral-torsional buckling experimental program. Two experiments were performed on the BT-54 test girder. The first experiment for the BT-54 involved obtaining temperature variations in the girder, thermal strains in the girder, solar radiation data, wind data, and for certain days due to experimental limitations, sweep and camber data. The non-destructive nature of the first experimental allowed for a stability experiment on the BT-54 as well. Details of the field BT-54 experimental study are presented in Chapter 3. Chapter 4 presents the

experimental setup for the seven stability experiments.   The results of the rectangular

beam experiments are presented in Chapter 5.

Chapter 5 also presents a comparison between the experimental results and the

analytical results utilizing the methodologies of previous researchers. Chapter 6 presents

the analytical developments to predict the lateral-torsional buckling behavior of

prestressed concrete flexural members. The first methodology predicted the load vs.

lateral displacement and load vs. rotation behavior; however, the rigorous and time

consuming nature of the methodology could possibly be unattractive to the practicing

engineering. Therefore, a simplified equation was developed that expedited the

analytical work and provided a prediction on the buckling load. Both analytical

procedures included the material characteristics of concrete and the effect of initial

imperfections. The stability results for the BT-54 girder and a comparison to analytical

procedures is presented in Chapter 7. Chapter 8 provides a commentary on the behavior

of prestressed concrete bridge girders with respect to lateral-torsional buckling and

rollover. Lastly, conclusions and recommendation from this research are presented in the

final chapter.

1.3 Background

1.3.1 Lateral-Torsional Buckling

<u>1.3.1.1 Reinforced Concrete Beams</u>

Classical theory had dealt with the behavior of linear elastic, isotropic materials;

however, reinforced concrete members needed solutions that incorporated the

complexities of concrete behavior. The elastic modulus could not be considered constant

because the stress-strain behavior would be nonlinear. Furthermore, after cracking, both the flexural and torsional rigidities of the member would be reduced.

Hansell and Winter (1959) approached the problem of lateral-torsional buckling of reinforced concrete beams by performing a set of experiments. Ten different beams were built with the same cross-section and longitudinal reinforcing and were loaded at quarter-points for five different spans. Each beam had the same dimensions; 13 in. (33 cm) deep, 2.5 in. (6.4 cm) wide and included one 0.75 in. (19 mm) diameter deformed bar centered 11.25 in. (28.6 cm) from the extreme compression fiber as shown in Figure 1.7. The additional details of the specimens are shown in Table 1.1.
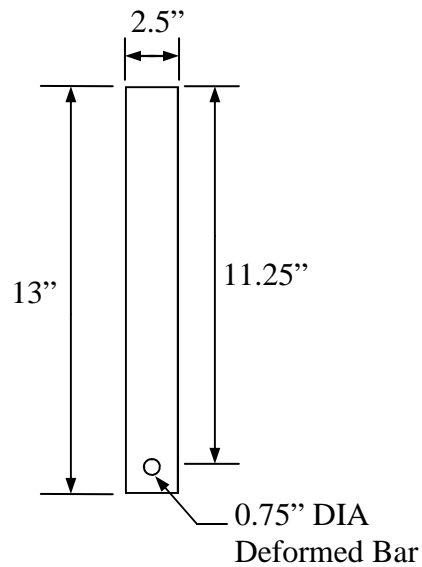
Figure 1.7 – Test beam geometry from Hansell and Winter (1959)

Table 1.1 - Test beam data from Hansell and Winter (1959)

Beam Mark	Span, ft. (m)	*L/b* Ratio	Stirrup Spacing, in. (cm)	Cylinder Strength, *fc'*, psi (MPa)
B6	6 (1.83)	28.8	5.5 (13.97)	4310 (29.72)
B9	9 (2.74)	43.2	5.5 (13.97)	4310 (29.72)
B12	12 (3.66)	57.6	7 (22.96)	4350 (29.99)
B15	15 (4.57)	72.0	7 (22.96)	4215 (29.06)
B18	18 (5.49)	86.4	7 (22.96)	4260 (29.37)

The test set-up was such that a 1.5 in. (38 mm) diameter ball attached to a roller assembly was used at the load points so that the beam was free to rotate and displace laterally to simulate gravity load. Additional testing was done (Hansell, 1959) to find that the maximum lateral restraining force provided by the loading apparatus was 0.1% of the vertical loads. The end conditions were simply supported with the additional use of vertical rollers so that the beams were restrained against torsion at the ends.

The results of the tests are shown in Table 1.2. Note that there was two of each beam type and were differentiated by a suffix of either 1 or 2. All ten of the beams failed in a flexural tension mode in good agreement with ultimate strength theory. The extreme slenderness of these test specimens not only did not buckle, but there was no reduction in capacity at all. Hansell and Winter (1959) believed that one potential influence on the results was the large web reinforcement ratio that probably contributed a significant amount of torsional restraint. Furthermore, Table 1.2 includes the amount of initial imperfections in each beam as well as the final observed lateral and vertical

17

displacements of the beams. Although not discussed significantly by Hansell and Winter (1959), the test specimens with larger initial imperfections correlated to larger final lateral displacements.

Table 1.2 - Test results from Hansell and Winter (1959)

Beam	B6	B9	B12	B15	B18	Suffix
L/b Ratio	28.8	43.2	57.6	72.0	86.4	1, 2
Observed Ultimate Moment, *Mtest*, kip-in. (kNm)	216 (24.4) 199 (22.5)	201 (22.7) 205 (23.2)	193 (21.8) 199 (22.5)	192 (21.7) 198 (22.4)	190 (21.5) 196 (21.1)	1 2
Calculated Ultimate Moment *Mcalc*, kip-in.	196.7 (22.2)	196.7 (22.27)	197 (22.26)	195.9 (22.13)	196.2 (22.17)	1,2
Mtest/Mcalc	1.10 1.01	1.02 1.04	0.98 1.01	0.98 1.01	0.97 1.00	1 2
Midspan Deflections at Yield Point, 0.001 in. (0.0254 mm)						
Vertical	192 188	330 330	460 495	825 1005	1015 1080	1 2
Lateral - Top	53 78	33 18	43 515	1260 97	72 500	1 2
Lateral - Bottom	66 82	56 25	14 620	1090 228	150 430	1 2
Initial Sweep, 0.01 in. (0.254 mm)	4 6	8 6	8 11	25 12	13 17	1 2

Although the experiments gave no results with respect to lateral-torsional buckling behavior, Hansell and Winter (1959) proposed an approximate buckling analysis for a reinforced concrete beam by taking the classical lateral-torsional buckling equation for an elastic rectangular cross-section with equal applied end moments that was given by:

$$M_b = \frac{\pi}{L}\sqrt{EI_y GJ} \tag{1.8}$$

and modifying it to give:

$$M_b = \frac{E_{hw}}{\sqrt{2(1+\nu)}} \times \frac{\pi}{L}\sqrt{I_y J} \tag{1.9}$$

where:

ν =   Poisson's ratio

E_{hw} =   modified modulus of elasticity from Hansell and Winter (1959)

Both cross-sectional properties, I_y and J, were to be calculated by the use of standard formulas except that the height of the section was to be taken as the depth of the compression block and reinforcement was to be neglected. The only way in which the longitudinal reinforcement was implicitly considered was by the effect it had on the depth of the neutral axis.

The reduced modulus was to be derived by using an established stress-strain relation for concrete such as the modification to Stüssi's flexural theory reported by

19

Hognestad (1955) to obtain the secant modulus at various points along the load history of the beam corresponding to the strain at the extreme compression fiber of the beam.

Hansell and Winter (1959) did not have any test data to confirm their method besides the fact that their method also predicted that their test specimens would not buckle. Furthermore, the approximations that were made with respect to the cross-section properties, although conservative, potentially neglected a significant amount of stiffness in the beams provided by other mechanisms such as the effect of the reinforcing steel and aggregate interlock, and, therefore, were overly conservative. A reduced modulus concept was a good method to represent the inelastic modulus of elasticity of the cross-section; however, the modulus at a specific load point was based on the extreme compression fiber and, therefore, did not accurately represent the elastic modulus at other locations in the depth of the cross-section or along the length, once again providing for conservative results.

Sant and Bletzacker (1961) also performed a set of tests on slender reinforced concrete beams. There were 11 beam specimens in total. Every beam was 20 ft. (6.1 m) long, 2.5 in. (63.5 mm) wide and the average concrete compressive strength was 5860 psi (40.4 MPa). Table 1.3 shows the results of the 11 tests.

Table 1.3 - Test results from Sant and Bletzacker (1961)

Beam Specimen	d/b Ratio	Test Moment kip-in. (kNm)	Theoretical Flexural Moment Capacity kip-in. (kNm)	M_{theory}/M_{test}	Failure Mode
B36-1	12.45	1620 (183)	3483.75 (393.6)	2.155	Instability
B36-2	12.45	1845 (208)	3483.75 (393.6)	1.890	Instability
B36-3	12.45	1350 (153)	3483.75 (393.6)	2.580	Instability
B30-1	10.20	2040 (230)	2250.8 (254.3)	1.105	Instability
B30-2	10.20	2160 (244)	2250.8 (254.3)	1.041	Instability
B30-3	10.20	1402 (158)	2250.8 (254.3)	1.600	Instability
B24-1	8.13	1260 (142)	1492.5 (168.6)	1.185	Instability
B24-2	8.13	1350 (153)	1492.5 (168.6)	1.105	Instability
B24-3	8.13	1440 (163)	1492.5 (168.6)	1.037	Instability
B12-1	3.78	300 (34)	330.0 (37.3)	-	Flexure
B12-2	3.78	210 (24)	330.0 (37.3)	-	Flexure

All of the beams failed by lateral buckling except for the two beams with the lowest d/b ratio. Sant and Bletzacker (1961) showed that it was possible to have reinforced concrete beams fail by lateral-torsional buckling. The reason Sant and Bletzacker's (1961) specimens were able to buckle while Hansell and Winter's (1959) specimens did not buckle was due to the differences in L/b and d/b ratios. In Sant and Bletzacker's (1961) tests, the L/b ratios all of the beams were 96 while the beams with the highest L/b ratio in Hansell and Winter's (1959) tests was 86.4, slightly less slender. Additionally, the transition between a stability failure and a flexural failure in Sant and Bletzacker's (1961) tests occurred between a d/b ratio of 8.13 and 3.78 which is consistent with the fact that all of the beams in Hansell and Winter's (1959) test had a d/b ratio of 5.2.

Sant and Bletzacker (1961) took the same approach as Hansell and Winter (1959) with respect to the analysis of the beams. The concrete not within the compression block

was neglected when the section properties were calculated. The difference in approach between the two was with respect to the modulus of elasticity. Sant and Bletzacker (1961) chose to use the reduced modulus given by Equation 3.3.

$$E_r = \frac{4 E_c E_{tan}}{\left(\sqrt{E_c} + \sqrt{E_{tan}}\right)^2} \qquad (1.10)$$

where:

E_c =   modulus of elasticity of concrete

E_{tan} =   tangent modulus of elasticity

E_r =   reduced modulus of elasticity

The analytical method used by Sant and Bletzacker (1961) was in fact a conservative approach. All of the specimens that buckled did so at a 4% to 116% higher load than predicted according to Sant and Bletzacker (1961). The variability of the experimental results was somewhat suspect though, particularly with respect to the B30 series and B36 series. The variability could have been attributed to the inherent variability of concrete, varying amounts of restraint provided by the test setup on a test-by-test basis, or a combination of reasons.

Massey (1967) performed small-scale experiments as well. The specimens used were 0.5 in. (12.7 mm) wide, 3 in. (76.2 mm) deep and no coarse aggregate was used in the "concrete" mix as shown in Figure 1.8. The results from the experiments are shown in Table 1.4.
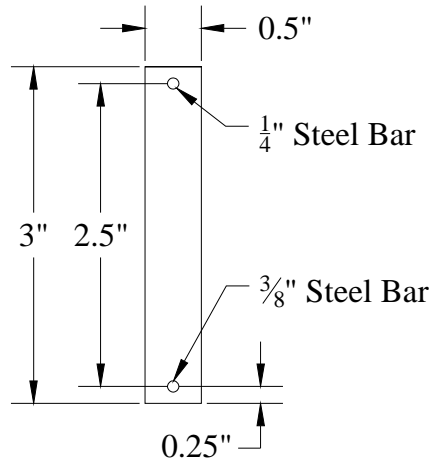
Figure 1.8 – Dimensions and reinforcement for specimens from Massey (1967)

Table 1.4 - Test results from Massey (1967)

Specimen	Reinforcement Pattern	Concrete Strength f_c' (psi)	Span (in.)	M_{fail} (lb-in.)	Failure Mode
1	Single	4500	48	5760	Buckling
2	Single	3750	48	5260	Buckling
3	Single	2740	36	5060	Buckling
4	Single	3400	24	5260	Flexure
5	Single	3620	60	4860	Buckling
6	Single	4430	72	4460	Buckling
7	Double	3340	48	7060	Buckling
8	Double	3520	48	6860	Buckling
9	Double	3140	36	7320	Buckling
10	Double	2680	24	7460	Buckling
11	Double	2950	72	5360	Buckling
12	Double	3800	72	5460	Buckling
13	Double	3740	60	5460	Buckling

The analytical portion of Massey's (1967) work expanded on the previous researchers' work. The following equation was derived to approximately solve the differential equation which considered warping of the section:

$$M_b = \frac{\pi}{L}\sqrt{BC}\sqrt{1 + \frac{4\pi^2 C_\omega}{CL^2}}$$ (1.11)

where:

B   =   weak-axis flexural stiffness

C   =   torsional stiffness

The lateral flexural rigidity proposed by Massey (1967) was similar to previous researchers except that Massey (1967) used the secant modulus of elasticity and included the effect of longitudinal steel as shown by:

$$B = \frac{cb^3}{12}E_{sec} + E_s \sum I_{sy}$$ (1.12)

where:

c   =   depth of neutral axis

b   =   breadth of cross-section

E_{sec} =   secant modulus of elasticity

E_s =   steel modulus of elasticity

I_{sy} =   moment of inertia of individual longitudinal steel reinforcing bar

Massey (1967) suggested that the longitudinal steel would have an effect on the torsional rigidity and that there was experimental evidence to suggest that the torsional rigidity should be based on the gross concrete section. Furthermore, Massey (1967) stated that the torsional rigidity would be reduced when major-axis bending was increased, and, therefore, the shear modulus should be modified as (Batdorf, 1949):

$$G_c' = G_c E_{sec}/E_c \qquad (1.13)$$

where:

G_c =   concrete shear modulus

G_c' =   modified concrete shear modulus

Based on the thin-membrane analogy (Plunkett, 1965), Massey (1967) considered the torsional rigidity to be:

$$C = \beta_T\, b^3 d_1 G_c' + \tfrac{1}{3}\left(G_s - G_c'\right)\sum b_s^{\,3} d_b \qquad (1.14)$$

where:

β_T =   parameter based on ratio d/b (Timoshenko and Goodier, 1951)

d_1 =   depth of area enclosed by steel reinforcing ties

b_s =   lateral distance between longitudinal steel reinforcing bars

d_b =   diameter of steel reinforcing bar

Furthermore, Massey (1967) added the stipulation based on Cowan (1953) that vertical ties would increase the torsional rigidity by:

$$C_s = \frac{\gamma b_1{}^2 d_1 A_t E_s}{2\sqrt{2p}} \qquad (1.15)$$

where:

C_s =   torsional stiffness from steel reinforcing bar

b_1 =   breadth of area enclosed by steel reinforcing ties

A_t =   area of individual steel reinforcing bar in reinforcing tie

p =   pitch of steel reinforcing ties

Massey (1967) also considered warping rigidity with the analysis, and it was suggested that neglecting the warping rigidity was accurate for singly-reinforced beams but not for doubly reinforced beams. The derivation arrived at the following equation:

$$C_\omega = E_s d'^2 \frac{I_1 I_2}{I_1 + I_2} \qquad (1.16)$$

where:

d' =   distance between top and bottom longitudinal reinforcing steel

I_1 =   moment of inertia of top longitudinal reinforcing steel

I_2 =   moment of inertia of bottom longitudinal reinforcing steel

More recently Revathi and Menon (2006) proposed their equations for the flexural and torsional rigidities which were based on previous research and experiments which they performed. Revathi and Menon (2006) considered the flexural rigidity by

modifying an equation originally proposed by Branson (Pillai and Menon, 2002) to

calculate flexural deflection in a reinforced concrete beam. Revathi and Menon's (2006)

equation once again neglected the concrete not in the compressed region. The steel was

thought to contribute to the rigidity but only in the case that the beam in question was

over-reinforced. The reason for this consideration was that in under-reinforced beams, it

was suspected the steel was close to yield, and, therefore, incapable of providing any

rigidity. Furthermore, Revathi and Menon (2006) considered the compression

reinforcement ineffective for flexural rigidity thus leaving the lateral flexural rigidity as:

$$B = E_c \left\{ \left[\frac{M_R}{0.8M_u} \right]^3 \left(\frac{b^3 h}{12} \right) + \left[1 - \left(\frac{M_R}{0.8M_u} \right)^3 \right] \left[\frac{b^3 c_u}{12} + \psi \left(\frac{E_s}{E_c} \sum I_{sy} \right) \right] \right\} \qquad (1.17)$$

where:

M_R = cracking moment of cross-section

M_u = ultimate flexural moment capacity of cross-section

h = height of cross-section

c_u = depth of neutral axis at ultimate load

ψ = 0 for $c_u \leq c_b$ (under-reinforced beam);

1 for $c_u > c_b$ (over-reinforced beam)

With respect to the torsional rigidity, Revathi and Menon (2006) used Tavio and Teng's (2004) torsional rigidity equation which considers the concrete cracking as well as the affect of longitudinal reinforcing and shear stirrups. The equation was as follows:

$$C = \frac{4\mu\, E_s\, A_0^2\, A_g}{p_0^2 \left(\dfrac{1}{\rho_l} + \dfrac{1}{\rho_t} \right)}$$
(1.18)

where:

μ =   rigidity multiplier (1.2 for under-reinforced and 0.8 for over-reinforced)

A_0 =   area enclosed by centerline of longitudinal reinforcing steel

A_g =   gross area of concrete

p_0 =   perimeter of centerline of longitudinal reinforcing steel

ρ_l =   longitudinal reinforcing steel reinforcement ratio

ρ_t =   transverse reinforcing steel reinforcement ratio

Revathi and Menon (2006) performed experiments on seven beam specimens in an attempt to validate their rigidity equations. The specifics of the beams tested shown in Table 1.5 and the failure loads of said beams are shown in Table 1.6. A comparative study that was included in Revathi and Menon (2006) is also included in Table 1.6. Revathi and Menon (2006) took the comparison one step further by comparing their

proposed formulation to the test beams used in Sant and Bletzacker (1961) and Massey

(1967). These comparisons have been included in Tables 1.7 and 1.8.

Table 1.5 - Test beam data from Revathi and Menon (2006)

Beam Label	Dimensions $b \times h \times L$, in. (mm)	L/b	d/b	2L 6 mm Stirrup Spacing, in. (mm)	Max Lateral Imperfection, in. (mm)
B1a	3.93 x 17.71 x 196.84 (100 x 450 x 5000)	50	4.0	7.87 (200)	0.47 (12)
B1b	3.93 x 21.65 x 196.84 (100 x 550 x 5000)	50	5.0	5.90 (150)	0.47 (12)
B1c	3.93 x 25.59 x 196.84 (100 x 650 x 5000)	50	6.0	3.93 (100)	0.31 (8)
B2a	3.93 x 17.71 x 236.21 (100 x 450 x 6000)	60	4.0	9.84 (250)	0.39 (10)
B2b	3.93 x 21.65 x 236.21 (100 x 550 x 6000)	60	5.0	9.84 (250)	0.51 (13)
B3a	3.14 x 11.81 x 236.21 (80 x 300 x 6000)	75	3.1	7.87 (200)	0.43 (11)
B3b	3.14 x 15.74 x 236.21 (80 x 400 x 6000)	75	4.3	9.84 (250)	0.35 (9)

The various analytical methods proposed to determine critical buckling loads for

reinforced concrete beams, were similar except for the way in which the rigidity

properties were calculated. A summary of the proposed expressions for the rigidity

properties from different researchers is included in Table 1.9.

Table 1.6 – Experimental results from Revathi and Menon (2006) with comparative study for under-reinforced beams

Beam Label	Flexural Capacity, kips (kN)	Failure Load, kips (kN)	Failure Mode	$Ptest/Pu$	Calculated Buckling Loads, kips (kN)			
					Hansell & Winter (1959)	Sant & Bletzacker (1961)	Massey (1967)	Revathi & Menon (2006)
B1a	22.86 (101.7)	20.88 (92.92)	Buckling	0.909	38.03 (169.2)	118.36 (526.5)	80.36 (357.5)	20.29 (90.27)
B1b	32.19 (143.2)	27.11 (120.6)	Buckling	0.834	49.57 (220.5)	145.02 (645.1)	95.92 (426.7)	26.61 (118.4)
B1c	50.22 (223.4)	39.22 (174.5)	Buckling	0.781	59.03 (262.6)	172.99 (769.5)	112.58 (500.8)	38.66 (172.0)
B2a	19.48 (86.68)	15.07 (67.04)	Buckling	0.765	38.17 (169.8)	114.31 (508.5)	78.81 (350.6)	13.87 (61.7)
B2b	27.62 (122.89)	19.31 (85.90)	Buckling	0.693	47.95 (213.3)	141.22 (628.2)	93.63 (416.5)	17.42 (77.5)
B3a	6.29 (27.89)	5.58 (24.85)	Buckling	0.837	11.21 (49.88)	37.88 (168.5)	29.69 (132.1)	4.87 (21.7)
B3b	12.96 (57.67)	8.17 (36.37)	Buckling	0.647	18.14 (80.71)	50.53 (224.8)	38.73 (172.3)	7.22 (32.15)
Percentage Error (Range)					50 to 153	340 to 658	186 to 431	1.4 to 12.6

Table 1.7 – Comparison of results for Sant and Bletzacker's (1961) over- reinforced test beams (Revathi and Menon, 2006)

Beam ID	b, in. (mm)	h, in. (mm)	L, in. (mm)	A_s, in.^{2} (mm^2)	Test M_b, kip-in (kNm)	Calculated M_b, kip-in (kNm)	
						Sant & Bletzacker (1961)	Revathi & Menon (2006)
B24	2.5 (63.5)	24 (610)	240 (6096)	1.9 (1264)	1359 (152.5)	976 (110.4)	1435 (162.2)
B30	2.5 (63.5)	30 (762)	240 (6096)	2.4 (1584)	1868 (211.1)	1161 (131.3)	1987 (224.6)
B36	2.5 (63.5)	36 (915)	240 (6096)	2.9 (1931)	1604 (181.3)	1327 (150.0)	1678 (189.7)
Percentage Error (Range)						17 to 27	4.6 to 6.3

Table 1.8 – Comparison of results for Massey's (1967) over-reinforced test beams
(Revathi and Menon, 2006)

Beam ID	b, in. (mm)	h, in. (mm)	L, in. (mm)	A_s, in.^{2} (mm^2)	A_v, in.^{2} (mm^2)	Test Mb, kip-in (kNm)	Calculated M_b, kip-in (kNm)	
							Massey (1967)	Revathi & Menon (2006)
B1	0.5 (12.5)	3.0 (75)	48 (1219)	0.1 (69.0)	-	6.03 (0.682)	6.03 (0.682)	5.69 (0.643)
B2	0.5 (12.5)	3.0 (75)	48 (1219)	0.1 (69.0)	-	5.07 (0.573)	5.58 (0.631)	5.30 (0.599)
B5	0.5 (12.5)	3.0 (75)	60 (1524)	0.1 (69.0)	-	4.68 (0.529)	5.03 (0.569)	4.37 (0.491)
B6	0.5 (12.5)	3.0 (75)	72 (1828)	0.1 (69.0)	-	4.30 (0.486)	4.71 (0.533)	3.83 (0.433)
B7	0.5 (12.5)	3.0 (75)	48 (1219)	0.1 (69.0)	0.05 (30.6)	6.80 (0.769)	7.47 (0.845)	6.14 (0.694)
B8	0.5 (12.5)	3.0 (75)	48 (1219)	0.1 (69.0)	0.05 (30.6)	6.61 (0.747)	7.02 (0.794)	6.03 (0.682)
B9	0.5 (12.5)	3.0 (75)	36 (914)	0.1 (69.0)	0.05 (30.6)	7.05 (0.797)	8.07 (0.913)	7.05 (0.797)
B10	0.5 (12.5)	3.0 (75)	24 (609)	0.1 (69.0)	0.05 (30.6)	7.18 (0.812)	8.36 (0.945)	7.72 (0.873)
B11	0.5 (12.5)	3.0 (75)	72 (1828)	0.1 (69.0)	0.05 (30.6)	5.16 (0.584)	6.24 (0.706)	4.72 (0.534)
B12	0.5 (12.5)	3.0 (75)	72 (1828)	0.1 (69.0)	0.05 (30.6)	5.26 (0.595)	6.17 (0.698)	4.75 (0.537)
B13	0.5 (12.5)	3.0 (75)	60 (1524)	0.1 (69.0)	0.05 (30.6)	5.26 (0.595)	5.90 (0.667)	5.00 (0.565)
Percentage Error (Range)							6.2 to 20	2.5 to 10

Table 1.9 – Summary of flexural and torsional rigidity expressions

Author	Flexural Rigidity $B = (EI)_{eff}$	Torsional Rigidity $C = (GJ)_{eff}$
Hansell & Winter (1959)	$B = E_{sec}\left(\dfrac{b^3 c}{12}\right)$	$C = \left(\dfrac{E_{sec}}{2(1+\nu_c)}\right)\left(\dfrac{b^3 c}{3}\left(1 - 0.35\dfrac{b}{d}\right)^2\right)$
Sant & Bletzacker (1961)	$B = E_r\left(\dfrac{b^3 d}{12}\right)$ $E_r = \dfrac{4 E_c E_{tan}}{\left(\sqrt{E_c} + \sqrt{E_{tan}}\right)^2}$ $E_{tan} = \dfrac{1}{2} E_c$	$C = \left(\dfrac{E_r}{2(1+\nu_c)}\right)\left(\dfrac{b^3 d}{3}\right)$
Massey (1967)	$B = \dfrac{b^3 c}{12} E_{sec} + E_s \sum I_{sy}$	$C = \beta b^3 d_1 G_c' + \tfrac{1}{3}(G_s - G_c')\sum b_s^3 d_s$ $+\dfrac{\gamma b_1^2 d_1 A_t E_s}{2\sqrt{2p}}$ $G_c' = G_c E_{sec}/E_c$ $G_c = \left(\dfrac{E_c}{2(1+\nu_c)}\right); \; G_s = \left(\dfrac{E_s}{2(1+\nu_s)}\right)$ $C_\omega = E_s h^2 \dfrac{I_1 I_2}{I_1 + I_2}$
Revathi & Menon (2006)	$B = E_c\left\{\left[\dfrac{M_R}{0.8M_u}\right]^3\left(\dfrac{b^3 h}{12}\right) + \left[1 - \left(\dfrac{M_R}{0.8M_u}\right)^3\right]\left[\dfrac{b^3 c_u}{12} + \psi\left(\dfrac{E_s}{E_c}\sum I_{sy}\right)\right]\right\}$	$C = \dfrac{4\mu E_s A_0^2 A_c}{p_0^2\left(\dfrac{1}{\rho_l} + \dfrac{1}{\rho_t}\right)}$

32

1.3.1.2 Prestressed Concrete

For prestressed concrete flexural members, the same complexities as reinforced concrete members needed to be considered. Furthermore, the behavior of the member with respect to the prestressing axial load needed to be considered. Several questions have been raised about the effect of the prestressing force. Would the prestressing cause a lower critical load like in the case of a steel beam-column or will the strands actually increase the critical load due to a restraint to lateral deformation from the strands? Would the prestressing force have any effect on the flexural and torsional rigidities?

Several authors such as Magnel (1950), Billig (1953), and Leonhardt (1955) had come to the conclusion that a prestressed concrete beam where the strands were bonded to the concrete cannot buckle. Billig (1953) stated that the prestressing force would only lead to a stability concern if the strands were unbonded over long distances. The reasoning behind not needing to perform stability calculations was due to the member being in equilibrium from the lateral reaction of the strand. Both Billig (1953) and Leondhardt (1955) cite Magnel (1944), in which Magnel's (1950) book on prestressed concrete incorporated the results published in the researcher's 1944 journal article (Magnel, 1944). Magnel (1950) used an example to analytically prove his theory. Magnel (1950) considered a beam with a prestressing tendon running through a duct sufficiently larger than the tendon where the tendon was rigidly attached only at the center by way of a cross-plate as depicted in Figure 1.9.
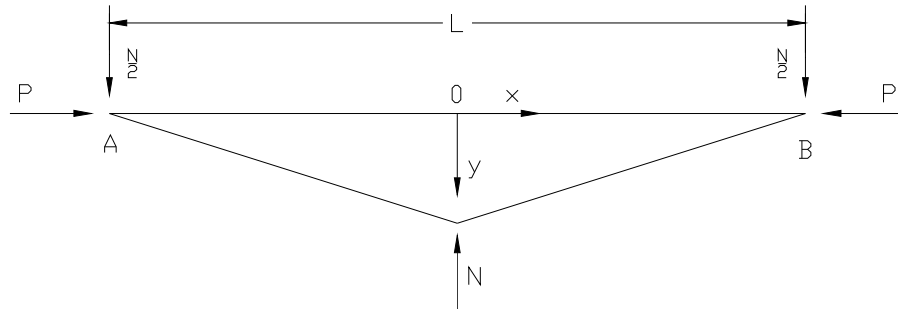
Figure 1.9 - System forces by Magnel (1950)

From equilibrium in Figure 1.9, the transverse load N was found to be $\dfrac{4\,y_0}{L}P$.

The second-order differential equation was then determined to be:

$$EI\frac{d^2y}{dx^2} = -Py + \frac{N}{2}\left(\frac{L}{2} - x\right) \tag{1.19}$$

where:

P   =   prestressing force

y   =   coordinate axis perpendicular to centroidal axis of girder (lateral)

N   =   lateral restoring force

Solving the differential equation by using the boundary conditions $y' = 0$ at $x = 0$ and $y = 0$ at $x = L/2$ gave the critical buckling load as:

$$P_b = \frac{4EI\pi^2}{L^2} \tag{1.20}$$

34

The critical buckling load was four times the Euler buckling load. Additional calculations would show that for n number of contact points between the tendon and the concrete would give n^2 times the Euler buckling load for the critical load. Therefore Magnel (1950) claimed that it was impossible to buckle a prestressed member if the tendon was continuously in contact with the concrete.

Tests were done by Magnel (1950) to try to prove these theories. The first of the relevant tests was performed on two concrete members that were 9.84 ft. (3 m) long with cross-sectional dimensions of 2 in. (5 cm) by 4 in. (10 cm) including a 5/8 in. (16 mm) longitudinal hole through the member. The compressive strength of the concrete was found to be 6000 psi (422 kg/cm^2) at the time when the prestressed members were tested. The first of the two members was tested with no prestressing wires and buckled at a load of 10,600 lbs. (4850 kg). The achieved buckling load was very close to the theoretical Euler buckling load for the member. The second specimen was prestressed with four 0.2 in. (5 mm) wires and loaded to 19,000 lbs. (8600 kg) with no signs of instability or failure of the concrete at that load.

The second relevant test was performed on a concrete member with a length of 20 ft. (6.10 m) with a cross-section that was 4 in. (10 cm) by 4 in. (10 cm). A 1.5 in. (4 cm) longitudinal hole was provided for a cable constructed of 16 - 0.2 in. (5 mm) wires. The compressive strength of the concrete at the time of the tests was found to be 3840 psi (270 kg/cm^2). These dimensions and material properties would give a buckling load of 14,100 lbs. (6300 kg) according to the Belgium regulations to which Magnel (1950) referred. The prestressing wires were stressed two at a time until the load was 49,400 lbs. (22 metric tons). This load would produce a stress in the concrete of 3740 psi (262

35

kg/cm^2). No sign of instability or of concrete crushing was initially noticeable but after

five minutes, the concrete failed in compression. The prestressed member had a

slenderness ratio of 185 but had the failure load that would normally be representative of

a member with a slenderness ratio of 14. Magnel (1950) believed that these test results

confirmed the theory that a member with prestressing tendons continuously in contact

with the concrete would not buckle.

Molke (1956) discussed a specific case study of a high school auditorium in

Springfield, Missouri that was framed with 146 ft. (44.5 m) prestressed roof girders. The

prestressed roof girders needed special investigation of their stability while being lifted

and placed before there was bracing from the roof slabs. In literature, it was well

established that with straight or curved concrete columns, there was no concern with

respect to stability failure as long as the prestressing strands were located at the centroid

of the section according to Molke (1956). Any bending moment created by the

prestressing force in the strands would then be countered by an equal and opposite

restoring force. Molke (1956) believed this had often been misconstrued to mean there

was never any stability concern in prestressed concrete members. Any externally applied

loads on the member could produce the same type of buckling failures as considered if

the member had not been prestressed. Furthermore, the buckling load could actually be

considered to be less than typical because the prestressing force would reduce the elastic

modulus of the concrete. The girders in question for the auditorium roof had sufficient

factor of safety when utilizing traditional formulas for lateral buckling of beams. Molke

(1956) believed that proof of a minimum factor of safety for buckling in concrete

structures should be calculated based on elastic theory and should be a code requirement.

The concept that Molke (1956) discussed in which the effect of the prestessing in the strands would not cause instability, but externally applied loads could potentially cause a buckling issue was repeated by Muller (1962). Muller (1962) stated that stability has become a concern due to the long spans of the precast beams and referred to handling and placing as the critical conditions for stability failure of the precast beams. The mechanics provided by Muller (1962) were obtained from LeBelle (1959). Essentially, the derivations by LeBelle (1959) included the loading not being at the shear center, the cross section not being thin-walled and rectangular, and the case of unsymmetrical flanges. These derivations were the same as what would be found in classical theory. Lebelle (1959) developed in-depth derivations for many different cases but no consideration was given to the prestressing force, changes in modulus of elasticity or the cracking of the concrete.

Additional research by Stratford, Burgoyne and Taylor (1999) and Stratford and Burgoyne (1999) used classical stability theory and assumed no inelastic behavior or cracking of the concrete. The cases considered by Stratford, Burgoyne and Taylor (1999) and Stratford and Burgoyne (1999) were beams on simple supports with torsional restraint at the ends and restrained rotation about the weak-axis, and beams on simple supports with torsional restraint at the ends and free rotation about the weak-axis. Furthermore, Stratford, Burgoyne and Taylor (1999) and Stratford and Burgoyne (1999) considered toppling of hanging girders and was expanded on by Stratford and Burgoyne (2000) to include a more detailed consideration of toppling of hanging girders. Stratford, Burgoyne and Taylor (1999) refer to a future paper with respect rollover (Burgoyne and Stratford, 2001) which is discussed in Section 1.3.2 on rollover stability. Muller (1962)

also considered toppling of a hanging girder as well as expanding on the classical theory presented in LeBelle (1959) for the case of elastic torsional restraint at the ends. An elastic torsional restraint was representative of the case of a girder in transport or on supports. The torsional stiffness was that provided by the truck trailer or elastomeric bearing pad.

An energy of deformations approach was used by Saber (1998) to derive a specific classical solution for stability of prestressed girders. Saber (1998) did, however, include the prestressing force, but it was done so by treating the prestressing force as an axial load at the end of the girder, or essentially treating the member as a beam-column. The girder was loaded by a prestressing force, P, which had an eccentricity, e, a uniform self-weight of the girder, W_b, and a uniform load from the deck, W_d. The theory of stationary potential energy was used to find the governing differential equations. The shear center was used as the location of the center of rotation. Some of the assumptions made during the analysis included that the plane cross-sections warp but their geometric shape did not change during buckling, the concrete was not cracked and the loads remained parallel with their initial orientations.

For example, Figure 1.10 shows a plot of the maximum effective prestressing force versus the unbraced length for an AASHTO Type III girder with various concrete compressive strengths and strand eccentricities. The deck weight was based on a deck thickness of 8 in. (20 cm) and a girder spacing of 11 ft. (3.35 m) to envelope all deck cases. Varying the deck dimensions and, therefore, the magnitude of the uniform deck load, did not significantly change the results. It appeared the reasoning for the insignificant effect of the deck weight was that the instability failure was controlled

38

mainly by the prestressing force in the member since it was large with respect to the deck weight. From this plot, it is also apparent that the eccentricity of the strands has little effect on the results, especially as the spans become large.
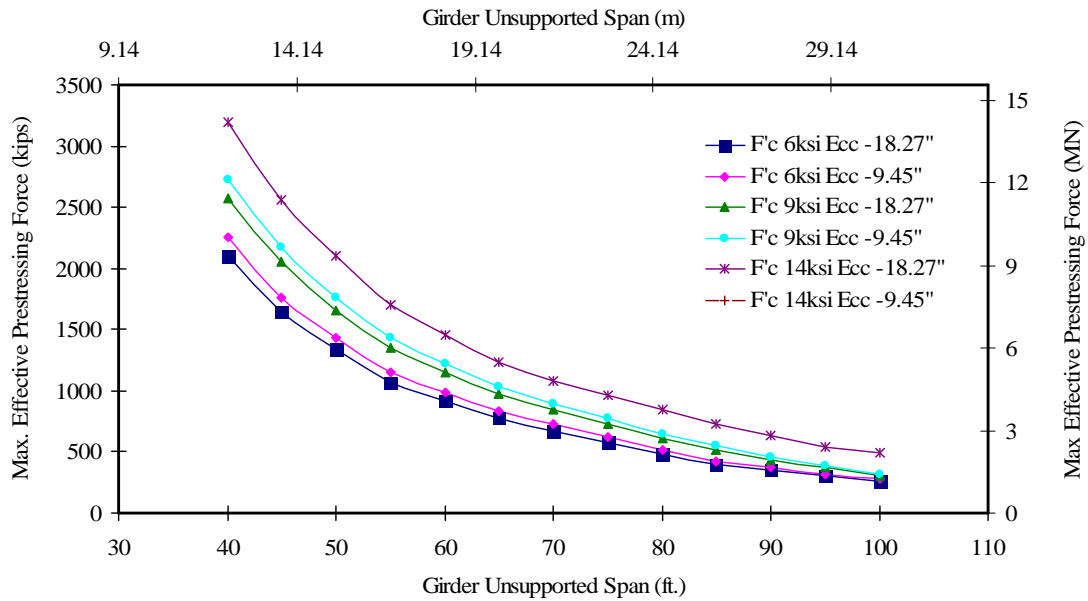
Figure 1.11 - Prestressing force for girder lateral stability for AASHTO Type III from Saber (1998)

It was evident to the author that the results of this analysis by Saber (1998) were not correct. For instance, the fabrication drawings for a Georgia Department of Transportation bridge, specifically Ramp 7 (NB C-D) over I-75 NB in Bibb County, Georgia, called for AASHTO Type III girders on the third span of the bridge. The length of these girders was specified to be 75 ft. 1¼ in. (22.9 m), the compressive strength of the concrete at prestressing strand release was specified as 5000 psi (352 kg/cm^2) and 5500 psi (387 kg/cm^2) at 28 days. Thirty prestressing stressing strands stressed at 33,818 lbs. (15,340 kg) each were used to prestress the girder which gives a total prestressing force

of 1,014,540 lbs. (460,195 kg). From looking at Figure 1.10, the analysis results
concluded that the girder would buckle after the strands were released as the deck load
had little effect, and, therefore, the maximum length of the girder should be less than 59
ft. (18 m). There were several instances of bridge girders of all types being fabricated,
but according to the analysis results reported in Saber (1998), the girders should have
buckled. Therefore, the girders would not behave ideally as an isotropic beam-column as
the analysis assumes.

Malangone (1977) used another mechanics approach to solve the problem but
attempted to include the effect of the prestressing force. The effect of the prestressing
force was included by utilizing the work done by the second order forces in finding
equilibrium of the system which gives an effective torsional rigidity that was dependent
on the prestressing force and location. The variation of the work was still equal to zero
such that:

$$\delta\left(L_2^* + W\right) = 0 \tag{1.21}$$

where:

      L_2*   =   second-order work of the system

      W   =   work of elastic system

The L_2^* term was the second order work of the system and was found as follows:

$$L_2^* = \int_0^L \int_A \sigma_z \varepsilon_{zz}^{(2)} dA dz + \int_0^L P \varepsilon_{zz}^{(2)} E_p dz \tag{1.22}$$

where:

σ_z =   longitudinal stress

$\varepsilon_{zz}^{(2)}$ =   second-order strain

After substituting the appropriate values for the terms in Equation 1.22 and plugging the second order work term into the equilibrium equation, the governing differential equation was found to be:

$$C_I \beta^{IV} - C\beta^{II} + P\left(\frac{I_x + I_y}{A_g} + e_x\beta_x + e_y\beta_y - e_x^2 - e_y^2\right)\beta^{II} = 0 \qquad (1.23)$$

where:

C_I =   warping stiffness (EC_w)

e_x =   individual strand eccentricity from x-axis

e_y =   individual strand eccentricity from y-axis

β_x =   section property $\dfrac{1}{I_y}\left(\int_A x^3 dA + \int_A xy^2 dA\right)$

β_y =   section property $\dfrac{1}{I_x}\left(\int_A y^3 dA + \int_A x^2 y dA\right)$

An effective torsional rigidity, C^*, could be found by subtracting the prestressing force stiffness term from the standard torsional rigidity of the section such that:

41

$$C_P = P\left(\frac{I_x + I_y}{A} + e_x\beta_x + e_y\beta_y - e_x^2 - e_y^2\right) \qquad (1.24)$$

$$C^* = C - C_P \qquad (1.25)$$

which gave the governing differential equation as:

$$C_1\varphi^{IV} - C^*\varphi^{II} = 0 \qquad (1.26)$$

where:

C_p = prestressing force torsional stiffness effect

C^* = effective torsional stiffness

Note that for the case of several prestressing strands in the section, C_P became:

$$C_P = P\left[\frac{I_x + I_y}{A_g} + e_x\beta_x + e_y\beta_y - \frac{1}{N}\sum_{i=1}^{n} P_i\left(e_{xi}^2 + e_{yi}^2\right)\right] \qquad (1.27)$$

From Equation 1.26, several solutions could be found for different cases and boundary conditions. The critical uniform transverse load for the case of perfect torsional restraint at each end was found to be:

$$w_b = \frac{28.911}{L^3}\sqrt{EI_y C^*}\sqrt{1 + \frac{\pi^2}{L^2}\frac{C_1}{C^*}} \qquad (1.28)$$

42

The results were essentially the same as classical theory for a uniformly loaded beam considering warping except that the torsional rigidity term was replaced by the effective torsional rigidity taking into account the magnitude and location of the prestressing force. Some examples were provided in Malangone (1977) which displayed the relatively small effect of the effective torsional rigidity. The first example gave a result of the critical uniform load to be 1268.0 lbs/ft. (18.87 kg/cm) while the results if the standard torsional rigidity was used gave 1247.2 lbs/ft. (18.56 kg/cm), a difference of 1.6%. Notice that the effective torsional rigidity actually increased the critical buckling load. The torsional rigidity could be increased or decreased depending on the magnitude of the prestressing force, the eccentricity and the section properties of the cross section. Generally, the effect was within a couple percent and would not change the results extensively. The minimal effect of consider the second-order work is why the effect of second-order behavior is neglected in most lateral-torsional buckling analyses (Trahair and Teh, 2000).

Analysis and experimental results were completed for post-tensioned concrete struts by Godden (1960) which was the basis for Wilby (1963). Godden (1960) referred to Billig (1952) and Magnel (1950) stating that a prestressed member would not buckle if the tendons were in contact with the concrete and that stability calculations should be performed based on a reinforced concrete column analysis. Godden (1960) also expressed the opinion that further research should be done considering flexural torsional buckling of slender prestressed beams since the tests performed only considered axially loaded members. Godden (1960) was unsure whether a prestressed strut would buckle if the tendons were in contact with the concrete, so the selection of struts for the

experiments used tendons with ducts such that they would buckle, and when the tendons

came into contact with the side of the duct, the behavior could be observed.

The theoretical analysis from Godden (1960) considered three cases. The first

case was that of a pinned ended strut with an axial load as depicted in Figure 1.11.
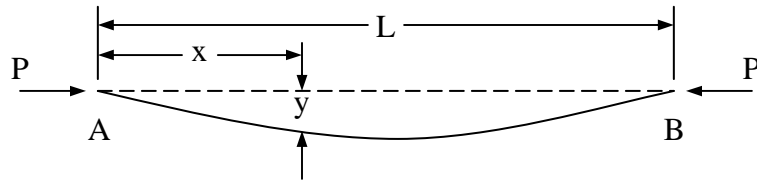
Figure 1.11 - Axial strut with pin jointed ends from Godden (1960)

The results of the first case gave the critical axial force equal to the Euler buckling load,

which was to be expected. Seldom have actual conditions allowed for perfect loading

with no error which was the cause for the derivation of the second case. The conditions

were the same except that the axial load was applied eccentrically as depicted in Figure

1.12.
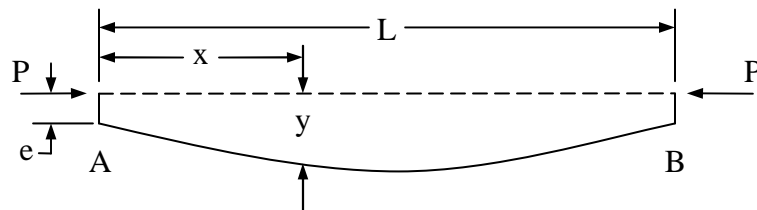
Figure 1.12 - Eccentrically loaded axial Strut with pin jointed ends from Godden (1960)

The deflection of the strut was found by first setting the internal moment equal to the externally applied moment:

$$EI \frac{d^2 y}{dx^2} = -Py \qquad (1.29)$$

by simplifying and substituting $k = \sqrt{\dfrac{P}{EI_y}}$:

$$\frac{d^2 y}{dx^2} + k^2 y = 0 \qquad (1.30)$$

The solution to the differential equation was of the form:

$$y = A \sin(kx) + B \cos(kx) \qquad (1.31)$$

Using the boundary condition that when x = 0, y = e, where e is the eccentricity at each end, gave the constant B = e. The boundary condition when x = L/2, y' = 0 resulted in A = e[tan(kL/2)]. After substituting and simplifying the final deflection was found to be:

$$y = e[tan(kL/2)] \sin(kx) + e[cos(kx)] \qquad (1.32)$$

and at the midspan of the strut the deflection was found to be:

$$y(L/2) = e\left[sec\left(\frac{kL}{2}\right)\right] = e\left[sec\left(\sqrt{\frac{PL^2}{4EI_y}}\right)\right] \qquad (1.33)$$

For a known value of the prestressing force, the deflection could be found at any point along the strut using Equation 1.32. However, Equation 1.32 only pertained to the case where the tendon did not come into contact with the duct. If the tendon comes into contact with the duct, an entirely new set of conditions would arise. The new conditions warranted the derivation for the third case where the strut had deformed enough such that the tendon and duct were in contact as shown by Figure 1.13.
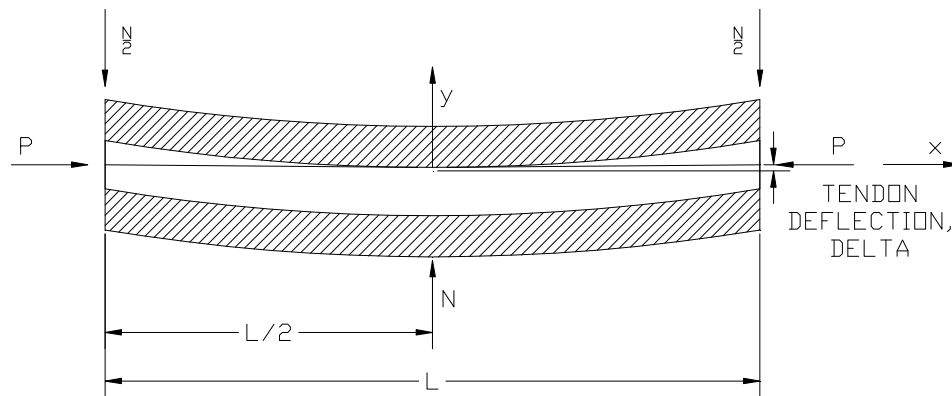
Figure 1.13 - Tendon in contact with duct from Godden (1960)

For the third case, the term Δ was introduced as the deflection of the tendon. Essentially, Δ was the deflection of the strut after the tendon came into contact with the duct. By making the assumption that after the tendon and duct came into contact, no

additional bending moment was developed at midspan of the strut, Godden (1960) was able to solve for the restoring force, N, by equilibrating it with the moment caused by the prestressing force multiplied by the tendon deflection which gave the restoring force to be:

$$N = \frac{4\Delta(P)}{L} \tag{1.34}$$

The internal moment had to equal the externally applied moment, therefore:

$$EI_y \frac{d^2y}{dx^2} = -Py + \frac{N}{2}\left(\frac{L}{2} - x\right) = -P\left[y - \Delta\left(1 - \frac{2x}{L}\right)\right] \tag{1.35}$$

After substituting $k = \sqrt{\dfrac{P}{EI_y}}$ into Equation 1.35, the solution to the governing differential equation became:

$$y = A\sin(kx) + B\cos(kx) + \Delta\left(1 - \frac{2x}{L}\right) \tag{1.36}$$

Using the first boundary condition, when x = 0, y' = 0, resulted in A = 2Δ/kL and the second boundary condition, when x = L/2, y = 0, resulted in Equation 1.37.

$$B = \frac{\frac{-2\Delta}{kL}sin(kL/2)}{cos(kL/2)} \qquad (1.37)$$

Note that the origin of the x-axis was set at midspan of the strut. Substituting into Equation 1.36 resulted in the deflection at any point along the length of the strut to be:

$$y = \Delta\left[\frac{2\,sin(kL)}{kL} - \frac{2/kL\,sin(kL/2)cos(kx)}{cos(kL/2)} + 1 - \frac{2x}{L}\right] \qquad (1.38)$$

The maximum deflection which occurred at midspan of the strut became:

$$y(0) = \Delta\left[1 - \frac{2}{L\sqrt{P/EI_y}}tan\left(\frac{L}{2}\sqrt{\frac{P}{EI_y}}\right)\right] \qquad (1.39)$$

Furthermore, the maximum deflection at midspan was the deflection of the tendon, Δ, in addition to the deflection before contact between the tendon and the duct. The deflection before contact between the tendon and the duct was just the clearance between the tendon and the duct; therefore, $y(0) = \Delta$ + clearance.

The important assumption made by the analysis for the third case was that when the tendon came into contact with the duct, a concentrated restoring force was applied at the point of contact between the tendon and the duct. The magnitude of the restoring

force was determined by assuming that the reactions from the restoring force produced a moment equivalent to the moment produced by the prestressing force multiplied by the deflection of the tendon.

Six struts were tested by Godden (1960), but only three tests produced load versus deflection plots that were included due to various experimental issues. The struts that had recorded load versus deflection plots were those designated by Godden as Beam II, Beam III and Beam VI. Figure 1.14 shows the specifics of each of the struts.
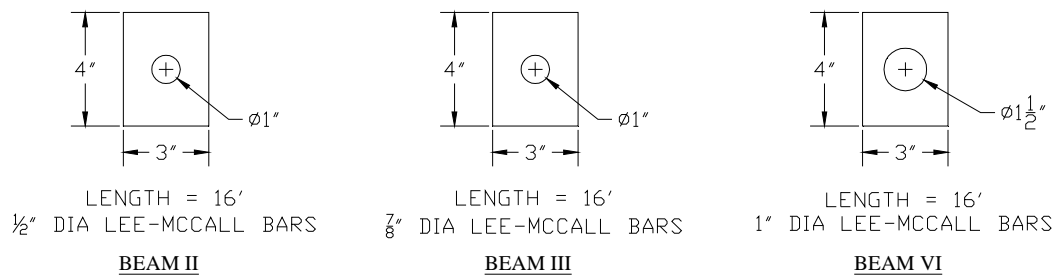
Figure 1.14 - Strut details from Godden (1960)

The load was applied to the struts but running the threaded Lee-McCall bars through the duct and turning the end nuts so that the end nut would apply a compressive force to the end of the strut. A diagram of the end condition is shown in Figure 1.15.
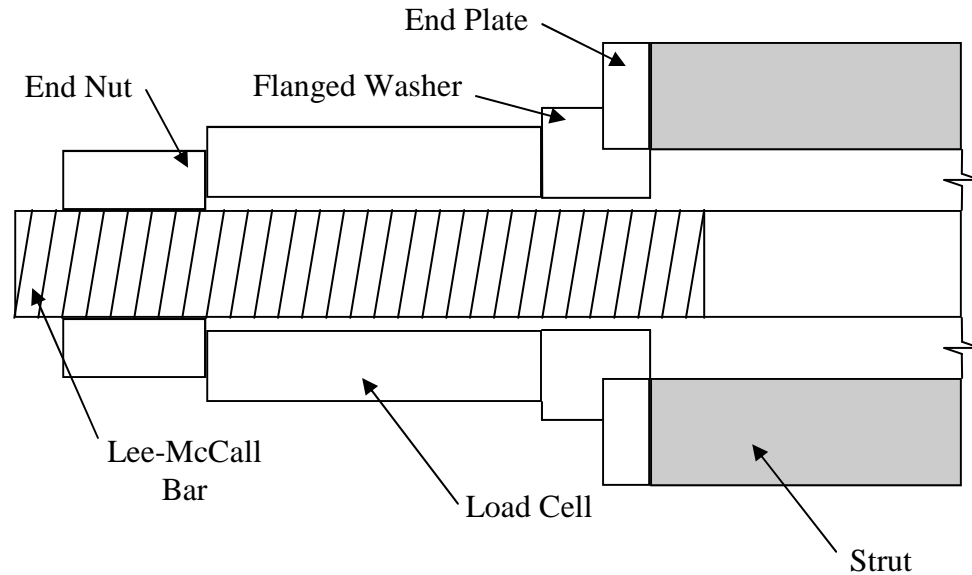
Figure 1.15 – End condition for struts from Godden (1960)

Godden (1960) stated that the experimental results demonstrated that the end

fixities of the beams were sufficiently close to the idealized assumption that end

conditions were pinned. The end fixity was determined by plotting the stress on both

sides of the strut at each of the ends. In theory, if the ends were completely free to rotate

then the stress on either side of the beam would be equivalent and the only induced stress

would be from the axially induced stress. An example of one of these plots is shown as

Figure 1.16. The stresses were difference on each side and it was apparent that there

were some end fixity issues to consider. Some of the plots that were included in Godden

(1960) did show a good representation of a free end condition but this only occurred in

approximately half of the end conditions of the beams.
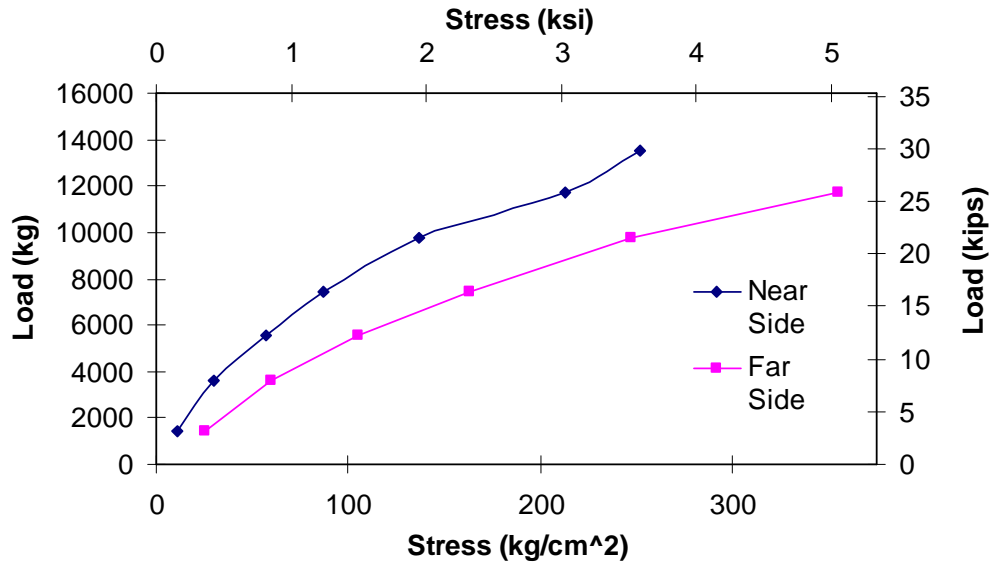
Figure 1.16 - Beam III load vs. stress at ends from Godden (1960)

For Beam I alone, Godden (1960) attached two strain gages at each location at both the top and the bottom of each side so that the stresses at these locations were compared. The comparison showed that the stress at the top and bottom of the side of the strut were the same; so, it was concluded that the deflection at the top and bottom was the same and, therefore, there was no rotation of the strut. Table 1.10 shows the material properties for each of the tested struts, while Figures 1.17, 1.18 and 1.19 show the lateral deflection versus the load for Beam II, Beam III and Beam VI, respectively.

Table 1.10 - Strut material properties from Godden (1960)

Beam	Cube Strength psi (kg/cm^2)	Modulus of Rupture psi (kg/cm^2)	Tensile Strength psi (kg/cm^2)	Modulus of Elasticity psi (kg/cm^2)
I	6640 (466.85)	467 (32.83)	498 (35.01)	4230 (297403)
II	5250 (369.12)	378 (26.58)	462 (32.48)	3630 (255219)
III	6500 (457.00)	378 (26.58)	466 (32.76)	4075 (286506)
IV	5070 (356.46)	409 (29.76)	429 (30.16)	3780 (265765)
VI	5356 (376.57)	428 (30.09)	498 (35.01)	5920 (416224)
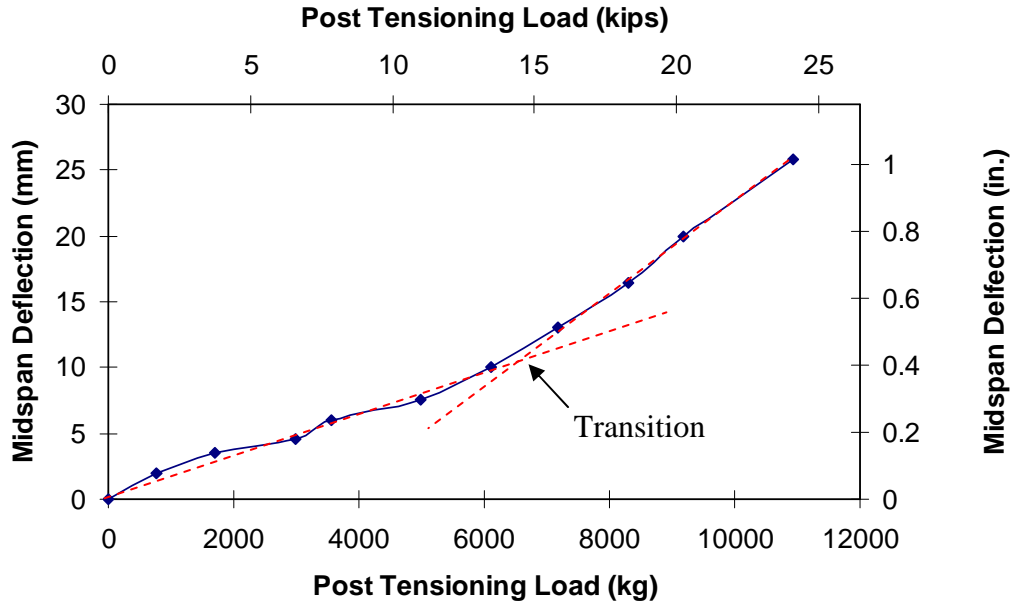
Figure 1.17 - Beam II experimental deflection versus load from Godden (1960)
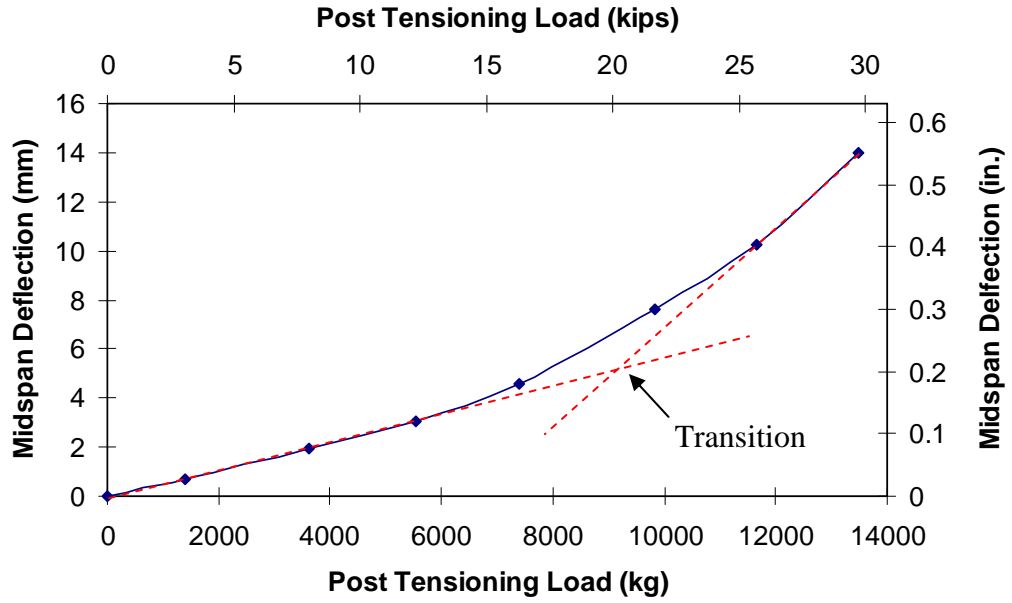
Figure 1.18 - Beam III experimental deflection versus load from Godden (1960)
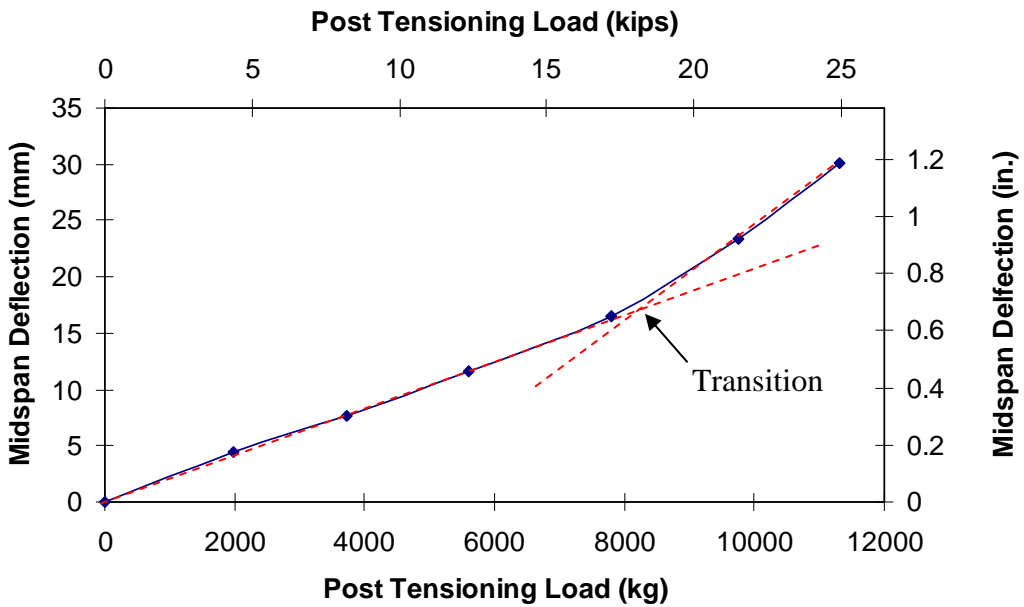
Figure 1.19 - Beam VI experimental deflection versus load from Godden (1960)

Godden (1960) considered each of the deflection versus load plots to be bilinear

with a transition zone between each of the linear segments. The thought was that the

transition zone where the deflection begins to increase at a higher rate was when the

tendon came into contact with the duct and began to move with the strut. This was

different then what Godden's cited references stated in which they believed there would

be a restraining effect when the tendon and duct came into contact. Furthermore, the

predicted behavior using the deflection formulation of Equation 1.39 was not accurate

either, which is apparent in Table 1.11 because the actual experimental deflections do not

match the theoretical deflection that was based on Equation 1.39. The comparison of the

theoretical deflection and the actual experimental deflection was especially different in

the case of Beam VI.

Table 1.11 - Experimental and theoretical results from Godden (1960)

Beam	Load kips (kg)	Actual Deflection in. (mm)	Theoretical Deflection in. (mm)	Euler Buckling Load kips (kg)
II	24.64 (11176.7)	1.05 (26.67)	1.33 (33.78)	8.75 (3967.5)
III	24.64 (11176.7)	0.37 (9.40)	0.27 (6.86)	9.82 (4453.9)
VI	24.64 (11176.7)	1.16 (29.46)	0.537 (13.64)	14.26 (6470.5)
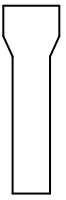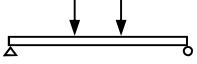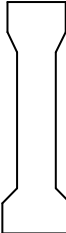
Notice that the transition region was at a deflection greater than the clearance

which Godden (1960) believed was due to the tendon rotating due to a couple at the end.

The couple induced in the tendon was quite probable since the end plate connection

between the strut and tendon was very rigid and would not allow complete freedom of

rotation of the strut without having an effect on the post-tensioned bar. The author

further calculated the Euler buckling load, which was believed by Godden (1960) to be the load of instability if the tendon had yet to come into contact with the tendon. The Euler buckling loads were such that the strut should have buckled before the transition zone. The author believed that there was some fixity at the ends of the strut which would result in a larger buckling load. These considerations lead the author to believe that when buckling was reached, the tendon came into contact with the duct, and then they moved together at a higher rate of deformation. Furthermore, there was obviously eccentricity and/or out of straightness errors in the struts because the lateral deflections increased at a high rate upon immediate loading. Godden (1960) did not include any measured eccentricities or fabrication errors within his thesis.

Similar tests were performed by Wilby (1963) where both the struts and experimental set-up were extremely similar. The analytical method developed by Wilby (1963) was the same as Godden (1960) except that the restoring force provided in the formulation was considered as a uniform load along the length in which the tendon had come into contact with duct. The results of the tests performed by Wilby (1963) are not presented here due to a lack of information the on struts' dimensions, material properties and errors. Furthermore, the data were not provided in a sufficient manner and were very incomplete.

To the author's knowledge, no lateral-torsional buckling tests were performed on prestressed concrete beams in the United States. In Germany however, a set of tests on reinforced concrete and prestressed concrete beams were performed by König and Pauli (1990). The six test specimens fabricated for the tests had the dimensions and reinforcement shown in Tables 1.12 and 1.13.

Table 1.12 – List of principle parameters from König and Pauli (1990)

Test No.	Cross-Section	Static System	Bottom Flange Reinforcement	Top Flange Reinforcement	Top Flange Width
1				4 - 12mm DIA 4 - 8mm DIA	25 cm
2			6 - 25mm DIA		
3					35 cm
4				4 - 25mm DIA 4 - 8mm DIA	25 cm
5			14 - 12.5mm Prestressed	4 - 12mm DIA 2 - 12.5mm	
6			24 - 12.5mm Prestressed	4 - 12mm DIA 4 - 8mm DIA	35 cm

Note: 1 in. = 25.4 mm

Table 1.13 – Cross-section dimensions from König and Pauli (1990)

	Units	Specimen					
		1	2	3	4	5	6
b top(/bottom)	in. (cm)	10.4 (26.5)	10.2 (26)	14.2 (36)	10.2 (26)	10.2 (26)	14.2/12.2 (36/31)
b web	in. (cm)	5.3 (13.5)	5.2 (13.3)	5.1 (13)	5.1 (13)	5.1 (13)	5.9 (15)
d	in. (cm)	51.2 (130)	51.2 (130)	51.2 (130)	51.2 (130)	51.2 (130)	53.1 (135)
As top	in.^{2} (cm^2)	0.80 (5.16)	0.80 (5.16)	0.80 (5.16)	3.16 (20.4)	0.80 (5.16)	0.80 (5.16)
As bottom	in.^{2} (cm^2)	4.74 (30.6)	4.74 (30.6)	4.74 (30.6)	4.74 (30.6)	14 Strands	24 Strands

56

The concrete material characteristics are shown in Table 1.14, and the steel characteristics are shown in Table 1.15. The concrete material properties were determined by casting six concrete cubes and six concrete cylinders for each specimen. The tensile strength of the concrete was determined by performing a split cylinder test on three of the six concrete cylinders.

Table 1.14 – Concrete material properties from König and Pauli (1990)

Test No.	Units	1	2	3	4	5	6
Cube Compressive Strength	ksi (MN/m^2)	8.27 (57)	8.27 (57)	8.25 (56.9)	8.88 (61.2)	8.34 (57.5)	6.38 (44)
Cylinder Compressive Strength	ksi (MN/m^2)	7.99 (55.1)	8.51 (58.7)	7.27 (50.1)	7.56 (52.1)	7.18 (49.5)	5.95 (41)
Tensile Strength	ksi (MN/m^2)	0.55 (3.8)	0.52 (3.6)	0.42 (2.9)	0.39 (2.7)	0.42 (2.9)	0.39 (2.7)
Core Compressive Strength	ksi (MN/m^2)	9.86 (68)	9.14 (63)	9.12 (62.9)	9.66 (66.6)	9.22 (63.6)	8.27 (57)
Elastic Modulus	ksi (MN/m^2)	5221 (36000)	5221 (36000)	5076 (35000)	5221 (36000)	5076 (35000)	4496 (31000)

Table 1.15 – Steel material properties from König and Pauli (1990)

	f_y ksi (MN/m^2)	ε_{sy} (%)	Es ksi (MN/m^2)
Reinforcing Steel	83.4 (575)	2.9	29000 (200000)
Prestressing Strand	227.7 (1570)	8.05	28300 (195000)

All of the specimens underwent the same unstable failure mechanism. As the transverse load increased, lateral deflections did so at a relatively small amount; however, when the critical load was reached, lateral deflections increased at a large magnitude, and there was very little load increase after the critical load was reached. The damage to the beams after the tests included diagonal cracks that developed on both the convex and concave sides of the specimens, and the cracks on the convex side of the specimens were perpendicular to those on the concave side. This type of diagonal cracking is representative of torsion cracking in reinforced concrete beams and is an indicator of lateral-torsional buckling. Furthermore, it was noted by König and Pauli (1990) that the amount of cracking was less on the concave side relative to the convex side, particularly in the case of the two prestressed beams. That makes intuitive sense because there was compression on the concave side due to weak-axis bending that acts to close the torsional cracks on that side; however, on the convex side, there was tension from the weak-axis bending that acts to amplify the torsional cracking on that side. It is important to note that weak-axis bending stresses and the torsional stresses were developed in the experiments by König and Pauli (1990) due to the end restraints. The end conditions that they used were: torsional restraint, vertical translation restraint, and horizontal translation restraint while allowing free rotation about horizontal axis and free rotation about vertical axis.

The results shown in Table 1.16 indicate that both widening the top flange and adding additional compression reinforcement increase the stability of the cross-section. Furthermore, the prestressing force did not produce any significant effect with respect to the specimens' stability because specimen 1 and specimen 5 were extremely similar with

respect to geometry, and amount and location of reinforcing steel; however, specimen 5 was prestressed, and the critical loads for the two case were very similar.

Table 1.16 – Test results from König and Pauli (1990)

Test No.	Units	1	2	3	4	5	6
Failure Load	kips (kN)	42.7 (190)	44.5 (198)	57.0 (253.5)	53.4 (237.5)	45.1 (200.5)	50.9 (226.5)
Horizontal Deformation	in. (mm)	6.38 (162)	3.27 (83)	5.55 (141)	1.85 (47)	7.24 (184)	8.66 (220)
Vertical Deformation	in. (mm)	4.57 (116)	2.40 (61)	4.61 (117)	3.74 (95)	2.80 (71)	5.51 (140)
Load Frame Tilt	%	0.5	0	1	0	0	0

A significant number of analytical procedures were also developed in Germany. Deneke, Holz and Litzner (1985) summarized the procedures available at the time by putting them in groups. The groups were determined by utilizing methods and characteristics employed by the various researchers. The groups in which Deneke, Holz and Litzner (1985) divided the various procedures are as follows:

Group 1: Thin-walled straight girders made from linear elastic materials. Large safety factors were used for reinforced and prestressed concrete.

Group 2: Like Group 1, but instead of large safety factors, the modulus of elasticity was reduced.

Group 3: Linear elastic equations were used but the rigidities were reduced with a dependence on the loading magnitude. The modulus of elasticity was also reduced in most methods.

Group 4: Instead of computational methods, the slenderness of the girders was limited. In the case of ACI 318-83, the ratio of compression flange width to unbraced length was limited.

Group 5: The buckling problem was idealized as a compression strut that has the dimensions of the compressed region of the beam under the total compressive force in the beam, thereby allowing initial imperfections to be more easily accounted for.

Group 6: The girder was broken into segments where each segment had its own stiffnesses based on the current load condition.

Table 1.17 summarizes the analytical procedures Deneke, Holz and Litzner (1985) considered available at the time by putting them in their procedural groups. Note that the methods deemed the most important and most accurate by Deneke, Holz and Litzner (1985) are in bold.

Table 1.17 – Available buckling procedures from Deneke, Holz and Litzner (1985)

Group 1	Group 2	Group 3	Group 4	Group 5	Group 6
Beck and Schack (1972)	Hansell and Winter (1959) Lebelle (1959) Petterson (1960) **Stiglat (1971)**	**Rafla (1969), (1973)** Jeltsch (1971) Nowak (1971) Mehlhorn (1974) Streit and Mang (1984)	CP 110 (1972) ACI 318-83 (1983)	**Mann (1976), (1985)**	**Röder and Mehlhorn (1981)** Röder (1982) Kraus and Kreuzinger (1983)

The methods highlighted in bold by Deneke, Holz and Litzner (1985) were deemed important and reasonable methodologies to determine the lateral-torsional buckling loads of prestressed concrete or reinforced concrete girders. Of these methodologies, Stiglat (1971) employed a relatively simple approach to the stability problem. Essentially, the elastic critical buckling load was determined for the cross-section and then the buckling load was reduced by multiplying the elastic critical buckling load by a ratio of the secant modulus to the elastic modulus. To employ the technique used by Stiglat (1971), any appropriate stress-strain diagram could be used to determine the secant modulus, but for the calculations performed by Stiglat (1971), the

stress-strain diagram published by Dilger (1966) was utilized. The reduction of the

elastic critical buckling load by Stiglat (1971) is shown by Equation 1.40.

$$M_b = \frac{E_{sec}}{E_c} M_{b\,elastic}$$ (1.40)

Rafla (1969) developed an approximate method based on both utilizing the secant

modulus as well as reducing the weak-axis moment of inertia to take into account the

weakening of the beam due to cracking. The torsional stiffness utilized the full

uncracked section of the beam which gives the following equations for material

properties and moments of inertia:

$$E_{sec} = \sigma_c / \varepsilon_c$$ (1.41)

$$G_c = 0.4 E_{sec}$$ (1.42)

$$I_y = \xi \frac{hb^3}{12}$$ (1.43)

where:

σ_c =   extreme compression fiber stress

ε_c =   extreme compression fiber strain

ξ =   factor controlling depth of neutral axis (Rafla, 1969)

The factor ξ represented the reduction based on the compression zone depth that created

equilibrium between the applied buckling moment and the internal moment.

Instead of using traditional methods of closed form solutions or iterative approaches to determine the neutral axis depth and secant modulus, Rafla (1973) constructed a series of diagrams to be used as design aids. These diagrams utilized several atypical parameters to associate concrete properties, reinforcement ratios and load height to the final rigidity properties to be substituted in the critical buckling moment equation which was altered to accommodate such parameters. The critical buckling moment equation was:

$$M_b = b_i d^2 \sqrt{\xi} E_{sec} A_R \tag{1.44}$$

where:

    b_i =   effective width of cross-section (Rafla, 1973)

    d   =   effective depth of cross-section

    A_R =   geometric relationship that considers load height (Rafla, 1973)

Within Equation 1.44, the term b_i represented an effective width of a rectangular cross-section that was based on the effective depth of the section, weak-axis moment of inertia and torsion constant and was given by:

$$b_i = \left[\frac{6}{d} \sqrt{I_y J} \right]^{\frac{1}{3}} \tag{1.45}$$

The term A_R in Equation 1.44 was a factor that takes into account the distance of the load application point on the critical buckling load that was given by Equation 1.46 for a uniformly distributed load and was given by Equation 1.47 for a midspan concentrated load.

$$A_R = \frac{0.37b^2}{dL}\left(1 - 0.90\frac{\bar{a}}{L}\right) \tag{1.46}$$

$$A_R = \frac{0.44b^2}{dL}\left(1 - 1.10\frac{\bar{a}}{L}\right) \tag{1.47}$$

The aforementioned factor ξ was a function of the reinforcement ratio, the strength ratio between concrete and steel, and the strain at the extreme compression fiber. It was most easily obtained by referring to Figure 6 in Rafla (1973).

Mann (1976) implemented a different technique where the compression zone of the beam was transformed into an equivalent compression strut that allowed for the effect of initial imperfections to be taken into consideration. The first parameter utilized by Mann (1976) was the χ-factor which was a function of the flexural and torsional stiffnesses based on the compression zone depth as well as the length and internal moment arm of the compression zone. The χ-factor could be obtained by utilizing Figure 5 from Mann (1976) or by using the following equation:

$$\chi = \frac{L}{\pi \, z_d} \sqrt{\frac{GJ_c}{EI_{yc}}} \qquad\qquad (1.48)$$

where:

    z_d =   internal moment arm between compression zone and tensile steel

            reinforcement

    I_{yc} =   weak-axis moment of inertia of compression zone

The idealized slenderness was based on the parameter in Equation 1.48 and was most easily obtained by using Figure 6 in Mann (1976), but also could be obtained by using the following equation:

$$\overline{\lambda} = \frac{L}{0.289b\sqrt{0.5 + \chi}\sqrt{C_b}} \qquad\qquad (1.49)$$

The slenderness parameter from Equation 1.49 utilized the method by Kasparek and Hailer (1973) to obtain a critical stress value for the derived equivalent compression strut.

      The initial imperfections were taken into consideration by using both the initial out-of-plane deformation in conjunction with the initial rotation to obtain an idealistic compression strut imperfection which was as follows (Mann, 1976):

$$\overline{e} = e_o\left[1 + \frac{0.4}{C_b\chi\sqrt{2}}\left(\chi^2 - \chi\sqrt{2} + 1 - \chi^2\frac{e_u}{e_o}\right)\right] \qquad\qquad (1.50)$$

where:

e_u =   out-of-plane eccentricity of bottom of beam

e_o =   out-of-plane eccentricity of top of beam

Furthermore, the equivalent compression strut needed a parameter that created an equivalent load eccentricity to the strut. This parameter was given by Equation 1.51.

$$m_o = \frac{6\bar{e}}{b} \qquad (1.51)$$

where:

$\bar{e}$ =   Idealistic compression strut imperfection

The area of the equivalent compression strut was simply given by the area of the compression zone of the beam at a given load condition. The critical stress of the equivalent strut was determined by using the previously derived characteristics and employing them in Kasparek and Hailer (1973). After obtaining the critical stress of the equivalent compression strut, the compressive force on the strut was the product of the critical stress and the area of the compression strut. The moment arm between the compression and the tensile steel reinforcing allowed for the critical moment in the beam to be determined. The resulting critical moment must then be compared to the moment of the steel reinforcing acting about the compression strut where the force in the steel was determined by using strain compatibility for the critical moment. If the two values were not equivalent, an iterative approach had to be utilized until the two moments were equal

66

(Mann, 1976). The previous methodology was further expanded and employed to T-shaped cross-sections by Mann (1985).

The last method considered important and viable by Deneke, Holz and Litzner (1985) was a very detailed analysis technique by Röder and Mehlhorn (1981). The method utilized a computer program that calculated the stresses and strains on a beam that included initial deformations. The stresses and strains were used to evaluate the stiffness values for separate segments of the beam. Combining the segments of the beam with varying stiffness properties, Röder and Mehlhorn (1981) were able to calculate a critical buckling load.

1.3.2 Rollover Stability

Rollover problems occur when an overturning moment is developed due to imperfections in the girder, imperfections in the support conditions, nonlinear behavior of the supports and in the case where cracking has occurred in girder and/or nonlinearity in the stiffness properties of the girder also occur. The solution to such a problem was not done with a traditional stability analysis but instead by considering the bending of the girder and the subsequent equilibrium. Some initial research was done on the topic by Imper and Laszlo (1987), but this work was expanded on by Mast (1989) for the case of a hanging girder, and by Mast (1993) for the case of a girder on elastic supports. The works by Mast had become the standard method used to determine rollover of bridge girders while being transported and placed. The Precast Prestressed Concrete Design Manual (2003) based its requirements on Mast's work and even included examples from Mast (1989) and Mast (1993).

A beam on elastic supports, such as that is shown in Figure 1.20, gives the equilibrium diagram (Mast, 1993) shown in Figure 1.21 depicting the overturning moment arm and the resisting moment arm.

Lateral Deflection of Beam

α = Superelevation
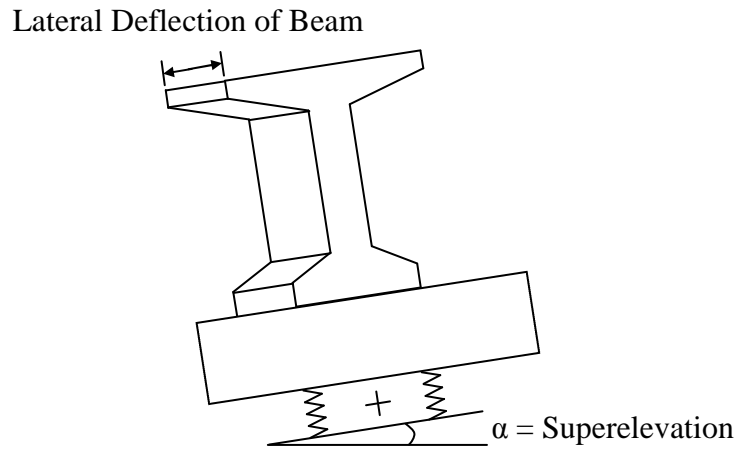
Figure 1.20 – Beam on elastic supports

The overturning moment arm was given by Equation 1.52 and the resisting moment arm was given by Equation 1.53 where the angle θ represents the total rotation of the beam from the vertical and the angle α represents the initial angle of the supports before deformations in the beam or supports occurred (Mast, 1993).
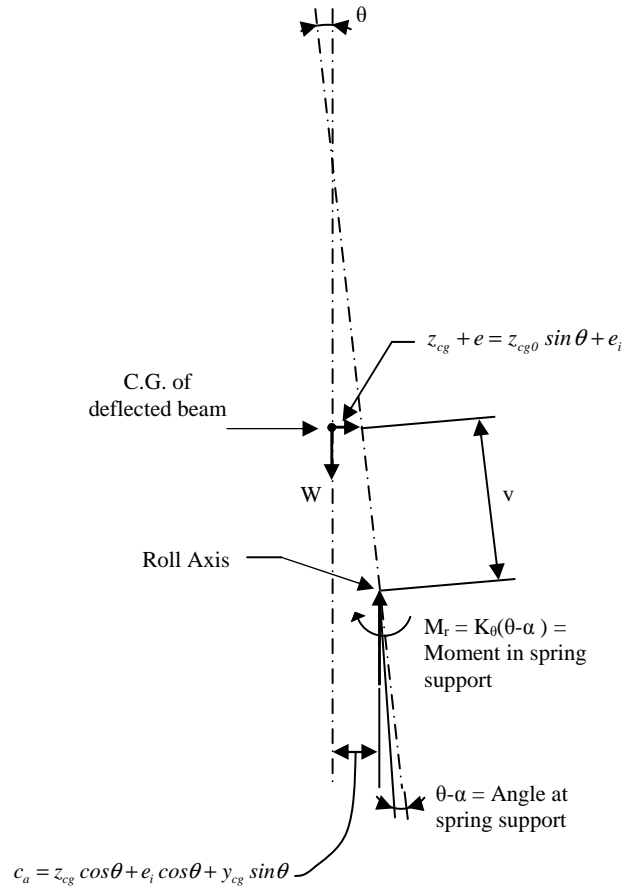
Figure 1.21 – Equilibrium of beam on elastic support (Mast, 1993)

$$c_a = z_{cg}\, cos\,\theta + e_i\, cos\,\theta + y_{cg}\, sin\,\theta \qquad (1.52)$$

where:

c_a =   overturning moment arm

z_{cg} =   lateral deflection of center of gravity of deflected beam

e_i =   eccentricity of girder center of gravity

y_{cg} =   height of center of gravity above roll axis

θ =   roll axis of beam with respect to vertical axis

$$c_r = \frac{K_\theta}{W_b}(\theta - \alpha) \qquad (1.53)$$

where:

K_θ = rotational spring constant of support

α = angle of support before deformations (superelevation)

To solve for the equilibrium angle, moments were summed about the roll axis and small angle approximation were made to give:

$$W_b\left[z_{cgo}\theta + e_i + y_{cg}\theta\right] = K_\theta(\theta - \alpha) \qquad (1.54)$$

A factor "r" was introduced (Mast, 1993) which was the quotient of the bearing rotational stiffness and the weight of the beam. The factor's physical meaning was that it was the height in which the weight of the beam could be placed such that the system was in neutral equilibrium as shown in Figure 1.22.

For Neutral Equilibrium
$W_b(r\theta) = M = M = \theta(K_\theta)$
$r = K_\theta/W_b$

$M = \theta(K_\theta)$
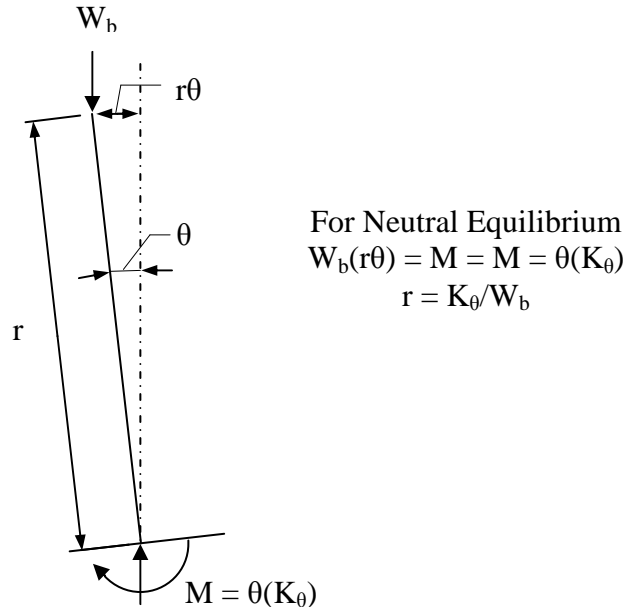
Figure 1.22 – Definition of radius of stability (Mast, 1993)

The factor r (radius of stability) was given by Equation 1.55. Solving the moment

balance resulted in the equilibrium angle and was given by Equation 1.56.

$$r = \frac{K_\theta}{W_b} \qquad (1.55)$$

$$\theta = \frac{\alpha r + e_i}{r - y_{cg} - z_{cgo}} \qquad (1.56)$$

The factor of safety against overturning was defined as the ratio of the resisting moment

arm to the overturning moment arm (Mast, 1993) shown as follows:

$$FS = \frac{c_r}{c_a} = \frac{r(\theta - \alpha)}{z_{cgo}\theta + e_i + y_{cg}\theta} \qquad (1.57)$$

At a certain angle, the beam would reach tensile stresses in one of the top flanges that would exceed the modulus of rupture of concrete, therefore resulting in decreased stiffness properties. The angle in which cracking occurs was defined by Mast (1993) as θ_{max}. The midspan biaxial stress state in a prestressed concrete girder is shown in Figure 1.23.
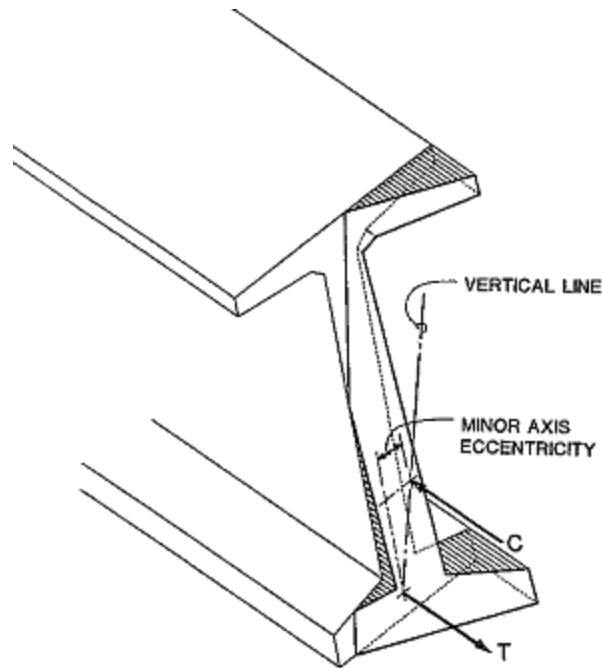
Figure 1.23 – Midspan biaxial stress state in a prestressed concrete girder (Mast, 1993)

Substituting the angle at the onset of cracking into Equation 1.57 resulted in the factor of safety against cracking (Mast, 1993). Mast (1993) believed it was very important to consider cracked conditions because many beams that had been shipped without collapse had factors of safety against cracking that were below unity. If the angle exceeded the cracking angle, Mast (1993) proposed an effective stiffness parameter shown by Equation 1.58. Furthermore, Mast (1993) noted the importance of considering wind force on the girder because wind would cause additional lateral deflections as well as additional overturning moment.

$$I_{eff} = I_y \big/ (1 + 2.5\theta) \qquad (1.58)$$

Burgoyne and Stratford (2001) also considered rollover by using a similar equilibrium methodology as Mast (1993). The primary difference was the way in which initial imperfections were considered. Mast (1993) included the initial imperfections within the derivation of equilibrium equations; however, Burgoyne and Stratford (2001) considered a perfect beam and then determined the stress distribution due to the initial sweep and the tensile stresses at critical locations. As the tensile stresses were large enough to induce cracking, it was said that the weak-axis flexural stiffness must be reduced.

The method to consider beams with flexible torsional restraints at the ends by Muller (1962) was based on classical stability theory. The coefficient in the lateral-

torsional buckling expression that included the effect of moment gradient, support

conditions and the constant, π, was reduced as a function of the torsional stiffness

provided by the bearing conditions. The phenomenon represented by the method was

still a lateral-torsional buckling mechanism and not a rollover mechanism. Within the

analytical techniques for rollover by Mast (1993) and Burgoyne and Stratford (2001), the

torsional stiffness, C, was considered to be infinite. However, in the analysis by Muller

(1962), infinite torsional stiffness, C, would result in an infinite buckling load.

Therefore, the failure mode consider was not that of rollover because a torsionally stiff

member could still be "tipped" over.

CHAPTER 2

SPECIMENS AND MATERIAL PROPERTIES

2.1 Rectangular Specimens

2.1.1 Specimen Descriptions

The first six specimens were rectangular prestressed concrete beams. The beams had a nominal length of 32 ft. (9.75 m), a width of 4 in. (10.2 cm) and a height of 40 in. (102 cm). The dimensions of these beams gave a span/width ratio of 96 and a depth/width ratio of 9.5. The reasons for the dimensions initially resulted from the selection of the width of the beams. The width was selected to be as small as possible to create a large slenderness. A width of 4 in. (10.2 cm) was the smallest that could be made by the precast plant and still guarantee the prestressing would be able to be properly done, and to assure no damage during the handling of the test beams. From the width, the length was determined by the need of a large span/width ratio, and the specific dimensional constraints allowed by the anchoring grid in the floor at the Georgia Institute of Technology Structural Engineering Laboratory. The depth was selected such that it would create the largest possible depth/width ratio, while being shallow enough that cracking would not occur when being tipped up from their sides after fabrication. The geometric ratios were compared with those of the reinforced concrete test specimens from Revathi and Menon (2006), and both ratios were found to be greater, and, therefore, more slender than the beams tested by Revathi and Menon (2006), in which all of their test specimens buckled.

All six of the rectangular beams had the same geometric dimensions. The reason for not varying the geometries of the beams was so that effect of the prestressing would be isolated. The six rectangular beams were split into three pairs. Each pair had a different prestressing strand pattern, but the same amount of mild steel reinforcement and approximate location of the mild steel reinforcement. The three different prestressing cases were: two strands located at the centroid of the cross-section (C2), two strands located at the bottom of the cross-section (B2) and one strand located at the bottom of the cross-section (B1). Either "A" or "B" was added to the end of the specimen designation to differentiate between the individual beams of a beam series. The strand patterns were selected such that the effect of strand location (eccentricity) was determined from a comparison of beams C2 and B2, because the prestressing force was approximately the same, but strand location was not. Furthermore, the effect of prestressing force was determined from a comparison of beams B2 and B1, because the center of gravity of the prestressing location was approximately the same, but the prestressing force was significantly different. The detailed design drawings of the three different layouts are shown in Figures A.1, A.2 and A.3 of Appendix A. Drawings of the beam specimens noting the important characteristics are shown in Figure 2.1 and photographs of the beams during fabrication are shown in Figures 2.2 and 2.3.
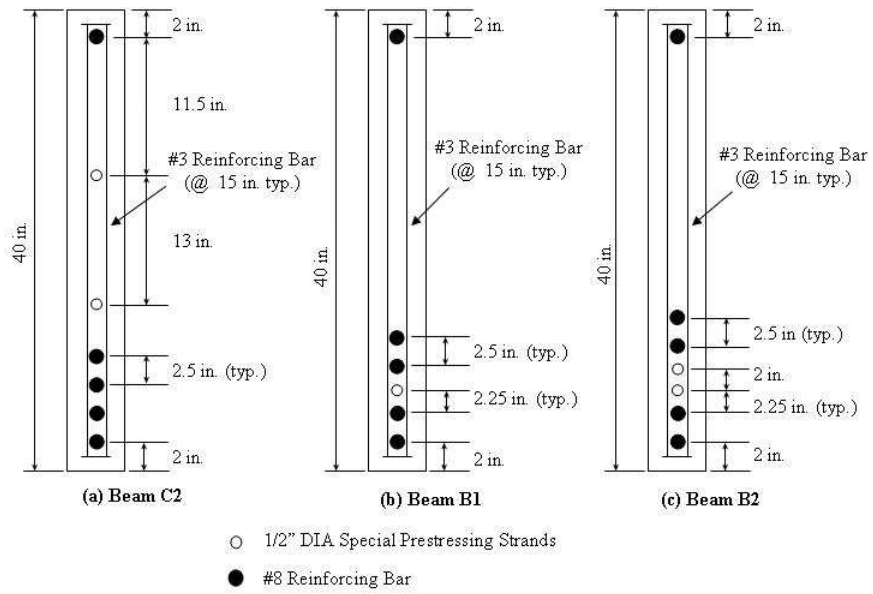
Figure 2.1 – Beam specimen drawings

Figure 2.2 – Reinforcement placement during fabrication of rectangular beams

Figure 2.3 – Finished rectangular beams

2.1.2 Initial Imperfections

Initial imperfections were measured for each test specimen. The initial horizontal, or weak axis displacement, was measured at five points along the length of each of the test specimens at both the top and the bottom of the cross-section. To measure the initial horizontal displacement, a taught wire was attached on either end of the beam length such that the distance between the wire and the beam specimen on the concave side of the beam was the initial horizontal displacement at that point. Knowing the initial horizontal displacement at the top and the bottom of the beam specimens allowed for the calculation of the initial rotation at each of the measurement points. Figures A.4 through A.15 depicts the initial horizontal displacements for each specimen with a comparison with an ideal sine curve. Table 2.1 summarizes the maximum initial imperfections for all of the specimens.

Table 2.1 – Summary of maximum initial imperfections

Beam ID	Sweep Top, in. (mm)	Sweep Bottom, in. (mm)	Rotation (radians)
B1A	-0.406 (-10.3)	-0.406 (-10.3)	0
B1B	-0.344 (-8.7)	-0.375 (9.5)	0.00078
B2A	1.50 (38.1)	1.06 (27.0)	0.011
B2B	-0.484 (-12.3)	-0.547 (-13.9)	0.00156
C2A	0.227 (5.8)	0.398 (10.1)	0.00430
C2B	-0.172 (-2.4)	-0.203 (-4.0)	0.00078

2.1.3 Material Properties

In order to predict the stability behavior of the rectangular prestressed concrete beams specimens, certain material properties were required. The prestressed concrete beams had three different materials to consider: concrete, mild steel and prestressing steel. To obtain the material properties for the concrete in the beam specimens, several concrete cylinders were cast according to ASTM C31-06. The material properties necessary for the analytical study were the compressive strength using ASTM C39-05, the initial modulus of elasticity using ASTM C469-02, and the Poisson's Ratio using ASTM C469-02. The concrete cylinder breaks occurred within one week of the testing of the specific beam. The cylinders were over a year old, and, therefore, changes in concrete material properties in a week would be negligible. The measured concrete material properties are summarized in Table 2.2.

Table 2.2 – Material properties for the rectangular beams specimens

Beam ID	# of Samples	f_c' (psi)	E_c (ksi)	ν
B1	3	10133	4713	0.19
B2	3	6015	4188	0.19
C2	3	11281	5156	0.20

The yield strength of the mild reinforcement given in the mill certificates was

71.7 ksi. Additional testing of the mild reinforcement was unnecessary because the stress

in the mild reinforcement never reached levels near the yield stress during the

experiments. Similarly, the stress level in the prestressing steel never reached levels of

nonlinear stress-strain behavior during the experiments either. However, the stress-strain

curve from the mill certificate for the prestressing strands, which was implemented in the

analytical study, is shown in Figure A.16 of Appendix A. Prestressing force was

important to monitor during the fabrication of the beam specimens. The desired

prestressing force in each of the test specimens was specified in the design drawings

shown in Figures A.1 through A.3 of Appendix A. Measured values of the prestressing

force in each of the beam specimens are shown in Table 2.3 and a photograph of the

prestressing force measurement is shown in Figure 2.4.

Table 2.3 – Measure prestressing force in each strand of the test specimens

Beam ID	Load LC1 (lbs)	Load LC2 (lbs)
B1	32,773	-
B2	30,398	30,832
C2	28,752	29,828

Note: Load LC1 measured the strand closest to the bottom of the beam.

Figure 2.4 – Measurement of prestressing strand force

2.2 PCI BT-54 Girder

2.2.1 Specimen Description

The seventh specimen was a 101 ft. (30.8 m) long PCI BT-54 bridge girder. The

BT-54 was prestressed with 40 – 0.6 in. diameter prestressing strands with each strand

having a jacking force of 43,940 lbs. (195.47 kN). Figure A.17, of Appendix A, shows

the detailed design drawing of the BT-54, while Figures 2.5 and 2.6 show photographs of

the BT-54 girder during fabrication and after completion, respectively. The specimen

length was selected without a detailed understanding of the stability behavior because the

planned thermal experiments needed to begin early in the research. The thought was that

additional initial imperfections could be introduced or a portion of the top flange could be

cut off if it was determined that the girder would not buckle at low enough load levels.

Figure 2.5 – BT-54 girder during fabrication

Figure 2.6 – Completed fabrication of BT-54 girder

2.2.2 Initial Imperfections

Initial imperfections of the BT-54 where measured at many different times. Many of the measurement were during the thermal study of the girder and are discussed in more detail in Chapter 3. The three important measurements of initial imperfections were immediately after the prestressing strands were cut, before testing the girder when the girder was on level supports, and before testing the girder when the girder was on the initially rotated supports. The maximum values for the initial imperfections and camber at these three times are shown in Table 2.4. Furthermore, initial horizontal displacement

measurements at nine points along the girder were measured at the top and the bottom of

the girder while the girder was on level supports and while the girder was on the initially

rotated supports. These values are presented in Figures A.18 through A.23 with a

comparison to an ideal sine curve. The same measurement technique as was described in

Section 2.1.2 for the rectangular test specimens was used for the BT-54.

Table 2.4 – Maximum Initial Imperfections for BT-54

Time	Sweep Top (in.)	Sweep Bottom (in.)	Rotation (radians)	Camber (in.)
After Strands Cut	0.875	-	0.00037	3.625
Level Support	1.944	1.484	0.01674	4.359
Initially Rotated Support	2.456	1.969	0.06524	4.391

For the BT-54 girder specimen, initial rotation was also introduced at the end supports to

cause the girder to be more unstable. The measured initial rotations on the bearing pads

and on the bottom flange of the girder are shown in Table 2.5.

Table 2.5 – End support initial rotations for BT-54

	Bearing Pad Rotations (radians)			Bottom Flange
	Front	Middle	Back	1' from Support
East Support	0.04817	0.04887	0.04887	0.04939
West Support	0.05131	0.05131	0.05079	0.05079

2.2.3 Material Properties

The BT-54 only had two different materials to consider: concrete and prestressing steel. The only mild reinforcement used in the specimen was the shear reinforcement. To obtain the material properties for the concrete in the beam specimens, several concrete cylinders were cast according to ASTM C31-06. The material properties necessary for the analytical study were the compressive strength using ASTM C39-05, the initial modulus of elasticity using ASTM C469-02, and the Poisson's Ratio using ASTM C469-02. The concrete cylinder breaks occurred within two days of the testing of the specific beam. The cylinders were over a year old, and, therefore, changes in concrete material properties in a two day period would be negligible. The measured concrete material properties are summarized in Table 2.6.

Table 2.6 – Material properties for the BT-54 specimen

# of Samples	f_c' (psi)	E_c (ksi)	ν
5	12188	4471	0.22

The stress level in the prestressing steel never reached levels of nonlinear stress-strain behavior during the experiments, and, therefore, the nonlinear material properties were not necessary. Prestressing force was unable to be measured accurately due to the immense number of strands. The design initial prestressing force is specified in Figure A.17 of Appendix A.

CHAPTER 3

SOLAR DEFORMATION EXPERIMENTAL STUDY

A preliminary investigation on the deformation behavior of the BT-54 girder specimen from the effects of solar radiation to determine if it was plausible that significant additional initial imperfections could be caused due to non-uniform heating of a bridge girder was performed. Subsequently, a more detailed experimental and analytical study was performed by another researcher at Georgia Institute of Technology (Lee, 2010).

3.1 Objectives

The solar deformation investigation was performed using the BT-54 girder specimen at the precast plant in which the girder was fabricated. Fabrication error resulted in an initial sweep in one direction, and, therefore, the convex side of the girder was directed towards the east such that the morning sun would heat the convex side serving to amplify the initial sweep in that direction. The objective was to obtain temperature variations in the girder, thermal strains in the girder, solar radiation data, wind data, sweep and camber data.

3.2 Experimental Setup

The induced thermal strains were found with vibrating wire strain gages embedded in the girder during casting. The temperature variations were found using internal thermocouples, external thermocouples and the thermistors that were included in vibrating wire strain gages. Solar radiation data were obtained using two Apogee

pyranometers, one on the top of the girder, and one attached to the side of the girder

directed horizontally to capture the magnitude of solar radiation on the side of the girder

due to the morning sun. The wind speed was found using an anemometer. Sweep and

camber data were found by hand measurements using a taught-wire system, as shown in

Figures 3.1 and 3.2. Additional sweep and camber measurements were taken on selected

days using string potentiometers to gain a better perspective on the displacements

throughout the day. The internal thermocouples and vibrating wire strain gage locations,

and external thermocouple locations, are depicted in Figure 3.3 and 3.4, respectively. A

photograph of the internal instrumentation is shown in Figure 3.5. Additionally, Figure

3.6 shows the locations of the pyranometers, anemometer and the string potentiometers.
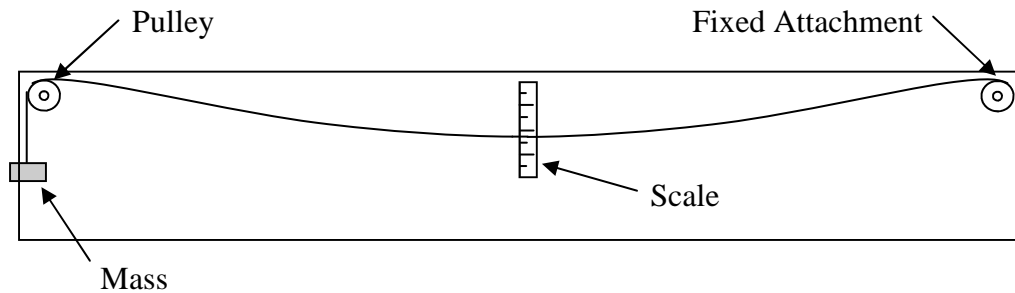
Figure 3.1 – Elevation view of taught wire system for camber measurements
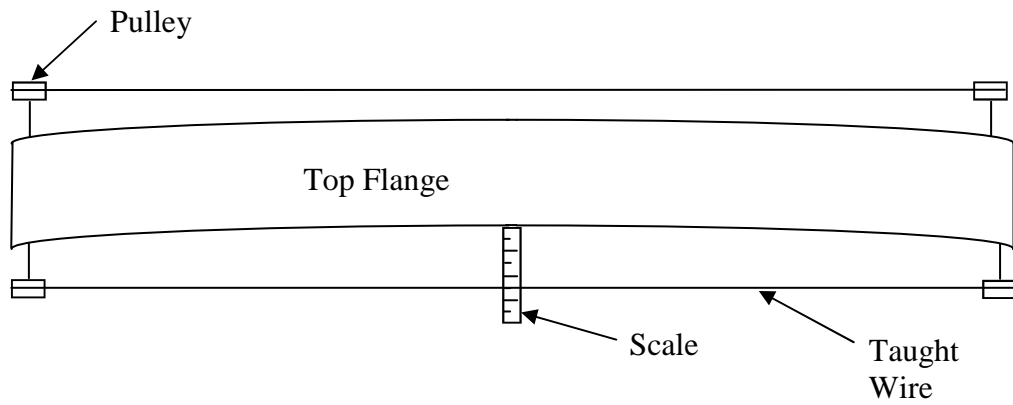
Figure 3.2 – Plan view of taught wire system for sweep measurements

Figure 3.3 – BT-54 internal vibrating wire strain gage and thermocouple locations
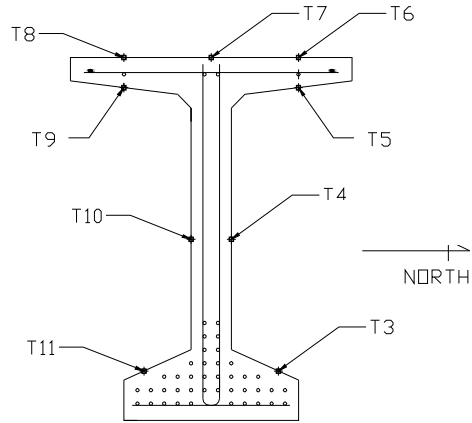
Figure 3.4 – BT-54 external thermocouple locations

Figure 3.5 – Internal vibrating wire strain gages and thermocouples
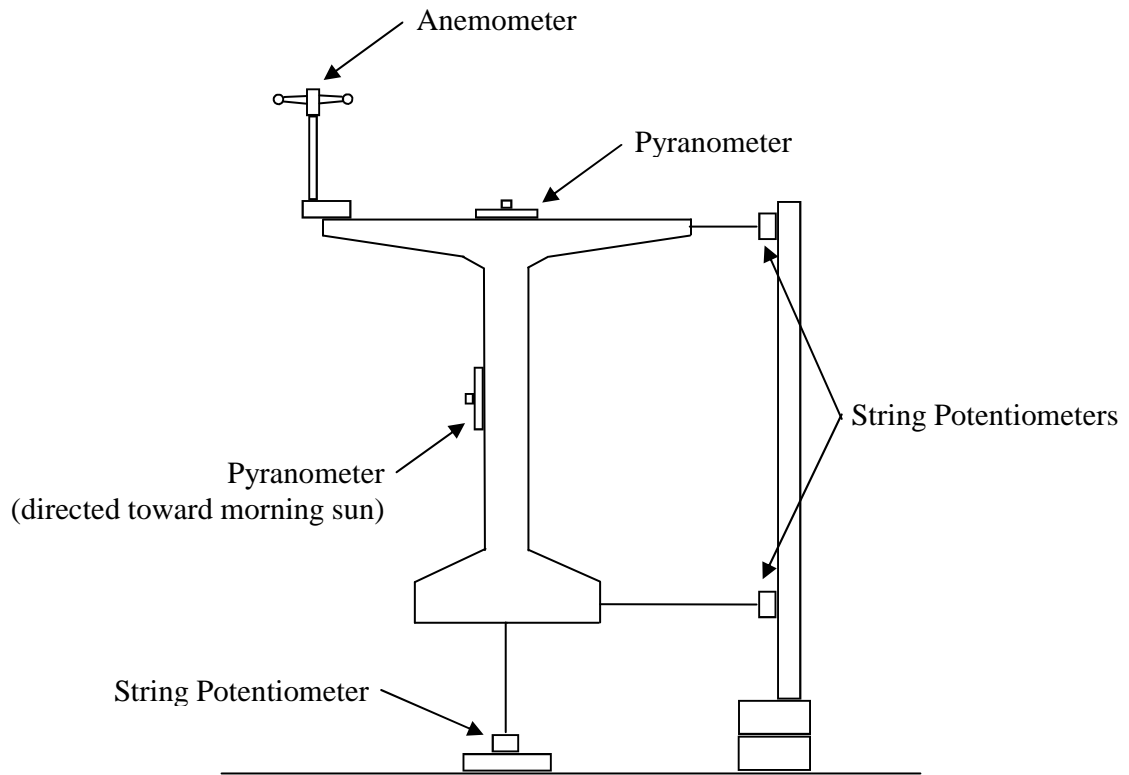
Figure 3.6 – BT-54 pyranometer, anemometer and string potentiometer locations

3.3 Experimental Results

Results from the experimental data for solar deformations and temperature

gradients in the BT-54 showed that the findings could be condensed to data from three

days during the summer of 2008. The days presented were deemed hot weather days,

where clear skies allowed a substantial amount of solar radiation to affect the girder, and

cool evenings created large temperature differentials. For all three days, the string

potentiometer set-up was used to gather accurate sweep and camber data. The plots of the solar radiation applied to the top of the girder and side of the girder (facing east) for each of the three days is shown below in Figure 3.7, 3.8 and 3.9.
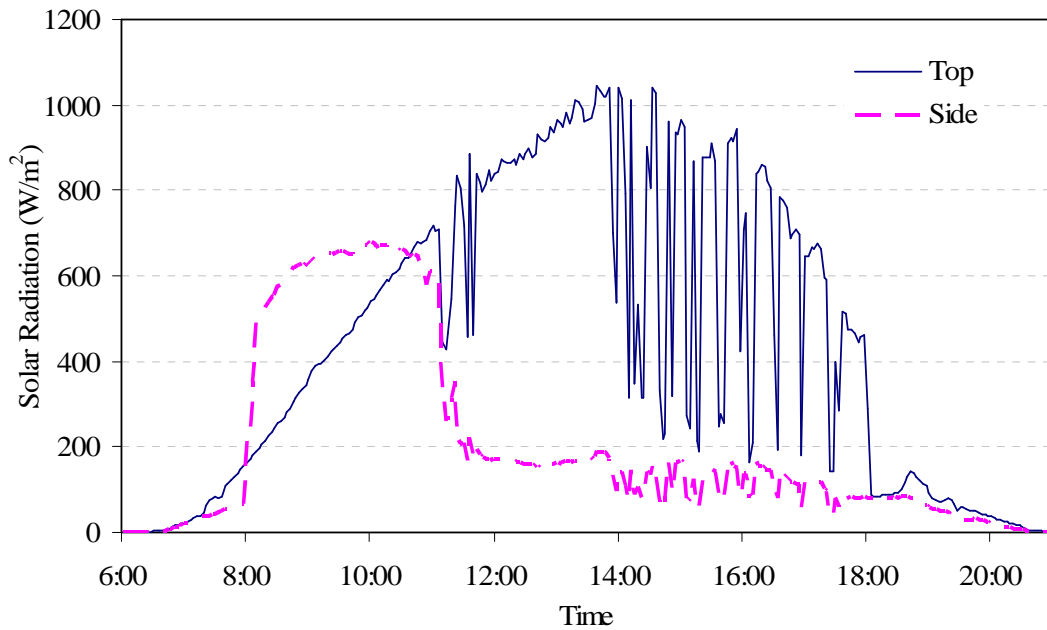
Figure 3.7 – Solar radiation on BT-54 for July 16, 2008
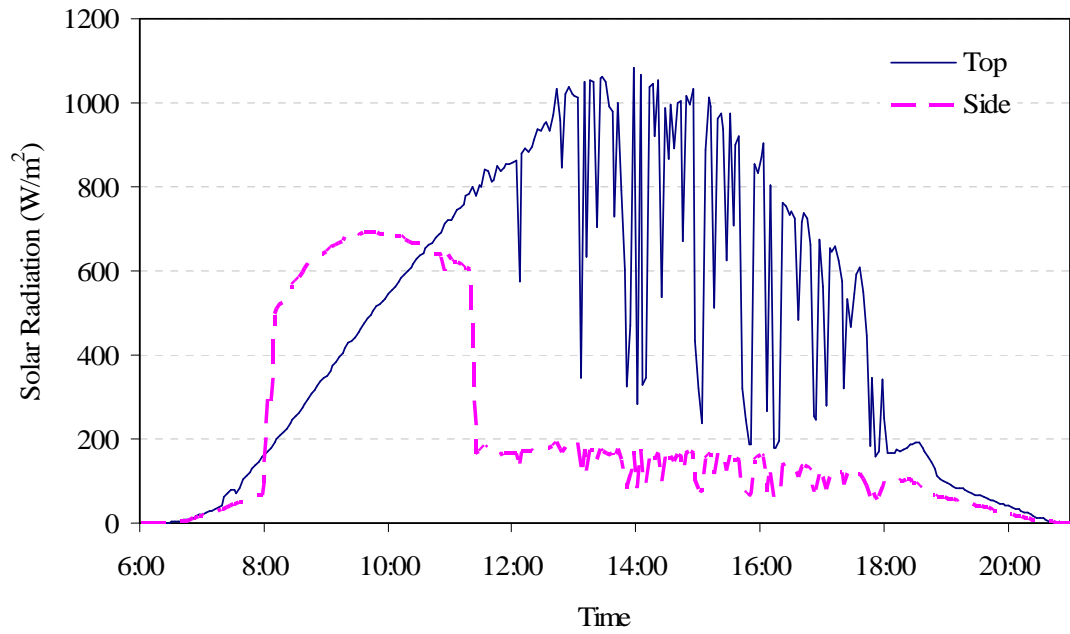
Figure 3.8 – Solar radiation on BT-54 for July 17, 2008
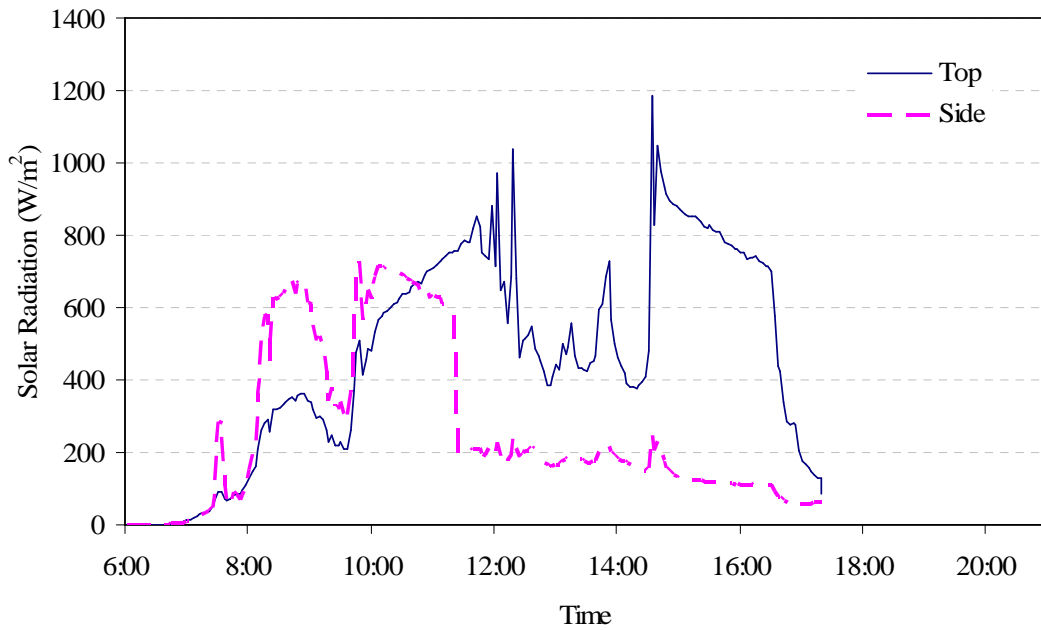
Figure 3.9 – Solar radiation on BT-54 for July 22, 2008

The curves do not come out perfectly smooth due to various disturbances and shadows that could occur at the precast plant where the BT-54 was being stored. For example, the gantry cranes often pass by the BT-54, and sometimes remain there for long periods of time.

The wind data for the three days presented are shown in Figures 3.10, 3.11 and 3.12. The wind speed was averaged over 15 minute increments. Gusting was deemed to be unimportant and extremely large amounts of data would have to be collected to represent the wind gusts.
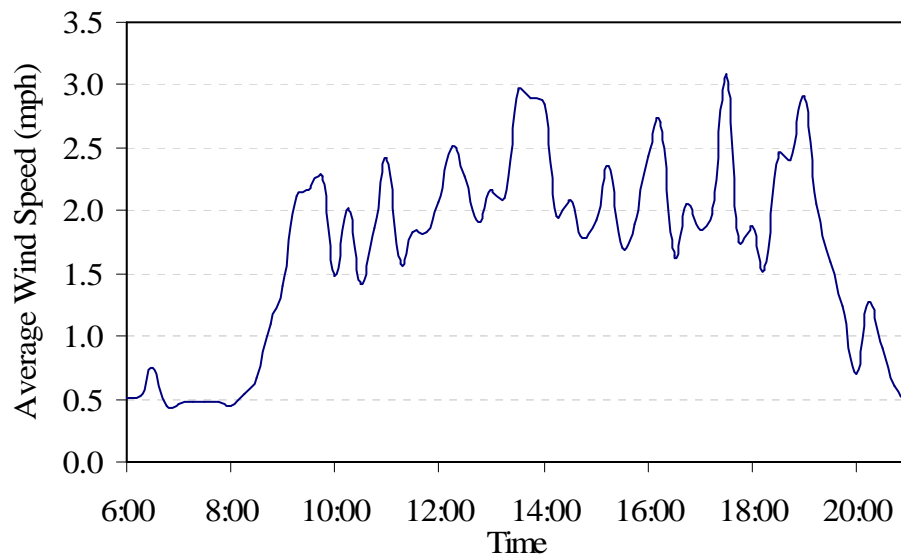
Figure 3.10 – Average wind speed at BT-54 on July 16, 2008
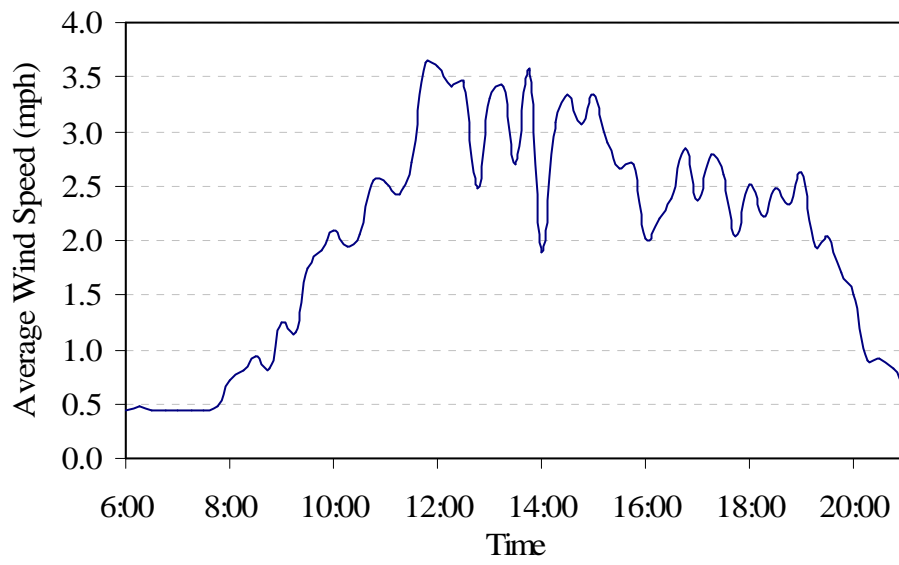
Figure 3.11 – Average wind speed at BT-54 on July 17, 2008
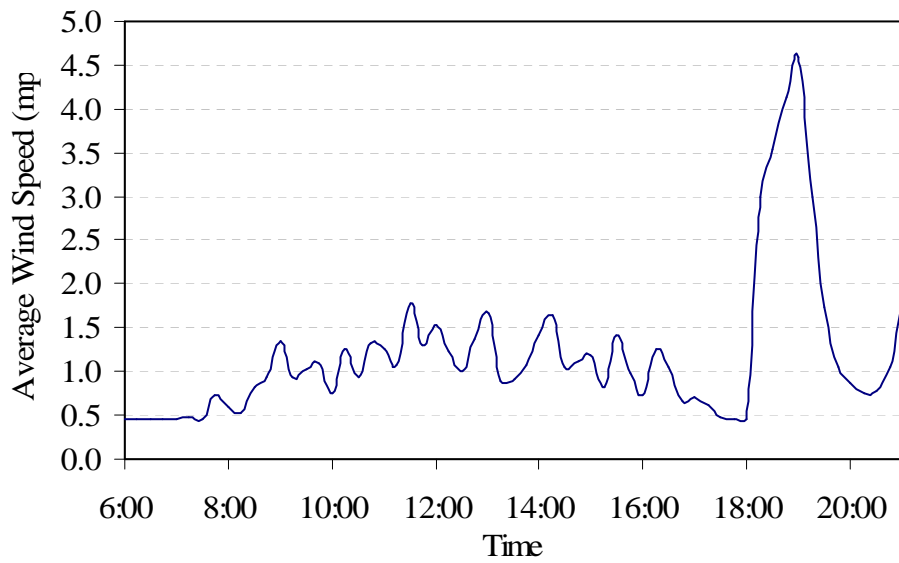
Figure 3.12 – Average wind speed at BT-54 on July 22, 2008

Internal and External temperature measurements were made at 15 minute increments throughout the presented days, at the locations shown previously in Figure 3.4 and 3.5. Temperature contours present the data in the most efficient way such that temperature gradients at midspan can be compared at various times throughout the day in question. Because MATLAB® (2006) cannot plot contours for inconsistent data points using the standard subroutines, a subroutine called "gridfit" (D'Errico, 2005) was used. The subroutine takes the sparse or irregular data, and converts it to a smooth surface. The smooth surface can then be plotted as a contour by MATLAB's® (2006) standard subroutines. The subroutine has many options that can be selected by the user, such as the interpolation method; the triangular interpolation method was chosen in this case. Further details on the subroutine, the algorithms used and the efficiency of "gridfit" (D'Errico, 2005) can be found within the text of the subroutine, and in Keim and Herrmann (1998). The temperature contours were plotted at 9:00 am, 12:00 pm and 3:00 pm for each of the three days and are shown in Figures 3.13, 3.14 and 3.15.
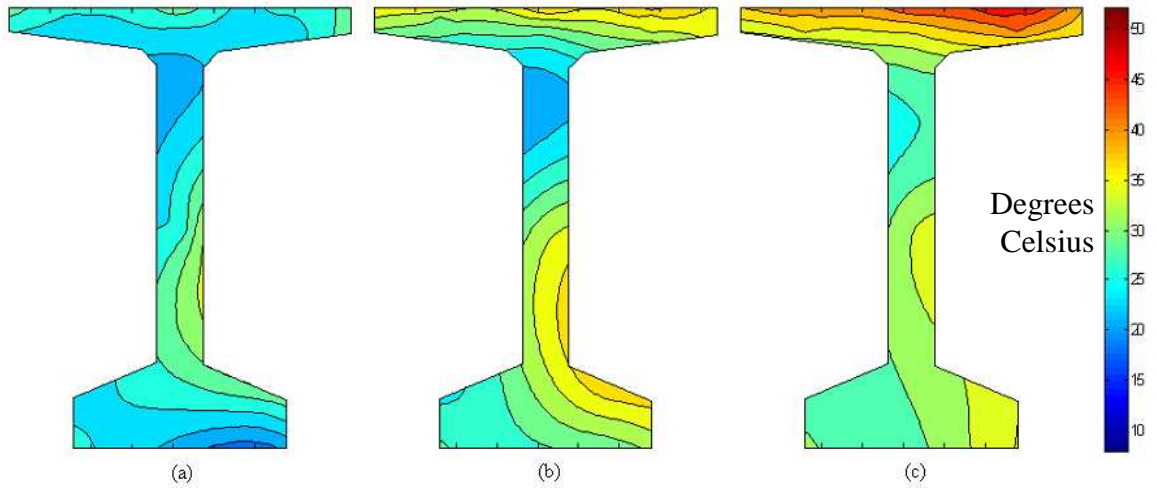
Figure 3.13 – BT-54 temperature contours at midspan on July 16, 2008 at (a) 9:00 am (b) 12:00 pm (c) 3:00 pm
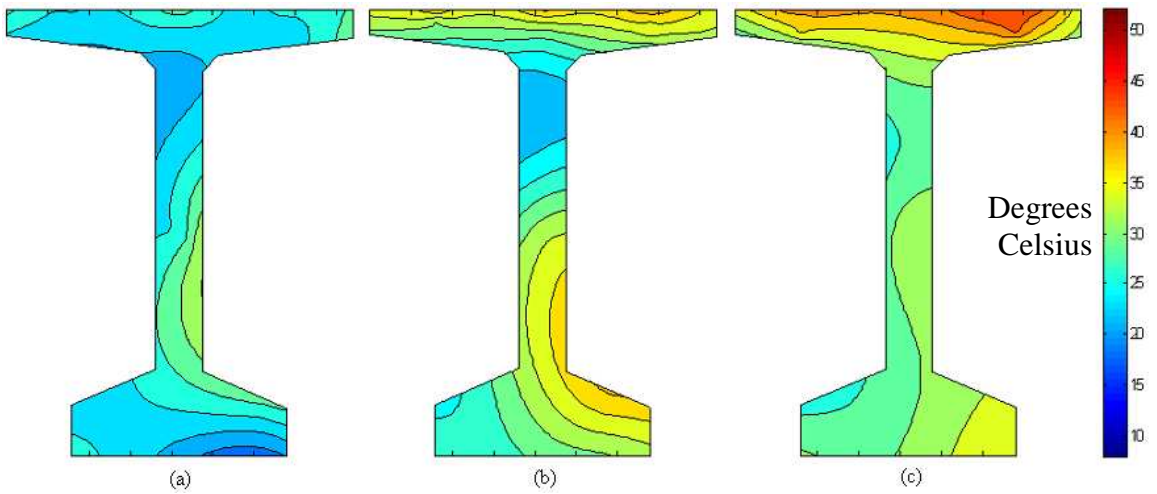
Figure 3.14 – BT-54 temperature contours at midspan on July 17, 2008 at (a) 9:00 am (b) 12:00 pm (c) 3:00 pm
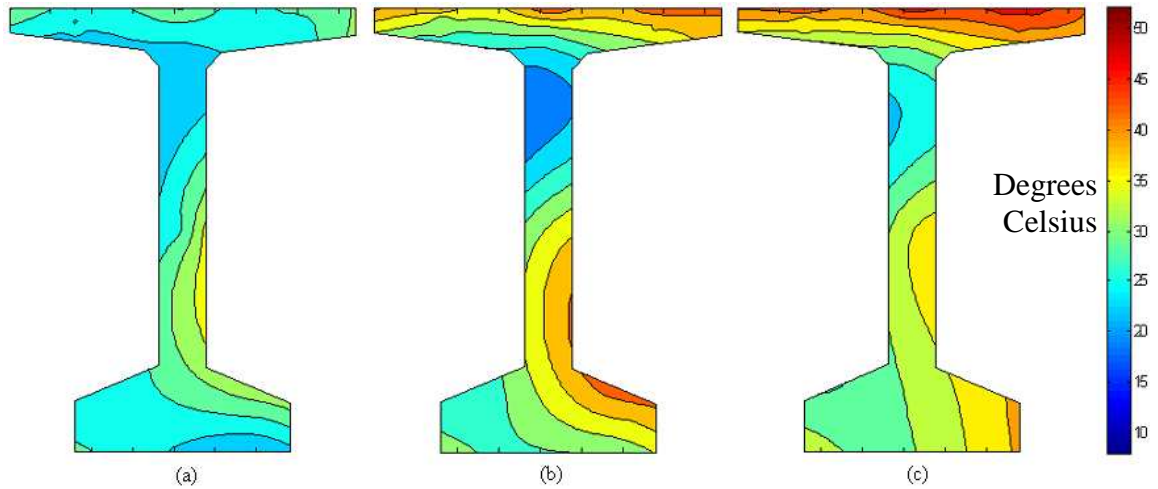
Figure 3.15 – BT-54 temperature contours at midspan on July 22, 2008 at (a) 9:00 am (b) 12:00 pm (c) 3:00 pm

The string potentiometer measurements determined the additional sweep and camber due to thermal effects throughout the day and were taken at 5 minute increments. The measured additional sweep and camber throughout the day from the differential heating of the BT-54 is shown for July 16, 2008, July 17, 2008 and July 22, 2008 in Figures 3.16, 3.17 and 3.18, respectively.
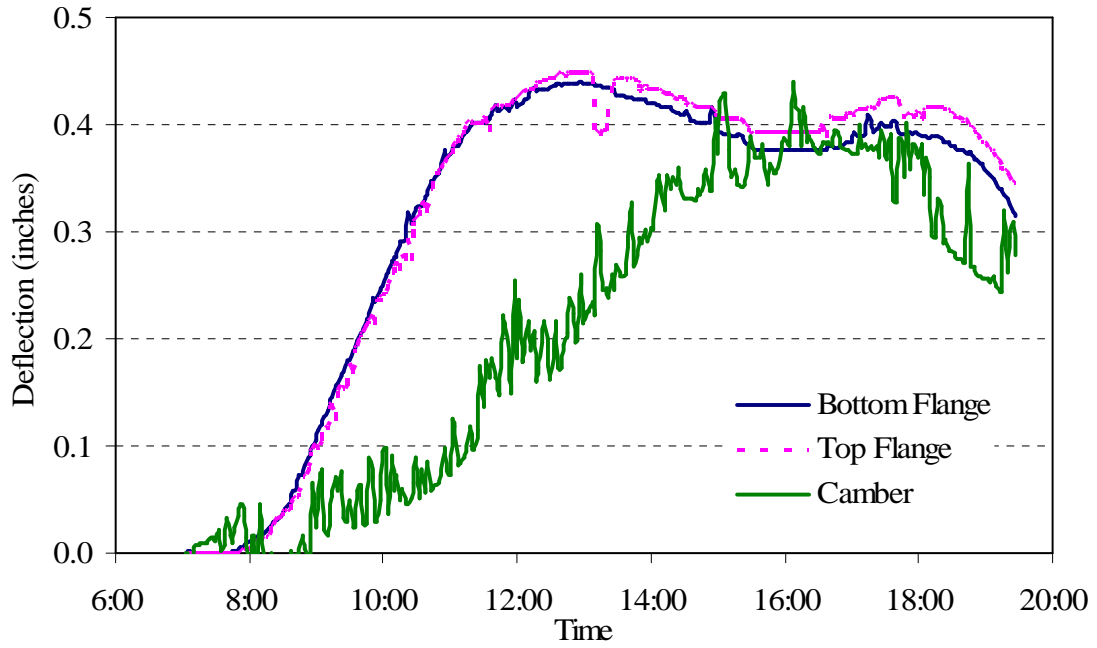
Figure 3.16 – BT-54 camber and sweep for July 16, 2008
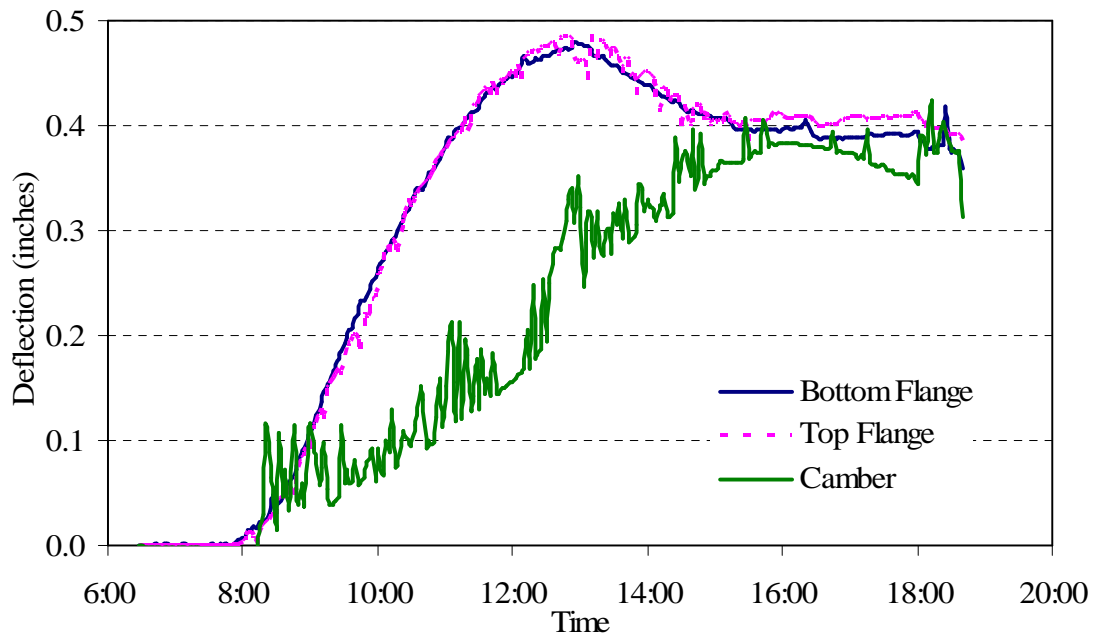
Figure 3.17 – BT-54 camber and sweep for July 17, 2008
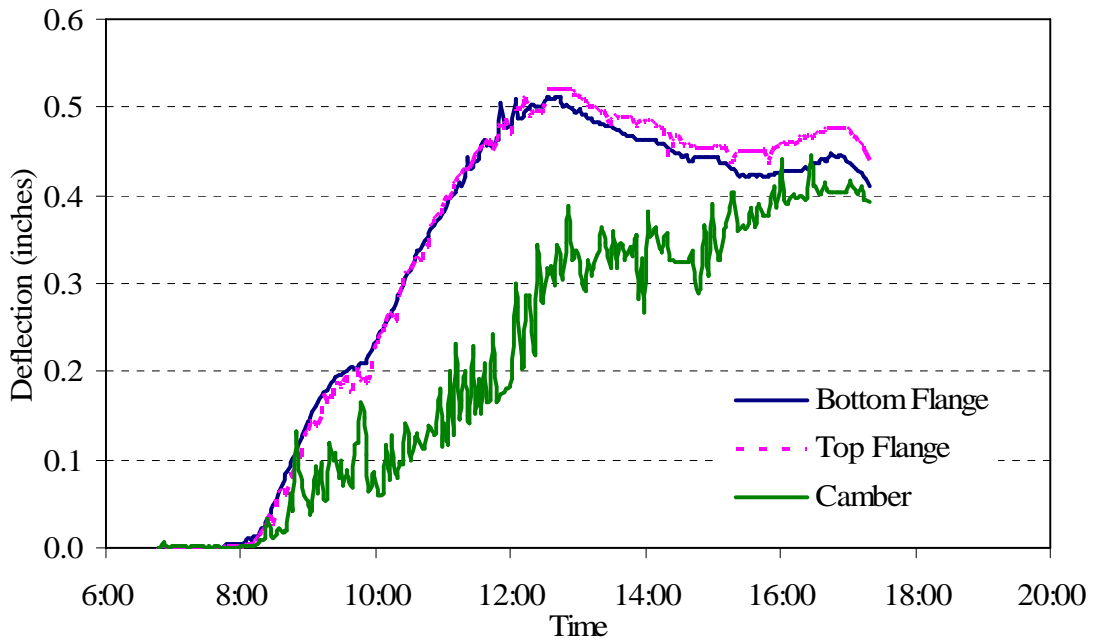
Figure 3.18 – BT-54 camber and sweep for July 22, 2008

The sweep data shown in Figures 3.16 through 3.18 indicated a maximum additional sweep in the range of 0.4 in. to 0.6 in. (10 mm to 15 mm). The PCI Bridge Design Manual (2003) tolerance for sweep is 1/8 in. (3.2 mm) per 10 ft. (3 m) of girder length which gives for the 101-ft. long BT-54 a maximum allowable girder sweep of 1.2625 in. (32 mm). The additional 0.6-in. sweep from thermal effects should not be considered negligible. The additional sweep from thermal effects on the BT-54 tested was in the range of 31% to 48% of the maximum allowable sweep in the girder. This was significant because a girder that is approaching the maximum allowable sweep could significantly surpass the allowable maximum when being erected at the bridge site, due to neglect of consideration to the potential for additional thermal sweep.

Furthermore, the sweep data presented in Figures 3.16 through 3.18 showed that the girder sweep went from its initial condition to a maximum sweep in a time frame of four hours for all cases. Additionally, the rapid increase was initiated as soon as the sun began to rise. Therefore, any stability failure attributed to the effect of thermal sweep from solar radiation would most probably occur within the first hours after sunrise.

The data also showed for this case, that the rotation of the girder due to thermal effects was minimal. The displacement of the top flange and bottom flange was shown in Figures 3.16 through 3.18. The top and bottom flange displacements were about equal throughout the mornings as the girder went from its initial conditions to the maximum thermal sweep condition. It was only in the afternoon when the top and bottom flange displacements began to differ. Even at that point in the day, the difference in top and bottom flange displacement resulted in rotations of the girder that were less than 0.001 radians.

CHAPTER 4

LATERAL-TORSIONAL BUCKLING EXPERIMENTAL SETUP

4.1 Objectives

To determine the behavior of prestressed concrete flexural members with respect to lateral-torsional buckling, the six aforementioned rectangular prestressed concrete beams were tested to determine the behavior for a simple geometry. Additionally, a BT-54 bridge girder specimen was tested to study the lateral-torsional buckling behavior of prestressed concrete flexural members with a more complex geometry with realistic bridge end support conditions.

4.2 Experimental Setup

Experimental methods were particularly important for the lateral-torsional buckling experiments on prestressed concrete beams. A typical beam flexure experiment would involve supporting the beam on a pin-support on one end and a roller-support on the other. The vertical load would then be applied from above via a hydraulic ram rigidly attached to a frame. For lateral-torsional buckling experiments, or any sway-permitted experiment, the load must be permitted to translate with the specimen, remain vertical (in the direction of gravity) and not provide restraint to deformation of the specimen. Failure to properly apply the load might either restrain or magnify lateral motions which would lead to incorrect determination of buckling loads. Incorrect experimental results would result in poor calibration of analytical procedures and result in poor design recommendations.

Different solutions to the load application problem were proposed throughout the literature. The most accurate to method would be to apply actual gravity load using water or sand. However, logistics and safety concerns arise at higher load levels. Another potential loading methodology (Stoddard, 1997) would be to constantly update or make adjustment to the load frame during the experiment; however, significant error could be introduced during the procedure, and the time for one experiment would be dramatically increased. Instead, Yarimici et al. (1967) designed a mechanism referred to as a "gravity load simulator". The gravity load simulator is an unstable mechanism that maintains a vertical load when the specimen experienced lateral translation. The gravity load simulator mechanism was implemented effectively in sway-frame testing of three story building frames (Yarimici et al., 1967), lateral-torsional buckling of steel wide-flange cross-sections (Yura and Phillips, 1992) and lateral-torsional buckling of polymer composite I-shaped cross-sections (Stoddard, 1997).

4.2.1 Gravity Load Simulator

The initial geometry and the deformed geometry of the gravity load simulator in Figure 4.1 and 4.2 shows the behavior of the gravity load simulator when a test specimen would require the load point to translate with the specimen. The gravity load simulator consisted of two incline members, a base, a rigid triangular frame and a hydraulic ram. All of the components were connected with pins which created an unstable mechanism. Therefore, the line of action of the load must always pass through the instantaneous center of rotation for equilibrium to be maintained. To utilize the gravity load simulator, the test specimen must span above the gravity load simulator such that the simulator would pull down on the specimen via a load frame.
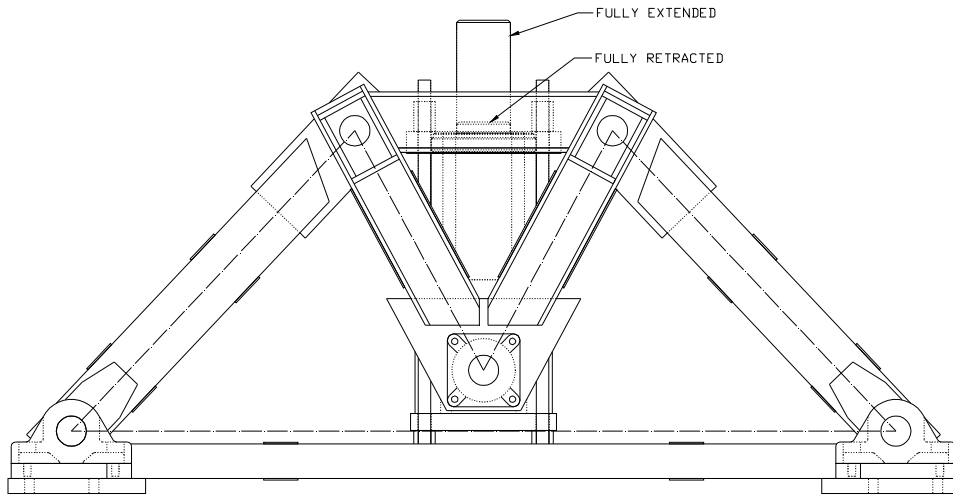
Figure 4.1 – Gravity load simulator
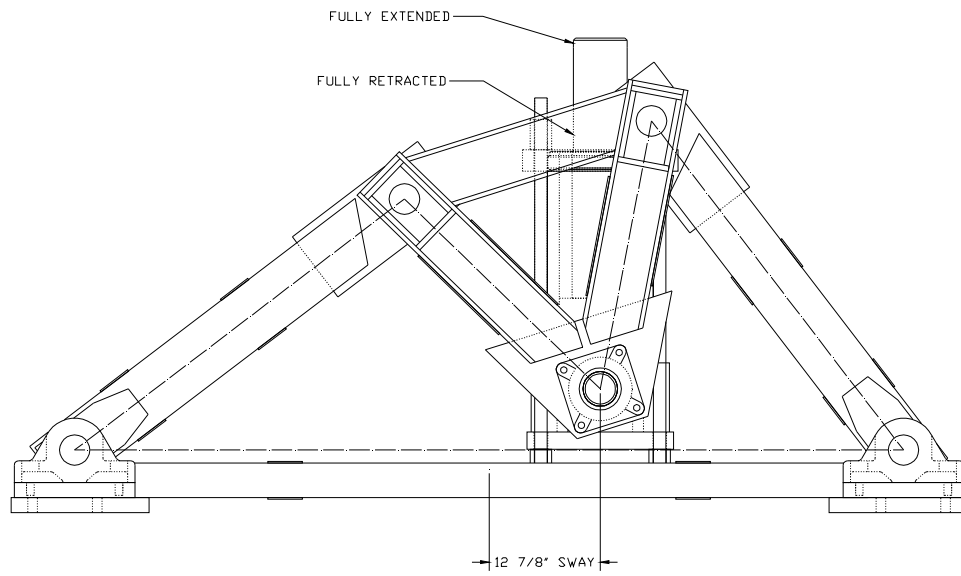
Figure 4.2 – Gravity load simulator in displaced configuration

A gravity load simulator was designed and fabricated to load the six rectangular prestressed concrete beams and the BT-54 girder specimen. The design was based on the ability of the gravity load simulator to achieve a load of 300 kips (1334 kN) to ensure that the BT-54 girder specimen would either buckle or fail in flexure before reaching the capacity of the gravity load simulator. Furthermore, the gravity load simulator was designed to accommodate a sway of 12.875 in. (32.7 cm) in. either direction. In theory, the design of the gravity load simulator's geometry was such that the center pin that connected the hydraulic ram to the rigid triangular frame would maintain the same elevation through the entire range of translation for the gravity load simulator. However, it was impossible to attain geometry such that the pin would coincide exactly with a horizontal line. Therefore, the line of action of the ram deviated from vertical as presented in Figure 4.3. The selected design geometry produced a maximum deviation angle for the line of action equal to 0.006 radians (0.344 degrees) at the extreme limits of the gravity load simulator. If the gravity load simulator was limited to a sway of 8 in. (20.3 cm), the maximum deviation angle for the line of action would be 0.00129 radians (0.074 degrees). A photograph of the gravity load simulator used for the experiments is shown in Figure 4.4. The detailed design is discussed and presented in Appendix B.
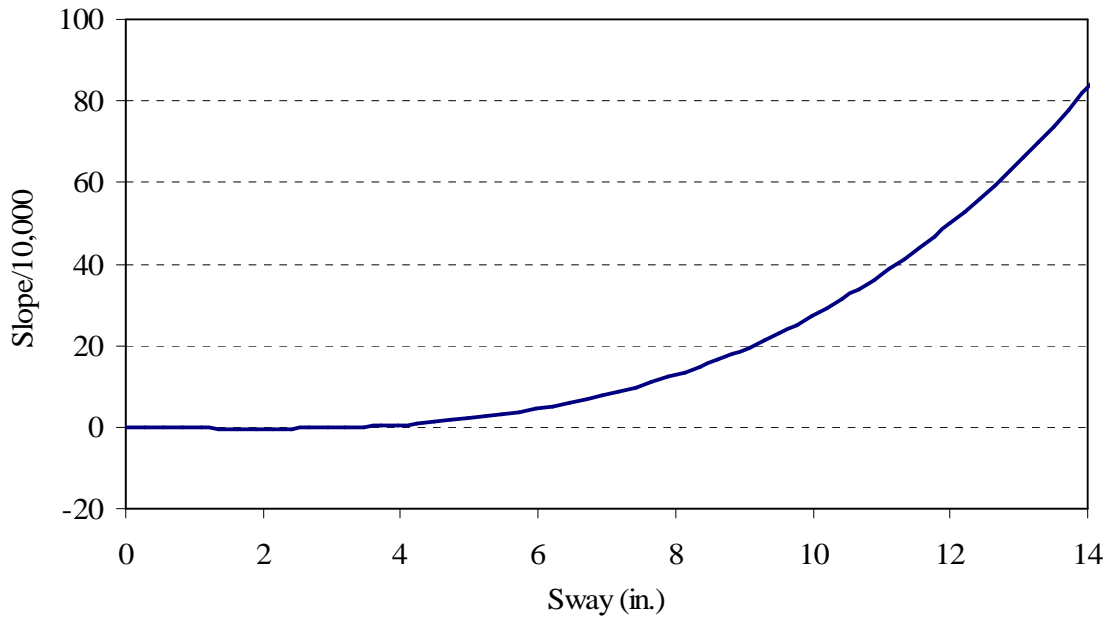
Figure 4.3 – Load deviation from vertical as a function of sway
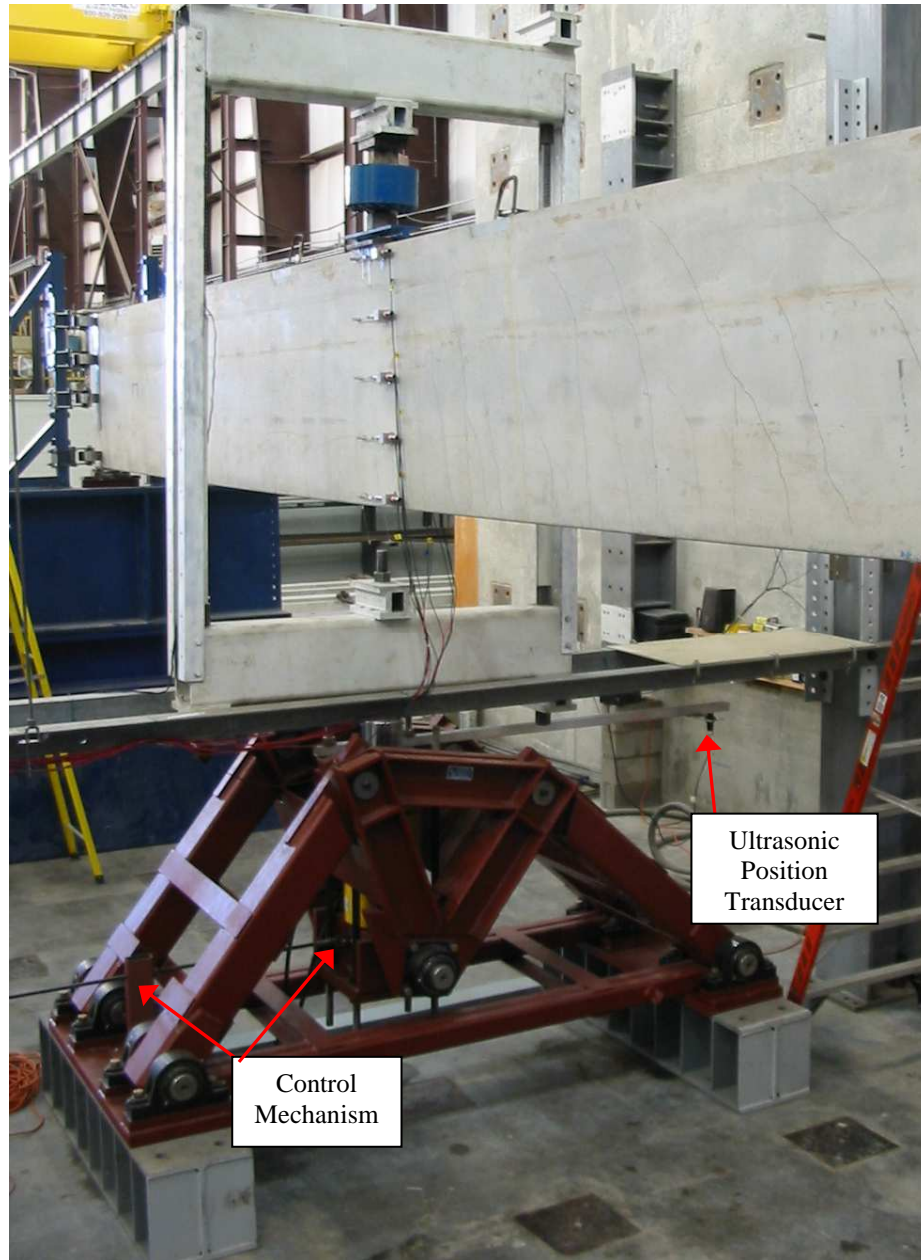
Figure 4.4 – Gravity load simulator in displaced configuration during an experiment

<u>4.2.1.1 Gravity Load Simulator Control Mechanism</u>

The intended behavior of the gravity load simulator was to allow the hydraulic ram to translate laterally while the hydraulic ram remained vertically oriented. The unstable mechanism that the gravity load simulator was based on would inherently provide that behavior given the assumption that the self-weight of the components were negligible. Due to the high capacity required for the experiments, the self-weight of the components were not negligible which caused the hydraulic ram angle to sway slightly from perfectly vertical until the angle was large enough to counteract the horizontal component of the self-weight of the gravity load simulator. The only position in which the hydraulic ram remained perfectly vertical was in the exactly undeformed position when the self-weight of the gravity load simulator did not create a horizontal component of force. Furthermore, at higher load levels, the magnitude of the error in load angle would reduce because the force being transferred through the hydraulic ram would be larger, and, therefore, the magnitude of the required error angle would decrease and still result in the equilibrium horizontal component.

A control mechanism was design for the gravity load simulator to remove the error angle from the effect of the self-weight of the gravity load simulator. The control mechanism caused the gravity load simulator to be a stable mechanism. Essentially, the mechanism consisted of a threaded rod attached to the center pin location where the base of the hydraulic ram was attached via a lubricated ball joint to allow free rotation of the threaded rod. The threaded rod was also threaded through a nut that was attached through structural components to the base plate of the gravity load simulator resulting in a self-reacting system. As the threaded rod was turned, the center pin location would

107

move allowing for the control of the gravity load simulator's position, and, thus, the angle of the applied load. Detailed design drawings of the control mechanism are shown in Figure B.17 through B.20 of Appendix B.

Because the addition of the control mechanism removed the automatic ability of the gravity load simulator to apply vertical load, the angle of load angle was monitored during the experiments in real-time so the position of the gravity load simulator was updated while the specimens were being loaded. To accomplish the acquisition of the load application angle, a long, stiff member was connected to the top of the hydraulic ram extending perpendicular to the angle of the applied load. At the end of the extension members, at 60 in. (152.4 cm), a Migatron RPS-401 self-contained ultrasonic position transducer was attached. The ultrasonic position transducer was used to measure the distance from an arbitrary, rigid, smooth and level surface because if there was a slight change in angle from vertical of the hydraulic ram, the ultrasonic position transducer would detect it. Furthermore, such a sensor was the only sensor capable of monitoring of this type because as the gravity load simulator translated, the sensor translated as well, while maintaining a measurement from the same reference datum. The string of a string potentiometer would remain attached at a specific location; therefore, when the gravity load simulator translated, the string would become diagonal and the reference displacement would no longer be the same. Figure 4.4 shown previously labels the control mechanism and the ultrasonic position transducer. The behavior of the ultrasonic position transducer load angle measurement method is depicted in Figure 4.5.
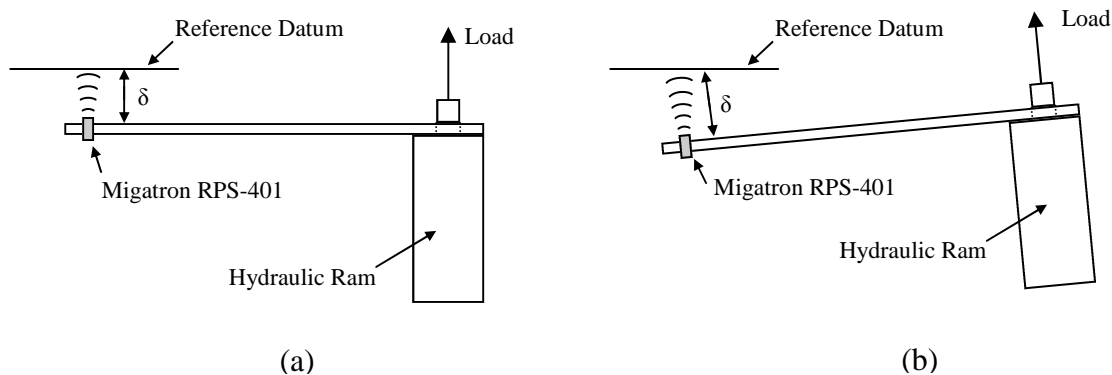
Figure 4.5 – Ultrasonic position transducer load angle measurement method in (a) vertical load configuration (b) angled load configuration

4.2.2 Rectangular Specimen Supports

To replicate classical theory, the end supports required the construction of lateral supports that restrain the beam in torsion, vertical translation and lateral translation at the ends, but allowed for rotation about the vertical axis. Furthermore, 1.5 in. (3.8 cm) rollers were used at both bearing supports to allow for axial lengthening of the beam specimens during the experiment and to provide symmetry about midspan. The rollers provided the restraint to vertical translation while a rigid frame was constructed and placed on both sides of the beam, at both ends, to restrict horizontal translation. The rigid frame was designed, constructed and used for the experiments of Kalkan (2009). For free rotation about the vertical axis, four 17 kip (75.6 kN) high-capacity casters were attached to the rigid frame at equal spacing along the depth of the test specimen. The caster wheels were forged steel with tapered roller bearings. The torsional restraint was provided by the couple created by the casters being spacing along the depth of the beam

109

on both sides. A photograph of the end supports for the rectangular tests is shown in

Figure 4.6.

Figure 4.6 – Rectangular setup end supports

Because the beam specimens must span longitudinally above the gravity load

simulator, the support conditions required the use of built-up pedestals to attain an

appropriate height that allowed for the proper function of the gravity load simulator. The

built-up pedestal was constructed of steel and concrete members that were remaining at

the laboratory from previous research activities. A photograph of the built-up pedestal is shown in Figure 4.7.

Figure 4.7 – Rectangular setup build-up pedestal

4.2.2.1 Secondary Restraint System

A restraint system was implemented because of the safety concerns of a potential sudden lateral stability failure. Due to the secondary objective of unloading and reloading the beam specimens to investigate the possibility of buckling load degradation, restraint was required during post-buckling to prevent excessive damage to the beam specimens. The system was composed of threaded rods connected to the beam specimen and to a rigid column support. The length of the threaded rods was controlled by the use

of turnbuckles; therefore, the threaded rods were continuously loosened so that there was zero restraint before significant post-buckling deflections occurred. A photograph of the system is shown in Figure 4.8. Strain gauges on the rods were calibrated so that the maximum restraint load was maintained at less than 10 lbs. (44.5 N). The turnbuckles were released to produce zero load at each displacement-load increment.

Figure 4.8 – Secondary restraint system

4.2.3 BT-54 Specimen Supports

For the stability experiment on the BT-54 girder specimen, the support conditions were different than for the rectangular experiments. In actual bridge conditions, there are not perfect pins located at the supports. In many cases, state Department of

Transportations use elastomeric bearing pads for the supports. In the case of the girder collapse in Arizona, elastomeric bearing pads were used at the bearings (Oesterle et al., 2007). The use of elastomeric bearing pads at the end supports added additional variables to the experimental study. Instead of the end boundary conditions being ideally rigid in the vertical direction, there was now a stiffness of the bearing pad in the vertical direction that needed to be considered. Furthermore, the torsional restraint at the ends of the specimens that was provided by the coupling effect of the casters attached to a rigid frame in the rectangular test setup was instead achieved by utilizing the relatively large width of the bottom flange of the BT-54 that provided torsional restraint. However, the torsional restraint provided by the bottom flange was not perfectly rigid because of the bearing pad stiffness; therefore, the bearing pad rotational stiffness was considered as well. The bearing pads also had relatively low stiffness properties in shear in both the longitudinal direction and transverse direction. The shear stiffness of the elastomeric bearing pads were relatively low compared to the vertical because the internal steel shims were not engaged during a shear or transverse loading. The minimal shear stiffness is beneficial in bridge design because it allows for free deformation in the longitudinal direction when the bridge is in service so that the girders are not stressed due to thermal strain behavior. In the case of the stability experiments, the shear stiffness in the transverse direction was also an important consideration because rotation of the girder caused a lateral component of force on the bearing pad.

4.2.3.1 Bearing Pad Properties

The bearing pads used for the BT-54 girder specimen experiment were 24 in. (61.0 cm) long, 14 in. (35.6 cm) wide and 2 7/8 in. (7.3 cm) thick steel reinforced

elastomeric bearing pads with four internal steel shims. The nomenclature for describing the axes of the bearing pad and the stiffness parameters is depicted in Figure 4.9.
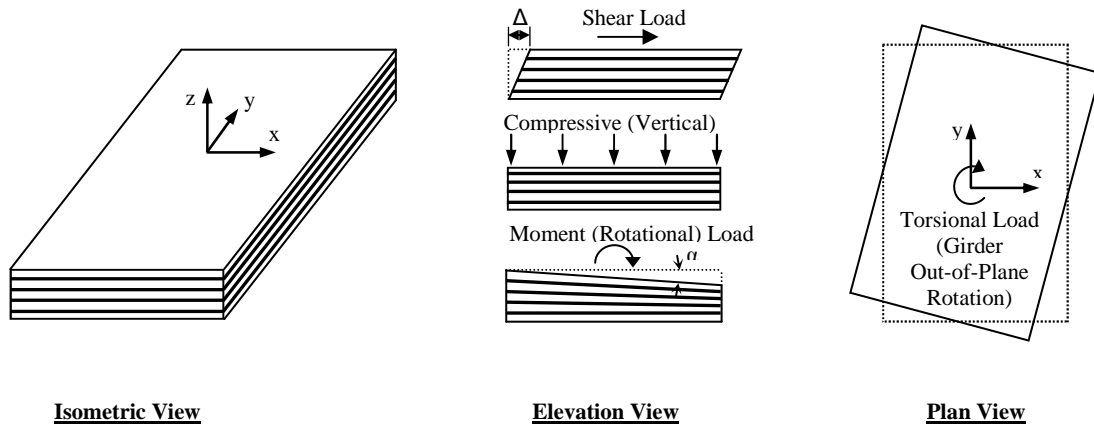
Figure 4.9 – Bearing pad axes

A bearing pad was tested to obtain the vertical stiffness of the bearing pad, K_z. The experimental testing consisted of placing a 1/8 in. (3.2 mm) sheet of steel that was larger in dimensions than the bearing pad on top of the bearing pad. On top of the thin sheet of steel, a stiffened wide flange stub with larger dimensions than the bearing pad was placed. The wide flange stub acted to distribute the load from the Baldwin test machine to the bearing pad so that the load was distributed uniformly. The thin sheet of steel was used below the wide flange stub to remove the effect of the small holes that were in the flanges of the wide flange stub. The displacement of the bearing pad in the axial direction was measured by using four dial gages located at the four corners of the bearing

114

pad. The total displacement was taken as the average of the displacements at the four

corners. The experimental setup was similar to that used in Consolazio et al. (2007). A

photograph of the test setup is shown in Figure 4.10. The resulting stress versus

displacement plot is shown in Figure 4.11.
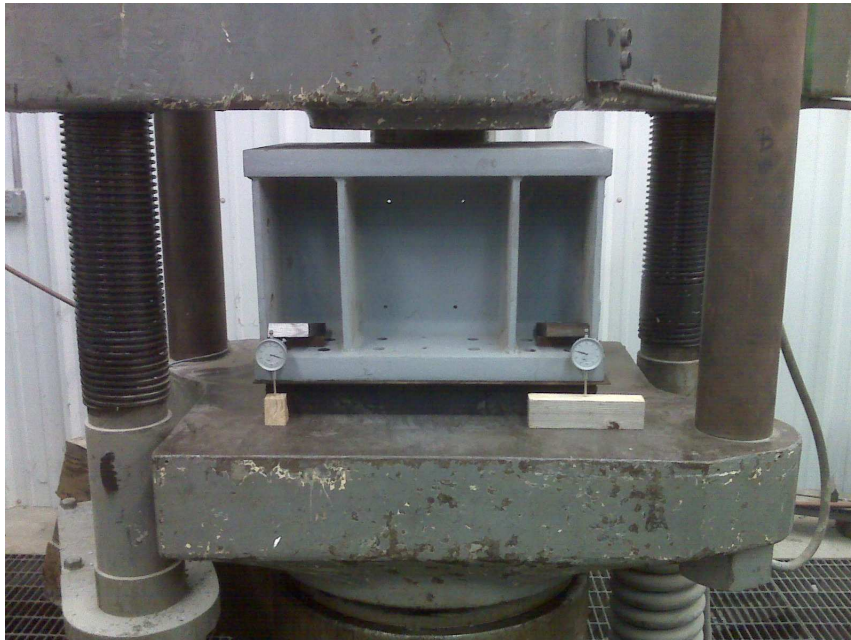
Figure 4.10 – Bearing pad axial stiffness testing
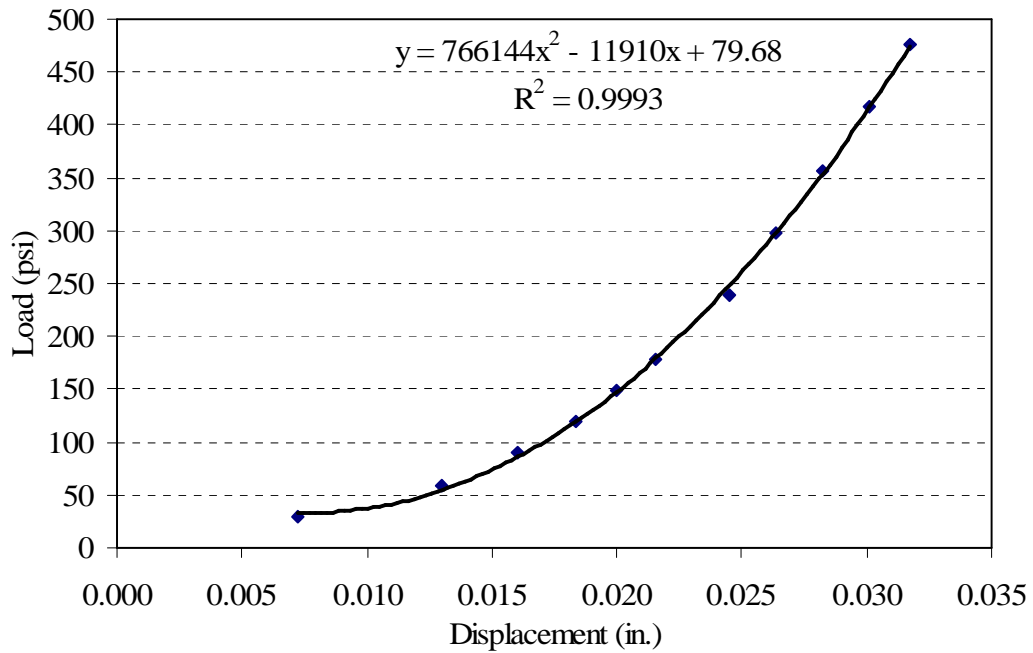
Figure 4.11 – Stress versus axial displacement of bearing pad 2nd-order polynomial fit

The load versus axial displacement plot in Figure 4.11 shows a nonlinear relationship because of the relatively low loads on the bearing pad. The nonlinearity stemmed from the settling of the thin elastomeric lips around the bearing pad edges that serve as a gasket seal in actual bridge condition to prevent water from seeping under and above the bearing pad. The bearing pad was only tested to 160 kips (711.7 kN) because 160 kips (711.7 kN) would well exceed the allowable load for the test setup. The behavior of the bearing pad was approximated by assuming a second-order polynomial fit as shown by the trend line in Figure 4.11. A linear approximation is shown in Figure 4.12 and considered the self-weight of the girder was 72 kips (320 kN) or 214 psi (1.48

MPa); therefore, the bearing pad initially underwent 36 kips (160 kN) or 107psi (0.74 MPa) before testing began.

The linear fit equation shown on the graph:
$$y = 26600x - 389.1$$
$$R^2 = 0.9853$$
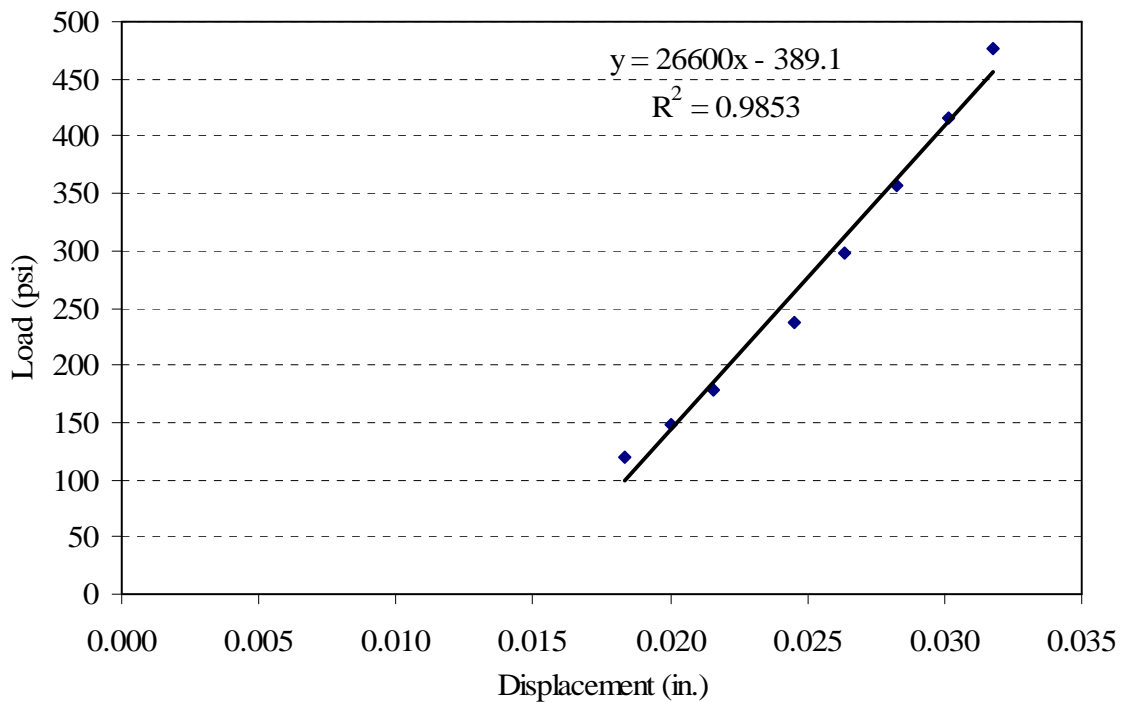
Figure 4.12 – Load versus axial displacement of bearing pad with linear fit

The axial stiffness values of the bearing pad resulted from the experimental testing; however, the rotational stiffness parameters had to be approximated analytically by assuming a rigid plate on the top of the bearing pad and applying a unit rotation which resulted in a triangular stress distribution. The approximation was determined to be accurate by using the results from Yazdani et al. (2000) and applying the approximation. Yazdani et al. (2000) used the equations from AASHTO (1996) to determine the effective

compressive modulus of the bearing pad based on the shape factor of the bearing pad and the shear modulus of the bearing pad. A finite model was created of the bearing pad including the steel shim plates. The vertical stiffness, K_z, of the bearing pad from the finite model was 5950 kip/in (1042 MN/m) and the rotational stiffness, K_{ry}, was 287,000 kip-in/rad (32,400 kNm/rad). Applying the rigid plate rotation approximation to determine the rotational stiffness, K_{ry}, from the axial stiffness, K_z, resulted in an approximate rotational stiffness, K_{ry}, of 285,600 kip-in/rad (32,270 kNm/rad) which was very close to the result given by the finite model. However, the nonlinear vertical stiffness at low loads meant that the true rotational stiffness of the bearing pad was different. A more accurate prediction was implemented in the analytical study which is presented in Chapter 7 and 8.

Additional error in the prediction of axial stiffness and rotational stiffness was apparent due to the poor flatness of the bottom flange of the BT-54. Figure 4.13 designates the orientation of the girder. Figure 4.14 shows the support at the east end of the girder, and Figure 4.15 shows the support at the west end of the girder before testing. The figures showed that the significant amount of curvature of the bottom of the flange caused a non-uniform bearing. The majority of the self-weight of the girder was resting in the middle of the bearing pad; in the case of the east support, the southern edge of the bottom flange was not in contact with the bearing pad at all.
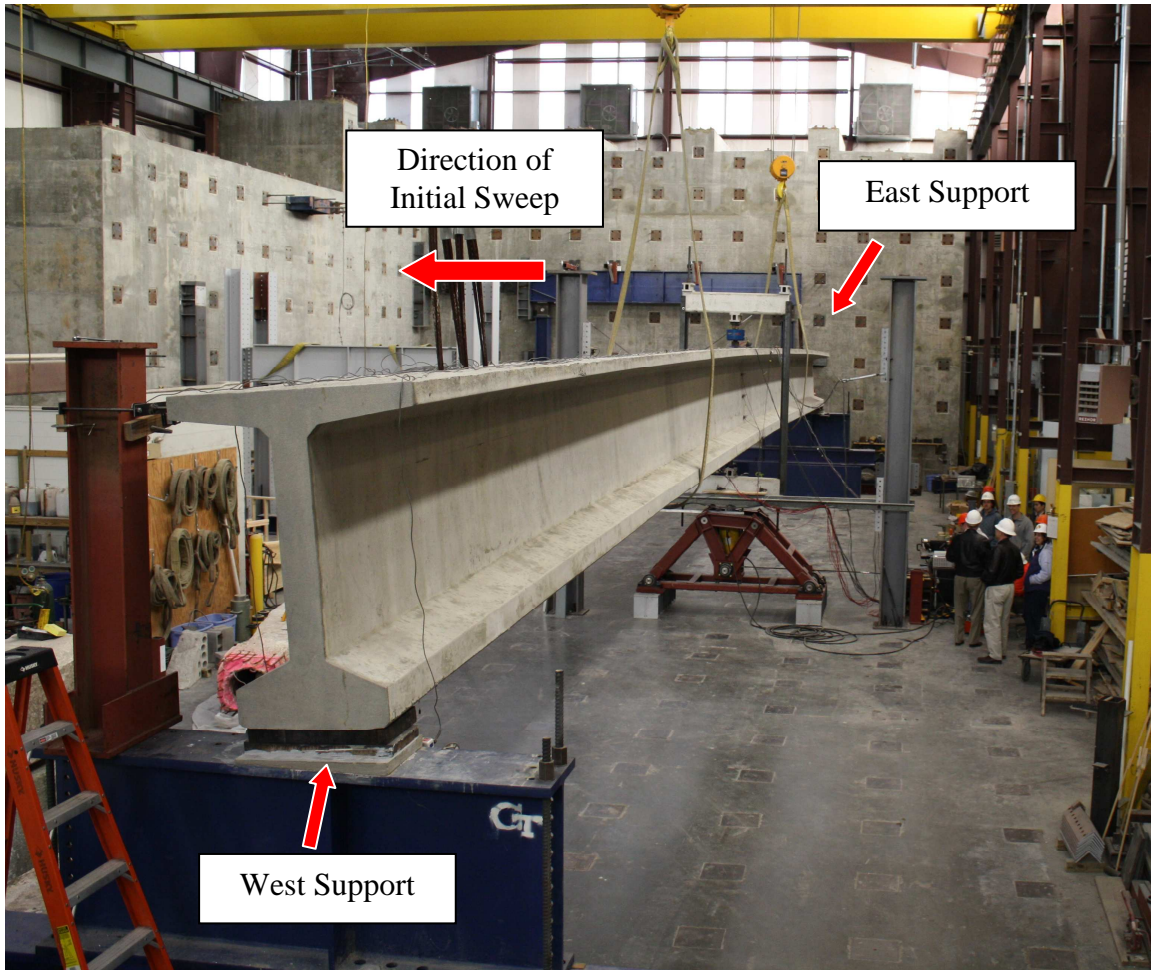
Figure 4.13 – BT-54 girder orientation

Figure 4.14 – East bearing pad support conditions
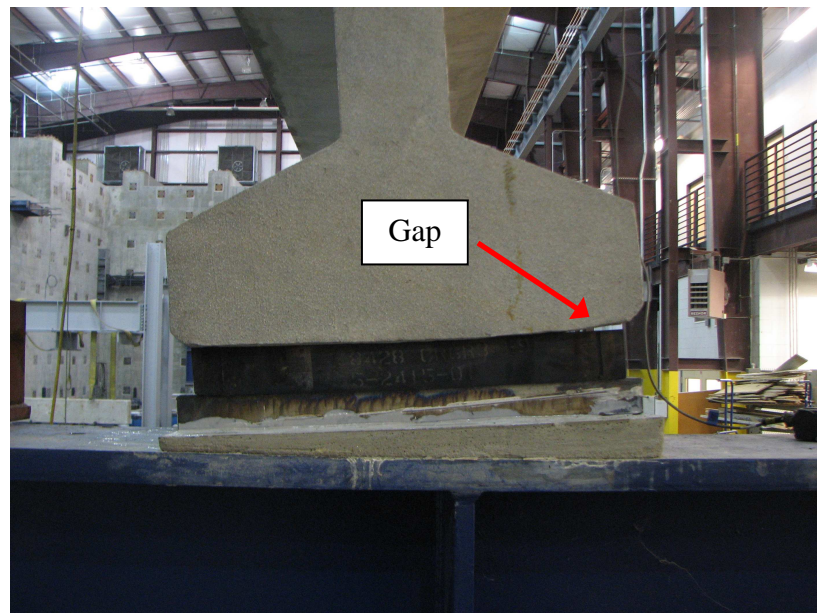
Figure 4.15 – West bearing pad support conditions

Initial testing of the BT-54 was performed to a load level of 29 kips (129 kN), and there was a significantly higher rotation at each of the supports than was anticipated due to the roundness of the bottom flange. Therefore, a retrofit was performed on the bottom flange at each of the supports before the entire load was applied to the girder in an attempt to remove the effect of the roundness of the bottom flange. The retrofit strategy was to use a high-strength, high-modulus epoxy on the bottom flange to create a level surface. The retrofitted bottom flange is shown in Figure 4.16. The effects of the roundness of the bottom flange are discussed in detail in Chapter 7.

Figure 4.16 – High-modulus epoxy leveling retrofit

4.2.3.2 Secondary Torsional Restraint System

Ideally, the torsional restraint was to be provided by the couple created by the width of the bottom flange. Because of uncertainties in the bearing pad behavior due to the non-uniform bearing, the lack of flatness in the bottom of the flange bearing on the bearing pad, and the nonlinear stiffness properties of the bearing pad at low loads, a secondary torsional restraint system was designed and implemented. The system involved a column segment at each support, adjacent to the BT-54 girder specimen. The columns were located on the north side of the girder, or the side towards which the girder was leaning due to the initial support rotation. Attached to the column segment was a load cell device that was implemented so that when contact was made between the top flange and the load cell device, torsional restraint was provided and the restraint load was known. The load cell device consisted of a built-up bracket that held the cylindrical, through-hole load cell in place and a threaded rod with both a threaded 1.5 in. (3.8 cm) diameter steel ball and a nut. The girder's top flange was to contact the steel ball, thus putting the threaded rod in compression. The nut that was on the threaded rod restrained the threaded rod from passing through the hole in the load cell, thus activating the load cell. A diagram of the device is shown in Figure 4.17.
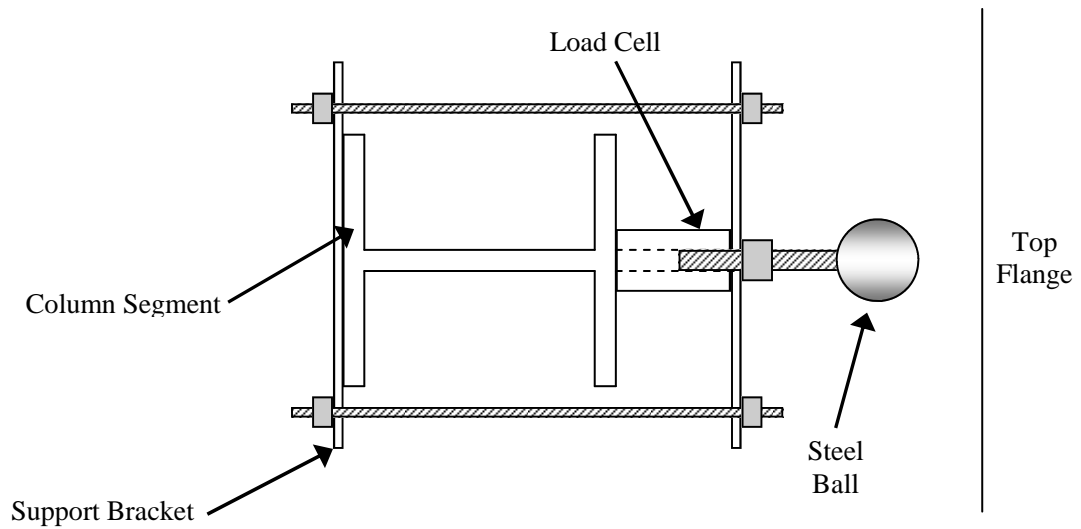
Figure 4.17 – Torsional restraint system load cell device

Initially, there was a gap between the top flange and the steel ball so that the behavior with only torsional restraint provided by the bottom flange was observed. If the rotation at the ends was substantial, the torsional restraint system was to be used. If the rotation at the end was close to what was predicted, the rod was backed-off so that there was always a gap between the top flange and the steel ball. Additionally, the torsional restraint system provided additional safety to the test setup. If the BT-54 girder specimen were to overturn suddenly, it would come into contact with the torsional restraint system which would provide some support. A photograph of the torsional restraint system is shown in Figure 4.18.
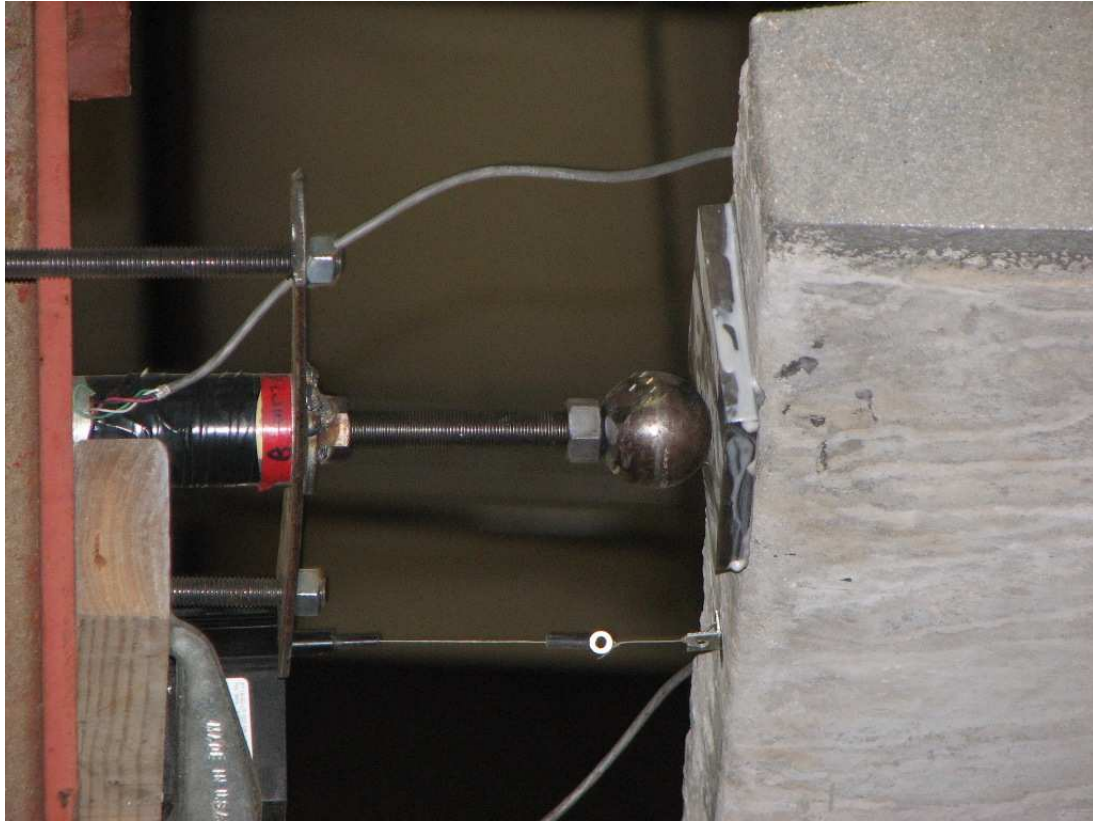
Figure 4.18 – Torsional restraint system

4.2.4 Load Application Details

It was required to apply the load provided by the gravity load simulator to the top of the beam specimen at midspan. Because the gravity load simulator was located below the beam specimen and applied the load to the specimen by pulling down on specimen, it was necessary to construct a frame that transferred the load from the gravity load simulator around the specimen, to the top of the specimen. Furthermore, the frame had to be constructed such that the geometry did not obstruct the specimen when the specimen wanted to rotate during the experiment.

To accomplish the load transfer, a rod from the gravity load simulator was connected through the center of a stiffened rectangular structural tube that was perpendicular to the specimen that was above. A high-capacity threaded rod was connected to each end of the rectangular structural tube. The high-capacity rods were connected to a similar stiffened rectangular structural tube that spanned perpendicular and above the beam specimen. Essentially, a rectangular frame was created. In addition to the high-capacity thread rods, 3x3x5/16 structural angles were connected to the rectangular structural tubes. The high-capacity threaded rods were sufficient for the tensile load being transferred, but were not stiff enough to restrain the frame from racking; therefore, the structural angles were used to restrain the shear racking behavior of the frame. The load was transferred from the top rectangular structural tube via a pin. The pin was parallel to the specimen's longitudinal axis which allowed the specimen to freely rotate about the load application point. The pin's length was small enough that the assumption of a point load would be adequate; however, it could have been considered a uniform load over a small distance. Figure 4.19 is a photograph of the rectangular load transfer frame with the important components labeled. Additionally, Figure 4.20 is a photograph of the pin at the load application point and Figure 4.21 is a diagram of the behavior of the pin during loading.
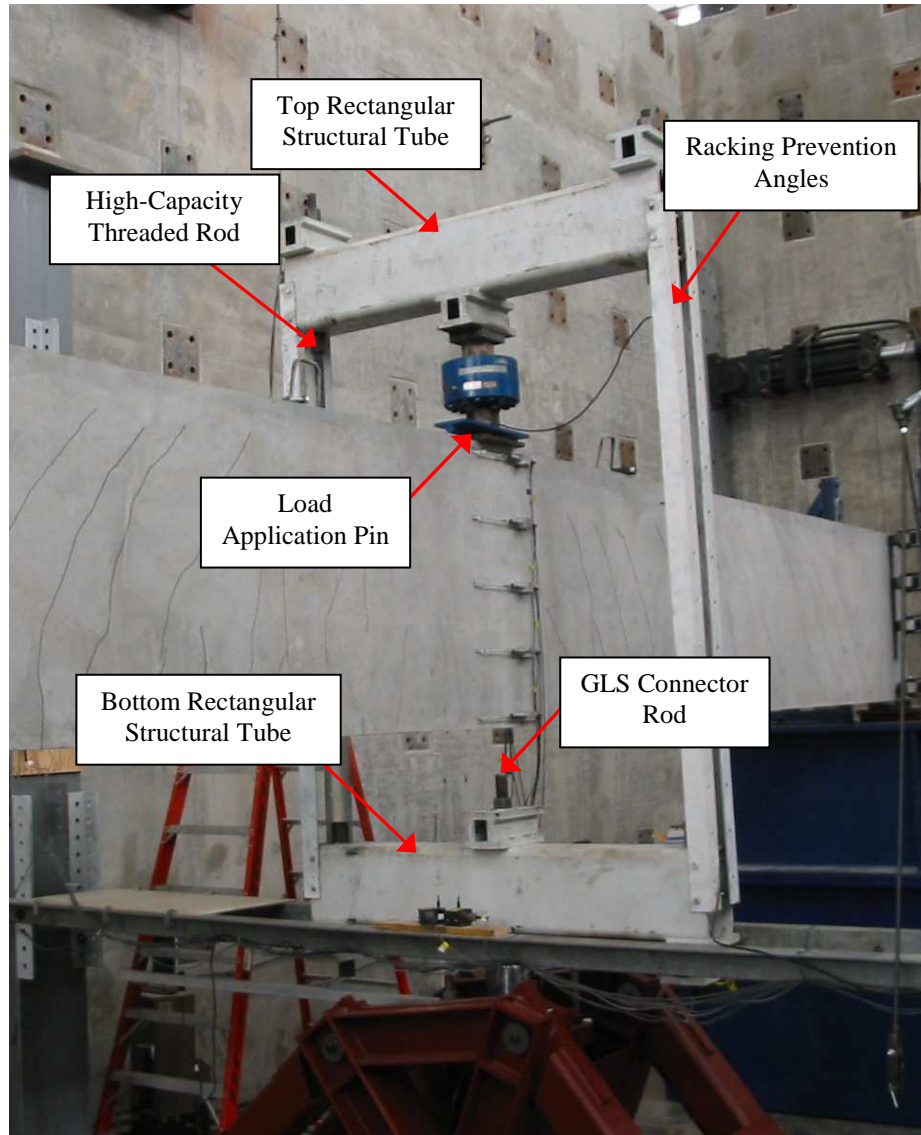
Figure 4.19 – Load transfer frame

Figure 4.20 – Load application pin
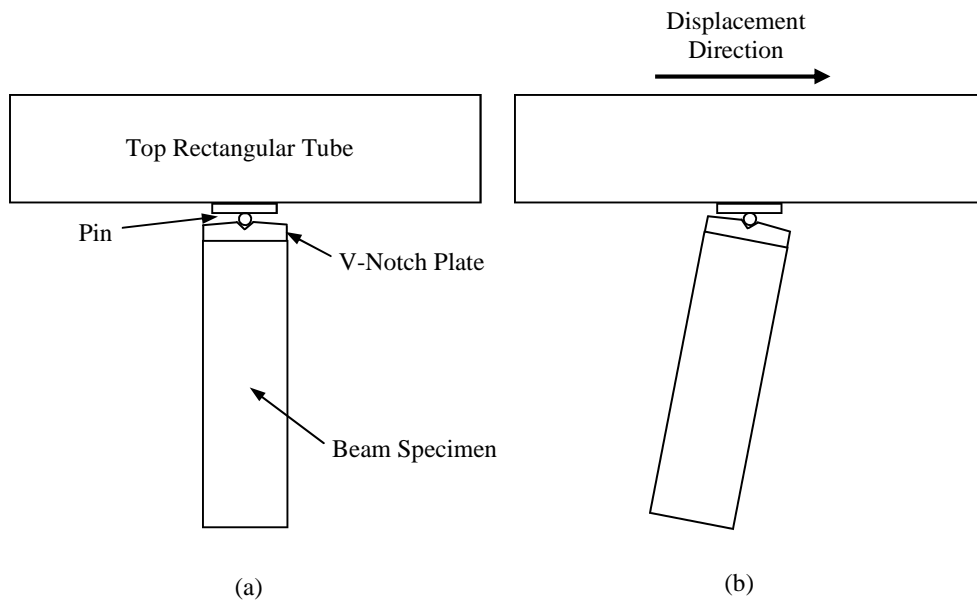
Figure 4.21 – Behavior of load application pin during loading (a) undeformed
configuration (b) deformed configuration

4.2.5 Experimental Measurements

All of the data acquisition was done using National Instruments hardware and the National Instrument's data acquisition software Labview. For all experiments, an Interface 200 kip (890 kN) load cell was mounted on the top member of the load transfer frame, attached to the load application pin, to measure the applied load on the specimens as was shown in Figure 4.20.

Strain measurements were made by positioning ten RDP linear variable displacement transducers (LVDTs) on the surface of all seven of the specimens at midspan. The LVDTs were mounted with a gage length of 10 in. (25.4 cm) so that the strain could be calculated from the displacement output. The ten LVDTs were positioned five on either side of the cross-section so that linear interpolation through the cross-section was made to determine the depth of the compression zone, the angle of the neutral axis and the extent of the biaxial behavior. Furthermore, the LVDTs were mounted on the specimens at a small distance off of the actual surface; therefore, interpolation was required to determine the actual surface strain. For the six rectangular beam specimens, the LVDTs were mounted at 1.5 in. (3.8 cm), 10.75 in. (27.3 cm), 20 in. (50.8 cm), 29.75 in. (75.6 cm) and 38.5 in. (97.8 cm) from the bottom of the beam cross-section. A photograph of the mounted LVDTs for the rectangular beam specimens is shown in Figure 4.22. The LVDTs were mounted in a slightly different configuration for the BT-54 girder specimen. The LVDT locations for the BT-54 girders specimens are presented in Figure 4.23.

Figure 4.22 – LVDT locations for rectangular specimens

12 1/2"

12 1/2"

LVDTs

12 1/2"

13 3/8"

2" from
Bottom
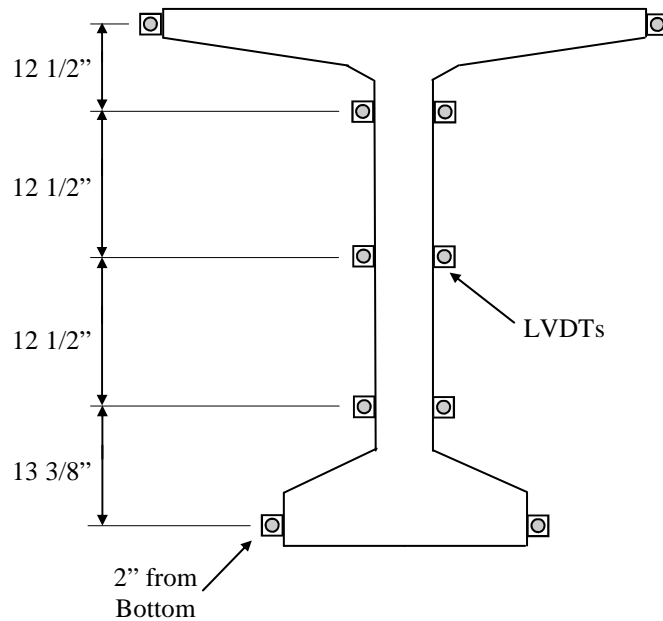
Figure 4.23 – LVDT locations for BT-54 girder specimen

4.2.5.1 Deflection and Rotation Measurements

The method to measure vertical displacements, horizontal displacements and

rotation of the specimens during testing was extremely important. Measuring the

displacements of the specimens using string potentiometers or LVDTs with respect to a

reference datum would provide inaccurate results because the specimens rotate and

translate during loading; therefore, the line of action of the measuring devices would no

longer be perpendicular to the specimen and would instead be measuring a diagonal

distance. To overcome this problem, past researchers (Turvey, 1995; Turvey and Brooks,

1996) attempted to measure the displacements by using an elaborate frame that

circumscribed the specimen and translated with the specimen. The measurement devices

then measured the horizontal and vertical displacements of the frame with respect to a

130

reference datum. In theory, the method provided accurate measurements of the vertical and horizontal displacements; although there were experimental error issues that arose when previous researchers used the method. The major objection to the method was that the rotation was unable to be determined using the method, and, therefore, an independent measurement of rotation had to be done using an inclinometer or theodolite.

For this research, due to the ease of implementation, string potentiometers were used to measure horizontal and vertical displacements. A post-processing procedure that was used by Stoddard (1997) was implemented in this research to correct the measured displacements. The details of the calculation procedure from Stoddard (1997) are included because the methodology was expanded on by the author in Section 4.2.5.1.1 for the case when the test specimens have initial rotation and in Section 4.2.5.1.2 for the case when the test specimens have unequal flange widths. Initial rotation and unequal flange widths were not considered in the calculation procedure by Stoddard (1997).

The correction method was based on the geometry of three string potentiometers and the coupling of the data to arrive at the correct displacements and rotation solution. The geometry and nomenclature used is shown in Figure 4.24. All potentiometers were attached rigidly to an independent frame to measure the displacements during testing. Two vertical string potentiometers and five horizontal string potentiometers were used. Although only one vertical and two horizontal string potentiometers were necessary for the post-processing procedure, the post-processing procedure was repeated for all the string potentiometers to get accurate measurement at each measurement location to ensure that the specimens were rotating and translating without the cross-sectional geometry changing significantly.
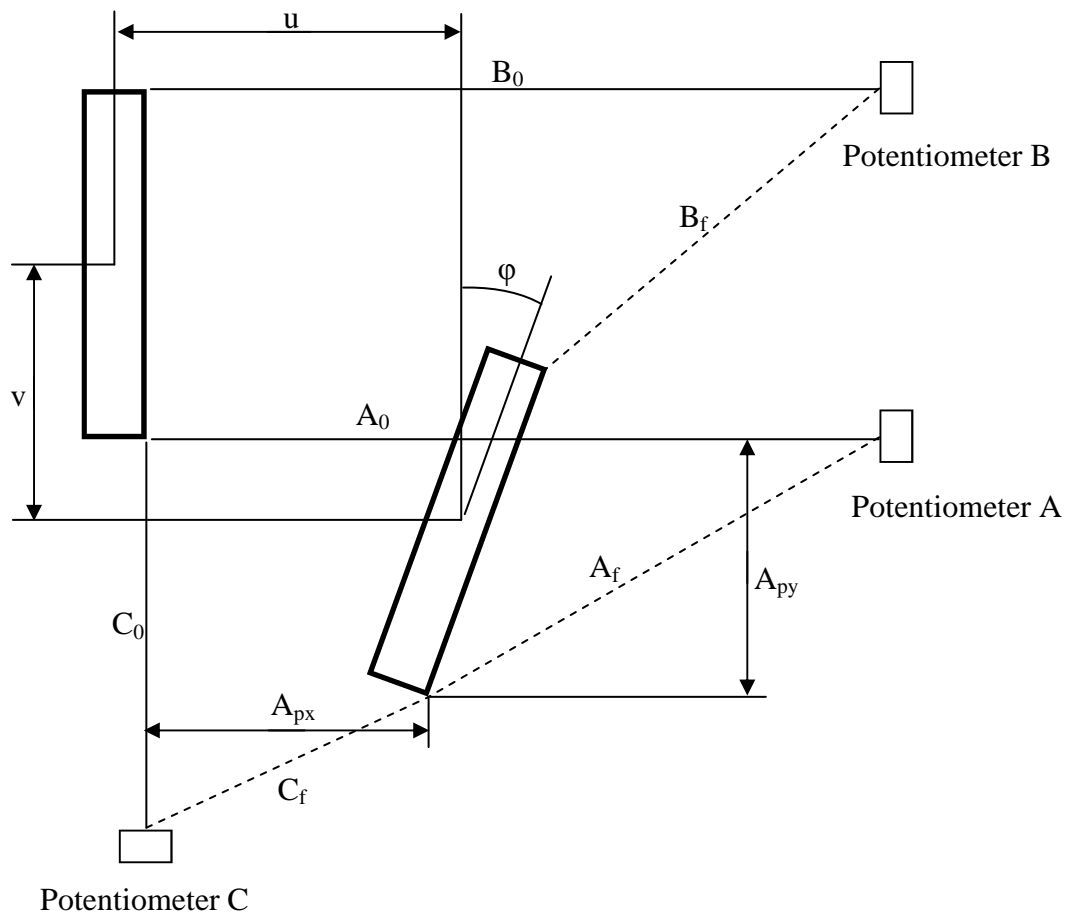
Figure 4.24 – Potentiometer configuration to measure vertical displacement, lateral displacement and rotation for rectangular specimens

The horizontal displacement, A_{px}, and the vertical displacement, A_{py}, was determined by utilizing the measurements from potentiometers A and C (Stoddard, 1997). The initial string lengths for each of the potentiometers had to be recorded prior to the experiments when the strings were still orthogonal. Pythagorean Theorem resulted in the following two equations to solve for the two unknowns A_{px} and A_{py}.

$$\left(A_0 - A_{px}\right)^2 + A_{py}{}^2 = A_f{}^2 \tag{4.1}$$

$$\left(C_0 - A_{py}\right)^2 + A_{px}{}^2 = C_f{}^2 \tag{4.2}$$

Solving Equations 4.1 and 4.2 simultaneously resulted in two roots.

Root Set #1:

$$A_{px} = \frac{K_p + C_0 L_p}{N_p} \tag{4.3}$$

$$A_{py} = \frac{M_p + A_0 L_p}{N_p} \tag{4.4}$$

Root Set #2:

$$A_{px} = \frac{K_p - C_0 L_p}{N_p} \tag{4.5}$$

$$A_{py} = \frac{M_p - A_0 L_p}{N_p} \tag{4.6}$$

where,

$$K_p = -\left(A_f{}^2 A_0\right) + A_0{}^3 + A_0 C_f{}^2 + A_0 C_0{}^2 \tag{4.7}$$

$$L_p = \sqrt{\begin{array}{l} -A_f{}^4 + 2A_f{}^2 A_0{}^2 - A_0{}^4 + 2A_f{}^2 C_f{}^2 + 2A_0{}^2 C_f{}^2 - C_f{}^4 \\ + 2A_f{}^2 C_0{}^2 - 2A_0{}^2 C_0{}^2 + 2C_f{}^2 C_0{}^2 - C_0{}^4 \end{array}} \tag{4.8}$$

$$M_p = A_f{}^2 C_0 + A_0{}^2 C_0 - C_f{}^2 C_0 + C_0{}^3 \tag{4.9}$$

$$N_p = 2\left(A_0{}^2 + C_0{}^2\right) \tag{4.10}$$

The two possible solution sets presented were the two theoretically possible displaced configurations of the displaced specimen. However, only one solution set actually made sense for the experiment. Figure 4.25 shows the two possible solutions which is a similar representation of what was presented in Stoddard (1997). The solution sets mirrored each other about a diagonal line passing from potentiometer C to potentiometer A.

A_f

Potentiometer A

True Solution

A_f

C_f

C_f

Alternative (Unrealistic) Solution
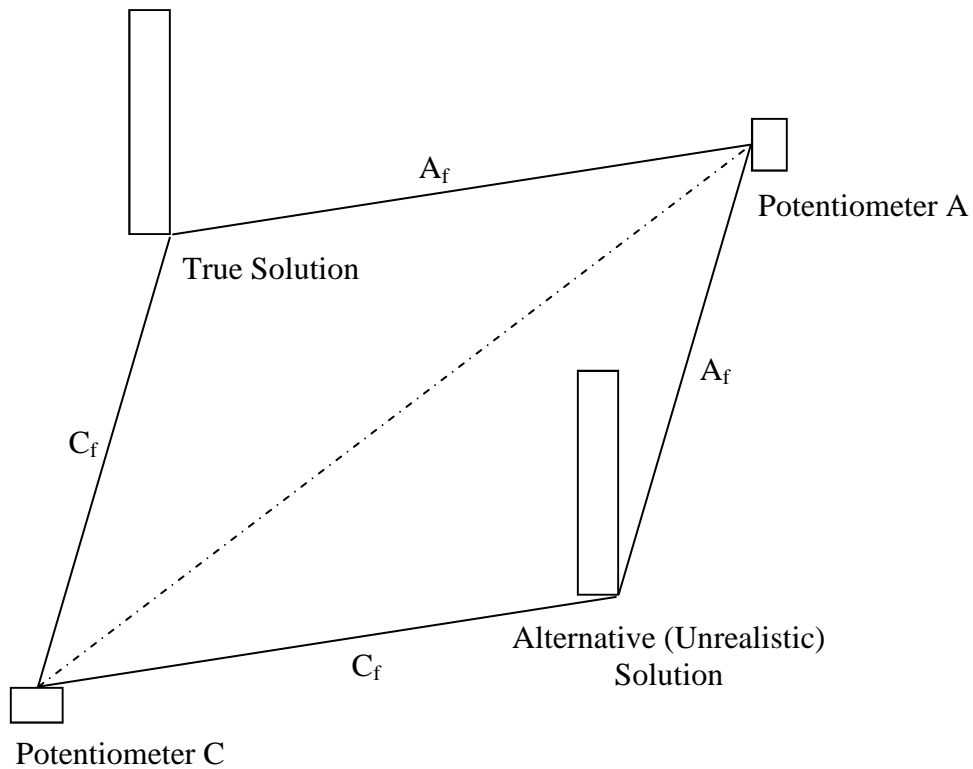
Potentiometer C

Figure 4.25 – Two possible solutions sets

Once the appropriate solution set was selected to determine the horizontal and vertical displacements, the torsional rotation, φ, was determined using the data and dimensions from potentiometers A and B. The height of the cross-section, h, or more accurately, the distance between the two horizontal potentiometers, was also necessary to determine the rotation, φ, of the cross-section. Figure 4.26 shows the required parameters and nomenclature for determining the rotation of the cross-section.
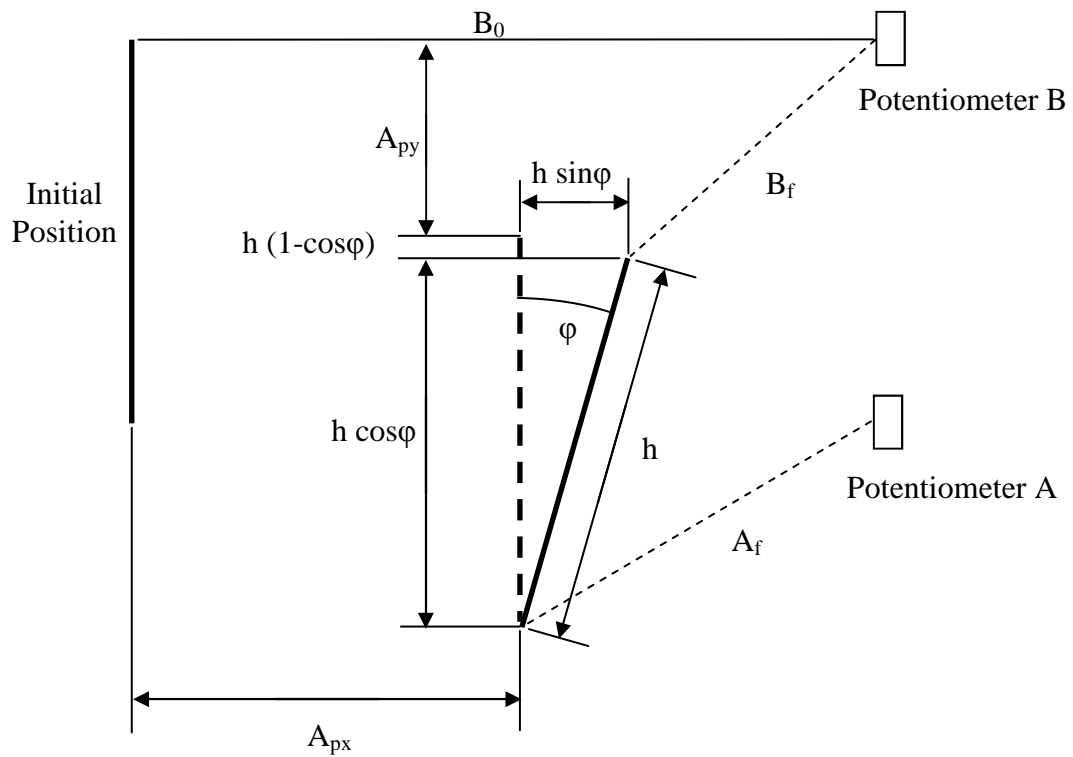
Figure 4.26 – Geometric parameters to determine rotation of cross-section

The following equation was constructed in terms of the parameters in Figure 4.25 in terms of one unknown: the rotation, φ.

$$[A_0 - A_{px} - h\sin\phi]^2 + [A_{py} + h(1 - \cos\phi)]^2 = B_f^2 \qquad (4.11)$$

The rotation, φ, was solved for resulting in two roots. Due to the relatively small rotation angles measured in the experiment, the appropriate root solution for the rotation was as follows.

$$\phi = 2\arctan\left[\frac{R_p + \sqrt{-S_p T_p}}{U_p}\right] \qquad (4.12)$$

where,

$$R_p = 2A_{px}h - 2A_0 h \qquad (4.13)$$

$$S_p = 2hB_f - 2A_{py}h - A_{px}^2 + 2A_0 A_{px} - A_0^2 + B_f^2 - A_{py}^2 \qquad (4.14)$$

$$T_p = -2hB_f - 2A_{py}h - A_{px}^2 + 2A_0 A_{px} - A_0^2 + B_f^2 - A_{py}^2 \qquad (4.15)$$

$$U_p = -A_0^2 + 2A_0 A_{px} - 4h^2 + B_f^2 - A_{px}^2 - A_{py}^2 - 4A_{py}h \qquad (4.16)$$

The displacement or coordinate location of any point of the cross-section could now be determined because the horizontal and vertical displacement of point A was known and the rotation of the cross-section was known.

4.2.5.1.1 Initial Rotation Considerations

The post-processing methodology used by Stoddard (1997) to calculate the actual displacements and rotation using the string potentiometer data needed to be adapted to the specific conditions of the experiments of this research. The procedure presented by Stoddard (1997) assumed that the initial rotation of the cross-section was zero. In the experiments of this research, that was not the case. The solution for the appropriate horizontal and vertical displacements was exactly the same as previously presented. This was because the reference point at the bottom of the cross-section was unchanged by the initial rotation, and, therefore, the coupled simultaneous equations that were solved for the horizontal and vertical displacement was the exactly the same. However, Equation 4.11 which was solved to determine the rotation was changed due to the initial rotation. The altered geometric considerations are shown in Figure 4.27.
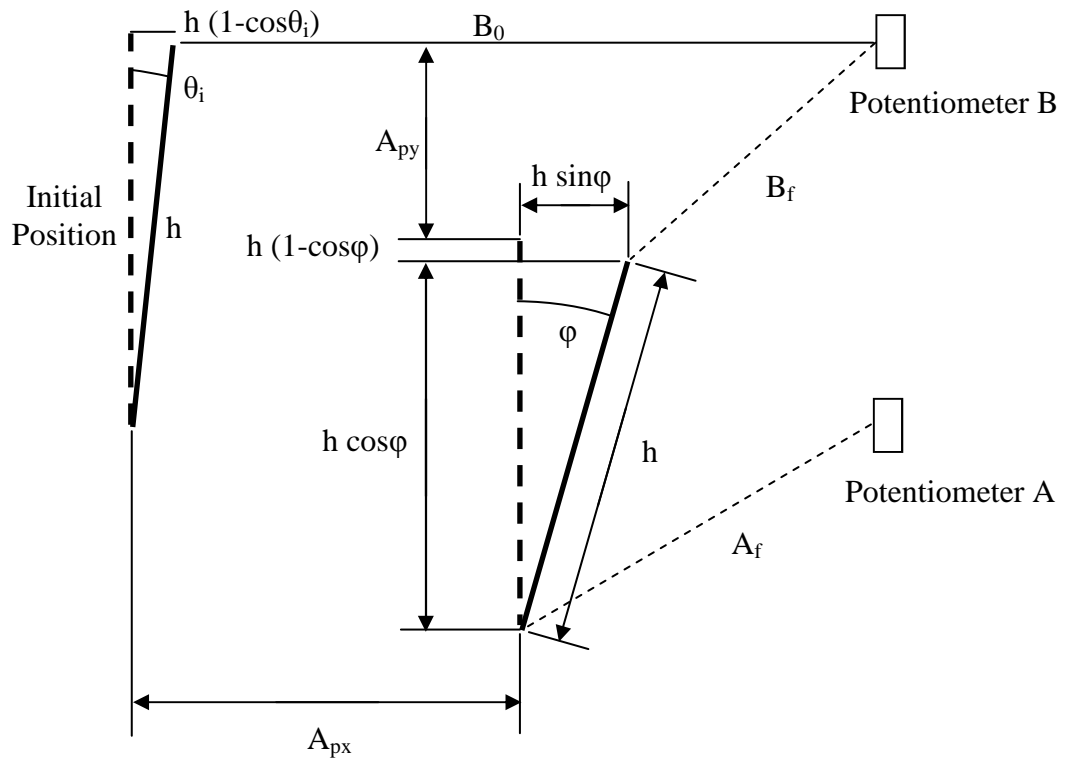
Figure 4.27 – Initial rotation geometric parameters to determine rotation of cross-section

The following equation was constructed in terms of the parameters in Figure 4.26 in terms of one unknown: the rotation, φ.

$$\left[A_0 - A_{px} - h \sin \phi \right]^2 + \left[A_{py} + h \left(\cos \theta_i - \cos \phi \right) \right]^2 = B_f^{\,2} \qquad (4.17)$$

The rotation, φ, was solve for resulting in two roots. Due to the relatively small rotation angles measured in the experiment, the appropriate root solution for the rotation was as follows.

$$\phi = 2\arctan\left[\frac{R_p + \sqrt{-S_p T_p}}{U_p}\right] \qquad (4.18)$$

where,

$$R_p = 2A_{px}h - 2A_0 h \qquad (4.19)$$

$$S_p = 2hB_f - 2A_{py}h - A_{px}^2 + 2A_0 A_{px} - A_0^2 + B_f^2 - A_{py}^2 \\ + \left(1 - \cos^2\theta_i\right)h^2 \qquad (4.20)$$

$$T_p = -2hB_f - 2A_{py}h - A_{px}^2 + 2A_0 A_{px} - A_0^2 + B_f^2 - A_{py}^2 \\ + \left(1 - \cos^2\theta_i\right)h^2 \qquad (4.21)$$

$$U_p = -A_0^2 + 2A_0 A_{px} - 4h^2\cos\theta_i + B_f^2 - A_{px}^2 - A_{py}^2 \\ - 4\left(1 + \cos\theta_i\right)A_{py}h \qquad (4.22)$$

It is important to note that the solution for the torsional rotation was the increment of additional rotation, in addition to the initial rotation; therefore, the change in rotation during the experiment was found as the difference between the total rotation solved for using Equation 4.18 and the initial rotation of the cross-section.

4.2.5.1.2 Unequal Flange Considerations

For the BT-54 lateral-torsional buckling experiment, the effect of unequal flange widths had to be considered in determining the corrected rotations. The procedure that was adapted from Stoddard (1997) was only appropriate for rectangular cross-sections or flanged cross-sections where the flanges had equal widths. Similar to the effect of initial rotation on the post-processing procedure, there was no effect of the unequal flange

widths on the computation of the horizontal and vertical displacements of the reference point. The unequal flange widths only affected the computation of the true rotation of the cross-section. The simplest method to account for the unequal flange widths was to create an equivalent rectangular section that utilized an effective height and effective initial rotation that was based on the actual distance between the horizontal measurement points, the initial rotation and the flange dimensions. The parameters for the effective section are shown in Figure 4.28.
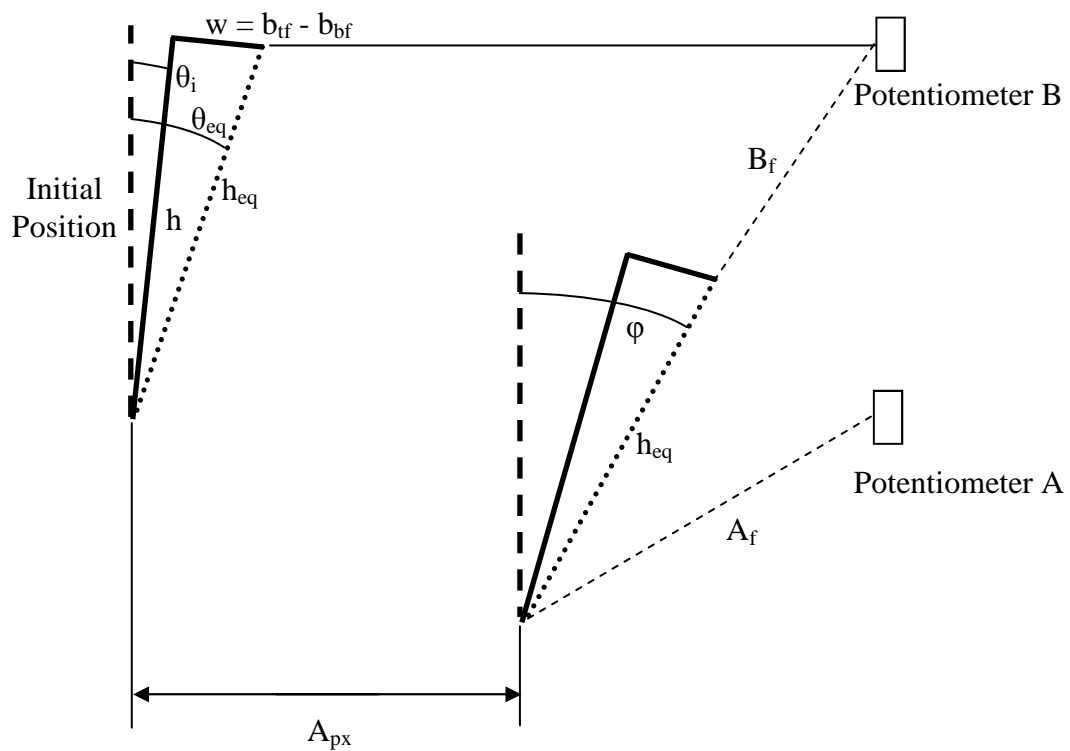
Figure 4.28 – Equivalent section height and initial rotation for unequal flange widths

The calculation procedure was exactly the same as the case of a rectangular cross-section with an initial angle except that the equivalent height, as calculated by Equation 4.23, was used instead of the actual height and the equivalent initial rotation, as calculated by Equation 4.24, was substituted into the computation procedure in place of the actual initial rotation.

$$h_{eq} = \sqrt{w^2 + h^2} \qquad (4.23)$$

$$\theta_{eq} = \theta_i + \arctan\left(\frac{w}{h}\right) \qquad (4.24)$$

4.2.5.2 BT-54 End Support Compliance Measurements

In addition to the load cell in each of the secondary torsional restraint systems, three string potentiometers were used at each end to monitor the rotation at the ends and the compliance of the bearing pad. The configuration of the string potentiometers was one lateral string potentiometer measuring the displacement of the top flange and two string potentiometers measuring the displacement at each edge of the bottom flange. The two bottom flange string potentiometers are shown in Figure 4.29.

Figure 4.29 – String potentiometer layout at end supports beneath the girder

The three string potentiometers at each end were necessary to monitor the rotation and displacements at the ends due to the compliance of the bearing pad so that the relative rotation and displacements at midspan could be determined. Furthermore, it was important to investigate the deformation behavior at the end supports to determine experimentally if the bearing pad compliance had a large effect on the overall behavior. The two vertical string potentiometers would have been sufficient to determine both the rotation at each end and the vertical displacement due to the compression of the bearing pad; however, the bearing pads also had the ability to undergo shear deformation. Therefore, the third, lateral, string potentiometer was implemented such that the rotation, vertical displacement due to the compression of the bearing pad and the horizontal displacement due to the shear deformation of the bearing pad could be determined.

CHAPTER 5

RECTANGULAR BEAM LATERAL-TORSIONAL BUCKLING

EXPERIMENTAL RESULTS

The six rectangular prestressed concrete beam specimens were tested in lateral-torsional buckling using the previously discussed test setup with a concentrated load at midspan. The load versus lateral displacement, load versus rotation and strain data were found to best identify the stability behavior of the beams. Load versus lateral displacement and load versus rotation data indicate when the rate of increase in deformation becomes substantial and, therefore, when the beam had become unstable. Furthermore, the data presented the maximum load achieved for the given geometric and material properties with a given initial imperfection profile. By investigating the strain data, the experimental neutral axis angle and depth were able to be determined. The strain data showed whether the concrete material properties were in the nonlinear region, areas of the cross-section that were in tension, and whether the reinforcing steel had yielded. For all of the beam specimens, the load was applied until buckling occurred, and then the load was removed slowly until there was a very small amount of load left on the beam. Then, the beam was reloaded. The procedure was repeated two to three times so that the effect of cracking and large initial imperfections could be studied.

5.1 Beam B2A

5.1.1 Beam B2A: Loading #1

The initial imperfections at midspan of the first test were 1 1/2 in. (38.1 mm) lateral sweep at the top of the beam, and 1 1/16in. (27.0 mm) lateral sweep at the bottom of the beam, which resulted in an initial rotation of 0.011 radians. The initial imperfections of all beams at midspan are presented in Table 2.1 of Chapter 2 and the detailed imperfections along the beams are presented in Appendix A. The load versus lateral displacement is shown in Figure 5.1. The maximum load reached was 35.26 kips (156.8 kN) at a lateral deflection of 2.17 in (55.1 mm) at the top of the beam, and 1.57 in. (39.9 mm) at the bottom of the beam. The load versus rotation plot is shown in Figure 5.2. Additionally, the loads versus vertical deflection data for each beam test are presented in Appendix C. When the maximum load level was reached, the restraint system held the beam from excessive lateral deflections. The turnbuckle, controlling the restraint system, was then released gradually, and allowed the beam to continue deflecting laterally, with no additional pumping of the hydraulic jack, as shown in Figure 5.3. The restraining system was released until the system was in equilibrium without the restraining system. Equilibrium occurred at a load of 27.6 kips (122.8 kN) at a lateral deflection of 5.66 in. (143.8 mm) at the top of the beam, and 3.91 in. (99.3 mm) at the bottom.

Figure 5.1 – Load vs. lateral deflection for Beam B2A, loading #1
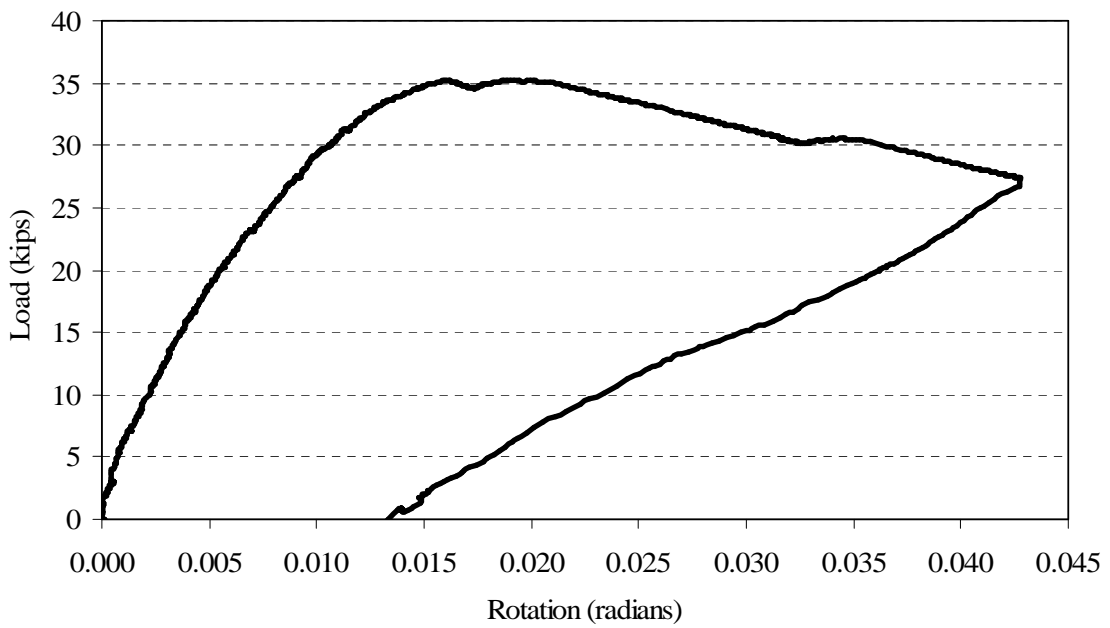
Figure 5.2 – Load vs. rotation for Beam B2A, loading #1

145

Figure 5.3 – Releasing restraint system during loading #1 of Beam B2A

The strain profile is plotted in Figure 5.4 for the load levels of 10 kips (44.5 kN),
20 kips (89.0 kN) and 30 kips (133.4 kN). Each horizontal gridline represents an LVDT
location. The nominal gage length for all beams was 10 in. (254 mm); however the
measured LVDT gage lengths for all beam tests are presented in Appendix C. The
bottom LVDT did not work properly during the experiment, and, therefore, was left out
of the data set. The strain values included the summation of the strain data points
collected, and the predicted initial strain in the cross-section due to prestressing and self-
weight of the beam. The effect of the initial strain due to prestressing and self-weight of
the beam is depicted in Figure 5.5. The effect of the initial strain was noticeable, but

146

small enough that at higher loads, the difference between predicted initial strain, and actual initial strains, would have a minimal effect. Figure 5.4 shows a high correlation to a linear strain distribution. It is also apparent, because of the relatively low strains in the bottom of the beam cross-section, that the steel did not yield, and, furthermore, the relatively small strains at the top of the beam cross-section correspond to a low enough concrete stress at mid-thickness, that the concrete could be considered linear-elastic. The initial strain in the prestressing strands was approximately 0.00103. With a yield strain of 0.0088, the increase in strain at the levels of the strands would be 7770 microstrains for the strands to have yielded. Similarly, strains would need to be greater than 2100 microstrains for the non-prestressed reinforcing steel to yield. However, it is important to note that these results were at mid-thickness, and, therefore, do not consider the strains due to out-of-plane behavior at the surface of the beam.
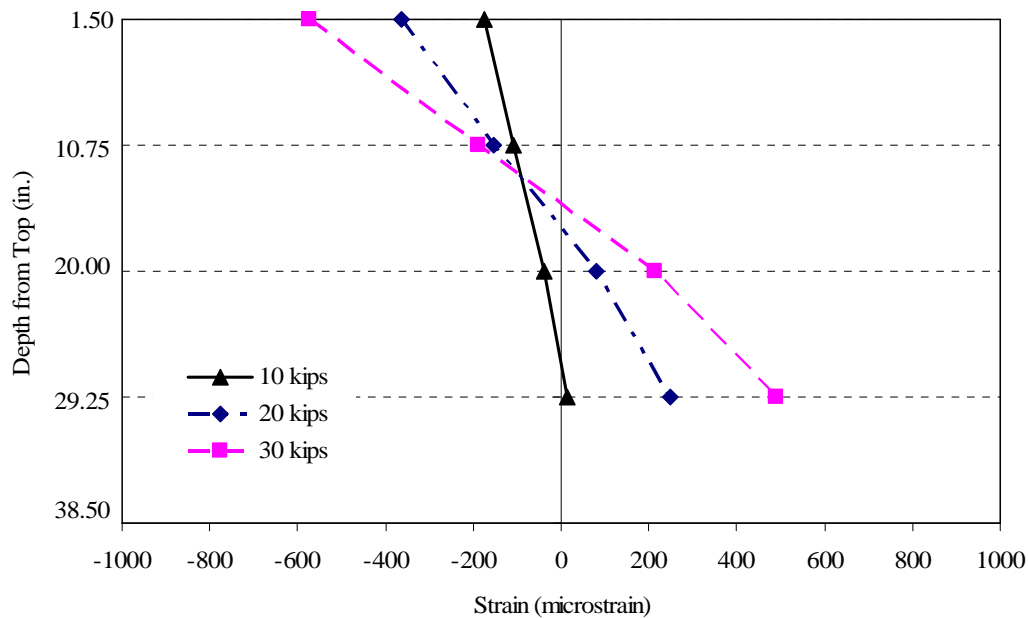
Figure 5.4 – Strain profile at mid-thickness at three load increments for Beam B2A, loading #1
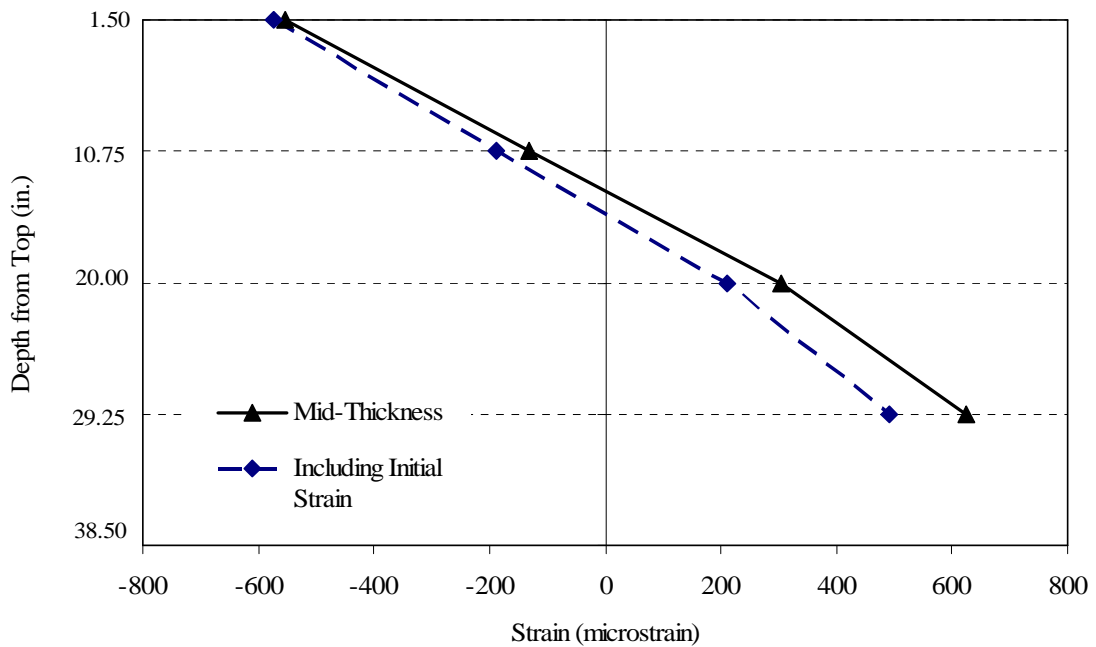
Figure 5.5 – Strain profile at mid-thickness at 30 kips (133.4 kN) for Beam B2A, loading #1

To capture the strain due to the out-of-plane behavior of the prestressed concrete beam, a linear interpolation from the locations of the LVDTs to the surface of the concrete was done. Figures 5.6, 5.7 and 5.8 show the surface strains for the concave and convex side of the beam for the load levels of 10 kips (44.5 kN), 20 kips (89.0 kN) and 30 kips (133.4 kN), respectively.
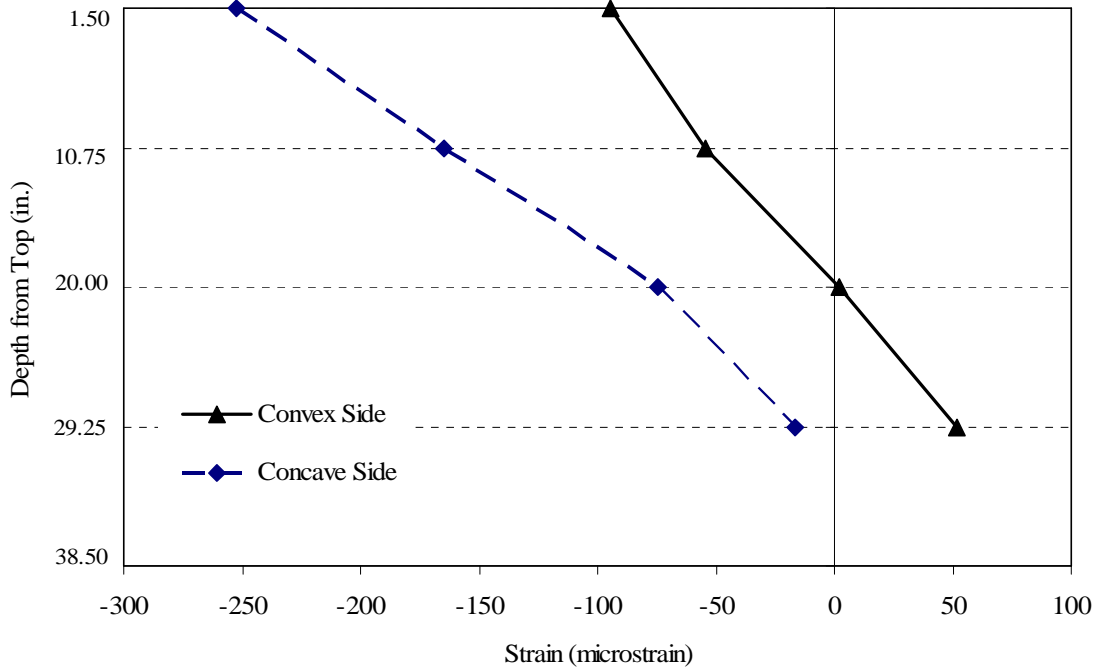
Figure 5.6 – Surface strain profile at 10 kips (44.5 kN) for Beam B2A, loading #1
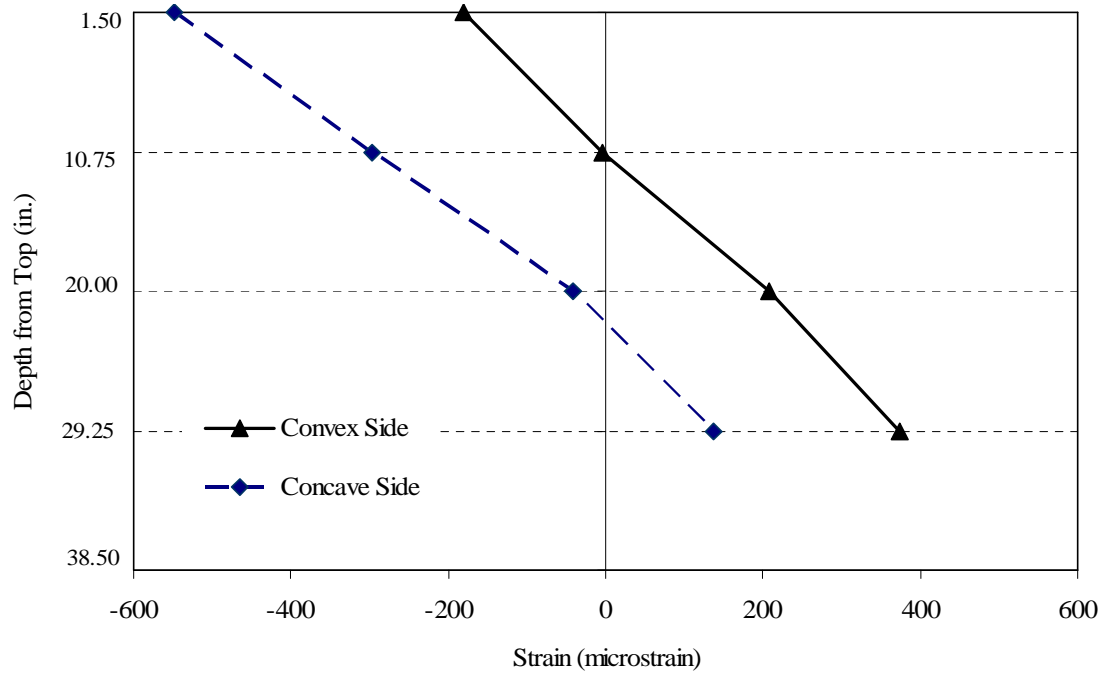
Figure 5.7 – Surface strain profile at 20 kips (89.0 kN) for Beam B2A, loading #1
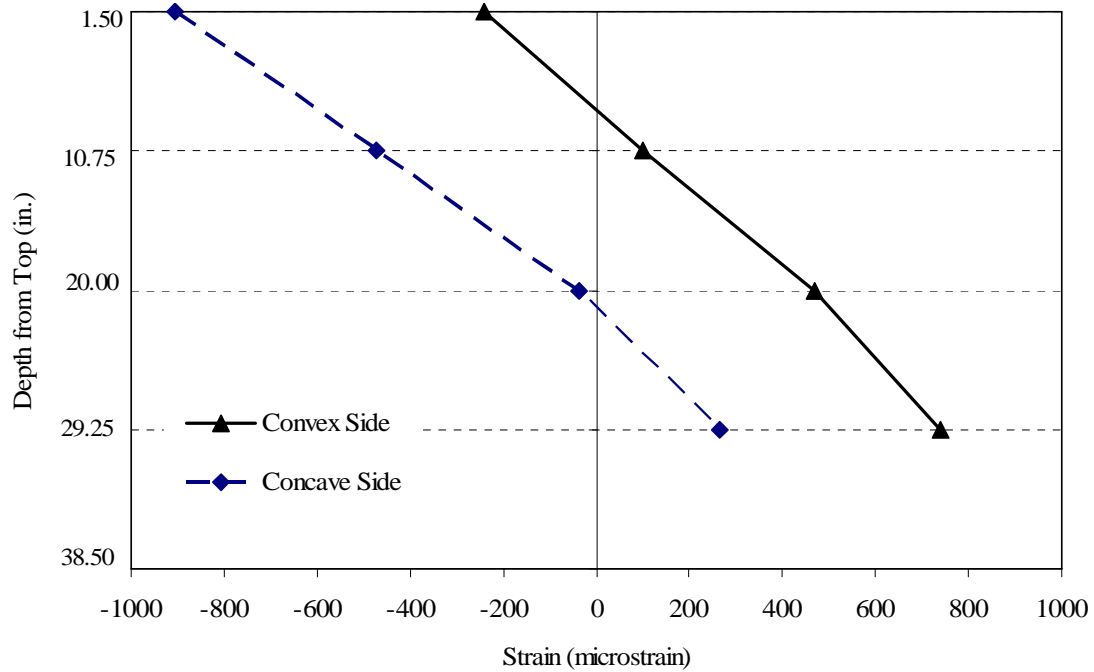
Figure 5.8 – Surface strain profile at 30 kips (133.4 kN) for Beam B2A, loading #1

The surface strain profiles in Figures 5.6 through 5.8 show that the concrete remained linear-elastic in the compression zone, including at the top corner on the concave side, where the highest biaxial compressive stresses occurred.   However, when the buckling load was reached and larger displacements occurred, large strains developed in the biaxially compressed region, as shown in Figure 5.9. Because of the larger compressive strains, the concrete could no longer be considered linear-elastic, and a reduced modulus should be used in that region from an analytical standpoint. Furthermore, the biaxially tensioned region, or the top of the beam on the convex side, developed tensile strains, and, therefore, it was possible that cracking occurred over the entire depth of the cross-section, at midspan, on the convex side of the beam. The level of cracking was not confirmed during the experiment due to safety concerns. Based on a

modulus of rupture of $7.5\sqrt{f_c{}'}$ the tensile cracking strain would be about 139

microstrains.
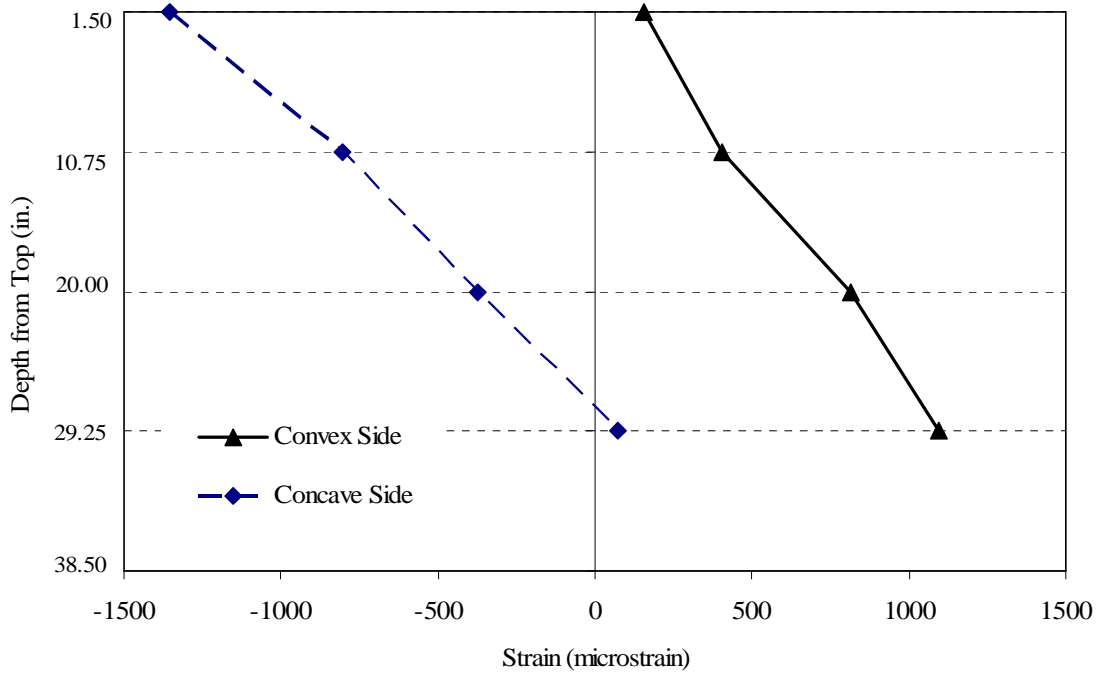
Figure 5.9 – Post-buckling surface strain profile at 31 kips (137.9 kN) for Beam B2A, loading #1

5.1.2 Beam B2A: Loading #2

The initial imperfections of the second test were 2 7/16 in. (61.9 mm) lateral

sweep at the top of the beam, and 1 13/16 in. (46.0 mm) lateral sweep at the bottom of the

beam, which resulted in an initial rotation of 0.0156 radians. The load versus lateral

displacement is shown in Figure 5.10 and the load versus rotation is shown in Figure

5.11. The maximum load reached was 28.62 kips (127.3 kN) at a lateral deflection of 4.13 in (104.9 mm) at the top of the beam, and 2.87 in. (72.9 mm) at the bottom of the beam. Because of the larger initial imperfections in the second loading, the restraining system restrained the beam after minimal load increments; consequently, data points were reported only at points when the load was increased and the restraint system was not restraining deformation of the beam.
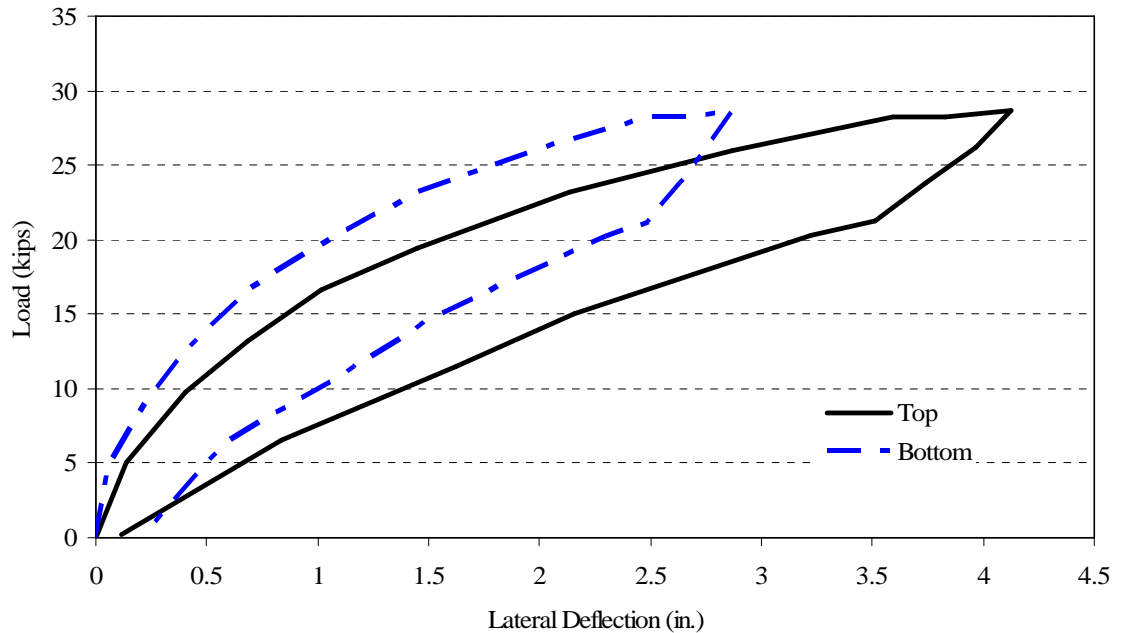
Figure 5.10 – Load vs. lateral deflection for Beam B2A, loading #2
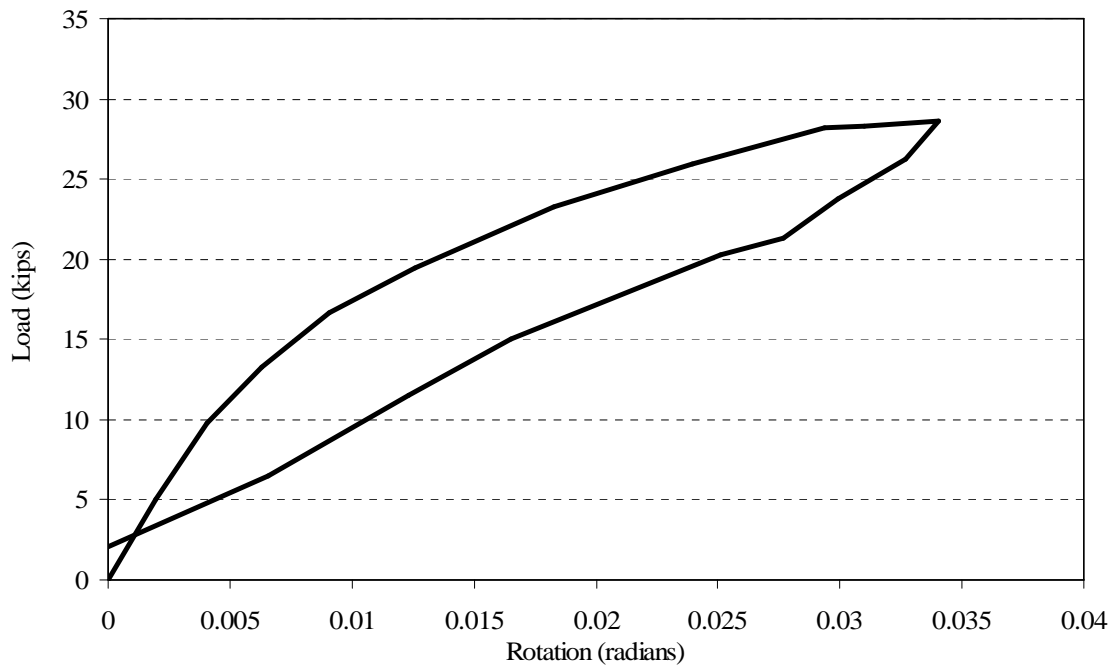
Figure 5.11 – Load vs. rotation for Beam B2A, loading #2

The strain profile is plotted in Figure 5.12 for load levels of 9.73 kips (43.3 kN),

19.47 kips (86.6 kN) and 28.19 kips (125.4 kN). The strain values included the

summation of the strain data points collected, and the predicted initial strain in the cross-

section due to prestressing and self-weight of the beam. The effect of the initial strain

due to prestressing and self-weight of the beam is depicted in Figure 5.13. Figure 5.12

shows nonlinearity, particularly with respect to the bottom LVDT. Therefore, the

behavior of the beam is creating a slightly nonlinear strain distribution. Torsion on the

cross-section due to the initial imperfections could have caused a nonlinear strain

distribution. The nonlinear strain distribution due to torsion was not apparent in the first

loading due to the much smaller initial imperfections. It was also apparent, because of

the relatively low strains in the bottom of the beam cross-section, that the steel did not

yield, and, furthermore, the relatively small strains at the top of the beam cross-section

corresponded to a low enough concrete stress at mid-thickness, that the concrete could be

considered linear-elastic. However, it is important to note that these results were at mid-

thickness, and, therefore, do not consider the strains due to out-of-plane behavior.

Furthermore, in the second test of Beam B2A, there were initial residual strains from the

first test of the beam; therefore, it was more difficult to predict the initial stress and strain

conditions in the beam, and, thus, the concrete could potentially have behaved

inelastically at the higher load levels.
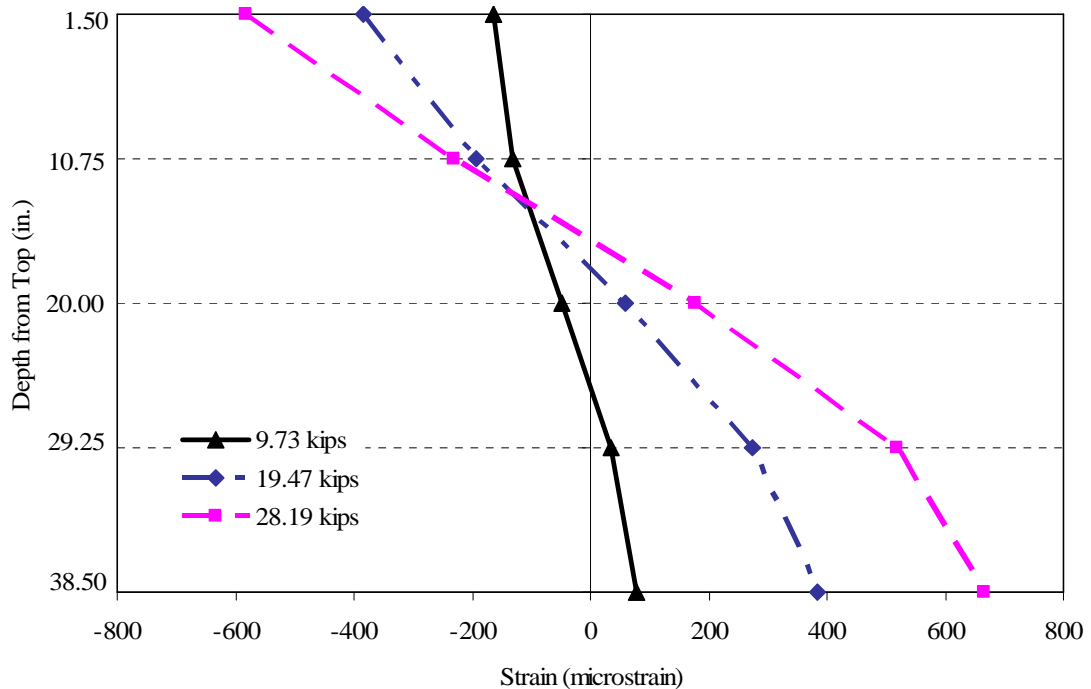
Figure 5.12 – Strain profile at mid-thickness at three load increments for Beam B2A,
loading #2

154
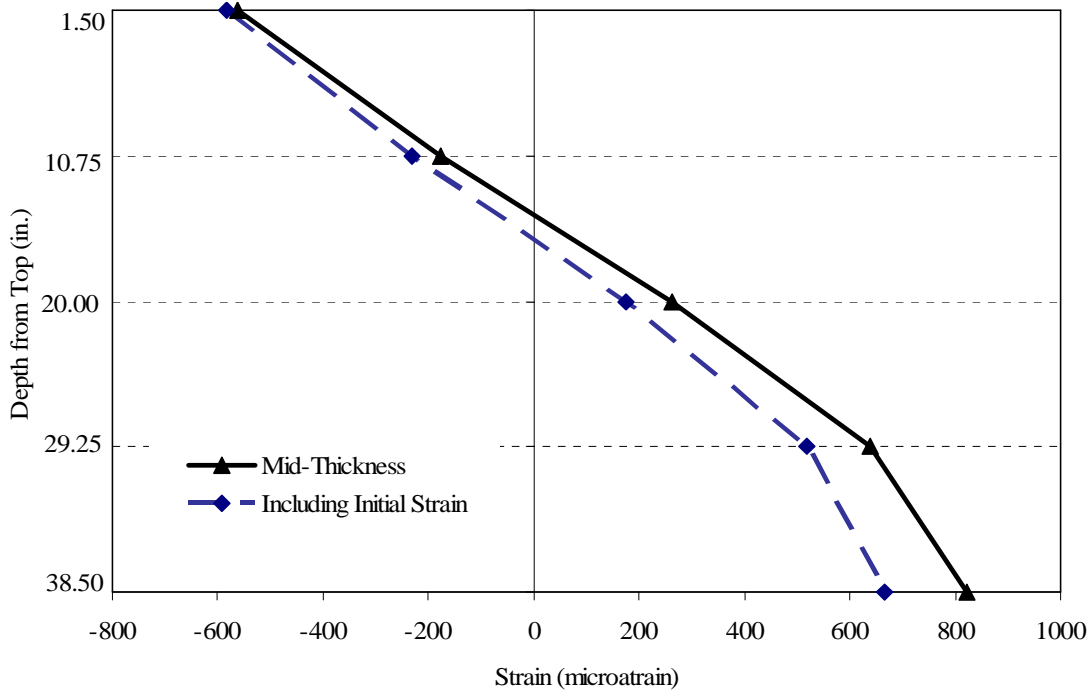
Figure 5.13 – Strain profile at mid-thickness at 28.19 kips (125.4 kN) for Beam B2A, loading #2

To capture the strain due to the out-of-plane behavior of the prestressed concrete beam, a linear interpolation from the locations of the LVDTs to the surface of the concrete was done. Figures 5.14, 5.15, and 5.16 show the surface strains for both the concave and convex side of the girder for load levels of 9.73 kips (43.3 kN), 19.47 kips (86.6 kN) and 28.19 kips (125.4 kN), respectively.
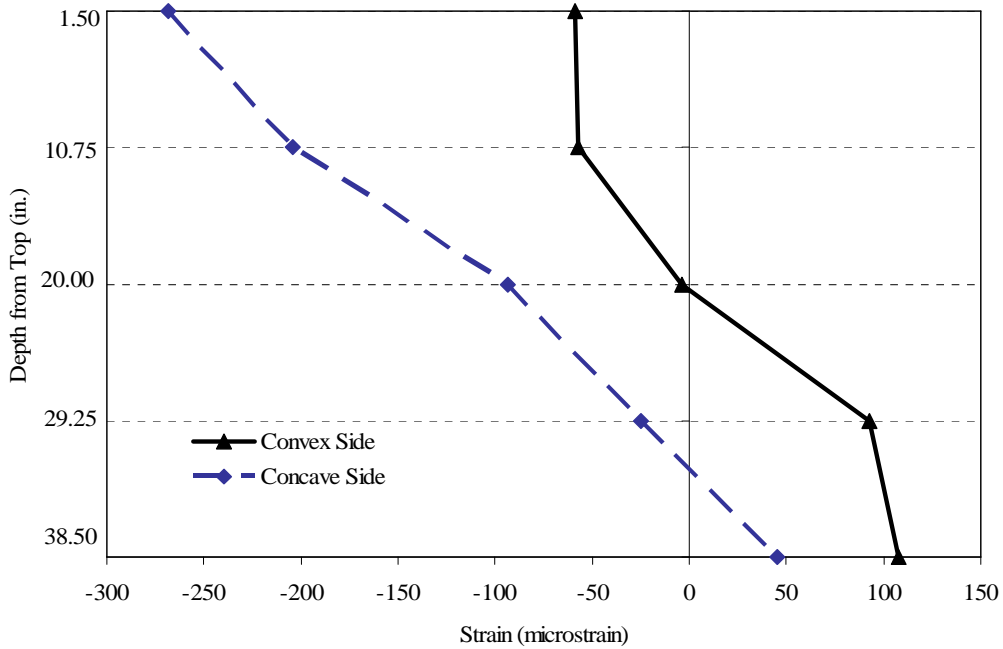
Figure 5.14 – Surface strain profile at 9.73 kips (43.3 kN) for Beam B2A, loading #2
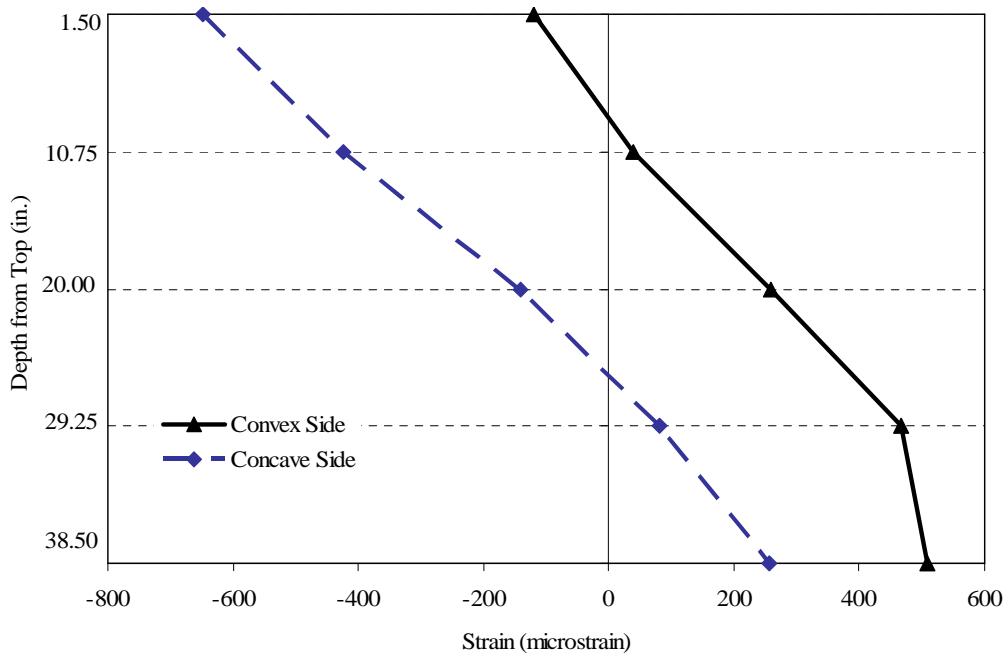
Figure 5.15 – Surface strain profile at 19.47 kips (86.6 kN) for Beam B2A, loading #2
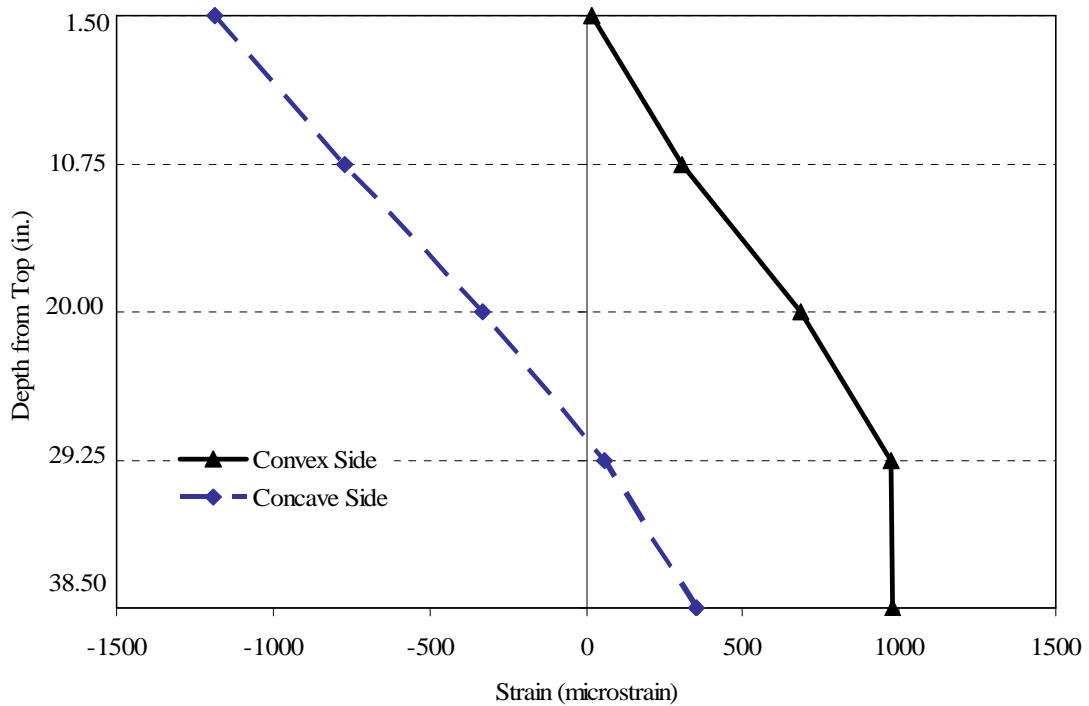
Figure 5.16 – Surface strain profile at 28.19 kips (125.4 kN) for Beam B2A, loading #2

The surface strain profiles in Figures 5.14 through 5.16 show that the concrete remained linear-elastic in the compression zone, including at the top corner on the concave side, where the highest biaxial compressive stresses occurred. However, at the maximum load attained, tensile strains began to develop at the top of the beam cross-section on the convex side. The tensile strain could have been slightly higher due to residual strains from the first test. Note that for the second test of Beam B2A, the beam was not loaded into the post-buckling range. Also, Figures 5.14 through 5.16 show the reason for the lower than expected values for the bottom strain at mid-thickness of the

cross-section from Figure 5.12. The LVDT located on the convex side near the bottom of the beam was reading significantly lower strains than expected.

5.1.3 Beam B2A: Loading #3

The initial imperfections of the third test were 2 5/8 in. (66.7 mm) lateral sweep at the top of the beam, and 1 7/8 in. (47.6 mm) lateral sweep at the bottom of the beam, which resulted in an initial rotation of 0.0187 radians. The load versus lateral displacement is shown in Figure 5.17 and the load versus rotation is shown in Figure 5.18. The maximum load reached was 25.00 kips (111.2 kN) at a lateral deflection of 4.94 in (125.5 mm) at the top of the beam, and 3.59 in. (91.2 mm) at the bottom of the beam. Figure 5.19 is a photograph showing approximately the maximum sweep and rotation of the third loading for Beam B2A. When the maximum load level was reached, increased jacking pressure significantly added to the lateral displacement with little, to no additional load increase. Furthermore, additional slack was provided in the restraint system for this loading, and all remaining tests, to provide for more deformation before having to release the restraint system.
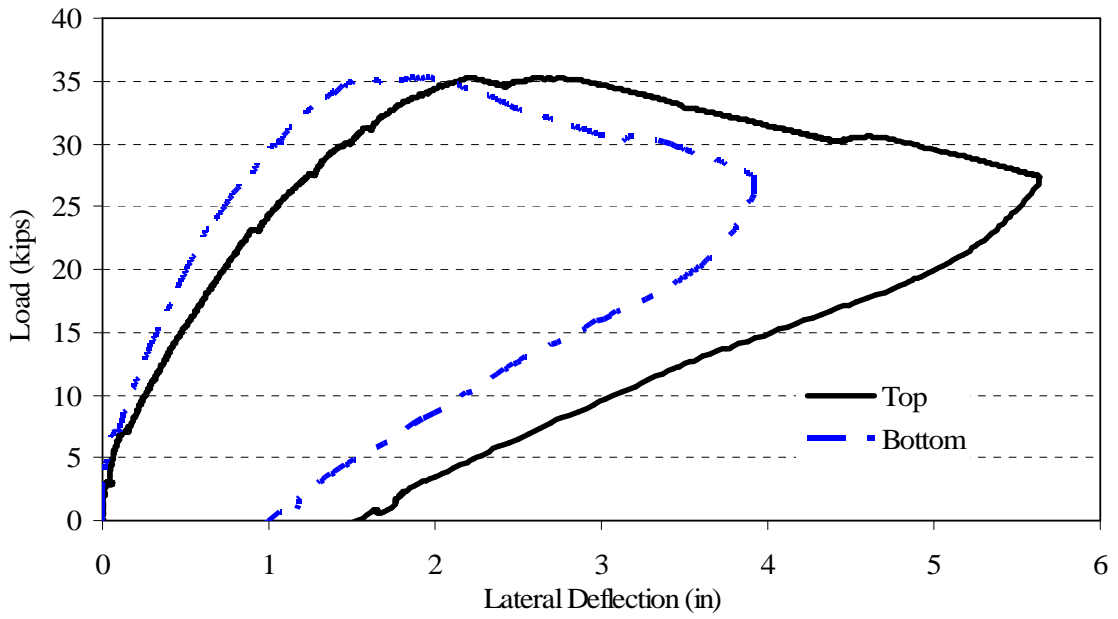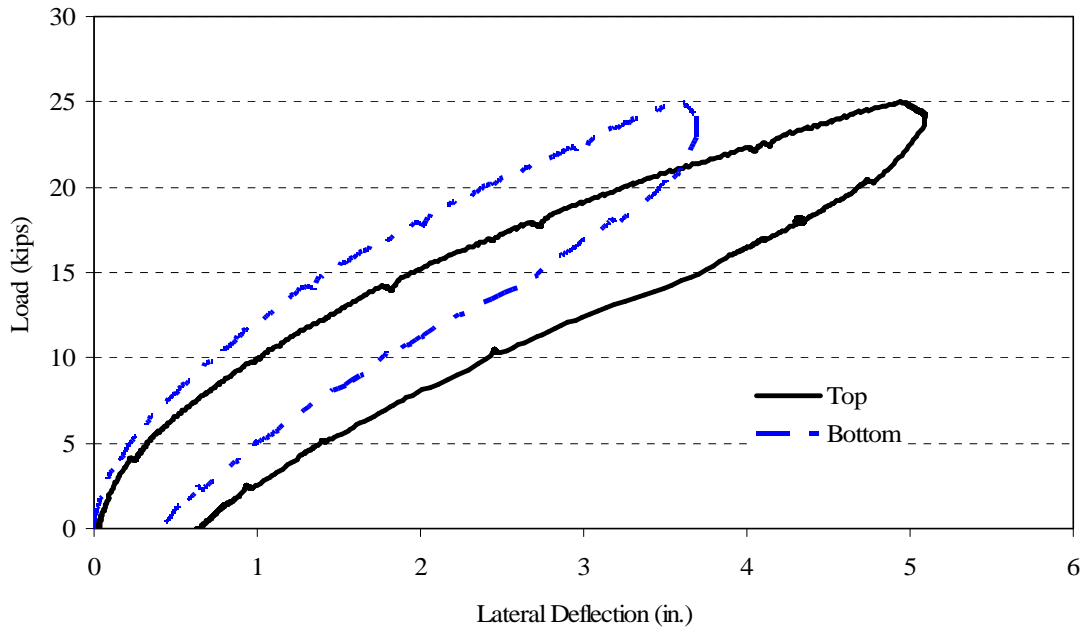
Figure 5.17 – Load vs. lateral deflection for Beam B2A, loading #3
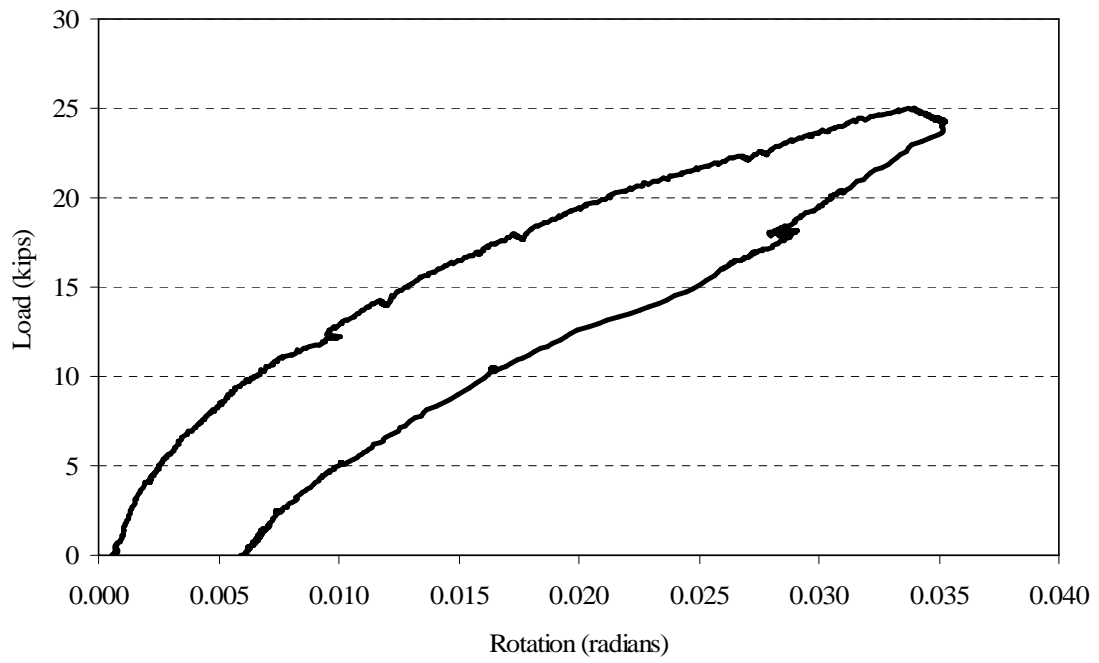
Figure 5.18– Load vs. rotation for Beam B2A, loading #3

Figure 5.19 – End view of sweep and rotation for loading #3 of Beam B2A

The strain profile is plotted in Figure 5.20 for the load levels of 10 kips (44.5 kN), 20 kips (89.0 kN) and 24 kips (106.8 kN). The strain values included the summation of the strain data points collected, and the predicted initial strain in the cross-section due to prestressing and self-weight of the beam. The effect of the initial strain due to prestressing and self-weight of the beam is depicted in Figure 5.21. Figure 5.20 shows a nonlinear strain distribution that appeared to become more linear at higher loads. The reason for the nonlinear strain distribution could be cracking and damage from previous testing, effects of torsion, as well as non-uniform residual strains. Additionally, the bottom LVDT on the convex side was reading smaller strain values than was to be

expected. It was also apparent, because of the relatively low strains in the bottom of the

beam cross-section, that the steel did not yield, and, furthermore, the relatively small

strains at the top of the beam cross-section corresponded to a low enough concrete stress

at mid-thickness, that the concrete could be considered linear-elastic. However, it is

important to note that these results were at mid-thickness, and, therefore, do not consider

the strains due to out-of-plane behavior.
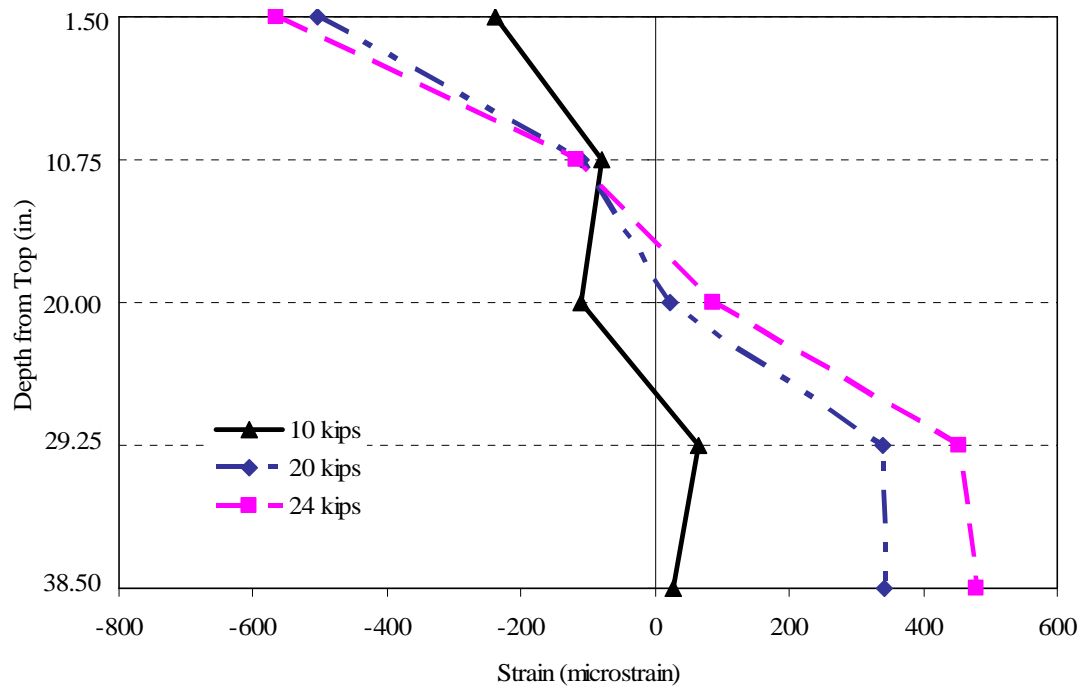
Figure 5.20 – Strain profile at mid-thickness at three load increments for Beam B2A, loading #3
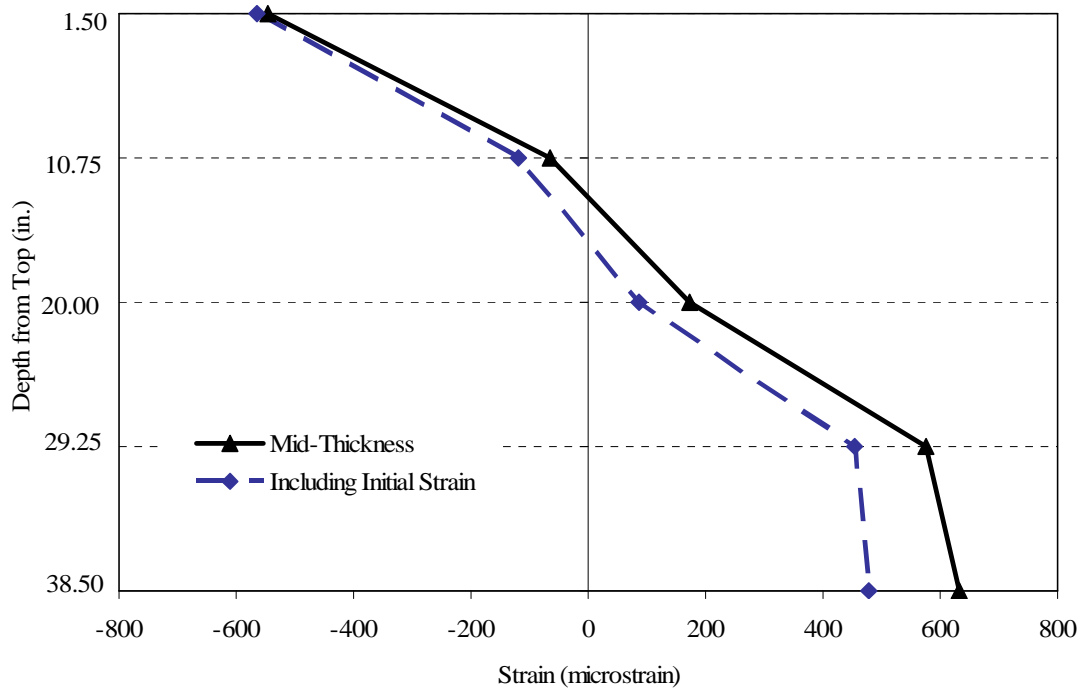
Figure 5.21 – Strain profile at mid-thickness at 24.0 kips (106.8 kN) for Beam B2A, loading #3

To capture the strain due to the out-of-plane behavior of the prestressed concrete beam, a linear interpolation from the locations of the LVDTs, to the surface of the concrete was done. Figures 5.22, 5.23, and 5.24 show the surface strains, for both the concave and convex side of the beam, for load levels of 10 kips (44.5 kN), 20 kips (89.0 kN) and 24 kips (106.8 kN), respectively.
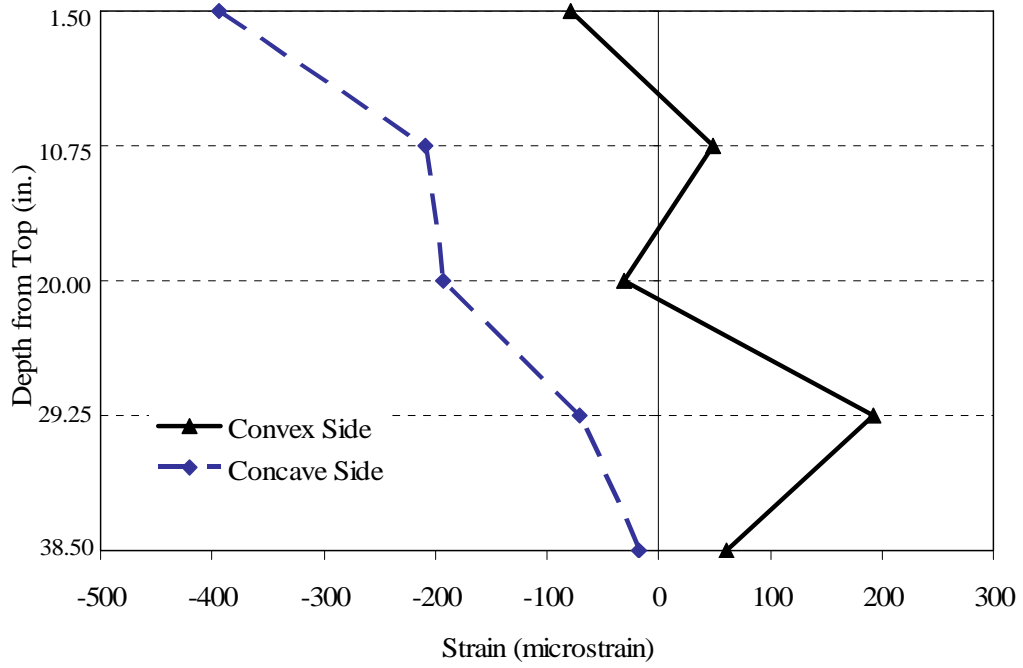
Figure 5.22 – Surface strain profile 10 kips (44.5 kN) for Beam B2A, loading #3
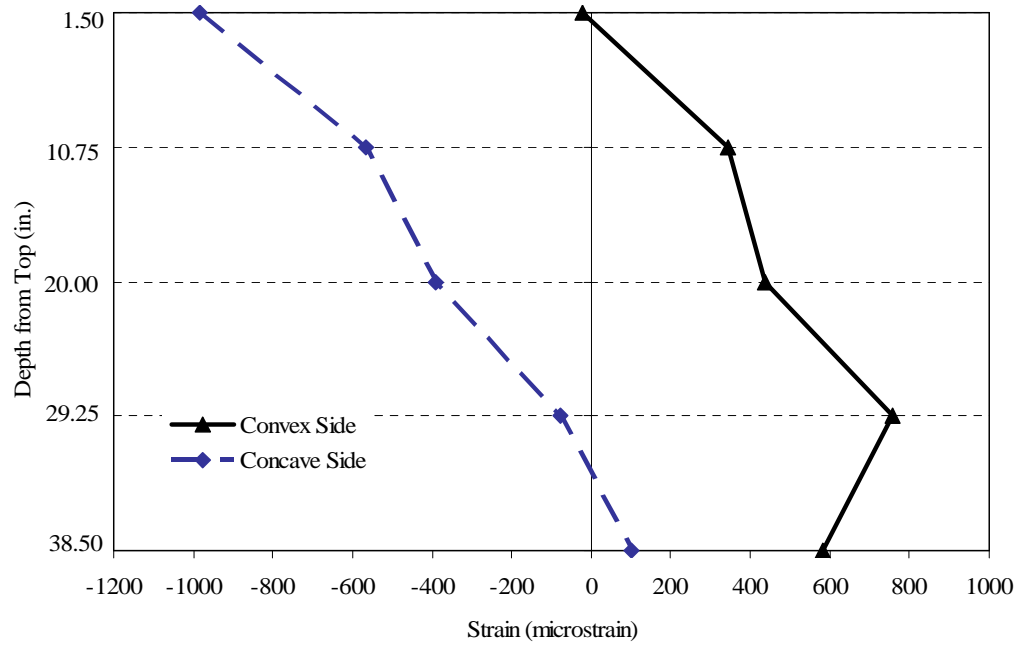
Figure 5.23 – Surface strain profile 20 kips (89.0 kN) for Beam B2A, loading #3

163
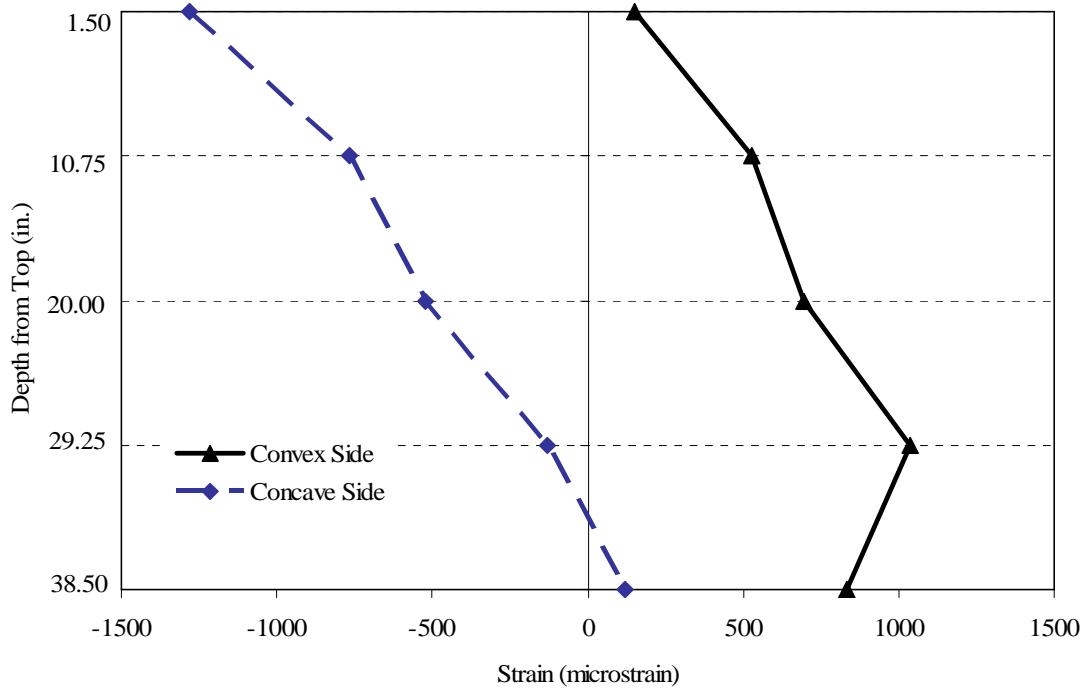
Figure 5.24 – Surface strain profile 24 kips (106.8 kN) for Beam B2A, loading #3

The surface strain profiles in Figures 5.22 through 5.24 show that the concrete remained linear-elastic in the compression zone, including at the top corner, on the concave side, where the highest biaxial compressive stresses occurred. However, due to residual strains from the previous two tests, it was possible that the concrete became inelastic. Also, at the maximum load attained, tensile strains developed at the top of the beam cross-section on the convex side. The tensile strain could have been slightly higher due to residual strains from the first two tests. Note that for the third test of Beam B2A, the beam was not loaded into the post-buckling path.

Unlike the first two tests, cracking was investigated briefly. After the maximum

load was reached, the load was reduced to 17 kips (75.6 kN) and the crack pattern was

quickly observed. The concave side, or compression side, showed no cracking. The

convex, or tension side of the beam, had a significant amount of diagonal cracking on the

order of 0.010 in. to 0.030 in. (0.25 mm to 0.75 mm) wide. The crack pattern on the

convex side of the beam is shown in Figure 5.25.
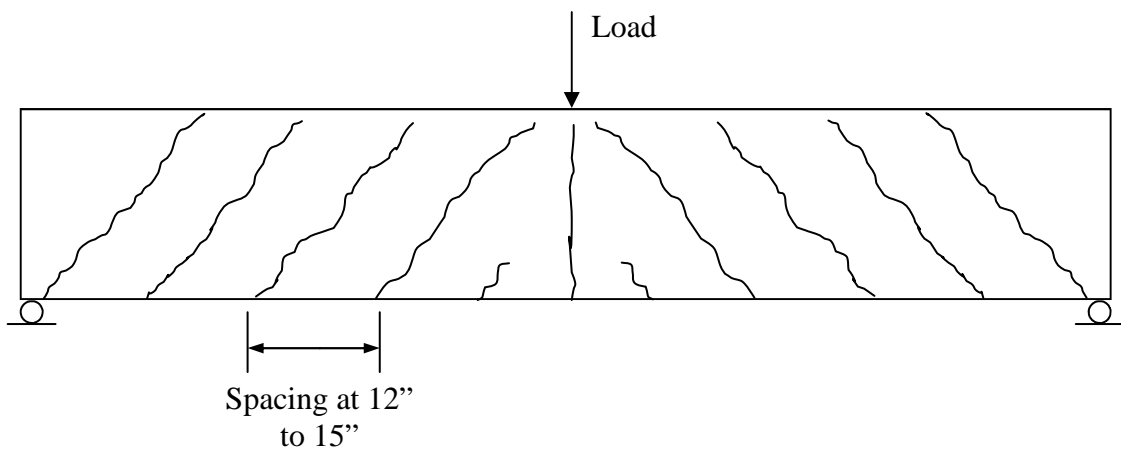
Figure 5.25 – Crack pattern on convex side of beam at 17 kips (75.6 kN) during
unloading for Beam B2A, loading #3

5.1.4 Beam B2A: Hysteresis

All three loadings were performed on the same beam, but with a large amount of

time between loadings. The load versus lateral deflection of all three loadings was

combined into a hysteresis, shown in Figure 5.26. Although, there was a large amount of

time between loadings, the hysteresis was useful to investigate the effect of initial

imperfections visually, such that a degradation of buckling capacity was apparent.
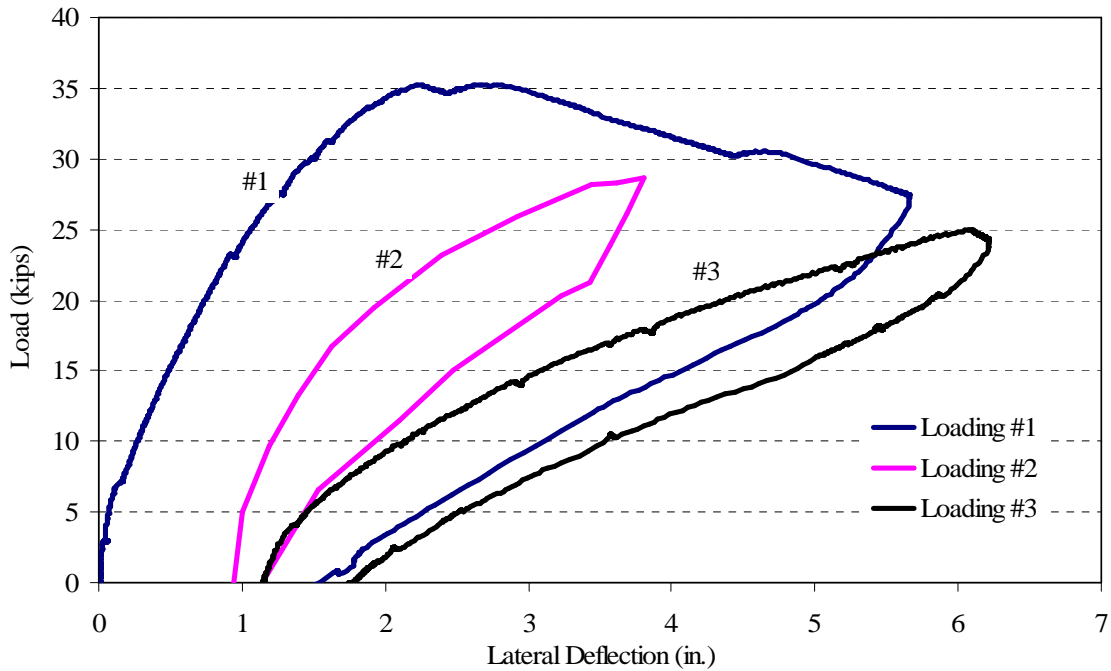
Figure 5.26 – Hysteresis of all three loadings on Beam B2A

Because of the large amount of time between tests, there was some loss of

residual deformations from one test to another. This was particularly apparent between

loadings 1 and 2 in Figure 5.26. Furthermore, Figure 5.26 shows that the increase in

initial imperfections and increase in initial damage caused the nonlinear load-deflection

curves to be shallower.

5.2 Beam B1A

Beam B1A was loaded to its critical buckling load and into its post-buckling path to a significant lateral displacement. After the beam was unloaded, the beam was immediately loaded again to a critical load where large displacements began again with little, to no additional load. The load versus lateral displacement is shown in Figure 5.27 and the load versus rotation is shown in Figure 5.28. The maximum load reached was 36.87 kips (163.9 kN) at a lateral deflection of 3.46 in (87.9 mm) at the top of the beam, and 2.92 in. (74.2 mm) at the bottom of the beam.
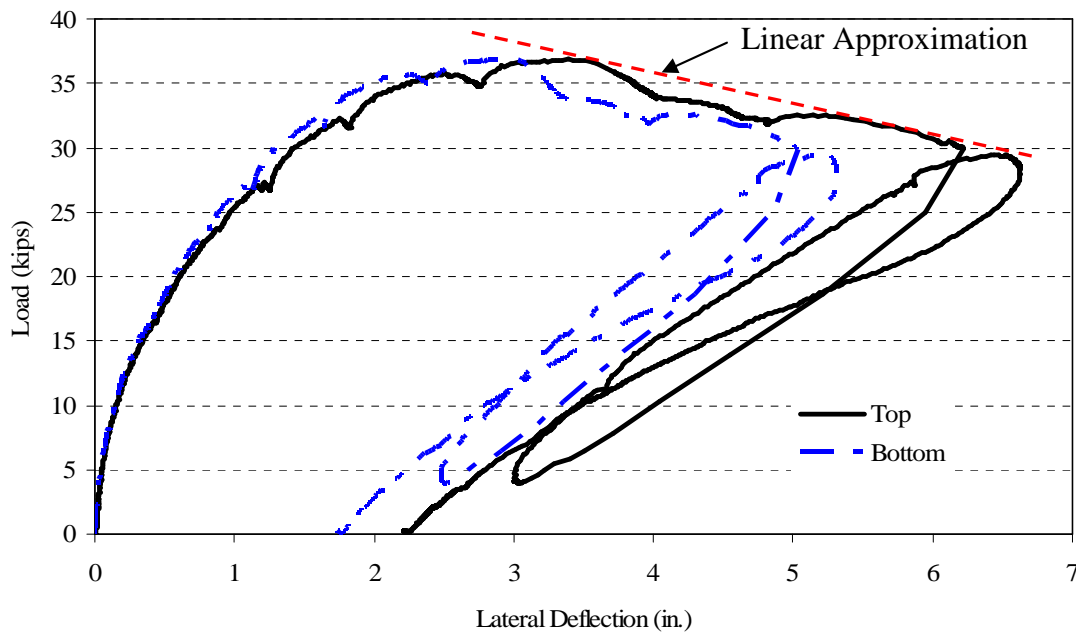
Figure 5.27 – Load vs. lateral deflection for Beam B1A
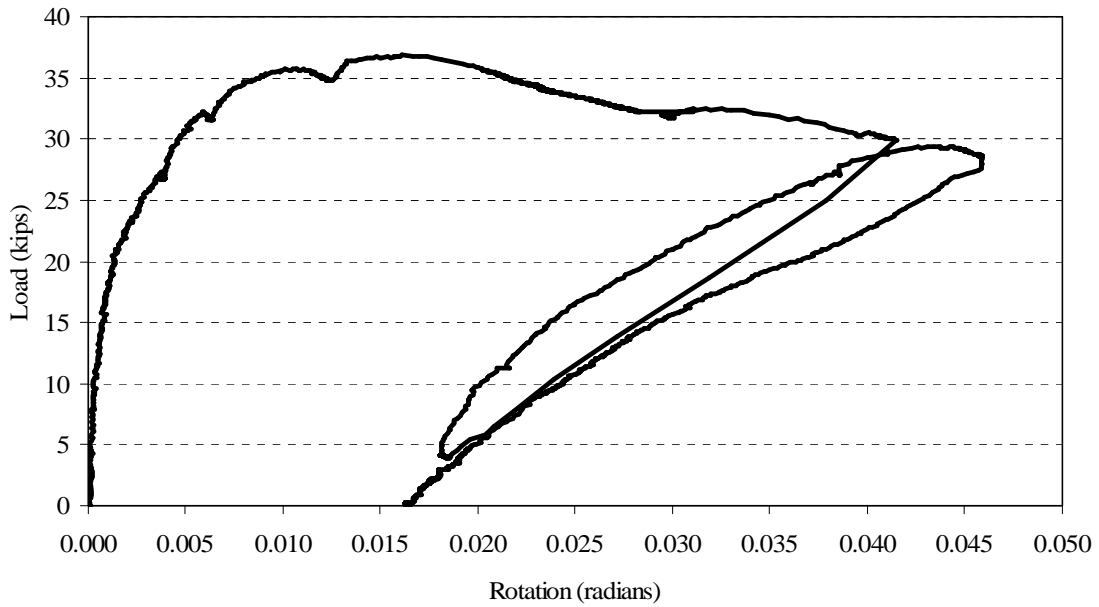
Figure 5.28 – Load vs. rotation for Beam B1A

Figure 5.27 shows that during the second loading of the beam, the maximum load for the second load was lower than the critical load during the first loading. Specifically, the second loading reached a load of 29.45 kips (130.9 kN). A linear approximation of the post-buckling path for the first loading was made, as shown in Figure 5.27; it appeared that the reloading brought the maximum to the initial load-deflection curve. A similar trend is noticeable the load versus rotation plot in Figure 5.28.

The strain profile is plotted in Figure 5.29 for the load levels of 10 kips (44.5 kN), 20 kips (89.0 kN) and 30 kips (133.3 kN). The mounted LVDTs at the midspan of the beam are shown in Figure 5.30. The strain values included the summation of the strain data points collected, and the predicted initial strain in the cross-section due to

168

prestressing and self-weight of the beam. The effect of the initial strain due to prestressing and self-weight of the beam is depicted in Figure 5.31. Figure 5.29 shows good linearity, particularly with respect to the top four LVDTs. Once again, one of the bottom LVDTs was reading a lower strain value than expected, and, therefore, the mid-thickness strain values presented were affected by the lower than expected reading. It was also apparent, because of the relatively low strains in the bottom of the beam cross-section, that the steel did not yield, and, furthermore, the relatively small strains at the top of the beam cross-section corresponded to a low enough concrete stress at mid-thickness, that the concrete could be considered linear-elastic. However, it is important to note that these results were at mid-thickness, and, therefore, do not consider the strains due to out-of-plane behavior.

Figure 5.29 – Strain profile at mid-thickness at three load increments for Beam B1A

169

Figure 5.30 – Photo of mounted LVDTs at midspan

Figure 5.31 – Strain profile at mid-thickness at 30 kips (133.3 kN) for Beam B1A

To capture the strain due to the out-of-plane behavior of the prestressed concrete beam, a linear interpolation from the locations of the LVDTs to the surface of the concrete was done. Figures 5.32, 5.33, and 5.34 show the surface strains for both the concave and convex side of the beam, for load levels of 10 kips (44.5 kN), 20 kips (89.0 kN) and 35 kips (155.6 kN), respectively.
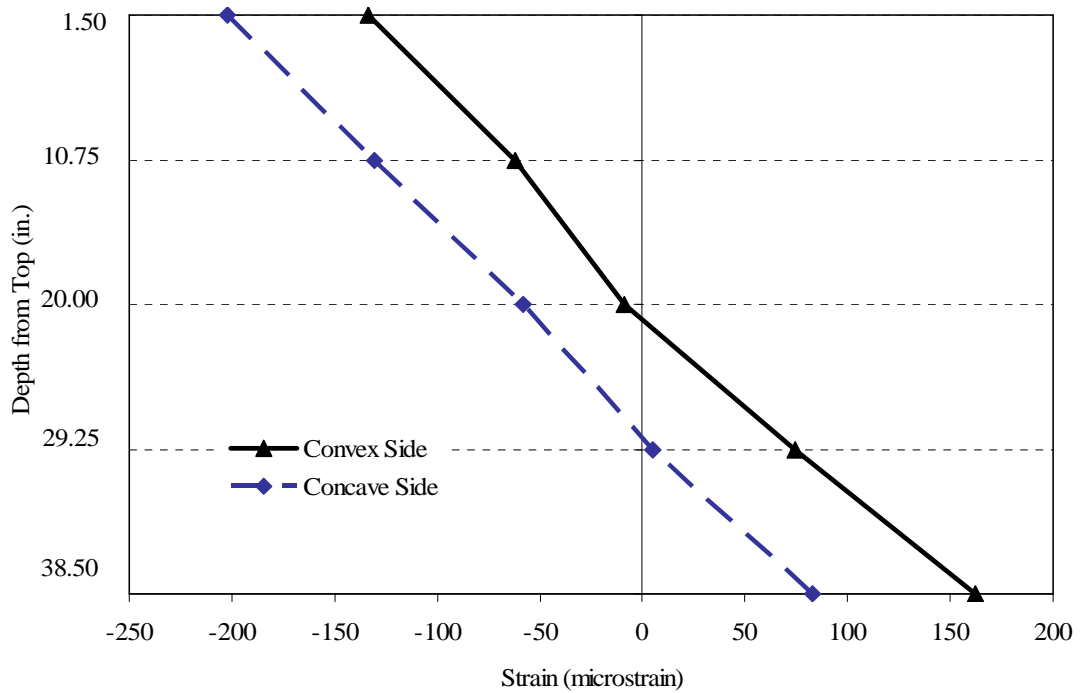
Figure 5.32 – Surface strain profile 10 kips (44.5 kN) for Beam B1A
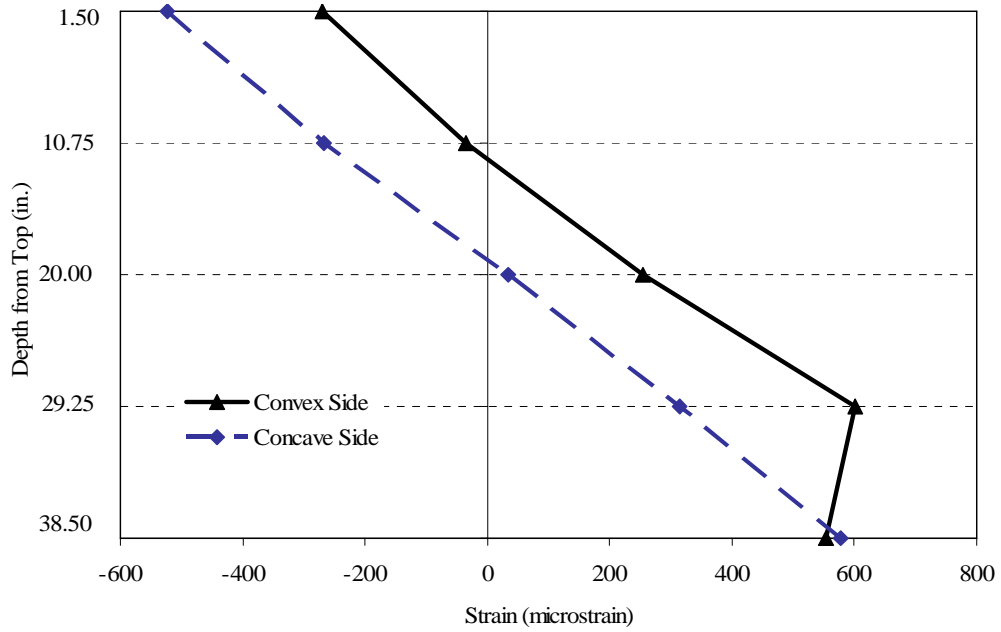
Figure 5.33 – Surface strain profile 20 kips (89.0 kN) for Beam B1A
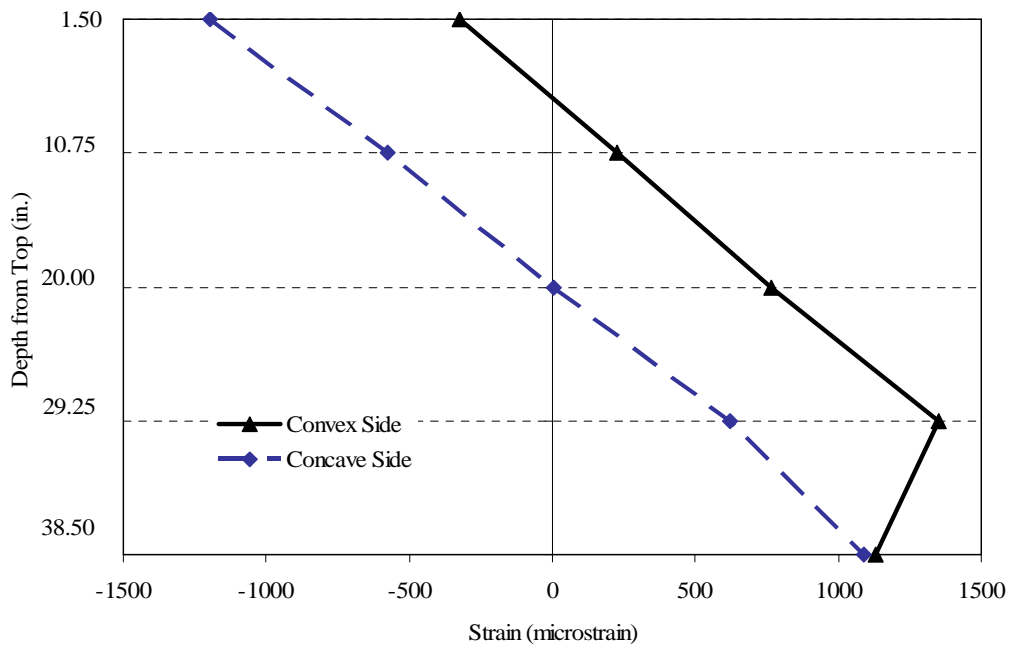
Figure 5.34 – Surface strain profile 35 kips (155.6 kN) for Beam B1A

The surface strain profiles in Figures 5.31 through 5.34 shows that the concrete remained linear-elastic in the compression zone, including at the top corner, on the concave side, where the highest biaxial compressive stresses occurred. Also, the strain distribution for 35 kips (155.6 kN), as shown in Figure 5.34, shows that tensile strains did not develop at the top of the beam cross-section on the convex side for this beam, but did for a significant percentage of the depth of the cross-section on the convex side of the beam. Additionally, it was apparent in Figures 5.33 and 5.34 that there was an error in the strain reading from the LVDT at the bottom of the convex side. After the experiment, it was found that the LVDT in that position was broken.

5.3 Beam C2A

Beam C2A was loaded to its critical buckling load and into its post-buckling path to a significant lateral displacement. After the beam was unloaded, the beam was immediately loaded again to a load where large displacements began with little, to no additional load. The load versus lateral displacement is shown in Figure 5.35 and the load versus rotation is shown in Figure 5.36. The maximum load reached was 33.68 kips (149.7 kN) at a lateral deflection of 3.88 in (98.6 mm) at the top of the beam, and 3.37 in. (85.6 mm) at the bottom of the beam. Additionally, Figure 5.37 is a photo of Beam C2A after buckling occurred showing the gravity load simulator with a shifted geometry.
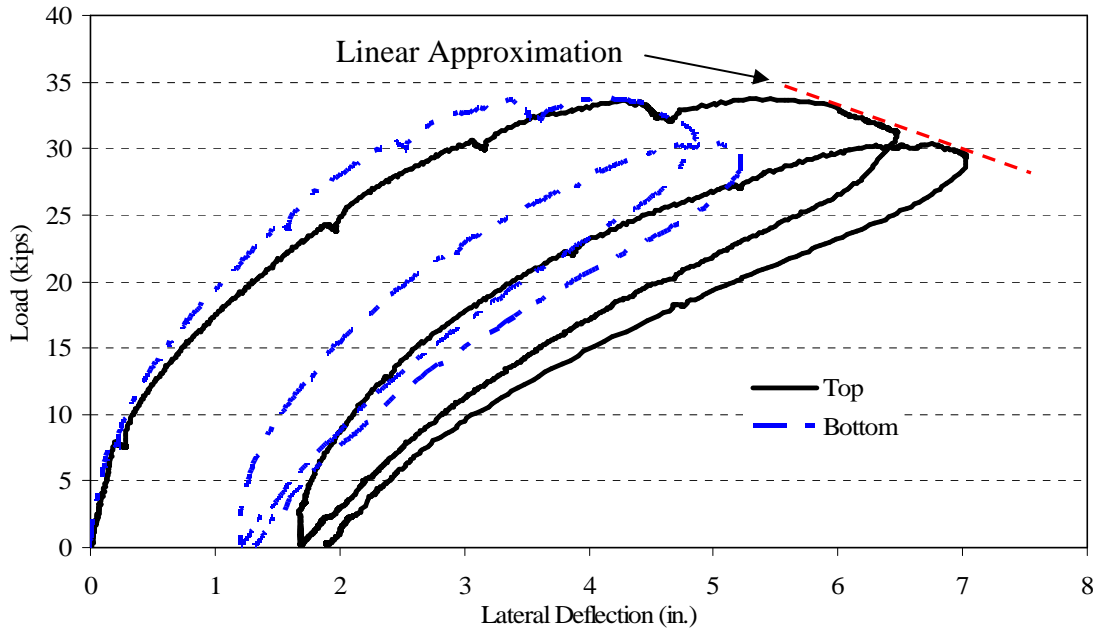
Figure 5.35 – Load vs. lateral deflection for Beam C2A
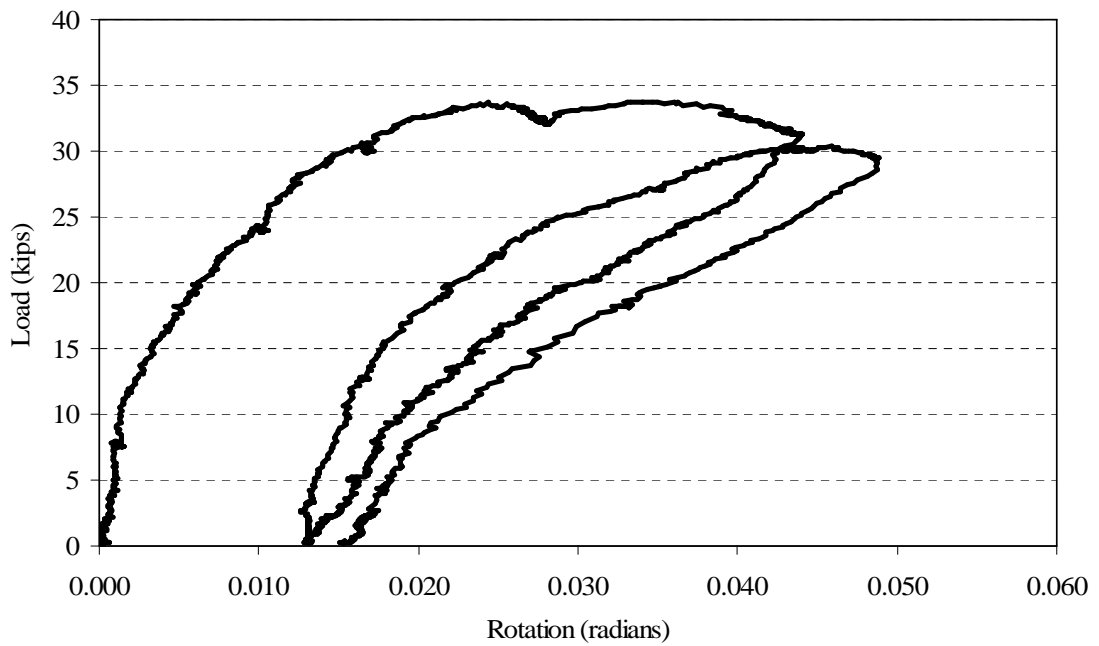
Figure 5.36 – Load vs. rotation for Beam C2A

174
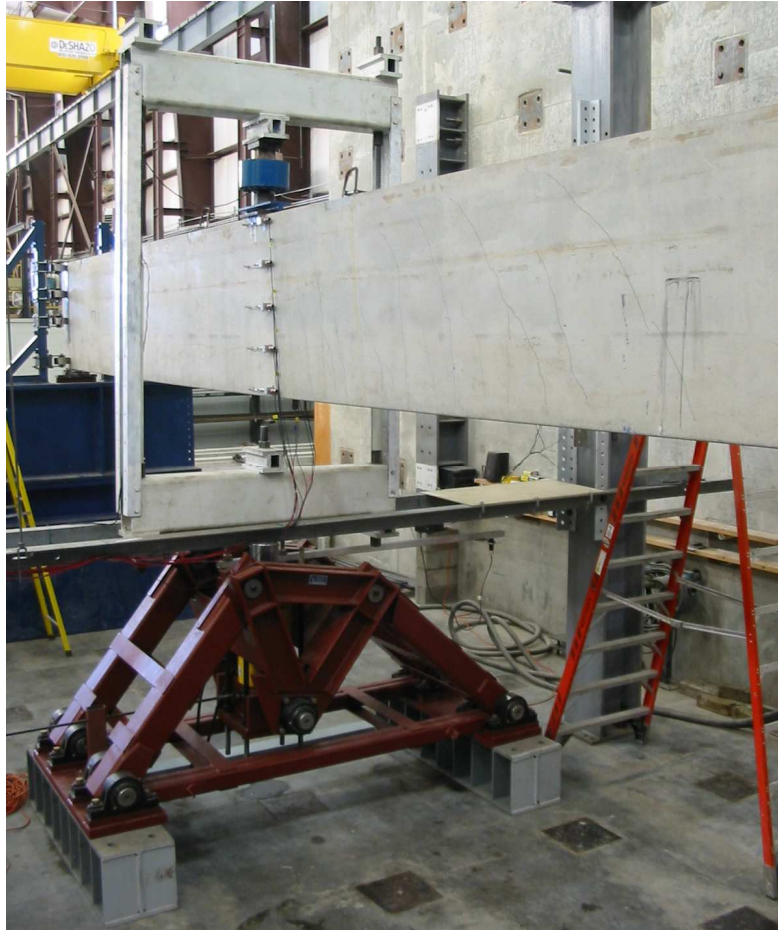
Figure 5.37 – Photo of shifted gravity load simulator

Figure 5.35 shows that during the second loading of the beam, the maximum load was lower than the critical load during the first loading. Specifically, the second loading reached a load of 27.23 kips (120.0 kN). A linear approximation of the post-buckling path for the first loading was made, like was done for Beam B1A, as shown in Figure 5.35, it appeared that reloading brought the maximum to the initial load-deflection curve. A similar trend is noticeable the load versus rotation plot in Figure 5.36. Therefore, the

trend that the critical load of subsequent loadings falls on the initial load-deflection curve was reaffirmed during the testing of Beam C2A.

The strain profile is plotted in Figure 5.38 for load levels of 10 kips (44.5 kN), 20 kips (89.0 kN) and 30 kips (133.3 kN). The strain values included the summation of the strain data points collected, and the predicted initial strain in the cross-section due to prestressing and self-weight of the beam. The effect of the initial strain due to prestressing and self-weight of the beam is depicted in Figure 5.39. Figure 5.38 shows a slight nonlinearity in the strain distribution through the cross-section particularly at higher loads most likely due to strains developed due to torsion on the cross-section. Furthermore, the higher tensile strain than expected at the bottom LVDT could be due to a crack developing within the gage length. It was apparent, considering the relatively low strains at the bottom of the beam cross-section, that the steel did not yield, and, furthermore, the relatively small strains at the top of the beam cross-section corresponded to a low enough concrete stress at mid-thickness, that the concrete could be considered linear-elastic. However, it is important to note that these results were at mid-thickness, and, therefore, do not consider the strains due to out-of-plane behavior.

Figure 5.38 – Strain profile at mid-thickness at three load increments for Beam C2A

Figure 5.39 – Strain profile at mid-thickness at 30 kips (133.3 kN) for Beam C2A

177

To capture the strain due to the out-of-plane behavior of the prestressed concrete beam, a linear interpolation from the locations of the LVDTs to the surface of the concrete was done. Figures 5.40, 5.41, and 5.42 show the surface strains for both the concave and convex side of the beam, for load levels of 10 kips (44.5 kN), 20 kips (89.0 kN) and 32 kips (142.2 kN), respectively.

Figure 5.40 – Surface strain profile 10 kips (44.5 kN) for Beam C2A

Figure 5.41 – Surface strain profile 20 kips (89.0 kN) for Beam C2A

Figure 5.42 – Surface strain profile 32 kips (142.2 kN) for Beam C2A

The surface strain profiles in Figures 5.40 through 5.42 show that the concrete remained linear-elastic in the compression zone, including at the top corner, on the concave side, where the highest biaxial compressive stresses occurred. Also, the strain distribution for 32 kips (142.2 kN), as shown in Figure 5.42, shows that tensile strains developed through most of the depth of the cross-section on the convex side for this beam. Note that the load level of 32 kips (142.2 kN) was only slightly less than the maximum load attained, 33.68 kips (149.7 kN). Additionally, linearity of the strain distributions throughout the loading of Beam C2A, confirmed that the occurrence of strain values that were unexpected in the previous tests were due to a faulty LVDT, and not due to the beams behavior.

5.4 Beam B1B

Beam B1B was loaded to its critical buckling load and into its post-buckling path to a significant lateral displacement. After the beam was unloaded, the beam was immediately loaded again to a load where large displacements began with little, to no additional load. The load versus lateral displacement is shown in Figure 5.43 and the load versus rotation is shown in Figure 5.44. The maximum load reached was 33.92 kips (150.8 kN) at a lateral deflection of 3.59 in (91.2 mm) at the top of the beam, and 3.19 in. (81.0 mm) at the bottom of the beam. Additionally, Figure 5.45 shows an end view of the buckled deflected shape of Beam B1B.
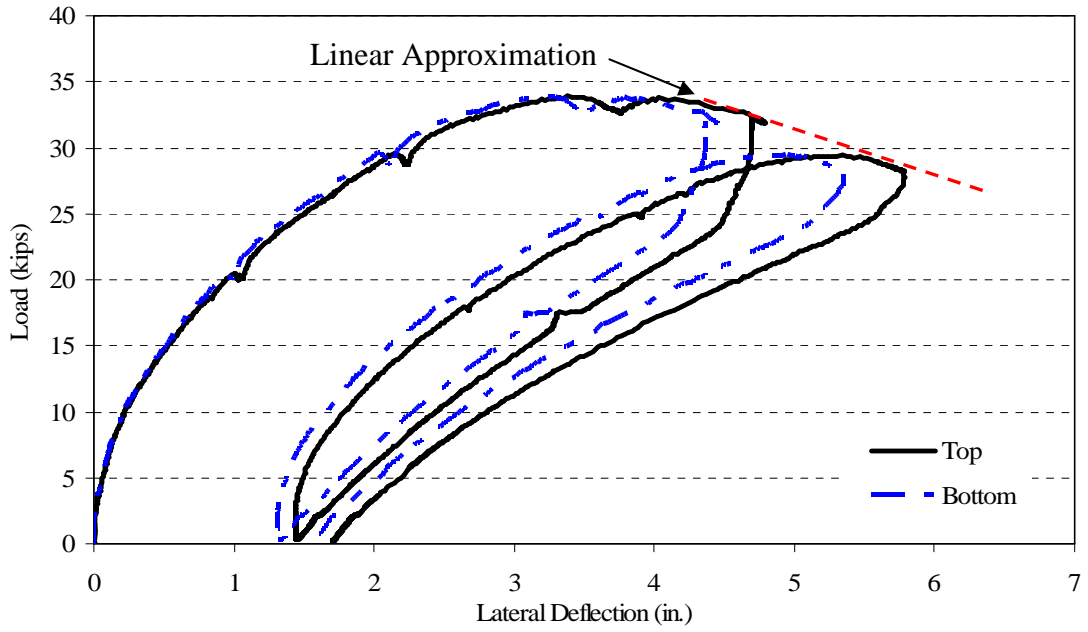
Figure 5.43 – Load vs. lateral deflection for Beam B1B
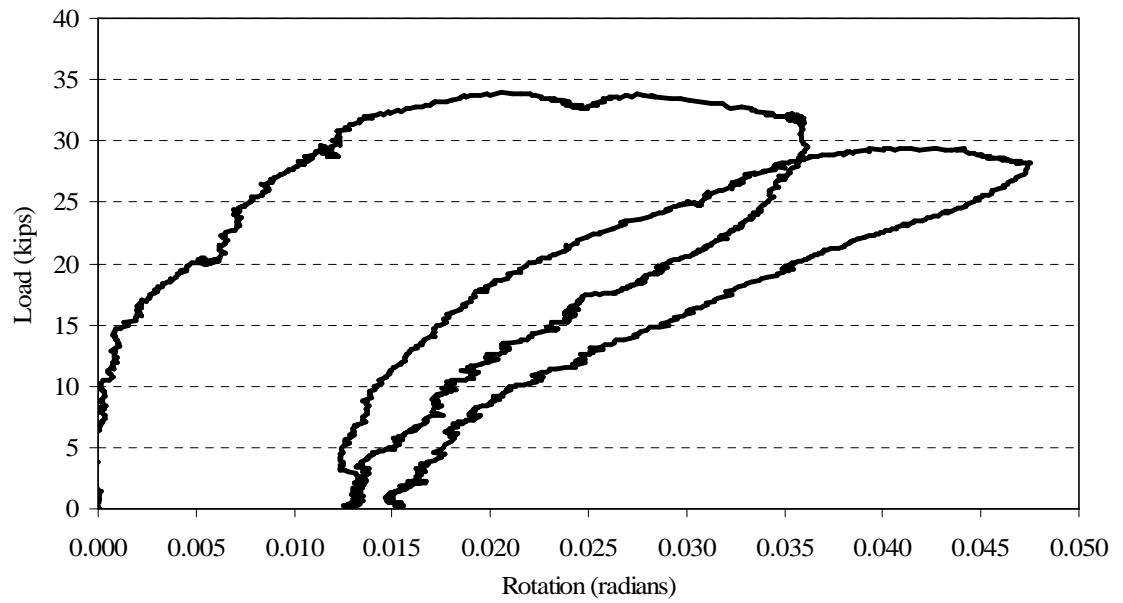
Figure 5.44 – Load vs. rotation for Beam B1B

Figure 5.45 –End view of Beam B1B in buckled position

Figure 5.43 shows that during the second loading of the beam, the maximum load during the second load was lower than the critical load during the first loading. Specifically, the second loading reached a load of 29.42 kips (130.8 kN). A linear approximation of the post-buckling path for the first loading was made, like was done for Beam B1A, as shown in Figure 5.43, and the reloading brought the maximum load to the initial load-deflection curve. A similar trend is noticeable in the load versus rotation plot in Figure 5.44. Therefore, the trend that the critical load of subsequent loadings falls on an initial load-deflection curve for the first loading was reaffirmed during the testing of Beam B1B.

The strain profile is plotted in Figure 5.46 for load levels of 10 kips (44.5 kN), 20 kips (89.0 kN) and 30 kips (133.3 kN). The strain values included the summation of the strain data points collected, and the predicted initial strain in the cross-section due to prestressing and self-weight of the beam. The effect of the initial strain due to prestressing and self-weight of the beam is depicted in Figure 5.47. Figure 5.46 shows a nonlinear strain distribution through the cross-section strains from torsion at higher loads and the possibility of cracking occurring through the gage length. It was apparent, considering the relatively low strains in the bottom of the beam cross-section, that the steel did not yield, and, furthermore, the relatively small strains at the top of the beam cross-section corresponded to a low enough concrete stress at mid-thickness, that the concrete could be considered linear-elastic. However, it is important to note that these results were at mid-thickness, and, therefore, do not consider the strains due to out-of-plane behavior.
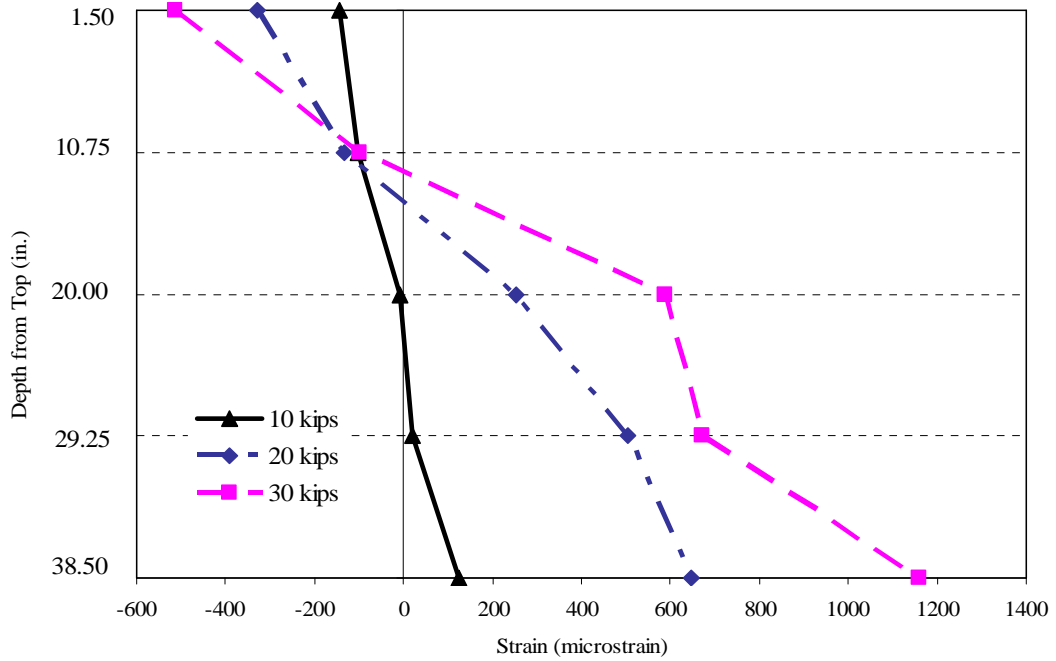
Figure 5.46 – Strain profile at mid-thickness at three load increments for Beam B1B
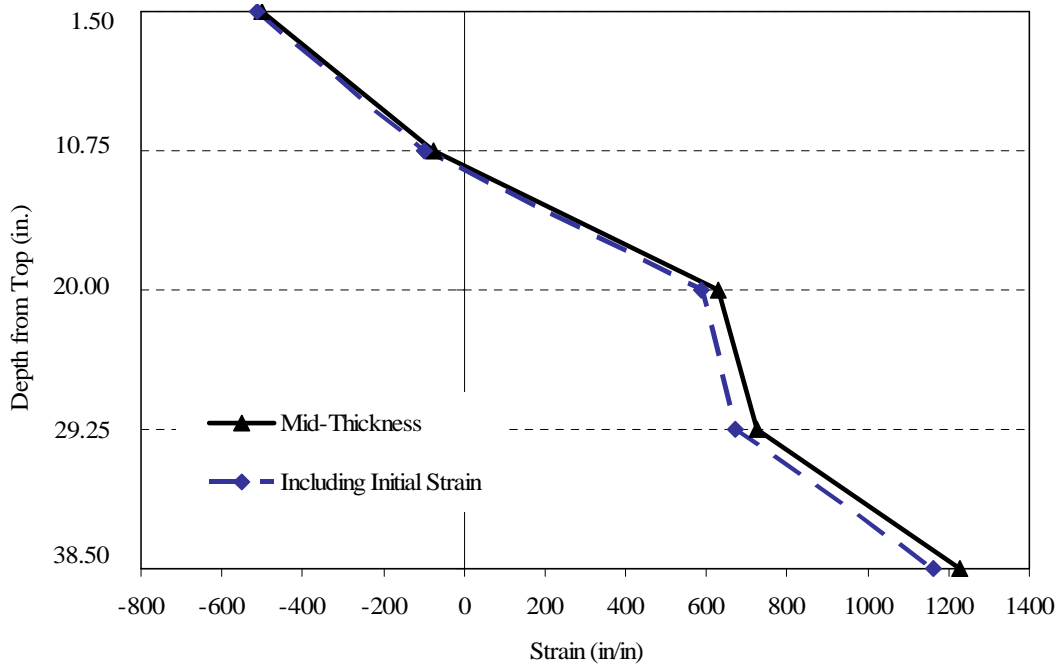
Figure 5.47 – Strain profile at mid-thickness at 30 kips (133.3 kN) for Beam B1B

184

To capture the strain due to the out-of-plane behavior of the prestressed concrete beam, a linear interpolation from the locations of the LVDTs, to the surface of the concrete was done. Figures 5.48, 5.49, and 5.50 show the surface strains for both the concave and convex side of the girder, for load levels of 10 kips (44.5 kN), 20 kips (89.0 kN) and 32 kips (142.2 kN), respectively.
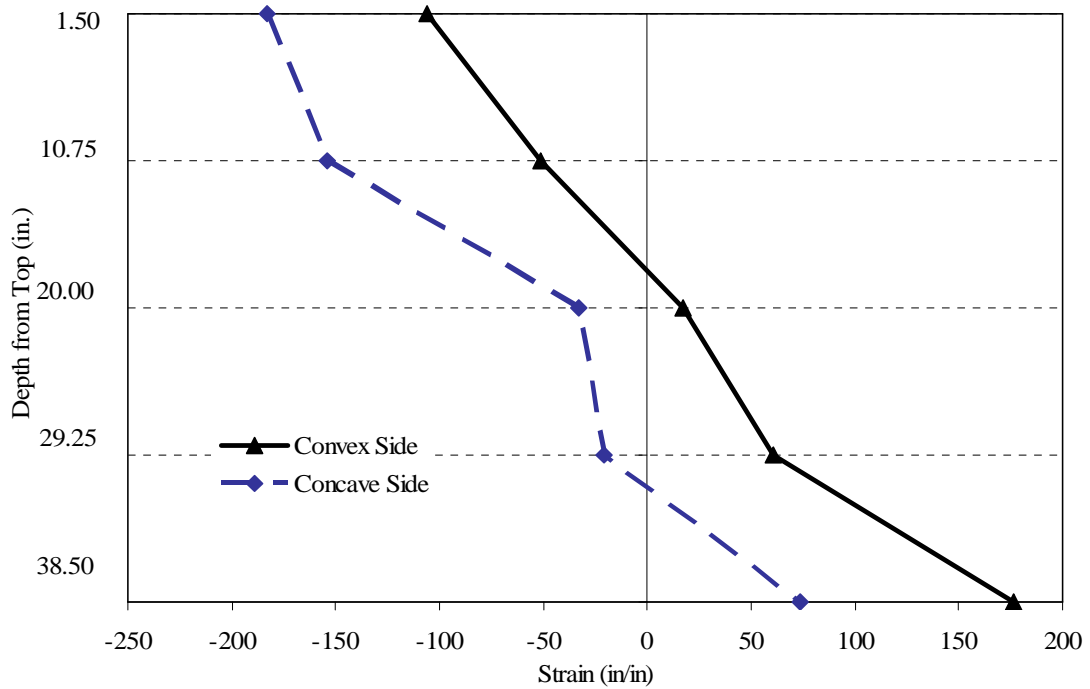
Figure 5.48 – Surface strain profile 10 kips (44.5 kN) for Beam B1B
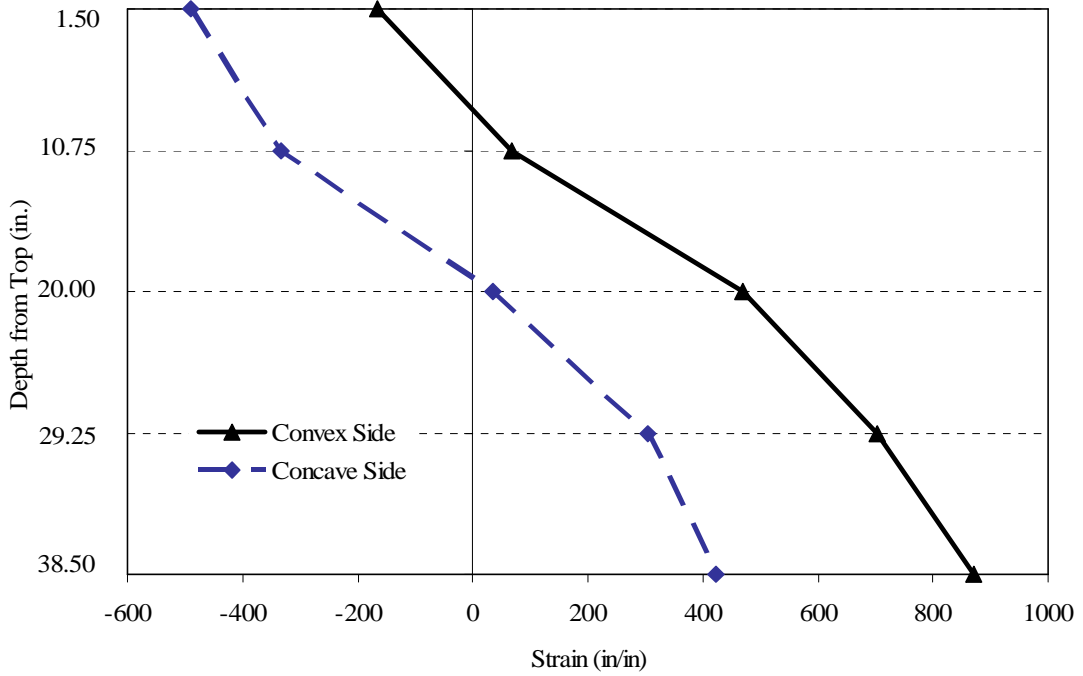
Figure 5.49 – Surface strain profile 20 kips (89.0 kN) for Beam B1B
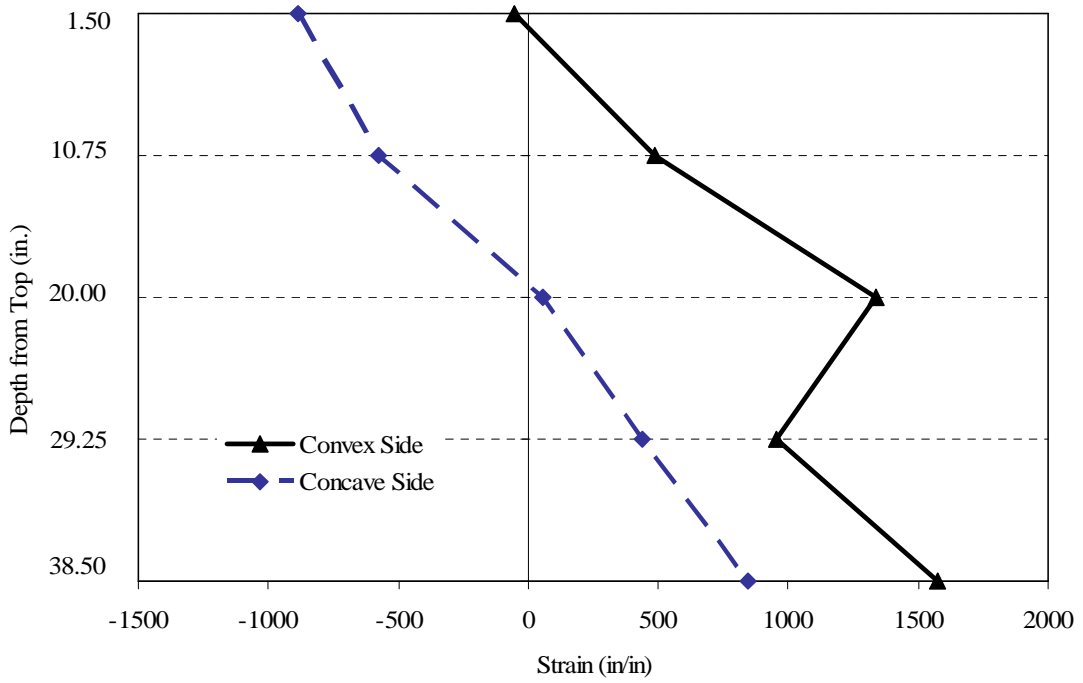
Figure 5.50 – Surface strain profile 32 kips (142.2 kN) for Beam B1B

186

The surface strain profiles in Figures 5.48 through 5.50 show that the concrete remained linear-elastic in the compression zone, including at the top corner, on the concave side, where the highest biaxial compressive stresses occurred. Also, the strain distribution for 32 kips (142.2 kN), as shown in Figure 5.50, shows that tensile strains developed through most of the depth of the cross-section on the convex side for this beam. Note that the load level of 32 kips (142.2 kN) was only slightly less than the maximum load attained, 33.92 kips (150.8 kN). Figure 5.50 also shows a larger than expected strain value at the mid-depth LVDT on the convex side of the beam. The unexpected strain value at that location was most likely due to a crack forming through the LVDT mount at that location. At the load of 32 kips (142.2 kN), significant cracking already occurred in the beam. Significant flexural cracking was observed at 20 kips (88.9 kN) and significant diagonal cracking was observed at 29 kips (128.9 kN). Figure 5.51 shows the vertical flexural cracking in the midspan region, as well as the flexural cracking that transformed into flexural-shear cracks as the load became closer to the buckling load. Furthermore, the cracking became predominantly diagonal in the support region. Also, the vertical flexural cracks can be seen in the region of the LVDTs, which could have been the reason for the mid-depth LVDT, on the convex side, recording unexpected strain values at high loads.
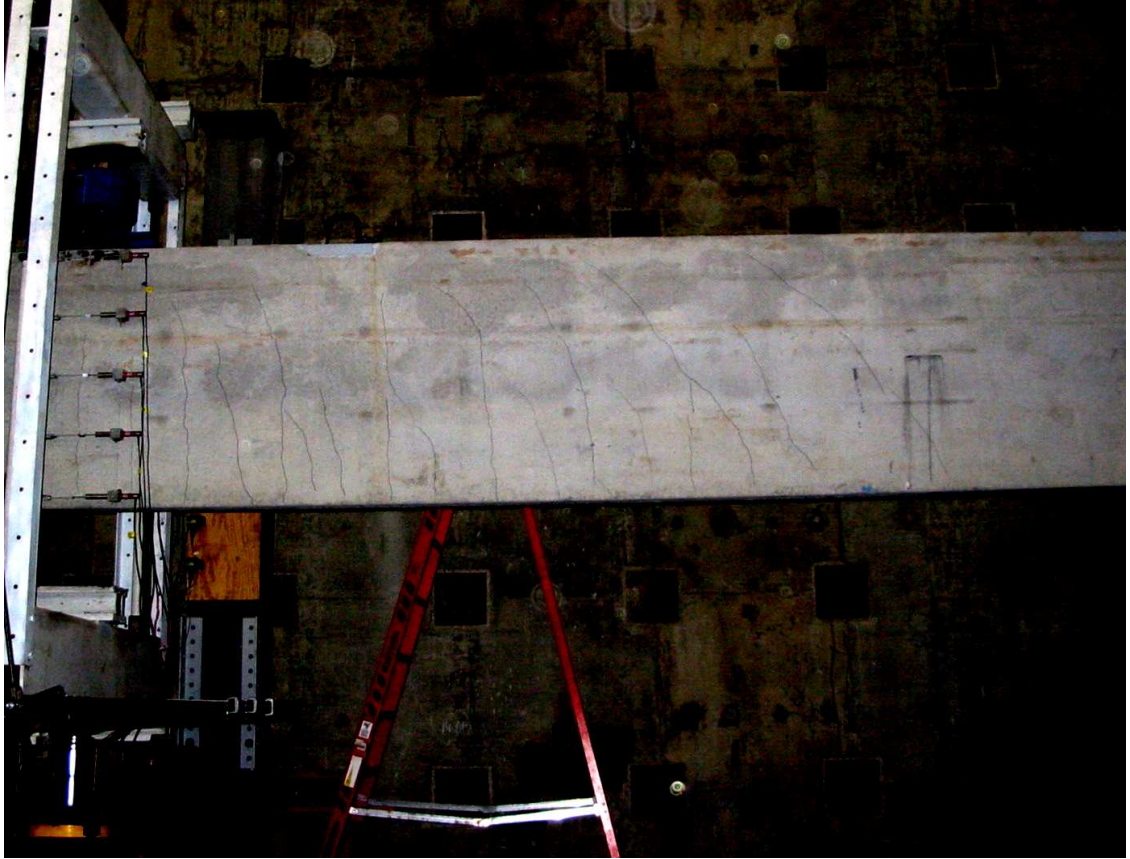
Figure 5.51 – Photo of cracking pattern after buckling of Beam B1B

5.5 Beam B2B

Beam B2B was loaded to its critical buckling load and into its post-buckling path to a significant lateral displacement. After the beam was unloaded, the beam was immediately loaded again to a load where large displacements began with little, to no additional load. The load versus lateral displacement is shown in Figure 5.52 and the load versus rotation is shown in Figure 5.53. The maximum load reached was 34.69 kips (154.2 kN) at a lateral deflection of 3.08 in (78.2 mm) at the top of the beam, and 2.82 in. (71.6 mm) at the bottom of the beam.
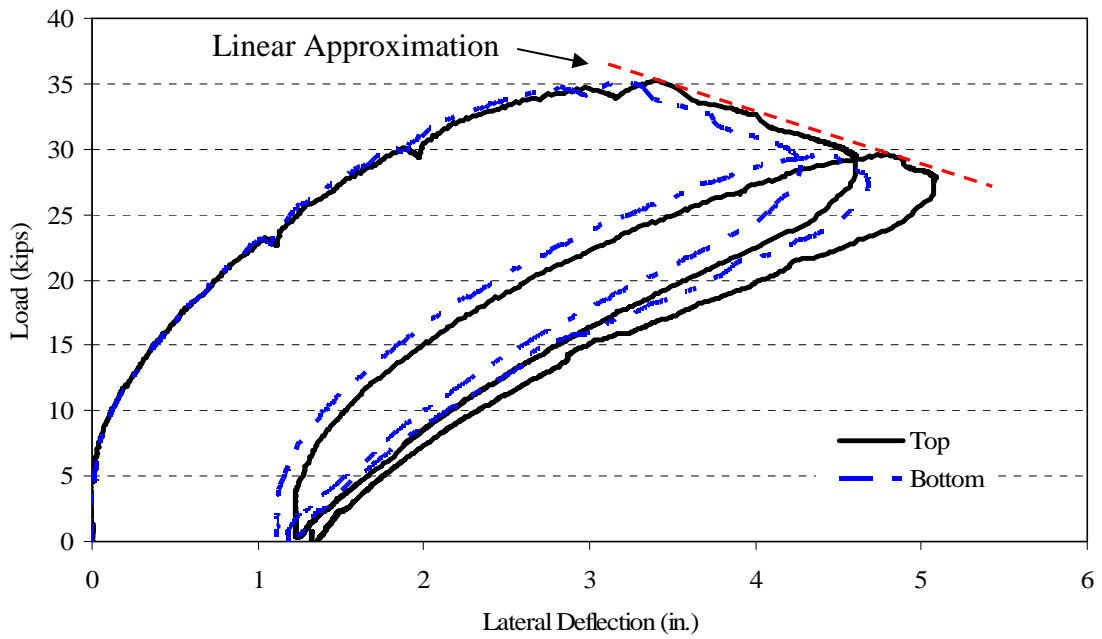
Figure 5.52 – Load vs. lateral deflection for Beam B2B
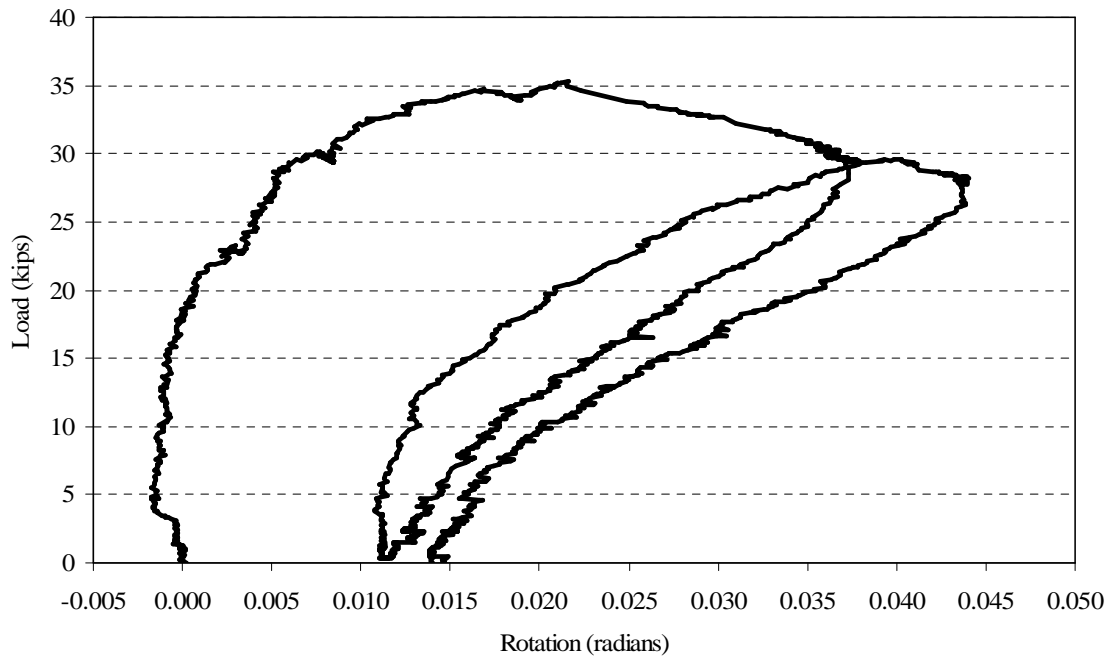
Figure 5.53 – Load vs. rotation for Beam B2B

Figure 5.52 shows that during the second loading of the beam, the maximum load of the reloading was lower than the critical load during the first loading. Specifically, the second loading reached a load of 29.62 kips (131.7 kN). A linear approximation of the post-buckling path for the first loading was made, like was done for Beam B1A, as shown in Figure 5.52, and it appeared that the reloading reaching the initial load-deflection curve. A similar trend is noticeable the load versus rotation plot in Figure 5.53. Therefore, the trend that the critical load of subsequent loadings falls on the load-deflection curve of the first loading was reaffirmed during the testing of Beam B2B.

The strain profile is plotted in Figure 5.54 for the load levels of 10 kips (44.5 kN), 20 kips (89.0 kN) and 30 kips (133.3 kN). The strain values included the summation of the strain data points collected, and the predicted initial strain in the cross-section due to prestressing and self-weight of the beam. The effect of the initial strain due to prestressing and self-weight of the beam is depicted in Figure 5.55. Figure 5.54 shows a slight nonlinearity in the strain distribution through the cross-section due to the effect of torsion on the strain distribution. It was apparent, considering the relatively low strains in the bottom of the beam cross-section, that the steel did not yield, and, furthermore, the relatively small strains at the top of the beam cross-section corresponded to a low enough concrete stress at mid-thickness, that the concrete could be considered linear-elastic. However, it is important to note that these results were at mid-thickness, and, therefore, do not consider the strains due to out-of-plane behavior.
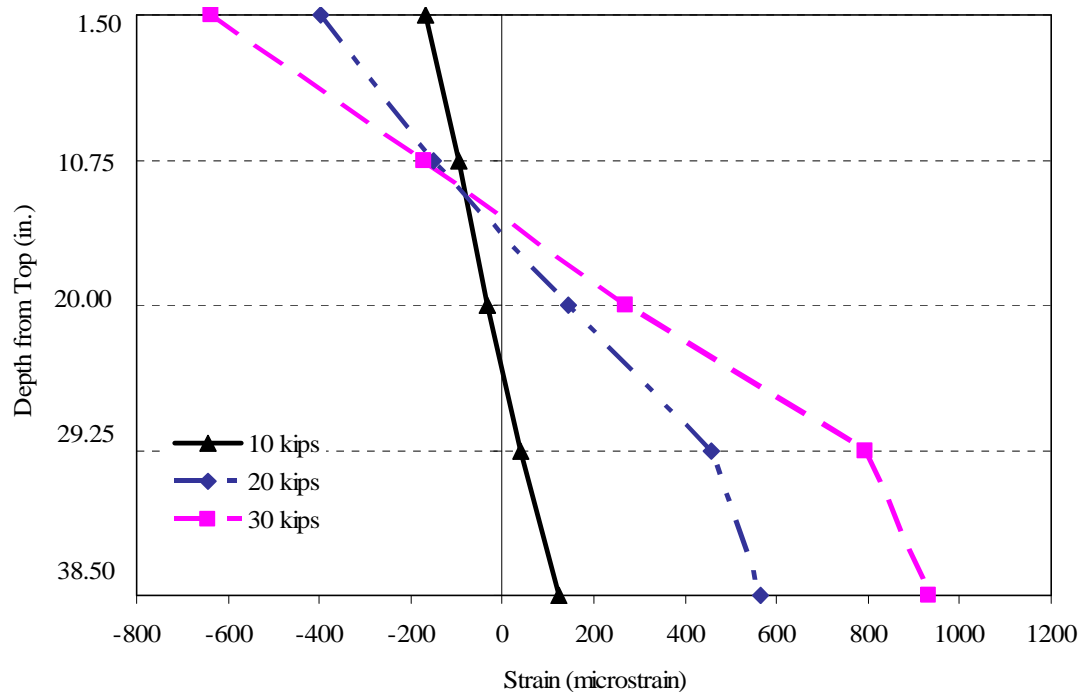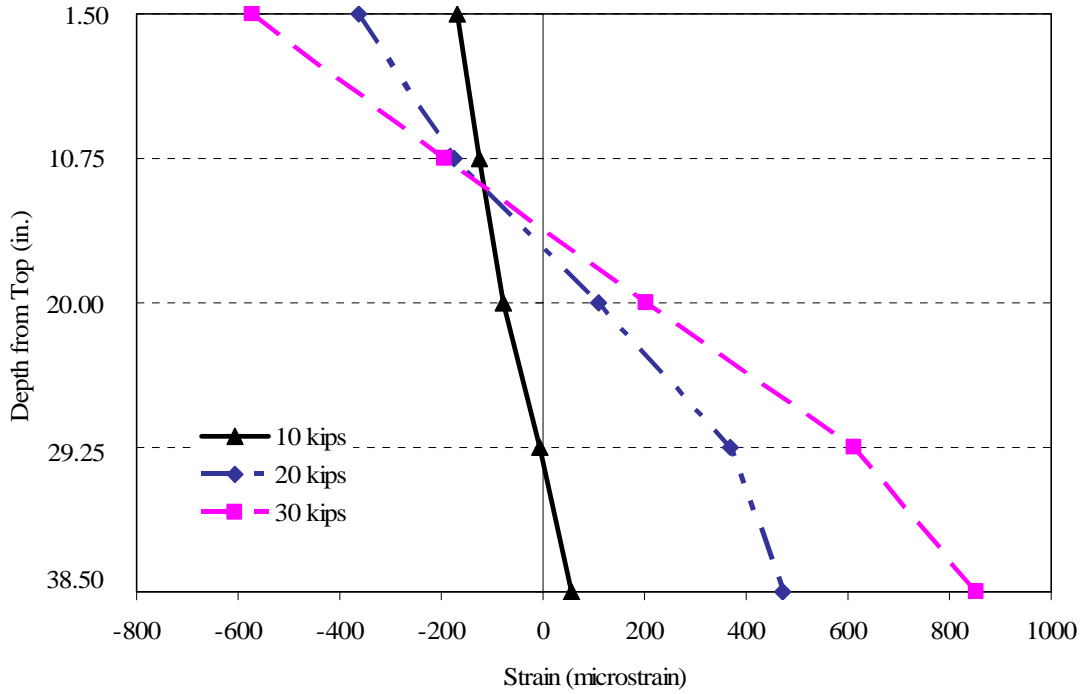
Figure 5.54 – Strain profile at mid-thickness at three load increments for Beam B2B
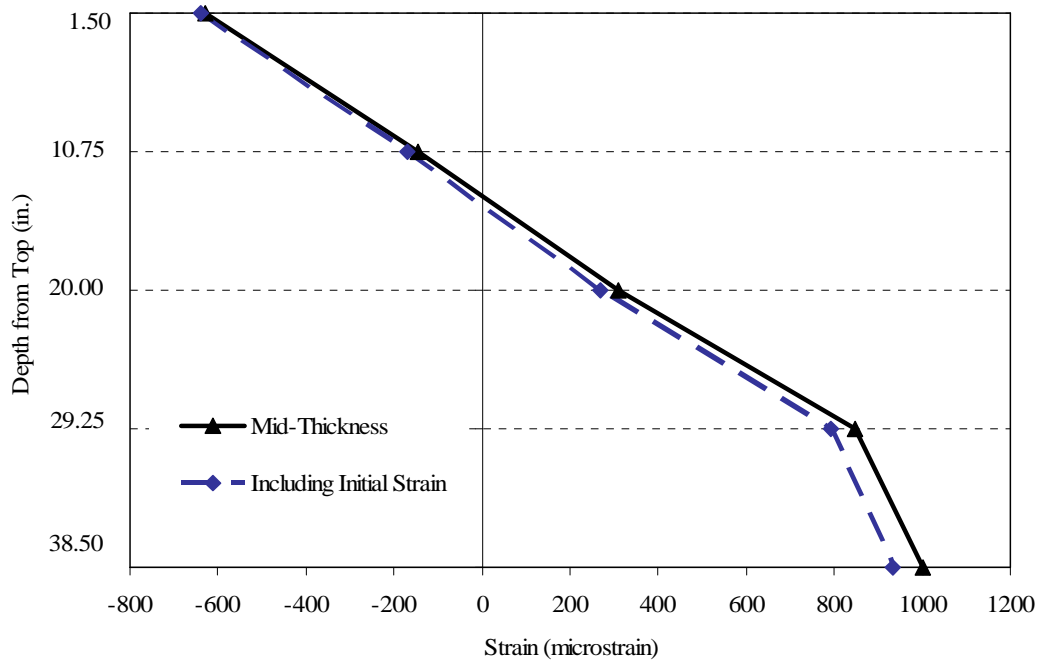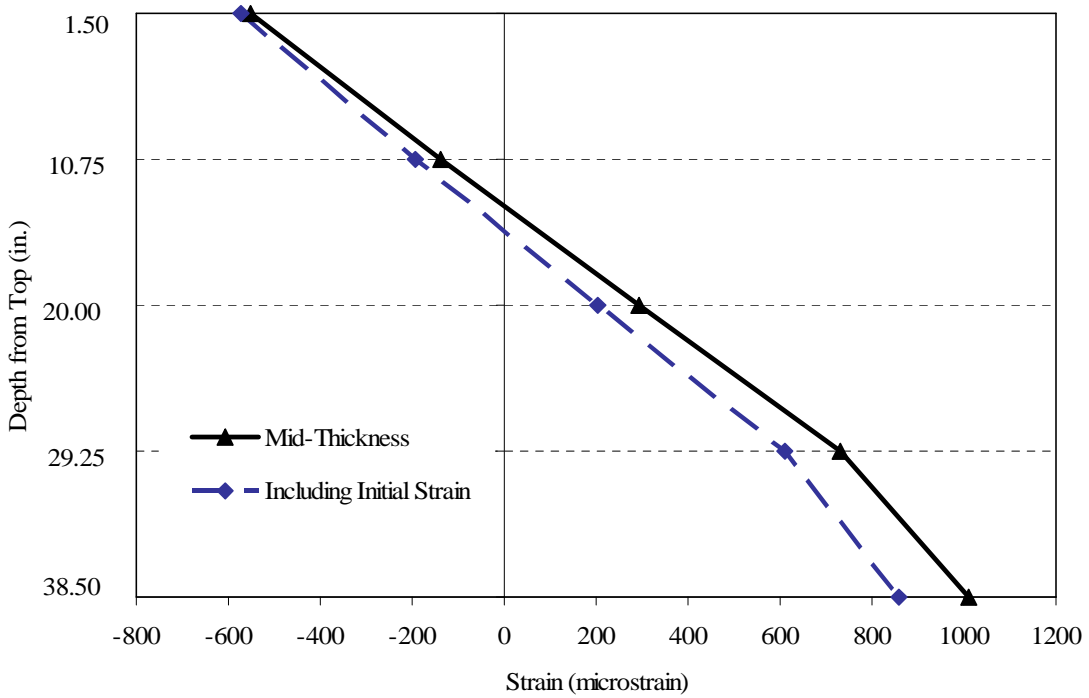

Figure 5.55 – Strain profile at mid-thickness at 30 kips (133.3 kN) for Beam B2B

191

To capture the strain due to the out-of-plane behavior of the prestressed concrete beam, a linear interpolation from the locations of the LVDTs, to the surface of the concrete was done. Figures 5.56, 5.57, and 5.58 show the surface strains for both the concave and convex side of the girder, for load levels of 10 kips (44.5 kN), 20 kips (89.0 kN) and 34 kips (151.1 kN), respectively.
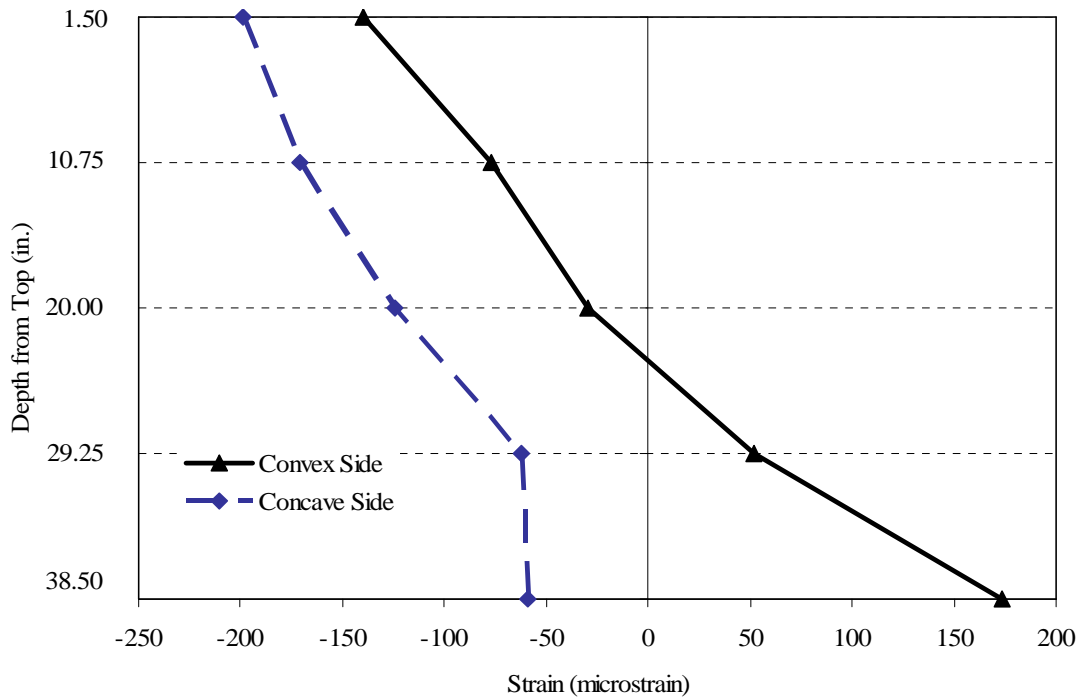
Figure 5.56 – Surface strain profile 10 kips (44.5 kN) for Beam B2B
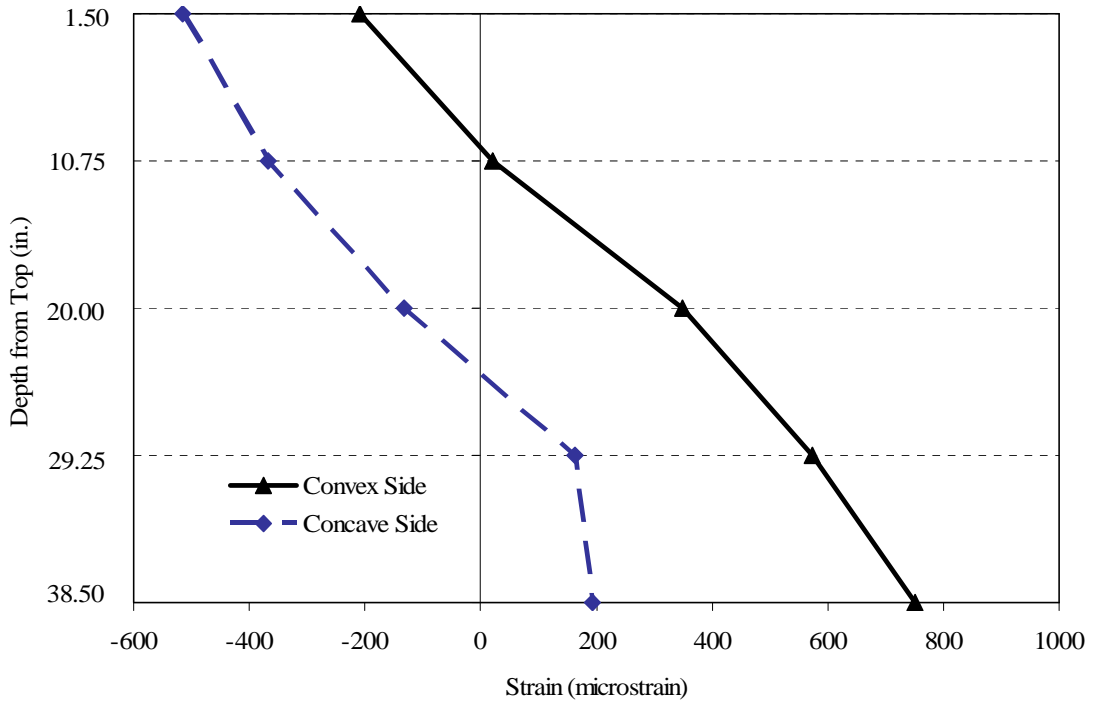
Figure 5.57 – Surface strain profile 20 kips (89.0 kN) for Beam B2B
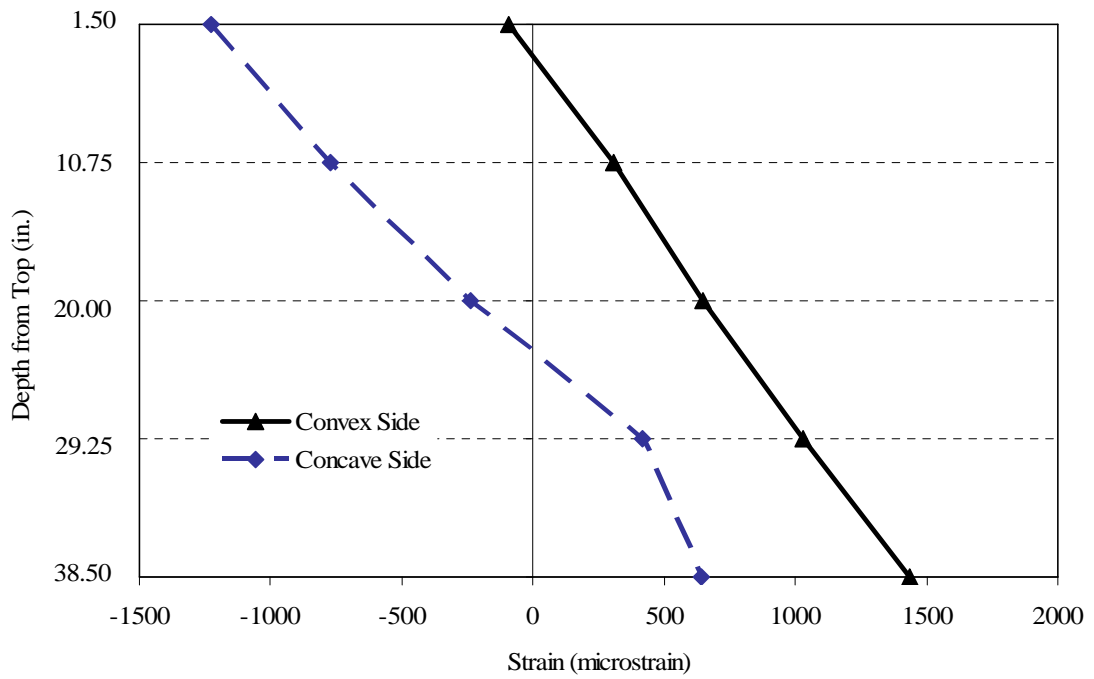
Figure 5.58 – Surface strain profile 34 kips (151.1 kN) for Beam B2B

The surface strain profiles in Figures 5.56 through 5.58 show that the concrete remained linear-elastic in the compression zone, including at the top corner, on the concave side, where the highest biaxial compressive stresses occurred. Also, the strain distribution for 34 kips (151.1 kN), as shown in Figure 5.58, shows that tensile strains developed through most of the depth of the cross-section on the convex side for this beam. Note that the load level of 34 kips (151.1 kN) was only slightly less than the maximum load attained, 34.69 kips (154.2 kN). At 30 kips (133.3 kN), cracking was investigated; flexural cracking was present, as well as a large amount of diagonal cracking. Figure 5.59 shows the large amount of diagonal cracking, particularly around the end supports. Notice that most of the diagonal cracks extend the complete depth of the beam.
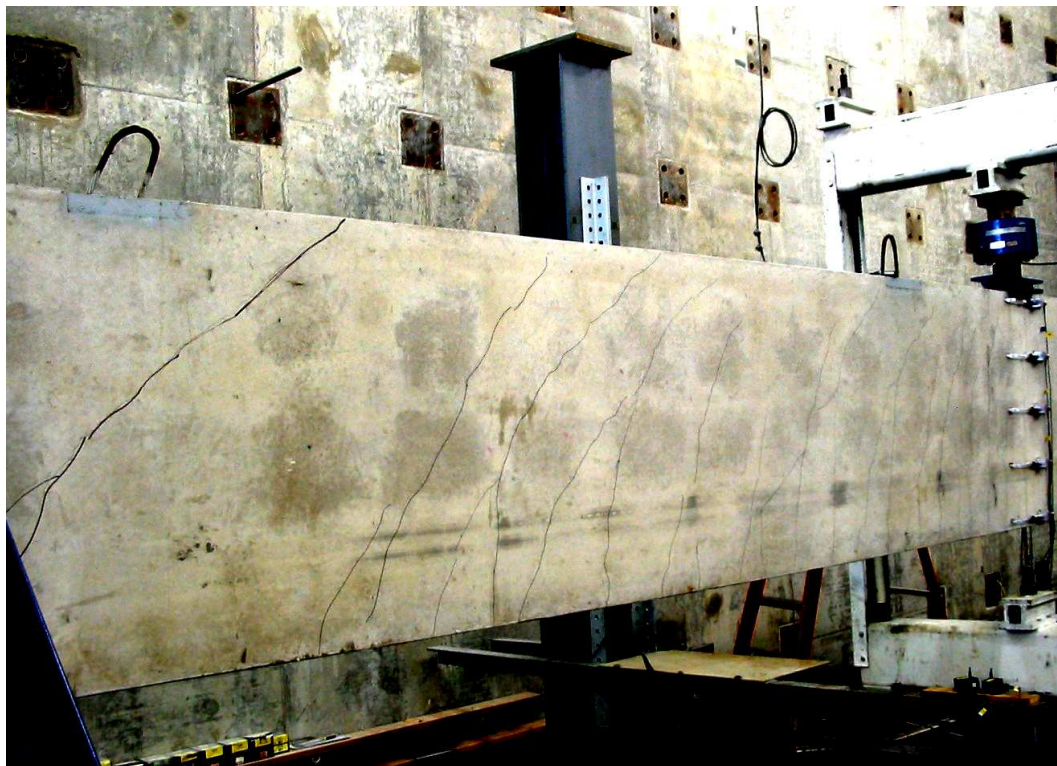
Figure 5.59 – Photo of diagonal cracking at supports after buckling of Beam B2B

5.6 Beam C2B

Beam C2B was loaded to its critical buckling load and into its post-buckling path to a significant lateral displacement. After the beam was unloaded, the beam was immediately loaded again to a load where large displacements began with little, to no additional load. The load versus lateral displacement is shown in Figure 5.60 and the load versus rotation is shown in Figure 5.61. The maximum load reached was 39.55 kips (175.8 kN) at a lateral deflection of 3.63 in (92.2 mm) at the top of the beam, and 4.10 in. (91.2 mm) at the bottom of the beam.
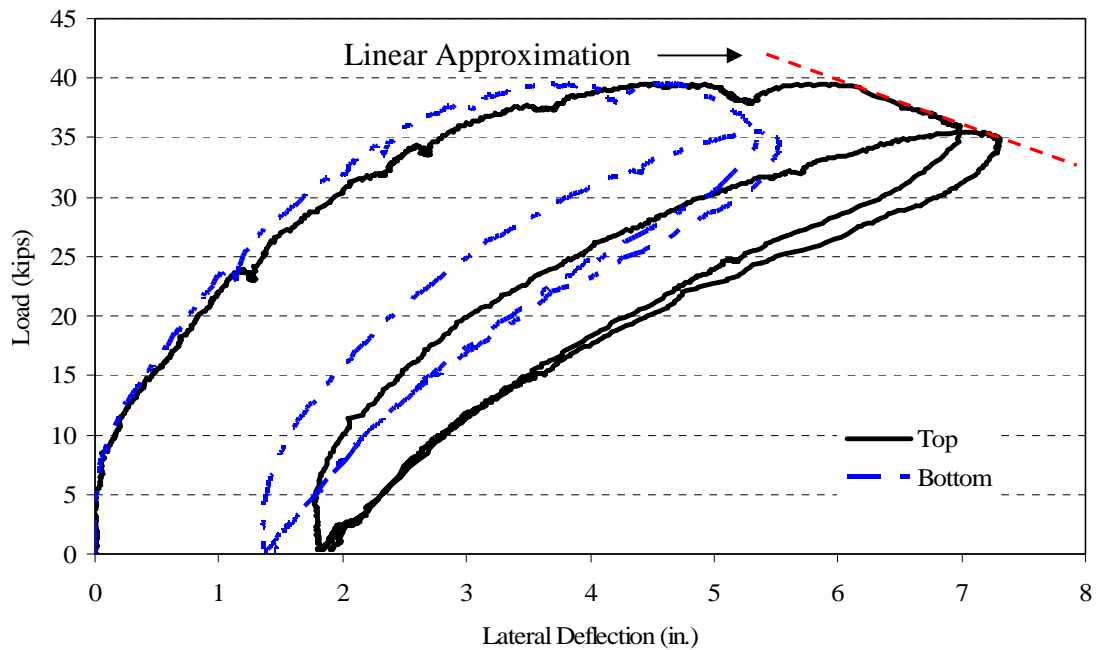
Figure 5.60 – Load vs. lateral deflection for Beam C2B
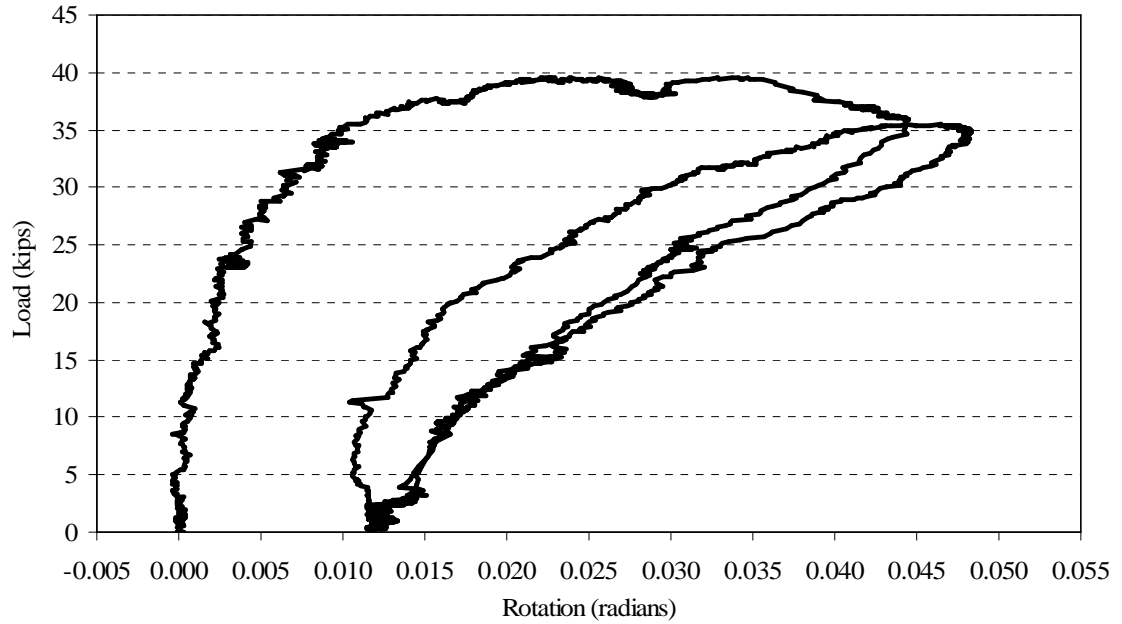
Figure 5.61 – Load vs. rotation for Beam C2B

Figure 5.60 shows that during the second loading of the beam, the maximum load during the reloading was lower than the critical load during the first loading. Specifically, the second loading reached a load of 35.49 kips (157.7 kN). A linear approximation of the post-buckling path for the first loading was made, like was done for Beam B1A, as shown in Figure 5.60, it appeared that the reloading reached the initial load-deflection curve and then unstable behavior began. A similar trend is noticeable in the load versus rotation plot in Figure 5.61. Therefore, the trend that the critical load of subsequent loadings falls on the load-deflection curve of the first loading was reaffirmed during the testing of Beam C2B.

The strain profile is plotted in Figure 5.62 for load levels of 10 kips (44.5 kN), 25 kips (111.1 kN) and 38 kips (168.9 kN). The strain values included the summation of the

strain data points collected, and the predicted initial strain in the cross-section due to prestressing and self-weight of the beam. The effect of the initial strain due to prestressing and self-weight of the beam is depicted in Figure 5.63. Figure 5.62 shows a slight nonlinearity in the strain distribution through the cross-section due to the effects of torsion on the strain distribution. It was apparent, considering the relatively low strains at the bottom of the beam cross-section, that the steel did not yield, and, furthermore, the relatively small strains at the top of the beam cross-section corresponded to a low enough concrete stress at mid-thickness, that the concrete could be considered linear-elastic. However, it is important to note that these results were at mid-thickness, and, therefore, do not consider the strains due to out-of-plane behavior.
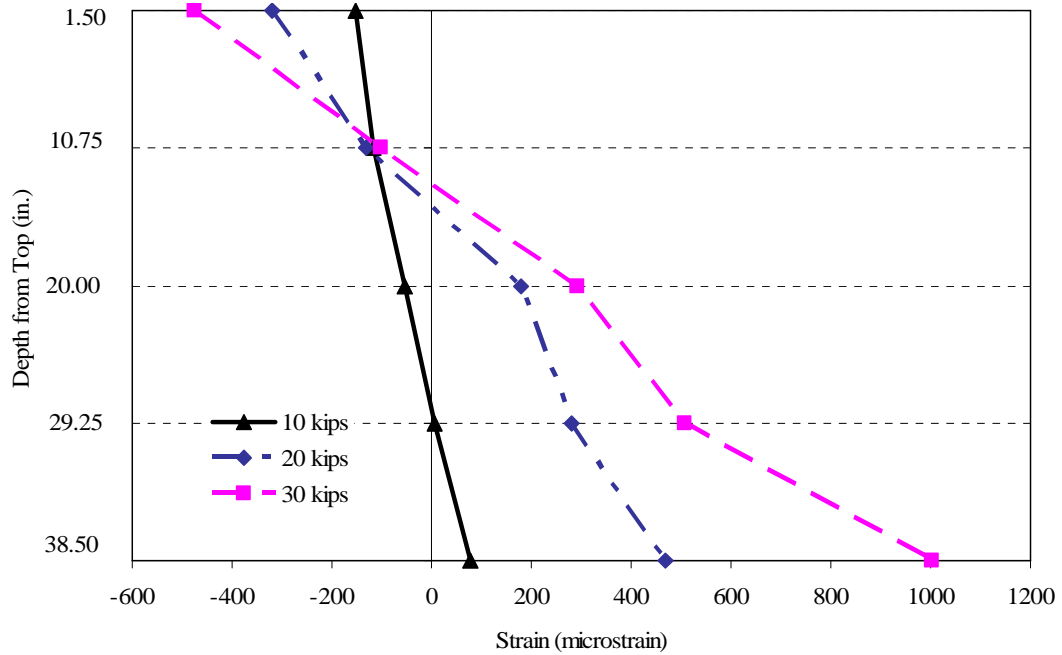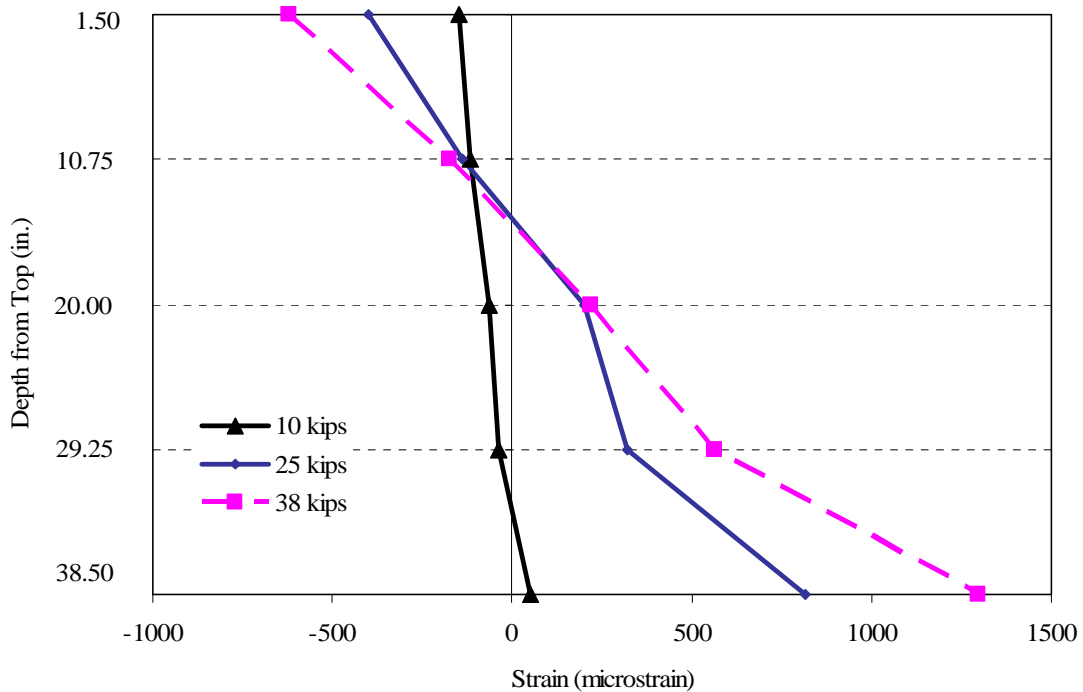

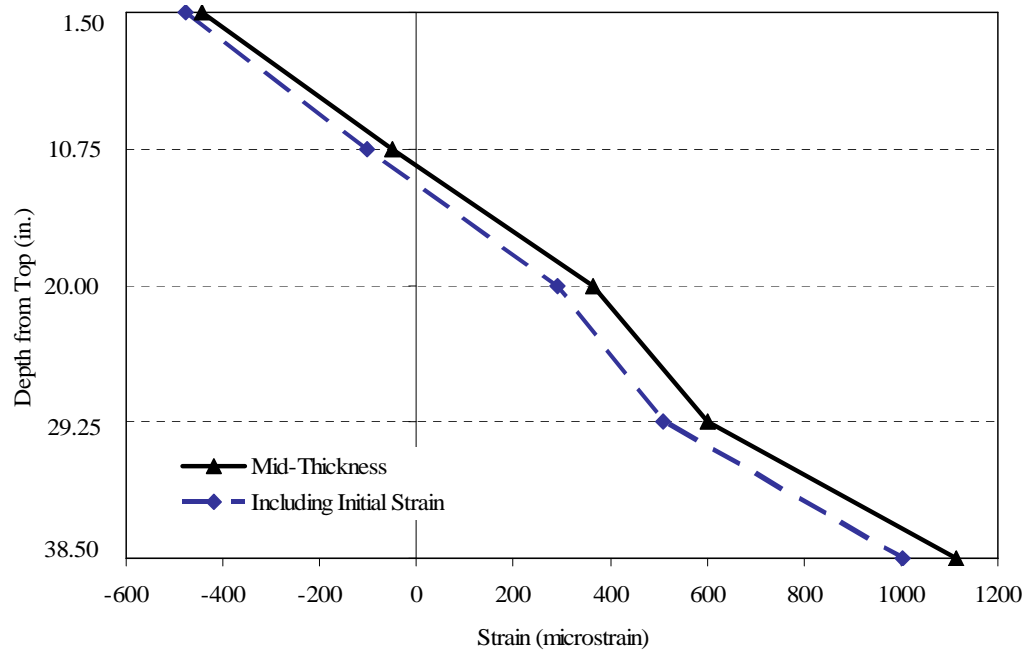Figure 5.62 – Strain profile at mid-thickness at three load increments for Beam C2B
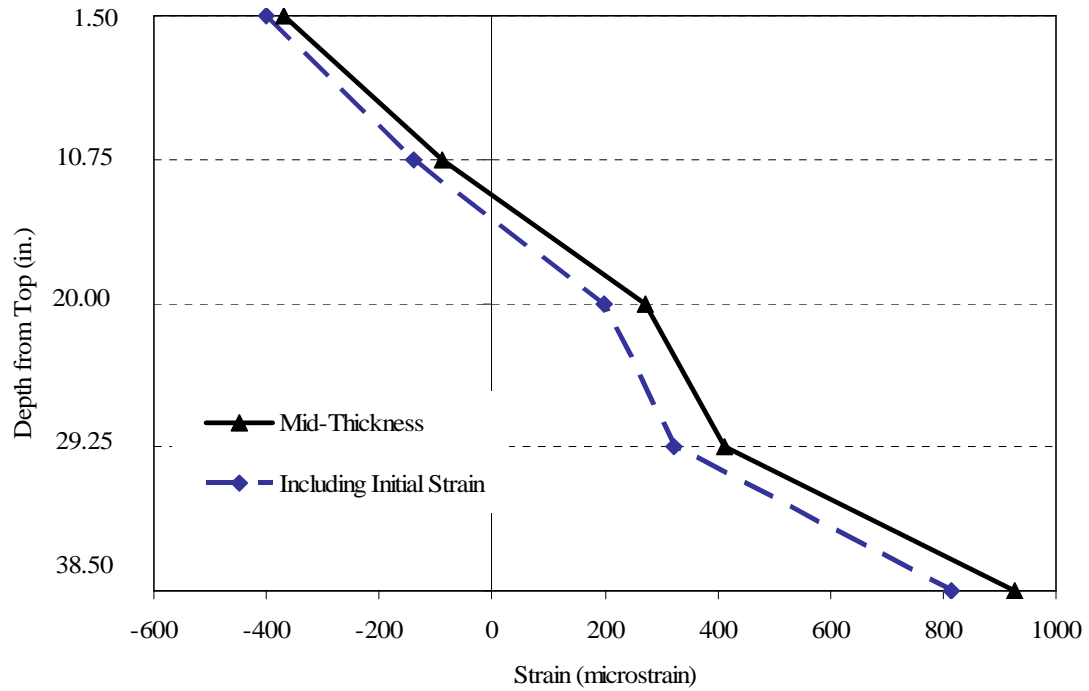
Figure 5.63 – Strain profile at mid-thickness at 25 kips (111.1 kN) for Beam C2B

To capture the strain due to the out-of-plane behavior of the prestressed concrete beam, a linear interpolation from the locations of the LVDTs, to the surface of the concrete was done. Figures 5.64, 5.65, and 5.66 show the surface strains for both the concave and convex side of the beam, for load levels of 10 kips (44.5 kN), 25 kips (111.1 kN) and 38 kips (168.9 kN), respectively.
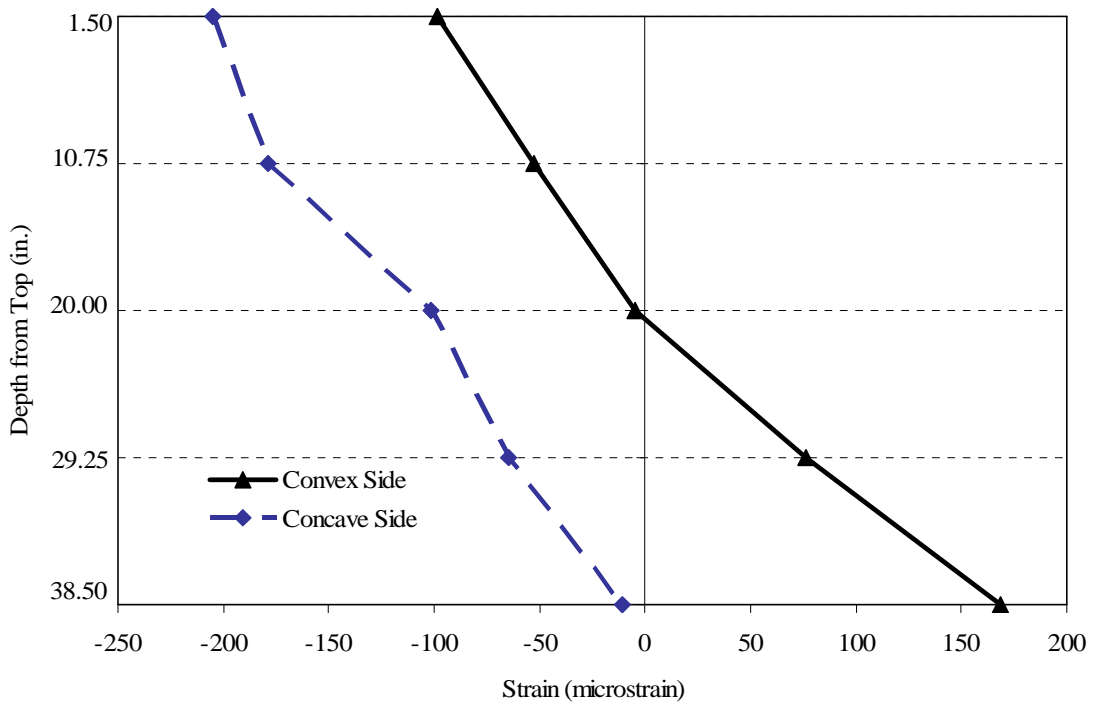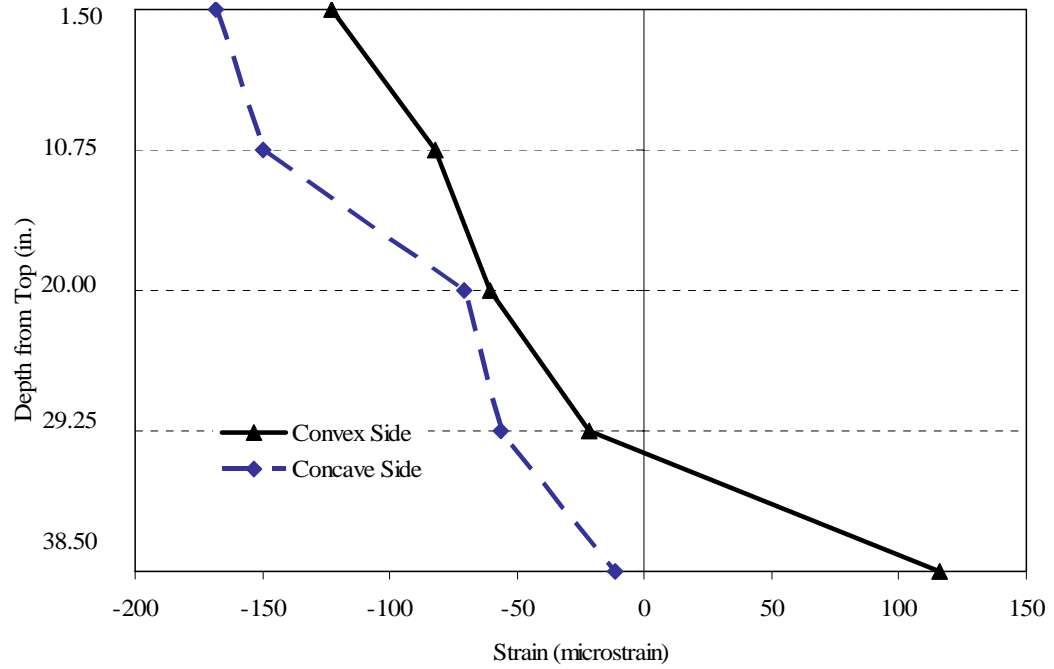
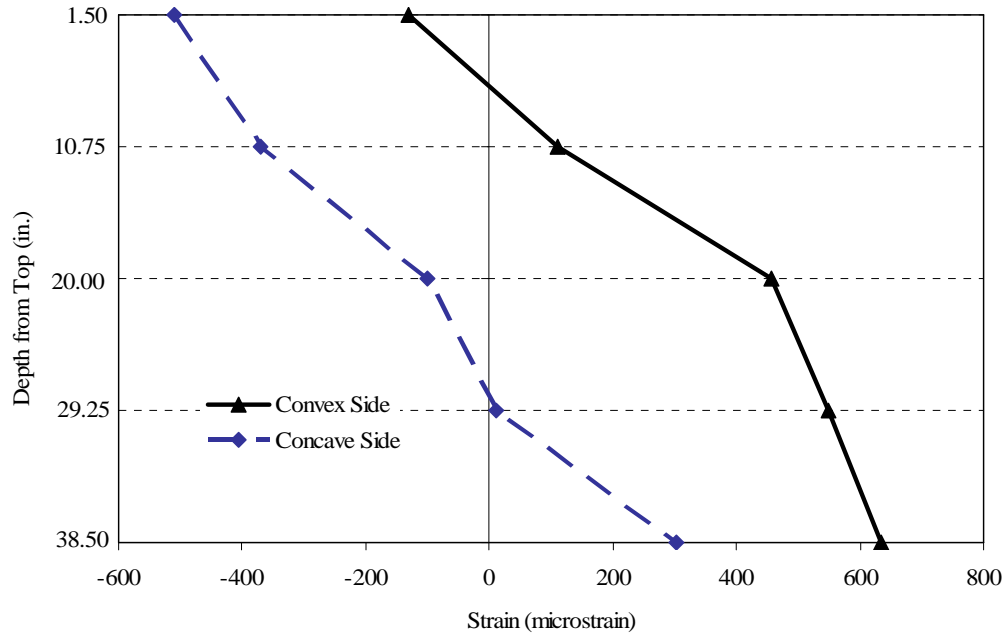Figure 5.64 – Surface strain profile 10 kips (44.5 kN) for Beam C2B

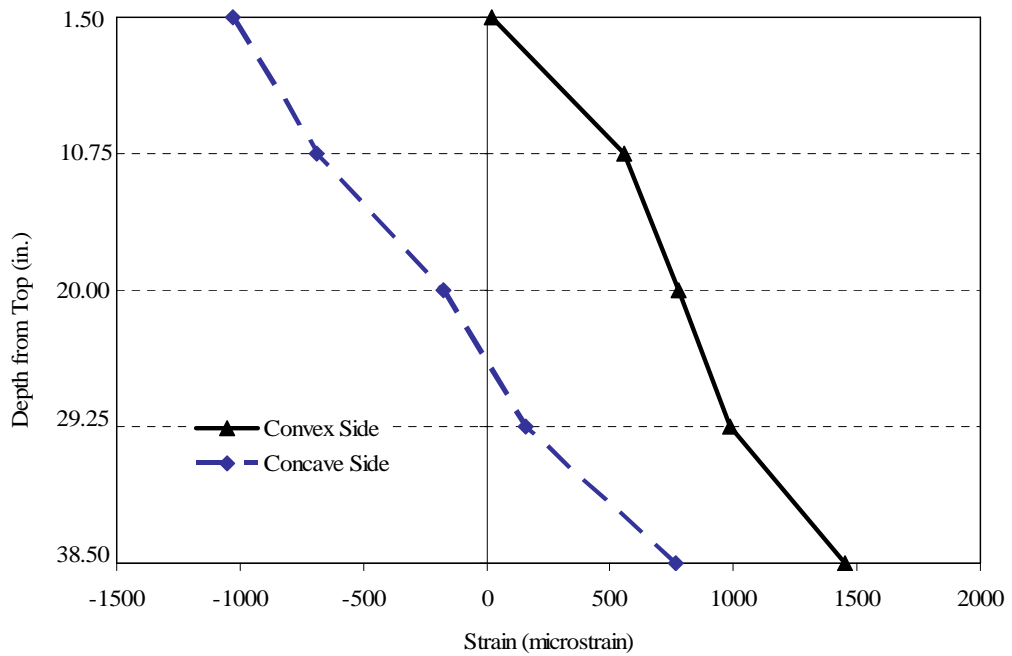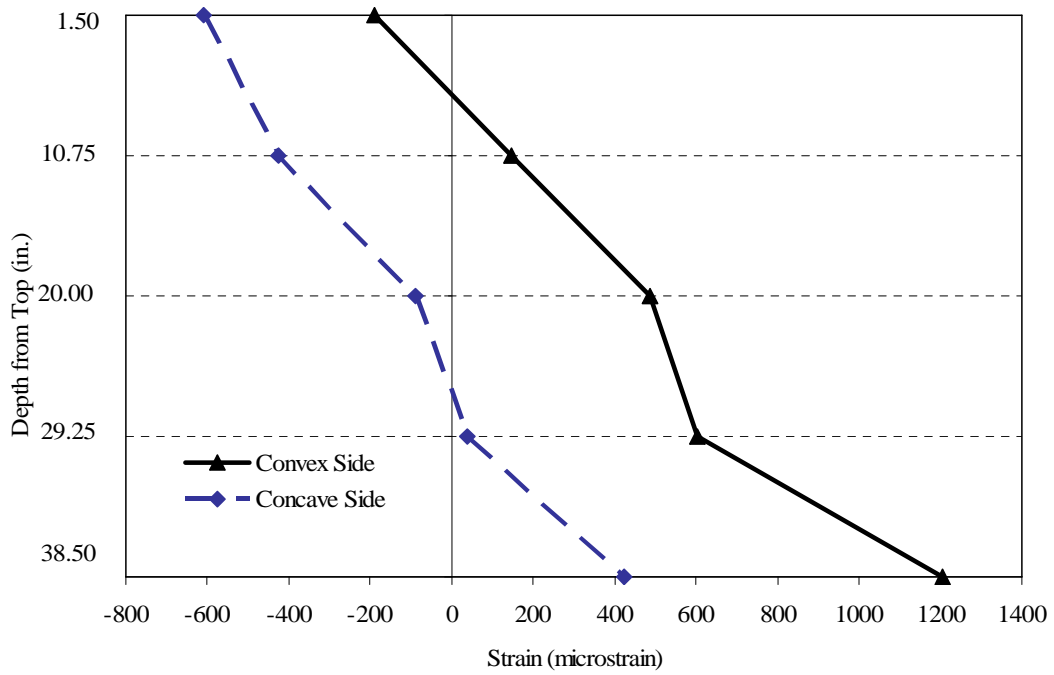Figure 5.65 – Surface strain profile 25 kips (111.1 kN) for Beam C2B

199
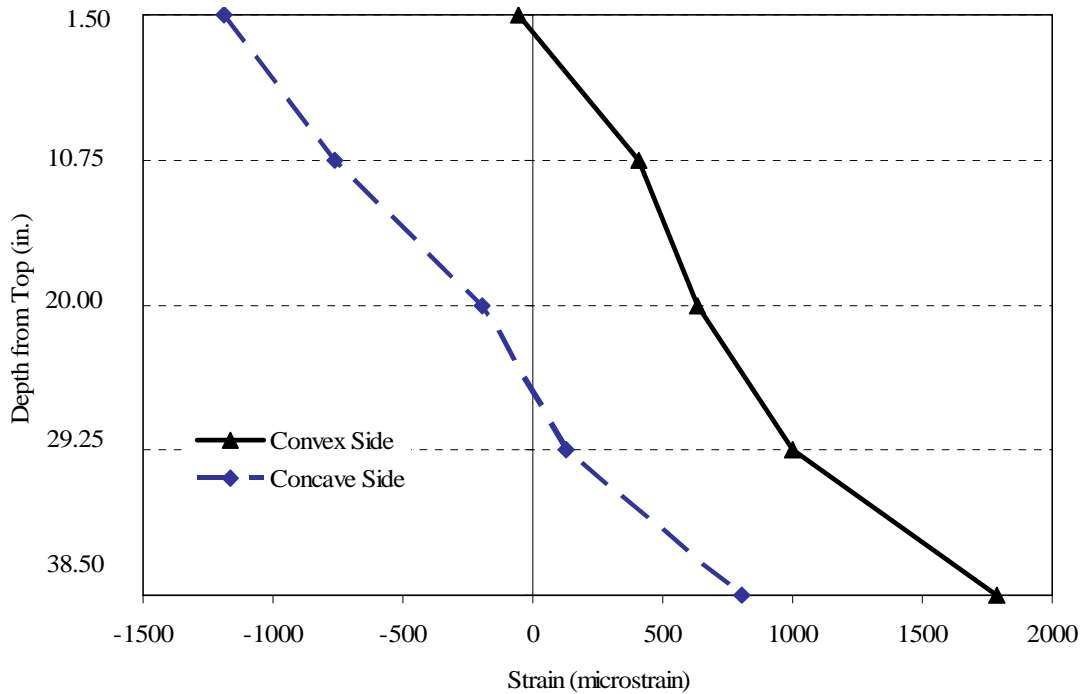
Figure 5.66 – Surface strain profile 38 kips (168.9 kN) for Beam C2B

The surface strain profiles in Figures 5.64 through 5.66 show that the concrete remained linear-elastic in the compression zone, including at the top corner, on the concave side, where the highest biaxial compressive stresses occurred. Also, the strain distribution for 38 kips (168.9 kN), as shown in Figure 5.66, shows that tensile strains developed though most of the depth of the cross-section on the convex side for this beam. Note that the load level of 38 kips (168.9 kN) was only slightly less than the maximum load attained, 39.55 kips (175.8 kN). Flexural cracking was the most prominent during this test and only around the critical load did diagonal cracking occur. Figure 5.67 shows the predominant flexural cracking before the critical load was reached and Figure 6.68 shows the transition to diagonal cracking when the critical load was reached. Beam C2B

had the smallest initial imperfections, particularly with respect to the initial rotation. Because of the relatively small initial imperfections, in-plane flexural behavior dominated until much higher loads than in the other cases, thus causing flexural cracking only until just before buckling when enough torsion developed to cause the flexural cracks to become flexural-shear cracks.
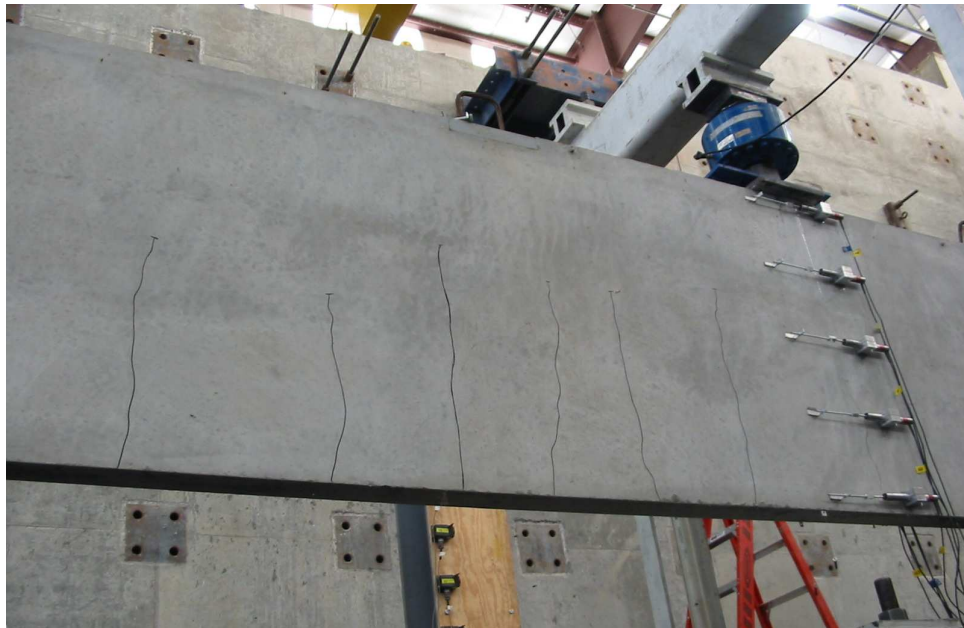
Figure 5.67 – Photo flexural cracking before buckling of Beam C2B

Figure 5.68 – Photo of diagonal cracking at the buckling load for Beam C2B

5.7 Additional Error Source

After the first experiment, it was deemed that the gravity load simulator did not remain perfectly vertical due to the self-weight of the gravity load simulator being so large. The gravity load simulator would rotate to a position where the horizontal force component was developed to equal the self-weight sway force of the gravity load simulator. To keep the load vertical at all times, a mechanism was devised to control the displacement of the gravity load simulator. The angle of the gravity load simulator was kept vertical by monitoring the angle of the bottom cross-bar of the load frame. However, after all testing on the rectangular beams were completed, it was found that the bottom cross-bar and hydraulic ram had not been perfectly perpendicular. The error

stemmed from a machined threaded rod coupler that connected the hydraulic ram threads with the threaded rod that connected with the bottom cross-bar of the load frame. The magnitude of the error was 0.012217 radians. To correct the error for future experiments, a new threaded rod coupler was fabricated that provided a much better accuracy and the initial load application angle was zeroed by measuring the angle of the hydraulic ram as opposed to the bottom cross-bar. The error was compensated for in the discussion of results and the conclusions drawn from the results. Furthermore, the error was taken into account during the analytical validation.

5.8 Results Summary and Discussion

5.8.1 Summary of Results

Several comparisons, observations and qualitative relationships were found from the analysis of the summary of results in Table 5.1. Note that positive values of displacement represent displacement away from the reaction wall, while negative displacements were those that were towards the wall, as shown in Figure 5.69. Additionally, Table 5.2 shows the depth of the compression zone and the applicable section properties that were based on the compression zone depth and shape. The compression zone depth values were found experimentally by using the strain values obtained at the surface of the beams and linearly interpolating to find the location of zero strain. Table 5.2 shows that the compression zone was not rectangular and the neutral axis had a significant angle. Table 5.2 will be important for later discussion.

Table 5.1 – Summary of experimental results

| Beam ID | Initial Imperfections | | | E_c, ksi (GPa) | P_{buckle}, kips (kN) | P_{buckle} Sweep Top, in. (mm) | P_{buckle} Sweep Bottom, in. (mm) |
	Sweep Top, in. (mm)	Sweep Bottom, in. (mm)	Rotation (radians)				
B1A	-0.406 (-10.3)	-0.406 (-10.3)	0	4713 (32.5)	36.87 (163.9)	3.46 (87.9)	2.92 (74.2)
B1B	-0.344 (-8.7)	-0.375 (9.5)	0.00078	4713 (32.5)	33.92 (150.8)	3.59 (91.2)	3.19 (81.0)
B2A	1.50 (38.1)	1.06 (27.0)	0.011	4188 (28.9)	35.26 (156.8)	2.17 (55.1)	1.57 (39.9)
B2B	-0.484 (-12.3)	-0.547 (-13.9)	0.00156	4188 (28.9)	34.69 (154.2)	3.08 (78.2)	2.82 (71.6)
C2A	0.227 (5.8)	0.398 (10.1)	0.00430	5156 (35.5)	33.68 (149.7)	3.88 (98.6)	3.37 (85.6)
C2B	-0.172 (-2.4)	-0.203 (-4.0)	0.00078	5156 (35.5)	39.55 (175.8)	4.10 (104.1)	3.59 (91.2)

The results from Beam B2A were left out of this discussion for several reasons. Beam B2A was the first beam tested, and, therefore the gravity load simulator's angle was not consistently controlled as was discussed in section 5.1.7 Additional Error. The data for Beam B2A did not reflect many of the apparent trends, and the author believes this was due to a failure to maintain the load in the direction of gravity nearly as well as in the subsequent tests. Furthermore, observations could have been made even though the load was not in the direction of gravity; however, it was unknown what the actual applied load angle was.

Table 5.2 – Experimental compression zone depth and section properties

Beam ID	Load, kips (kN)	Beam Rotation, radians	Compression Zone Depth, in. (mm)			phi, radians	I_x, in^4 (cm^4)	I_y, in^4 (cm^4)
			Convex Side	Concave Side	Center			
B1A	10 (44.5)	0.00023	20.97 (533)	28.47 (723)	24.72 (628)	1.08	14111 (587344)	131 (5454)
	20 (89.0)	0.00133	11.87 (301)	18.98 (482)	15.42 (392)	1.06	14549 (605575)	81 (3382)
	30 (133.3)	0.00472	8.87 (225)	19.04 (484)	13.96 (354)	1.20	14929 (621392)	72 (3005)
B1B	10 (44.5)	0.00013	17.64 (448)	31.29 (795)	24.47 (621)	1.29	14395 (599165)	128 (5320)
	20 (89.0)	0.00477	8.80 (224)	19.10 (485)	13.95 (354)	1.20	14927 (621309)	72 (3002)
	30 (133.3)	0.01195	3.13 (79.5)	19.28 (490)	11.21 (285)	1.33	15470 (643910)	53 (2217)
B2A	10 (44.5)	0.00217	19.67 (500)	31.90 (810)	25.79 (655)	1.25	14628 (608863)	135 (5639)
	20 (89.0)	0.00530	10.95 (278)	22.15 (563)	16.55 (420)	1.23	14288 (594711)	86 (3574)
	30 (133.3)	0.01059	8.02 (204)	21.13 (537)	14.58 (370)	1.27	14705 (612068)	74 (3086)
B2B	10 (44.5)	-0.00107	23.34 (593)	38.41 (976)	30.88 (784)	1.31	17236 (717416)	162 (6742)
	20 (89.0)	0.00076	9.95 (253)	24.13 (613)	17.04 (433)	1.30	14220 (591881)	87 (3626)
	30 (133.3)	0.00786	5.72 (145)	22.56 (573)	14.14 (359)	1.34	14709 (612235)	69 (2887)
C2A	10 (44.5)	0.00132	20.32 (516)	31.66 (804)	25.99 (660)	1.23	14626 (608780)	137 (5697)
	20 (89.0)	0.00614	8.44 (214)	26.06 (662)	17.25 (438)	1.35	14224 (592048)	86 (3589)
	30 (133.3)	0.01541	3.84 (98)	23.97 (609)	13.91 (353)	1.37	14622 (608614)	65 (2722)
C2B	10 (44.5)	0.00059	27.09 (688)	31.03 (788)	29.06 (738)	0.78	15406 (641246)	155 (6443)
	25 (111.2)	0.00428	8.15 (207)	24.85 (631)	16.50 (419)	1.34	14305 (595419)	83 (3440)
	38 (169.0)	0.01788	3.96 (101)	24.90 (632)	14.43 (367)	1.38	14512 (604035)	68 (2819)
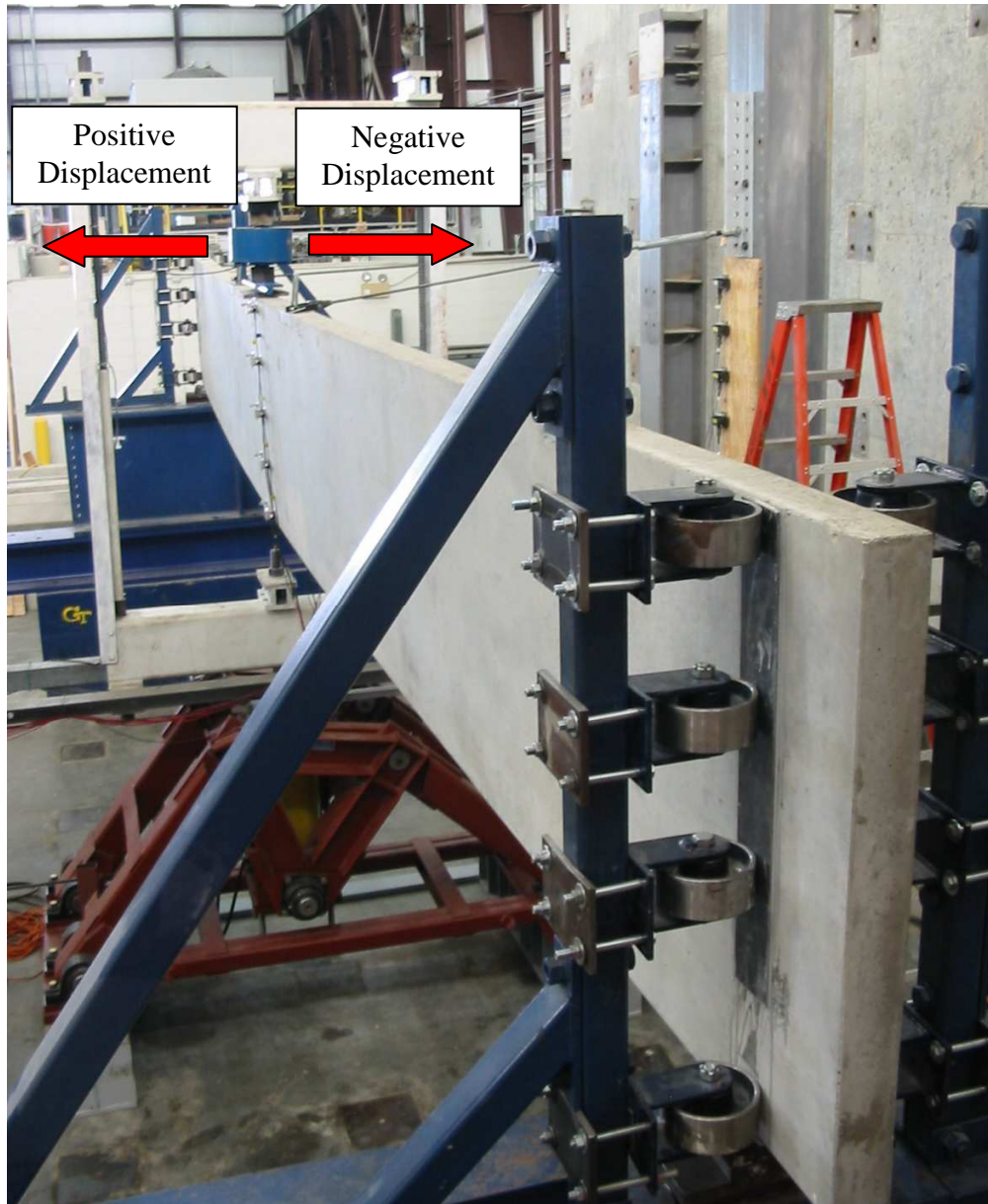
Figure 5.69 – Test setup with positive and negative displacement convention noted

The first observation was made by comparing the experiments of Beams B1A and B1B, and the experiments of Beams C2A and C2B. Note that many of the beams had sweep in the negative direction which was not the direction of buckling. Therefore, a lower magnitude of negative sweep caused the beam to be more prone to buckling, and, furthermore, as the loading increased, the negative sweep would become positive due to the angle of the load from the error in the set-up pushing the beams in the positive displacement direction. When making the comparisons, the effect of the concrete's modulus of elasticity, prestressing strand pattern and prestressing force was eliminated, and, therefore, the only difference between beams was the initial imperfections. In the case of the B1 beam series, B1A had slightly larger sweep measurements than Beam B1B, but in both cases the sweep was in the negative direction, and, furthermore, Beam B1B had twice the initial rotation of Beam B1A. Both beams of the series B1 had rotations that opposed the sweep direction, but buckled in the positive direction, or the direction that was favored by the rotation, and not the sweep. That would suggest that the direction of buckling was governed by the direction of the rotation, and not necessarily by the direction of the sweep; however, it cannot be determined from these experiments due to the error in the applied load angle. Beam B1B, the beam with the larger initial rotation, buckled at a load approximately 8% less than beam B1A, which suggested that an increased initial rotation reduced the buckling load. Figure 5.70 shows a plot of the buckling loads versus initial rotation for both the B1 and C2 series. Figure 5.70 makes the effect of rotation more apparent. Note that the rotation plotted in Figure 5.70 was the initial rotation not including the error in load application angle because that was a constant throughout the testing. Furthermore, Figure 5.71 shows a plot of the buckling

loads versus initial sweep at mid-depth for both the B1 and C2 series. From Figures 5.70 and 5.71, the trend was that a larger positive initial rotation combined with a larger initial sweep (in the positive direction) resulted in lower buckling loads. In the case of the C2 beam series, Beam C2A had a larger sweep (in the positive direction) and larger initial rotation than Beam C2B. Beam C2A, the beam with the larger initial rotation, buckled at a load that was approximately 15% less than beam C2B.
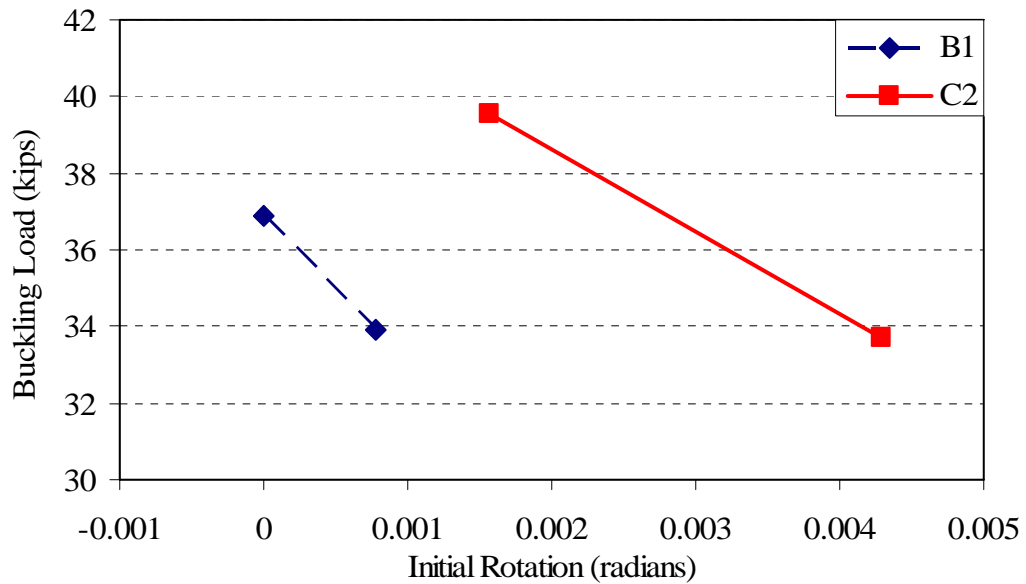
Figure 5.70 – Buckling load versus initial rotation
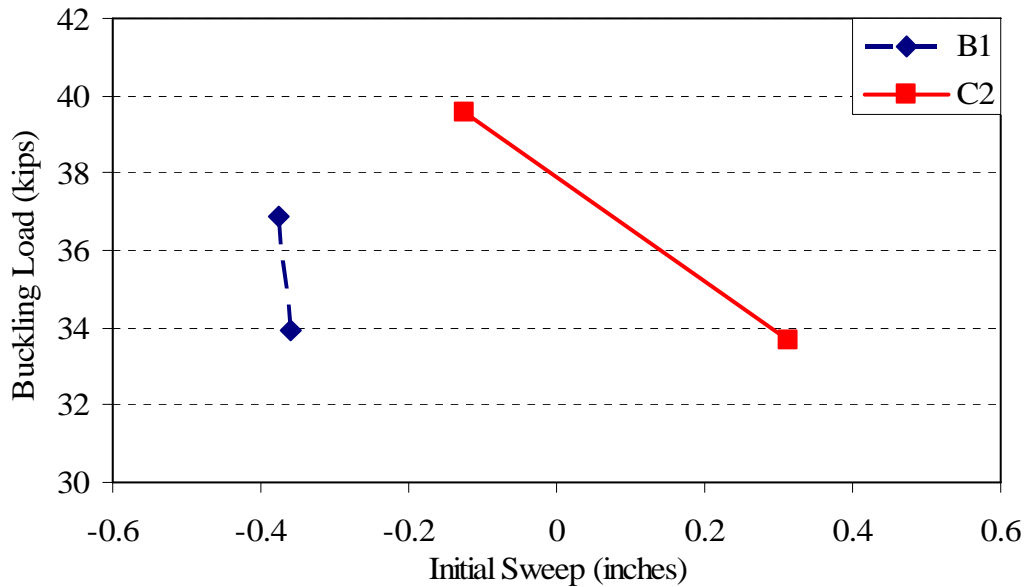
Figure 5.71 – Buckling load versus initial sweep

The effect of the prestressing strand location and force as well as the initial concrete modulus of elasticity cannot be inferred directly from the experimental data. Because of the variability of the concrete modulus of elasticity between series, it was difficult to determine whether the difference in buckling loads was due to the modulus of elasticity or the influence of prestressing strand location and force. To determine the effect of the prestressing force and strand location, the buckling load was normalized by the initial concrete modulus of elasticity because the classical lateral-torsional buckling formulation was a linear function of the modulus of elasticity. By normalizing the buckling load with respect the modulus of elasticity, the effect of the modulus of elasticity was removed from consideration. The normalized results are shown in the last column of Table 5.3.

Table 5.3 – Normalized buckling load with respect to initial concrete modulus

Beam ID	Initial Imperfections			f_c' (ksi)	E_c (ksi)	P_{buckle} (kips)	P_{buckle}/f_c' (in^2)	P_{buckle}/E_c (in^2)
	Sweep Top (in.)	Sweep Bottom (in.)	Rotation (radians)					
B1A	-0.406	-0.406	0	10.133	4713	36.87	3.46	7.82E-03
B1B	-0.344	-0.375	0.00078	10.133	4713	33.92	3.59	7.20E-03
B2A	1.500	1.060	0.01100	6.015	4188	35.26	2.17	8.42E-03
B2B	-0.484	-0.547	0.00156	6.015	4188	34.69	3.08	8.28E-03
C2A	0.227	0.398	0.00430	11.281	5156	33.68	3.88	6.53E-03
C2B	-0.172	-0.203	0.00156	11.281	5156	39.55	4.10	7.67E-03

From Table 5.3, Beam C2B had a larger normalized buckling load than Beam B1B even though Beam C2B had twice the initial rotation and an initial sweep that was more favorable to buckling than the initial sweep for Beam B1B. Therefore, two prestressing strands located at the center of the cross-section created a more stabilizing effect than one strand located near the bottom of the cross-section. That conclusion was consistent with concept that a larger compression zone would create a higher buckling load. Beam B2B also had a larger normalized buckling load than Beam B1B and had a larger initial rotation. Although the initial sweep was more favorable to buckling in the case of Beam B1B, because the normalized buckling load for Beam B2B was 15% larger and the initial sweep was twice as large as Beam B1B, the conclusion that a larger compression zone creates a higher buckling load was further verified.

5.8.2 Current Analytical Techniques vs. Experimental Results

A summary of the analytical results from the current analytical methods discussed in Chapter 1, applied to all of the beams tested, is shown in Table 5.4. Additionally, Table 5.4 shows a summary of the experimental buckling loads for all of the tested

rectangular beams, with a comparison between the experimental and analytical results. The percent difference was calculated by using Equation 5.1; therefore, a positive percent difference was conservative.

Table 5.4 – Comparison of analytical methods to experimental results

	Beam Specimen ID					
	B1A	B1B	B2A	B2B	C2A	C2B
Experimental Buckling Load, kips (kN)	36.87 (163.9)	33.92 (150.8)	35.26 (156.7)	34.69 (154.2)	33.68 (149.7)	39.55 (175.8)
Elastic kips (kN)	153.13 (680.6)	153.13 (680.6)	133.47 (593.3)	133.47 (593.3)	167.06 (742.6)	167.06 (742.6)
% Difference	-315.32	-351.44	-278.53	-284.75	-396.02	-322.40
Hansell & Winter (1959) No Prestressing Force	47.04 (209.1)	47.04 (209.1)	39.53 (175.7)	39.53 (175.7)	50.68 (225.3)	50.68 (225.3)
% Difference	-27.58	-38.68	-12.11	-13.95	-50.48	-28.14
Hansell & Winter (1959)	57.12 (253.9)	57.12 (253.9)	45.65 (202.9)	45.65 (202.9)	63.33 (281.5)	63.33 (281.5)
% Difference	-54.92	-68.40	-29.47	-31.59	-88.03	-60.13
Sant & Bletzacker (1961)	71.41 (317.4)	71.41 (317.4)	62.07 (275.9)	62.07 (275.9)	80.81 (359.2)	80.81 (359.2)
% Difference	-93.68	-110.52	-76.04	-78.93	-139.93	-104.32
Massey (1964)	68.44 (304.2)	68.44 (304.2)	56.69 (252.0)	56.69 (252.0)	69.96 (311.0)	69.96 (311.0)
% Difference	-85.63	-101.77	-60.78	-63.42	-107.72	-76.89
Rafla (1969)	90.481 (402.2)	90.48 (402.2)	61.49 (273.3)	61.49 (273.3)	101.44 (450.9)	101.44 (450.9)
% Difference	-145.41	-166.75	-74.39	-77.26	-201.19	-156.49
Stiglat (1971)	95.92 (426.3)	95.92 (426.3)	61.43 (273.0)	61.43 (273.0)	105.78 (470.2)	105.78 (470.2)
% Difference	-160.16	-182.78	-74.22	-77.08	-214.07	-167.46
Malangone (1977)	158.21 (703.2)	158.21 (703.2)	140.55 (624.7)	140.55 (624.7)	166.03 (737.0)	166.03 (737.0)
% Difference	-329.10	-366.42	-298.61	-305.16	-392.96	-319.80
Revathi & Menon (2006)	20.12 (89.4)	20.12 (89.4)	24.63 (109.5)	24.63 (109.5)	21.81 (96.9)	21.81 (96.9)
% Difference	45.43	40.68	30.15	29.00	35.24	44.85

$$\% \ Difference = \frac{\left(Experimental - Analytical\right)}{Experimental} \qquad (5.1)$$

The primary observation that was taken from Table 5.4 was the extremely large

scatter in predicted results for all of the analytical methods presented. From Table 5.4, it

was apparent that the analytical methods by Hansell and Winter (1959) and Revathi and

Menon (2006) were the most accurate analytical approaches. Essentially, the analytical

procedure of Hansell and Winter (1959) used classical lateral-torsional buckling

equations, but used the secant modulus of elasticity for the modulus of elasticity, and

calculated both the moments of inertia, and torsion constant, based on the depth of the

compression zone. The analytical procedure of Revathi and Menon (2006) used a

flexural rigidity formula originally proposed by Branson (Pillai and Menon, 2002), with a

modification where 80% of the ultimate flexural moment was used instead of the entire

ultimate flexural moment capacity to determine the flexural rigidity. For the torsional

rigidity, Revathi and Menon (2006) used Tavio and Teng's (2004) torsional rigidity

equation which was based on torsionally cracking reinforced concrete member. The

details of these methods were presented in Chapter 1.

Table 5.4 includes two rows for Hansell and Winter (1959); the first row included

the effect of the area of steel of the prestressing strands, but not the prestressing force,

while the second row included the effect of the prestressing force on the compression

zone of the cross-section. The predicted buckling loads for the case where the effect of

the prestressing force was considered were larger than the predicted buckling loads when

the effect of the prestressing force was neglected. That was because the prestressing

force caused a larger compression zone depth, and, therefore, the rigidity properties

calculated were larger based on the method by Hansell and Winter (1959).

For both cases of predicted buckling loads determined by using the method by

Hansell and Winter (1959), the buckling load was over-predicted, and, therefore,

unconservative. There were some possibilities why the method was over-predicting the

results. First, the torsion constant was based on the compression zone depth, but the

coefficient k_1 in the equation for the torsion constant, shown in Equation 5.2 from

Timoshenko and Goodier (1970), was calculated using the entire depth of the beam

instead of the compression zone depth. Using the entire depth of the cross-section would

result in a larger k_1, and, thus, a larger torsion constant than if the depth of the

compression zone was used in the equation.

$$J = k_1 cb^3 \qquad\qquad (5.2)$$

where:

$$k_1 \quad = \quad \frac{1}{3}\left[1 - \frac{192b}{\pi^5 d}\sum_{n=1,3,5...}^{\infty}\frac{1}{n^5}\tanh\left(\frac{n\pi d}{2b}\right)\right]$$

Secondly, the moments of inertia and the torsion constant were based on a

rectangular compression zone with the dimensions as the width of the beam and the depth

213

of the compression zone. However, unless the beam was initially perfect, the

compression zone would not be rectangular, but instead a trapezoid. The compression

zone depth on each side of the beams, the associated neutral axis angle, and moments of

inertia based on the compression zone depth was shown in Table 5.2. Table 5.2 shows

that the compression zone was in fact a trapezoid and the angle of the neutral axis was

substantial. To visualize the actual shape of the compression zone, the surface strain

profiles for Beam C2B at 10 kips (44.5 kN) and 38 kips (168.9 kN) are presented in

Figures 5.72 and 5.73, respectively. In the case that the compression zone was

rectangular, the lines representing the surface strain would intersect the ordinate at the

same value. Beam C2B had relatively minimal initial imperfections; however, at a

loading of 10 kips (44.5 kN), the lines representing the surface strains did not intersect

the ordinate at the same value, as shown in Figure 5.72. Furthermore, at a loading of 38

kips (168.9 kN), the lines representing the surface strains intersect the ordinate at

significantly different values. The compression zone shapes at the two presented load

values are shown in Figure 5.74. As the load increased, the compression zone shape

changed from a rectangle, to a trapezoid, and then it approached a triangle.
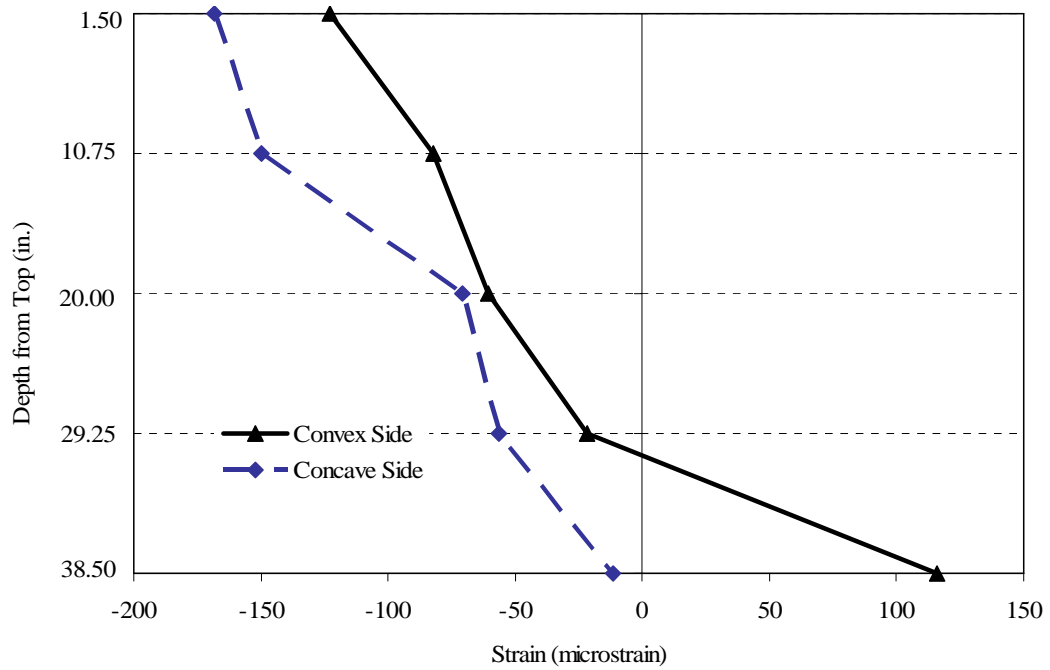
Figure 5.72 – Surface strain profile 10 kips (44.5 kN) for Beam C2B
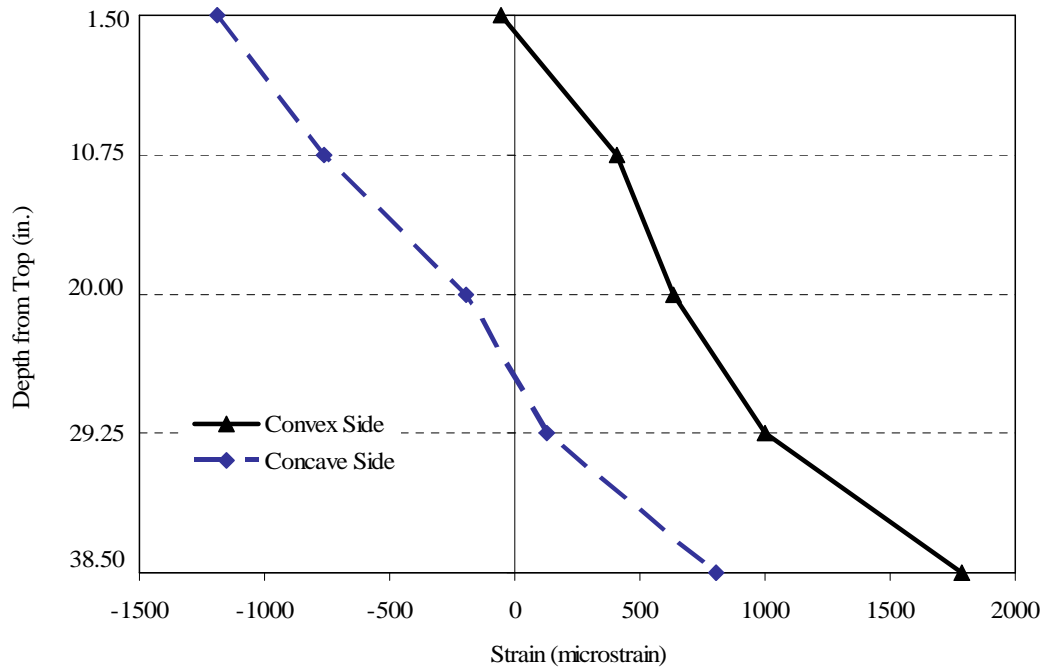
Figure 5.73 – Surface strain profile 38 kips (168.9 kN) for Beam C2B
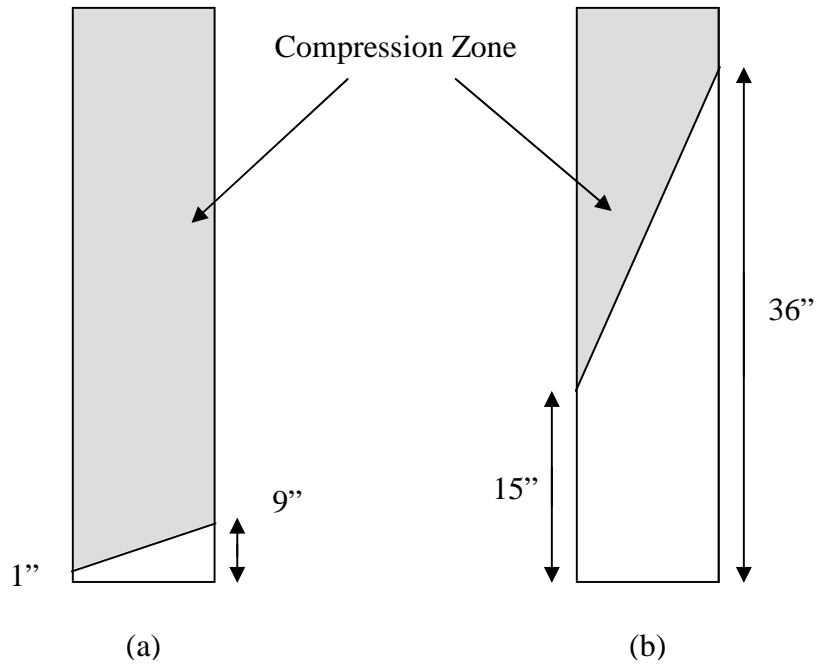
Figure 5.74 – Compression zones for Beam C2B at (a) 10 kips (44.5 kN) (b) 38 kips (168.9 kN)

Lastly, none of the aforementioned analytical procedures considered initial imperfections. Initial imperfections would serve to reduce the buckling load, and, therefore, any analytical procedure should take initial imperfections into account or the buckling load would be less than what was predicted. Figure 5.75 shows a plot of the normalized buckling moment to ultimate flexural moment ratio versus the slenderness ratio for the experimental data from the current study, Hansell and Winter (1959), Sant and Bletzacker (1961) and Kalkan (2009). Also in Figure 5.75 is the predicted buckling moment to ultimate flexural moment ratio versus slenderness ratio for the analytical method by Hansell and Winter (1959). Note that a constant value for the reinforcing bar yield strength, when calculating the ultimate flexural strength in all cases was used so that the data were comparable. Figure 5.75 shows a general trend that Hansell and

216

Winter (1959) over predicts the buckling load; however, not all data points show that trend. The experimental data of Hansell and Winter (1959) matches very well with the analytical procedure by Hansell and Winter (1959) because the test beams failed in flexure and not by stability. More apparent was the overall variability in the experimental results.   The parameters not considered by Hansell and Winter (1959) that could be causes for the variability in results were the initial imperfections of the test beams, the experimental error and the differences in experimental setups. Furthermore, the data presentation method of Figure 5.75 is a decent method to investigate general behavior but cannot be used quantitatively due to the assumption that the ultimate moment and buckling moment differ by the same ratio depending on amount and location of reinforcement, which was not necessarily the case.
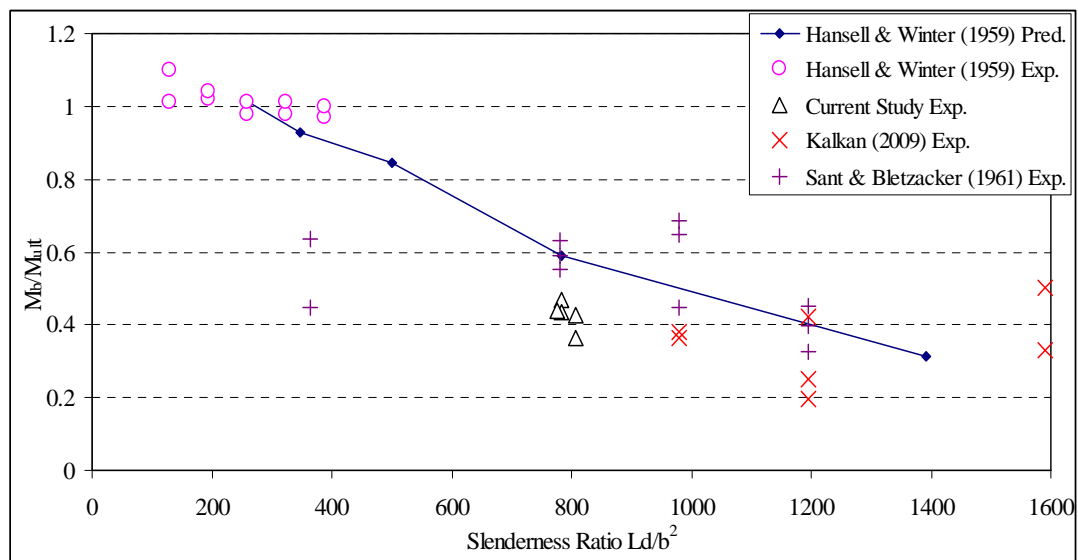
Figure 5.75 – Buckling moment to ultimate flexural moment ratio versus slenderness ratio for test data compared with Hansell and Winter (1959) analysis

217

The analytical procedure by Revathi and Menon (2006) under-predicted the experimental buckling loads by a non-negligible amount. That would be good from a safety standpoint, but would not be good for design economy or from the theoretical standpoint of understanding the actual behavior. Furthermore, the analytical procedure by Revathi and Menon (2006) did not consider initial imperfections; therefore, any modification to their method that included the effect of initial imperfections would decrease the accuracy of the prediction. A similar plot to the one in Figure 5.75 is shown in Figure 5.76 except that the experimental data were compared with the analytical procedure by Revathi and Menon (2006). Figure 5.76 shows that all the experimental results were higher than what was predicted by Revathi and Menon (2006), and, therefore, does not represent the actual behavior and would potentially be too conservative.
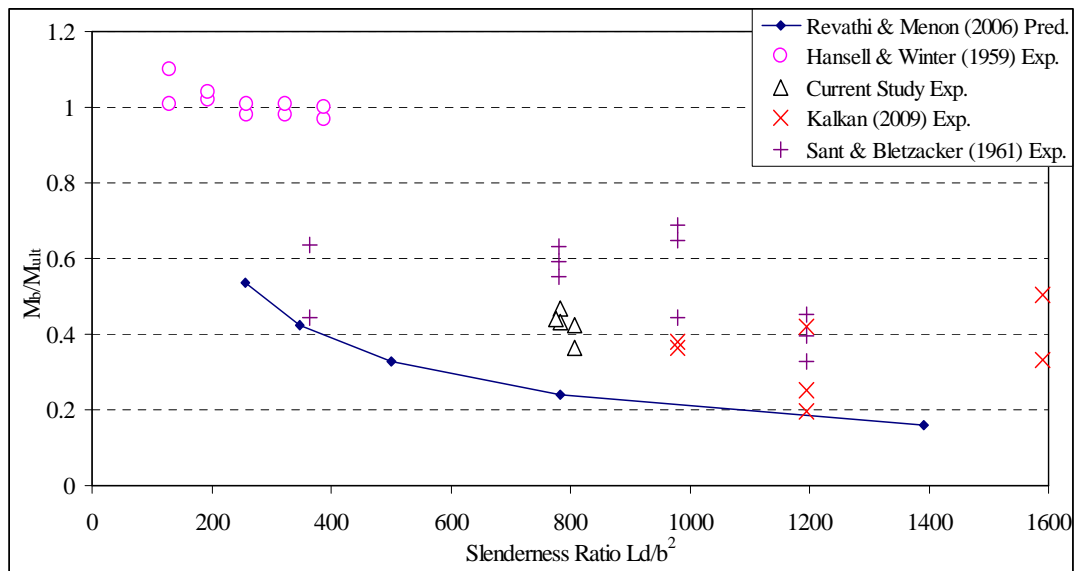
Figure 5.76 – Buckling moment to ultimate flexural moment ratio versus slenderness ratio for test data compared with Revathi and Menon (2006) analysis

5.8.3 Discussion of Secondary Loading

For every test beam, the beam was initially loaded until buckling occurred, and
lateral deflections were increased into the post-buckling range; then the load was
removed, and each beam was reloaded until buckling occurred a second time. The results
of the secondary tests are summarized in Table 5.5.

Table 5.5 – Results of secondary loading of beam specimens

| Beam ID | Residual Imperfections | | | Residual + Initial Imperfections | | | E_c, ksi (GPa) | P_{buckle}, kips (kN) |
	Sweep Top, in. (mm)	Sweep Bottom, in. (mm)	Rotation (radians)	Sweep Top, in. (mm)	Sweep Bottom, in. (mm)	Rotation (radians)		
40B1A	**	**	NA	**	**	**	4713 (32.5)	29.45 (130.9)
40B1B	1.861 (47.3)	1.550 (39.4)	0.00778	2.174 (55.2)	1.925 (48.9)	0.00623	4713 (32.5)	29.42 (130.8)
* 40B2A #2	0.938 (23.8)	0.750 (19.1)	0.00469	2.438 (61.9)	1.810 (46.0)	0.01569	4713 (32.5)	28.62 (127.3)
* 40B2A #3	1.125 (28.6)	0.810 (20.6)	0.00789	2.625 (66.7)	1.870 (47.5)	0.01888	4188 (28.9)	25.00 (111.2)
40B2B	1.407 (35.7)	1.122 (28.5)	0.00713	1.891 (48.0)	1.669 (42.4)	0.00555	4188 (28.9)	29.62 (131.7)
40C2A	1.460 (37.1)	1.202 (30.5)	0.00645	1.663 (42.2)	1.515 (38.5)	0.00370	5156 (35.5)	27.23 (120.0)
40C2B	1.618 (41.1)	1.364 (34.6)	0.00635	1.721 (43.7)	1.520 (38.6)	0.00503	5156 (35.5)	35.49 (157.7)

From Table 5.5, the most obvious trend was that the buckling load of the second
loading was always less than the buckling load of the secondary loading. The initial
imperfections due to the residual deformations from the first loading did not appear to

have a trend with respect to the buckling load of the secondary loading. For instance, the buckling load of Beam C2B was 30% larger than the buckling load of Beam C2A, although the initial sweep and rotation for the secondary loading was larger for beam C2B. More observations of the secondary loading behavior were made by investigating a plot of the load versus lateral displacement at the top of the beam. As an example, Figure 5.77 shows the lateral displacements for Beams C2A and C2B.
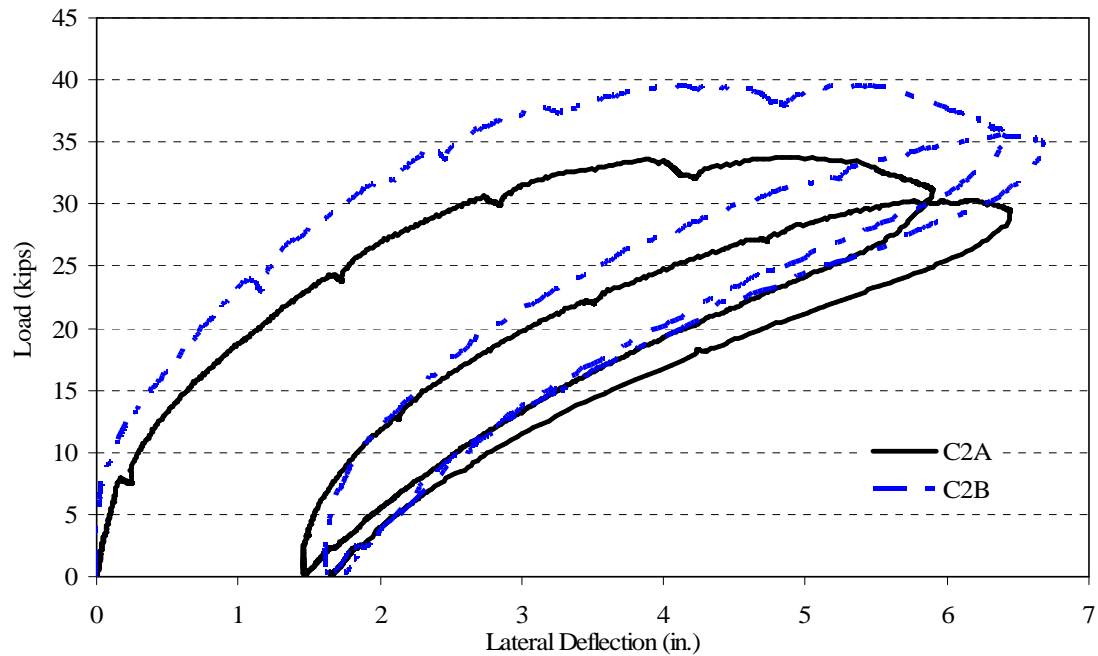
Figure 5.77 – Load vs. top lateral displacement for Beams C2A and C2B

Figure 5.77 shows graphically that the residual deflection after the first loading was larger for Beam C2B. This was attributed to the fact that Beam C2B had a larger

maximum displacement during the first loading, and probably was in a more damaged at the end of the first loading than was Beam C2A. In both cases, the secondary loading load-displacement curve was shallower than the load-displacement curve of the first loading. During the secondary loading for all of the test beams, a trend was noticed. When the secondary loading reached the post-buckling path of the first loading, the load-deflection curve would continue along what was inferred as the post-buckling path of the first loading if the beam was displaced to that level during the first loading. Furthermore, the displacement at buckling during the secondary loading for every test beam was greater than the largest displacement reached during the first loading.

CHAPTER 6

ANALYTICAL DEVELOPMENT

6.1 Analytical Development Objectives

The current analytical procedures to predict buckling loads of prestressed concrete beams were inadequate based on the comparisons between theoretical and experimental results presented in Chapter 5. The objective of the analytical portion of this research was to develop a methodology that predicted load versus lateral displacement and load versus rotation behavior of a prestressed concrete beam subjected to lateral-torsional buckling. Furthermore, it was desired to develop a simplified approach that predicted the lateral-torsional buckling load of a prestressed concrete beam that was less computationally rigorous and which could be used for design.

The analysis that predicted the load versus deflection and load versus rotation plots was developed first. The procedure involved a fiber model with a material and geometric nonlinear incremental analysis. The nonlinear behavior was compared to the experimental results to validate the fiber model approach. After validation was accomplished, the analysis was run for various imperfections for the different beams such that the accuracy of a proposed simplified equation was verified. Lastly, the simplified technique was compared with available experimental results where the initial imperfections of the beams were published to determine the validity of the technique.

6.2 Nonlinear Analysis

The nonlinear analysis program was developed by first creating a fiber model of the beam cross-sections to obtain a moment-curvature relationship. The moment-curvature relationship was used in the nonlinear analysis at each load increment to determine section and material properties. The fiber model and nonlinear analysis are discussed in the following sections. Additional information is provided in Appendix H.

6.2.1 Fiber Model

The fiber model was created for the experimental beam cross-sections with 320 fibers in each segment, where each fiber was 1 in. (25.4 mm) in height by 0.5 in. (12.7 mm) in width. Each fiber was 0.5 in^2 (323 mm^2) in cross-sectional area. Each individual fiber was composed of a value representing the area of concrete, the area of mild steel, and the area of prestressing steel. The total area of the three components summed to 0.5 in^2 (323 mm^2), the total area of fiber. The procedure utilized was based on that performed by Liang (2008). The assumptions of the fiber model were that plane sections remained plane after deformation, there was perfect bond between the concrete and steel reinforcing, strain hardening was not included in the steel material models, the influence of creep was not included and the concrete followed the assumed stress-strain relationship during strain reversals. There was no hysteretic behavior considered during strain reversals within the applied concrete stress-strain model.

The procedure began by cycling through a range of angles of rotation for the beam; at different load stages, the beam was oriented at different angles. For each angle of orientation, the curvature was incremented to obtain the weak-axis and strong-axis

flexural moment at each curvature value. However, to obtain the weak-axis and strong-axis flexural moment at each curvature, several steps had to be taken.

The first step was to assume a neutral axis angle, φ, (the axis of zero strain) and depth of the neutral axis. From the assumed neutral axis angle, φ, and neutral axis depth, geometric relations were used to find the strain in each fiber. The relations, which were similar to those used by Liang (2008) are shown in the following equations and the variables are depicted in Figure 6.1. Note that the sign conventions for Equations 6.1 through 6.4 assume compressive strains were positive and tensile strains were negative. At a certain angle of applied load, for a specific level of curvature and for the assumed angle of the neutral axis, φ, the strain in each fiber was determined from Equations 6.1 through 6.4.

$$c_1 = \frac{d_n}{\cos(\theta_{NA})} \tag{6.1}$$

$$y_{n,i} = \left| x_i - \frac{b}{2} \right| \tan(\theta_{NA}) + \left(\frac{h}{2} - c_1 \right) \tag{6.2}$$

$$d_{e,i} = \left| y_i - y_{n,i} \right| \cos(\theta_{NA}) \tag{6.3}$$

$$\varepsilon_i = \begin{cases} \phi d_{e,i}, & for \; y_i \geq y_{n,i} \\ -\phi d_{e,i}, & for \; y_i < y_{n,i} \end{cases} \tag{6.4}$$
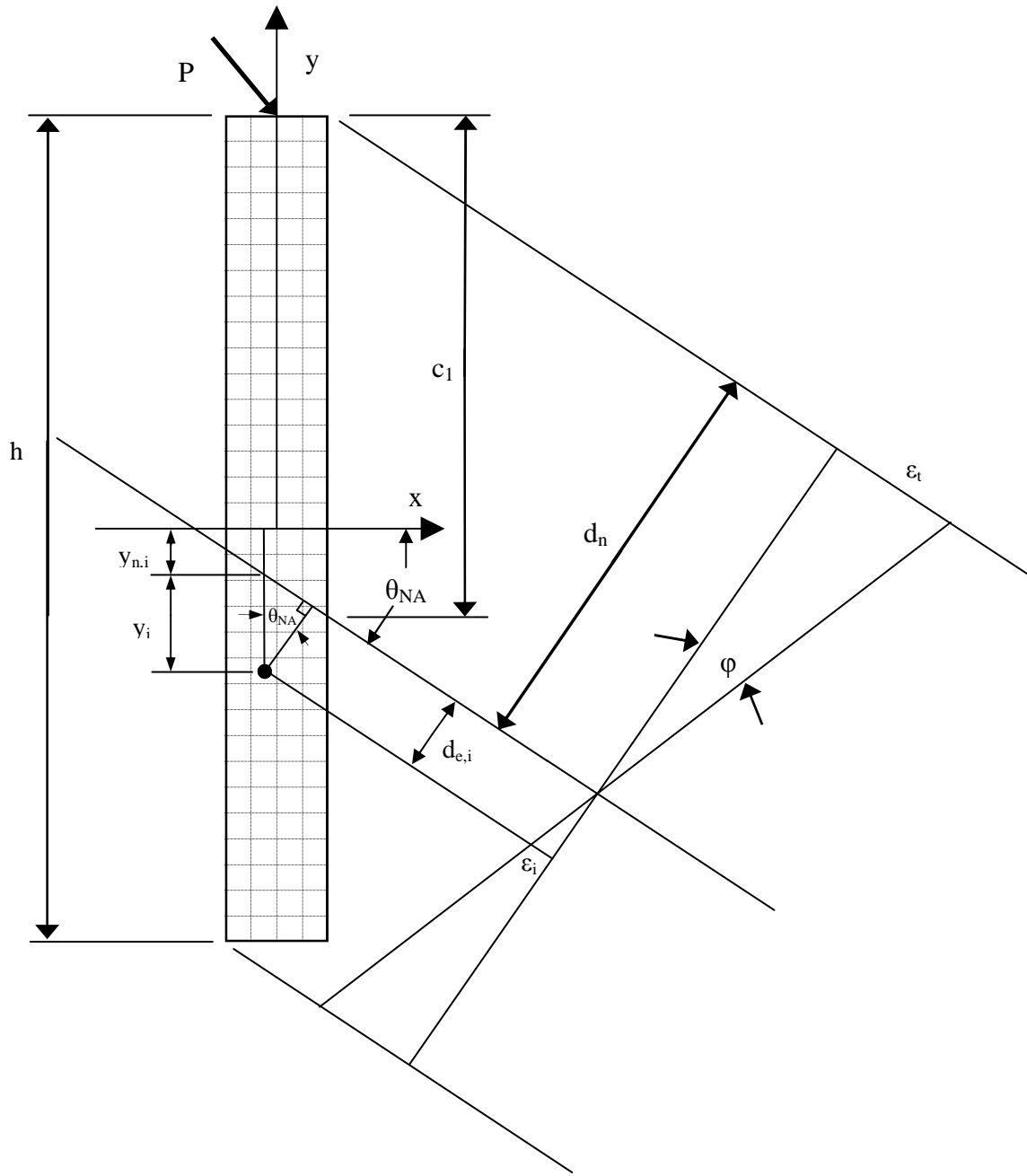
Figure 6.1 – Fiber geometric relations and strain distribution for biaxial flexure

Knowing the fiber strains allowed for the use of material models to determine the stress in each fiber. An elastic, perfectly plastic model was used for the nonprestressed

reinforcement. The stress-strain curve for the prestressing strand was obtained using the curve provided by the manufacturer. The initial stress in the prestressing strands was determined from the measured load in each strand during fabrication immediately before the strands were cut. Then, estimates were made to take into account prestress losses due to elastic shortening, concrete shrinkage, steel relaxation and creep. For the concrete of the rectangular prestressed beams, the stress-strain relationship presented by Thorenfeldt et al. (1987) for concrete strengths from 2.2 ksi (15 MPa) to 18.1 ksi (125 MPa) was used; however, strain values never reached levels in which the selection of the concrete constitutive model affected the results until post-buckling.

Member forces were determined by summing the stress resultants in the beam by using the following equations from Liang (2008):

$$P = \sum_{i=1}^{ns} \sigma_{s,i} A_{s,i} + \sum_{1=1}^{nc} \sigma_{c,i} A_{c,i} \tag{6.5}$$

$$M_x = \sum_{i=1}^{ns} \sigma_{s,i} A_{s,i} y_i + \sum_{j=1}^{nc} \sigma_{c,i} A_{c,i} y_j \tag{6.6}$$

$$M_y = \sum_{i=1}^{ns} \sigma_{s,i} A_{s,i} x_i + \sum_{j=1}^{nc} \sigma_{c,i} A_{c,i} x_j \tag{6.7}$$

In Equations 6.5 through 6.7, the subscript "s" referred to stresses and areas of steel fibers and the subscript "c" referred to stresses and areas of concrete fibers. Furthermore, "ns" means the number of steel fibers, and, similarly, "nc" means the number of concrete fibers.

The calculated value of axial force "P", based on the assumed neutral axis angle, φ, and neutral axis depth, d_n, was compared with the applied axial load on the cross-section; in this case, the applied axial load was the prestressing force. If the calculated axial force was not equivalent to the applied axial load (within a set amount of error), the assumed value of the neutral axis depth had to be iterated until force equilibrium was met. Once force equilibrium was met, moment equilibrium had to be met. If the internal moment was not equivalent to the external moment, the neutral axis angle, φ, was iterated until the moment equilibrium was met. Note that for each iteration of the neutral axis angle, φ, the depth of the neutral axis to fulfill force equilibrium had to be determined once again.

The nested loops tended to become computationally cumbersome, and, therefore, a more efficient method of iterating values was used to arrive at the correct values more quickly. A secant algorithm similar to that used by Liang (2008) was utilized for the neutral axis depth and neutral axis angle, φ, and proved to be much more efficient.

Once force and moment equilibrium were met, and the proper values for the neutral axis angle, φ, and neutral axis depth were obtained, the fiber program would output the moment, maximum compression strain, the depth of the neutral axis, neutral axis angle, φ, and the average tangent modulus of the concrete fibers. Essentially, the tangent modulus of elasticity was calculated for each concrete fiber and was averaged over the number of concrete fibers in compression. All of the properties were used in the nonlinear analysis; therefore, the fiber analysis was used as a subroutine to the nonlinear analysis.

6.2.2 Nonlinear Analysis Program

To perform the nonlinear analysis, the beam specimens were divided into eight segments, 47.1 in. (1.20 m) in length; however, symmetry was used so that the analysis was only performed on four segments. The symmetry boundary conditions were to restrain rotation about the strong-axis and weak-axis at midspan. At each node, the degrees of freedom applied within the member stiffness matrix were lateral translation (x-direction), vertical translation (y-direction), strong-axis rotation (about x-axis), weak-axis rotation (about y-axis) and torsional rotation (about z-axis). The axial displacement was neglected, and, therefore, catenary or membrane behavior was not captured by the analysis. The initial rotation, θ_0, and lateral displacement of each beam were applied as an assumed sine curve along the length of the beam. Figure 6.2 shows the symmetric boundary conditions and the segment locations.
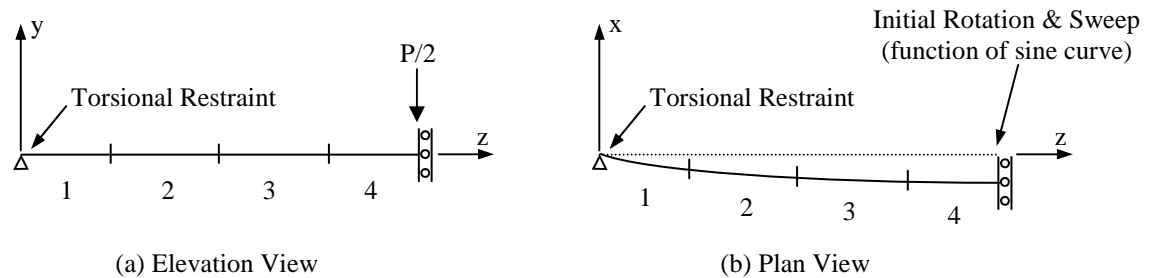
Figure 6.2 – Symmetric boundary conditions (a) elevation view and (b) plan view

The nonlinear analysis was performed by stepping the vertical load, P, at a small increment until large lateral displacements were achieved. Note that at a vertical point load of zero, the self-weight moment was already applied to the cross-section to ensure that the analytical load versus displacement curves could be compared with the

experimental load versus displacement curves. The load increment used was 0.10 kips (0.45 kN) and was determined to be a small enough load increment to provide sufficient accuracy. The accuracy was determined by running the analysis for 0.25 kips (1.11 kN) and 0.10 kips (0.45 kN) increments and finding that the difference in maximum loads achieved was less than 1%. In addition to the accuracy achieved from numerical experimentation in determining a sufficiently small load increment, it was assumed that the number of segments along the length was large enough to provide sufficient accuracy.

For each load increment, the applied moment and initial rotation, θ_0, of the beam was used as an input to the fiber subroutine to obtain the depth of the neutral axis, the angle of the neutral axis, φ, and the average tangent modulus of the compression zone for each segment along the length of the beam. The depth of the neutral axis and angle of the neutral axis, φ, were used to calculate the moments of inertia based on the shape of the compression zone and the transformed area of the steel. The torsion constant was calculated by using the approximate method for non-circular solid sections presented by Dooley (1979). The method was basically a summation of a series of thin-walled hollow sections. The approximate method had to be used because the torsion constant was based on the compression zone which was not rectangular, but instead was trapezoidal or triangular. Longitudinal and transverse reinforcement were not considered in the expression for the torsion constant because Hsu (1984) determined through analytical and experimental study that the longitudinal and transverse reinforcement increased the torsional cracking moment but did not affect the torsionally uncracked torsional stiffness.

For each load increment, the section and material properties were determined using the fiber subroutine for each segment along the length of the beam. Then the

stiffness matrix was formed for each individual segment and was combined by eliminating restrained degrees of freedom to form the global stiffness matrix. The incremental load vector was then formulated by applying the load increment to the appropriate degree of freedom and applying torsion to the beam which was determined by the increment of applied load on the deformed beam using the displacements and rotations along the length of the beam from the previous load increment. The incremental displacement and rotation vector was then found by multiplying the inverse of the stiffness matrix and the incremental load vector as shown in Equation 6.8. The inversion of the stiffness matrix was performed by an included subroutine "mldivide" in MATLAB® R2009a (2009). For the specific case of a square stiffness matrix and a column load vector, the solution will be exact and the method of solution was based on Cholesky decomposition because the stiffness matrix was square, symmetric and had real positive diagonal elements. The stiffness matrix was positive definite until unstable behavior occurred and computational errors arose within the analysis at which point the analysis was halted.

$$\{u\} = [K]^{-1}\{P\} \qquad\qquad (6.8)$$

Once the lateral displacement and rotation, θ, were determined for a load increment, the process was repeated for the next load increment. Essentially, for every load increment, there was a different value of the rotation and applied moment; therefore, the fiber subroutine was used for every load increment for each segment along the length of the beam to determine the section properties for the specific load increment.

Furthermore, when the stresses became high enough, the average tangent modulus of elasticity of the compressed fibers was less than the initial modulus of elasticity, and, therefore, the modulus of elasticity used in the global stiffness matrix would change with each load increment and for each segment along the length of the beam. The process can be best summarized in the flowchart shown below in Figure 6.2. A more detailed flowchart and the associated subroutine flowcharts are presented in Appendix G.
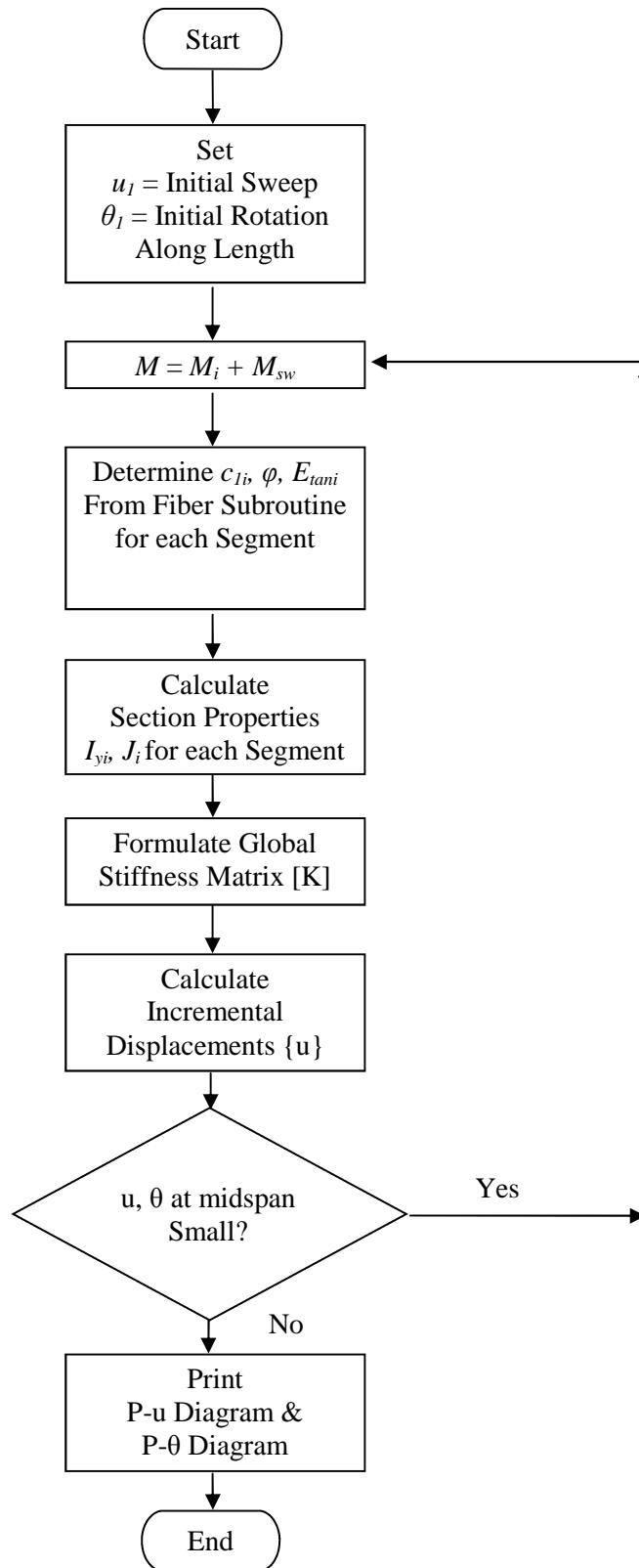
Figure 6.3 – Nonlinear analysis flowchart

6.2.3 Nonlinear Analysis Results

The nonlinear analysis was run for all of the beams except for B2A because that was the beam where the angle of the applied load was unknown. For all of the other test beams, there was a 0.01222 radian (0.7 degrees) error in the applied vertical load; however, it was a known quantity that was taken into account in the analysis.

6.2.3.1 Method to Account for Error in Load Angle

The error in the load angle was taken into account in the nonlinear analysis by an additional term in the incremental load vector, {P}. The incremental load vector of a beam loaded with a perfectly vertical load would have an applied load in the horizontal direction as the product of the applied vertical load and the sine of the rotation, θ, of the cross-section at midspan. Because of the error in applied load angle, the component of horizontal load at midspan was a product of the applied vertical load and the sine of the summation of rotation, θ, and the error in applied load angle. Similarly, additional torsion was applied to the cross-section due to the error in applied load angle. The component of torsion due to the horizontal load acting about the shear center included the component of horizontal load due to the error in applied load angle.

6.2.3.2 Nonlinear Analysis Results vs. Experimental Results

The results of the nonlinear analyses are depicted in Figures 6.4 through 6.18 for Beams B1A, B1B, B2B, C2A and C2B. For each of the beams, the load versus lateral displacement, load versus rotation and load versus vertical displacement are shown. The

initial imperfections used in the analysis were those measured prior to each of the

experiments.
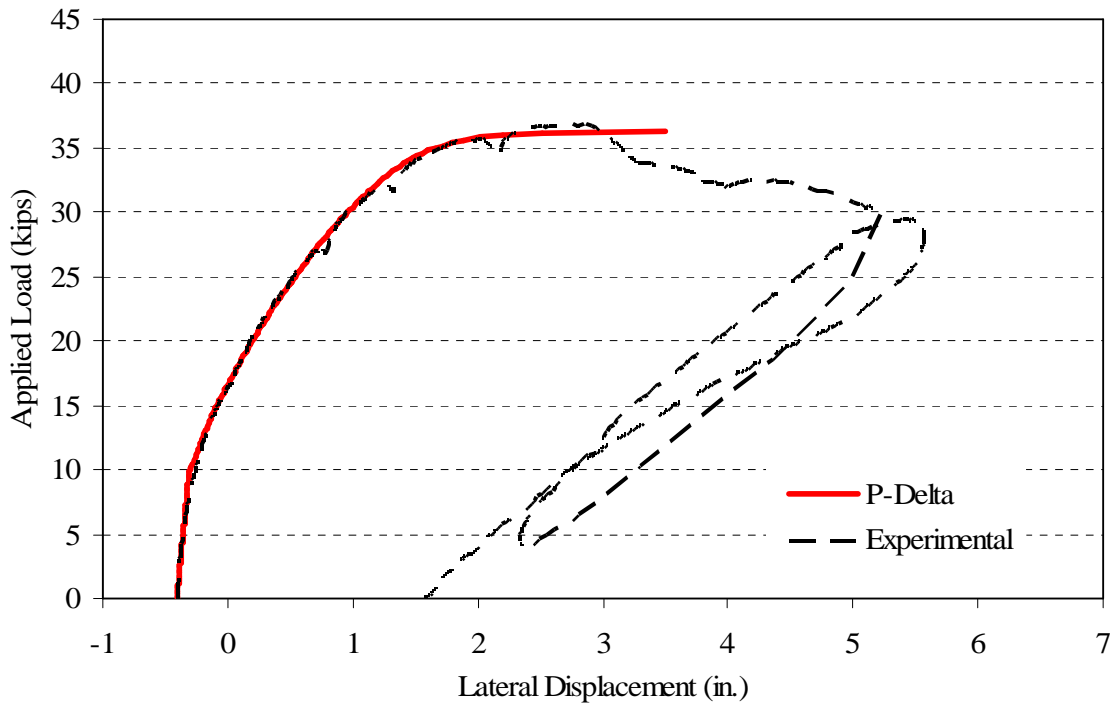
Figure 6.4 – Load versus lateral displacement for Beam B1A
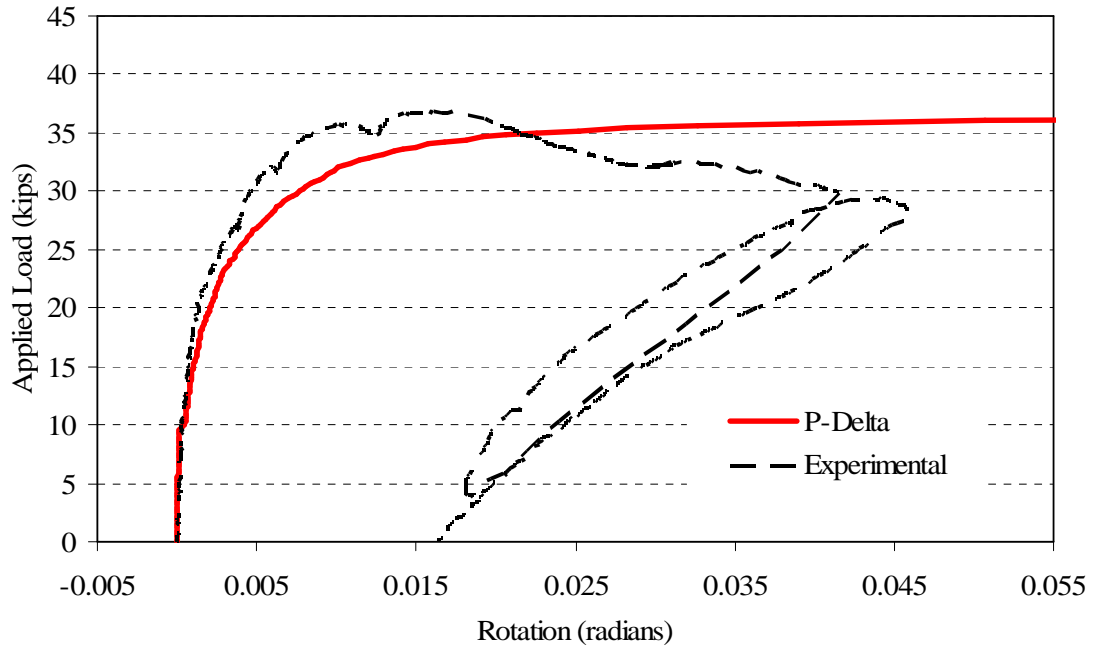
Figure 6.5 – Load versus rotation for Beam B1A
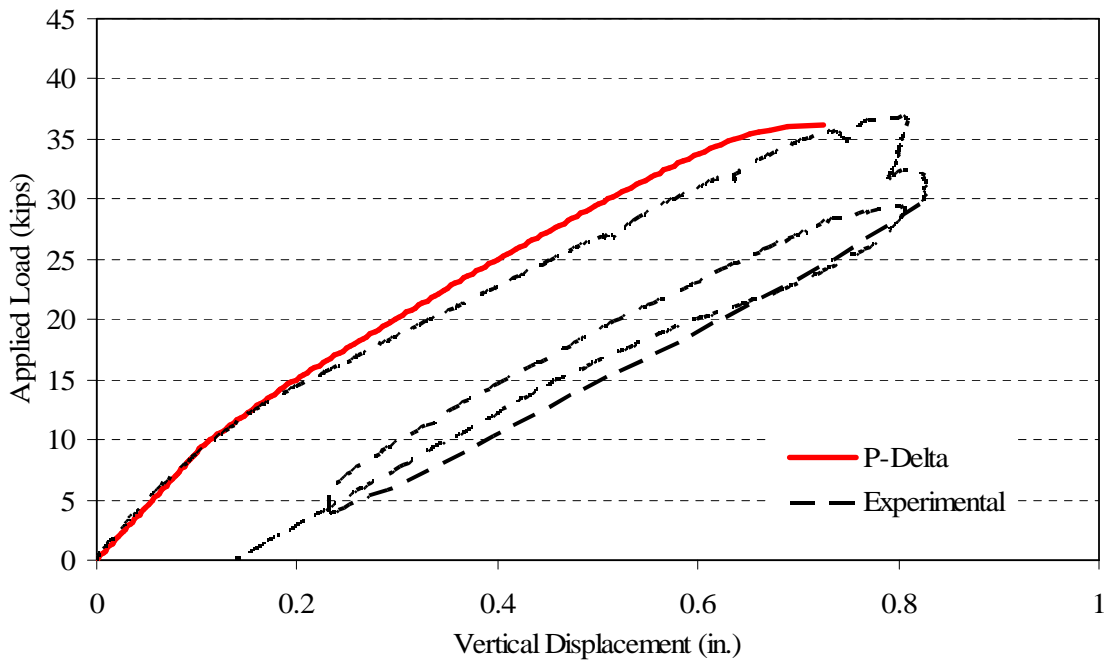
Figure 6.6 – Load versus vertical displacement for Beam B1A
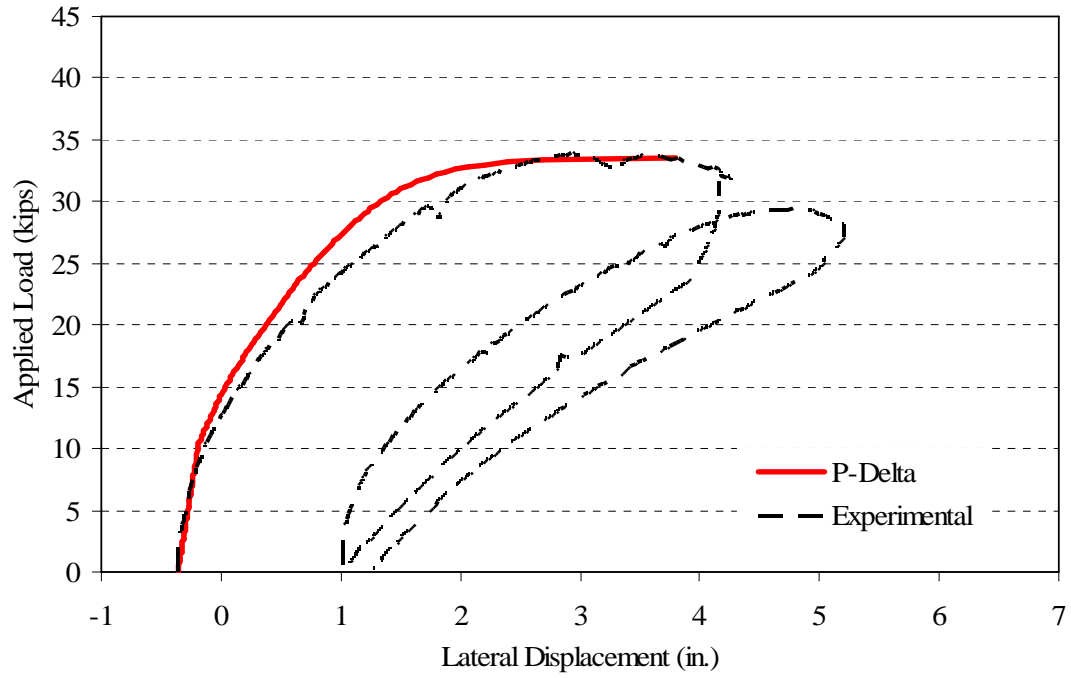
Figure 6.7 – Load versus lateral displacement for Beam B1B
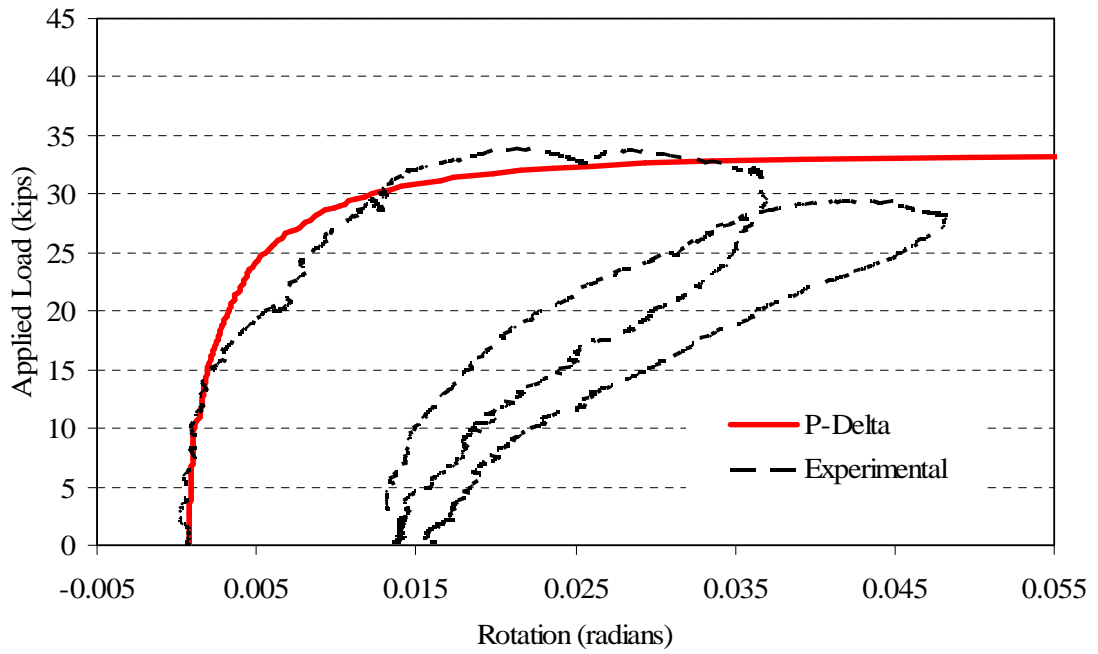
Figure 6.8 – Load versus rotation for Beam B1B
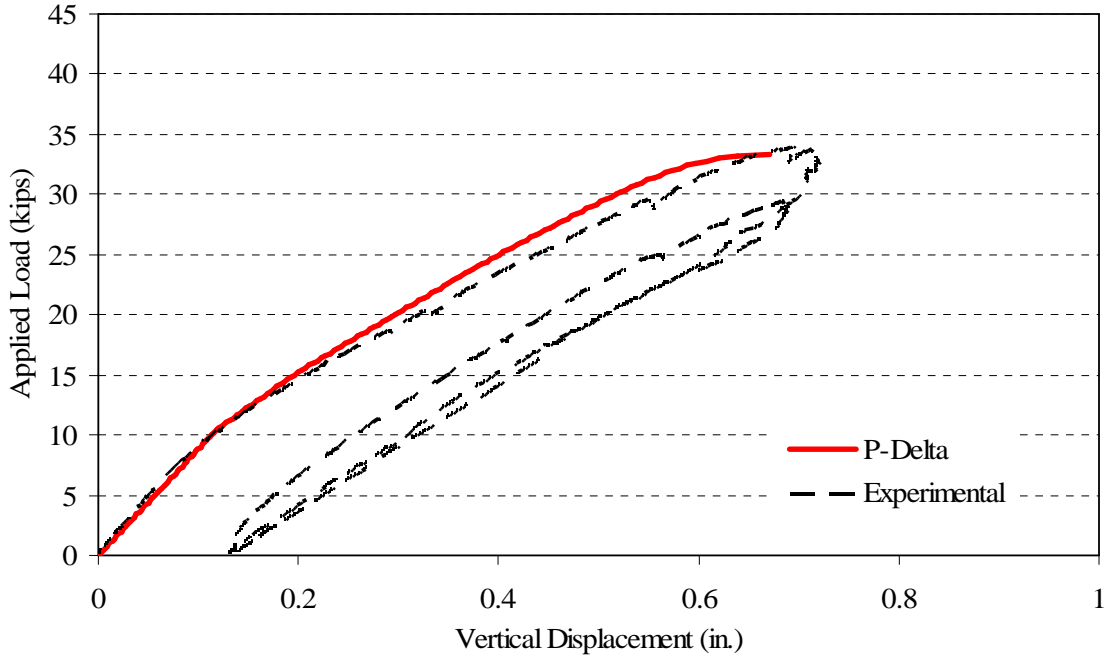
Figure 6.9 – Load versus vertical displacement for Beam B1B
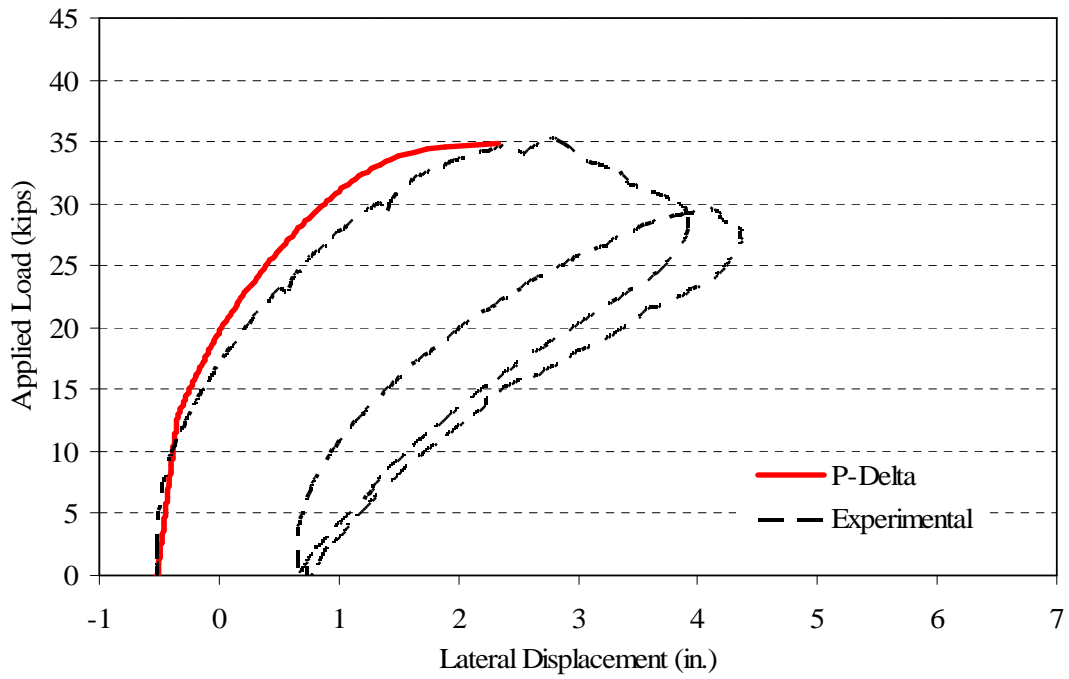
Figure 6.10 – Load versus lateral displacement for Beam B2B

237
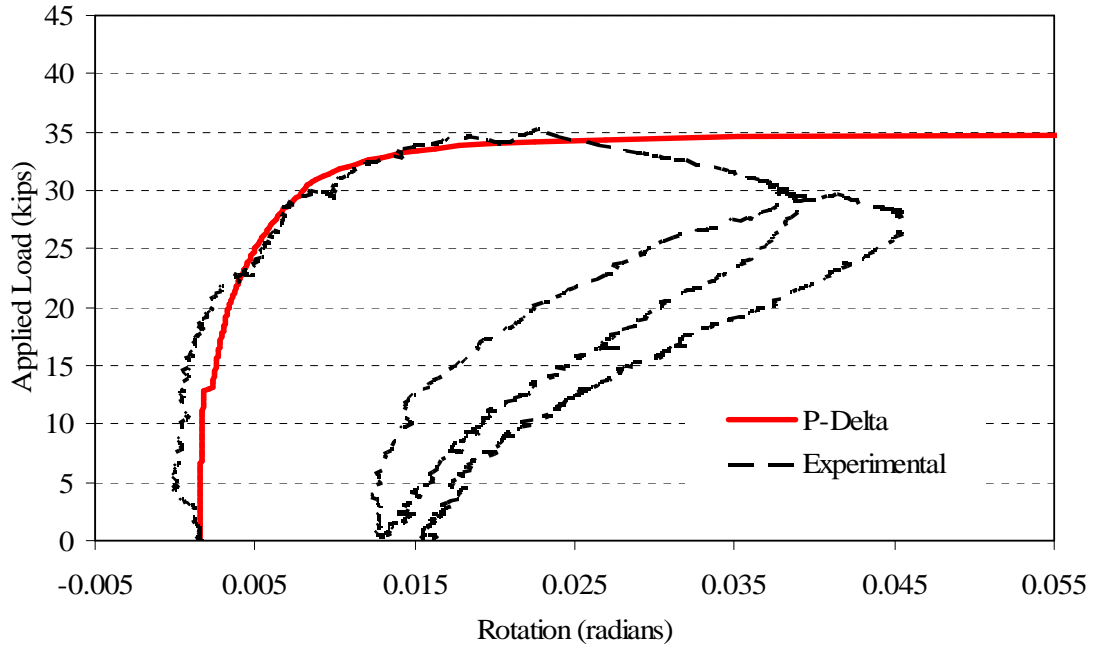
Figure 6.11 – Load versus rotation for Beam B2B
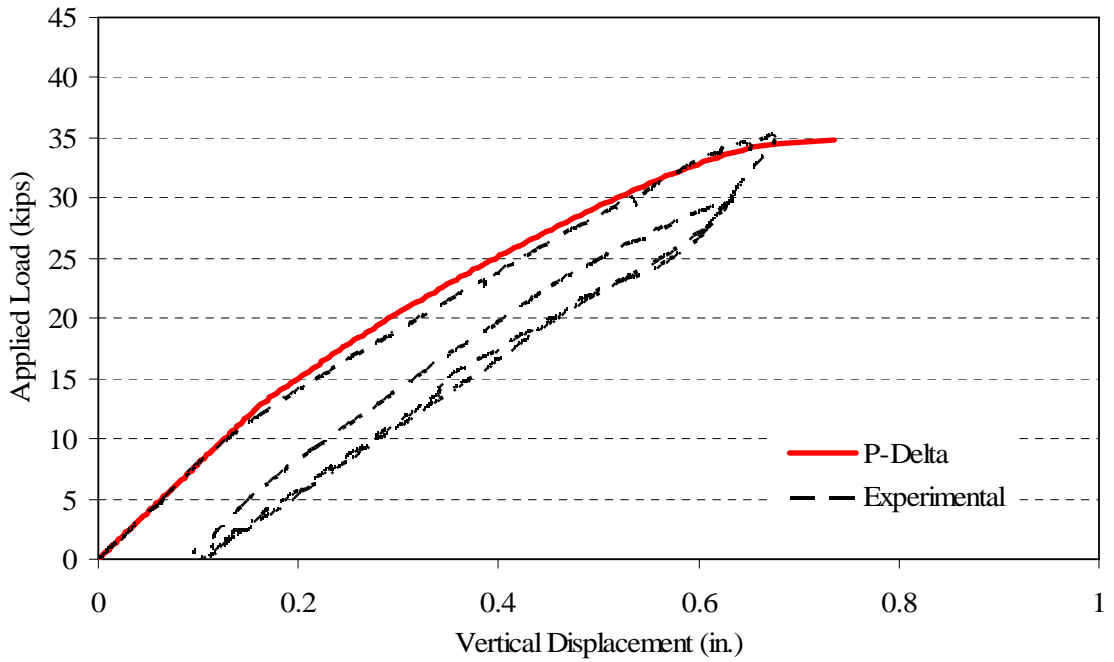
Figure 6.12 – Load versus vertical displacement for Beam B2B
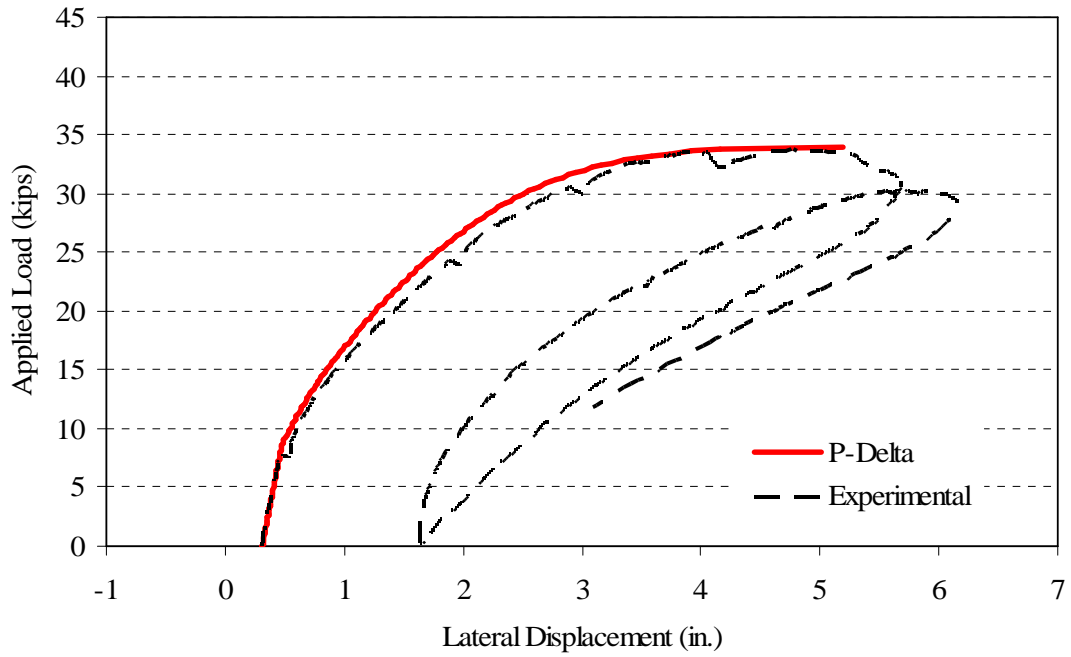
Figure 6.13 – Load versus lateral displacement for Beam C2A
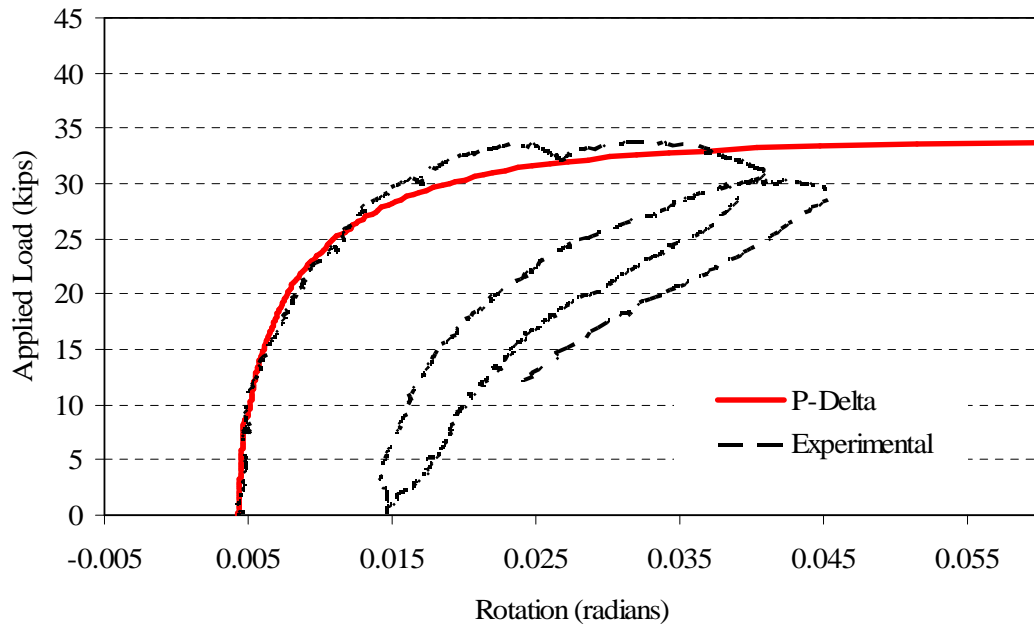
Figure 6.14 – Load versus rotation for Beam C2A
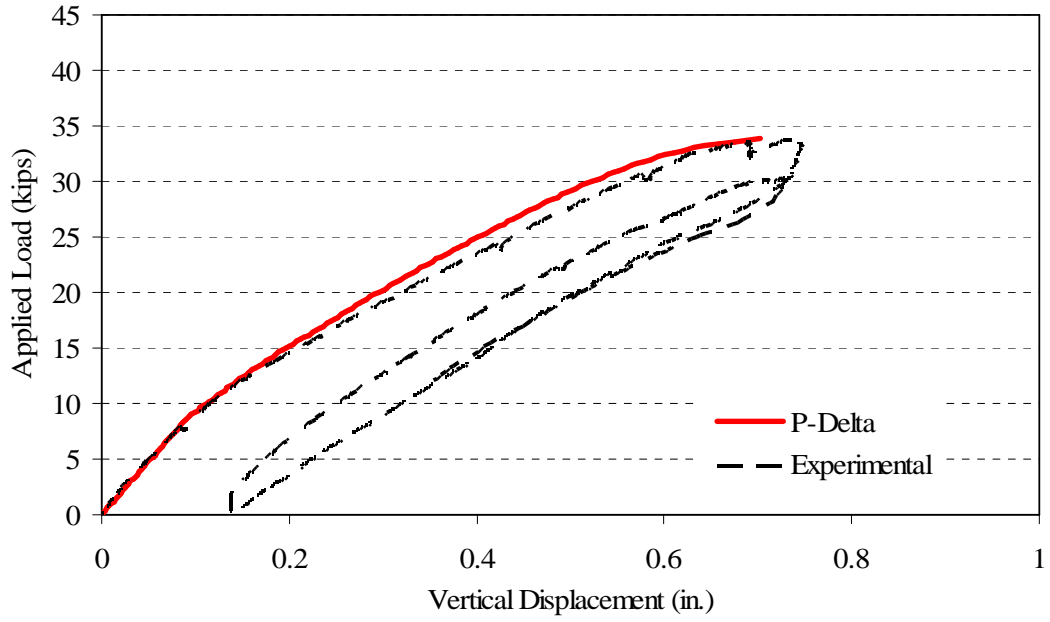
Figure 6.15 – Load versus vertical displacement for Beam C2A
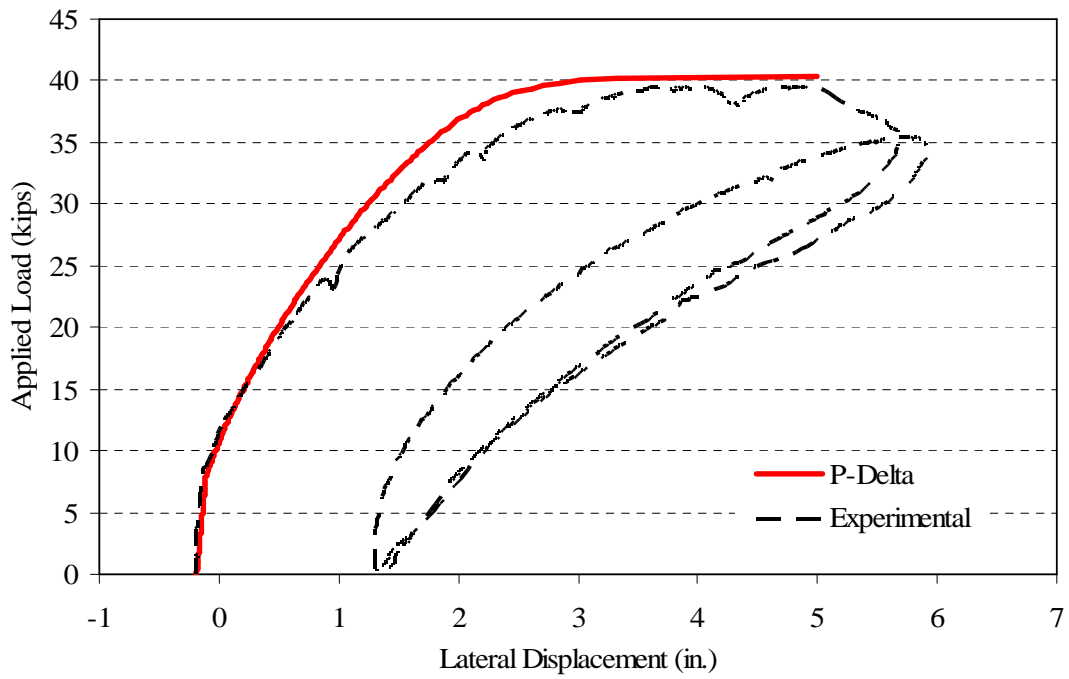
Figure 6.16 – Load versus lateral displacement for Beam C2B

240
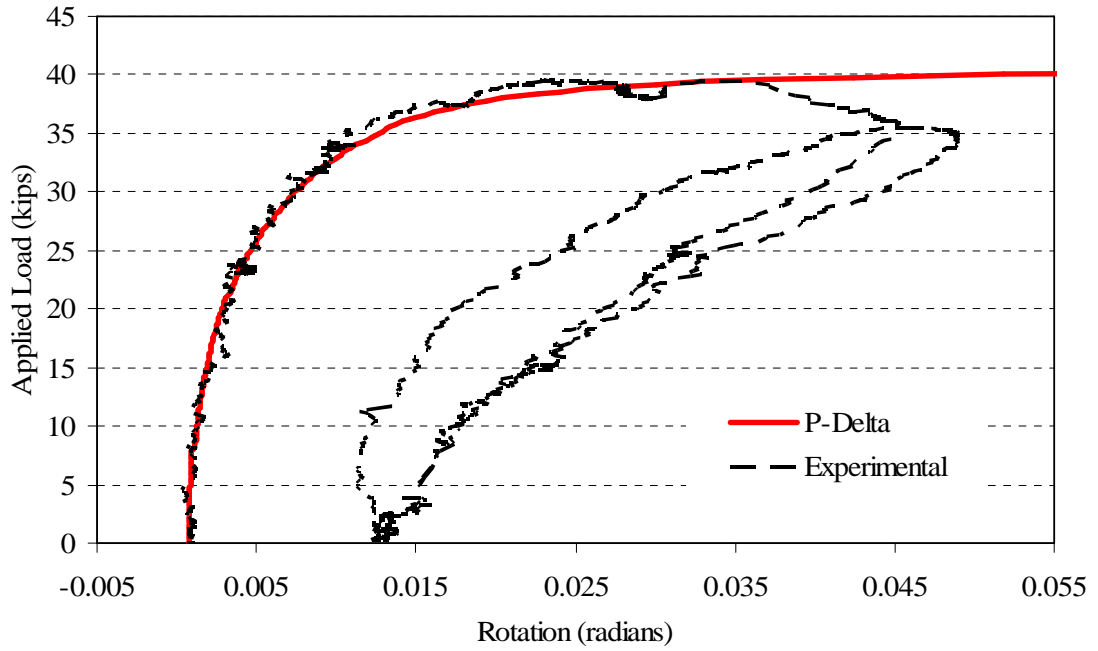
Figure 6.17 – Load versus rotation for Beam C2B
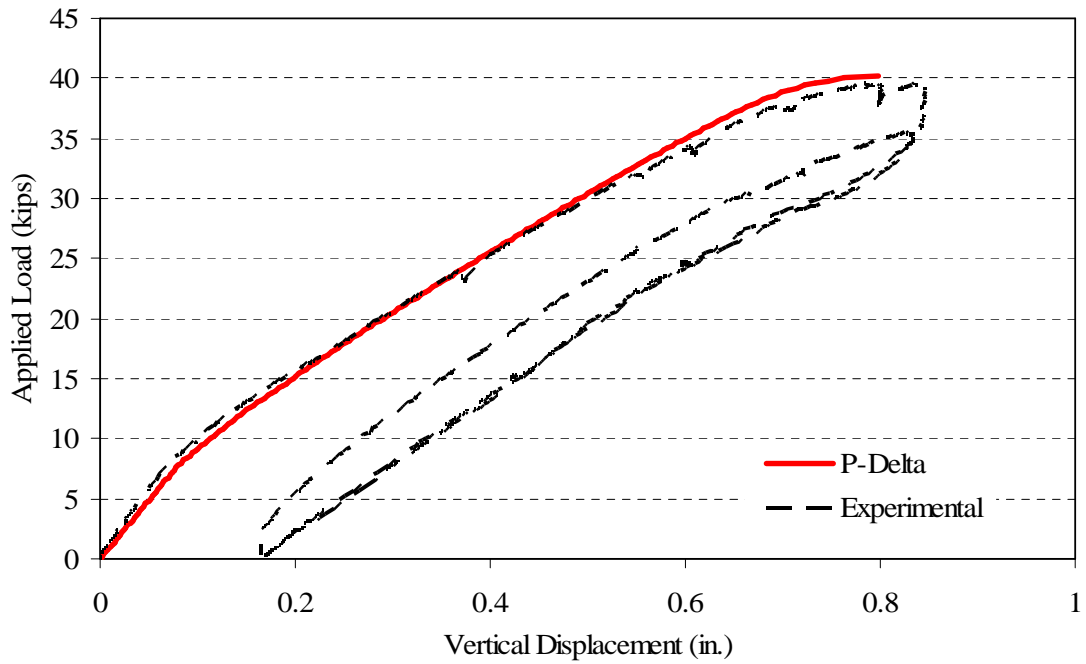
Figure 6.18 – Load versus vertical displacement for Beam C2B

It was apparent from Figures 6.4 through 6.18 that the nonlinear analysis matched the experimental load versus horizontal displacement, load versus rotation curves, and load versus vertical displacement well with little deviation. The nonlinear analysis sufficiently predicted the leveling of the experimental load versus lateral displacement and load versus rotation curves when the beams became unstable and continued to deform with no additional load. The nonlinear analysis was able to successfully predict the nonlinear behavior of the vertical displacements when the beams became unstable. The nonlinear behavior shown in the experimental curves for the vertical displacement was due to the large rotations causing the lateral displacement about the local axes of the beam becoming a significant component of displacement in the global vertical direction. Furthermore, the nonlinear analysis predicted the maximum load well. The differences in predicted maximum load can be attributed to error in measuring the initial imperfections and the possibility of "settlement" in components of the test set-up, such as the end supports, once loading began. The possibility of error in measuring the initial imperfections was a strong possibility because the nonlinear analysis results varied significantly with varying initial imperfections with all other parameters equivalent.

The nonlinear analysis never "softened" like the experimental results because the nonlinear analysis was a load-controlled analysis. Using the fiber model to determine stiffness properties as inputs into a matrix analysis based approach does not allow for a displacement controlled analysis unless the system was assumed to be one degree of freedom system. The fiber model required knowing the moment at the cross-section in question to determine moment equilibrium of the section. To obtain the descending, softening portion of the curve, an incremental approach with a predictor-corrector

algorithm such as the arc length method (Riks, 1979; Crisfield, 1981; Clarke and

Hancock, 1990; Lam and Morley, 1992; Hellweg and Crisfield, 1998) would have had to

be used. An arc length approach was successfully employed for concrete cracking by

Foster (1992); however, the use of finite was necessary to perform the analysis. The use

of nonlinear finite analysis was outside the scope of this research and should be

performed in future research on the subject.

Because the nonlinear analysis did not predict the descending portion of the load

versus lateral displacement, in all plots and tables the nonlinear analysis buckling load

was the maximum load at which the analysis became computationally unstable. At a

certain load increment, the stiffness quantities in the global stiffness matrix created a

global stiffness matrix that was approaching singularity. A comparison of the maximum

load from the nonlinear analysis and from the experiments is given in Table 6.1.

Table 6.1 – Comparison of nonlinear analysis results to experimental results

Beam ID	Experimental P_{buckle}, kips (kN)	Nonlinear Analysis P_{buckle}, kips (kN)	% Difference
B1A	36.87 (163.9)	36.2 (161)	1.82
B1B	33.92 (150.8)	33.4 (149)	1.53
B2B	35.26 (156.8)	34.8 (155)	1.30
C2A	33.68 (149.7)	33.8 (150)	-0.36
C2B	39.55 (175.8)	40.2 (179)	1.64

Additional comparisons between the experimental results and the nonlinear analysis results were made to further validate the nonlinear analysis. From the experiments, the compression zone depths on both surfaces of the beams were determined from the strain measurements on the surfaces. The nonlinear analysis program output the compression zone depths on both sides of the beam so that a comparison with the experimental compression zone depths could be made. The results from the comparison are shown in Table 6.2.

Table 6.2 – Comparison of experimental and analytical compression zone depths

Beam ID	Load, kips (kN)	Experimental Compression Zone Depth, in. (mm)			Analytical Compression Zone Depth, in. (mm)		
		Convex Side	Concave Side	Center	Convex Side	Concave Side	Center
B1A	10 (44.5)	17.0 (432)	26.4 (671)	21.7 (551)	16.0 (406)	24.1 (612)	20.1 (511)
	20 (89.0)	11.8 (300)	18.9 (480)	13.9 (353)	7.04 (179)	24.2 (615)	15.6 (396)
	30 (133.3)	8.88 (226)	19.0 (483)	14.2 (361)	3.58 (90.9)	25.0 (635)	14.3 (363)
B1B	10 (44.5)	14.2 (361)	26.4 (671)	22.7 (577)	12.7 (323)	26.3 (668)	19.5 (495)
	20 (89.0)	6.17 (157)	20.5 (521)	13.3 (338)	5.56 (141)	25.3 (643)	15.4 (391)
	30 (133.3)	2.23 (56.6)	19.9 (505)	11.1 (282)	0.00 (0.00)	27.4 (696)	13.7 (348)
B2B	10 (44.5)	22.3 (566)	40.0 (1020)	31.3 (795)	22.7 (577)	33.0 (838)	27.9 (709)
	20 (89.0)	8.29 (211)	27.4 (696)	17.9 (455)	8.39 (213)	29.2 (742)	18.8 (478)
	30 (133.3)	5.35 (136)	24.1 (612)	14.7 (373)	4.26 (108)	28.6 (726)	16.5 (419)
C2A	10 (44.5)	15.4 (391)	30.1 (765)	22.8 (579)	11.0 (279)	29.6 (752)	20.3 (516)
	20 (89.0)	8.18 (208)	25.6 (650)	16.9 (429)	5.49 (139)	27.2 (691)	16.4 (417)
	30 (133.3)	3.70 (94.0)	23.7 (602)	13.7 (348)	0.00 (0.00)	30.2 (767)	13.8 (351)
C2B	10 (44.5)	16.9 (429)	30.2 (767)	23.6 (599)	13.5 (343)	27.7 (704)	20.6 (523)
	20 (89.0)	7.79 (198)	23.6 (599)	15.7 (399)	8.72 (221)	24.8 (630)	16.8 (427)
	30 (133.3)	6.63 (168)	23.9 (607)	15.3 (389)	5.27 (134)	25.1 (638)	15.2 (386)

Table 6.2 shows reasonable correlation between the compression zone depth at the center of the cross-section for the experimental results and the analytical results. For some specific load levels and beam cases the experimental results and analytical results for the compression zone depths on the surfaces of the beams matched well; however, there were many cases where there were apparent differences. The general trend with respect to the compression zone depths on the surfaces of the beams was similar between the experimental and analytical cases, and the results showed better correlation at the load level of 20 kips (89.0 kN) than at the other load levels presented. There were some reasons for the discrepancies between the experimental and analytical results. The predicted initial strain due to prestressing and self-weight was added to the experimental results so that the experimental and analytical results could be compared accurately. At higher load levels a direct superposition may not be accurate. Also, the sensitivity of the compression zone depth on the surfaces of the beam was very high at low loads, below 10 kips (44.8 kN) and when the applied load approached the buckling load. The high sensitivity is apparent in a plot of the analytical results for the surface compression zone depth shown in Figure 6.19.
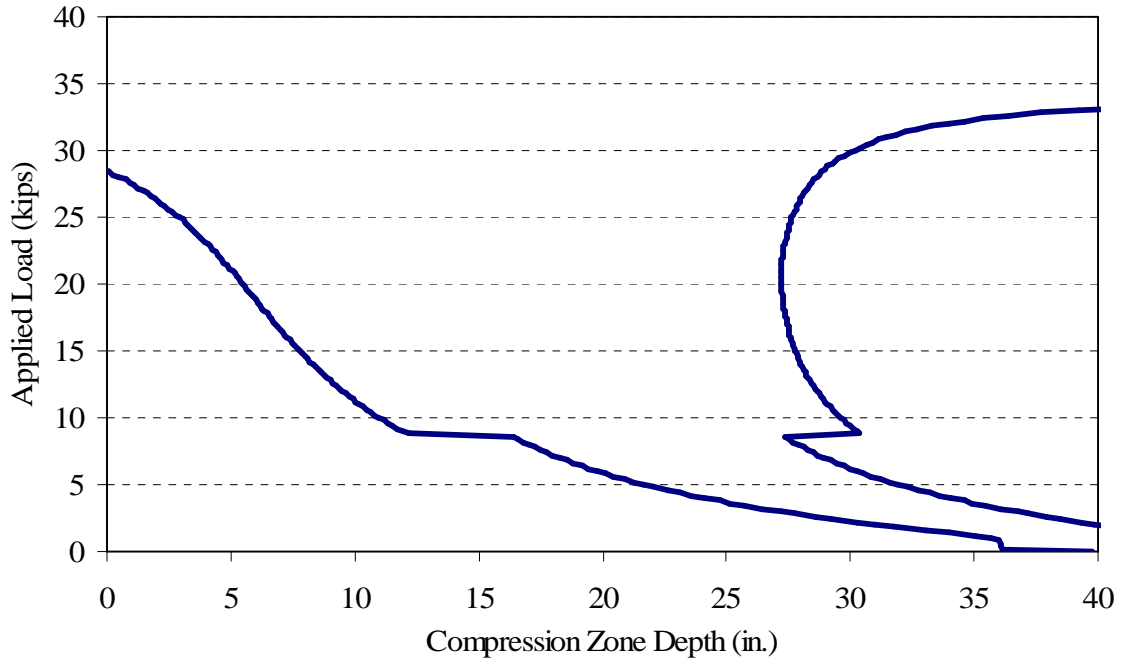
Figure 6.19 – Nonlinear analysis compression zone depth for Beam B1B

From Figure 6.19, the rate of change of the compression zone on each side of the

beam was high at low load levels and at high load levels as the load approached the

buckling load. This trend was apparent in all the beam cases. Because of the trend,

comparisons of the compression zone depth from the experimental results and the

analytical results were more accurate in the middle of the applied load range where the

rate of change of the compression zone depth was smaller. Because the compression

zone depth at the center of the cross-section showed good correlation between the

experimental and analytical results, the discrepancies potentially originated from

differences between the analytical and experimental results for the neutral axis angle, φ.

Plots of the neutral axis angle, φ, as a function of applied load for each rectangular beam

are shown in Figures 6.20 to 6.24 for the experimental data and the nonlinear analysis data.
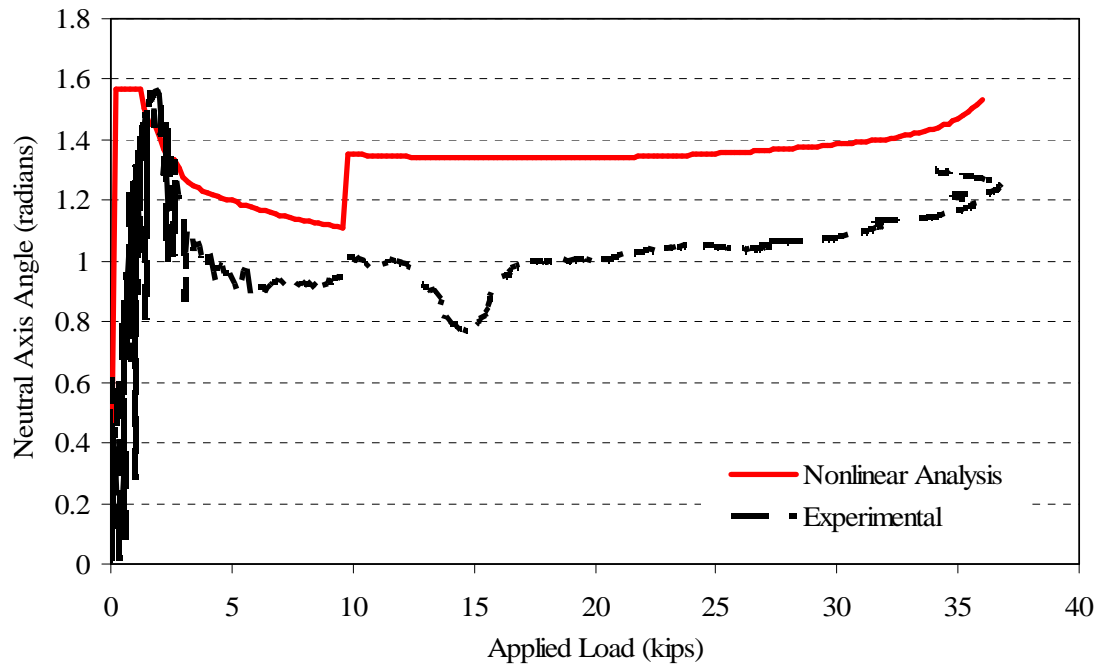
Figure 6.20 – B1A neutral axis angle for experimental data and nonlinear analysis
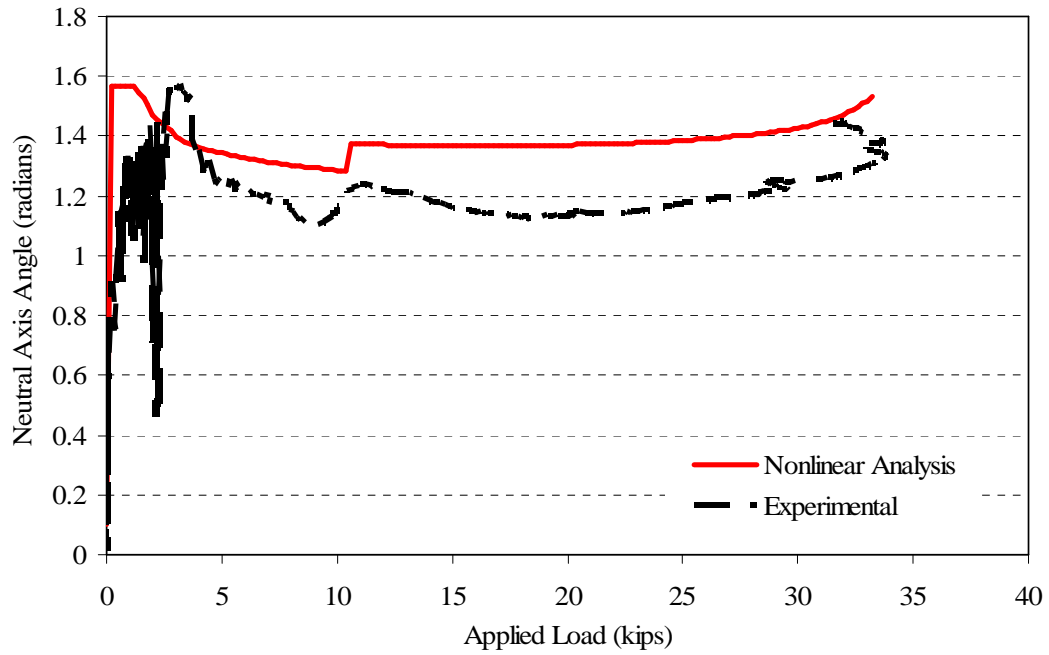
Figure 6.21 – B1B neutral axis angle for experimental data and nonlinear analysis
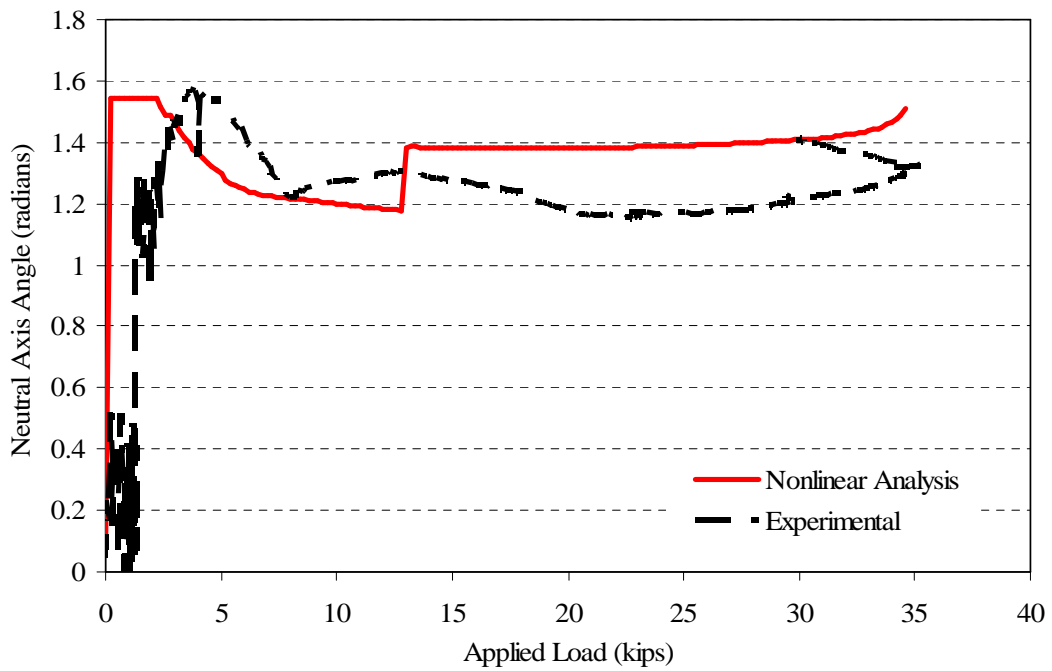
Figure 6.22 – B2B neutral axis angle for experimental data and nonlinear analysis
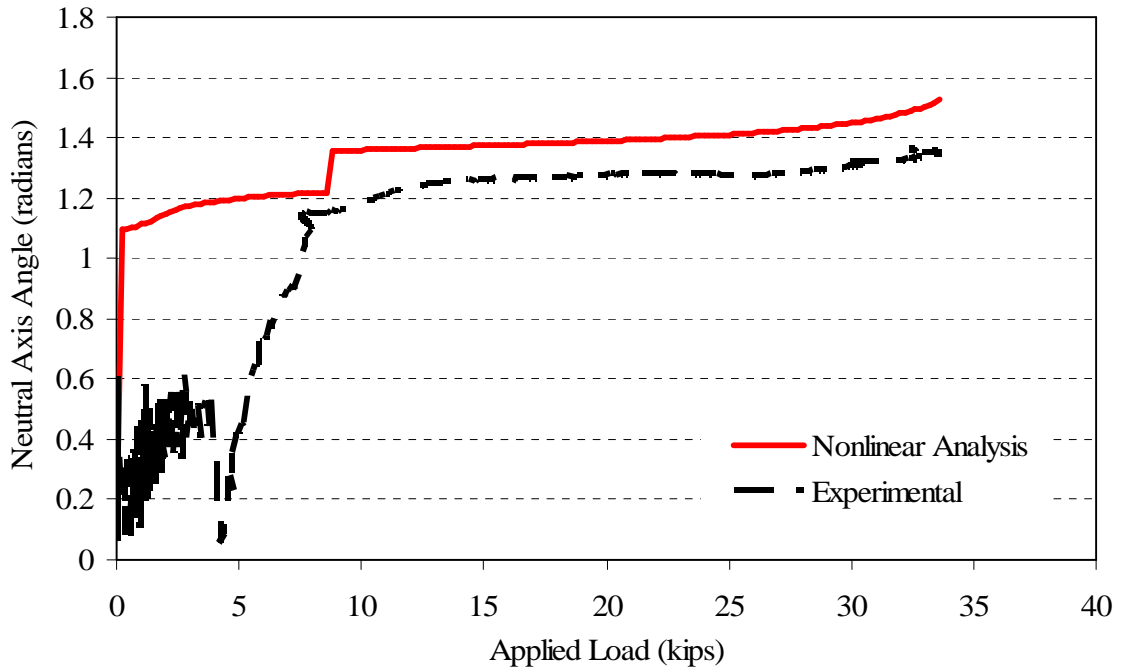
Figure 6.23 – C2A neutral axis angle for experimental data and nonlinear analysis
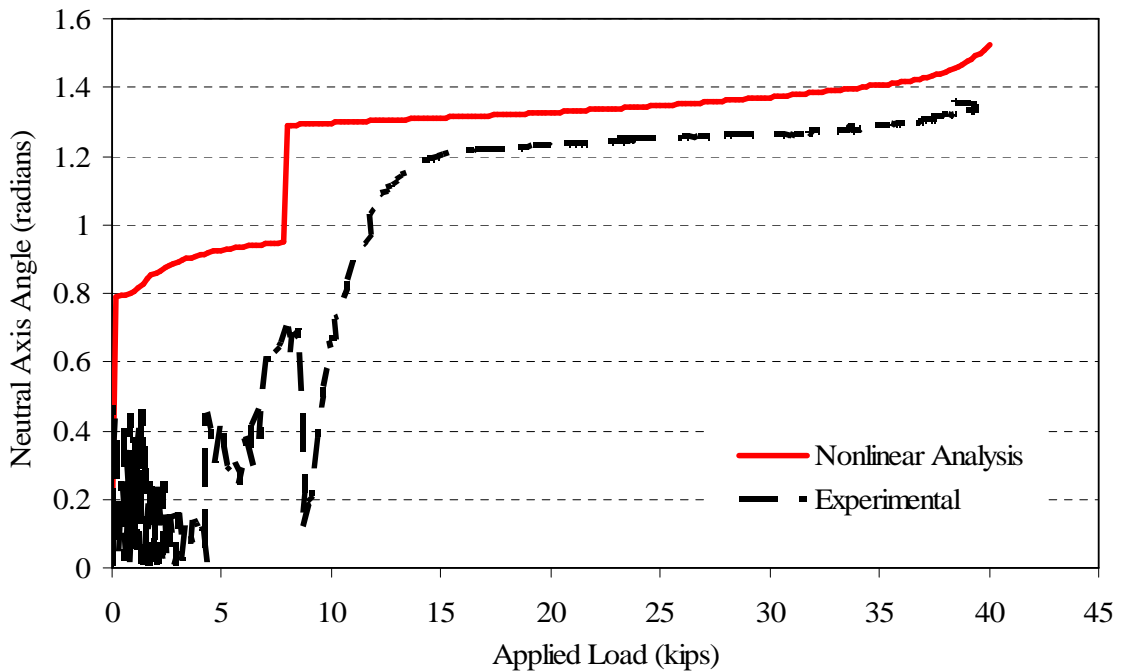
Figure 6.24 – C2B neutral axis angle for experimental data and nonlinear analysis

Figures 6.20 through 6.24 show good correlation between the analytical and experimental results with respect to the behavior of the neutral axis angle, φ, as a function of the applied load, but in most cases, there was an appreciable amount of error between the experimental and analytical results for the neutral axis angle, φ. The error was in the range of 5% to 30% during the applied loading after the cross-section had cracked at midspan in flexure. There were three potential causes of the differences between the analytical and experimental results. First, the experimental neutral axis angle, φ, was calculated using the experimental data and the assumed initial strain values due to the prestressing force and self-weight of the beam; however, there was no compensation made for the initial rotation, θ_0, causing a component of self-weight moment acting about the weak-axis of the beams. Secondly, the location of the additional longitudinal #3 reinforcing bars that spanned continuously along the length of the beam affected the neutral axis angle, φ, predicted in the nonlinear analysis. If the #3 reinforcing bars were located further from mid-thickness of the cross-section than specified in the design drawings, the neutral axis angle, φ, predicted in the nonlinear analysis would be reduced. Lastly, the nominal gage length of the LVDT's was 10-in. (254 mm), and for such a small gage length, flexural cracking did not necessarily cross the LVDT's. If cracking did not intersect the LVDT gage length, the measurements of strain would be smaller and incur an experimental error.

6.2.3.3 Nonlinear Analysis Results for Theoretical Cases

The nonlinear analysis was extrapolated to various initial imperfection cases for both beam series B1 and C2. Performing the nonlinear analysis for several different initial imperfection conditions made the lateral-torsional buckling behavior with respect

to initial sweep and initial rotation, θ_0, more apparent by uncoupling the two types of initial imperfection. Uncoupling the behaviors of initial sweep and initial rotation, θ_0, was achieved by performing the nonlinear analysis for a series of initial rotation, θ_0, values with a constant initial sweep and by performing the nonlinear analysis for a series of initial sweep values with a constant initial rotation. For the both beam series', the load versus deflection for the case of an initial sweep of ¼ in. (6.35 mm) is shown in Figure 6.25 for series B1 and Figure 6.26 for series C2 for several initial rotation angles. Additionally in Figures 6.25 and 6.26, the case of near zero imperfections both with respect to initial sweep and rotations was included.
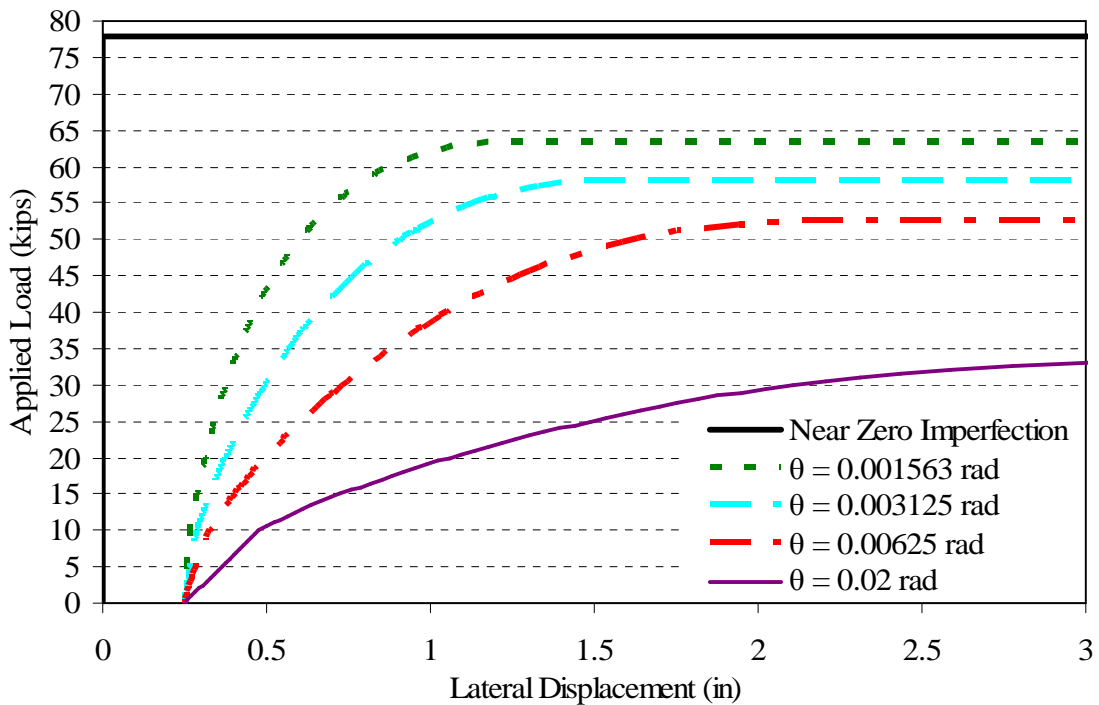
Figure 6.25 – Nonlinear analysis load vs. lateral displacement for Beam Series B1 with ¼ in. (6.35 mm) initial sweep and various initial rotations, θ_0
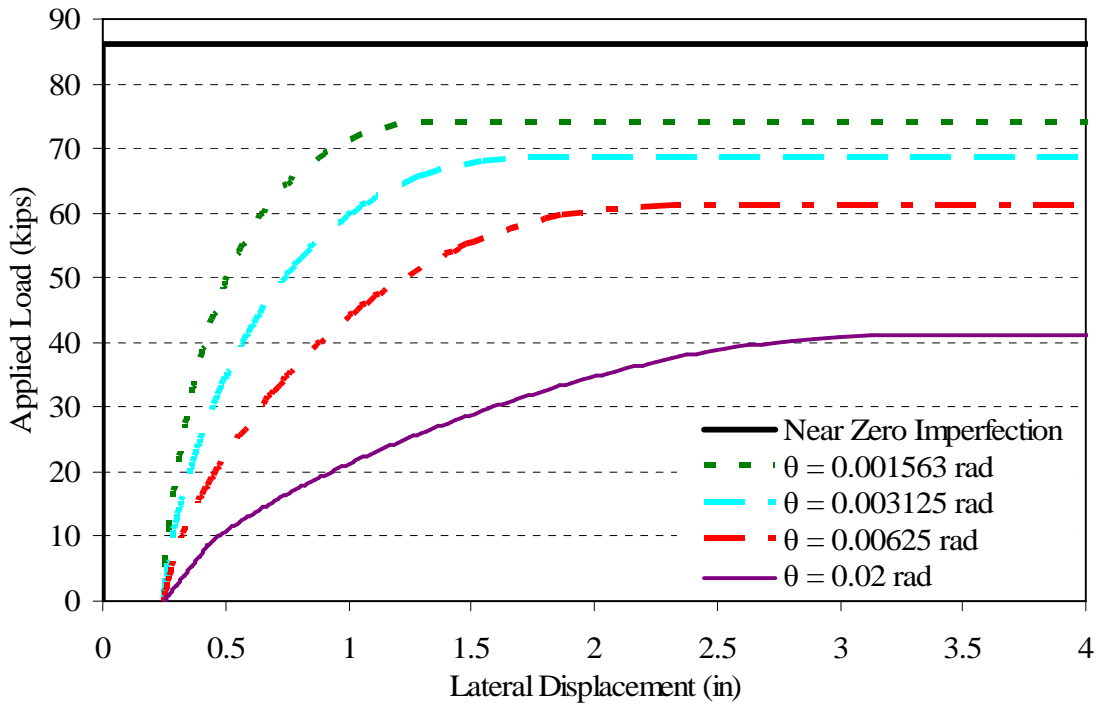
Figure 6.26 – Nonlinear analysis load vs. lateral displacement for Beam Series C2 with ¼ in. (6.35 mm) initial sweep

From Figures 6.25 and 6.26, it was apparent that the lateral deflection behavior was not a linear function between the initial rotation, θ_0, and the reduction in maximum load. Similarly, the rotation was held at a constant value of 0.001563 radians and the load versus lateral displacement results for several values of initial sweep at the top were obtained for series B1 and series C2. The plots of the results are shown in Figures 6.27 and 6.28.
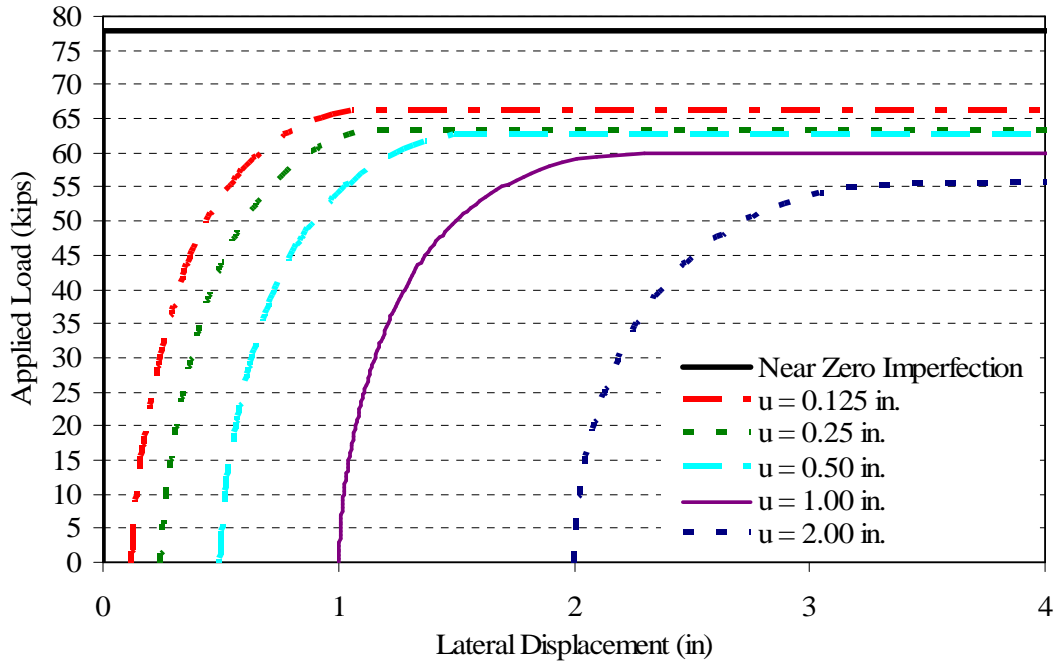
Figure 6.27 – Nonlinear analysis load vs. lateral displacement for Beam Series B1 with
0.001563 radians initial rotation for several initial sweep displacements, u
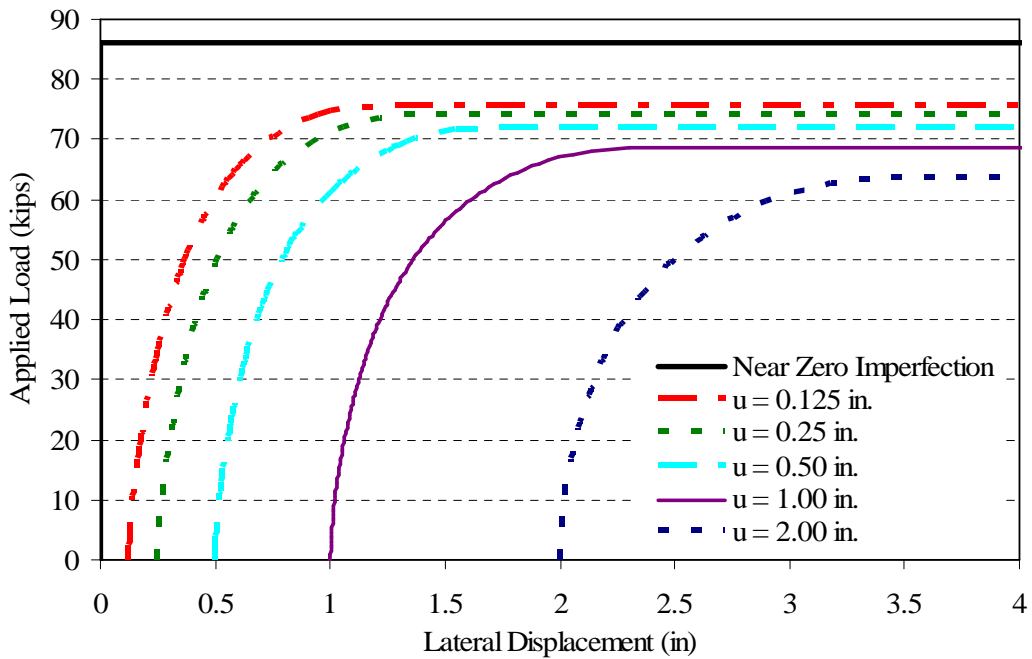
Figure 6.28 – Nonlinear analysis load vs. lateral displacement for Beam Series C2 with
0.001563 radians initial rotation for several initial sweep displacements, u

The analysis shows that the lateral displacement and rotation of the cross-section can continue to increase indefinitely which is not the case. Figures 6.27 and 6.28 depict the effect the initial sweep has on the lateral displacement behavior of the beams. However, for the beams to achieve the displacements required for the beam to support the maximum load, the beams must not crack in torsion. When the beams crack in torsion, the torsion constant used in the analysis would no longer be accurate, and a torsion constant for a torsionally cracked prestressed beam should be used. However, torsion constant expressions for a torsionally cracked beam are substantially less than the calculated torsion constant based on a rectangular compression zone; therefore, the beam would no longer remain stable. Therefore, when torsional cracking occurs at the ends of the beams, the descending portion of the load versus lateral displacement curve would initiate. With respect to the effect steel reinforcing had on the torsion behavior, Hsu (1984) established via experimental results that both transverse and longitudinal steel reinforcement act to increase the cracking torque of the cross-section but do not influence the uncracked torsional stiffness of the cross-section.

6.2.4 Torsional Cracking Behavior

The torsional cracking behavior was investigated by determining the point on the load versus lateral displacement curve where the torsion on the cross-section had reached the cracking torque. The cracking torque expression used in the analysis was the cracking torque expression from ACI 318-05 as presented in Equation 6.17.

$$T_{cr} = 4\sqrt{f_c'}\left(\frac{A_{cp}^2}{p_{cp}}\right)\sqrt{1+\frac{f_{pc}}{4\sqrt{f_c'}}} \qquad (6.17)$$

Each of the load versus lateral displacement plots for the experimental beams (except B2A) are presented in Figure 6.29 to 6.33. The plots include the experimental and analytical data as well as the point on the analytical load versus lateral displacement curve at which the cracking torque was exceeded.
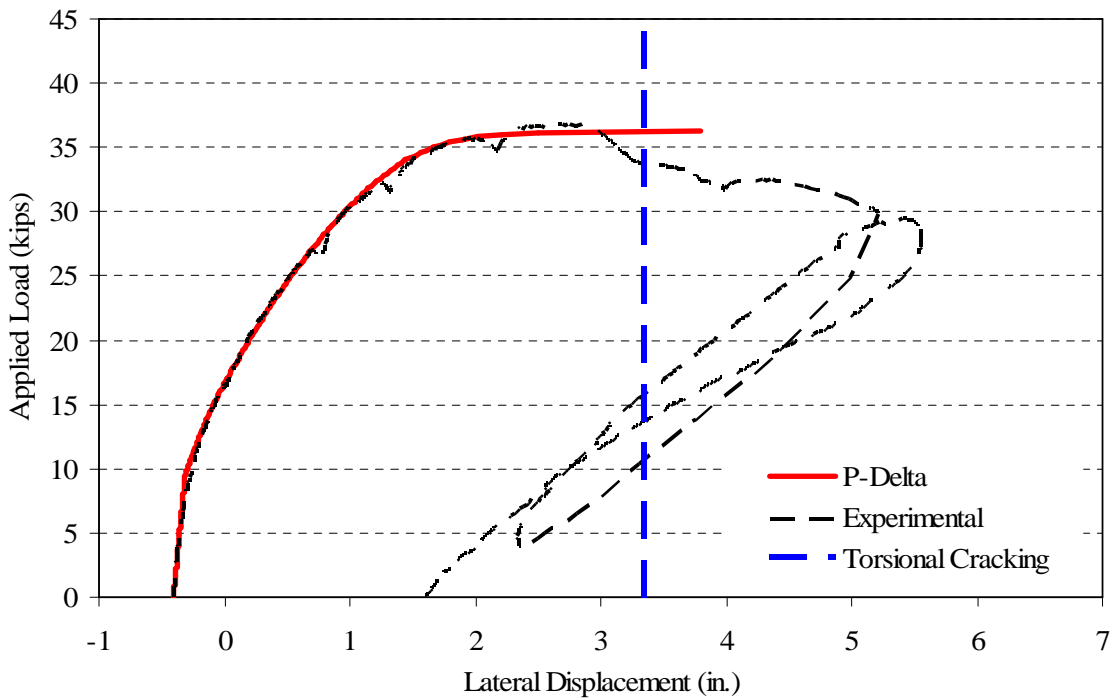
Figure 6.29 – Load vs. lateral displacement with cracking torque threshold for B1A
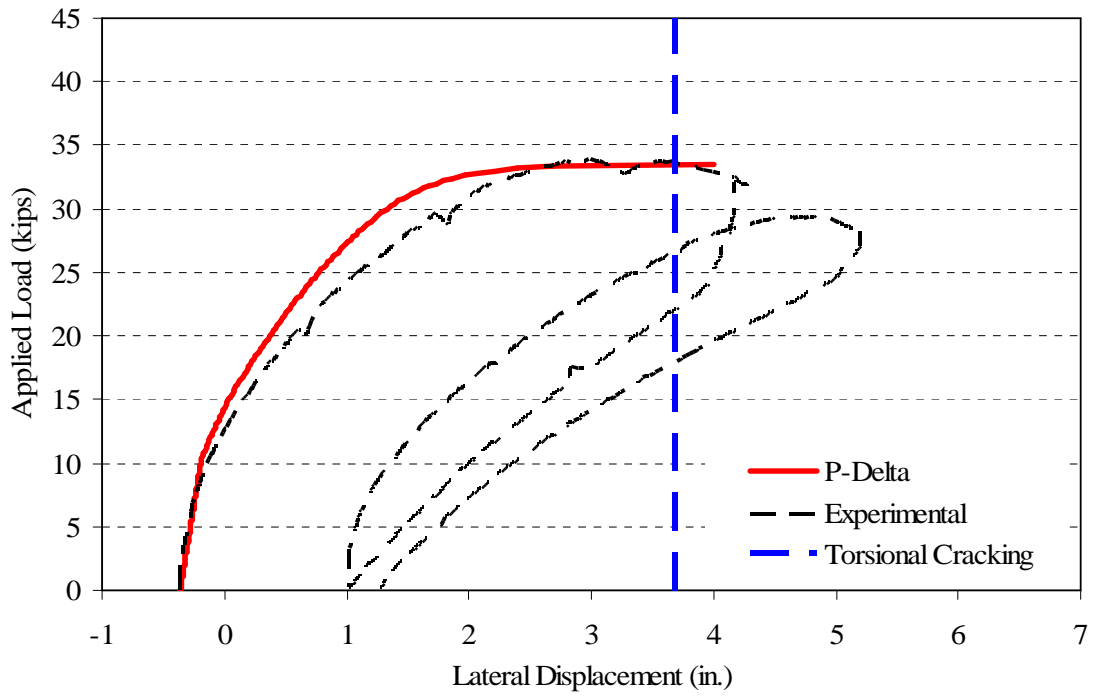
Figure 6.30 – Load vs. lateral displacement with cracking torque threshold for B1B
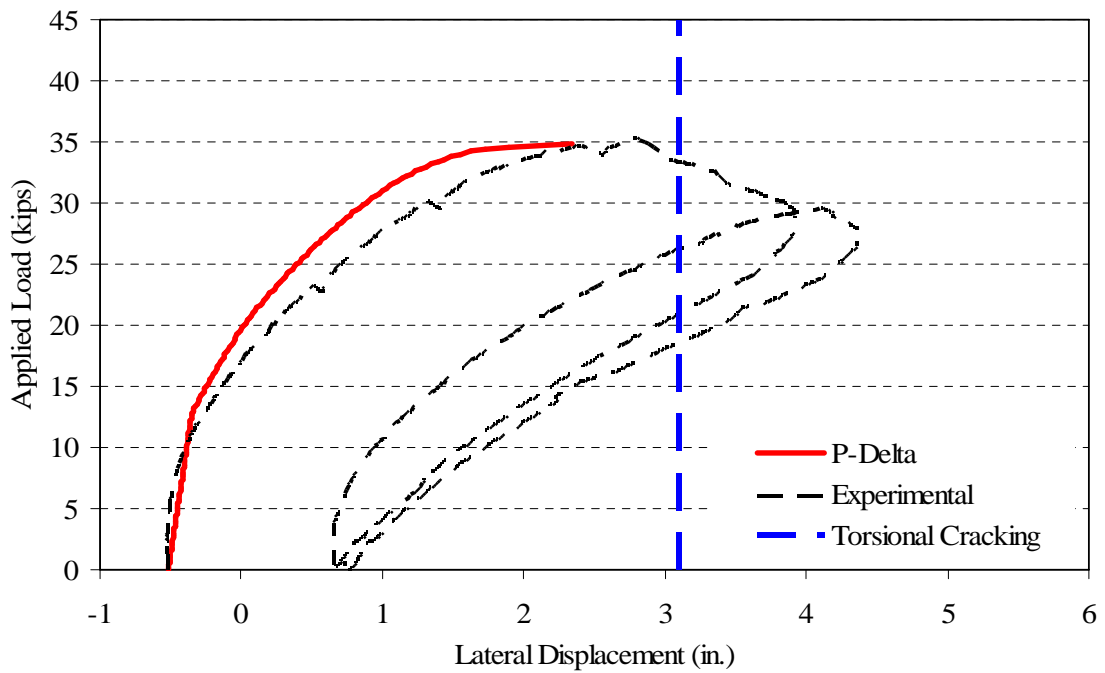
Figure 6.31 – Load vs. lateral displacement with cracking torque threshold for B2B
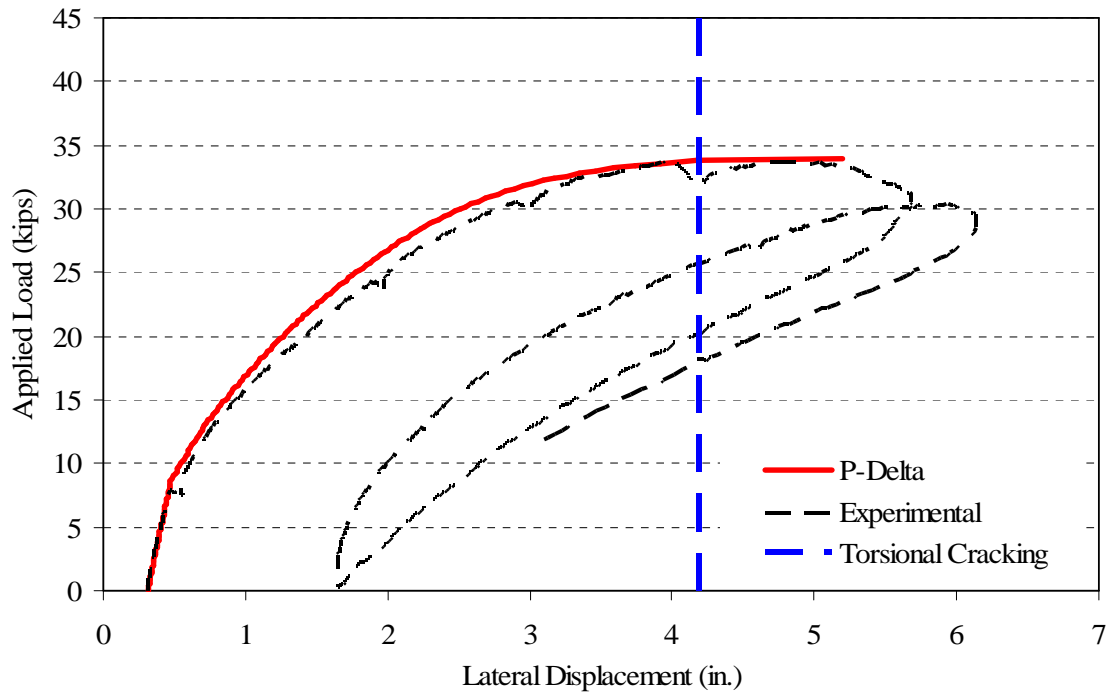
Figure 6.32 – Load vs. lateral displacement with cracking torque threshold for C2A
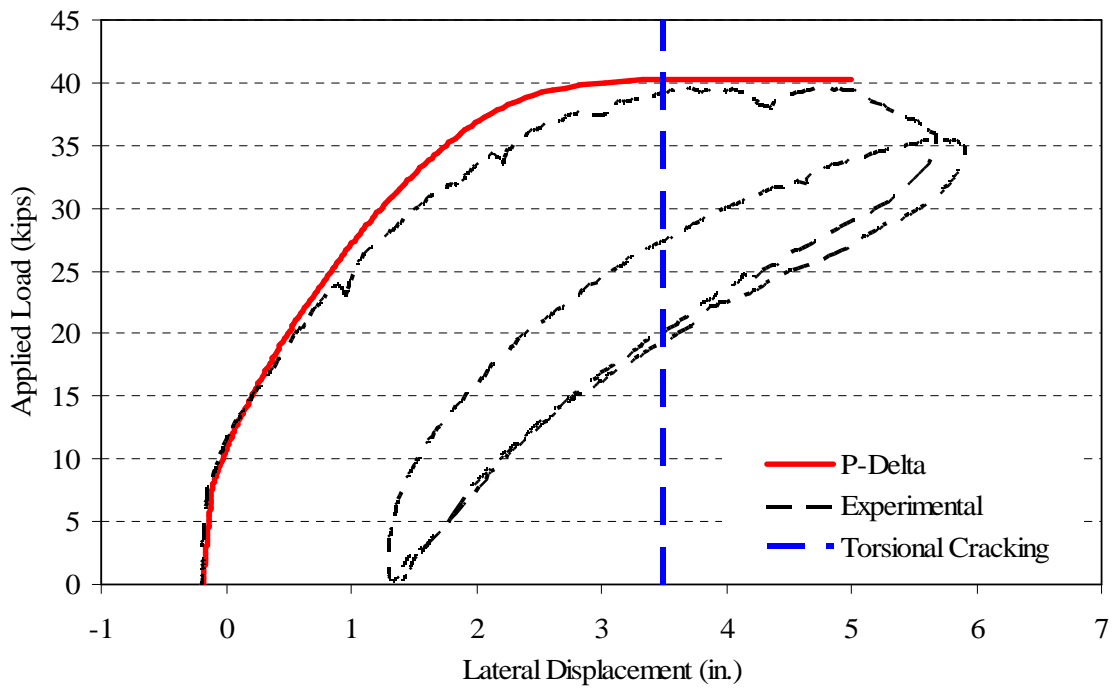
Figure 6.33 – Load vs. lateral displacement with cracking torque threshold for C2B

From Figures 6.29 to 6.33, the line designating the threshold for a torsionally uncracked cross-section coincided very well with the maximum experimental load, or the point at which the descending portion of the experimental load versus lateral displacement curve began. After large displacements occurred, torsional cracking was apparent at the ends of the beams during the experiments. However, cracking was not investigated immediately before buckling so it was not known whether torsional cracking occurred and then buckling happened as a result or if large post-buckling displacements occurred which led to torsional cracking at the ends. From the nonlinear analysis and predictions of the cracking torque for the cross-section, it was hypothesized that the torsional cracking occurred due to large post-buckling displacements. The flexural and flexural-shear cracking was observed as predicted by the nonlinear analysis at load much less than the buckling loads (10 kips to 18 kips).

6.3 Simplified Stability Analysis

A simplified stability analysis was developed to predict the buckling load that included the effects of the initial sweep and rotation imperfections. The simplified analysis was based on the approach by Hansell and Winter (1959) and by Sant and Bletzacker (1961). The secant modulus of elasticity of the extreme compression fiber of the beam was used for the concrete modulus of elasticity. The weak-axis moment of inertia was based on the ratio of the applied moment to the cracking moment as shown by Equation 6.18. The compression zone depth at midspan was used to calculate the weak-axis moment of inertia along the length of the beam in which the strong-axis flexural cracking moment had been exceeded. For the distance along the beam in which the

strong-axis flexural cracking moment had not been exceeded, the full height of the cross-section was used to calculate the weak-axis moment of inertia.

$$I_{yeff} = \left(\frac{M_a}{M_{crack}}\right)^2 \left(I_{gy} - I_{cry}\right) + I_{cry} \qquad (6.18)$$

Equation 6.18 was derived by considering that the weak-axis moment of inertia at midspan had more effect on the lateral displacement of the beam because the moment increased when approaching midspan. Therefore, the area of the moment diagram in the cracked portion of the beam along the length and the area of the moment diagram in the uncracked portion of the moment diagram along the length of the beam were used to determine the effective moment of inertia. Note that the derivation was based on the assumption of a concentrated load at midspan. For a different loading condition, a similar methodology could be used based on a different moment diagram. The ratio is shown in Equation 6.19, and when simplified, Equation 6.19 resulted in Equation 6.18.

$$I_{y\,eff} = \frac{\frac{L}{2}\left(\frac{M_{crack}}{M_a}\right)M_{crack}I_{gy} + \left[\frac{L}{2}M_a - \frac{L}{2}\left(\frac{M_{crack}}{M_a}\right)M_{crack}\right]I_{cry}}{\frac{L}{2}M_a} \qquad (6.19)$$

The longitudinal reinforcement was included in the calculation of weak-axis moment of inertia, although for the test beams of this study, there was a negligible effect on the weak-axis moment of inertia due to the proximity of the reinforcement to the weak-axis centroidal axis. In the analysis of the flange cross-sections from König and Pauli (1990), the longitudinal reinforcement contributed a non-negligible amount because the reinforcement in the flanges was at a significant distance, 1.28-in. to 5.31-in. (32.5 mm to 135 mm), from the weak axis. For cases where the analysis was performed on cross-sections that were at strain levels greater than the yield strain of the reinforcement, the effect of the reinforcement on the weak-axis moment of inertia should be neglected similarly to the methodology of Revathi and Menon (2006), because when the longitudinal steel yields, there will be minimal stiffness provided by the reinforcement.

An effective torsion constant considering flexural cracked and uncracked sections was developed as presented in Equations 6.20 and 6.21. The method employed in developing the effective torsion constant was similar to that of the effective weak-axis moment of inertia. Instead though, the largest torque was at the ends of the beam, and, therefore, the uncracked cross-section had more of an effect on the torsional stiffness of the beam than the cracked cross-section. A parabolic lateral displacement state was assumed, and, therefore, the torsion diagram was also parabolic. The assumed torsion diagram was integrated over half of the length of the beam to find that the area of the

torsion diagram for half of the beam was L/6. Furthermore, the assumed torsion diagram

was integrated from the end support to the point in which the strong-axis flexural

cracking moment was exceeded resulting in the following ratio for the effective torsion

constant:

$$J_{eff} = \frac{\left[\frac{4}{3L^2}\left(\frac{M_{crack}L}{2M_a}\right)^3 - \frac{2}{L}\left(\frac{M_{crack}L}{2M_a}\right)^2 + \left(\frac{M_{crack}L}{2M_a}\right)\right]J_g + \left[\frac{L}{6} - \frac{4}{3L^2}\left(\frac{M_{crack}L}{2M_a}\right)^3 - \frac{2}{L}\left(\frac{M_{crack}L}{2M_a}\right)^2 + \left(\frac{M_{crack}L}{2M_a}\right)\right]J_{cr}}{\frac{L}{6}} \quad (6.20)$$

Equation 6.20 can then be simplified to:

$$J_{eff} = \left[\left(\frac{M_a}{M_{crack}}\right)^3 - 3\left(\frac{M_a}{M_{crack}}\right)^2 + 3\left(\frac{M_a}{M_{crack}}\right)\right](J_g - J_{cr}) + J_{cr} \quad (6.21)$$

The technique used by the author to determine the buckling load was to assume a

strain value for the extreme fiber of the compression zone and solve for the compression

zone depth that resulted in force equilibrium within the cross-section. For rectangular

beams, a good initial estimate for the compression zone depth was one third of the height

of the cross-section. Then, the value for the compression zone depth based on an

assumed extreme compression fiber strain was used to calculate the internal moment in

262

the cross-section. The cracked section properties and secant modulus of elasticity were calculated, and, therefore, the buckling moment was able to be calculated for the assumed extreme compression fiber strain. The secant modulus was used because it best represents the "effective" modulus that would be determined from the average tangent modulus in the nonlinear analysis. Then, the internal moment in the cross-section was compared to the buckling moment, and the assumed value of the extreme compression fiber strain was iterated until the internal moment and the buckling moment were equivalent, arriving at the buckling moment for the cross-section. The value for the buckling moment was for the case of the perfect beam. Three parameters were introduced to reduce the buckling load based on the initial sweep and initial rotation, θ_0, of the beam. The three parameters were a weak-axis flexural stiffness reduction parameter, B_r, an initial sweep buckling load reduction parameter, Δ_r, and an initial rotation buckling load reduction parameter, Θ_r

6.3.1 Weak-Axis Flexural Stiffness Reduction Parameter, B_r

The weak-axis flexural stiffness was reduced to compensate for the effect of the compression zone not being in the shape of a rectangle, but instead, an initially imperfect beam has a rotated neutral axis. The reduction to the weak-axis flexural stiffness was calculated by using Equation 6.22.

$$B_r = B\left[1 - \frac{1}{3}\tan^{-1}\left(\frac{I_{gx}}{I_{gy}}\theta_0\right)\frac{2}{\pi}\right] \tag{6.22}$$

In Equation 6.22, the 1/3 coefficient resulted from the worst case for the weak-axis moment of inertia with respect to the compression zone shape without reducing the web thickness in the calculation of the weak-axis moment of inertia; this reduction created essentially a triangular compression zone. The assumption of a triangular compression zone was based upon the realization that a neutral axis angle, φ, coinciding with the weak-axis would actually be the worst case; however, the reduction would then be a function of the width of the cross-section and the compression zone depth.

The ratio of the triangular compression zone weak-axis moment of inertia to the rectangular compression zone weak-axis moment of inertia was 2/3; therefore, the weak-axis moment of inertia in the weak-axis flexural stiffness term was reduced by 1/3 in the worst case scenario. Because the reduction was based on a worst case scenario, the actual reduction was a function of the true neutral axis angle. For example, in the case of zero initial rotation, the neutral axis angle, φ, would be zero; therefore, the compression zone would be rectangular until post-buckling and no reduction in weak-axis flexural stiffness was necessary. So the reduction in weak-axis moment of inertia should be a function of the ratio of the actual neutral axis angle, φ, to the limiting neutral axis angle, φ$_{limit}$, resulting in the triangular compression zone as shown in Equation 6.23.

$$B_r = B\left[1 - \frac{1}{3}\frac{\phi}{\phi_{\lim it}}\right] \tag{6.23}$$

The limiting neutral axis angle, φ$_{angle}$, was a function of the cross-section as shown by Equation 6.24.

$$\phi_{\text{lim}\,it} = \tan^{-1}\left(\frac{h}{b}\right) \qquad (6.24)$$

The limiting neutral axis angle, ϕ_{angle}, was approximated as $\pi/2$ for two reasons. The first reason was that as the slenderness of a cross-section increased, the limiting neutral axis angle, ϕ_{limit}, approached $\pi/2$. For example, in the case of the rectangular test beams, the limiting neutral axis angle, ϕ_{limit}, was 1.471 radians. Secondly, it was an assumption that the worst case was a triangular compression zone; the actual worst case was if the neutral axis was at $\pi/2$. The limiting neutral angle was substituted into Equation 6.23 to arrive at:

$$B_r = B\left[1 - \frac{1}{3}\left(\frac{2\phi}{\pi}\right)\right] \qquad (6.25)$$

To determine the actual neutral axis angle, ϕ, which was substituted in Equation 6.25, the assumption that the material was elastic and homogeneous was employed. Therefore, the equation for the neutral axis angle, ϕ, given by Beer et al. (2001) was:

$$\phi = \tan^{-1}\left(\frac{I_x}{I_y}\tan(\theta_0)\right) \qquad (6.26)$$

Equation 6.26 was further simplified by the assumption that the tangent of the initial rotation, θ_0, of the cross-section was equal to the initial rotation angle, θ_0. The assumption was validated by investigating Figure 6.35.
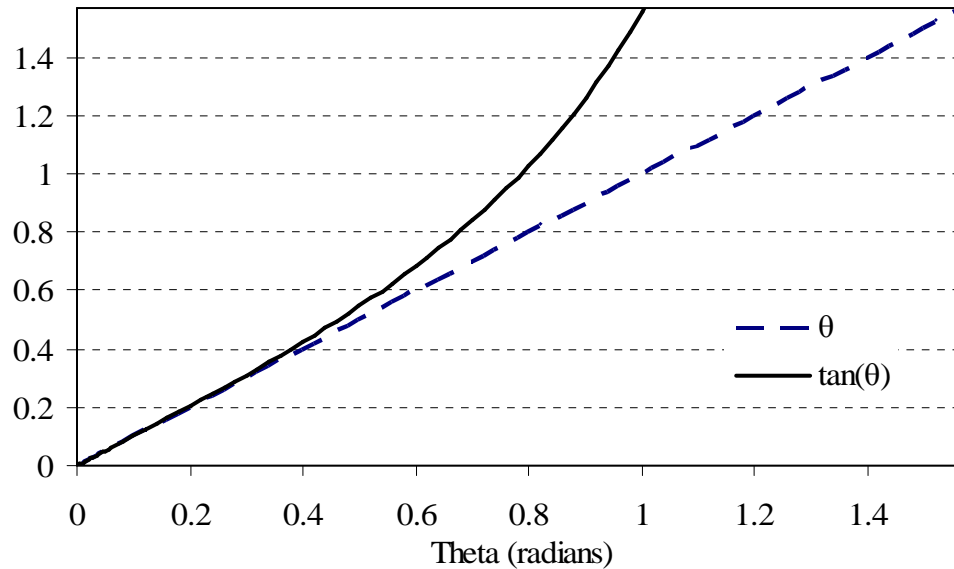
Figure 6.34 – Comparison of tangent of rotation angle to rotation

From Figure 6.34, it was apparent that for small initial rotation angles the simplification was accurate. For the approximation to remain below 1% error from the actual response, the initial rotation angle, θ_0, must be less than 0.173 radians or approximately 10 degrees. In most practical situations, a structural member should not have an initial rotation error exceeding 3 degrees; therefore the approximation was valid and Equation 6.27 can be used instead of Equation 6.26.

$$\phi = \tan^{-1}\left(\frac{I_x}{I_y}\theta_0\right) \tag{6.27}$$

Substituting Equation 6.27 into Equation 6.25 resulted in the weak-axis flexural stiffness reduction parameter in Equation 6.22. Additionally, for small initial rotation angles and depending on the specifics of the cross-section, the reduction parameter of Equation 6.22 can be further simplified to Equation 6.28 by removing the inverse tangent from the equation.

$$B_r = B\left[1 - \frac{1}{3}\left(\frac{I_{gx}}{I_{gy}}\theta_0\right)\frac{2}{\pi}\right] \tag{6.28}$$

The response of the reduction parameter of Equation 6.22 and the simplified reduction parameter of Equation 6.28 as a function of the initial rotation angle, θ_0, for different ranges of strong-axis to weak-axis moments of inertia is shown in Figure 6.35. The moments of inertia used in the analysis were the gross moments of inertia because the actual moments of inertia vary along the length of the beams. Furthermore, the difference between the ratio of strong-axis to weak-axis moment of inertia for the gross section and fully cracked section at midspan was typically less than 0.1% with respect to the resulting predicted buckling loads for the rectangular cross-sections. Strong-axis

moment of inertia to weak-axis moment of inertia ratios on the order of 100 are

representative of slender rectangular cross-sections (the 4x40 in. sections used had and

Ix/Iy ratio of 115), and strong-axis moment of inertia to weak-axis moment of inertia

ratios on the order of 10 are representative of flanged cross-sections (a BT-54 has and

Ix/Iy = 8.75).
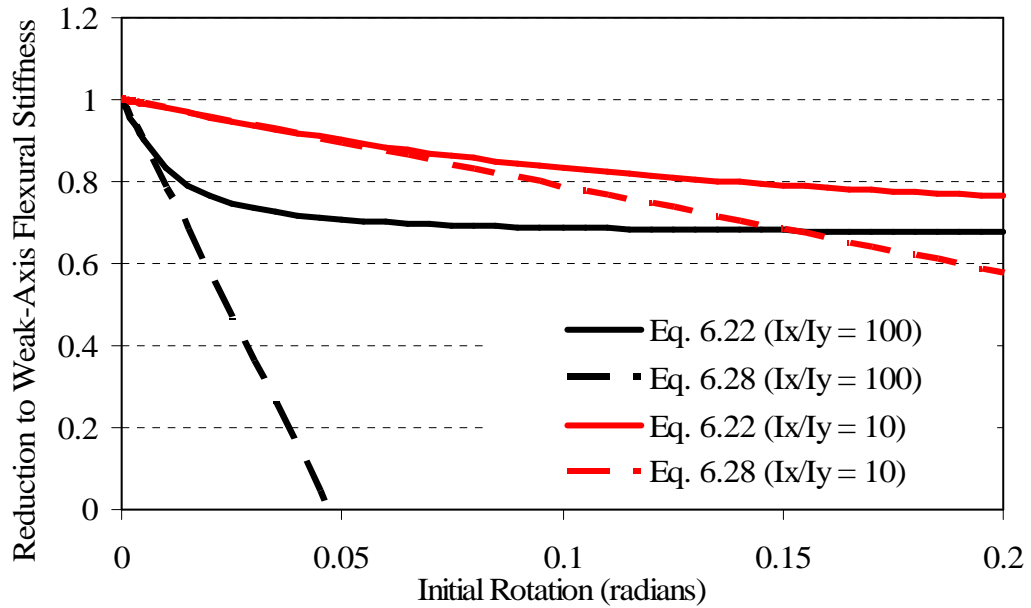
Figure 6.35 – Comparison of reduction parameter and simplified reduction parameter

Figure 6.35 shows that for small initial rotations less than 0.01 radians, the weak-

axis flexural stiffness reduction parameter and the simplified reduction parameter

produced very similar results. Furthermore, for smaller ratios of strong-axis to weak-axis

moment of inertia, the simplified reduction parameter was accurate at initial rotations up

to 0.06 radians. However, due to the limited computational benefit of the simplified expression of Equation 6.28, Equation 6.22 is recommended.

The effect that the reduction parameter B_r of Equation 6.22 had on the buckling moment for varying strong-axis to weak-axis moment of inertia ratios is shown in Figure 6.36. Note that the reduction to the buckling load due to the weak-axis flexural stiffness reduction parameter, B_r, asymptotes to a reduction of 18.3% because that corresponds to the largest reduction possible due to a reduced weak-axis moment of inertia from the rotation of the neutral axis, φ.
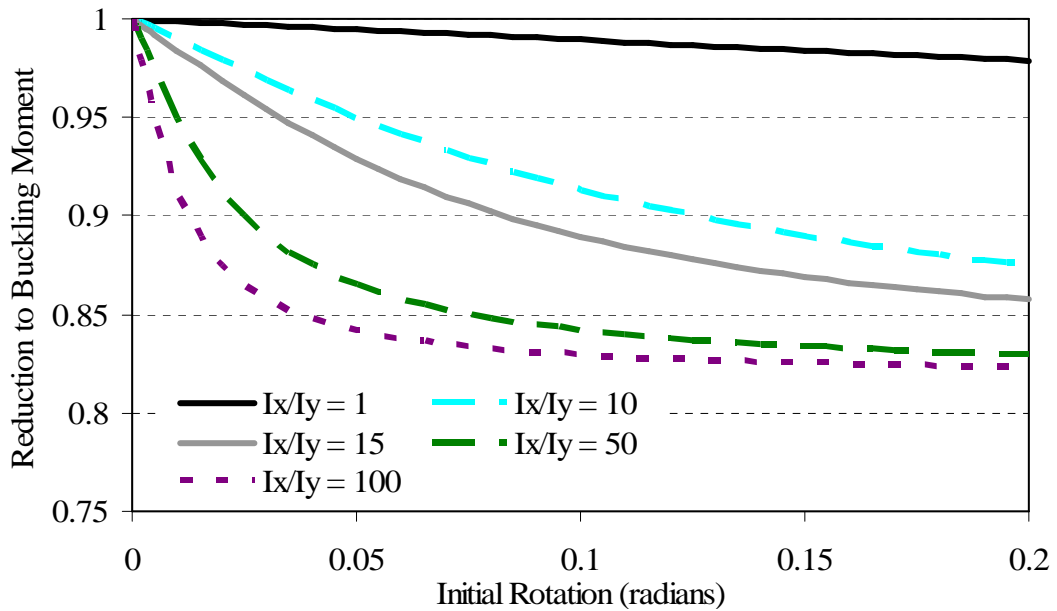
Figure 6.36 – Effect of reduction parameter B_r on buckling load

Figure 6.36 shows that the reduction parameter B_r corresponds qualitatively to what intuitively would occur. For slender rectangular beams ($I_x/I_y = 100$) the reduction to the buckling load was substantially more than for an AASHTO bridge girder ($I_x/I_y = 6$-10) or a PCI BT bridge girder ($I_x/I_y = 7$-15). The reason was that a specific rotation angle had more of an effect on the neutral axis angle, φ, for a slender rectangular beam than on a flanged girder.

The 1/3 coefficient within Equation 6.22 was determined by considering a rectangular cross-section, but how accurate was the coefficient for a cross-section with flanges? The coefficient for flange cross-sections was a function of the specific geometry and the range of the neutral axis angle, φ. Essentially, if the neutral axis angle, φ, was small enough that the neutral axis did not cut through the flange and reduce the flange width, then the 1/3 coefficient over-predicted the reduction, or was conservative. However, for relatively large neutral axis angles, the reduction to the weak-axis moment of inertia was significant and the 1/3 coefficient under-predicted the reduction because the neutral axis would then cut through the flange and reduce the flange width. The specific range of neutral axis angle, φ, in which the coefficient transitions between conservative and unconservative depends on the specific geometry of the flange cross-section. The transition would occur at a neutral axis angle, φ, approximated by Equation 6.29.

$$\phi_{transition} = \tan^{-1}\left(\frac{y_t}{\left(b_{tf}/2\right)}\right) \tag{6.29}$$

The initial rotation angles, θ_0, for practical conditions are relatively small. The tolerance for the flatness of the support from the PCI Bridge Design Manual (2003) is 1/16" (1.6 mm) which results in a maximum initial rotation, θ_0, of 0.0035 radians for an 18" (460 mm) wide bearing pad. The PCI Bridge Design Manual (2003) also limits the sweep of a girder to 1/8 in. (3.2 mm) per 10-ft. (3 m) of girder length which results in a maximum rotation of 0.026 radians for a 150-ft. (45.7 m) long girder that is 72-in. (1.8 m) in depth. To the author's knowledge, no other tolerances have been specified in accepted design guides or construction manuals that affect the slope of the girder at midspan. If the amount of rotation, θ, due to the compliance of the bearing pad is negligible, the neutral axis angle, φ, for typical AASHTO and PCI BT cross-sections would be on the order of 0.20 radians to 0.50 radians. The neutral axis angle, φ, would have to exceed approximately 0.90 radians to 1.00 radians for the weak-axis flexural stiffness reduction parameter, B_r, to become unconservative. However, larger initial rotations can occur due to bearing pad compliance if there is a non-uniform bearing condition or if the girder is placed eccentrically on the bearing pad. A maximum end rotation of 0.079 radians was measured after the collapse of the bridge girders in Arizona (Oesterle et al., 2007). The approximate initial rotation, θ_0, given by the summation of the reported maximum initial end rotation and the tolerance of initial rotation, θ_0, along the length of the girder resulted in a neutral axis angle, φ, of approximately 1.00 radians for an AASHTO or PCI BT cross-section. Therefore, if a large initial end rotation occurs due to a non-uniform bearing condition or an eccentric placement of the girder, the weak-axis flexural stiffness reduction parameter, B_r, can become unconservative.

6.3.2 Buckling Load Reduction for Initial Imperfections

The buckling load was reduced due to initial imperfections in addition to the effect of the initial rotation, θ_0, on the neutral axis angle, φ. Although small displacement theory for an elastic beam showed that initial imperfections affect the load versus lateral displacement and load versus rotation behavior, the same maximum load was achieved for any value of initial imperfection. However, the inelastic behavior of a prestressed concrete beam did not necessarily attain the same maximum load independent of the initial imperfections. Because varying initial imperfections varied the cracking behavior, the concrete nonlinear material properties, and the torsion constant, the buckling load was reduced to approximate the effects of the initial imperfections.

Two terms were introduced: one reduction parameter for the effect of initial lateral displacement, Δ_r, and one parameter for the effect of initial rotation Θ_r. The reduction term for initial rotation, θ_0, was chosen as an exponential function because the reduction of the buckling load for initial rotation, θ_0, was asymptotic. The terms were as follows:

$$\Delta_r = 1 - \left(\frac{\delta_0}{L} \right)^m \tag{6.30}$$

$$\Theta_r = e^{-n\theta_0} \tag{6.31}$$

The reduction term for initial lateral displacement in Equation 6.30 was a function of the ratio of the initial lateral displacement to the span of the beam. Such a ratio was used so that the term was unitless and because it was hypothesized that a constant quantity of initial lateral displacement should have a varying effect on the stability depending on the span of the beam. The rotation term in Equation 6.31 was a function of only the initial rotation, θ_0, so that the term was unitless and because the initial rotation, θ_0, was already a ratio of the change in initial lateral displacement at the top and bottom of the beam over the height of the cross-section. Furthermore, the ratios were reductions to behavior of an initially perfect beam; therefore, the ratio for initial lateral displacement was subtracted from unity to attain a simple multiplier. The reason the reduction for initial lateral displacement was a power expression and the reduction for initial rotation, θ_0, was an exponential expression was because the uncoupled behavior of the two types of initial imperfection most closely followed the specific type of equation specified. Figures 6.25 to 6.28 depict this behavior.

The exponent variables in Equations 6.30 and 6.31, m and n, were determined by performing nonlinear analysis on nine B1 beams with varying initial imperfection combinations and on nine C2 beams with varying initial imperfections. The results of the 18 nonlinear analyses were compared with predictions from the simplified analysis. By using a least-squares, best-fit methodology, the selection of the variables m and n ideally would have been m = 0.31 and n = 26.5 with an average residual of 1.33 and an average percent error of 1.67%. Equations 6.32 and 6.33 show the final initial lateral displacement and initial rotation reduction parameters, respectively. Table 6.3 shows the least squares methodology for the case of m = 0.31 and n = 26.5.

$$\Delta_r = 1 - \left(\frac{\delta_0}{L}\right)^{0.31} \tag{6.32}$$

$$\Theta_r = e^{-26.5\theta_0} \tag{6.33}$$

Table 6.3 – Least squares analysis on reduction parameters

Parameters								
Δr Power =	0.31	θr Power =	26.5					
Beam C2 Constant Displacement								
P_{buckle} (kips)	u (in)	Rotation (rad)	Br	Δr	θr	$P_{predict}$ (kips)	Si	% error
86	0	0	1	1	1	86	0	
74.2	0.25	0.001563	0.98341	0.896541	0.95943	72.74711977	2.110861	1.95806
68.8	0.25	0.003125	0.96733	0.896541	0.92052	68.65592916	0.020756	0.209405
61	0.25	0.00625	0.93886	0.896541	0.84736	61.33952549	0.115278	0.556599
41.3	0.25	0.02	0.87467	0.896541	0.5886	39.69531163	2.575025	3.885444
						S (C2) =	4.82192	
Beam B1 Constant Displacement								
P_{buckle} (kips)	u (in)	Rotation (rad)	Br	Δr	θr	$P_{predict}$ (kips)	Si	% error
76.2	0	0	1	1	1	76.2	0	
63.5	0.25	0.001563	0.98341	0.896541	0.95943	64.4573317	0.916484	1.507609
58.6	0.25	0.003125	0.96733	0.896541	0.92052	60.83234654	4.983371	3.809465
52.7	0.25	0.00625	0.93886	0.896541	0.84736	54.34967259	2.72142	3.130309
34.3	0.25	0.02	0.87467	0.896541	0.5886	35.1718924	0.760196	2.54196
						S (B1) =	9.381471	
Beam C2 Constant Rotation								
P_{buckle} (kips)	u (in)	Rotation (rad)	Br	Δr	θr	$P_{predict}$ (kips)	Si	% error
86	0	0	1	1	1	86	0	
75.6	0.125	0.001563	0.98341	0.916546	0.95943	74.37033166	1.512084	1.626545
74.2	0.25	0.001563	0.98341	0.896541	0.95943	72.74711977	2.110861	1.95806
72.1	0.5	0.001563	0.98341	0.871741	0.95943	70.73481149	1.86374	1.893465
68.7	1	0.001563	0.98341	0.840997	0.95943	68.24013742	0.211474	0.669378
						S (C2) =	5.698158	
Beam B1 Constant Rotation								
P_{buckle} (kips)	u (in)	Rotation (rad)	Br	Δr	θr	$P_{predict}$ (kips)	Si	% error
76.2	0	0	1	1	1	76.2	0	
66.3	0.125	0.001563	0.98341	0.916546	0.95943	65.89557293	0.163561	0.609996
63.5	0.25	0.001563	0.98341	0.896541	0.95943	64.4573317	0.916484	1.507609
62.6	0.5	0.001563	0.98341	0.871741	0.95943	62.67433297	0.005525	0.118743
60	1	0.001563	0.98341	0.840997	0.95943	60.46393571	0.215236	0.773226
						S (C2) =	1.300807	
						S_{total} =	21.20236	
						Mean =	1.325147	1.672242

The reduction parameters from Equations 6.22, 6.32 and 6.33 were developed and calibrated for a specific range of initial sweep and initial rotation, and, therefore, if these maximums are exceeded, the reduction parameters are not necessarily accurate due to a lack of verification. The limit on the maximum initial sweep is 5/16-in. (7.94 mm) per 10-ft. (3.05 m) of span, which is 150% larger than the PCI tolerance (PCI, 2000). The limit on the maximum initial rotation is $\theta_i/h < 0.8$. The total critical buckling moment equation for prestressed concrete beam considering initial imperfections is:

$$M_{b\,imperfections} = \frac{\pi}{L} A\sqrt{B_r C}\ \Delta_r \Theta_r \qquad (6.34)$$

In Equation 6.34, the parameter "A" was the parameter that takes into consideration the effect of load height on the buckling moment given in Equation 6.35 where $\bar{a}$ is the load height above the shear center.

$$A = 1 - 1.74\frac{\bar{a}}{L}\sqrt{\frac{EI_y}{GJ}} \qquad (6.35)$$

6.3.3 Simplified Equation vs. Experimental Results

Because the experimental results from this study include an effect of the error in the load application angle, the error in load application angle was included as part of the initial rotation, θ_0, of the beam in the simplified equation. Furthermore, because the initial sweep of some of the beams was in the negative direction, which created a

stabilizing effect, the initial sweeps that were negative were input into the simplified

equation as zero value. The results of the comparison are shown in Table 6.4.

Table 6.4 – Comparison between the experimental results and the simplified equation

Beam ID	Initial Sweep, in. (mm)	Initial Rotation, radians	Experimental Buckling Load, kips (kN)	Simplified Equation Buckling Load, kips (kN)	Percent Difference
B1A	-0.406 (-10.3)	0	36.87 (163.9)	37.5 (167)	-1.7
B1B	-0.360 (-9.1)	0.00078	33.92 (150.8)	36.2 (161)	-6.7
B2B	-0.516 (-13.1)	0.00156	34.69 (154.2)	32.1 (143)	7.5
C2A	0.313 (7.9)	0.00430	33.68 (149.7)	32.8 (146)	-2.6
C2B	-0.188 (-4.8)	0.00078	39.55 (175.8)	41.8 (186)	-5.7

There was good correlation between the results from the experiments of this study

and the predicted buckling loads using the simplified equation proposed in Equation 6.34.

However, the simplified equation was developed to determine buckling loads for beams

with a perfect vertical load such as gravity load. Furthermore, the simplified equation

was not developed to account for an initial lateral displacement in the opposite direction

of buckling. The predicted buckling load for Beam C2A using the simplified equation

was the second lowest absolute percent error, and it was the only beam case that had the

initial lateral displacement in the direction of buckling. To further validate the procedure,

the simplified equation was also compared with the experimental results from König and

Pauli (1990) and Kalkan (2009). The comparisons are shown in Table 6.5 and 6.6,

respectively.

Table 6.5 - Comparison between the experimental results from König & Pauli (1990) and
the simplified equation

Konig & Pauli Beam #	Initial Sweep, in. (mm)	Initial Rotation, radians	Experimental Buckling Load, kips (kN)	Simplified Equation Buckling Load, kips (kN)	Percent Difference
1	0.787 (20)	0.005	42.7 (190)	39.1 (173.9)	8.4
2	0.118 (3)	0.003	44.5 (198)	43.8 (194.8)	1.6
3	0.236 (6)	0.013	57.0 (253.5)	53.9 (239.8)	5.4
4	0.098 (2.5)	0.0015	53.4 (237.5)	51.6 (229.5)	3.4
5	0.827 (16)	0.003	45.1 (200.5)	47.6 (211.7)	-5.5
6	0.433 (11)	0.004	50.9 (226.5)	50.4 (224.2)	1.0

Table 6.6 - Comparison between the experimental results from Kalkan (2009) and the simplified equation

Kalkan Beam #	Initial Sweep, in. (mm)	Initial Rotation, radians	Experimental Buckling Load, kips (kN)	Simplified Equation Buckling Load, kips (kN)	Percent Difference
B18 - 2	0.125 (3.2)	0	12 (53.4)	12.3 (54.7)	-2.5
B30	0.625 (14.3)	0.00417	22 (97.9)	22.7 (101.0)	-3.2
B36	0.219 (5.6)	0.00087	39.2 (174.4)	39.5 (175.7)	-0.8
B44 - 1	0.250 (6.4)	0.00284	15.2 (67.6)	15.1 (67.2)	0.7
B44 - 2	0.781 (19.8)	0.00284	12 (53.4)	13.6 (60.5)	-13.3

Refer to König and Pauli (1990) and Kalkan (2009) for the details of the individual beam properties such as the geometry, reinforcement layout, initial imperfections and the material properties. Beams 1 through 4 from König and Pauli (1990) did not have any prestressed reinforcing, only mild reinforcing. Beams 1 through 4 all had a top flange, but not a bottom flange. In König and Pauli's (1990) study, they varied the top flange width and the amount of compression reinforcement to parametrically study these effects (Beams 1 through 4). Table 6.5 shows that the simplified equation predicted buckling loads within 8% of the experimental results. Beams 5 and 6 were both prestressed concrete beams. Beam 5 had a top flange, while Beam 6 included both a top and a bottom flange. The simplified equation predicted the buckling loads for the prestressed beams within 6%. The difference between the experimental results and predicted results for Beams 5 and 6 were most likely due to the

limited information published on the prestressing strands and prestressing force. Additionally, error in all beam cases could be attributed to the relative crudeness of the measured initial rotations. With the exception of Beam 5 of the test beams from the study by König and Pauli (1990), the simplified equation was conservative and under-predicted the actual behavior which was consistent with the previous discussion on the simplified equation's 1/3 coefficient. The previous discussion stated that for flanged cross-sections, the 1/3 coefficient was conservative for most cases.

The test beams from Kalkan (2009) were all slender, rectangular concrete beams with mild reinforcement. From Table 6.6, the simplified equation matched very well with the experimental buckling loads. The error was from -4% to 1% for all of the beams with the exception of B44-2. The error was attributed to experimental error, the fact the simplified equation is an approximate technique, the thin beam sections (less than 3-in. (76 mm)), extreme slenderness with length to width ratios of 96 to 156, and relatively low buckling load. The simple analysis was very sensitive to the many parameters. The sensitivity of the simplified equation with respect to initial imperfections for the test beams of Kalkan (2009) is shown in Table 6.7. The lower bound simplified equation buckling load was the buckling load using the maximum initial imperfections possible within the resolution of the initial imperfection measurements. Similarly, the upper bound simplified buckling load was the buckling load using the smallest initial imperfections possible within the resolution of the initial imperfection measurements. The initial rotation, θ_0, was never taken as less than zero.

Table 6.7 - Comparison between the experimental results from Kalkan (2009) and the
simplified equation with bounds

Kalkan (2009) Beam #	Experimental Buckling Load, kips (kN)	Simplified Eq. Buckling Load, kips (kN)	Lower Bound Simplified Eq. Buckling Load, kips (kN)	Upper Bound Simplified Eq. Buckling Load, kips (kN)	Percent Difference Range
B18 - 2	12 (53.4)	12.3 (54.7)	11.3 (50.3)	12.7 (56.5)	-5.8 to 5.8
B30	22 (97.9)	22.7 (101.0)	21.8 (97.0)	23.8 (105.9)	-3.6 to 0.9
B36	39.2 (174.4)	39.5 (175.7)	37.8 (168.1)	41.4 (184.2)	-5.6 to 3.6
B44 - 1	15.2 (67.6)	15.1 (67.2)	13.8 (61.4)	16.5 (73.4)	-8.6 to 9.2
B44 - 2	12 (53.4)	13.6 (60.5)	13.1 (58.3)	15.6 (69.4)	-30 to -9.2

No other researchers included the initial imperfections when they published their experimental results; therefore, the simplified equation developed in this study was not compared with any other experimental results. A sample calculation using the simplified technique is presented in Appendix D.

CHAPTER 7

PCI BT-54 BRIDGE GIRDER INVESTIGATION

7.1 PCI BT-54 Study Objectives

An experimental study was performed on a 100-ft (30.5 m) long BT-54 bridge girder to investigate the stability behavior of an actual bridge girder with a relatively large amount of prestressing force and with construction tolerances which modeled inaccuracies similar to those noted in the Arizona bridge collapse. This full-size girder also allowed the application of the analyses developed for the simple rectangular beams to be verified for a large section with top and bottom flanges and with torsional restraint only provided by the torsional resistance of the couple created by the bearing pad and bottom flange of the girder rather than by a method which modeled a theoretical restraint condition. All previous lateral-torsional buckling research on prestressed concrete beams included within this research assumed perfect torsional restraint at the supports. Perfect torsional restraints were not provided in the girders that collapsed in Arizona and Pennsylvania; instead, the only torsional resistance was provided by the couple created between the bearing pad and the bottom flange. Photographs of the test setup are shown in Figures 7.1 to 7.3.

The design and construction of the BT-54 is presented in Chapter 2. The field thermal studies presented in Chapter 3 showed that the midspan sweep of the 100-ft (30.5 m) long girder was 1.94-in. (49.3 mm) at the top flange and 1.48-in. (37.6 mm) at the bottom flange. These sweeps increased by as much as 0.6-in. (15.2 mm) due to solar radiation; however, there was minimal additional rotation due to solar radiation. The PCI

Bridge Design Manual (2003) permits a total sweep tolerance of ⅛-in. (3.18 mm) per 10

ft. (3.05 m) length of beam, or 1.25-in. (31.8 mm) sweep for this 100-ft span girder.

Figure 7.1 – BT-54 test setup

Figure 7.2 – BT-54 data acquisition and initial leveling

Figure 7.3 – End view of BT-54 test setup

The specific objectives were to experimentally investigate the effects of the

bearing pad on the torsional restraint at the ends of the beam, to study the effect of initial

end rotation due to bearing seat tolerances on the stability, and to compare to the rollover

factor of safety as calculated by using the method from Mast (1993) with that found from

the test.

7.2 Discussion of Experiment Design

A nominal initial end rotation of 0.05 radians was used in the stability testing of

the BT-54 girder for several reasons. Initial imperfections, especially initial rotation,

proved to be a large contributing factor to destabilization of beams both with respect to

lateral-torsional buckling and rollover based on the method by Mast (1993). Therefore, it

was desired to study the effect of initial end rotation on the stability behavior. Although,

the initial rotation of 0.05 radians was large, it was still within the range of end rotations

measured after the collapse of the bridge girders in Arizona (Oesterle et al., 2007).

Experimental design economy was also a concern. The load application frame

that was used for the rectangular test specimens and was detailed in Chapter 2 had a

capacity of 170 kips (756 kN). The rollover prediction method by Mast (1993) predicted

instability at approximately 120 kips (543 kN), and, therefore, it was predicted that the

BT-54 girder would fail by rollover before the capacity of the load application frame was

exceeded, thereby eliminating the need of a higher capacity load application frame. The

simplified analysis predicted a lateral-torsional buckling load of 183 kips (814 kN);

however, the girder was anticipated to become unstable in a rollover mode. It was

hypothesized that for prestressed concrete bridge girders, the rollover limit state would

govern over the lateral-torsional buckling limit state because concrete cracking and inelastic behavior would be required for a bridge girder of a standard shape to become unstable. Prestressed concrete bridge girders are designed such that the concrete does not crack during the erection. Therefore, the focus of the BT-54 girder experiment was on the rollover behavior.

7.3 Bottom Flange Bearing Flatness

The BT-54 was loaded twice. The first experiment loaded the girder to 29 kips (129 kN), an applied moment of 8,700 in-kips. During the loading, the torsional rotation of the girder at the supports was substantially larger than was expected – 0.0042 radians as compared to 0.00072 radians. Further loading was suspended, and the load was removed to investigate the cause of the unexpected rotation. The cause was deemed to be the lack of flatness of the bottom of the cross-section which was bearing on the elastomeric bearing pad. The profile of the roundness of the bottom flange was measured and is shown in Figure 7.4.

Tilt

1/8 in.   5/16 in.

17 in.
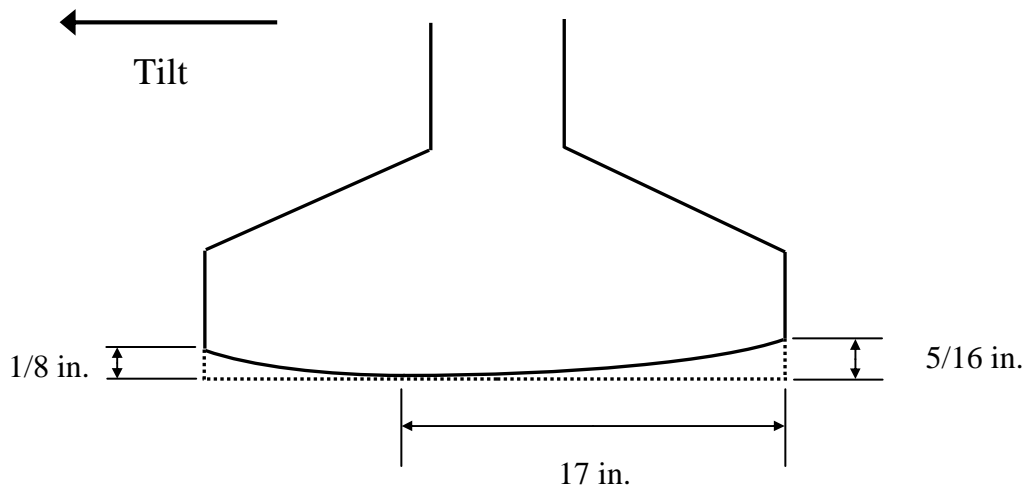
(a) West end support looking east

Tilt

1/8 in.   1/8 in.

12 in.
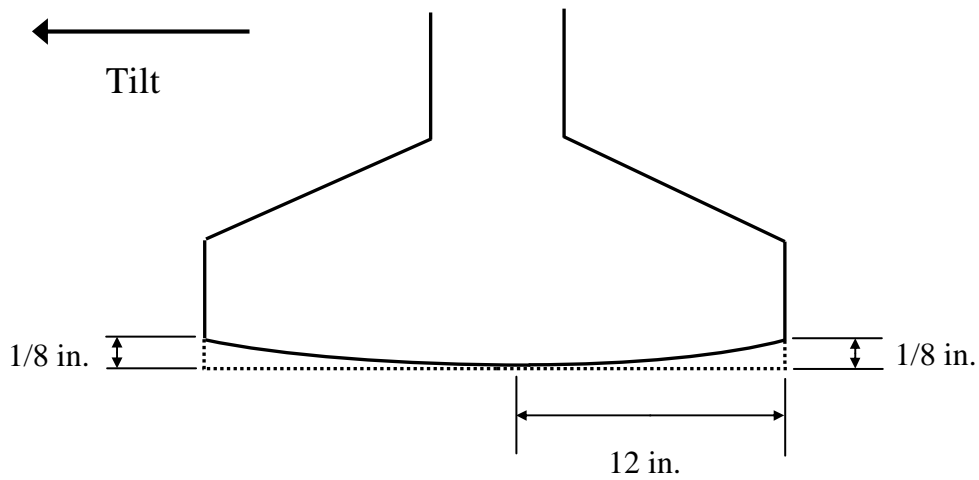
(b) East end support looking east

Figure 7.4 – Bottom flange profile for (a) west end support (b) east end support

The rotation resulting from the bottom roundness resulted in approximately

0.0042 radians of rotation at the 29-kip load as shown in Figure 7.5. This rotation was far

greater what was planned or desired for comparison with analysis. Also, both the

nonlinear, fiber-model nonlinear analysis and the rollover analysis based on Mast (1993) did not consider the effect of roundness of the bottom flange. It was desired to only study the effect of the rotational stiffness provided by the bearing pad. Furthermore, the rollover analysis method by Mast (1993) involved an input for the rotational stiffness of the bearing pad. There was no adequate method to determine the effective rotational stiffness of a bearing pad without the assumption of uniform bearing. Future studies are required to determine the typical magnitudes of the bottom flange roundness, and tolerances need to be established to reduce the risk of rollover failure from such an imperfection. The use of embedded steel plates at bearing locations would provide an easy solution to ensuring a flat bearing surface on the bottom flange of the girder.

To provide a flat bearing surface on the bottom flange of the BT-54, a retrofit was performed to the bottom flange at each of the supports so that there was uniform bearing on the pad. Also, due to the camber of the girder, it was observed during the first experiment that the beam was not bearing uniformly along the length of the pad as shown in Figure 7.6. The retrofit strategy to level the bearing pad also removed the non-uniform bearing condition in the longitudinal direction as well. The details of the retrofit construction are provided in Chapter 4.
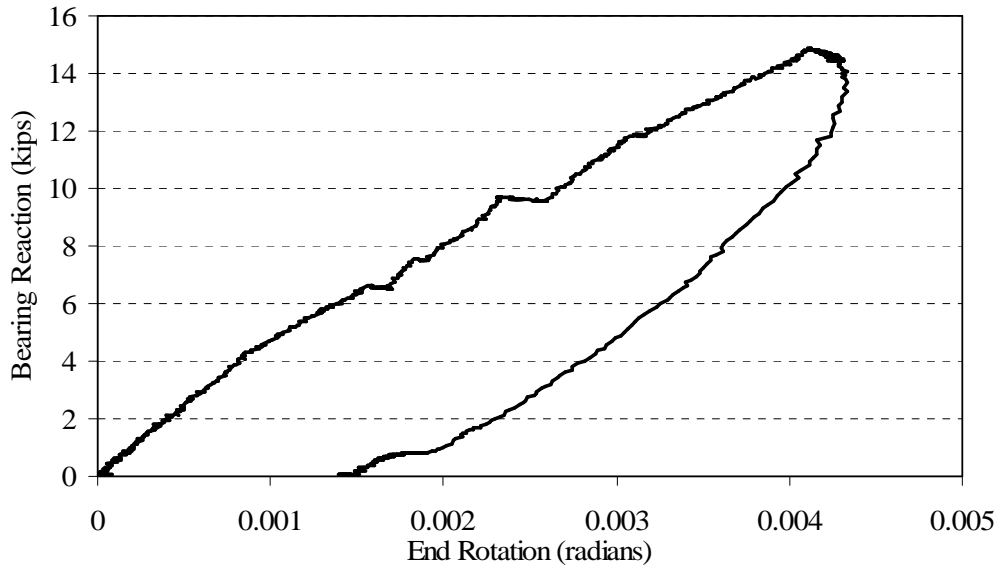
Figure 7.5 – Bearing pad reaction vs. end rotation for BT-54, loading #1
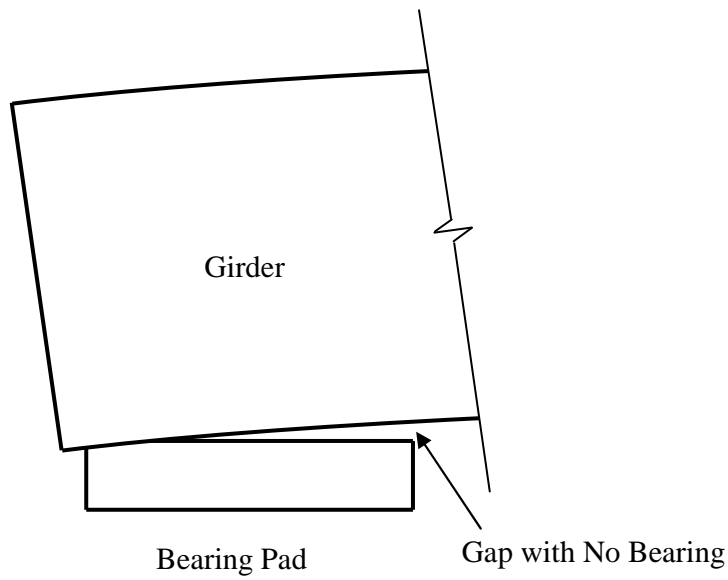
Figure 7.6 – Non-uniform bearing due to camber

The effectiveness of the retrofit with respect to the gap caused by the camber of the girder is shown in Figure 7.7 by comparing the east support before, and after the retrofit.

(a) East End Support before Retrofit   (b) East End Support after Retrofit

Figure 7.7 – Retrofit effectiveness on non-uniform bearing due to camber

The effectiveness of the retrofit strategy with respect to the flatness of the bottom flange was best observed by a comparison of the amount of rotation when placing the girder. Initially when the girder was being placed on the initially rotated supports, the girder rotated at the end supports a significant amount. After the retrofit was completed and the girder was replaced on its supports, there was almost no rotation which was the originally predicted behavior. Table 7.1 shows the comparison between the initial end rotations under only the self-weight of the girder for the before and after retrofit cases.

The bearing pad rotation was measured at three locations along the length of the bearing. These rotations would ideally be the same; however, there were small differences (less than 1%) which were believed due to the bearing pads and the underlying support system. Figure 7.8 shows the rotation measurement locations.

Table 7.1 – Comparison of end support initial rotations for BT-54

	Bearing Pad Rotations (radians)			Before Retrofit	After Retrofit
				Bottom Flange 1' from Support	Bottom Flange 1' from Support
	Front	Middle	Back		
East Support	0.04817	0.04887	0.04887	0.07016	0.04939
West Support	0.05131	0.05131	0.05079	0.06301	0.05079
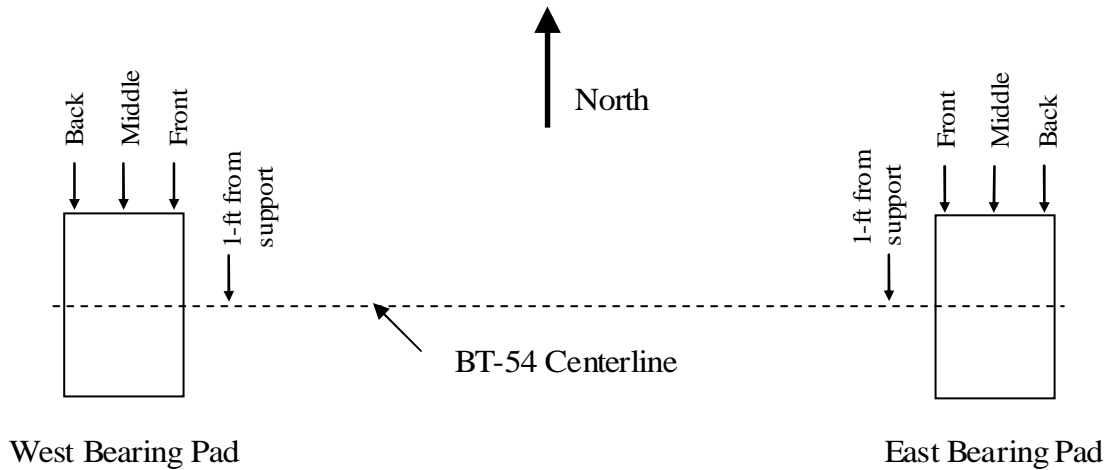
Figure 7.8 – Rotation measurement locations

From Table 7.1, it was apparent that significant rotations occurred simply under the self-weight of the girder due to the lack of flatness of the bottom flange. After the retrofit was performed, under the self-weight of the girder only, the end rotation was essentially equivalent to the initial rotation of the bearing before the girder was placed.

7.4 Experimental Results

7.4.1 BT-54 Rollover Behavior, Loading #1

Prior to the retrofit, the girder was first loaded to 29 kips (129 kN) when large end rotations were noted. The load was then released. The load versus lateral displacement plot is shown in Figure 7.9, and the load versus rotation plot is shown in Figure 7.10. The end rotation for all plots was the rotation at the east end of the girder. Both sides behaved similarly; however, one of the vertical string potentiometers on the west end of the girder displayed significant "noise" in the measurements. Therefore, the discussion is mainly focused on the end rotation at the east end of the girder.
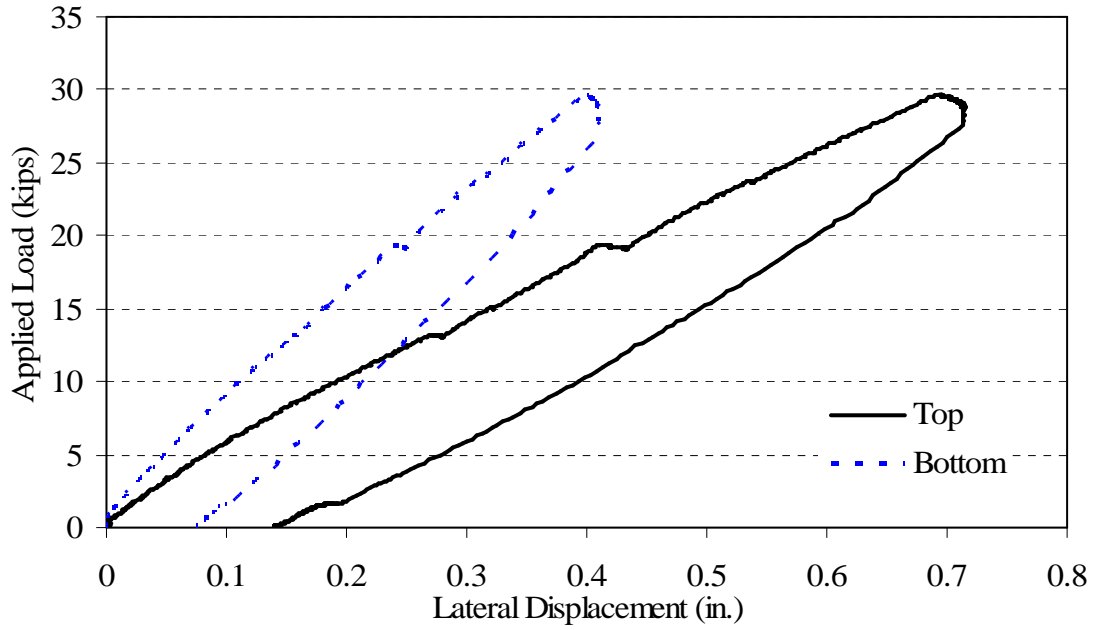
Figure 7.9 – Load vs. lateral displacement at midspan for BT-54, loading #1, before retrofit
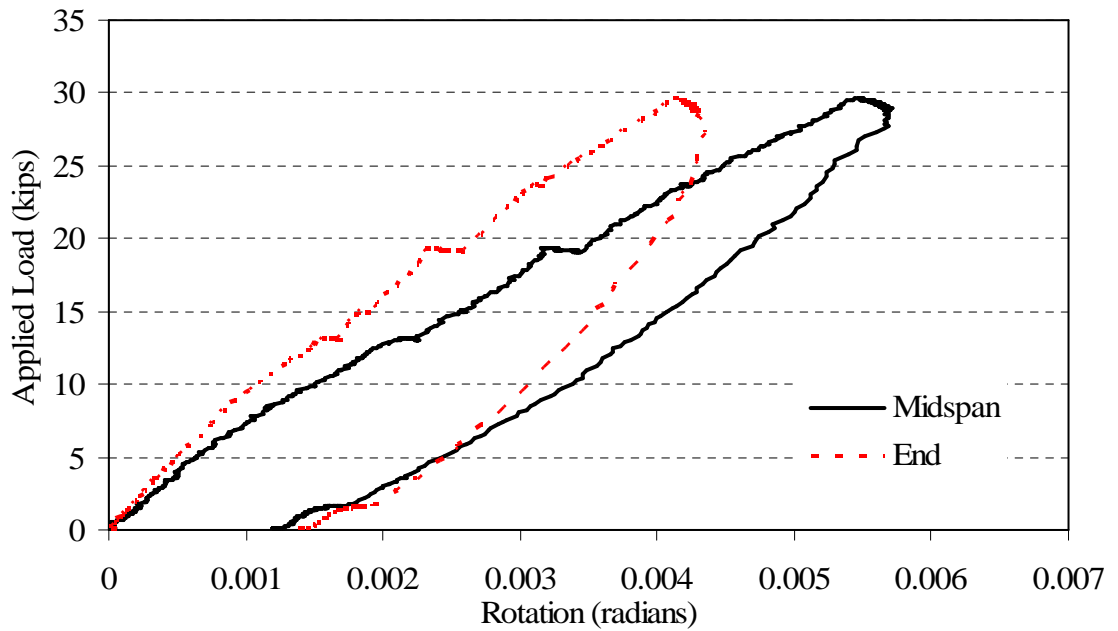
Figure 7.10 – Load versus rotation for BT-54, loading #1, before retrofit

Figure 7.9 shows that the lateral displacements at the top and the bottom of the beam were significant, 0.29-in. (7.4 mm) at 29 kips. The behavior showed the predominance of rotation. In the rectangular beam tests, the lateral displacements at the top and the bottom of the beams were very similar until buckling was about to occur. The cause of the significant difference between the top and bottom displacements of the girder was the large torsional rotation behavior at the end supports. Figure 7.10 shows the midspan rotation as well at the end rotation, and it was noticeable that the majority of the midspan rotation was actually due to the end rotation. Furthermore, the rotation at each end was significantly higher than the estimated end rotation before the experiment. The fact that the bottom flange was rounded at the supports reduced the effective rotation stiffness so much that behavior was similar to an out-of-plane roller than a torsionally fixed condition. Figure 7.10 also shows that there was a significant residual rotation; however, the residual rotation at each end and at midspan were almost equivalent; therefore, the majority of the residual rotation occurred due to the "rolling" at the ends.

The shear stiffness of the bearing pad was also a factor in the behavior of the girder. Due to the large additional initial torsional rotation (rolling) when the girder was placed with only the self-weight on the bearing pad and the rapid increase in end rotation during loading, a larger transverse shear load was applied to the bearing pad than was anticipated. It was anticipated that only the initial slope of the bearing and its effect on the gravity load would cause transverse shear. Figure 7.11 shows the applied load versus shear displacement of the bearing pad, and Figure 7.12 shows the shear force in the bearing pad versus shear displacement of the bearing pad. Figure 7.13 shows the load versus lateral displacement of the centroid of the cross-section at midspan with the

bearing pad shear displacement included, without the bearing pad shear displacement included, and without both the bearing pad shear displacement and effective centroid displacement due to the large rotations at the ends. The shear displacement was determined by the experimental data from the two vertical string potentiometers and the horizontal string potentiometers at each end of the beam. The two vertical string potentiometers were used to determine the end rotation of the girder. The end rotation was used to determine the lateral displacement due to end rotation at the top of the girder where the lateral string potentiometer measured displacements. It was calculated by multiplying the end rotation calculated using the vertical string potentiometer by the vertical distance between the lateral string potentiometer and the center of bearing. The shear displacement was then determined as the measured lateral displacement minus the lateral displacement due to rotation. Furthermore, the end rotation was used to calculate the effective centroid lateral displacement due to end rotation because the lateral displacement presented in Figure 7.13 was at the centroid of the cross-section at midspan.
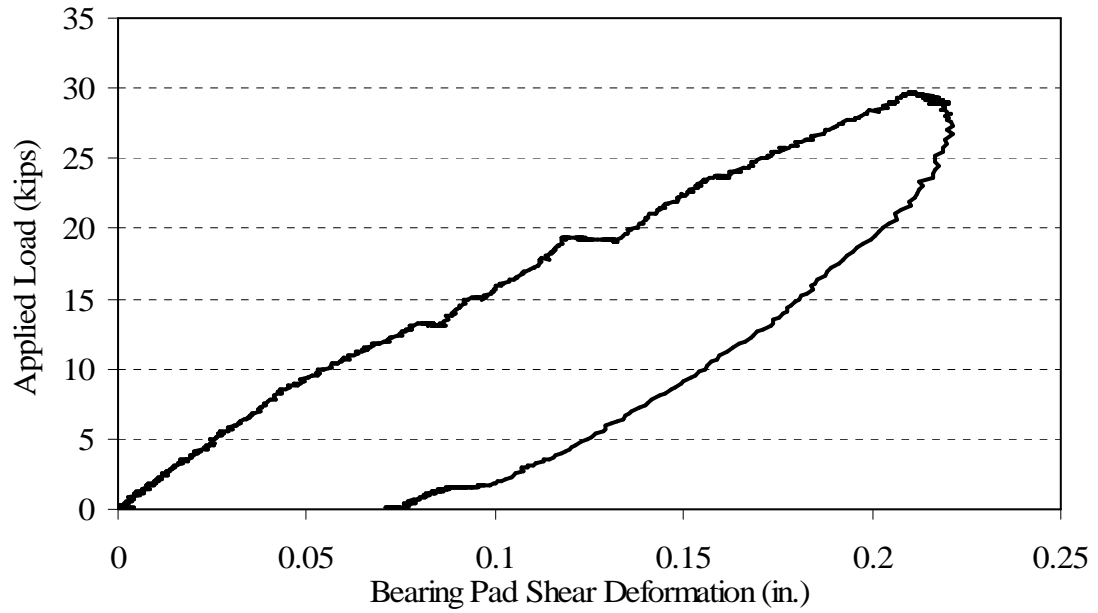
Figure 7.11 – Applied load vs. bearing pad shear deformation, loading #1
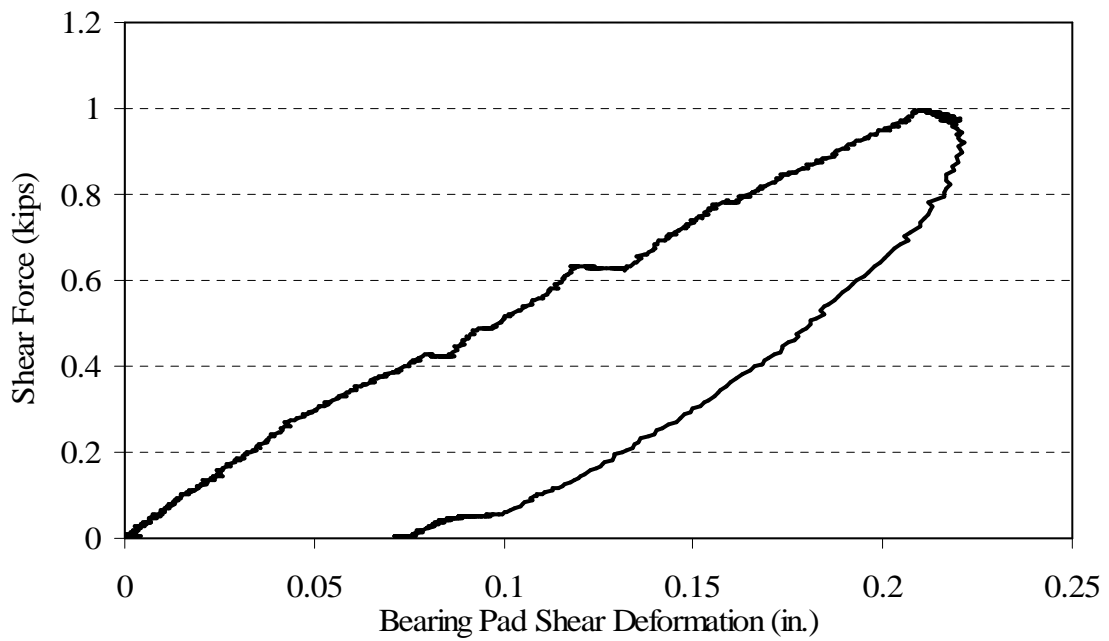
Figure 7.12 – Calculated bearing pad shear force vs. measured shear deformation, loading #1
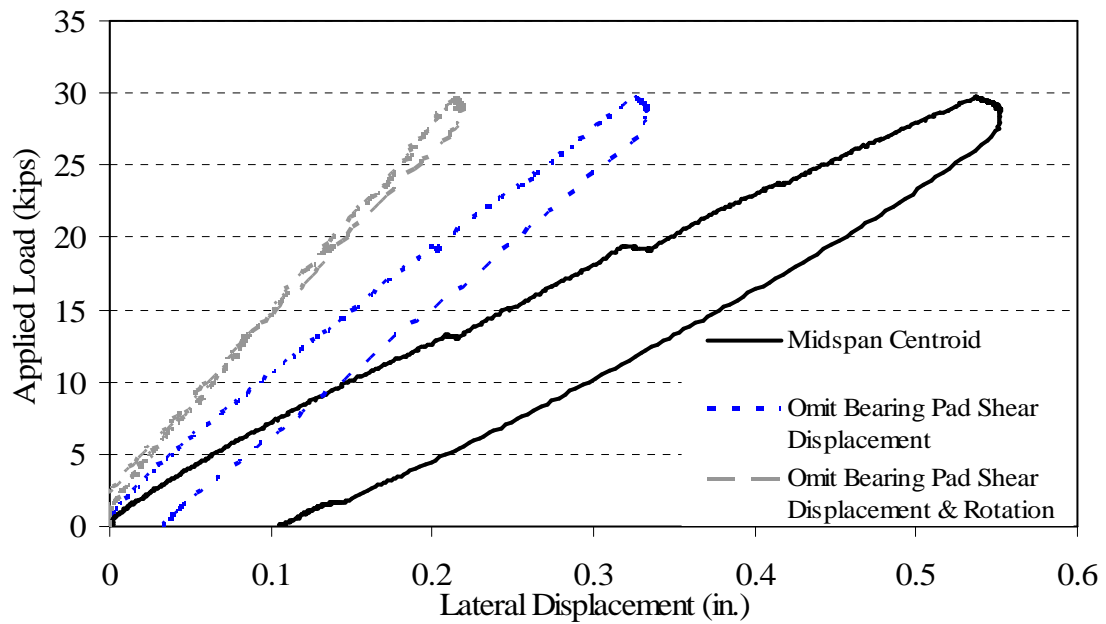
Figure 7.13 – Midspan lateral displacement including & excluding bearing pad effects, loading #1

Figure 7.11 shows that there was a significant amount of shear deformation in the bearing pad during loading; furthermore, residual shear deformations in the bearing pad occurred. A significant amount of the residual shear deformation in the bearing pad was not due to plastic deformation of the bearing pad, but instead, the fact that there was residual rotation of the girder at the ends due to the girder "rolling" on the rounded bottom flange. The residual end rotation caused an additional shear component of load on the bearing pad that was not there at the beginning of loading. From Figure 7.12, the shear deformation stiffness of the bearing pad was 4.7 kip/in (820 kN/m). Figure 7.13 shows that 0.32-in. (8.2 mm) of the 0.54-in. (13.7 mm) lateral displacement of the centroid at midspan was due to the rigid body rotation and lateral displacement caused by the behavior of the bearing pads. Although the curve with the bearing pad effects

included shows a residual lateral displacement of 0.1-in (2.5 mm), there was actually an insignificant amount of residual lateral displacement in the girder which was evident from the curve in Figure 7.13 which omitted all of the bearing pad effects on the measured lateral displacement values. The curve omitting the bearing pad effects showed an almost perfect elastic return of the girder to its initial conditions.

7.4.2 BT-54 Rollover Behavior, Loading #2

After the bottom of the girder was leveled as discussed in Chapter 4, the girder was re-loaded. At about 100 kips (445 kN), the girder was allowed to contact the torsional restraints at the ends of the girder because the lateral displacements were becoming large (0.6-in.) and the end rotation was such that the girder was no longer in complete contact with the bearing pad (0.0055 radians). Safety became a concern, and the load was reduced to approximately 70 kips (311 kN).

With safety conditions assured, load was increased. The slope of the load versus lateral displacement and the load versus rotation curves, shown in Figure 7.14 and 7.15, respectively, were very similar to the initial loading when at the 70-to-100 kip (311-to-445 kN) load level. However, the curve was offset compared to the initial curve due to the residual deformation and residual rotation behavior that was observed from the partial unloading. Once the load achieved 104 kips (463 kN), the lateral displacement and rotation began to increase more rapidly such that there was once again a safety concern. Figures 7.14 and 7.15 also highlight the behavior discussed.
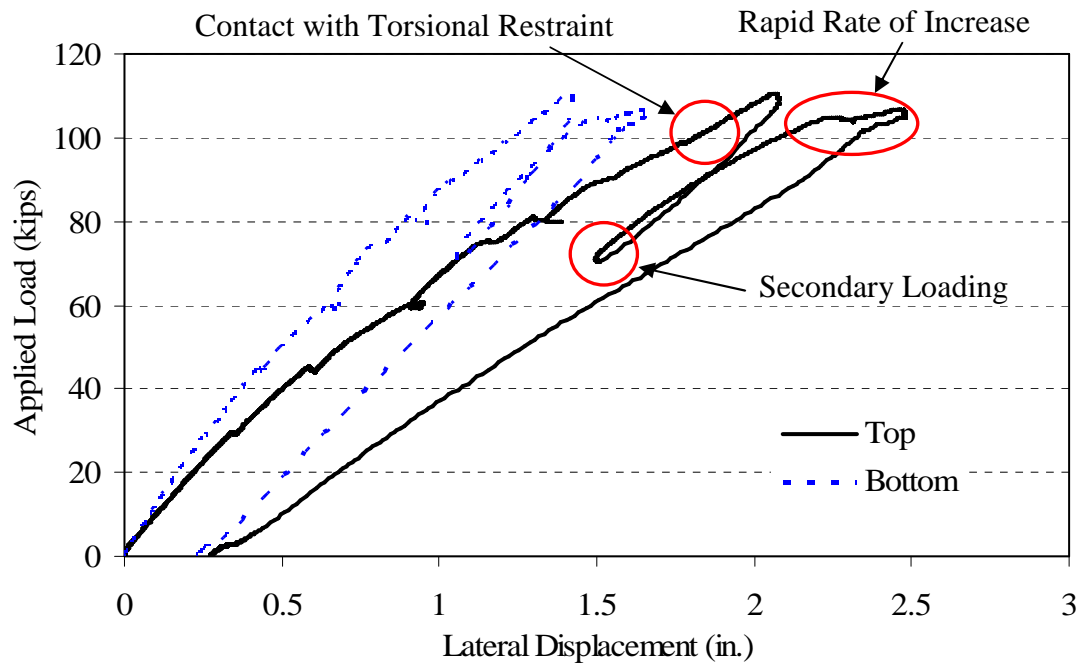
Figure 7.14 – Load vs. lateral displacement for BT-54, loading #2
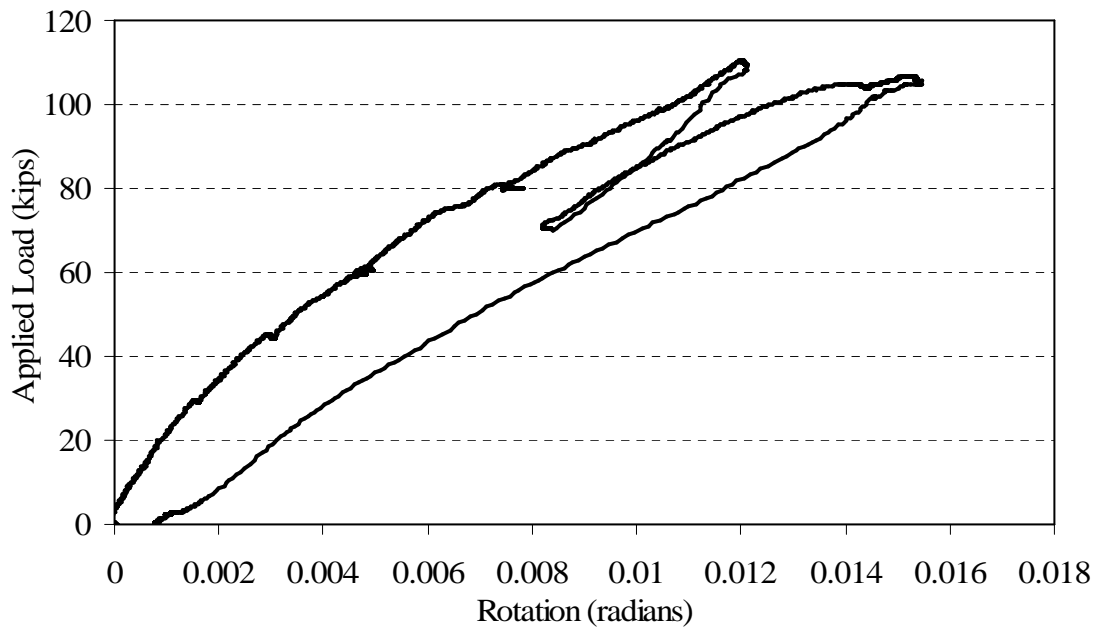
Figure 7.15 – Load vs. rotation for BT-54, loading #2

The bearing pad effect on the BT-54 during the second loading is shown in

Figures 7.16 through 7.18.
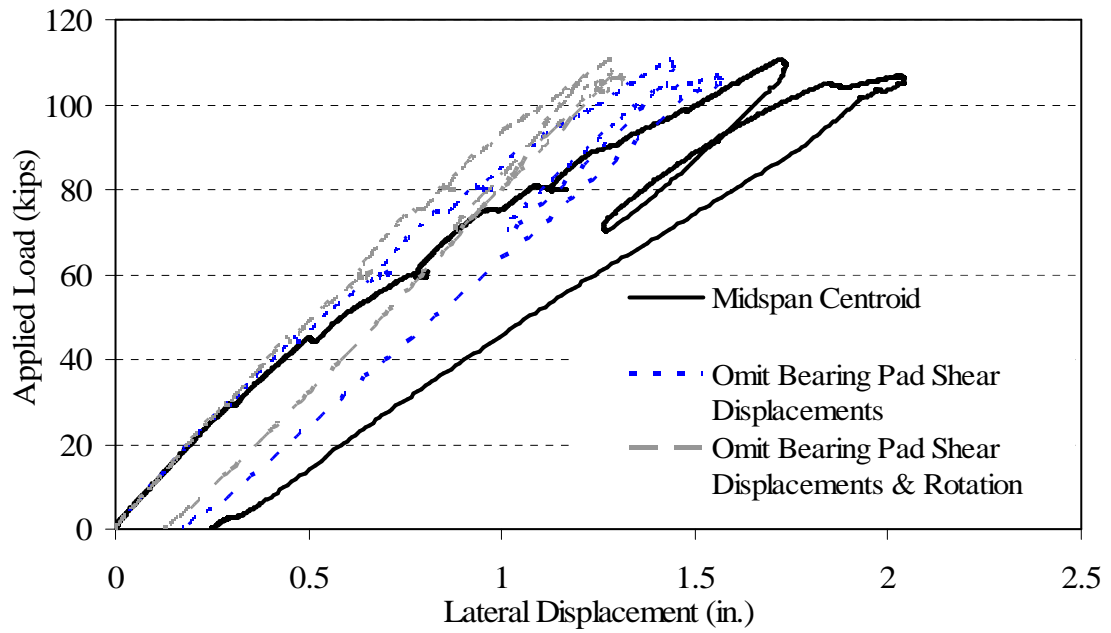
Figure 7.16 - Midspan lateral displacement including & excluding bearing pad effects, loading #2
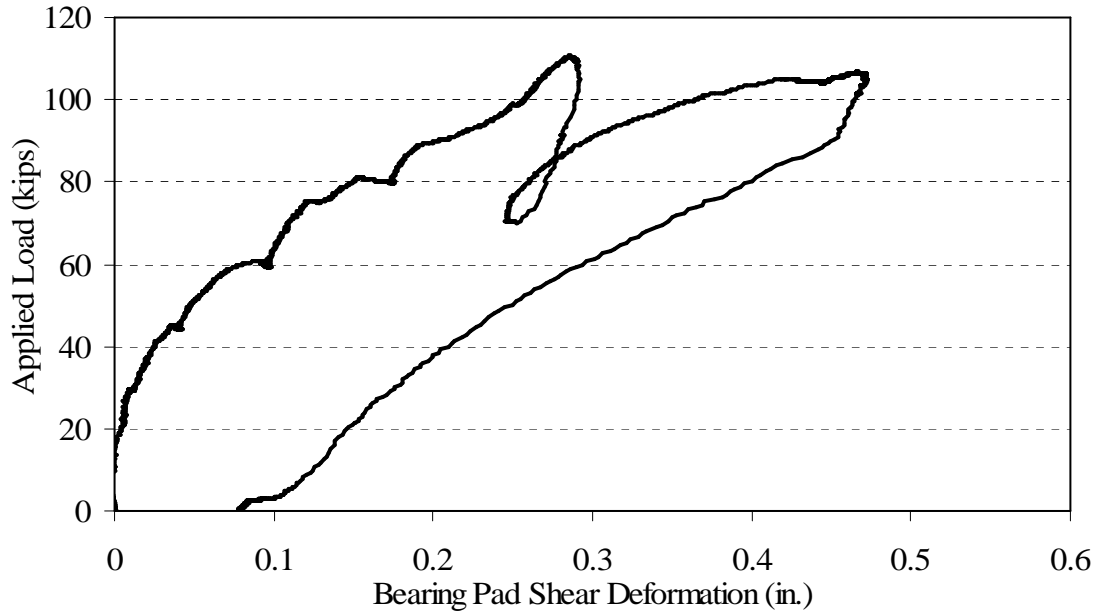
Figure 7.17 – Bearing pad shear deformation, loading #2
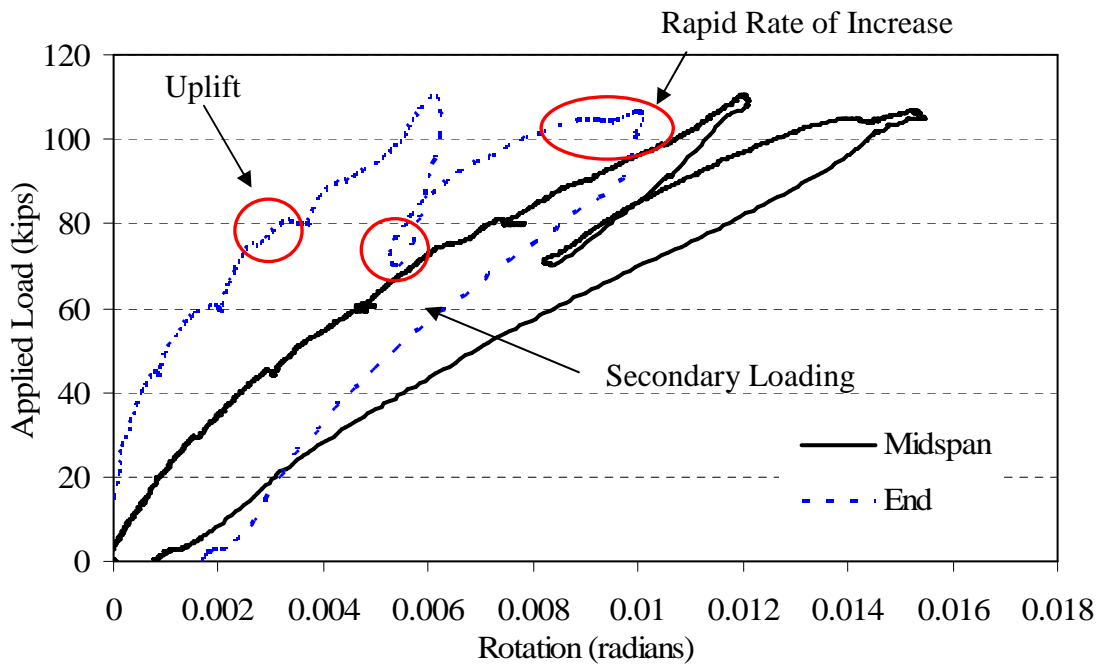
Figure 7.18 - Load versus rotation and end rotation for BT-54, loading #2

Figure 7.16 shows that during the second loading, the shear deformation of the bearing pad and the effect which the end rotation had on the midspan lateral displacement were much less compared to those during the first loading. Figure 7.17 shows the bearing pad shear deformation with respect to the applied load on the girder. For the initial ascent of the load versus bearing pad shear deformation, the bearing pad deformed only 20% more than in the first loading even though it was loaded to a 270% higher load. The leveling retrofit did not necessarily have a direct effect on the stiffness with respect to shear deformation, but instead, the moment resistance provided by the bearing pad with leveled bottom flange allowed for much smaller rotations at the end during the second loading.

Figure 7.18 shows that there was still a non-negligible amount of end rotation at the supports due to the bearing pad even with the retrofit. For the first 20 kips (89 kN) of loading, there was essentially a negligible amount of end rotation, but from that load on, the bearing pad did not provide the torsional moment stiffness that was expected. Although the end torsional stiffness was not as high as was predicted by the ideal conditions, the leveling retrofit strategy was much better at providing partial torsional restraint at the end supports than the case of the first load with the rounded bottom flanges as is evident from Figure 7.19.
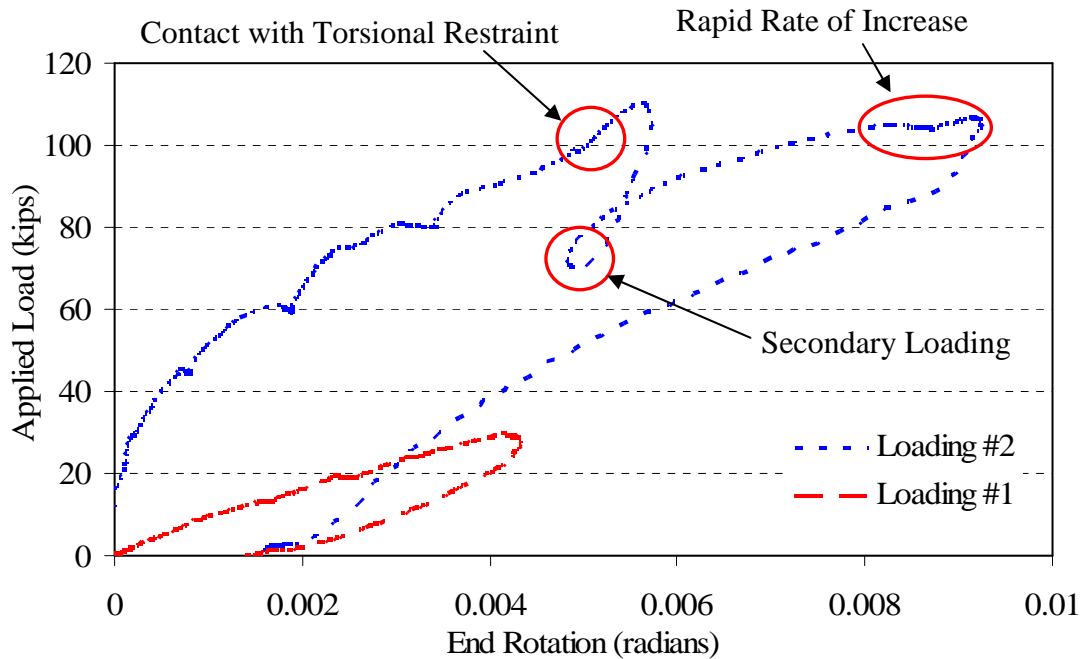
Figure 7.19 – Comparison of end rotations for loadings #1 and #2

From Figure 7.19, the end rotation achieved at 29 kips (129 kN) during the first experiment was equivalent to the end rotation during the second loading at 94 kips (418 kN). Furthermore, Figure 7.19 illustrates the rigid body unstable nature witnessed during the second experiment during the reloading from 70 to 104 kips (311 to 463 kN). Beginning at an end rotation of 0.0078 radians, additional load application brought the end rotation to 0.0092 radians with an increase in load of only 0.6 kips (2.7 kN). Therefore, it was suspected during testing that the lack of torsional restraint at the ends caused the limit state of the girder to be that of a rollover phenomenon.

7.4.2.1 BT-54 Strains and Cross-Section Results, Loading #2

The strain behavior of the girder was captured via the LVDT layout discussed in

Chapter 4. The initial strain values due to the effect of prestressing were extremely

important for understanding the behavior of the BT-54 girder. For the rectangular beams,

the relatively small magnitude of prestressing force only contributed a minimal amount to

the strain profiles recorded during loading; therefore, an approximation of the actual

prestressing force after prestressed losses was sufficiently accurate. For the BT-54, the

strain profile was affected by the prestressing force significantly. The effective

prestressing force during the experiment was determined by utilizing the internal

vibrating wire strain gages. There were known values for the initial strains before the

prestressing strands were released during the fabrication of the girder. Therefore, the

measured strain values of the vibrating wire strain gages immediately before the

experiment were used to determine prestress losses due to creep and shrinkage.

Relaxation losses were calculated based on Nawy (2006) for low relaxation strands. The

effective prestressing force at the time of testing was found as the initial stress minus the

losses due to creep, shrinkage and relaxation. The effective prestressing stress in the

strands was determined to be 166.4 ksi (1131 MPa) and the total effective prestressing

force was 1444 kips (6425 kN). The effect of the prestressing force and self-weight on

the strain profile at 35 kips (156 kN) is shown in Figure 7.20. In Figure 7.20, the solid

black line is just the flexural strains due to the 35 kip load determined at midspan and at

the center of the cross section (y-axis). The dashed blue line combines these flexural

strains with the axial and flexural strains due to the effective prestressing force plus self

weight of the beam.

304

The total strain profile at mid-thickness for three different load increments, 35 kips (156 kN), 70 kips (311 kN) and 104 kips (463 kN), is shown in Figure 7.21.
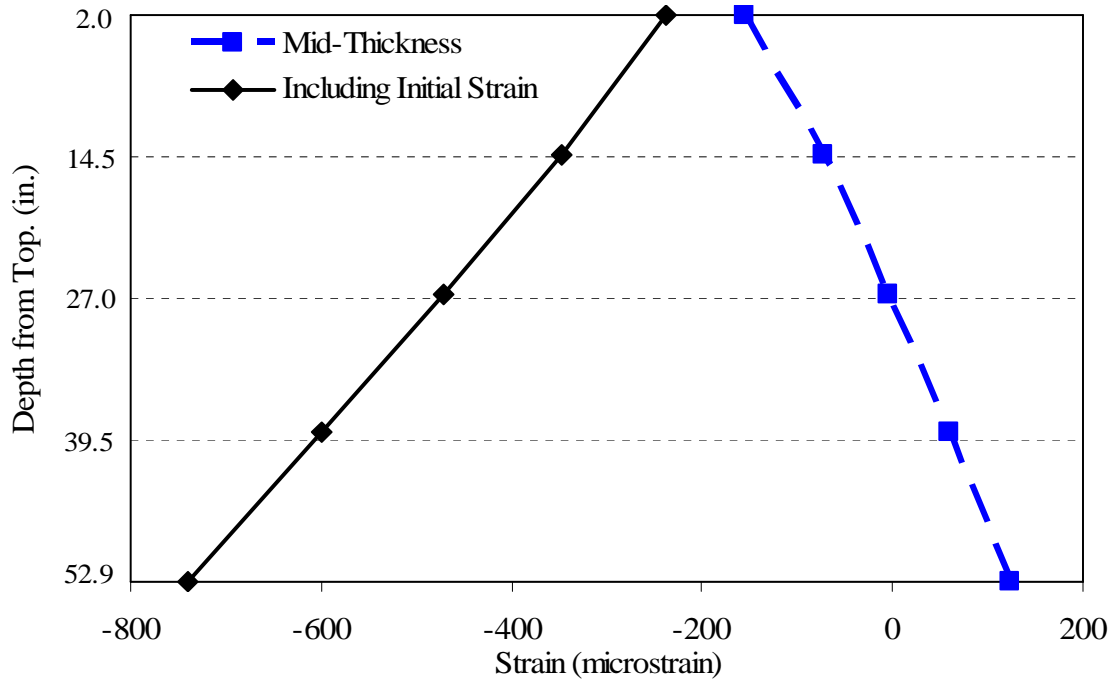
Figure 7.20 – Effect of prestressing force & self-weight on strain profile at mid-thickness at 35 kip (156 kN)
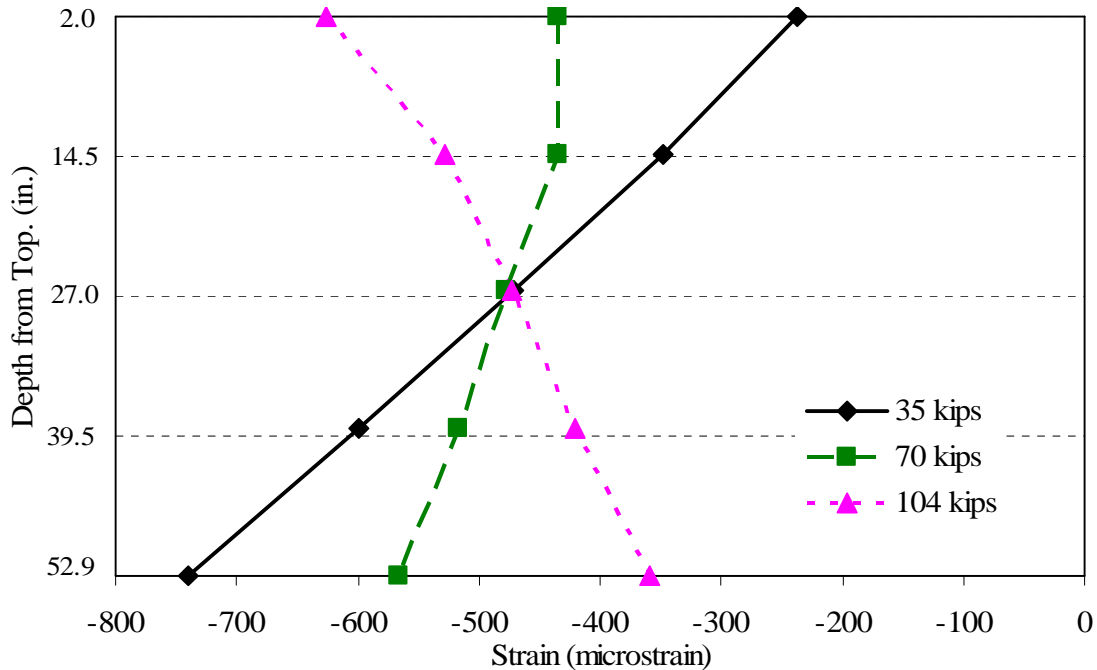
Figure 7.21 – Strain profiles at mid-thickness for load increments of 35 kips (156 kN), 70 kips (311 kN) and 104 kips (463 kN)

Figure 7.20 shows that it was necessary include the effects of initial prestressing force and self-weight on the strain profile because there was a significant strain contribution due to the prestressing force and self-weight. The strain profiles in Figure 7.21 show good correlation with a linear strain distribution with the exception of a slight deviation from linearity at the top of the girder at 104 kips (463 kN). The strain profile at 104 kips (463 kN) was approaching the maximum load applied of 110 kips (489 kN), and, although the strain profile showed that the condition of less compressive strain at the bottom of the girder than at the top of the girder had been attained, the bottom of the girder was not close to reaching tensile strain levels. However, the strains on the concrete surface were significantly different than at mid-thickness due to out-of-plane

306

bending. Figures 7.22 through 7.24 show the surface strain profiles for 35 kips (156 kN), 70 kips (311 kN) and 104 kips (463 kN), respectively. Note that the strain profiles were not and should not be linear on the surface of the girder because the girder was not a constant width, as was the case for the rectangular beams.
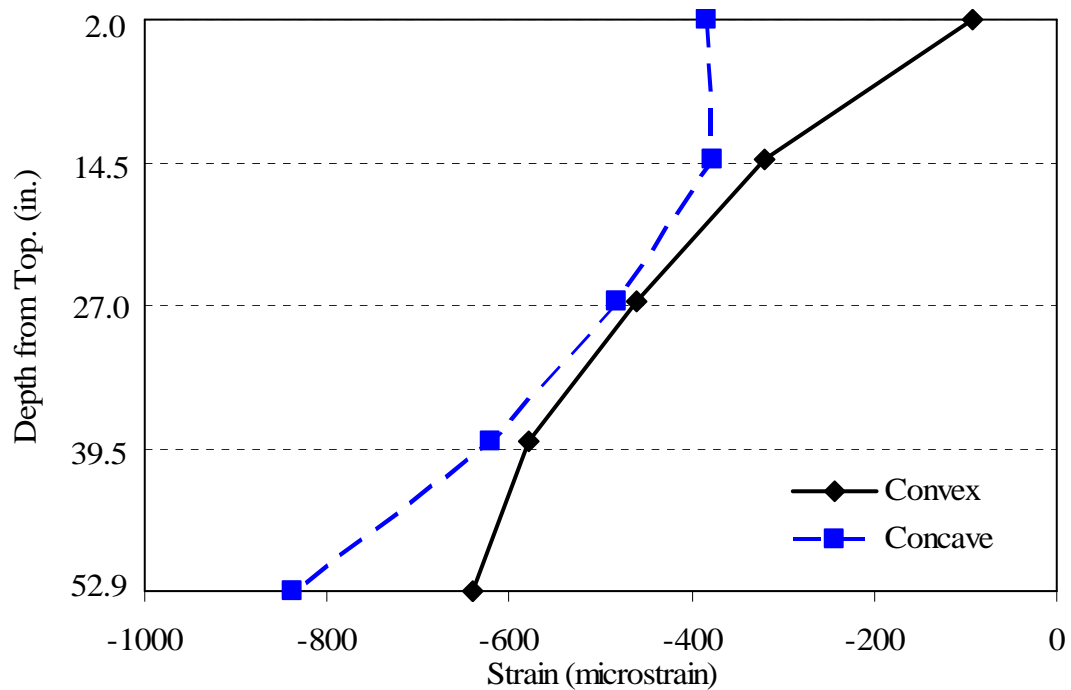
Figure 7.22 – Surface strain profiles for BT-54 at 35 kips (156 kN)
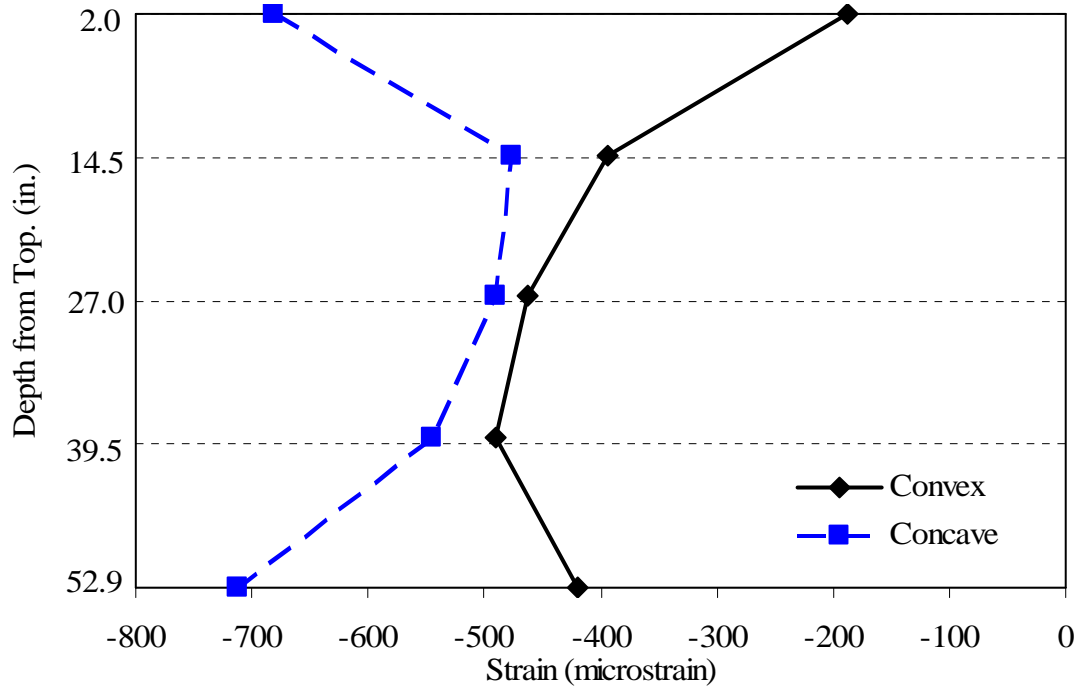
Figure 7.23 – Surface strain profiles for BT-54 at 70 kips (311 kN)
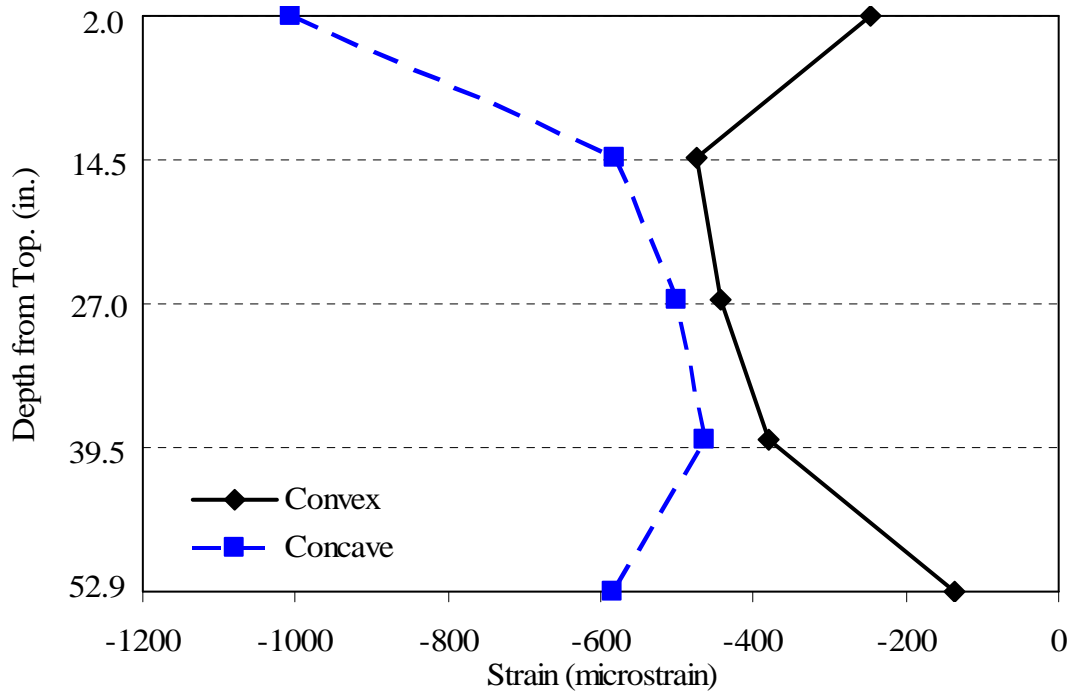
Figure 7.24 – Surface strain profiles for BT-54 at 104 kips (463 kN)

308

Figures 7.22 through 7.24 show the significant differences in the strains at the surface of the girder as opposed to mid-thickness due to the biaxial flexure. The surface strains on the top and bottom flange were particularly different from the mid-thickness strain values due to the large distance from center to the concrete surface. The strain on the concrete surface on the convex side of the bottom flange of the girder had much less compressive strain than at mid-thickness; even at a load level of 104 kips (463 kN), the surface strains were in compression and not tension. Therefore, the data show that cracking did not occur during the first load ascent of the second loading, which was consistent with the load versus lateral-displacement behavior. The girder reached levels of unstable rollover behavior due to excessive rotations at the supports; however, the uncoupled load versus lateral displacement plot only included lateral displacement due to the deformation of the girder and showed no significant softening or stiffness reduction. Larger displacements and rotations occurred during the second load ascent, but once again, the unstable behavior was representative of rollover instability and not softening or a stiffness reduction of the girder. Figure 7.25 shows the surface strain profile at 104 kips (463 kN) during the second load ascent. The surface strain profile shows that tensile strain values were not achieved during the second load ascent, either.
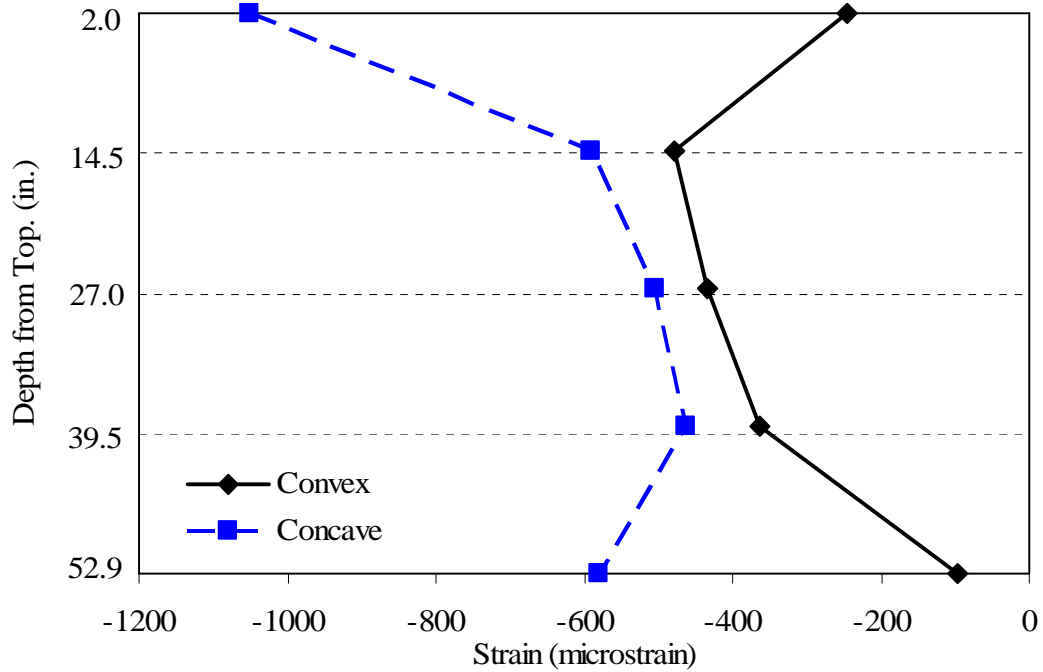
Figure 7.25 – Surface strain profiles for BT-54 at 104 kips (463 kN), 2nd load ascent

The effect of the initial strains due to the weak-axis component of the girder self-weight moment was non-negligible and had to be considered. The weak-axis component of the self-weight was calculated by multiplying the self-weight moment by the sine of the initial rotation angle. Then the stress was calculated at each strain measurement location using the weak-axis self-weight moment, the gross weak-axis moment of inertia and the distance from the weak-axis centroidal axis of the cross-section to the strain measurement location. The strains were then determined by dividing the calculated stresses by the initial concrete modulus of elasticity. The accuracy of the calculation was verified by calculating the strain from the weak-axis component of moment due to the applied load of 35 kips (156 kN) and comparing to the experimental values. The

calculated strain from the weak-axis component of moment at the top of the cross-section was 70 microstrains, and the experimental strain value was 78 microstrains. The values were 10% different and the error was due to the potential for error in the assumed weak-axis moment of inertia and the modulus of elasticity. Furthermore, an error of 0.1 degrees (0.00175 radians) would add an additional 2.5 microstrains to the calculated strain value. Figure 7.26 shows the surface strain profile at 35 kips (156 kN) showing the effect of the weak-axis component of the girder self-weight on the strain profile.
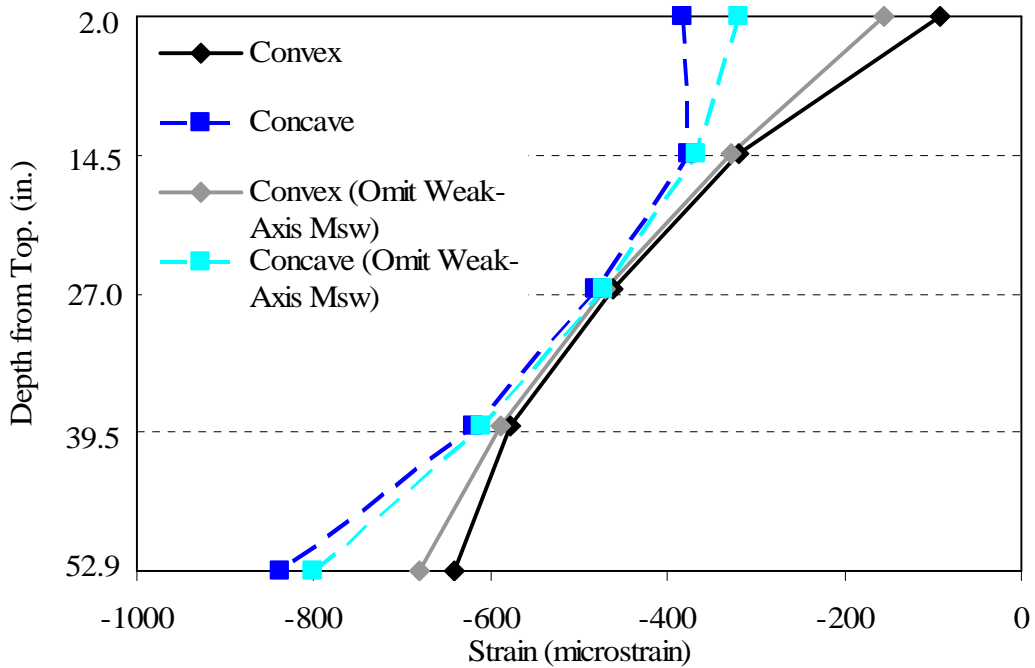
Figure 7.26 – Surface strain profiles at 35 kips (156 kN) omitting weak-axis self-weight moment

The differences in strain values in Figure 7.26 when the weak-axis component of the self-weight moment was neglected were minimal within the web of the girder.

Because of the large distances from mid-thickness to the surfaces of the flanges, the additional strains due to self-weight moment were significant and the additional strains should not be neglected.

Figure 7.22 showed that at 35 kips (156 kN), the strain on the surface of the top flange on the convex side of the girder had a relatively small compressive strain. The relatively small compressive strain at the top flange was consistent with Mast (1993) where it was stated that for certain initial imperfections and support conditions, the stiffness of the girder should be reduced when considering rollover because there was a possibility that the top flange could crack. Therefore, Figure 7.27 is presented to investigate the initial strain condition for this girder.
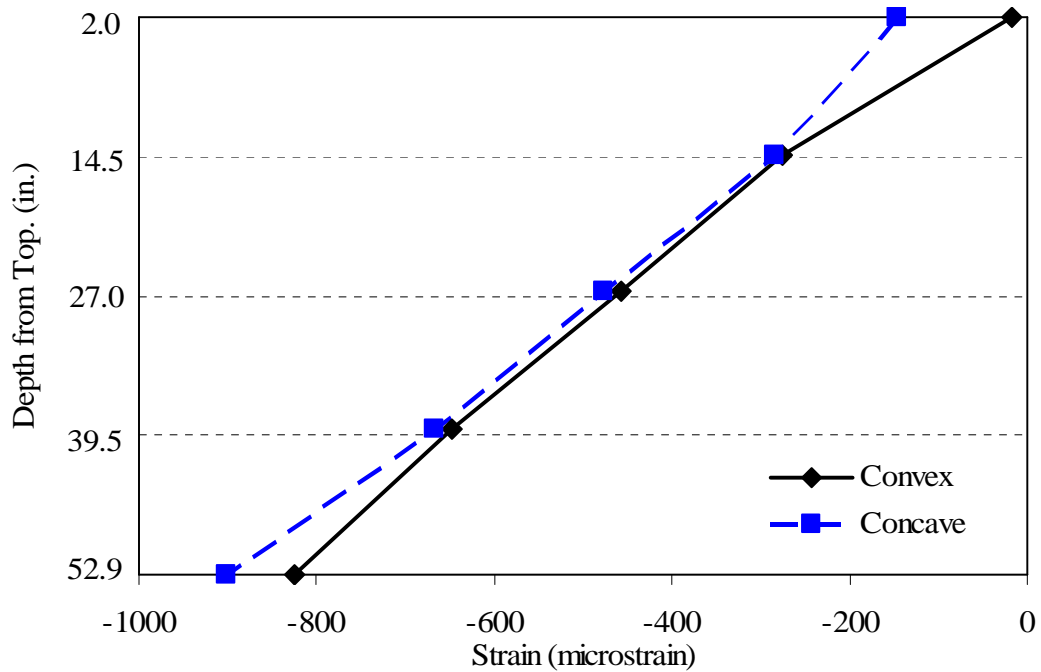
Figure 7.27 – Initial surface strain profile due to effective prestressing and self-weight

Figure 7.27 shows that tensile strains were not present in the top flange of the

girder initially; however, the compressive strain on the convex side due to the effects of

prestress and self weight was only 18 microstrains. Figure 7.27 shows that girders with a

longer span and similar initial imperfections could have initially cracked top flanges on

the convex side of the girder. Additional experimental data and photographs are

presented in Appendix E.

7.5 Analytical Investigation

The analytical study was performed using three different methods. The first

method was to perform the nonlinear analysis with the inclusion of a stiffness model that

represented the support rotational stiffness provided by the bearing pad. The second

method was to compare the simplified equation with the experimental results and the

nonlinear analysis results. Lastly, the rollover method from Mast (1993) was used to

predict the rollover load. The rollover load was important because of the rigid body

unstable behavior witnessed during the experiment.

7.5.1 Nonlinear Analysis

The nonlinear analysis was done for the BT-54 much the same way that it was

done for the rectangular beam experiments. The primary differences were with respect to

modeling the bearing pad behavior. The nonlinear analysis considering the effect of

imperfect torsional stiffness at the ends due to the compliance of the bearing pad was not

taken into consideration by applying a stiffness term within the global stiffness matrix,

[K]. Instead, perfect torsional restraint was assumed within the global stiffness matrix,

[K], at the beginning of a specific load increment. After the incremental displacement

vector, {u}, was calculated, the restraint was released by applying the increment of torque to the bearing pad model. The rigid body rotation and displacements were then determined from the bearing pad model and added to the total system deformation to determine the deformed geometry and loading condition for the following load increment. The methodology was accurate assuming small enough load increments were used.

7.5.1.1 Bearing Pad Model

The bearing pad model was implemented as a subroutine to the nonlinear analysis program. The subroutine received the amount of torque and axial load on the end supports for a given load increment of the nonlinear analysis. The bearing pad was divided into 48 0.5-in. (1.27 mm) strips along the width of the bearing pad as illustrated in Figure 7.28. The one-dimensional strip model was used as opposed to a two-dimensional fiber model because it was assumed that there was uniform bearing along the width of the bearing pad. A uniform bearing was not actually the case; however, an assumption had to be made because the exact bearing stress distribution was not known. The program iterated both the axial deformation on the side of the bearing pad that was more highly compressed and the end rotation of the girder to determine the axial deformation and end rotation required to satisfy both force equilibrium and moment equilibrium due to the torque applied to the bearing pad. The force in each strip of the bearing pad was determined by using a bilinear force versus displacement model for the bearing pad determined from axial stiffness experiments on the bearing pad described in Section 4.2.3. The pad's load versus axial displacement model is shown in Figure 7.29.

314
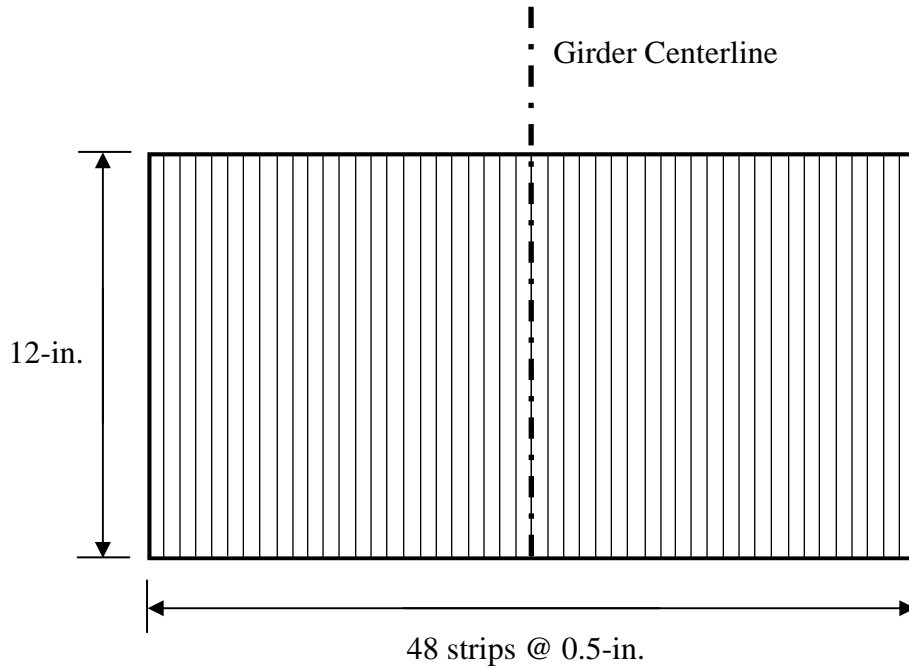
Figure 7.28 – Bearing pad strip model layout
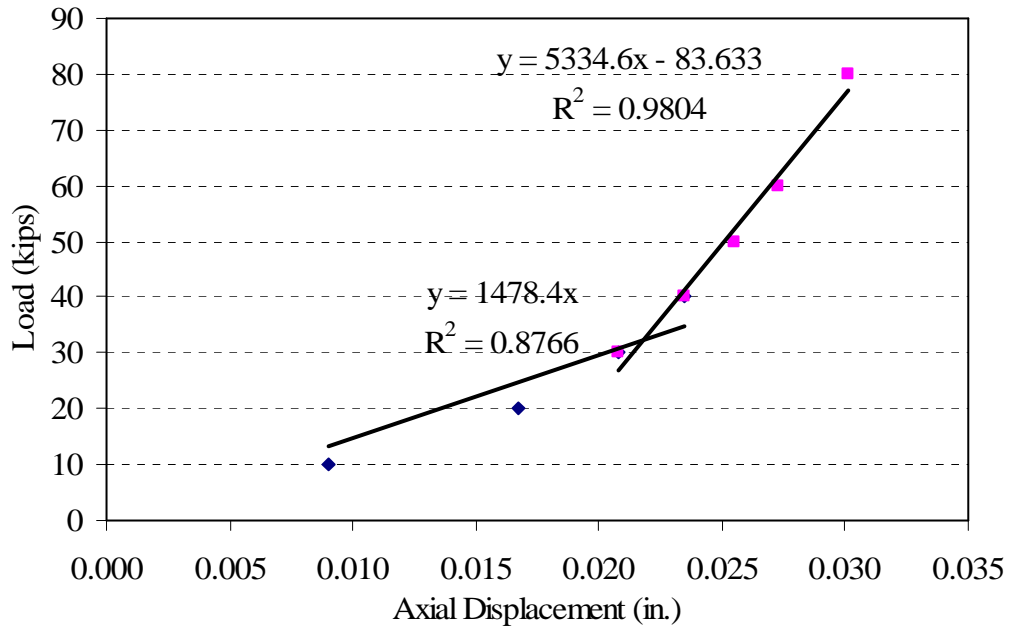
Figure 7.29 – Bearing pad bilinear axial (vertical) load vs. displacement model

Bearing pad strips that underwent tensile forces were taken as zero force elements when force and moment equilibrium were determined. The bearing pad model subroutine outputted the end rotation and the axial displacement of each edge of the bearing pad. The nonlinear analysis summed the end rotation and the rotation due to the deformation behavior of the girder for input into the subroutine that considered the concrete material model, the calculation of the neutral axis angle, and the section properties. With the exception of the effect which the bearing pad behavior had on the neutral axis angle, material properties and section properties, the deformation behavior of the girder was uncoupled from the rigid body rotation behavior due to the bearing pads. However, the rigid body rotation behavior was not uncoupled from the girder deformation behavior because the girder deformation behavior had a significant effect on the magnitude of torque applied to the bearing pads at the end supports.

7.5.1.2 Nonlinear Analysis Results

The comparison of the analytical and experimental data was split into two different cases. The first case was used to determine the accuracy of the analytical model for predicting the elastic response of the girder. With respect to the experimental data, the elastic response of the girder was determined by taking the rotation, θ, at midspan and subtracting the end rotation (rigid body rotation) of the girder as determined from the experimental data from the end string potentiometers. Similarly, the shear deformation of the bearing pads and the lateral displacement due to the rigid body rotation about the bottom of the girder to the centroid of the cross-section was subtracted from the experimental data at midspan to determine the elastic response of the girder. Although the altered data represented the elastic deformation response of the girder, the

316

experimentally applied load was still a function of the total deformation state including the rigid body deformation.

The analysis used the total deformation state including the rigid body deformation to calculate the incremental load vector, {P}; however, the stiffness matrix, [K], did not include the bearing pad stiffness properties. Instead, the stiffness matrix, [K], assumed perfect torsional restraint. After the load increment was applied, the elastic response of the girder was computed. Then, the bearing pad model was used to determine the shear deformation and rotation of the bearing pad for each load increment. Therefore, the next load increment was updated with the new displaced configuration including the rigid body deformation when determining the incremental load vector, {P}.

For the second case, the bearing pad deformation response was simply added to the elastic response of the girder to find the total response. The total response was directly compared with the "raw" data at midspan from the experiment.

The nonlinear analysis showed reasonably good correlation to the experimental results. The analytical data included the initial effect of the self-weight of the girder on the girder deformations and bearing pad deformations. Thus, at the point in the analytical data of zero applied load, the self-weight had already been applied. The initial vertical deformation of the bearing pad from the analytical model after the self-weight was applied was 0.01871-in. (0.475 mm) on the axially compressed side of the bearing pad and 0.016394-in. (0.416 mm) on the side of the bearing pad prone to uplift.

The experimental load versus lateral displacement data are shown both as post-processed raw data and with corrections to the lateral displacement data. The corrected

317

lateral displacement curves excluded the rigid body lateral displacement of the girder due to shear deformation of the bearing pads and the lateral displacement at the centroid of cross-section from the rigid body rotation of the girder due to the bearing pad compliance. By not including the lateral displacement at midspan due to the shear deformation of the bearing pad and the lateral displacement of the girder centroid from the end rotation, the displacement response due to the elastic girder deformation alone was confirmed. By removing the rigid body behavior and the girder deformation, while still maintaining accuracy, allowed for sources of error to be determined more easily. The experimental data for load versus lateral displacement compared to the results from the nonlinear analysis is shown in Figure 7.30. The self-weight of the girder was already applied in the analysis at the point of zero applied load in the following plots.
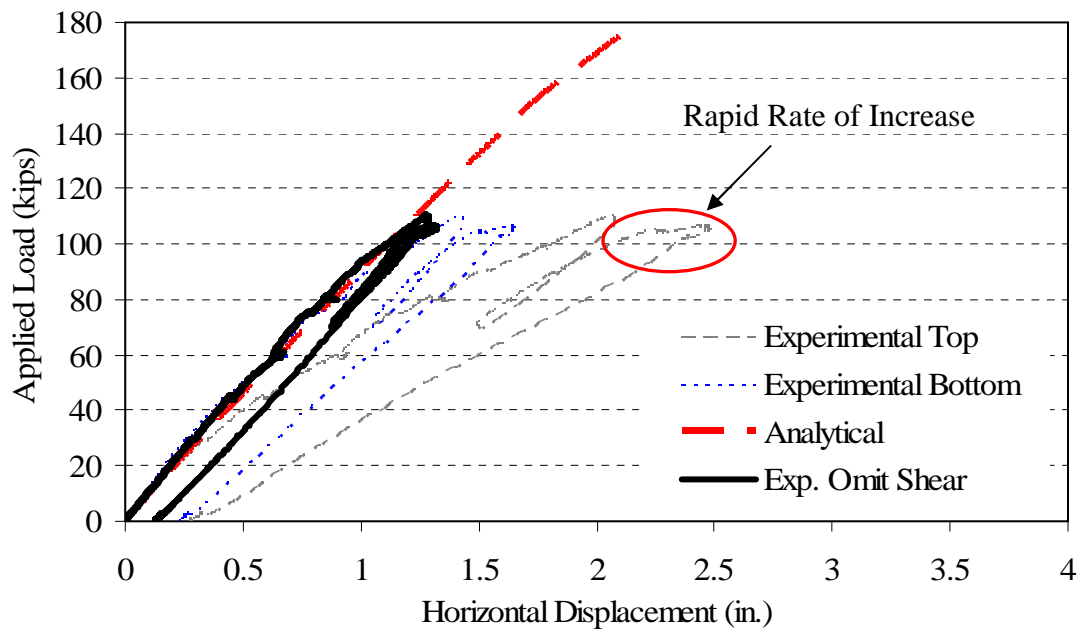
Figure 7.30 – Nonlinear analysis load vs. lateral displacement compared to the experimental results

318

The nonlinear analysis load versus displacement curve from Figure 7.30 matched very well with the experimental results representing the girder deformation behavior. A comparison between the nonlinear analysis load versus midspan rotation behavior and the experimental girder rotation is shown in Figure 7.31. Similar to the comparison between the load versus lateral displacement analytical and experimental curves, the experimental end rotation was subtracted from the experimental midspan rotation to compare the analytical girder rotation behavior at midspan to the experimental girder behavior, as opposed to the total girder rotation including the rigid body rotation from the compliance of the bearing pad. Such a correction was necessary to confirm the accuracy of the nonlinear analysis in predicting the elastic girder deformation response, thereby showing that the error of in the total behavior of the system was due to the model predicting the behavior of the bearing pad.
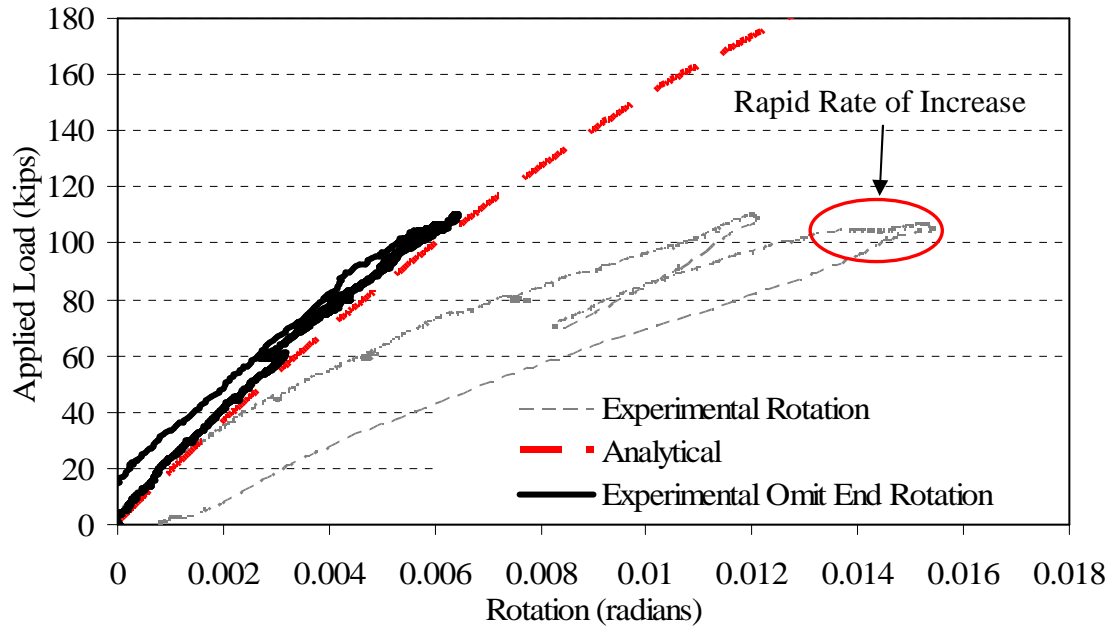
Figure 7.31 – Nonlinear analysis load vs. rotation compared to the experimental results

From Figure 7.31, the analytical load versus rotation curve matched very well with the experimental curve with the bearing pad rotation omitted. Furthermore, the rapid rate of increase in rotation shown by the experimental data for the entire system, as noted in Figure 7.31, was not apparent in the midspan rotation behavior omitting the rigid body rotation behavior. That shows that the system did not become unstable due to unstable girder deformation as in a lateral-torsional buckling failure mode, but instead as an unstable rigid body rotation or a rollover failure mode.

The analytical and experimental curves of Figure 7.31 coincided until the applied load reached approximately 60 kips (267 kN). The cause of the offset between the two curves at 60 kips (267 kN) was that a long pause in loading occurred at that load level and the bearing pads at the end supports crept. Once loading began again, the slope of

the experimental load versus rotation curve matched very well with the analytical curve. The creep behavior was shown by the load versus vertical displacement at the girder ends as shown in Figure 7.32. The vertical displacements of each side of the bearing pad are shown in Figure 7.32 and creep behavior is apparent at load levels of 60 kips (267 kN) and 80 kips (356 kN) which is consistent with long time periods where increased loading was suspended during the experiment. The creep behavior at 80 kips (356 kN) was less noticeable in Figure 7.31 because the magnitude of creep rotation was less than at 60 kips (267 kN) and because the unloading curve after the first load ascent and the unloading curve of the second load ascent intersect the creep response making the behavior less apparent.
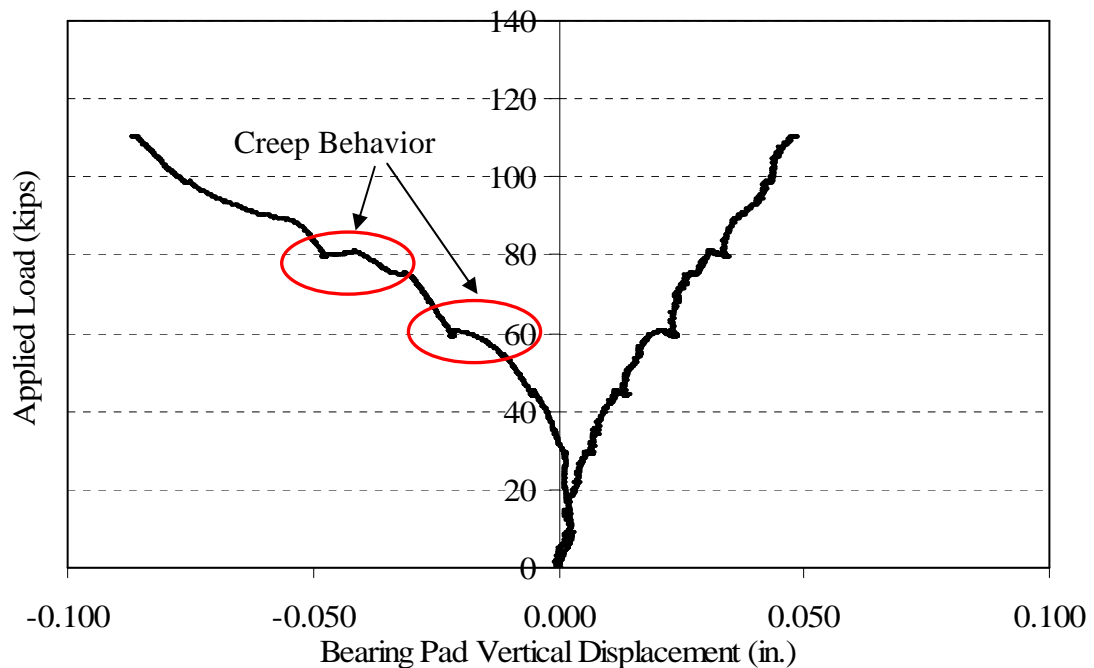
Figure 7.32 – Applied load vs. bearing pad vertical displacement showing bearing pad creep behavior

During the experiment, torsional cracking did not occur and was not a factor in the nonlinear analysis as was the case for the rectangular beam specimens. The nonlinear analysis was performed to an applied load of 145 kips (645 kN) and the torque on the cross-section was on the order of 600 kip-in (68 kN-m), but the calculated cracking torque was approximately 1600 kip-in (181 kN-m).

The analysis included the vertical deformation of the bearing pad; however, Figure 7.32 shows that the bottom flanges of the south side of the girder began to uplift from the bearing pad once load commenced. Uplift did not occur immediately because the self-weight of the girder resulted in an initial axial deformation in the bearing pad. The nonlinear analysis predicted that there was an initial axially compressed deformation of the bearing pad of 0.0187-in. (0.475 mm) on the side of the girder that was compressed during rollover (north side) and 0.0164-in. (0.416 mm) on the side that was prone to uplift during rollover of the girder (south side). Therefore, true uplift did not occur until the load was approximately 60 kips (267 kN).

During the experiment, rollover was the concern at the maximum loads. Although Figure 7.31 does not show the unstable behavior during the first ascent of the second loading because of the restraint provided at the end supports, the second load ascent shows an initiation of large rotations with minimal additional load. The rollover behavior is better shown in a plot of the applied load versus the end rotation as shown in Figure 7.33. Both contact with the torsional restraint system and uplift are noted in Figure 7.34.
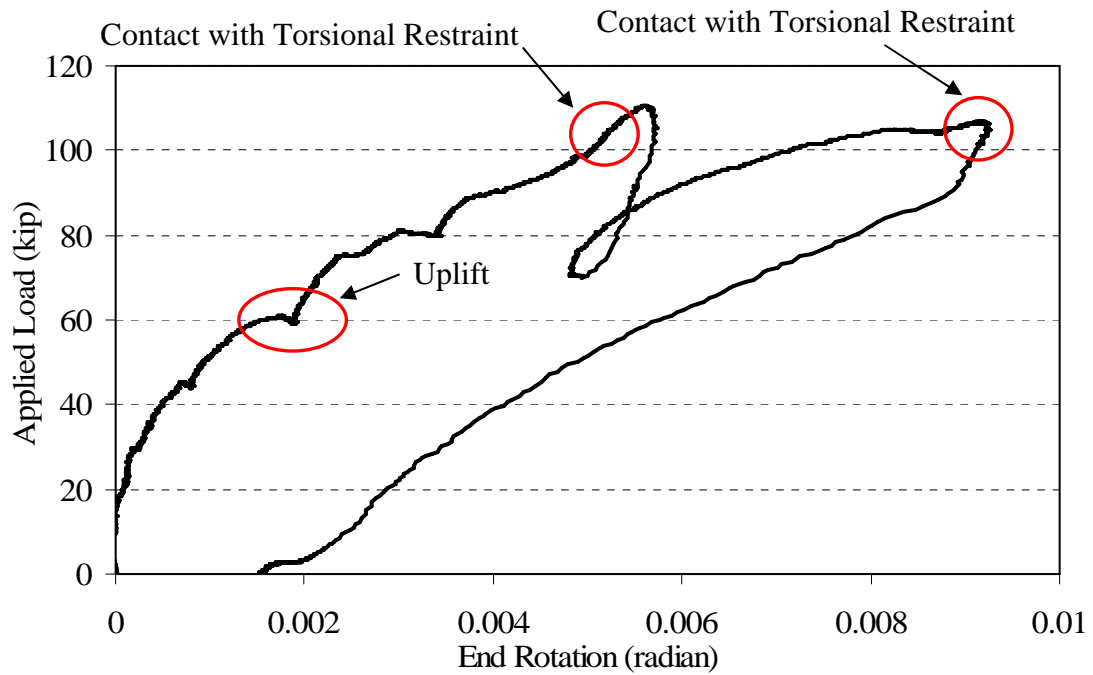
Figure 7.33 – Applied load versus end rotation

Figure 7.33 shows that during the first load ascent, the rate of increase of end rotation increased until the torsional restraint impeded the continuation of significant end rotations. During the second load ascent, the torsional restraint was removed and large end rotations began at approximately 104 kips (463 kN) which caused the girder to again contact the torsional restraint system. Although the nonlinear analysis was developed to capture lateral-torsional buckling behavior, the model should also predict rollover behavior because of the effect of the bearing pad model on the nonlinear analysis. Because Figure 7.30 and 7.31 presented the girder deformation behavior neglecting the rigid body deformation, the plots did not show the complete behavior as predicted by the

analysis. Therefore, the second analytical case where the total deformation including the elastic deformation of the girder and the rigid body behavior were summed was considered. The applied load versus total rotation was investigated to determine the adequacy of the nonlinear analysis in predicting the rollover behavior of the girder. A plot of the total rotation behavior predicted by the nonlinear analysis is shown in Figure 7.34.
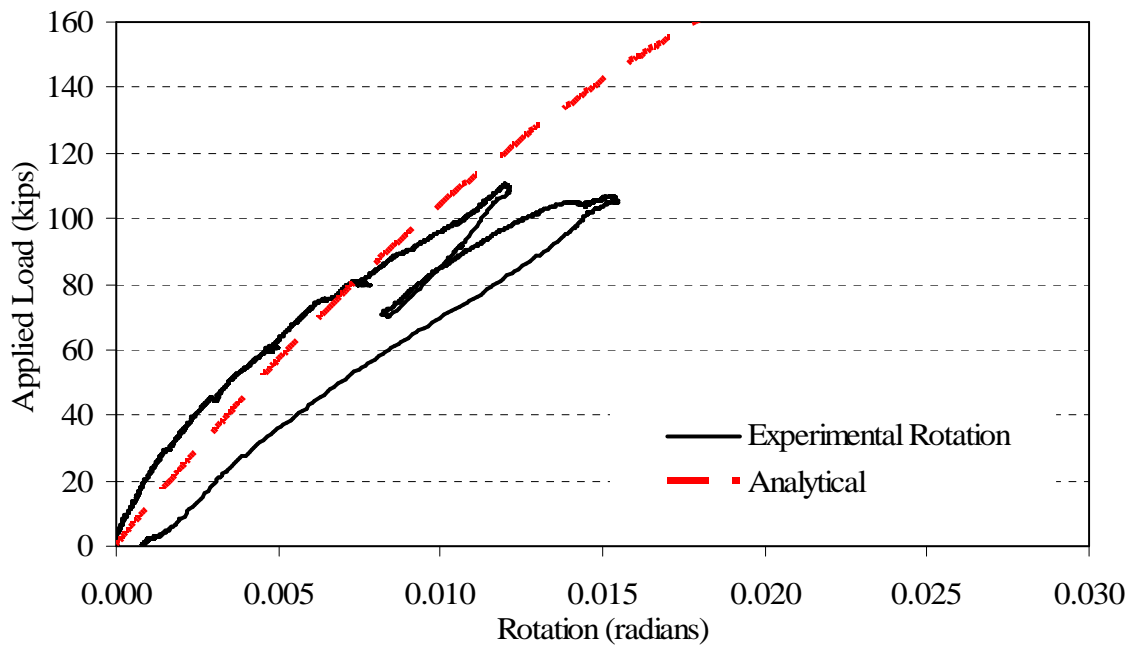
Figure 7.34 – Applied load vs. total rotation (girder rotation + end rotation)

Figure 7.34 shows that the nonlinear analysis model predicted the total rotation from the experiment at loads less than 80 kips (356 kN) reasonably well. However, there was significant deviation between the experimental and analytical curves at relatively low

loads. Because the uncoupled girder rotation behavior was proven to predict the

experimental girder rotation behavior well, particularly at lower loads, it was apparent

that the analytical model under-estimated the rotational stiffness of the bearing pads. At

high loads, in excess of 80 kips (356 kN), the analytical model appeared to over-estimate

rotational stiffness of the bearing pads. Furthermore, the analytical model never achieved

a completely unstable condition, although the rate of increase in total rotation was

increasing. The differences in behavior are presented more clearly in a comparison plot

between the experimental end rotation and the end rotation predicted by the nonlinear

analysis with respect to the torque applied to the girder ends as shown in Figure 7.35.
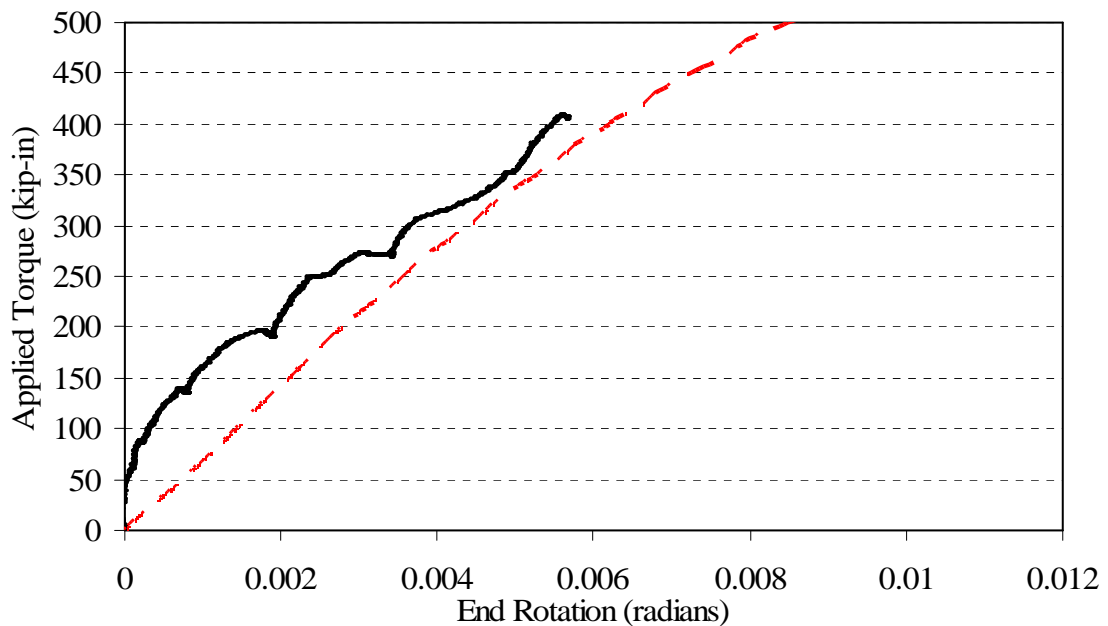
Figure 7.35 – Applied torque vs. end rotation

Figure 7.35 shows that the stiffness behavior of the actual bearing pad was stiffer than the analytical bearing pad model. At lower loads the rotational stiffness of the bearing pad was larger than the analytical model represented, and the effective rotational stiffness of the bearing pad at higher loads was lower than the analytical model represented. The detailed bearing pad behavior was further investigated by considering a plot of the bearing pad vertical displacements at each edge of the girder for both the analytical and experimental data. Figure 7.36 shows a plot of this comparison with compressive displacements as positive. The raw data for the bearing pad vertical displacements had to be corrected to account for the effect of the rotation about the strong-axis of the girder because the string potentiometers were not located directly under the center of rotation of the bearing pad. The correction procedure is presented and discussed in Appendix F.
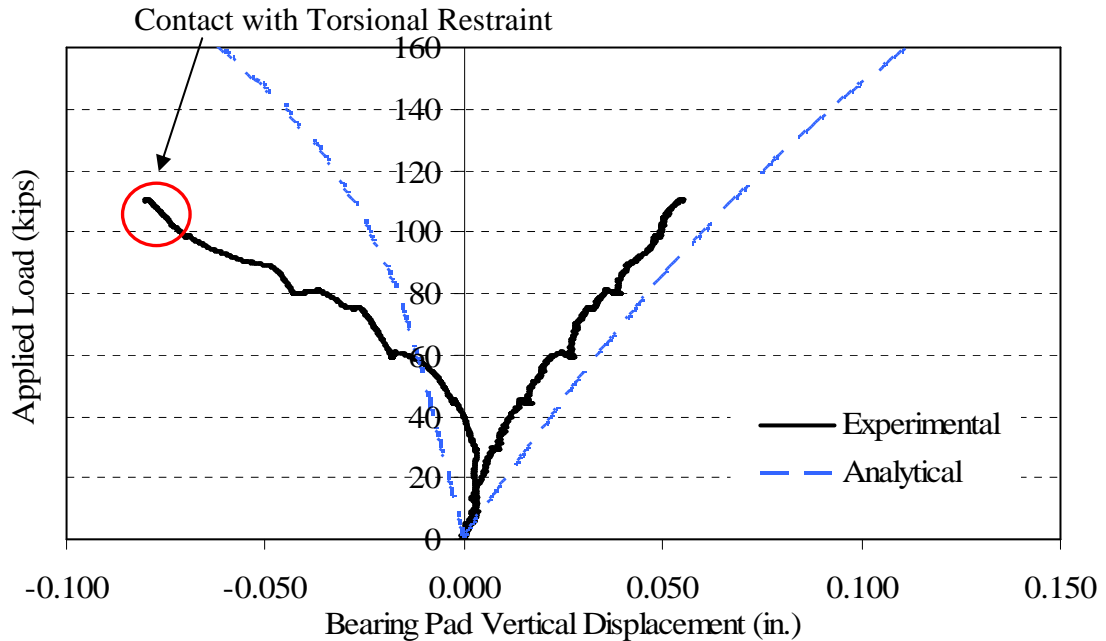
Figure 7.36 - Corrected bearing pad vertical displacements at edges (positive compression)

The experimental data of Figure 7.36 shows that the bearing pad had a substantially larger nonlinear response than the analytical model predicted. Furthermore, the rate of increase in uplift became very high at higher loads, and the analytical model did not predict the behavior. The experimental data in Figure 7.36 also shows that both sides of the bearing were being compressed upon initial loading; however, that is most likely not the case. The vertical displacement correction procedure presented in Appendix F was sensitive to the assumption of the distance from the vertical string potentiometers and the center of strong-axis rotation at the bearing. Therefore, the assumed center of strong-axis rotation was probably slightly in error.

There were a few potential error sources in the analytical model that caused the discrepancies between the experimental and analytical bearing pad responses. The first was that a relatively simple model was used to represent the stiffness properties of the bearing pad. For small vertical displacements, the bearing pad response was shown to be highly nonlinear; therefore, a more detailed experimental and analytical study on bearing pad properties was needed. Consolazio et al. (2007) presented a detailed study on bearing pad response; however, higher loads were dealt with and uplift was not considered. Also, the retrofit to the bottom flange of the girder was intended to level the bearing surface so that uniform contact was made between the bottom flange of the girder and the bearing pad. The author cannot be certain that the retrofit completely removed the roundness of the bottom flange.

Furthermore, the retrofit was supposed to provide a uniform bearing condition in the longitudinal direction, and although the bearing was improved compared to actual bridge bearing conditions, at the end of the second load ascent, the distance along the width of the bearing pad that had underwent complete uplift was measured. On the west side of the girder, the back side of the bearing pad, as shown in Figure 7.37, was not in contact with the bearing pad for a distance of 10.25-in. (260 mm), and the front side of the bearing pad was not in contact with the bearing pad for a distance of 6.5-in. (165 mm). On the east side of the girder, the back side of the bearing pad had was not in contact with the bearing pad for a distance of 4.75-in. (121 mm) and the front side of the bearing pad was not in contact with the bearing pad for a distance of 3-in. (76 mm). If uniform bearing was achieved in the longitudinal direction, the uplift distance on the back side and front side of the bearing pad would be equivalent, which was not the case.

Figure 7.37 depicts the region of uplift on each of the bearing pads. Non-uniform bearing in the longitudinal direction was another source of error and the effects should be studied because the camber in actual bridge girders causes all girders to have a non-uniform bearing condition when being erected.
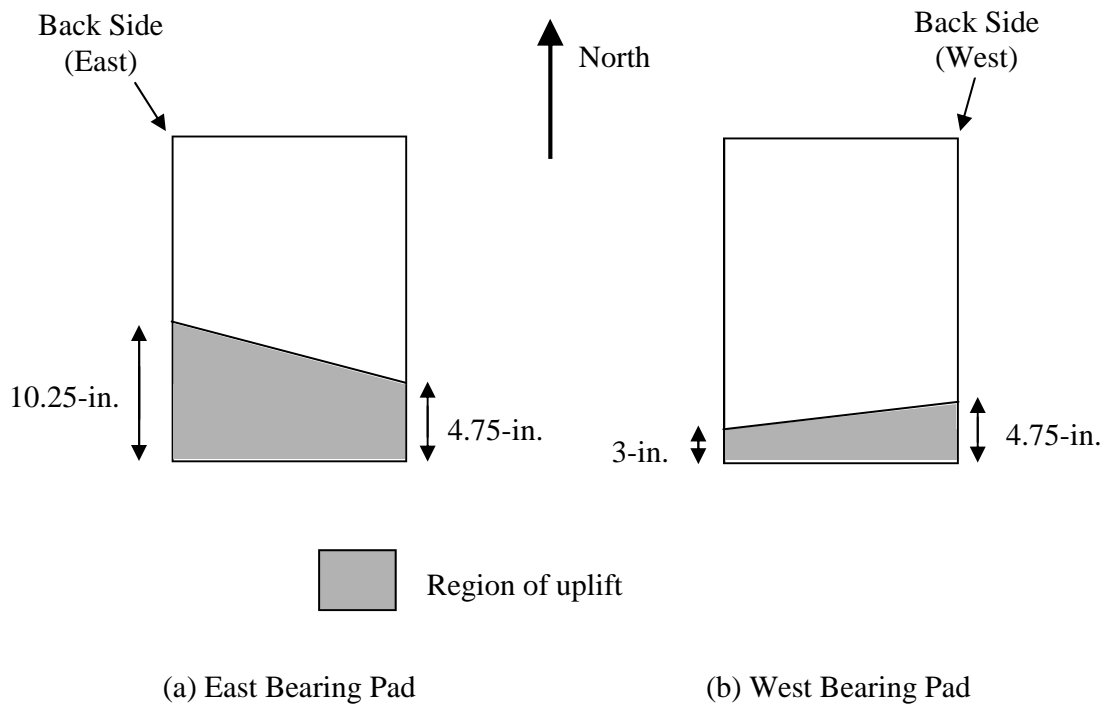
Figure 7.37 – Region of uplift for (a) west bearing pad and (b) east bearing pad. Note, the girder was spanning east-west and was laterally displacing toward the north.

The last possible cause of the highly nonlinear bearing pad response, particularly at higher loads, was the possibility of a second-order effect due to the shear deformation of the bearing pad as shown in Figure 7.38. Because of the relatively larger shear displacements that the bearing pad incurred during the experiment, on the order of 0.3-in.

(7.6 mm) for the first load ascent and 0.5-in (12.7 mm) for the second load ascent, it was

hypothesized that the shear deformation caused a softening of the bearing pad on the

compressed edge of the bearing pad.
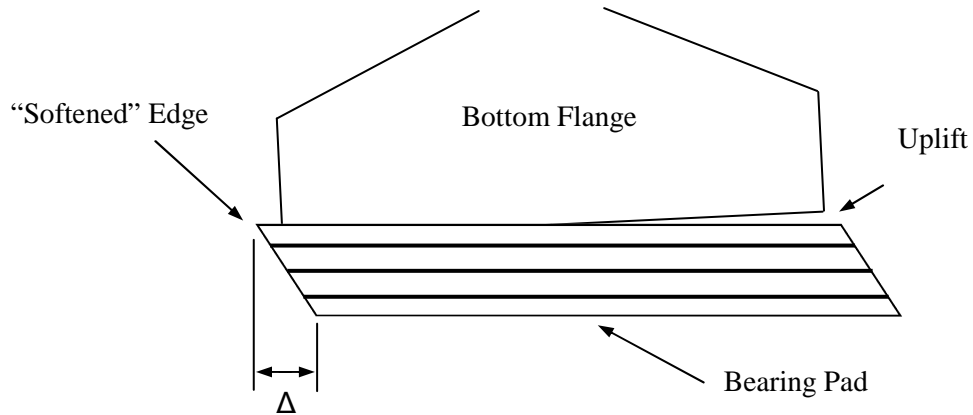
Figure 7.38 – "Softened" bearing pad edge due to bearing pad shear deformation

7.5.2 Simplified Equation Prediction

The simplified equation from Equation 6.34 proposed in Chapter 6 for lateral-

torsional buckling of prestressed concrete beams considering initial imperfections was

applied to the BT-54 specimen with the initial imperfections measured before the

experiment. The simplified equation does not consider effects of bearing pad

deformations. The predicted lateral-torsional buckling load using the simplified equation

was 23.5 kips (104.5 kN). If cracked properties are not used, the elastic lateral-torsional

buckling load would be 466 kips (2073 kN).

The BT-54 never failed in a lateral-torsional buckling mode, but instead failed by rollover at a higher load than was predicted by the simplified equation. The cause of the large under-prediction by the simplified equation was that the girder never cracked or became inelastic. The simplified equation was derived for inelastic lateral-torsional buckling and does not apply when a cross-section remains elastic because the lateral-torsional buckling load does not decrease with imperfections for an elastic beam. A detailed discussion of this behavior, the limits and the applicability of the simplified equation are presented in Chapter 8. Additionally, because of the sensitivity of lateral-torsional buckling and rollover to initial rotation, tighter tolerances on these initial imperfections are needed, particularly for long-span girders.

7.5.3 Rollover Stability

For conditions where the end of a bridge girder is not braced, rollover is expected to govern over lateral-torsional buckling for AASHTO and PCI BT bridge girders and imperfection conditions. The nonlinear analysis detailed in Chapter 6 and applied to the BT-54 test girder in Chapter 7 predicts the response of a bridge girder with respect to both lateral-torsional buckling and rollover; however, the analysis proved to be extremely sensitive to the bearing conditions and the bearing pad stiffness assumptions. Mast (1993) provided a simple approach to check the factor of safety against rollover of a prestressed concrete bridge girder on elastic supports. Figure 7.39 shows a plot of the rollover prediction using the methodology from Mast (1993) compared to the nonlinear analysis and experimental data.
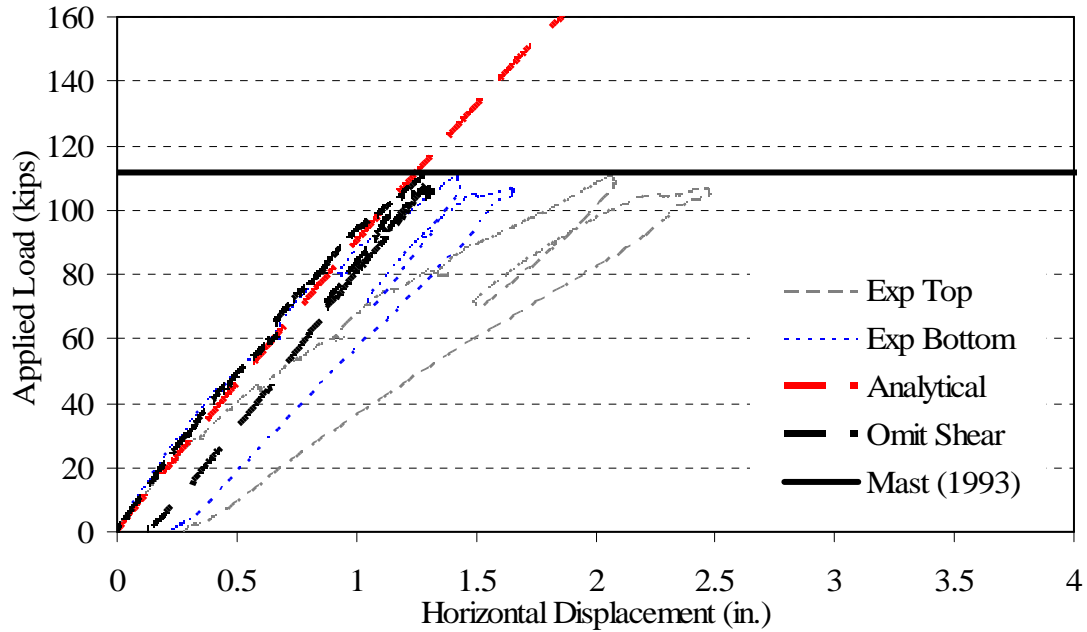
Figure 7.39 – Mast (1993) rollover prediction vs. experimental and nonlinear analysis data

The predicted rollover load using Mast (1993) was 111.7 kips (497 kN). It was apparent from Figure 7.39 that methodology from Mast (1993) effectively predicted the rollover load. However, the method required the assumption of rotational stiffness of the bearing pad. A more detailed discussion of the bearing pad rotational stiffness is presented in Chapter 8.

CHAPTER 8

ROLLOVER & LATERAL-TORSIONAL BUCKLING STABILITY: DISCUSSION OF RESULTS

The lateral-torsional buckling behavior of the rectangular prestressed concrete beams of this study, the BT-54 girder of this study, and the test specimens from König and Pauli (1990) and Kalkan (2009) were studied in Chapters 6 and 7. Furthermore, Chapter 7 discussed the rollover behavior of the BT-54 girder. The discussion on the lateral-torsional buckling behavior for bridge girders has been limited to the BT-54 girder of this study thus far. Limitations to the applicability of the simplified equation arise for cases when inelastic behavior is not expected and these limitations are discussed in the following sections. A parametric study of the lateral-torsional buckling behavior of a PCI BT-72 bridge girder that is laterally braced at the ends is provided within this chapter. The limitations of the simplified analysis are highlighted using the parametric study. Additionally in this chapter, the rollover of bridge girders without lateral bracing at the end is examined, and the effects of the bearing pad stiffness on the rollover behavior are discussed

8.1 Braced Girder Lateral-Torsional Buckling Discussion

8.1.1 Limitations on Simplified Equation Applicability

There are limitations to the applicability of the simplified equation to predict lateral-torsional buckling of prestressed concrete cross-sections. The simplified equation

and the associated reduction parameters from Equation 6.22 and Equations 6.32 through 6.34 are presented again below.

$$B_r = B\left[1 - \frac{1}{3}\tan^{-1}\left(\frac{I_{gx}}{I_{gy}}\theta_0\right)\frac{2}{\pi}\right] \qquad (8.1)$$

$$\Delta_r = 1 - \left(\frac{\delta_0}{L}\right)^{0.31} \qquad (8.2)$$

$$\Theta_r = e^{-26.5\theta_0} \qquad (8.3)$$

$$M_{b\,imperfections} = \frac{\pi}{L}A\sqrt{B_r C}\ \Delta_r \Theta_r \qquad (8.4)$$

To present the limitations, the way in which the reduction parameters were derived must first be considered. The buckling load of the beam was determined by first neglecting the effect of initial imperfections. Section properties were based on the compression zone depth, the longitudinal mild reinforcing and prestressing strands. The secant modulus of elasticity of the concrete was used. Therefore, the inelastic lateral-torsional buckling load was determined for the case of zero imperfections where the term

"inelastic" refers to the flexural cracking of the concrete and the nonlinear material properties of the concrete (modulus of elasticity).

As sections that have greater slenderness or a larger precompression were considered, the compression zone depth at buckling was larger and the secant modulus of elasticity of the concrete approached the initial modulus of elasticity of the concrete. When either the slenderness or precompression became large enough, the entire cross-section was effective when calculating the section properties; and the secant modulus of elasticity of the concrete was equivalent to the initial modulus of elasticity of the concrete. At this point the critical buckling moment was equivalent to the elastic lateral-torsional buckling moment. Essentially the lateral-torsional buckling load would be the same as if the beam was assumed to be a linear-elastic material that could not crack.

The effect of initial imperfections on the critical buckling moment was determined by plotting several load versus lateral displacement curves for several different initial imperfection conditions. The results of the imperfections parametric analyses were used to develop reduction parameters for initial lateral displacement and initial rotation as shown qualitatively in Figure 8.1. The reduction parameters acted to reduce the critical buckling moment with zero initial imperfections.
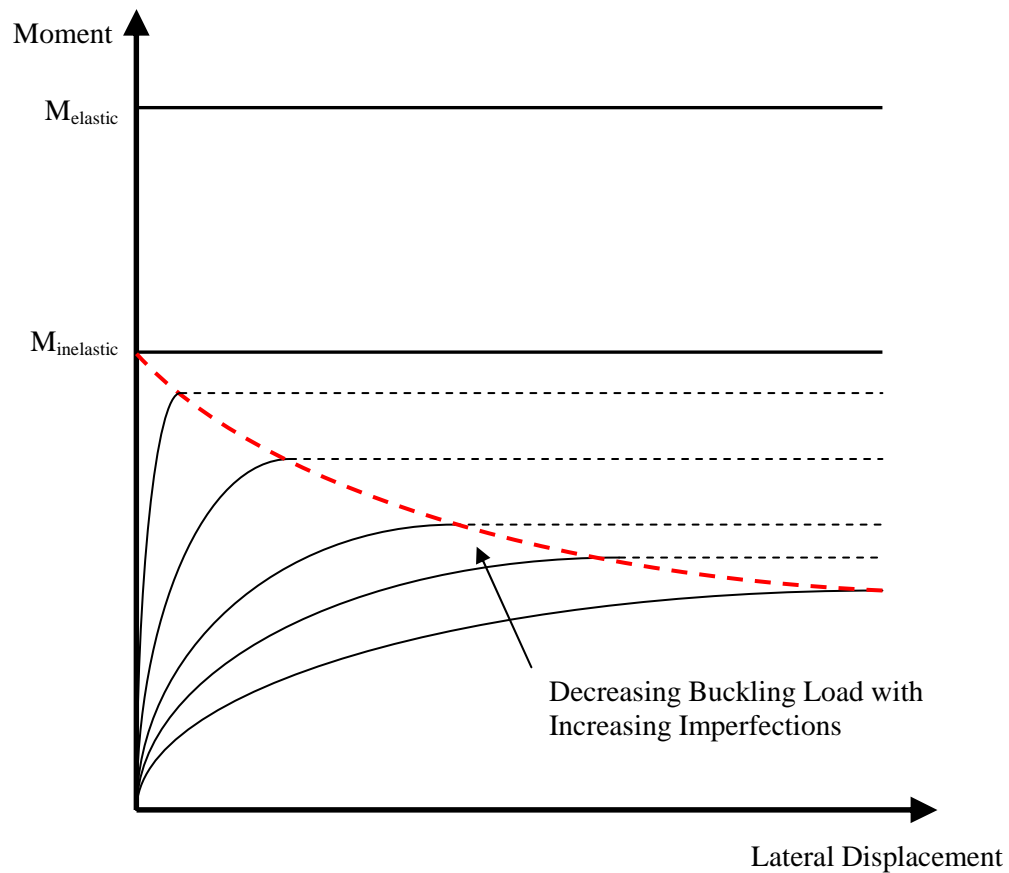
Figure 8.1 – Reduction of buckling moment due to increasing initial imperfections

The reduction to the zero initial imperfection buckling load due to initial imperfections stemmed from the effect of initial imperfections on the extent of cracking, the angle of neutral axis, the progression of cracking, and the reduction of the modulus of elasticity from initial to the secant modulus. For beams with greater slenderness, the inelastic behavior was present for a smaller portion of the load versus lateral displacement curve as shown in Figure 8.2. Consider qualitatively an example case where beam 1, represented by curve 1 in Figure 8.2, had less slenderness than beam 2, represented by curve 2 in Figure 8.2. Beam 2 will buckle at a larger ratio of applied

moment to the theoretical elastic buckling moment than beam 1 because less severe

inelastic behavior will occur in the case of beam 2.
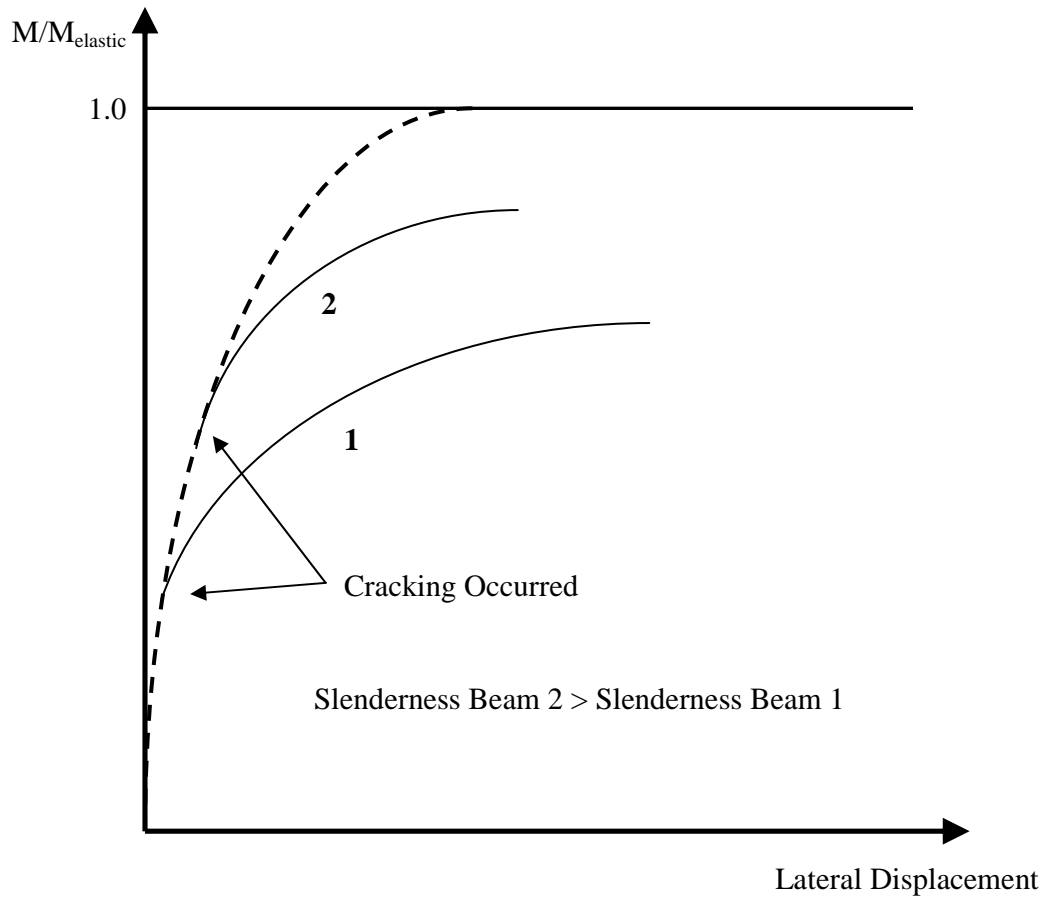
Figure 8.2 – Effect of slenderness on the ratio of buckling moment to the theoretical
elastic buckling moment

As the beam slenderness increases, the ratio of buckling moment to elastic

buckling moment will approach 1.0. At a certain slenderness no inelastic behavior will

occur, and the elastic buckling load will govern. A similar example can be considered to

investigate the effect of precompression as shown in Figure 8.3. Two beams were

compared that had equivalent slenderness ratio; however, beam 1, represented by curve 1

in Figure 8.3, had less precompression than beam 2, represented by curve 2 in Figure 8.3.

Beam 2 will buckle at a larger ratio of applied moment to the theoretical elastic buckling

moment than beam 1 because less severe inelastic behavior will occur in the case of beam

2. Essentially, the larger precompression will cause the beam to have a large

compression zone.
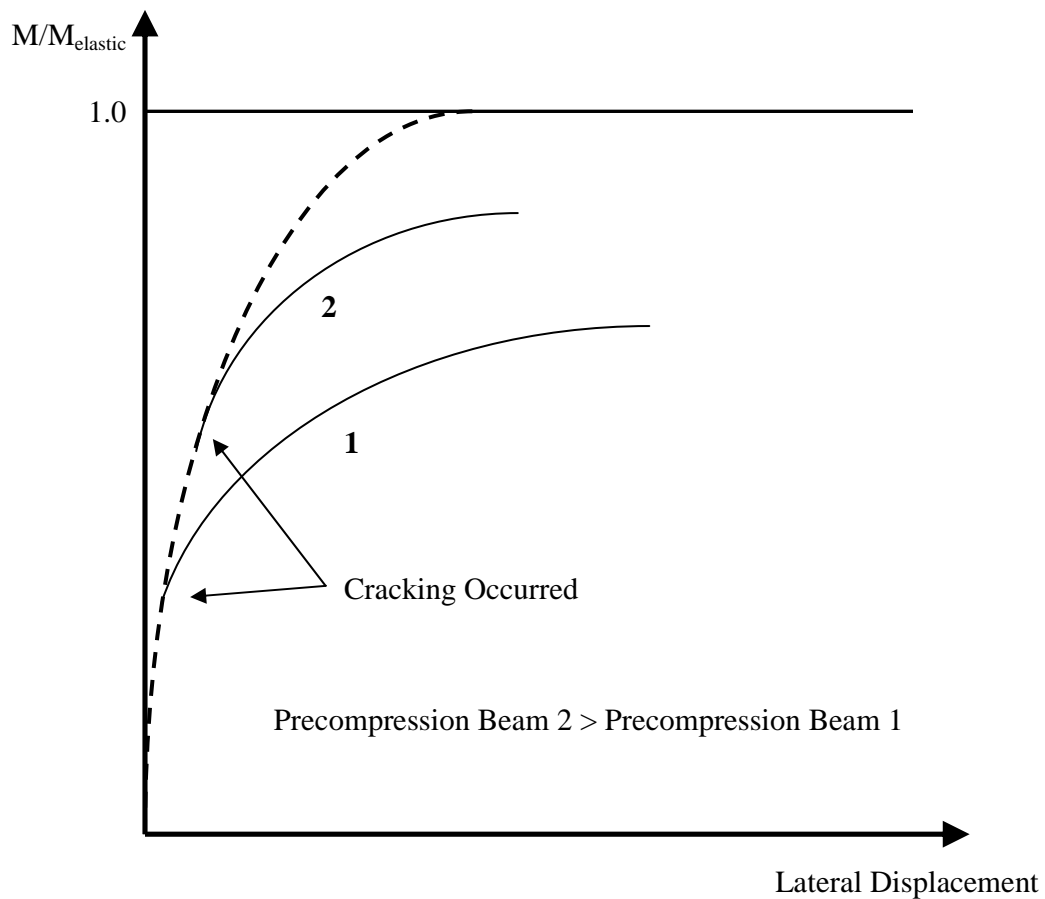
Figure 8.3 – Effect of precompression on the ratio of buckling moment to the theoretical elastic buckling moment

For the case of elastic lateral-torsional buckling, initial imperfections affect the load versus lateral displacement and load versus rotation response, but not the maximum load achieved, as shown in Figure 8.4. In Figure 8.4, curve 1 represents a beam with less severe initial imperfections than curve 2 and curve 2 represents a beam with less severe initial imperfection than curve 3.
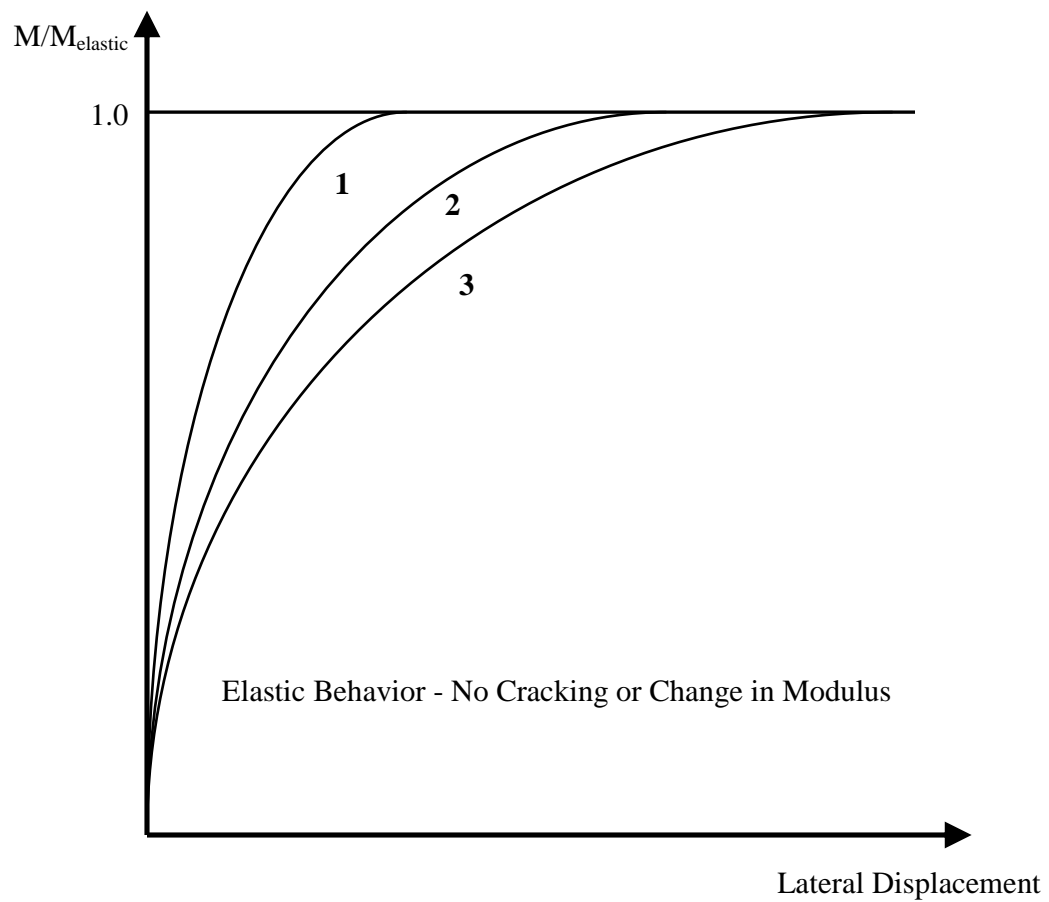
Figure 8.4 – Effect of initial imperfections of elastic lateral-torsional buckling response

Because the initial imperfections for an elastic case do not affect the maximum load achieved, the reduction parameters for initial imperfections do not apply for the elastic case. The reduction parameters were derived for cases where inelastic behavior was anticipated.

The author hypothesizes that there is a transition between the elastic buckling load and the inelastic buckling load. The lateral-torsional buckling load calculated by the simplified equation and reduced by the associated reduction parameters was based on a reinforced concrete or prestressed concrete beams that had significant cracking behavior.

Consider first a beam with zero initial imperfections and significant prestressing force such that there was no cracking behavior. For prestressed concrete bridge girders, the prestressing force is large enough that no flexural cracking is developed under the self-weight and the neutral axis would be below the bottom flange. The beam would then buckle elastically. If the buckling load was slightly less than the cracking load, the neutral axis would be slightly below the bottom of the cross-section and perfectly horizontal as shown in Figure 8.5.

Now consider the same beam configuration but with initial imperfections. The beam will not buckle at the elastic buckling load as was discussed and presented in Figure 8.4 because the neutral axis will no longer be horizontal and cracking could occur at the corner of the cross-section as shown in Figure 8.5.
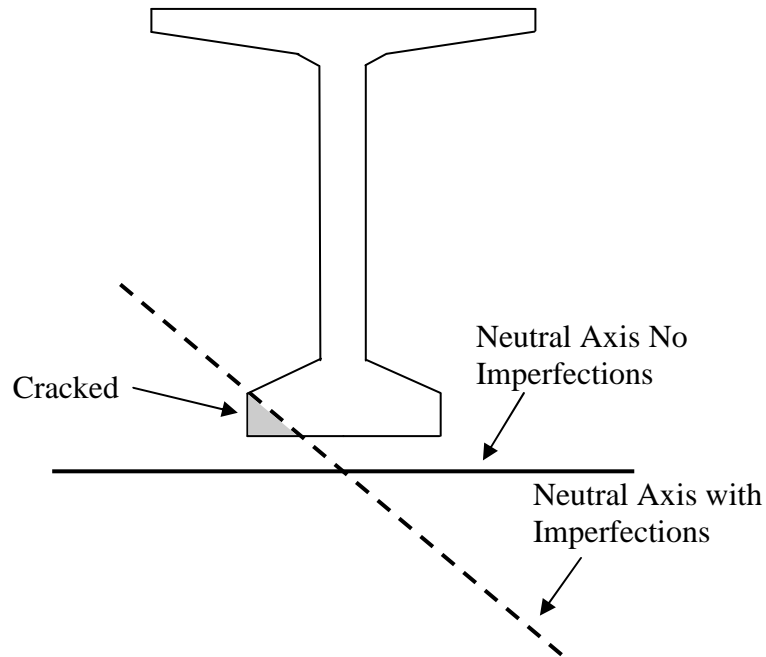
Figure 8.5 – Cracking behavior during transition behavior between elastic and inelastic lateral-torsional buckling

The reduction in stiffness due to the cracking behavior shown in Figure 8.5 would be less than the reduction predicted by the reduction parameters from the simplified equation. The reduction parameters would therefore be conservative; however, the reduction parameters potentially could be overly conservative because the reduction parameters were developed for prestressed concrete and reinforced concrete beams that were fully cracked. The difference between reinforced concrete and prestressed concrete beams would be the extent or depth of cracking. The depth of cracking and the associated effect on the lateral-torsional buckling load was inherent to the simplified equation because it was a function of the calculated depth of the compression zone. Additional research is required on the transition behavior.

There is additional transition behavior to be considered for the case of large initial imperfections and no anticipation of flexural cracking in the bottom flange. For example, if the initial imperfections are large enough, the load versus lateral displacement response could cause the modulus of rupture of the concrete to be exceeded at one edge of the top flange of a prestressed concrete bridge girder as shown in Figure 8.6.
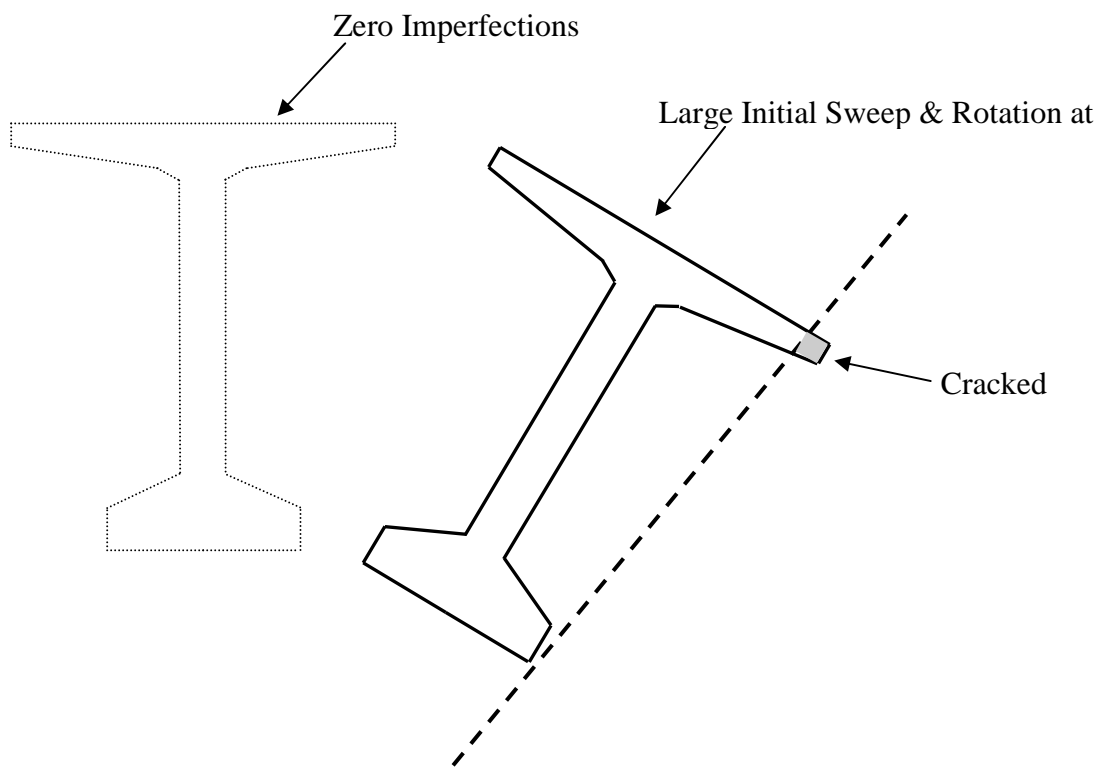
Figure 8.6 – Top flange cracking due to excessive initial imperfections

The reduction parameters introduced in this research do not apply to such a case because the parameters were derived for flexural cracking initiating at the bottom flange and progressing upward through the beam. Instead, a reduction to stiffness should be based the weak-axis moment of inertia reduction equation from Mast (1993) given by Equation 1.66 and presented again here as:

$$I_{eff} = I_y / (1 + 2.5\theta) \qquad (8.5)$$

Equation 8.5 was derived by using experimental results for several prestressed concrete bridge girders that were continually rotated at their end to determine the weak-axis displacement characteristics. When the girder reached a large enough angle, the top flange on the convex side of the girder began to crack and there was a loss of weak-axis stiffness. Equation 8.5 was determined by a fit to the experimental data (Mast, 1993). Additional research is required to determine the validity of Equation 8.5 as a stiffness reduction parameter for lateral-torsional buckling when cracking of the top flange is anticipated.

8.1.2 PCI BT-72 Lateral-Torsional Buckling Parametric Study

To investigate the potential of lateral-torsional buckling for a typical bridge girder cross-section, a PCI BT-72 was studied parametrically using the rollover analysis by Mast (1993). A PCI BT-54 was not studied parametrically because girder spans for BT-54's are typically less than 140-ft. (42.7 m) in practice. From preliminary analyses, a

span of 140-ft. (42.7 m) was not long enough to cause a BT-54 to be prone to lateral-torsional buckling. Figure 8.7 shows the ratio of applied load to self-weight load that would cause lateral-torsional buckling of span for a BT-72 with 40 ½-in. (12.7 mm) diameter prestressing strands for several different initial imperfection conditions. The applied load to self-weight load ratio for each of the representative conditions was computed as the ratio of the critical uniform load that caused buckling over the self-weight uniform load of the girder. Therefore, an applied load to self-weight load ratio of 1.0 corresponded to the self-weight of the girder causing buckling. The different initial imperfection conditions used are listed below.

1. The girder with zero imperfections.

2. The girder with the maximum allowable sweep of 1/8-in. (3.2 mm) per 10-ft. (3.0 m) of length and no rotation.

3. The girder with the maximum rotation at midspan as the allowable sweep over the height of the cross-section, but no sweep applied in the reduction parameters.

4. The girder with the maximum sweep of 1/8-in. (3.2 mm) per 10-ft. (3.0 m) of length and maximum rotation at midspan as the allowable sweep over the height of the cross-section in addition to 0.05-in. (1.3 mm) per 10-ft. (3.0 m) of length of additional sweep due to thermal effects (standard imperfections). The 0.05-in. (1.3 mm) per 10-ft. (3.0 m) of length was approximated by using data from the BT-54 thermal deformation study

344

from Chapter 3 where thermal deformations were measured as approximately 0.5-in. (13 mm) for the 100-ft. long girder.

5. The girder with standard imperfections, including the imperfections from thermal deformation, in addition to a bearing rotation of 0.005 radians that was representative of the rotation caused by the support flatness tolerance. The support flatness tolerance that is presented in Chapter 1 allows for 1/16-in. (1.6 mm) perturbations in the concrete surface. A 24-in. (610 mm) bearing was assumed, and the worst case of a 1/16-in. (1.6 mm) increased elevation on one side of the bearing and a 1/16-in. (1.6 mm) decreased elevation on the other side of the bearing was assumed, which resulted in approximately a 0.005 radian initial bearing rotation.

6. The girder with standard imperfections, including imperfections due to thermal deformation, plus an additional 0.05 radians of initial rotation at the supports were applied to consider an extreme condition. The extreme condition was in the range of initial bearing rotation angles for the girders at the Arizona bridge collapse (Oesterle et al., 2007). The addition of a large initial end rotation was representative of the case of imperfections in the girder causing additional rotation of the girder due to the compliance of the bearing pad. Furthermore, a rounded bottom flange would allow a girder to "roll" to a significant initial end rotation.
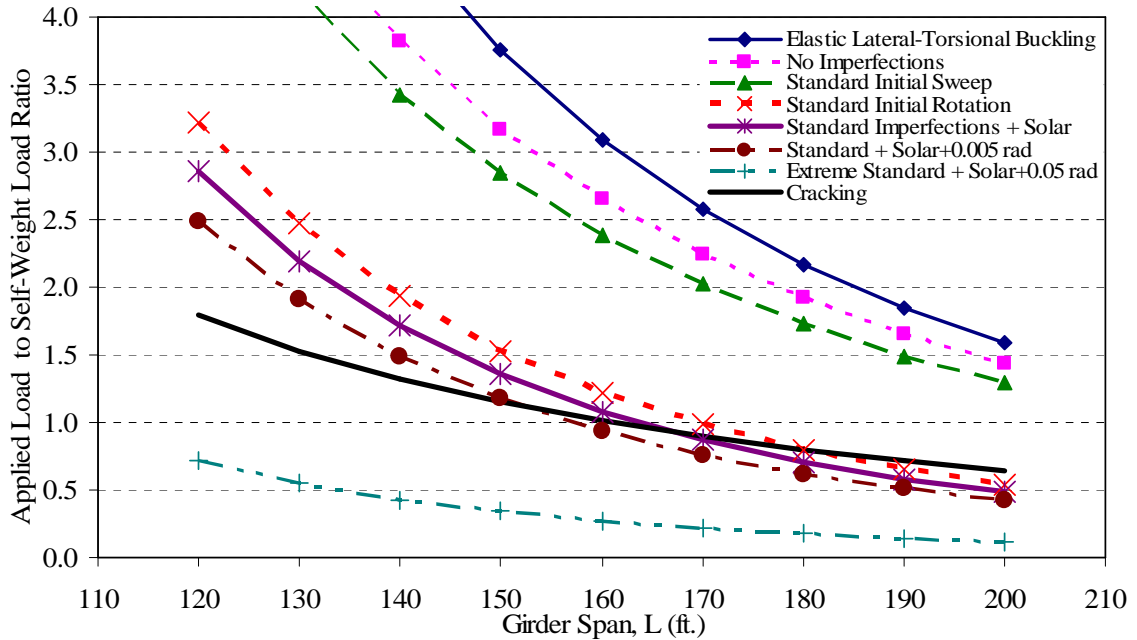
Figure 8.7 –Lateral-torsional buckling load over self-weight loads for BT-72 girder with 40 ½-in. diameter strands and with lateral bracing at the supports

The line labeled as "Cracking" in Figure 8.7 represents the applied load to self-weight load ratio in which cracking would occur for the cross-section given the assumed prestressing force. Below the "Cracking" curve, the cross-section was not cracked and above the curve, the cross-section was cracked. Figure 8.7 shows that at spans greater than 160-ft. (48.8 m), with standard initial imperfections or extreme initial imperfections, lateral-torsional buckling could occur for a girder braced at the ends. However, at spans exceeding 160-ft. (48.8 m), more prestressing force would typically be used than what was used in the analysis for the plot of Figure 8.7. Therefore, a similar plot is shown in Figure 8.8 for a BT-72 with 40 0.6-in. (15.2 mm) diameter prestressing strands, an increase of 42% in area of strands and in the amount of prestressing force.

346
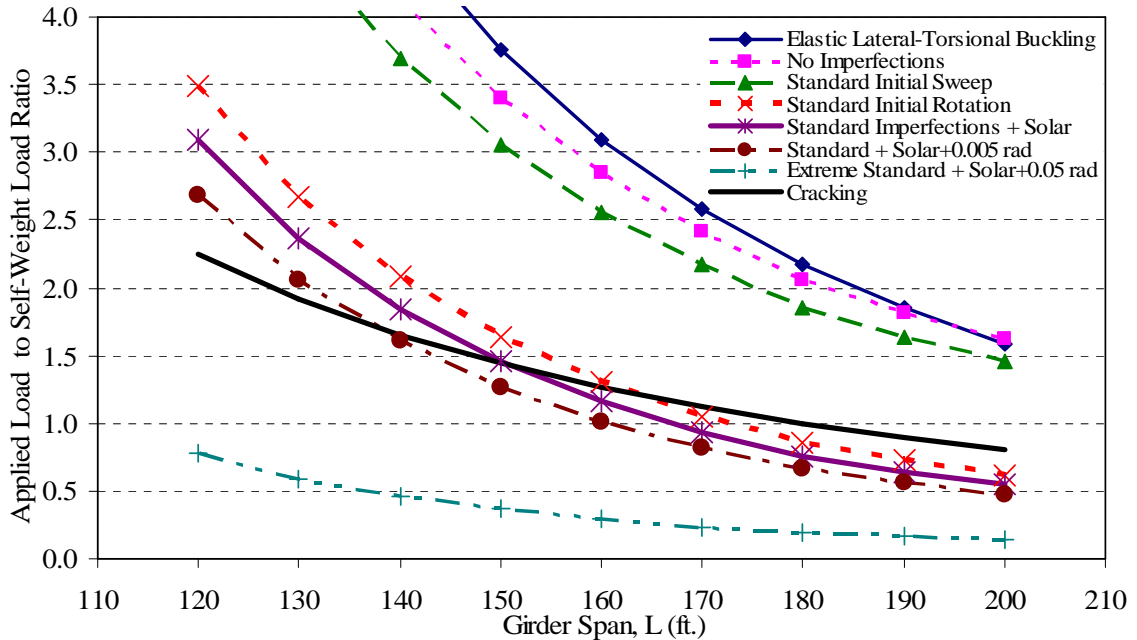
Figure 8.8 – BT-72 lateral-torsional buckling loads for 40 0.6-in. diameter strands with lateral bracing at the supports

Figure 8.8 shows that with standard imperfections or extreme initial imperfections, spans exceeding 170-ft. (51.8 m) are predicted to be in danger of lateral-torsional buckling. However, that is not necessarily the case. For points in Figure 8.8 that are above the cracking curve, the cross-section has cracked, and, therefore, the simplified equation is applicable because inelastic behavior is present. For points below the cracking curve, the cross-section has not cracked, and, therefore, the simplified equation does not apply. For those cases, the elastic lateral-torsional buckling load would be the true buckling load if it was not for the aforementioned hypothesized transition behavior that is depicted in Figure 8.5. Therefore, the simplified equation applies to cases in Figures 8.7 and 8.8 where the ratio of uniform buckling load to self-weight load

is below unity and above the cracking curve. In Figure 8.8, it is shown that there is such a possibility when the span is greater than 180-ft. (801 m) because the factor of safety against cracking is less than unity. However, for girders in excess of 180-ft. (801 m), a larger prestressing force would be used because design practice is such that prestressed bridge girders will not crack under self-weight alone. Because of the amount of prestressing in typical long span girders and the transition from inelastic buckling to elastic buckling, typical bridge girder cross-sections with typical prestressing forces and typical initial imperfections will not be in danger of lateral-torsional buckling with the ends properly braced. Bracing stiffness and strength criterion needs to be developed and is beyond the scope of this research. For unusual cases or if a high factor of safety is desired, the simplified analytical technique would provide a conservative factor of safety.

8.2 Unbraced Girder Rollover Discussion

The author concludes that the Arizona girders collapsed due to rollover. It is predicted in Section 8.1 that lateral-torsional buckling failures are unlikely for AASHTO and PCI BT bridge girders because such girders are designed to have no cracking under self-weight and because the cross-sectional geometries are not slender enough for elastic lateral-torsional buckling to occur for typical spans. However, any new bridge girder geometric design should be checked for the elastic lateral-torsional buckling capacity. Rollover failures are more feasible than lateral-torsional buckling failures for prestressed concrete bridge girders and are possible when no cracking behavior is expected. For girders that are being placed on supports, the estimation of the bearing pad rotational stiffness is of utmost importance.

8.2.1 Determination of Bearing Pad Rotational Stiffness

To determine the rotational stiffness of a bearing pad, an axial stiffness of the bearing pad must be determined first. AASHTO (2007) specified that elastomeric bearing pads must have a shear modulus between 95 psi to 200 psi (0.655 MPa to 1.379 MPa). The shape factor of the bearing pad as specified by AASHTO (2007) is presented in Equation 8.6.

$$S = \frac{LW}{2h_{ri}(L+W)}$$ (8.6)

In Equation 8.6, L is the length of the bearing pad, W is the width of the bearing pad, and h_{ri} is the thickness of an individual layer of elastomer. AASHTO (2007) states that the bearing pad response is nonlinear; however, the compressive modulus for an elastomeric bearing pad can be estimated as:

$$E_{bp} = 6GS^2$$ (8.7)

In Equation 8.7, G is the shear modulus for the elastomer. The vertical or axial stiffness was then determined using Yazdani et al. (2000):

$$k_z = \frac{E_{bp} A_z}{H}$$ (8.8)

In Equation 8.8, A_x is the cross-sectional area of the bearing pad and H is the total height of the elastomer layers. It was assumed that the rotation was sufficiently small such that uplift did not occur, and, therefore, the rotational stiffness of the bearing pad was calculated by Yazdani et al. (2000):

$$k_{rx} = \frac{E_{bp} I_x}{H}$$ (8.9)

In Equation 8.9, I_x is the moment of inertia about the axis that was parallel to the longitudinal axis of the girder.

The rollover load calculated by using Mast (1993) for the PCI BT-54 test girder from this study shown in Figure 7.40 was based on the experimental vertical stiffness test on the bearing pad. The vertical stiffness used in the analysis was 4573 kip/in (801 kN/mm) and the rotational stiffness was 219,500 kip-in/rad (24,800kN-m/rad). However, using the conservative value of the shear modulus as 95 psi (0.655 MPa) from AASHTO (2007) and the analysis technique from Yazdini et al. (2000), the theoretical vertical stiffness of the bearing pad was determined to be 7296 kip/in (1278 kN/mm) and the theoretical rotational stiffness was determined to be 350,200 kip-in/rad (39,570 kN-m/rad). The predicted stiffness was greater than the experimentally determined bearing pad stiffness because the bearing pad exhibited nonlinear behavior. For small loads, the

stiffness properties were reduced; however, in the case of bearing pad design, the load on the bearing from an in service bridge was significantly larger than the self-weight of the girder. Therefore, the theoretical stiffness of the bearing pad over-predicted the bearing pad stiffness properties at relatively low applied loads.

The current experimental measurement of elastomeric bearing pad stiffness by the Georgia Department of Transportation is to load the elastomeric bearing pad to 150% of the design service load for the bearing pad and to measure the final axial (vertical) shortening of the bearing pad. No preload is used, that is the dial gages that are used to measure the vertical displacement of the bearing pad at each of the four corners of the bearing pad are zeroed when there is zero load on the bearing pad. From the experimental results, the axial and rotational stiffness are calculated based on the method outlined in AASHTO (2007). Therefore, the nonlinear stiffness behavior at low loads is not captured by the method because the total bearing pad vertical displacement is averaged over the entire loading to 150% of the design service load. The experimental vertical stiffness of the bearing pad was 9387 kip/in (1644 kN/mm) when the load on the bearing pad exceeded 80 kips (356 kN), corresponding to a shear modulus of 122 psi (MPa). A shear modulus of 122 psi (MPa) was well within the designated range of allowable shear moduli presented in AASHTO (2007). However, the maximum load a single bearing experienced during the experiment was 86 kips (383 kN). In fact, for the bridge girders that collapsed in Arizona (Oesterle et al., 2007) the ratio of self-weight load to service load was approximately 0.31.

8.2.2 Rollover Sensitivity to Bearing Pad Stiffness

The stiffness parameters that should be used in the rollover analysis ideally would not be the assumed linear bearing pad stiffness based on relatively large loads on the bearing pad. The use of a high stiffness value would be unconservative. Additional research is required to determine bearing pad axial and rotational stiffnesses with applied loads in the range of girder self-weights. Figure 8.9 shows the rollover analysis by Mast (1993) on a 100-ft. (30.5 m) long PCI BT-54 bridge girder for the experimental bearing pads used by the author as a function of the assumed rotational stiffness to depict the relatively low sensitivity.
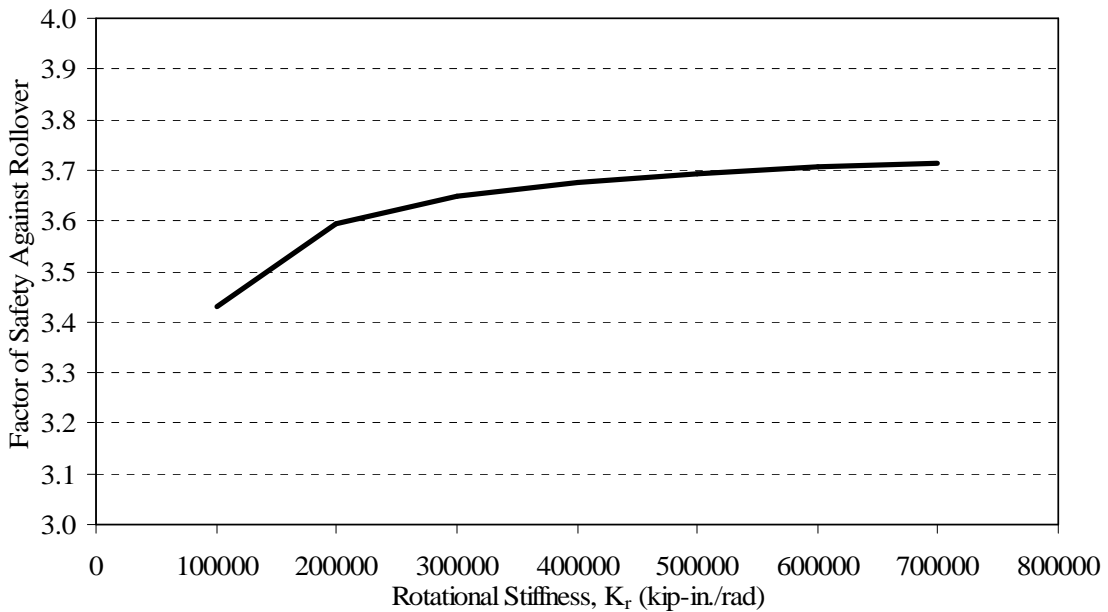
Figure 8.9 – Factor of safety against rollover under self-weight vs. 24-in. (610 mm) bearing pad rotational stiffness

The sensitivity to rotational stiffness was based on the 24-in. (610 mm) wide bearing pad used in the experiments. The effect an 18-in. (457 mm) wide bearing pad had on the rollover behavior was considered, and, furthermore, the sensitivity of the rollover load to reasonable rotational stiffness approximations for an 18-in. (457 mm) wide bearing pad was investigated.

A lower bound approximation for the rotational stiffness for an 18-in. by 10-in (457 mm by 254 mm) bearing pad was determined to be 77,160 kip-in./rad (8718 kN-m/rad) as labeled in Figure 8.10. Figure 8.10 shows the sensitivity to the assumed rotational stiffness. The predicted factor of safety against rollover under self-weight loading using Mast (1993) for the BT-54 was 2.56. The rollover factor of safety reduced 39% if an 18-in. (457 mm) wide bearing pad was used as opposed to the 24-in. (610 mm) wide bearing pad.
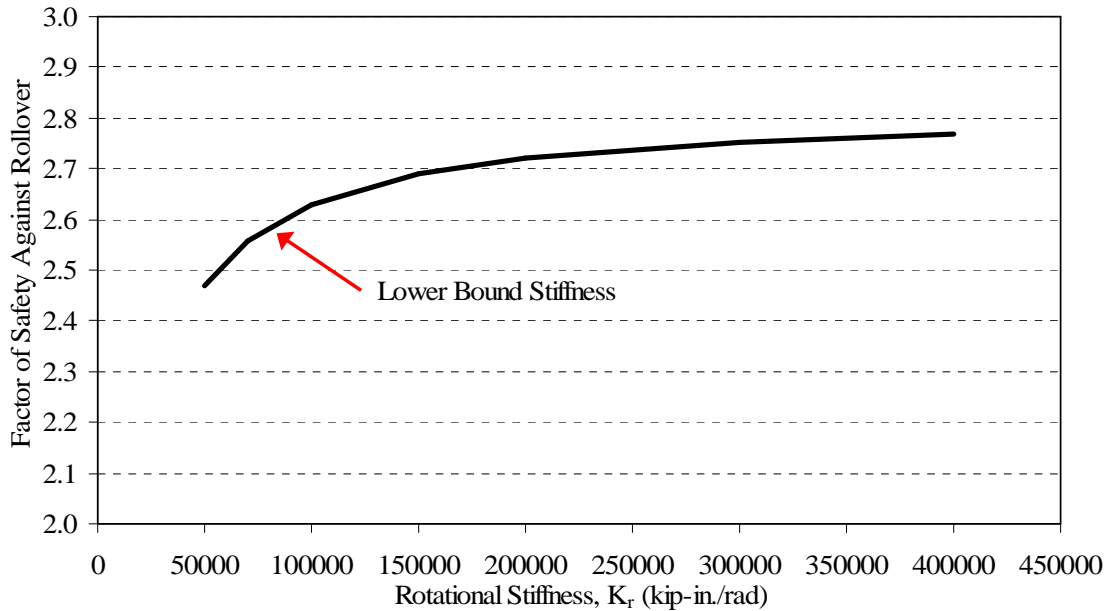
Figure 8.10 – Factor of safety against rollover under self-weight vs. 18-in. (457 mm) bearing pad rotational stiffness

Figure 8.10 shows that the sensitivity to the assumed rotational stiffness was higher for the 18-in. (457 mm) wide bearing pad. To determine whether the sensitivity of the rollover failure load to the estimated bearing pad rotational stiffness is too large, a factor of safety needs to be established. Additional research is required to establish an adequate factor of safety. Mast (1993) recommends a factor of safety of 1.5 against rollover; however, Mast stated that this factor of safety was based on experience.

8.2.3 Rollover with respect to Non-Uniform Bearing

All of the rollover analyses were predicated on the assumption that the bottom flange was flat and provided a uniform bearing surface. The effective rotational stiffness would be less for a rounded bottom flange. Mast (1993) stipulated that if the load was

354

outside of the kern (the bearing pad has uplifted), then the shape factor should be computed as the perimeter of the area that is in contact with the bearing pad. Although the proposition needs to be verified, the author proposes that a similar consideration be made for girders with imperfect bottom flanges. Research needs to be done to verify the requirement, and, furthermore, a survey of initial bottom flange inaccuracies needs to be performed to quantify the extent of the imperfections in practice.

CHAPTER 9

CONCLUSIONS & RECOMMENDATIONS

9.1 Summary

An experimental and analytical study was performed to determine the stability behavior of prestressed concrete beams. Two stability phenomenons were investigated: (1) lateral-torsional buckling and (2) rollover. An emphasis was placed on the effects of initial imperfections on the stability behavior; the effect elastomeric bearing pads and support rotational stiffness was investigated. The experimental study consisted of testing six 40-in. (1016 mm) deep, 4-in. (102 mm) wide, 32-ft. (9.75 m) long rectangular prestressed concrete beams with varying prestressing force and prestressing strand eccentricity and testing one 100-ft. (30.5 m) long PCI BT-54 bridge girder. Elastic and nonlinear analyses were performed on the seven test specimens, on a hypothetical rectangular beam with a series of varying initial imperfections and a PCI BT-72 with varying imperfections.

The first set of experiments was performed on the six rectangular beams. The beams were designed to fail by lateral-torsional buckling. The boundary conditions were constructed so that the test setup replicated classical theory; at each support lateral translation, vertical translation and torsional rotation were restrained. The beams were free to rotate about the horizontal and vertical axes. The results showed that the prestressing strands did not restrain the beams from buckling out-of-plane or destabilize the beam like in the case of a beam-column. The beams buckled after flexural cracking had occurred and did so at a load much less than what elastic lateral-torsional buckling

theory predicted. The reinforced concrete analytical methods by Hansell and Winter (1959) and by Sant and Bletzacker (1961) over-predicted the buckling loads because the effect of initial imperfections was not considered. Initial imperfections were shown to decrease the inelastic lateral-torsional buckling load due to a rotated neutral axis, additional torsion on the cross-section and progressive rotation that led to a larger component of flexure about the weak-axis (P-delta effect).

A material and geometric nonlinear, incremental load analysis was performed on the six rectangular beams. The nonlinear analyses matched the experimental load versus lateral displacement and load versus rotation behavior, and the analysis predicted the experimental maximum load within an error of 2%.

The nonlinear analysis was extrapolated to several different initial imperfection conditions to parametrically study the effect of initial lateral displacement and initial rotation on the inelastic lateral-torsional buckling load. A simplified expression for lateral-torsional stability of beams with initial imperfections was developed based on an elastic stability expression (Goodier, 1941 and 1942). The data from the parametric study were used to develop reduction parameters for both initial sweep and initial rotation. A reduction parameter was derived for the reduction to the weak-axis stiffness due to a rotated neutral axis and reduction parameters were fit to reduce the lateral-torsional buckling load for initial lateral displacement and initial rotation. A simple procedure was presented to calculate the zero imperfection inelastic lateral-torsional buckling load and the reduction parameters were applied to determine the inelastic lateral-torsional buckling load of the imperfect case. The simplified technique predicted the buckling loads of the rectangular experimental beams of this study very well with a

maximum error of 7.5% and an average absolute error of 4.8%. The simplified technique prediction for the experimental results from König and Pauli (1990) resulted in a maximum error of 8.4% and an average absolute error of 4.2%. The simplified equation predicted the experimental results from reinforced concrete beams by Kalkan (2009) with a maximum error of 13.3% and an average absolute error of 4.1%.

The first experiment with the PCI BT-54 was a study on the deformation of the girder due to solar radiation. Solar radiation on the top and side of the girder, wind speed, internal strain, air temperature, internal temperature and surface temperature were recorded to determine additional sweep or rotation in the girder due to non-uniform heating. The research showed that the initial sweep of the 101-ft. (30.8 m) PCI BT-54 girder increased up to 40% due to the effect of solar radiation on the girder, an additional sweep of 0.0515-in. (1.31 mm) per 10-ft. (3.05 m) of girder length. However, only 0.000212 radians of additional rotation was developed due to the non-uniform heating of the girder.

The PCI BT-54 was tested under midspan point load to examine its rollover behavior. For the stability experiment, full torsional restraint was not provided at the supports. Instead, torsional restraint was only provided by the couple created by the bottom flange and the elastomeric bearing pads. The girder was first loaded to 29 kips (129 kN) and the rigid body rotation of the girder was significantly more than anticipated. The large rigid body rotation was due to the lack of flatness of the bottom flange of the girder at the supports which allowed the girder to "roll" on the elastomeric bearing pad. A retrofit was performed to provide a flat bearing surface. Upon the second loading of the girder, the load versus lateral displacement and load versus rotation response

corresponded well with the prediction from the nonlinear incremental analysis that included a bearing pad model. A rollover failure occurred well before an inelastic lateral-torsional buckling mode was anticipated. In fact, the girder never cracked during the testing. The nonlinear incremental analysis did not predict the rollover failure because of the assumption made in the elastomeric bearing pad model. Imperfect bearing conditions were not modeled and nonlinear bearing stiffness behavior at large rotations was most likely inaccurate. The rollover methodology proposed by Mast (1993) predicted the rollover limit state very well.

From the research, it was apparent that rollover is the controlling stability phenomenon for prestressed concrete bridge girders. The nonlinear lateral-torsional stability failure is unlikely because prestressed concrete bridge girders are designed to not crack under self-weight alone. Therefore, the inelastic lateral-torsional buckling simplified equation initial imperfection reduction parameters do not apply to bridge girders with large flanges. Instead, the elastic lateral-torsional buckling predictions should be used. However, the elastic lateral-torsional buckling loads were found to be greater than the rollover limit for girders with no end support lateral bracing.

9.2 Conclusions

The following conclusions were made based on the experimental and analytical research.

1. For prestressing strands fully bonded to the concrete, the prestressing force did not have a destabilizing effect on the beams. In fact, the prestressing strands increased the stability of the beams because the prestressing caused a larger

compression zone depth, and, therefore, a higher lateral and torsional stiffness. Any prestressing strand design (force and strand location) that increases the compression zone depth increases the lateral-torsional buckling stability of the cross-section.

2. Imperfections had a significant effect on the stability behavior of prestressed concrete beams. For inelastic lateral-torsional buckling, imperfections caused a rotated neutral axis angle, and, therefore, reduced the weak-axis moment of inertia more than was predicted with a rectangular compression zone. Furthermore, increased initial imperfections increased that rate of additional lateral displacement and rotation, thereby increasing the torsion on the cross-section which inevitably led to torsional cracking when the beams reached unstable behavior. The initial imperfections significantly affected the load versus lateral displacement and load versus rotation behavior. The rate of increase of lateral displacement and rotation increases due to increased initial imperfections, and, therefore, lead to rollover at lower loads. The BT-54 girder reached a rollover behavior without becoming inelastic.

3. The existing analytical methods to predict the lateral-torsional buckling loads of prestressed concrete and reinforced concrete beams were inadequate. The methods that were reasonable neglected the effect initial imperfections had on the stability behavior. The existing methods thus serve as upper bounds and are not conservative.

4. A material and geometric nonlinear incremental-load analysis was performed to predict the load versus lateral displacement and load versus rotation behavior of prestressed concrete beams in flexure. The analysis predicted the maximum loads well with a maximum error of 2%. The analysis predicted the lateral displacement and rotation behavior well; however, there were some inconsistencies between the experimental and analytical load-deflection curves because of the assumptions made in the analysis and experimental error.

5. The simplified equation predicted the buckling loads of the rectangular experimental beams of this study well with a maximum error of 7.5% and an average absolute error of 4.8%. The simplified equation was also compared with the experimental results for the reinforced concrete and prestressed concrete beams from König and Pauli (1990) and the reinforced concrete beams from Kalkan (2009). The simplified equation prediction for the experimental results from König and Pauli (1990) resulted in a maximum error of 8.4% and an average absolute error of 4.2%. The simplified equation tended to slightly under-predict the buckling load of the flanged cross-sections of the experimental study by König and Pauli (1990). The simplified equation predicted the experimental results from Kalkan (2009) with a maximum error of 13.3% and an average absolute error of 4.1%. Note that the reduction parameters from Equations 6.22, 6.32 and 6.33 were developed and calibrated for a specific range of initial sweep and initial rotation, and, therefore, if these maximums are exceeded, the reduction parameters are not necessarily accurate due to a lack of verification. The limit on the maximum initial sweep is 5/16-in. (7.94 mm) per 10-ft. (3.05 m) of span,

which is 150% larger than the PCI tolerance (PCI, 2000). The limit on the maximum initial rotation is $\theta_i/h < 0.8$.

6. The nonlinear incremental analysis was applied to the BT-54 girder experiment and the analytical results matched very well with the experimental load versus lateral displacement and load versus rotation when the shear displacement of the bearing pads and the end rotation of the girder due to the compliance of the bearing pads were omitted. The nonlinear incremental analysis predicted the general trend of the end rotation behavior due to the bearing pad compliance but did not match perfectly because of the assumptions and simplifications used in the bearing pad analytical model.

7. Rollover behavior controlled for the BT-54 experimental girder and rollover will control for typical bridge girders and typical bridge girder conditions because prestressed concrete bridge girders are designed to not crack under self-weight. For girders that are extremely long, and for new bridge girder cross-section geometries, elastic lateral-torsional buckling should be checked even if the ends are braced.

8. It is hypothesized from this research that there is a transition between inelastic lateral-torsional buckling and elastic lateral-torsional buckling for cases where flexural cracking is not anticipated. In such a transition case, the inelastic simplified stability analysis will under-predict the buckling load because the cracking will be less extensive than the conditions that the simplified equation was based on and the elastic buckling load will over-predict the buckling load.

9. The nonlinear incremental analysis can be used to predict the lateral-torsional buckling load and the rollover behavior assuming the bearing pad stiffness model used is accurate. The analytical procedure by Mast (1993) predicted the rollover load well, but the procedure is dependent on the assumed rotational stiffness of the support.

10. The rollover behavior was very sensitive to bearing pad width. Using a wider bearing pad increases the factor of safety against rollover significantly. The 18-in. (457 mm) wide bearing pads used as bearings for the girders that collapsed in Arizona coupled with the large initial bearing rotations were probably the most significant contributing factors to the collapse. Furthermore, a rounded bottom flange will significantly increase the equilibrium rotation when the girder is placed, thereby causing a girder to become more unstable.

11. The research showed that the initial sweep of the 101-ft. (30.8 m) PCI BT-54 girder increased up to 40% due to the effect of solar radiation on the girder. Little additional initial rotation was observed during the study.

9.3 Recommendations

The following recommendations are made for the analysis and design of slender reinforced and prestressed concrete members.

9.3.1 Analysis & Design Recommendations

1. Use the simplified Equation 6.34 including the reduction parameters from Equation 6.22, 6.32 and 6.33 given below that take into account initial

imperfections to estimate the inelastic lateral-torsional buckling load of slender

reinforced concrete and prestressed concrete beams. The inelastic lateral-

torsional buckling load simplified analysis should be used when flexural cracking

is anticipated. Note that the reduction parameters from Equations 6.22, 6.32 and

6.33 were developed and calibrated for a specific range of initial sweep and initial

rotation, and, therefore, if these maximums are exceeded, the reduction

parameters are not necessarily accurate due to a lack of verification. The limit on

the maximum initial sweep is 5/16-in. (7.94 mm) per 10-ft. (3.05 m) of span,

which is 150% larger than the PCI tolerance (PCI, 2000). The limit on the

maximum initial rotation is $\theta_i/h < 0.8$.

$$B_r = B \left[1 - \frac{1}{3} \tan^{-1} \left(\frac{I_{gx}}{I_{gy}} \theta_0 \right) \frac{2}{\pi} \right] \tag{9.1}$$

$$\Delta_r = 1 - \left(\frac{\delta_0}{L} \right)^{0.31} \tag{9.2}$$

$$\Theta_r = e^{-26.5\theta_0} \tag{9.3}$$

$$M_{b\,imperfections} = \frac{\pi}{L} A \sqrt{B_r C} \; \Delta_r \Theta_r \tag{9.4}$$

2. To increase the lateral-torsional buckling load of a slender reinforced concrete or prestressed concrete beam, the span can be decreased, intermediate bracing can be added, the geometry can be changed to decrease the slenderness, or prestressing force can be increased. Increasing the prestressing force results in a higher cracking moment and a larger compression zone, thereby increasing the weak-axis moment of inertia and torsion constant so long as the effects of prestressing do not cause tension in the compression flange.

3. For cases where the inelastic behavior (concrete cracking) is not expected, initial imperfections will not reduce the lateral-torsional buckling load for most cases, and, therefore, the elastic lateral-torsional buckling load applies. The specific cases where initial imperfections could still reduce the lateral-torsional buckling load are if the initial imperfections are so large that cracking initiates at the top flange or if the stresses in the bottom flange are very close to the rupture stress, and, therefore, imperfections can cause cracking at the corner of the bottom flange. For cracking of the top flange, different stiffness reduction parameters are required because the simplified equation was developed for flexural cracking progressing from the bottom flange. For a small amount of cracking at the corner of the bottom flange, the reduction parameters of the simplified equation would under-predict the lateral-torsional buckling load.

4. For prestressed concrete bridge girders, rollover will control over lateral-torsional buckling for cases where the ends are not laterally braced. Prestressed concrete bridge girders are designed to not crack under self-weight; therefore, the elastic lateral-torsional buckling load applies. For AASHTO and PCI BT bridge girder

cross-sections, the elastic lateral-torsional buckling load will be greater than the self-weight, thus rollover controls. Furthermore, the rollover methodology from Mast (1993) predicted the rollover load of the BT-54 from this research, and, therefore, should continue to be used as the method to predict the factor of safety against rollover failure.

5. Lack of flatness of the bottom flange of a prestressed concrete bridge girder was shown in this research to increase the initial rotation of the girder which can cause a premature rollover failure. Using an embedded steel plate in the bottom flange at the location of bearing is recommended to remove the effect of imperfections in forming the concrete of the bottom flange. Furthermore, the embedded steel plates have additional benefits in the fabrication of prestressed concrete bridge girders such as the reduction of bearing zone cracking (Kelly, 2006).

6. From rollover analyses using Mast (1993), the width of the elastomeric bearing pads should be selected as the width of the bottom flange of the prestressed concrete bridge girder (minus the edge chamfers). The factor of safety against rollover failure for a 100-ft. (30.5 m) PCI BT-54 was 39% lower for an 18-in. (457 mm) wide elastomeric bearing pad as opposed to a 24-in. (610 mm) wide elastomeric bearing pad

7. Future long-span prestressed concrete bridge girder geometries should have increased bottom flange widths to decrease susceptibility to rollover failures of girders while being erected. Increasing the bottom flange width is the most effective way to change the geometry and increase the factor of safety against

rollover of the girder. The weak-axis moment of inertia is affected favorably by an increase in the bottom flange width and the larger bottom flange width allows for a wider elastomeric bearing pad to be used. The implementation of a wider bottom flange only at the support locations coupled with a wider bearing pad provide the best economy with respect to the use of materials in increasing the factor of safety against rollover of a prestressed concrete bridge girder; however, an efficient and economical fabrication methodology to create a wider bottom flange only at a specific location needs to be explored.

8. A prestressed concrete bridge girder should be laterally braced adequately at the supports as soon as possible after the girder is erected. Such bracing will reduce the possibility of rollover failures.

9.3.2 Future Research Recommendations

1. Finite element modeling should be done to further verify the simplified equation (Equation 6.34) and to improve upon the equation. Furthermore, the transition behavior between inelastic and elastic buckling can be investigated by the use of finite element modeling that has been verified with fully inelastic experiments.

2. An experimental study needs to be performed on the axial and rotational stiffness of elastomeric bearing pads at loads in the range of the self-weight of a prestressed concrete bridge girder. Because the assumed rotational stiffness is important to the rollover behavior it is crucial to have an accurate prediction of the actual support rotational stiffness. Traditionally the elastomeric bearing pad stiffness is found by assuming a linear axial stiffness based on the loading the

elastomeric bearing pads will encounter under service conditions; however, rollover failures occur under the self-weight of the girders alone when the stiffness of the bearing pad has been shown to be nonlinear.

3. The extent of bottom flange flatness error must be determined from a survey of prestressed concrete girders from many different precast plants. The extent of the bottom flange flatness error can be used to help determine if requiring an embedded steel plate is necessary.

4. A criterion is required for the initial rotation of prestressed concrete bridge girders. The PCI Bridge Design Manual (2003) specifically states a tolerance on initial sweep in a prestressed concrete girder, but does not explicitly state a tolerance on initial rotation.

5. A criterion is necessary to determine the required lateral bracing strength and stiffness that will prevent a rollover failure. It is stipulated in Section 9.3.1 that a prestressed concrete bridge girder should be laterally braced adequately at the supports to prevent rollover failures due to unforeseen circumstances. Therefore, "adequate" bracing must be defined.

6. Methods to increase the factor of safety against rollover of a prestressed concrete bridge girder when the girder is hanging from a crane or when the girder is in transport needs to be researched. This study focused on prestressed concrete girders supported from below on rollers or elastomeric bearing pads; however, hanging girders and girders in transport are also prone to rollover failures.

APPENDIX A

SUMMARY OF SPECIMEN CHARACTERISTICS
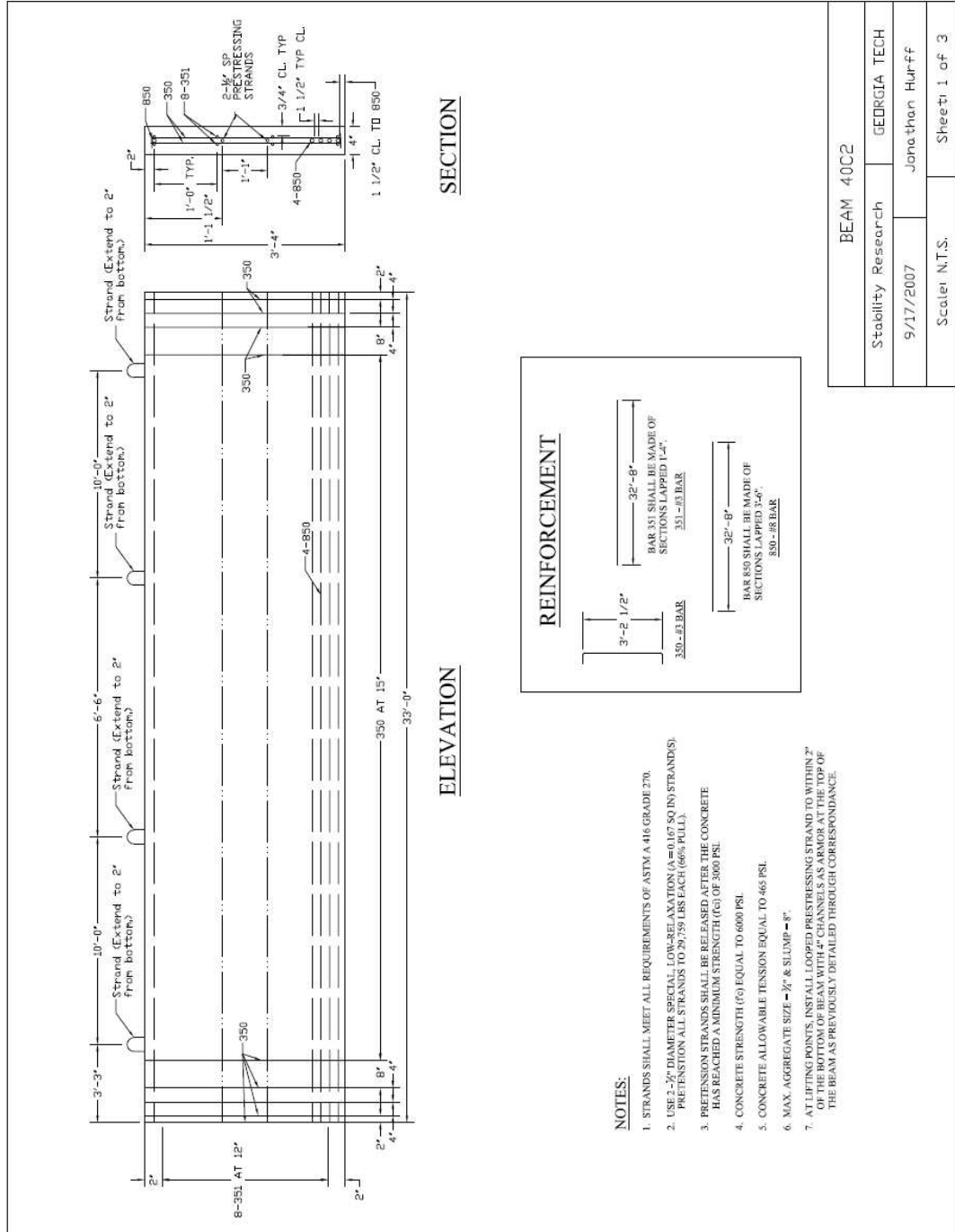
Figure A.1 – Design drawing C2
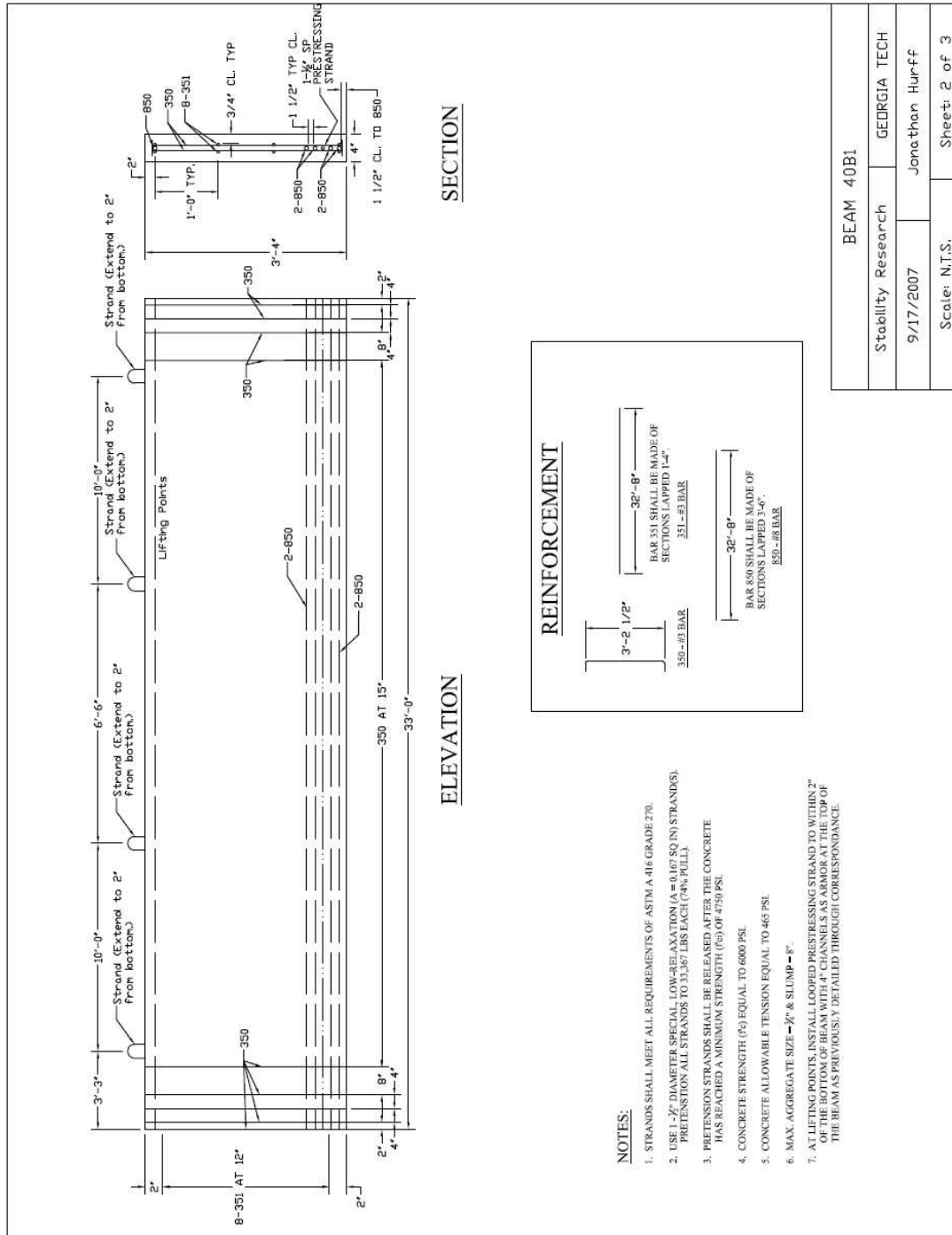
Figure A.2 – Design drawing B1
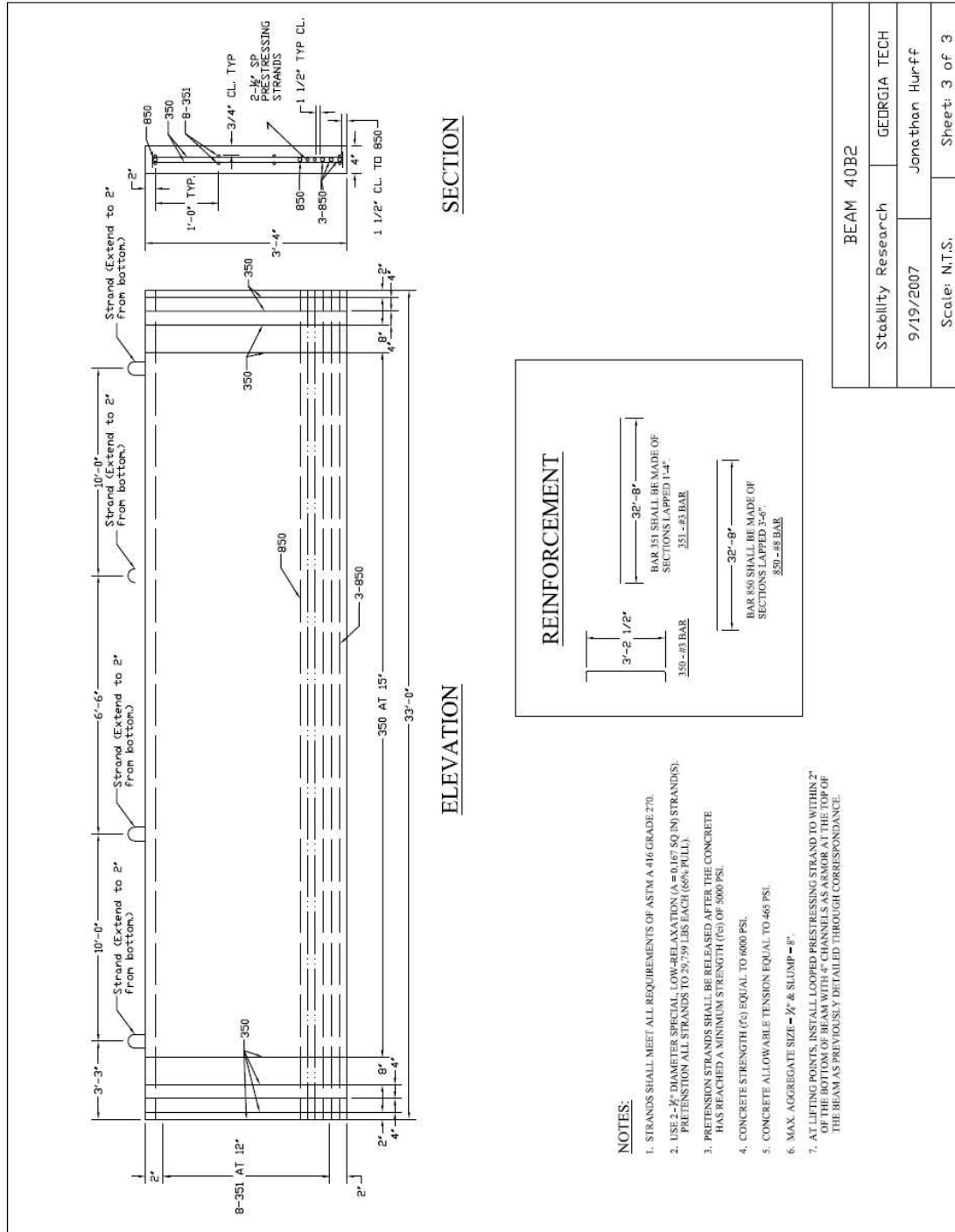
Figure A.3 – Design drawing B2
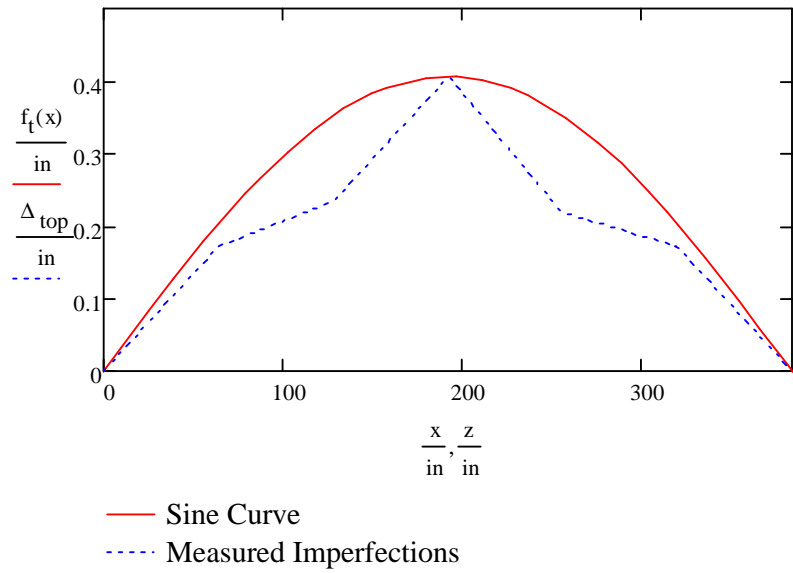
Figure A.4 – Initial horizontal displacement at top of Beam B1A
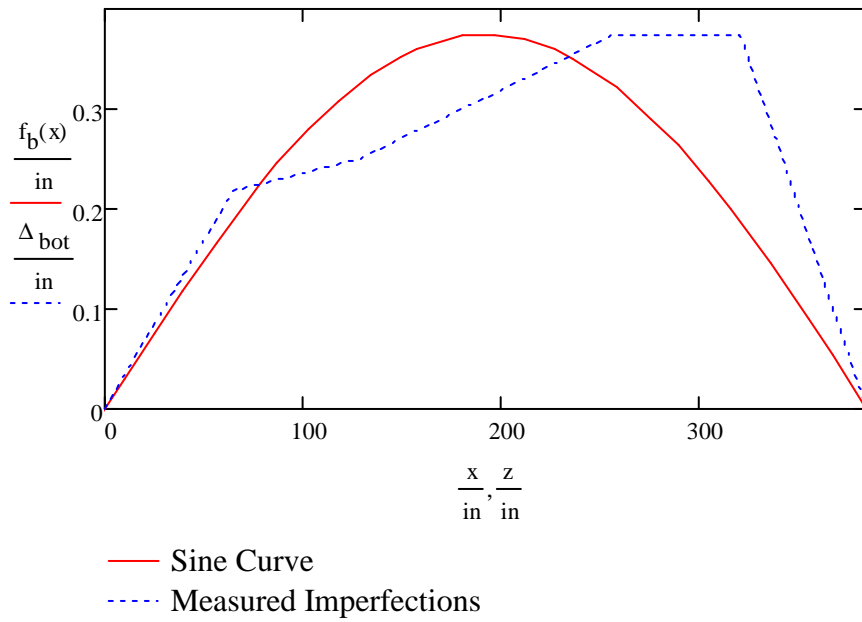
Figure A.5 – Initial horizontal displacement at bottom of Beam B1A
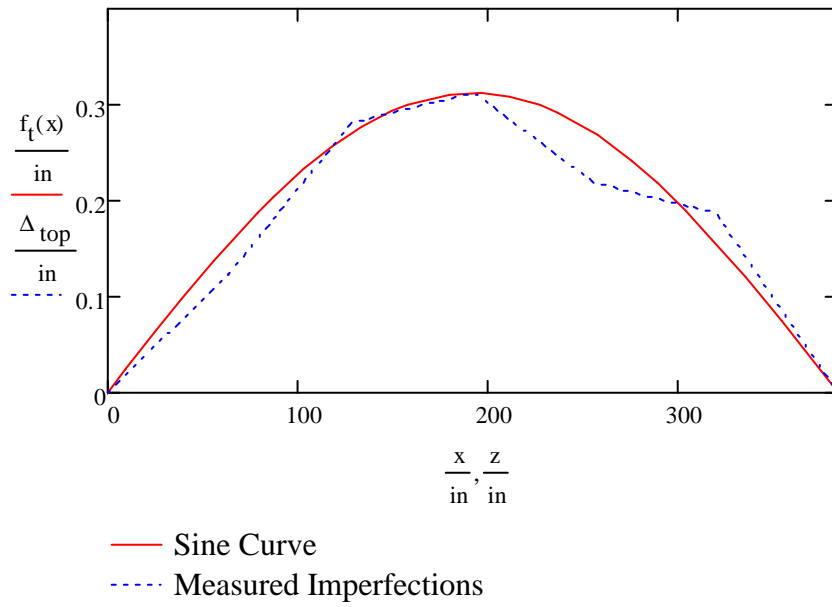
Figure A.6 – Initial horizontal displacement at top of Beam B1B
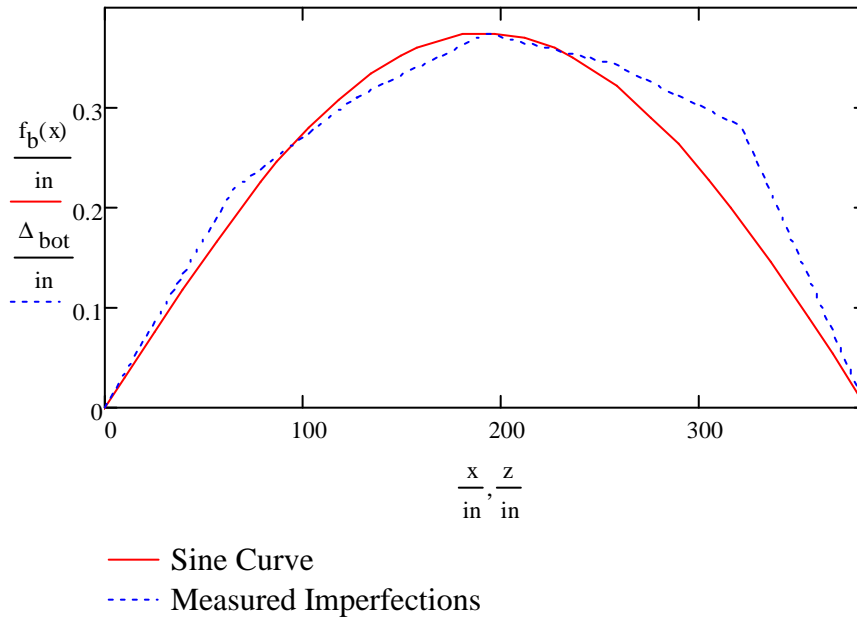
Figure A.7 – Initial horizontal displacement at bottom of Beam B1B
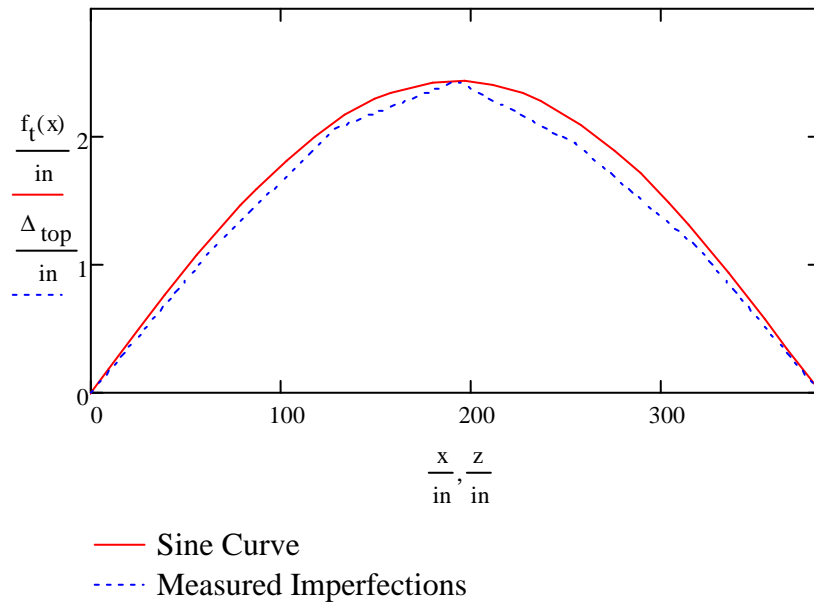
Figure A.8 – Initial horizontal displacement at top of Beam B2A
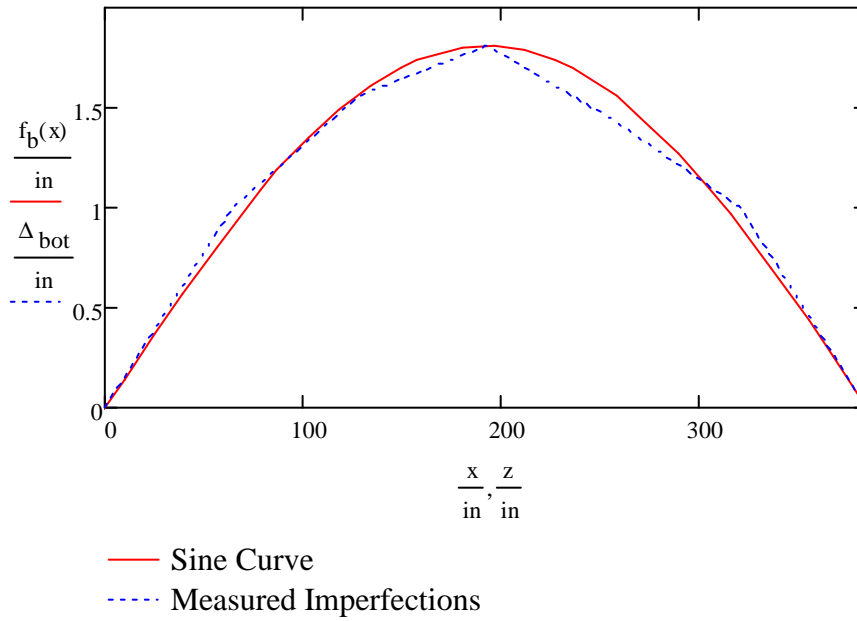
Figure A.9 – Initial horizontal displacement at bottom of Beam B2A
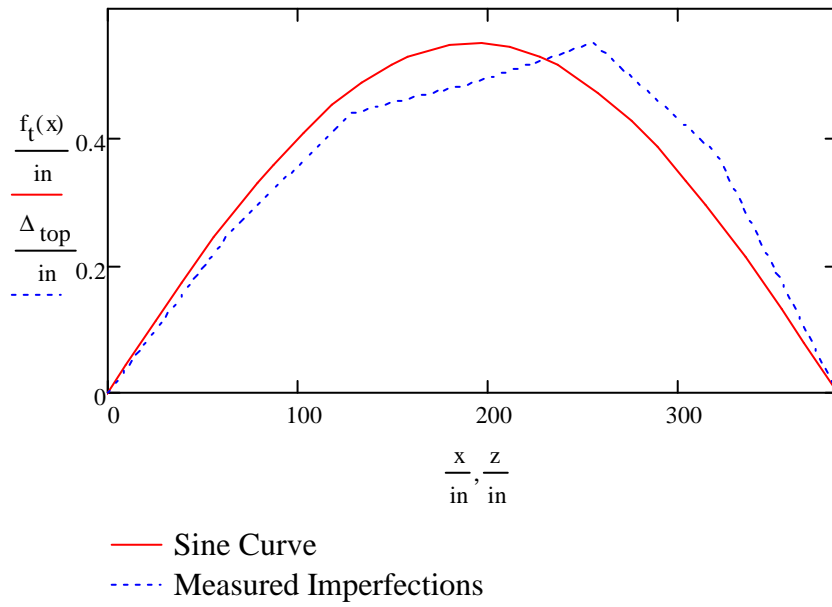
Figure A.10 – Initial horizontal displacement at top of Beam B2B
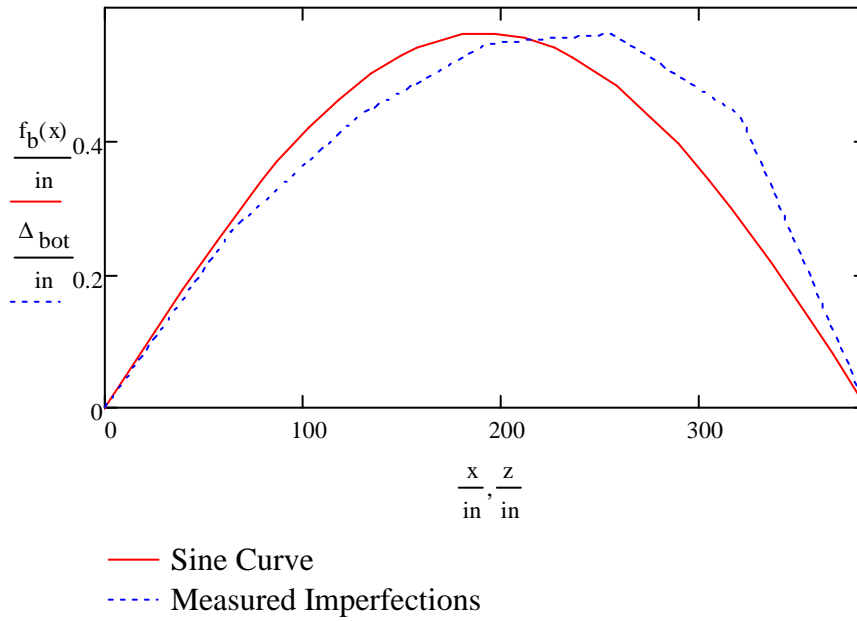
Figure A.11 – Initial horizontal displacement at bottom of Beam B2B
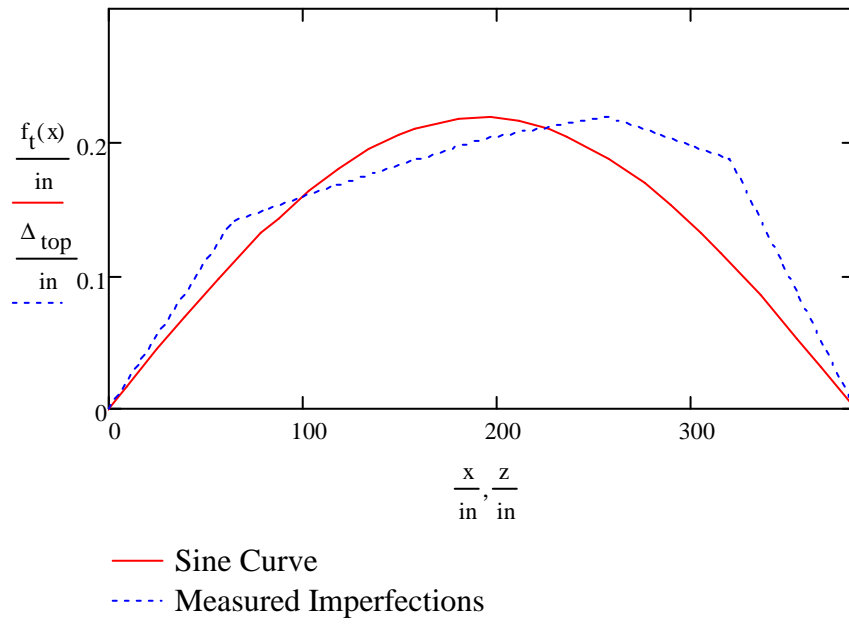
Figure A.12 – Initial horizontal displacement at top of Beam C2A
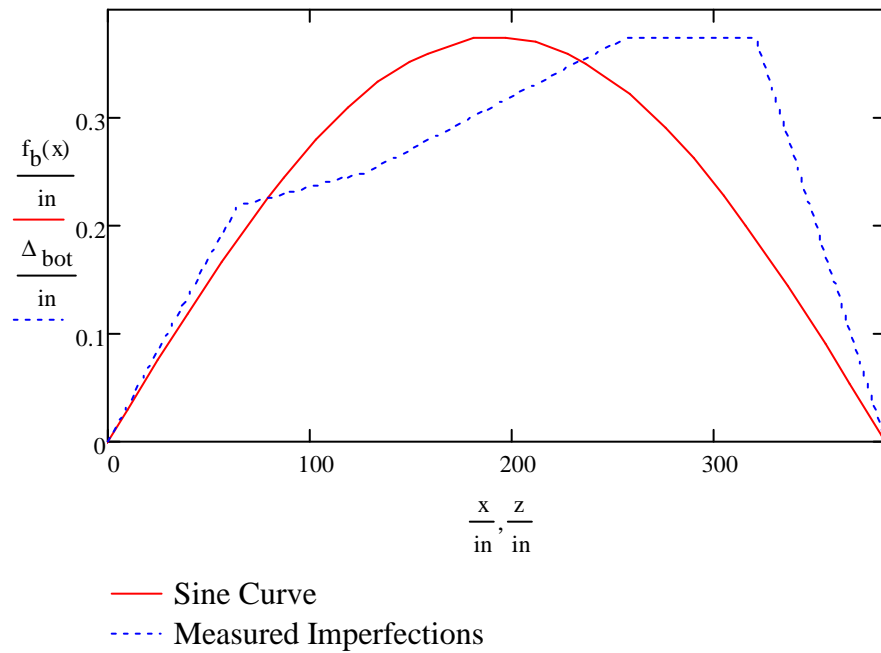
Figure A.13 – Initial horizontal displacement at bottom of Beam C2A
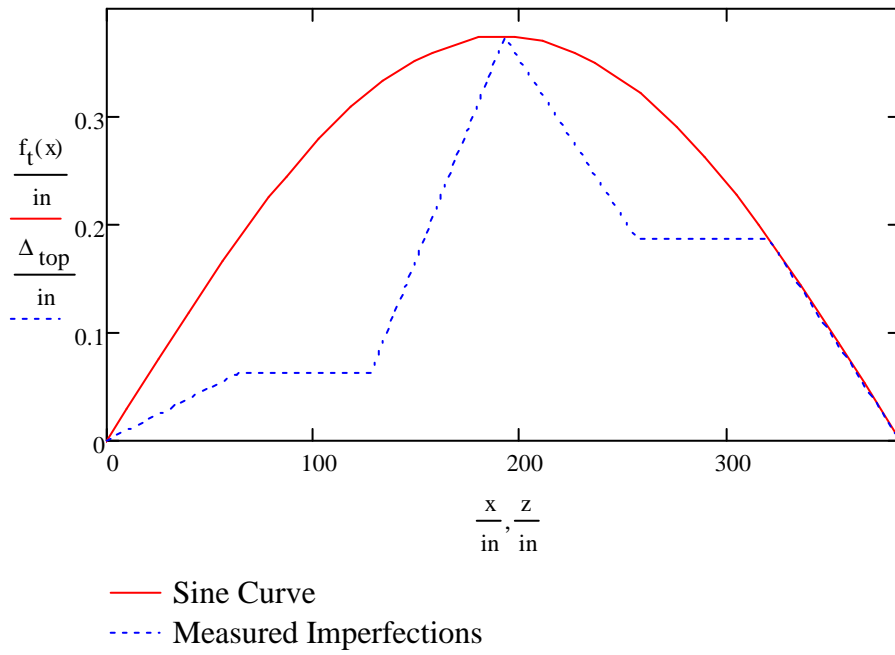
Figure A.14 – Initial horizontal displacement at top of Beam C2B
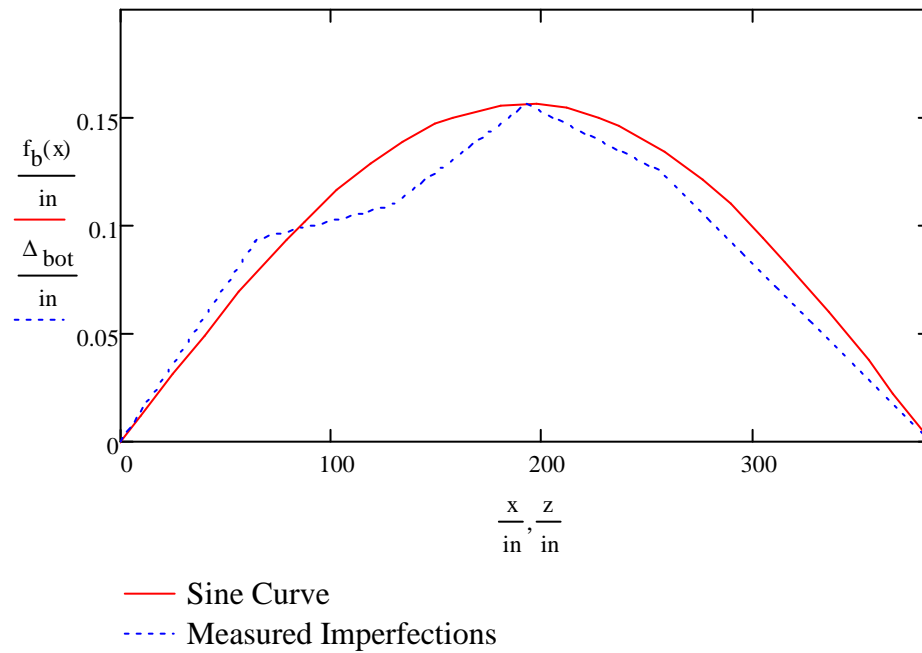
Figure A.15 – Initial horizontal displacement at bottom of Beam C2B

Figure A.16 – Prestressing strand stress-strain curve from mill certificate
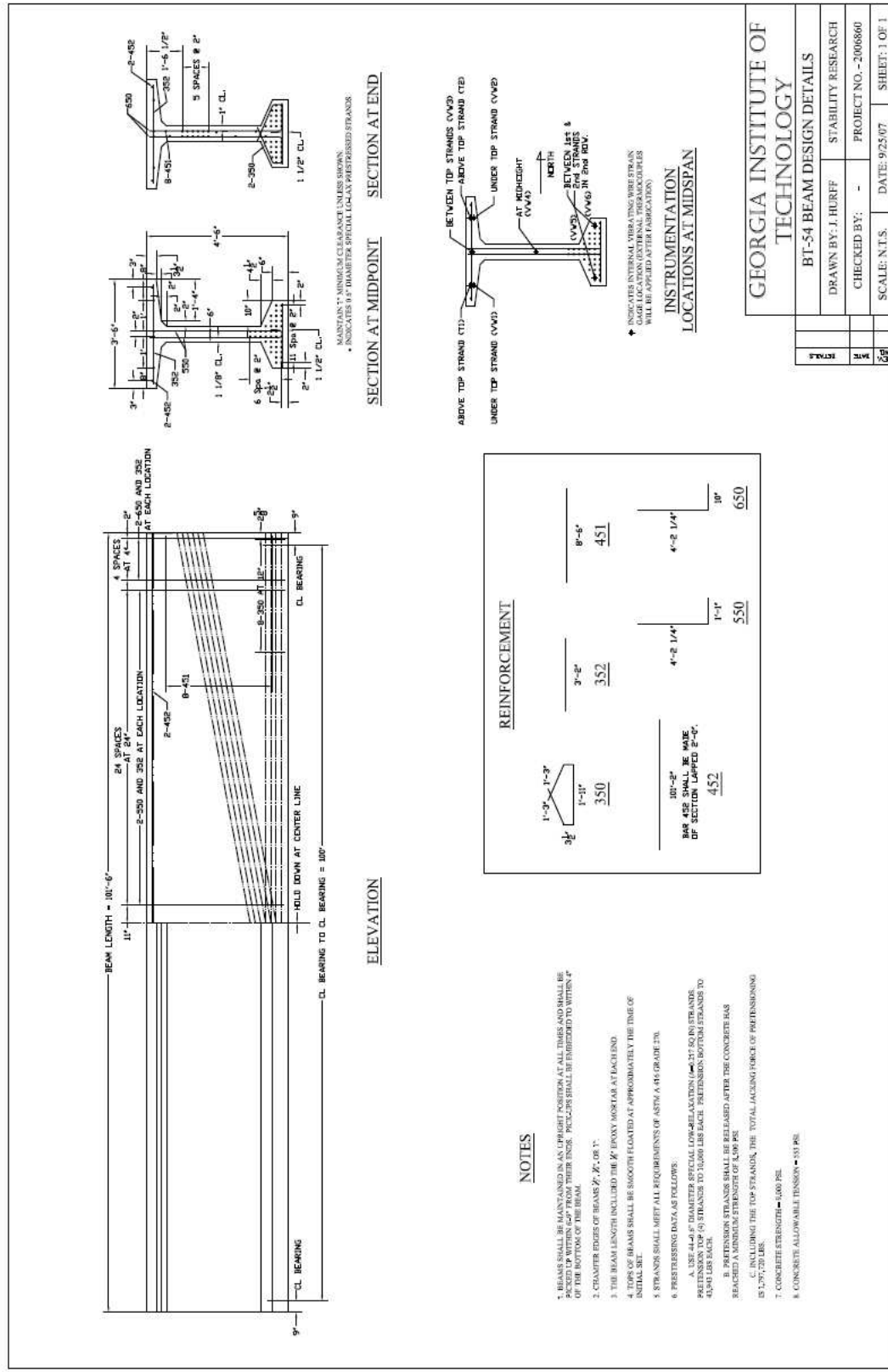
Figure A.17 – BT-54 detailed design drawing
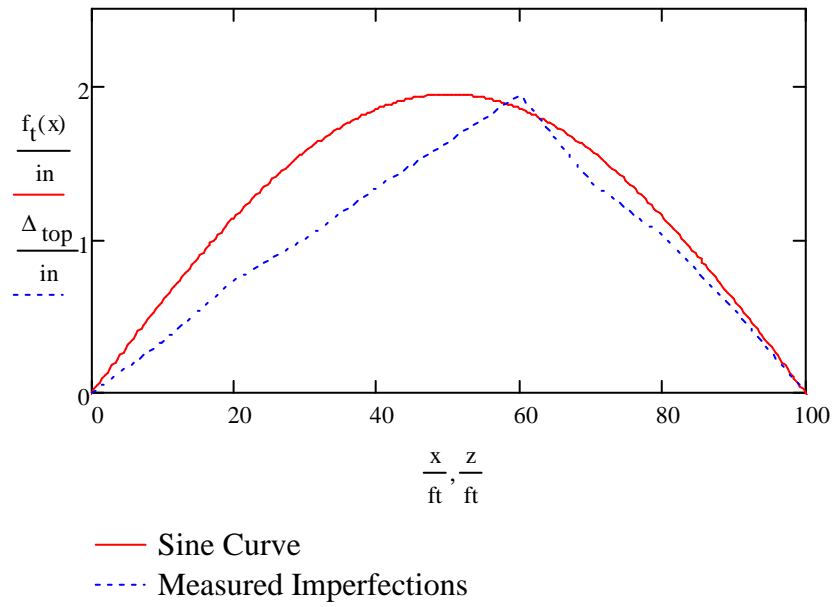
Figure A.18 – Initial horizontal displacement at top of BT-54 with level supports
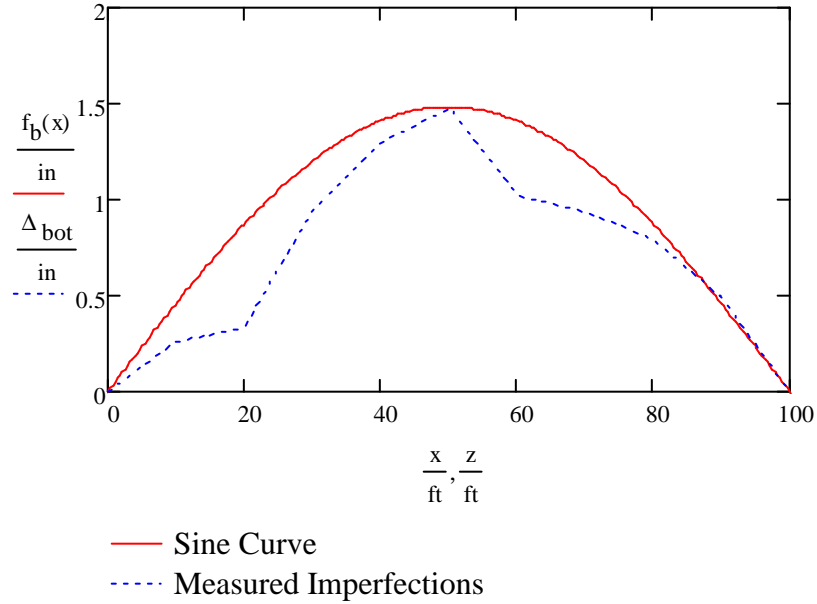
Figure A.19 – Initial horizontal displacement at bottom of BT-54 with level supports
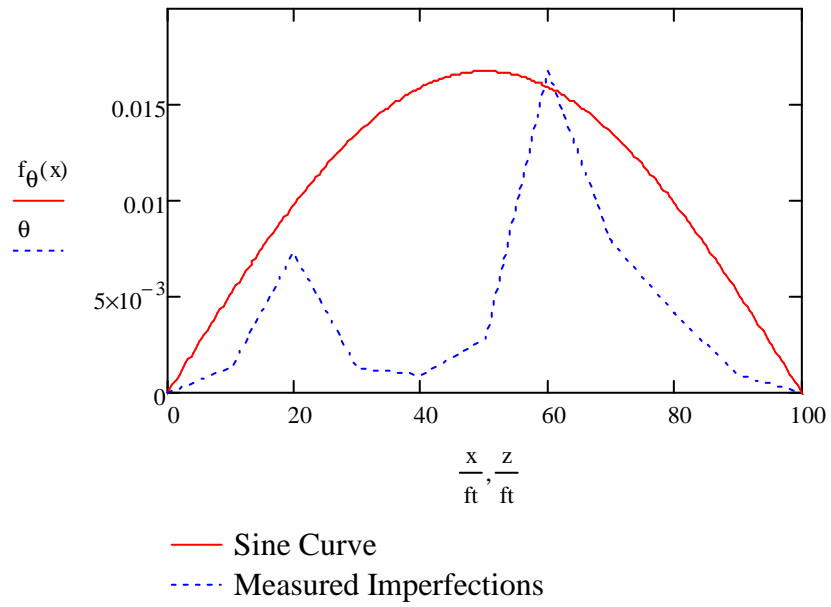
Figure A.20 – Initial rotation of BT-54 with level supports
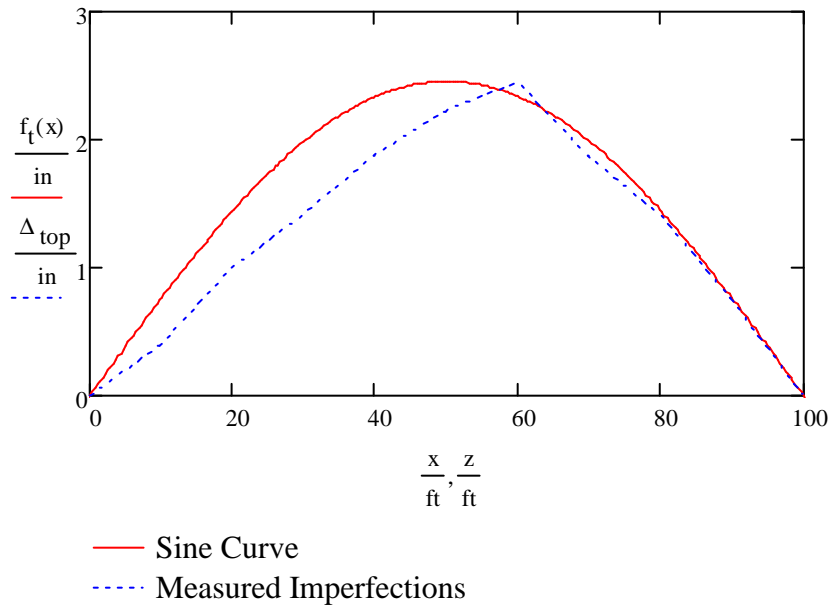
Figure A.21 – Initial horizontal displacement at top of BT-54 with rotated supports
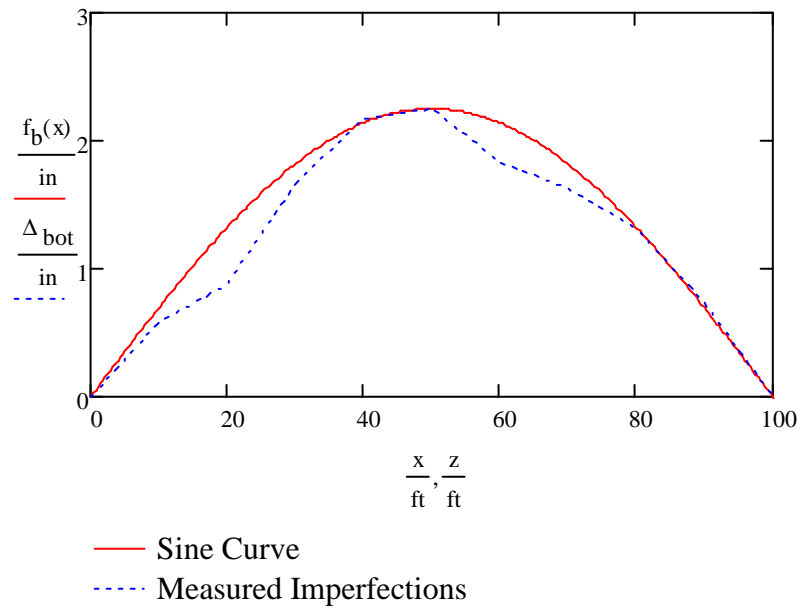
Figure A.22 – Initial horizontal displacement at bottom of BT-54 with rotated supports
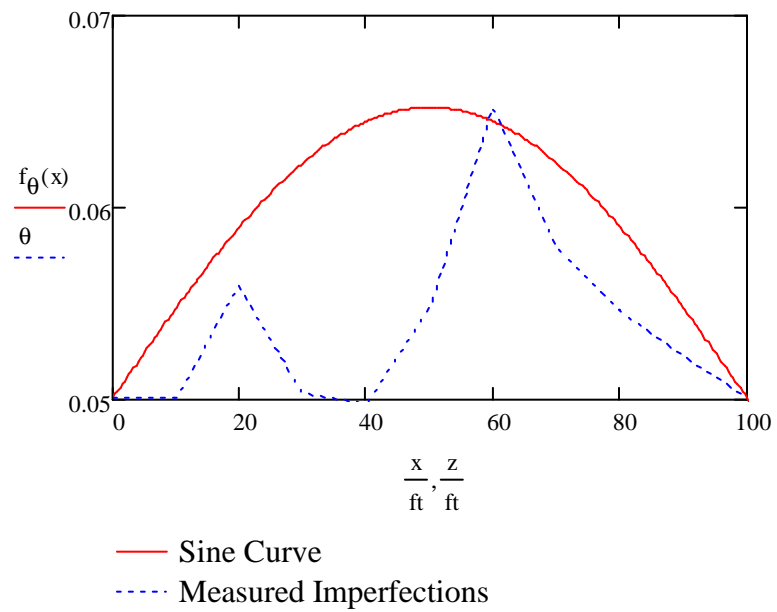
Figure A.23 – Initial rotation of BT-54 with initially rotated supports

APPENDIX B

GRAVITY LOAD SIMULATOR DESIGN & DETAILS

The design of the gravity load simulator required selecting the geometry such that the capacity could be reached, the required lateral sway could be achieved and the mechanism would function properly. To achieve a capacity that was much larger than previous gravity load simulators, the gravity load simulator was essentially designed as two parallel frames where the hydraulic ram was located between them. It was necessary for such geometry for two reasons: to reduce the load in each frame of the gravity load simulator in half because bulky members would inhibit the free movement of the gravity load simulator, and, secondly, the high loads required the use of a high capacity hydraulic ram which was large itself. There was no way to fit a large-capacity hydraulic ram in one frame; however, with two frames, the distance between them was selected based on the size of the hydraulic ram.

There was a secondary advantage to design the gravity load simulator's geometry this way. Previous gravity load simulators, due to the rigid triangular frame undergoing significant compression forces, were susceptible to out-of-plane buckling. In this design, the rigid triangular frames were braced to each other which restricted the ability for the rigid triangular frames to buckle about their pin locations, but, instead, they would have to overcome the resistance of two sets of pins separated by a relatively large distance which provided a significant couple. Details of this buckling phenomenon were discussed in Yaramici et al. (1967). Furthermore, detailed calculation procedures for

determining the geometric characteristics, as well as some "rules of thumb", were

presented in Stoddard (1997). The detailed design drawings are presented in Figures B.1

through B.16.
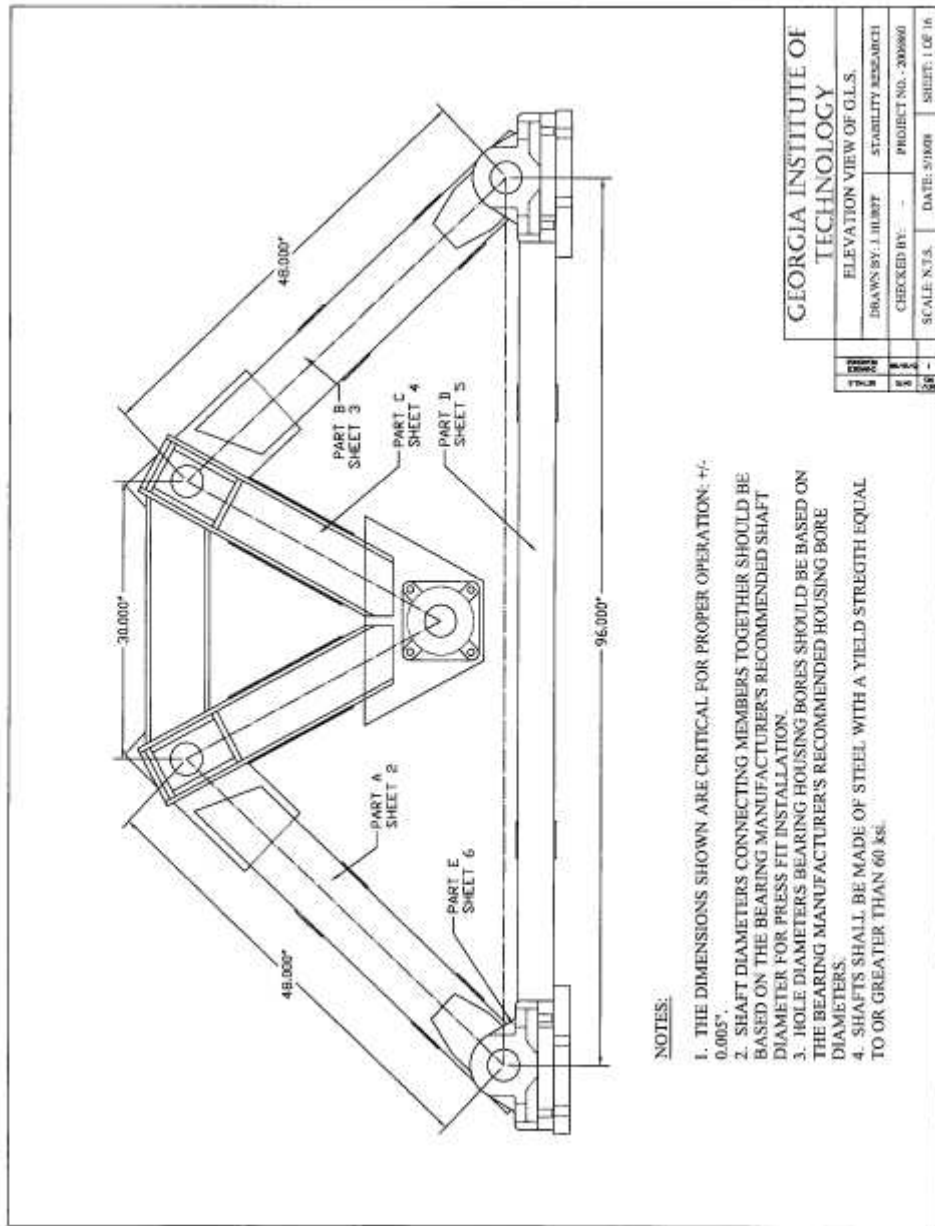
Figure B.1 – Gravity load simulator design (Sheet 1 of 16)

385
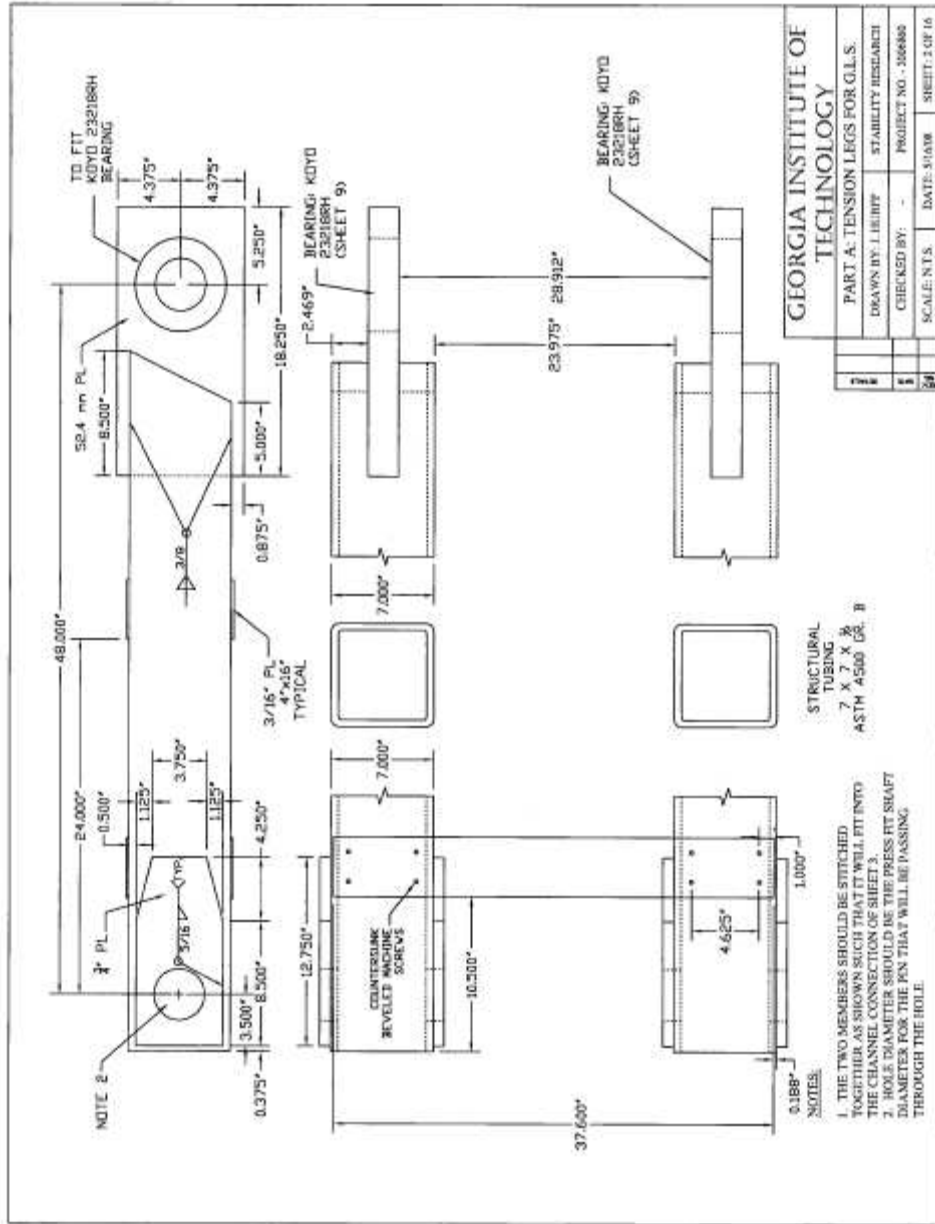
Figure B.2 – Gravity load simulator design (Sheet 2 of 16)

386
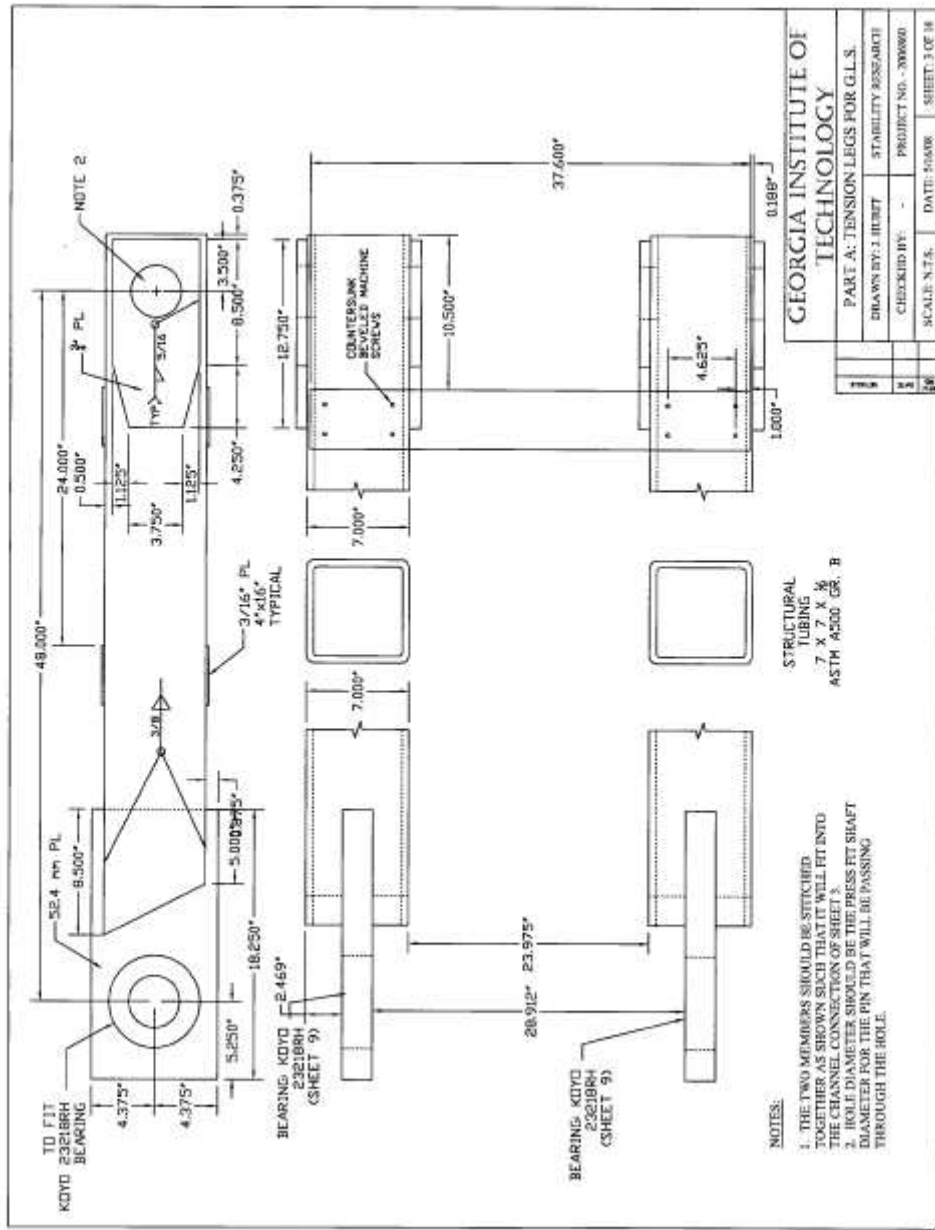
Figure B.3 – Gravity load simulator design (Sheet 3 of 16)
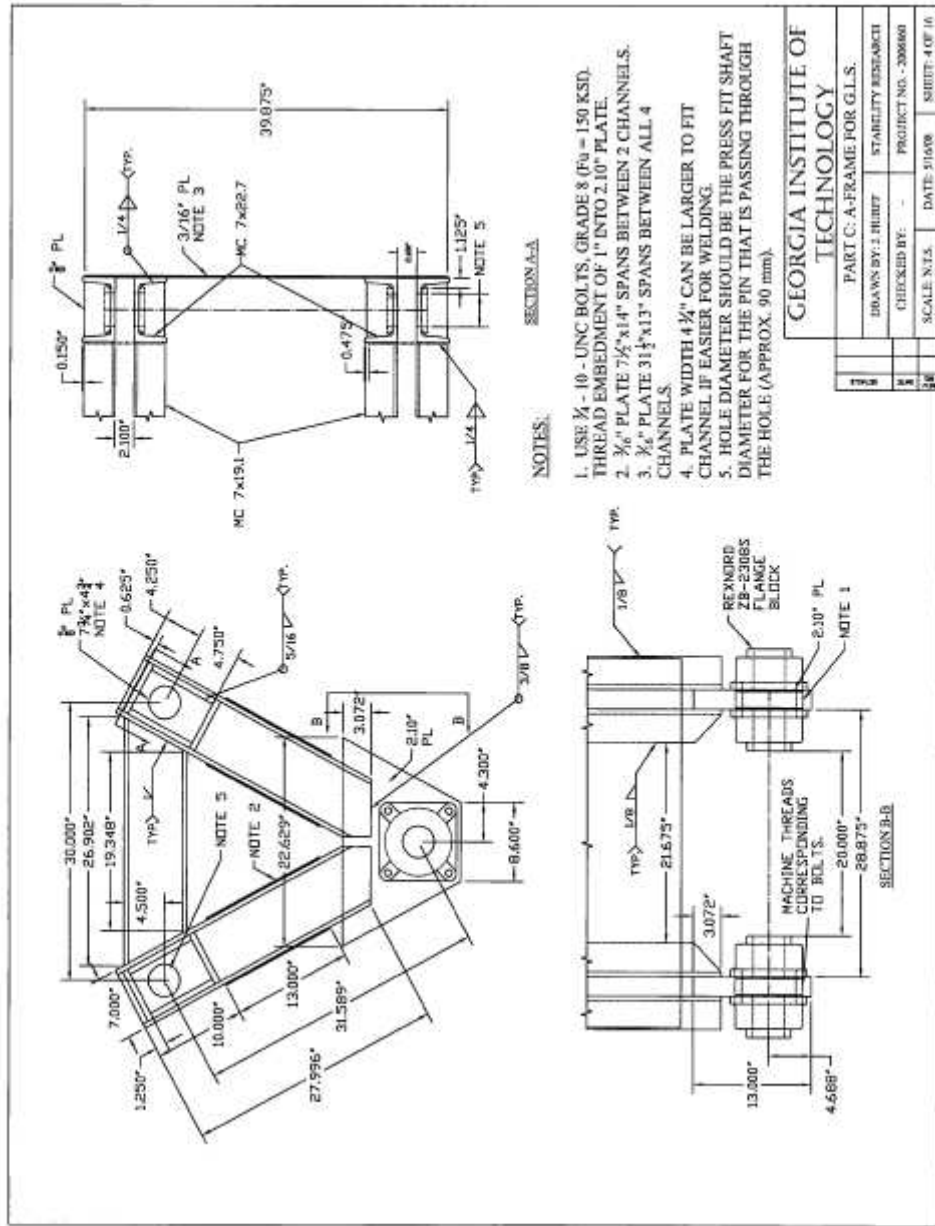
Figure B.4 – Gravity load simulator design (Sheet 4 of 16)
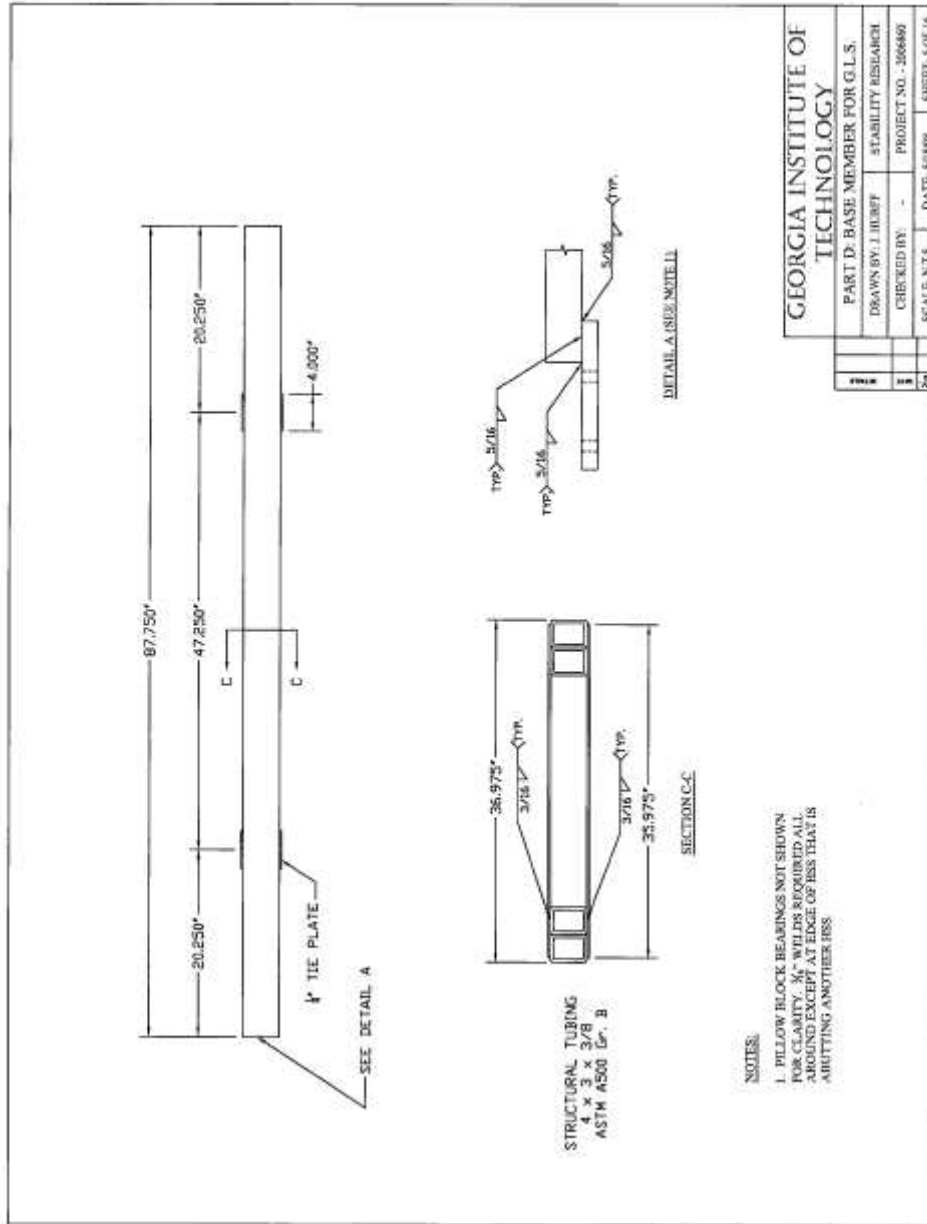
Figure B.5 – Gravity load simulator design (Sheet 5 of 16)

389

Figure B.6 – Gravity load simulator design (Sheet 6 of 16)

390
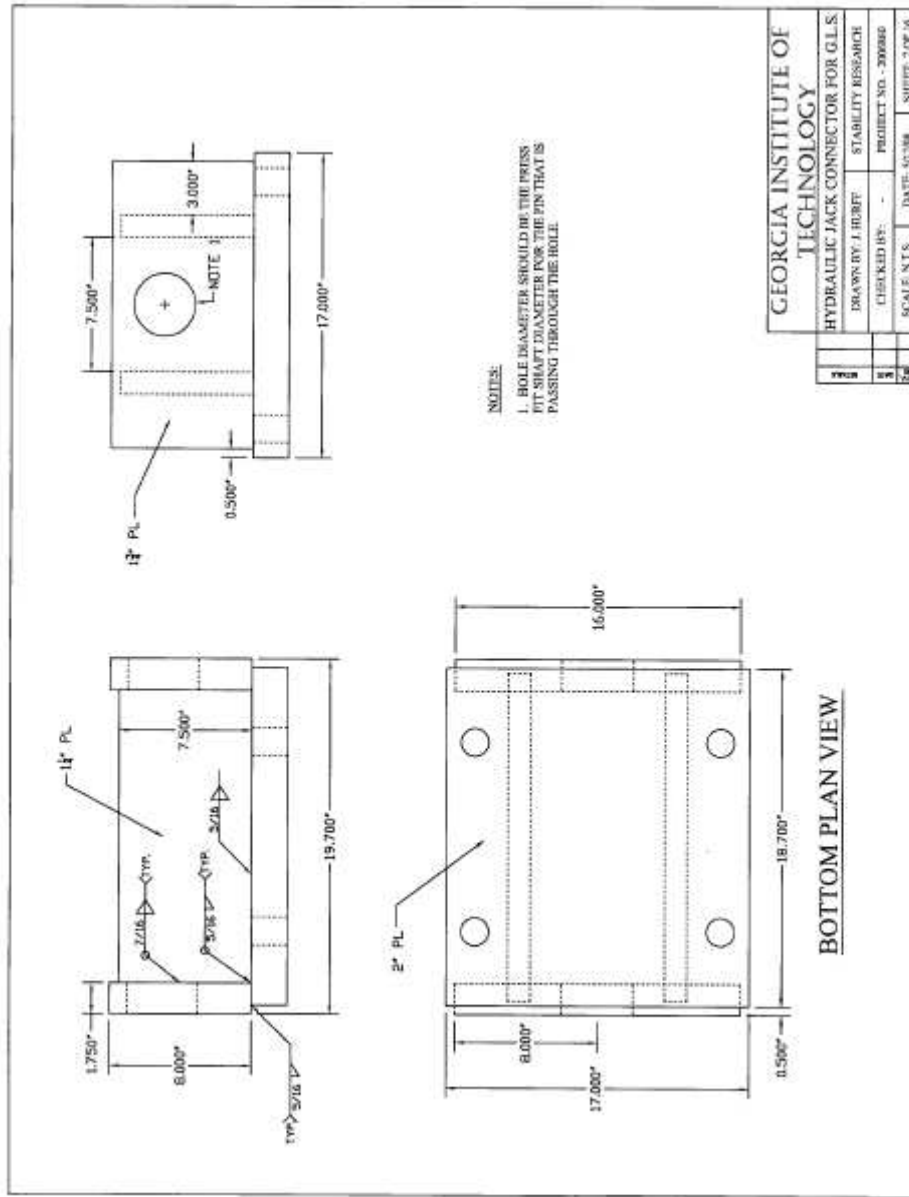
Figure B.7 – Gravity load simulator design (Sheet 7 of 16)

391
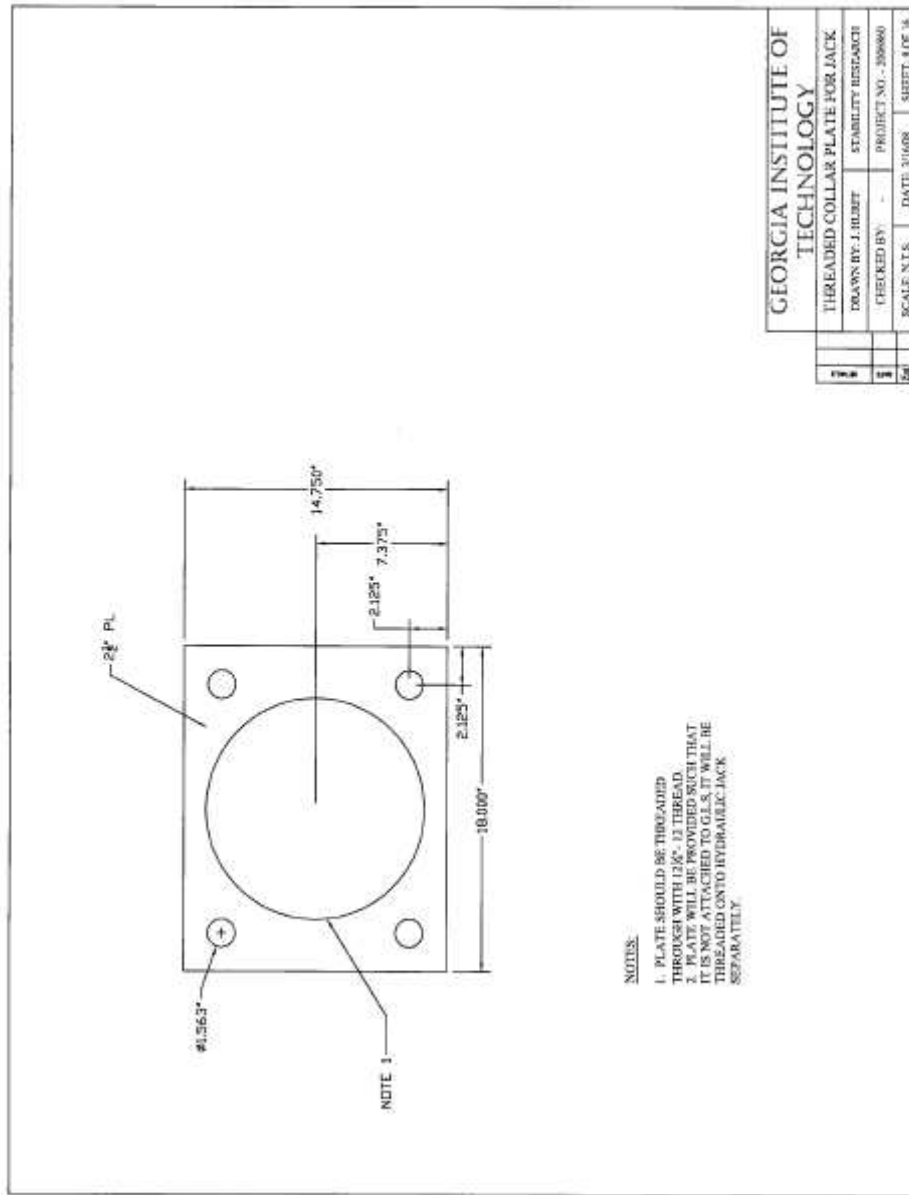
Figure B.8 – Gravity load simulator design (Sheet 8 of 16)
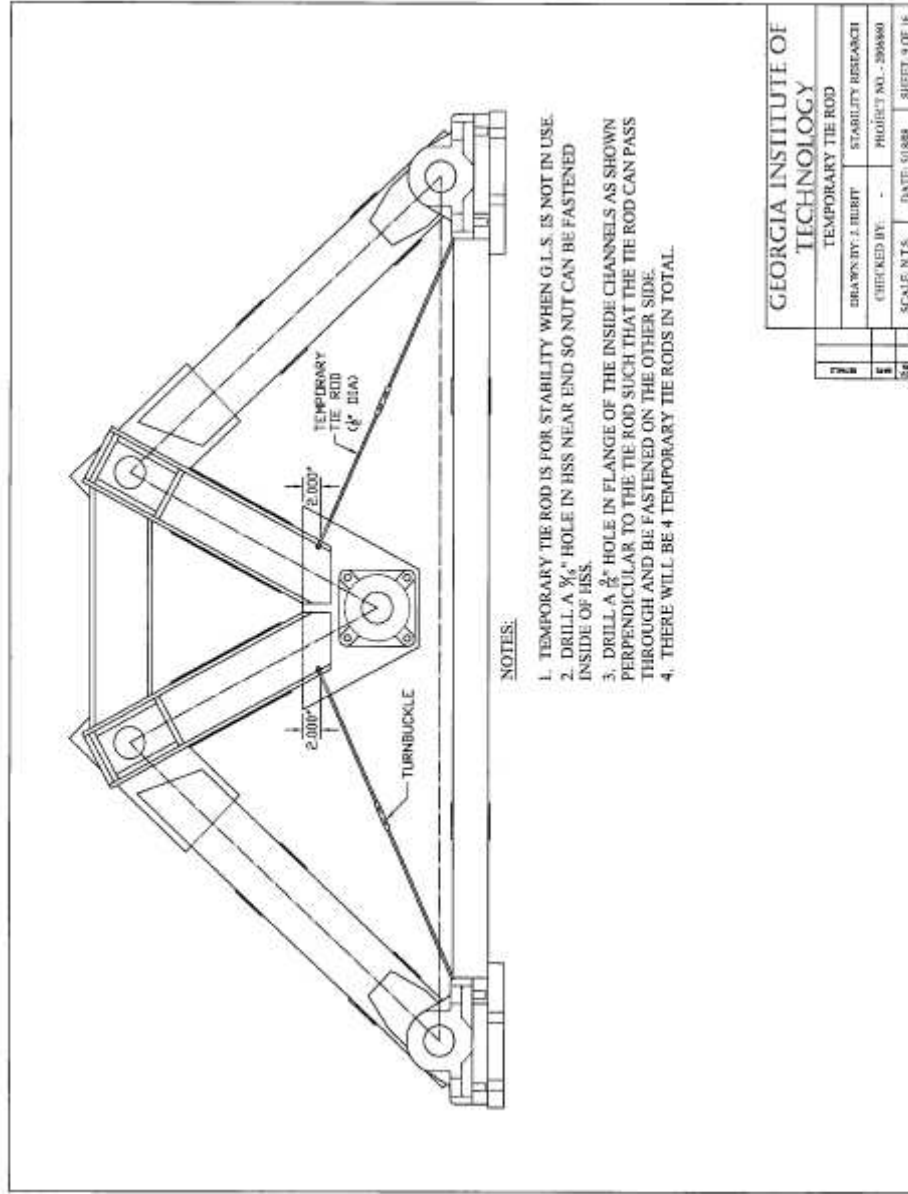
Figure B.9 – Gravity load simulator design (Sheet 9 of 16)

393
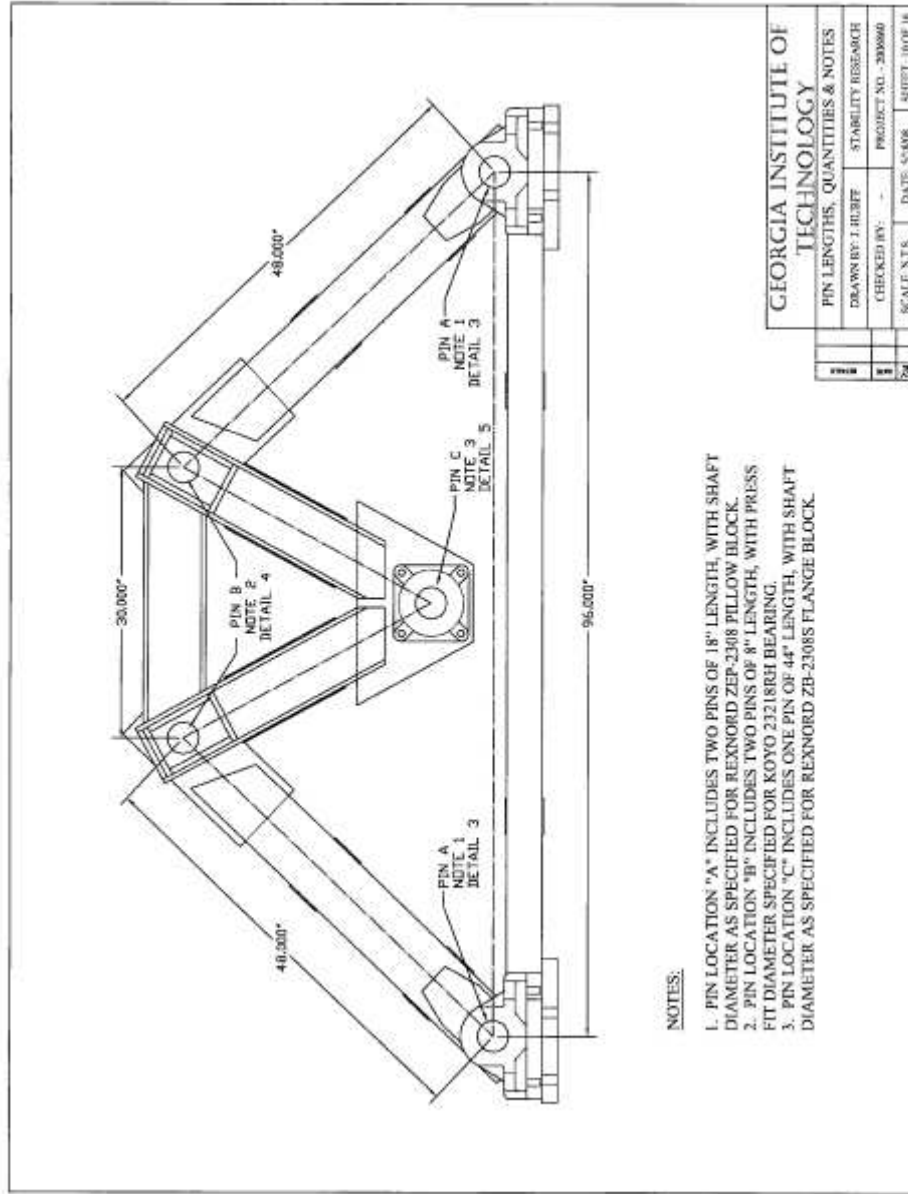
Figure B.10 – Gravity load simulator design (Sheet 10 of 16)

Figure B.11 – Gravity load simulator design (Sheet 11 of 16)
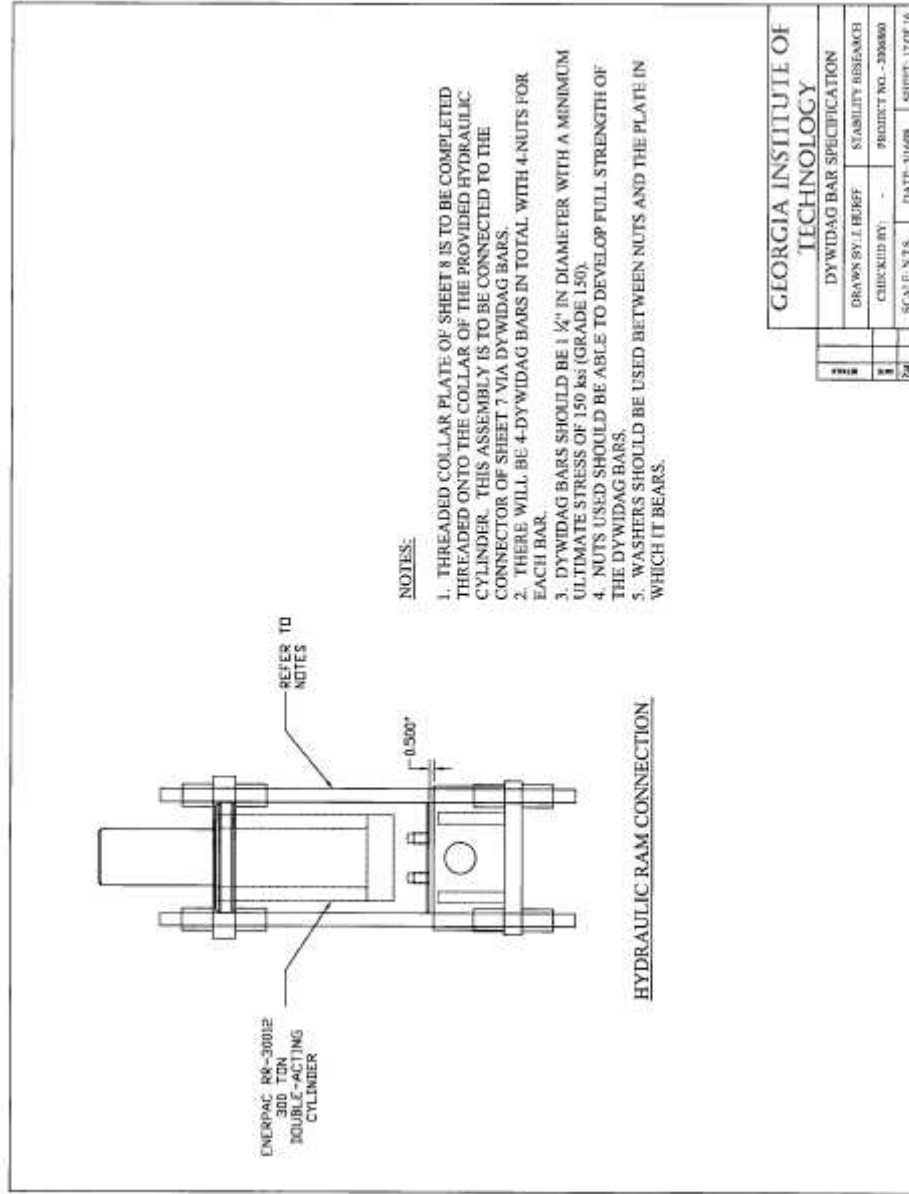
Figure B.12 – Gravity load simulator design (Sheet 12 of 16)
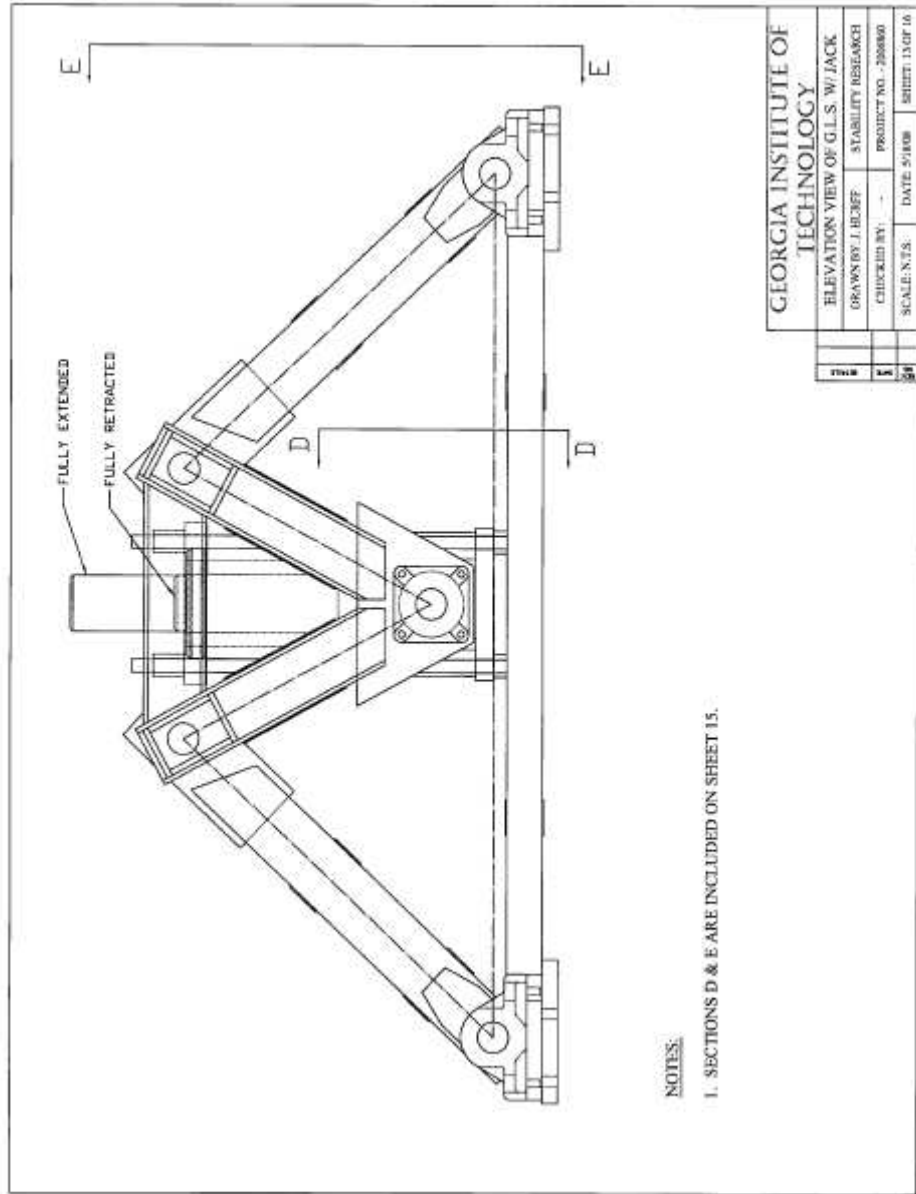
396

Figure B.13 – Gravity load simulator design (Sheet 13 of 16)
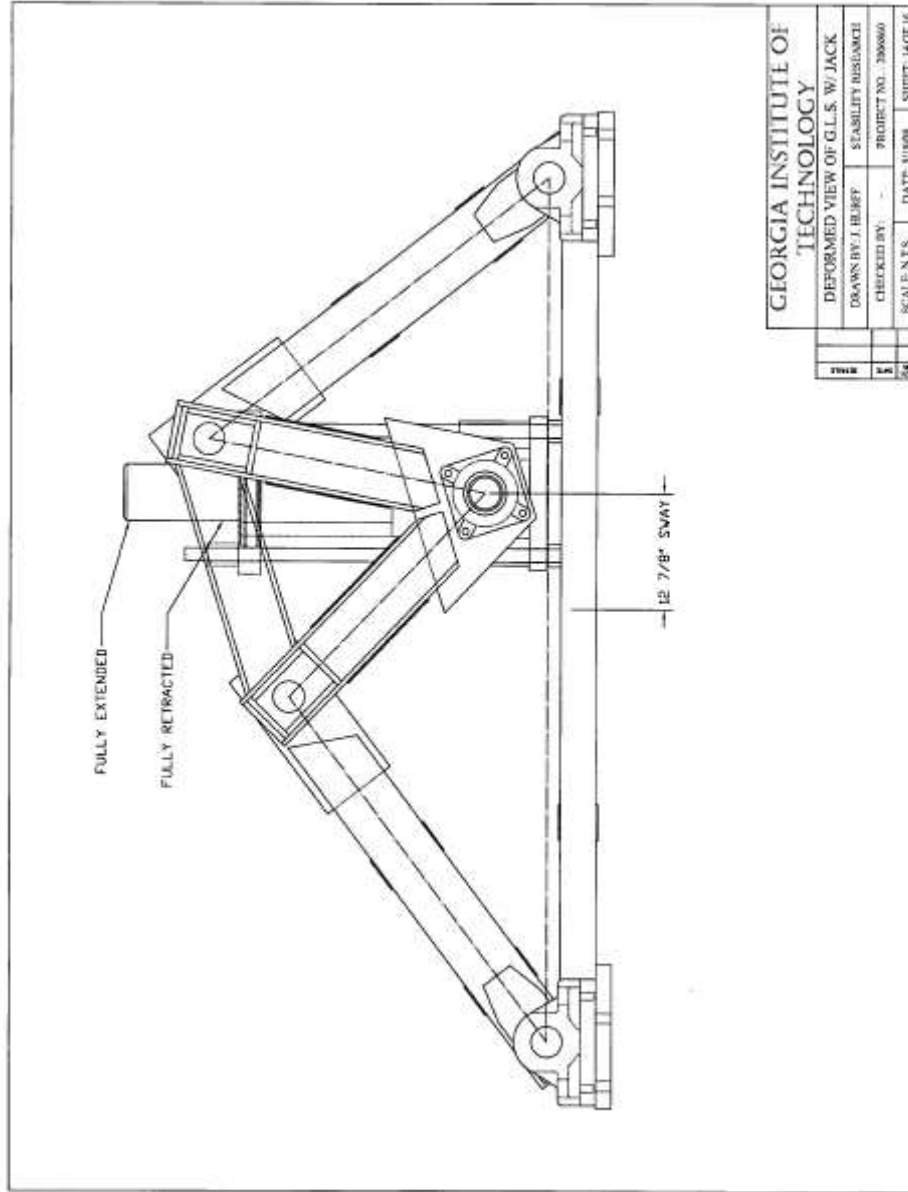
Figure B.14 – Gravity load simulator design (Sheet 14 of 16)

SECTION E-E

SECTION D-D

NOTES:

1. BRACING PLATES ON DOUBLE CHANNELS LEFT OUT OF SECTION VIEWS FOR CLARITY.

GEORGIA INSTITUTE OF TECHNOLOGY

SECTIONS OF G.L.S. W/ JACK

TITLE			DRAWN BY: J. HURFF	STABILITY RESEARCH
			CHECKED BY: -	PROJECT NO. - 2000860
			SCALE: N.T.S.	DATE: 5/1/06	SHEET: 15 OF 16
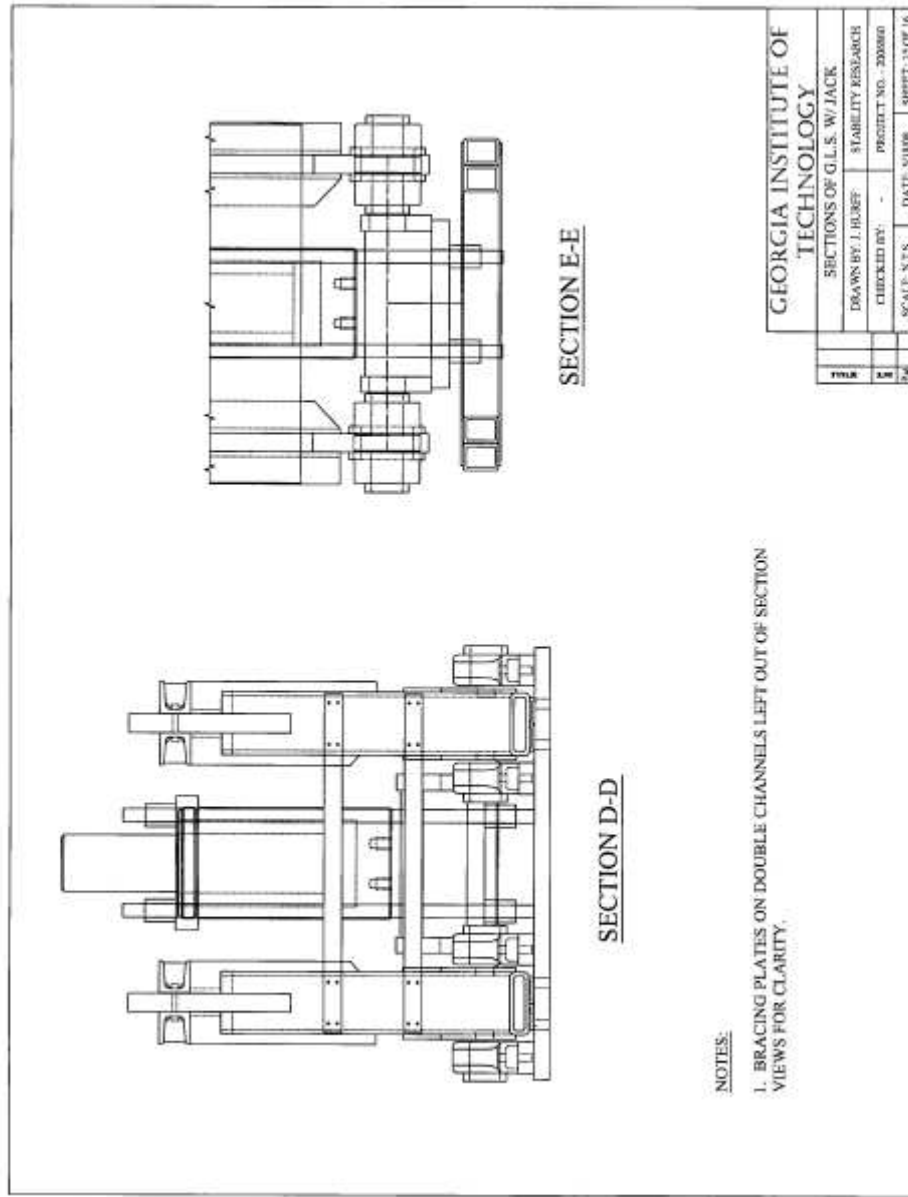
Figure B.15 – Gravity load simulator design (Sheet 15 of 16)

399
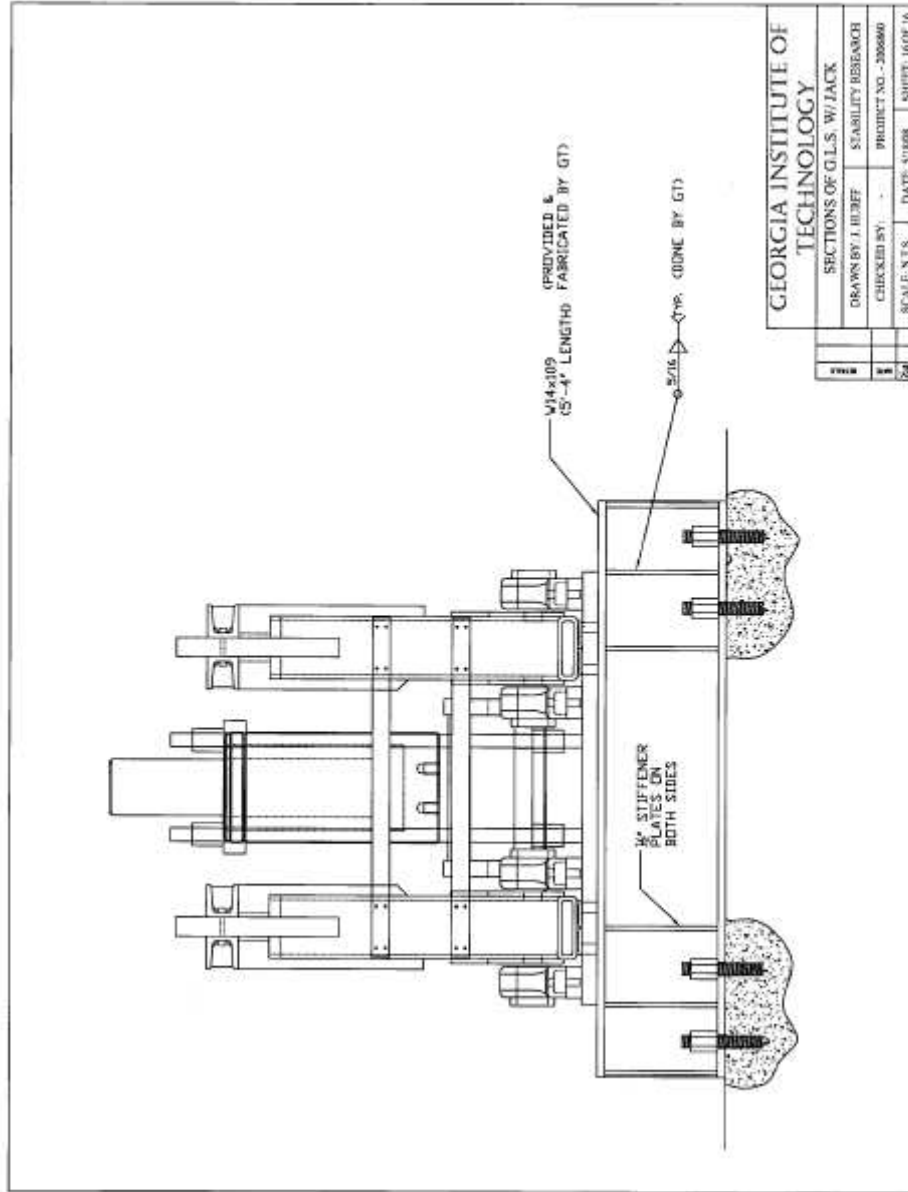
Figure B.16 – Gravity load simulator design (Sheet 16 of 16)
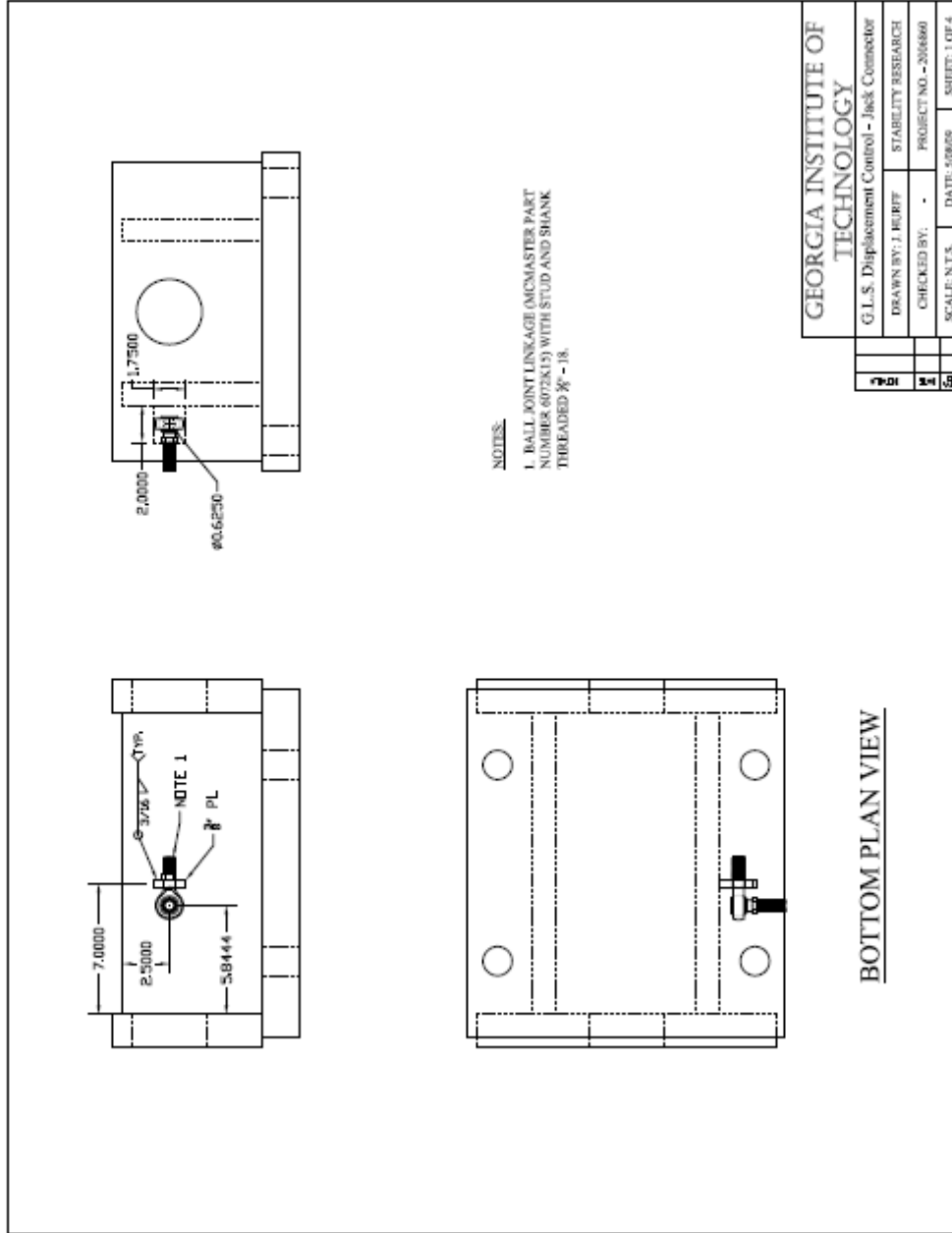
Figure B.17 – Gravity load simulator control mechanism (Sheet 1 of 4)
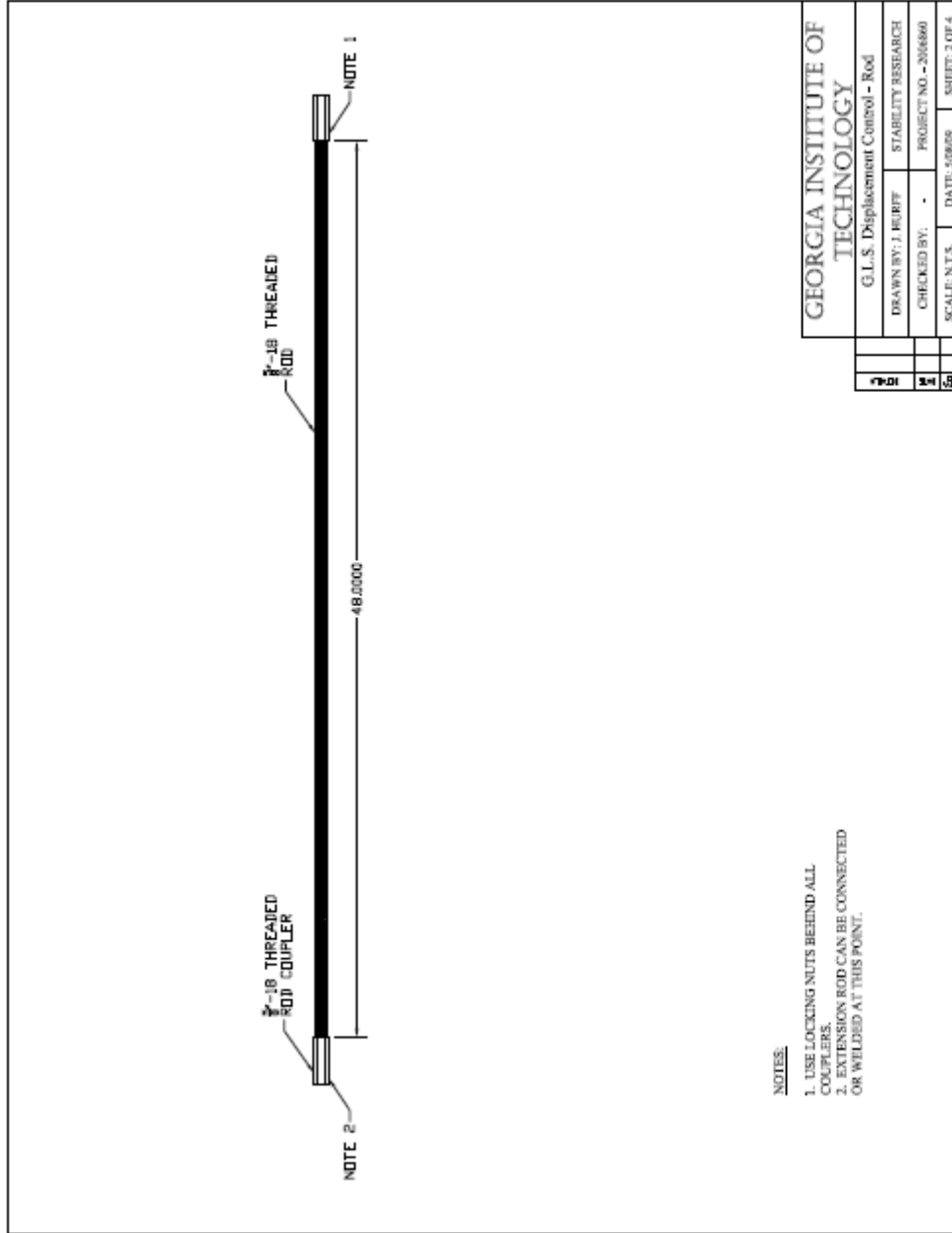
Figure B.18 – Gravity load simulator control mechanism (Sheet 2 of 4)
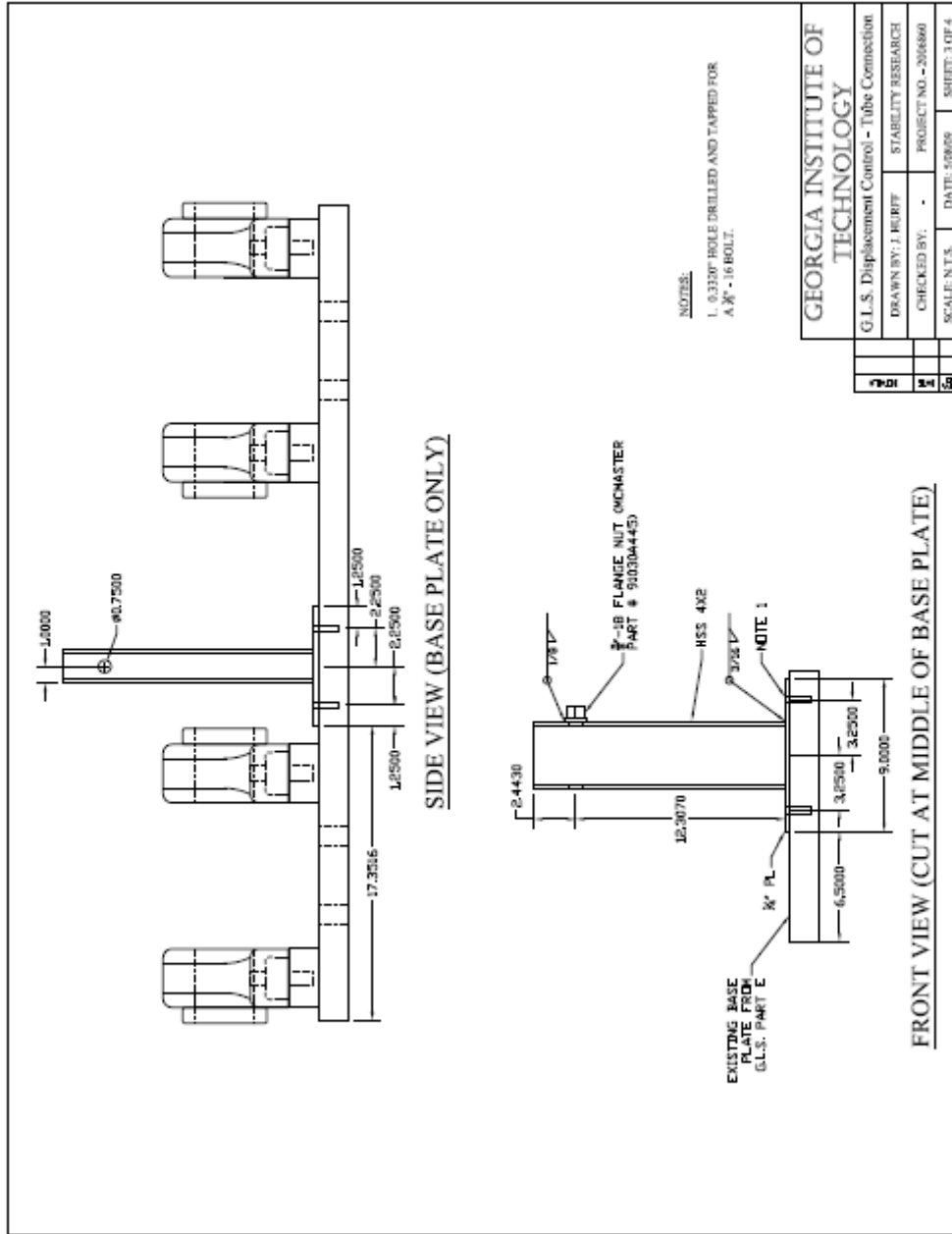
Figure B.19 – Gravity load simulator control mechanism (Sheet 3 of 4)
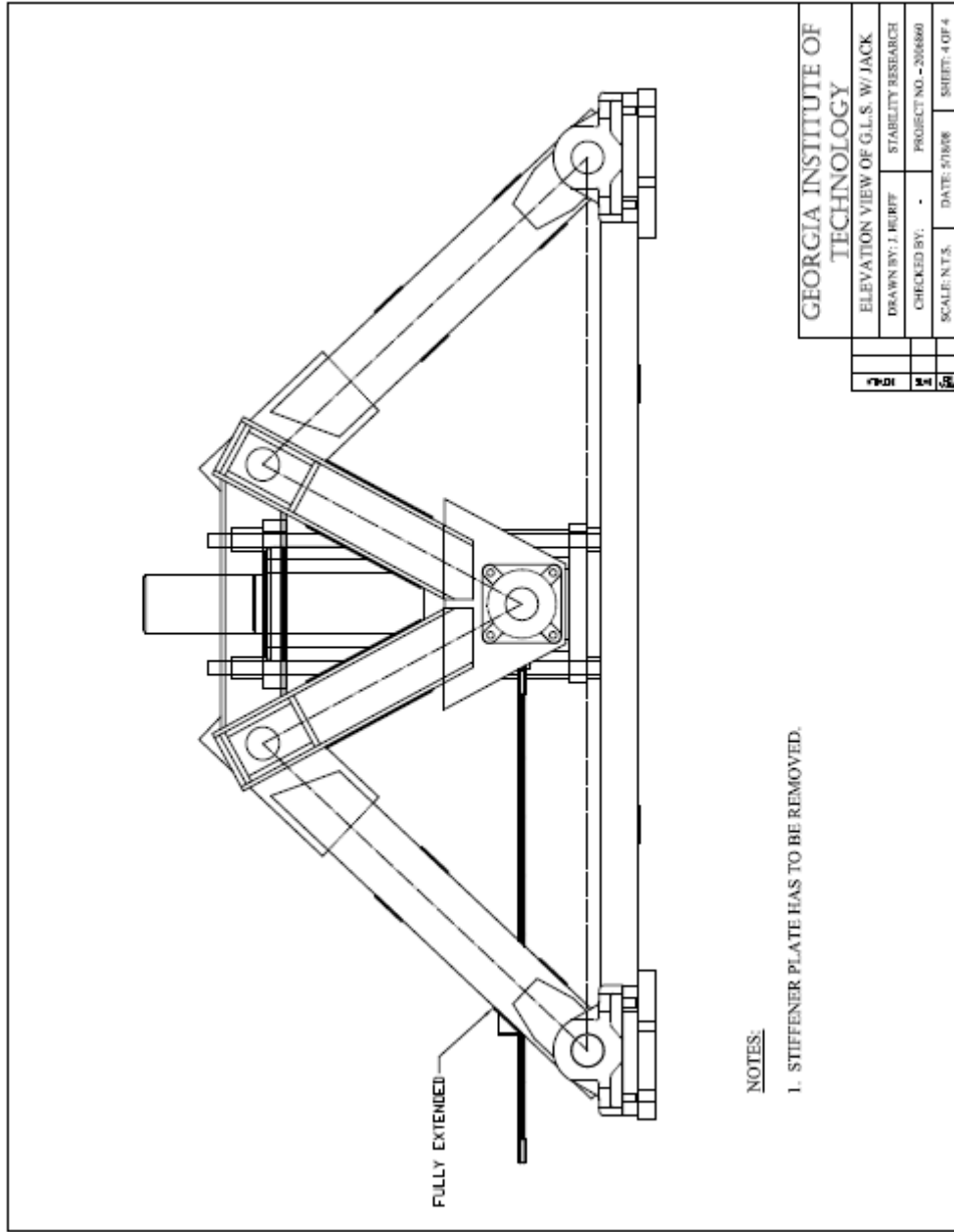
Figure B.20 – Gravity load simulator control mechanism (Sheet 4 of 4)

404

APPENDIX C

ADDITIONAL RECTANGULAR BEAM MEASUREMENTS & DATA
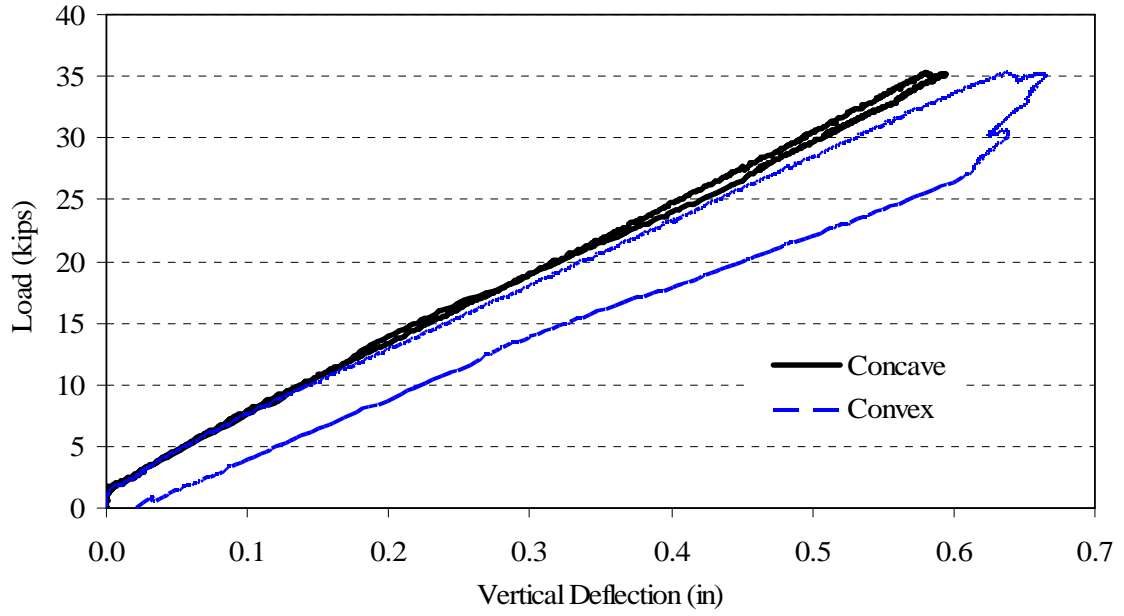
Figure C.1 – Load vs. vertical displacement Beam B2A, loading #1
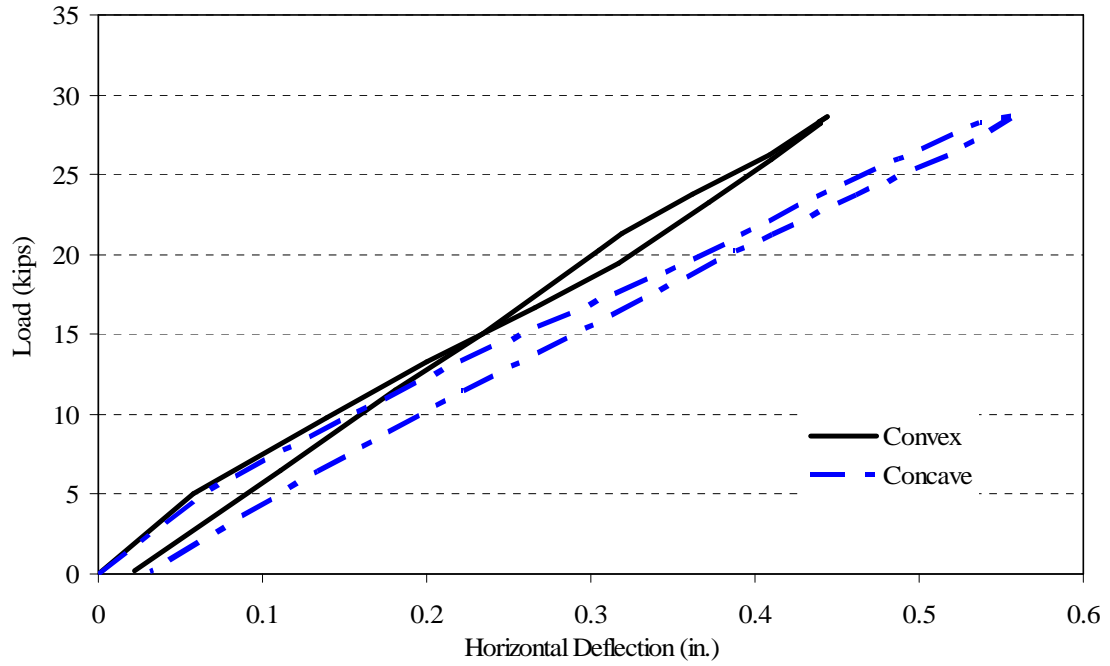
Figure C.2 – Load vs. vertical displacement Beam B2A, loading #2
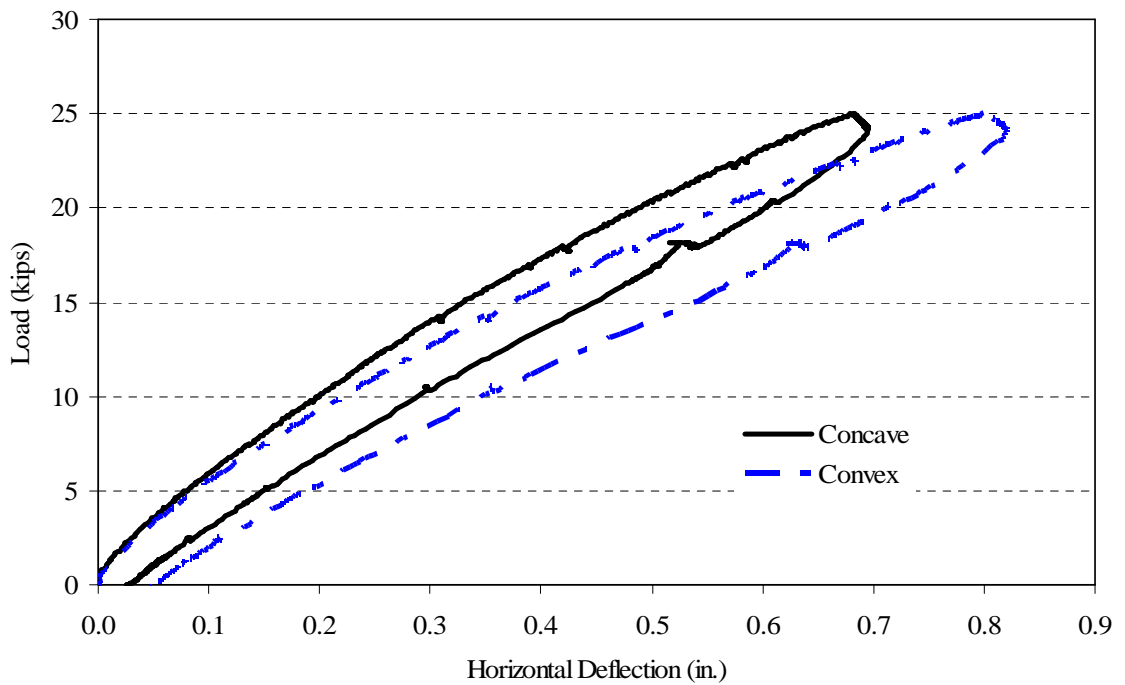
Figure C.3 – Load vs. vertical displacement Beam B2A, loading #3

406
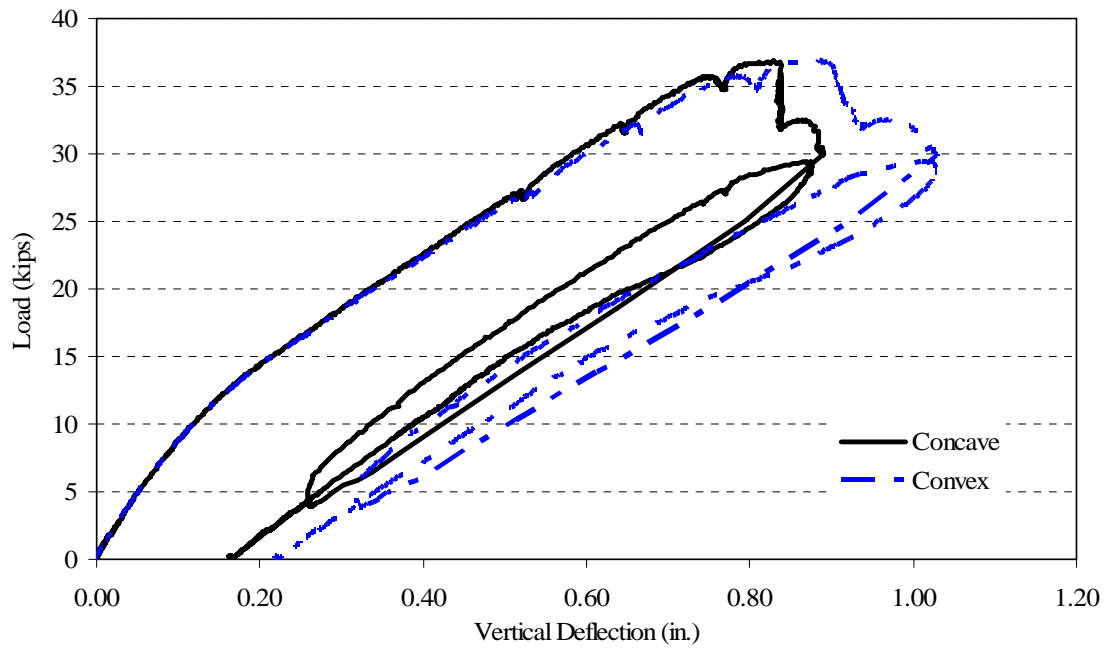
Figure C.4 – Load vs. vertical displacement Beam B1A
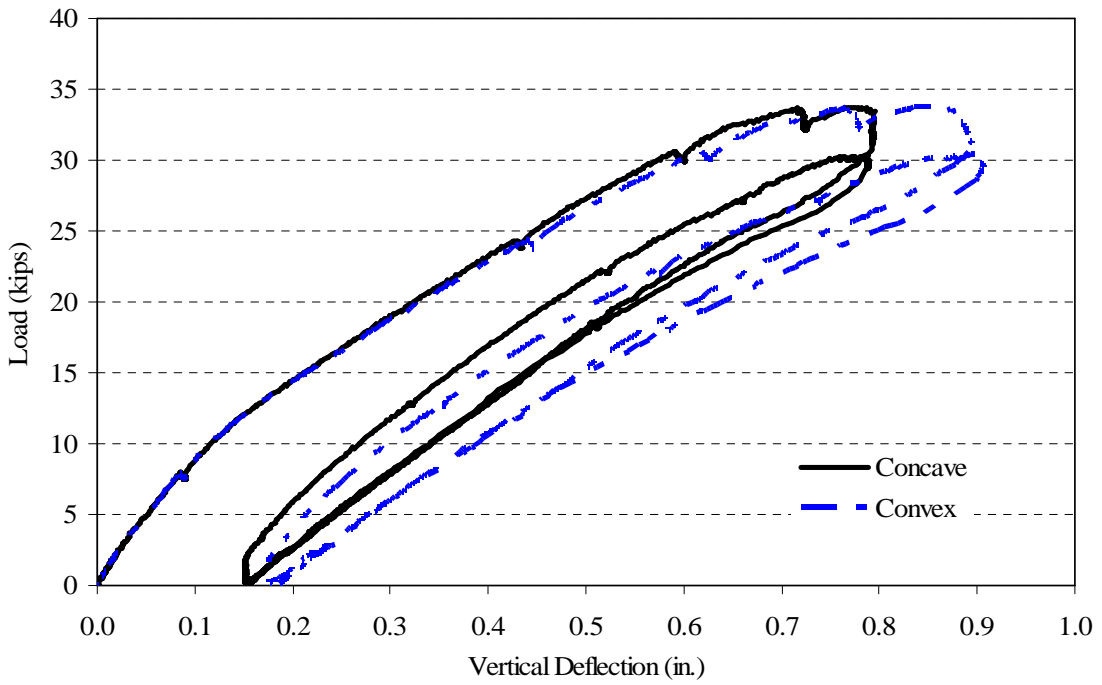
Figure C.5 – Load vs. vertical displacement Beam C2A
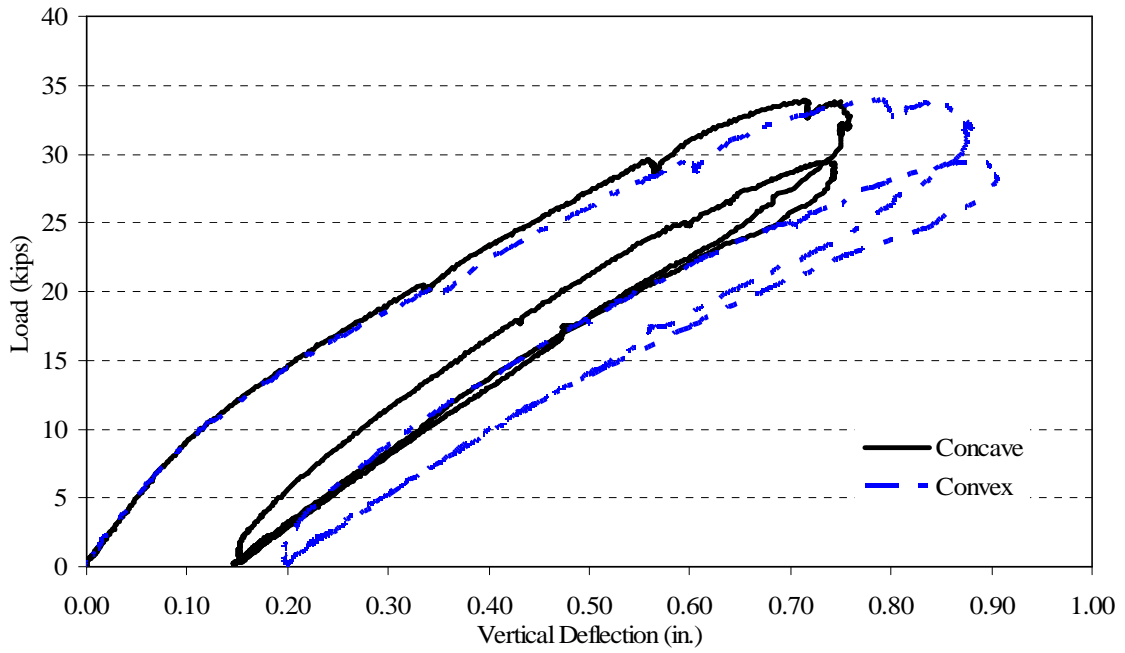
Figure C.6 – Load vs. vertical displacement Beam B1B
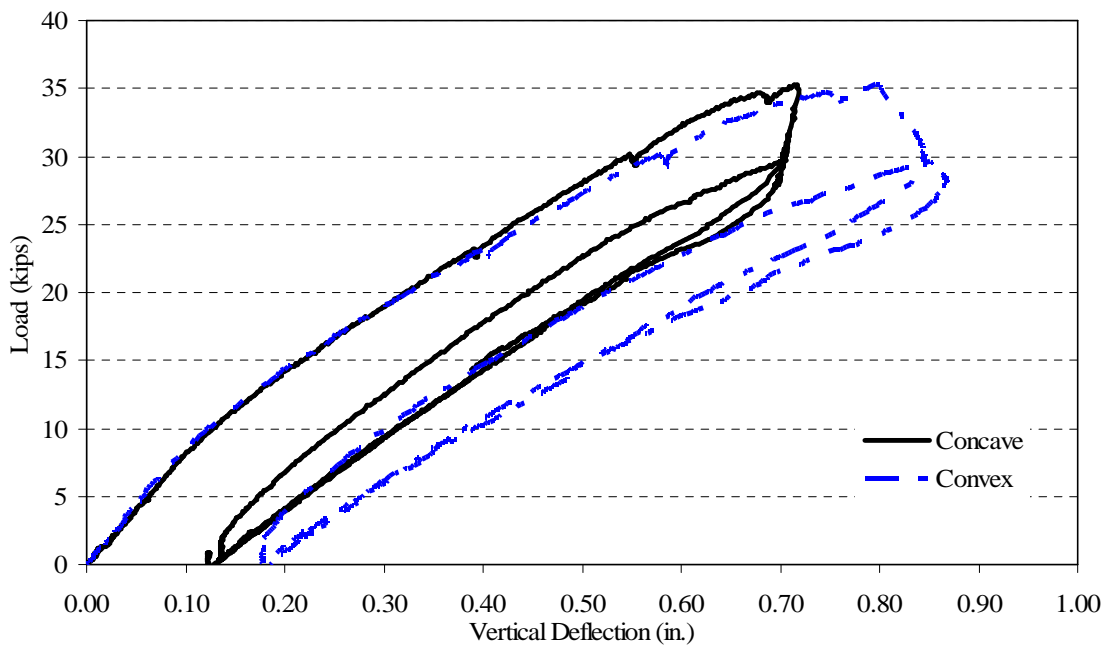
Figure C.7 – Load vs. vertical displacement Beam B2B
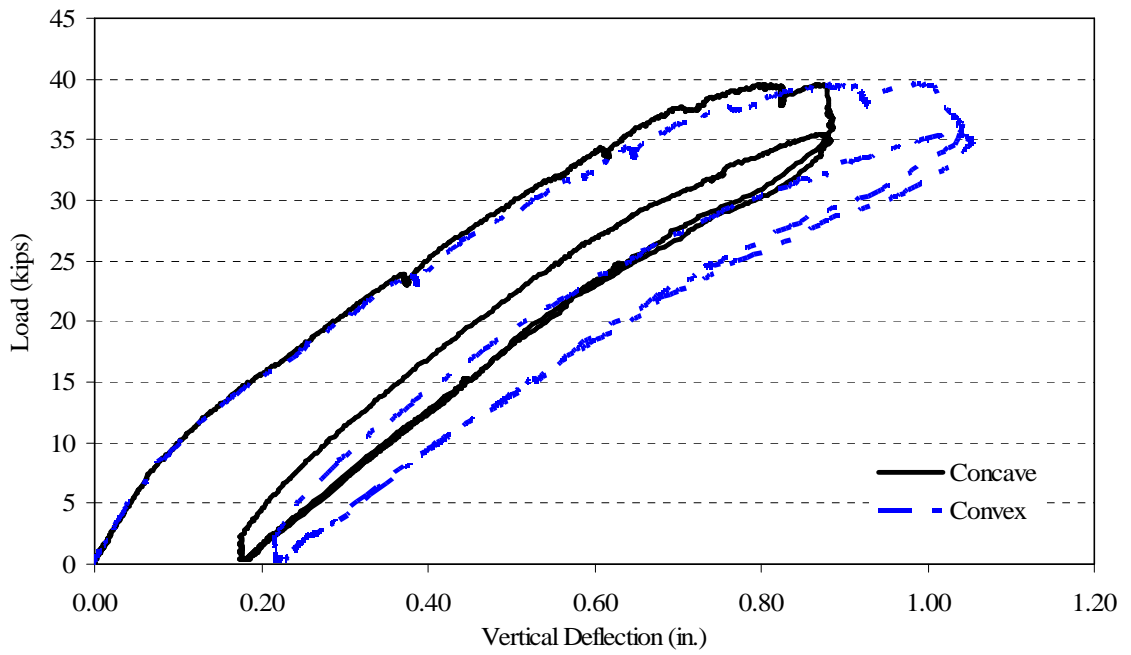
Figure C.8 – Load vs. vertical displacement Beam C2B

(a) South Side   (b) North Side
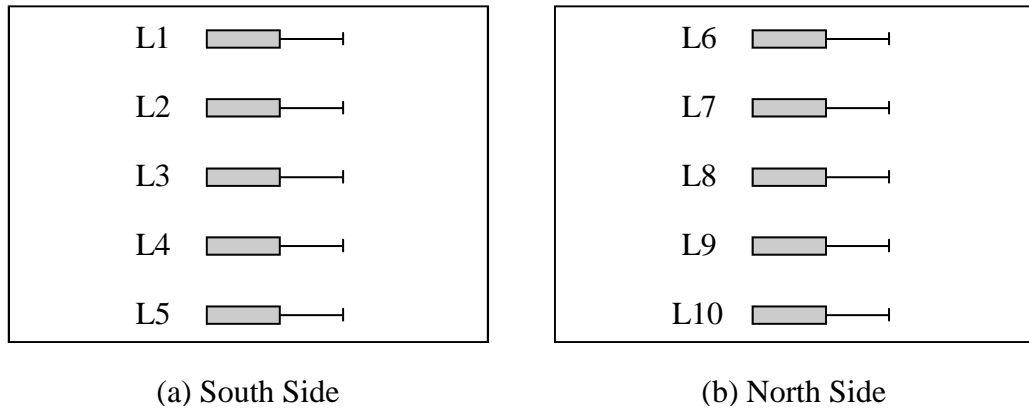
Figure C.9 – LVDT nomenclature for rectangular beam tests

Table C.1 - Actual LVDT gage lengths for rectangular beams (inches)

LVDT #	B2A	B1A	C2A	B1B	B2B	C2B
L1	10 3/16	10 13/16	10 1/16	10 1/8	9 31/32	10
L2	10	10 7/8	10 1/32	10 3/16	10 1/8	9 31/32
L3	10 1/32	10 3/4	10	10 1/8	10	10
L4	9 29/32	10 13/16	10	10 1/32	9 31/32	10 1/16
L5	10 1/32	10 11/16	9 29/32	10 1/32	9 31/32	10 1/32
L6	9 15/16	10 23/32	9 29/32	9 7/8	10 1/16	10 1/32
L7	9 31/32	10 13/16	10 1/16	10	10 1/32	10
L8	9 15/16	10 3/4	10 5/32	10	10 1/32	9 15/16
L9	10	10 27/32	9 31/32	9 31/32	9 15/16	10
L10	10 3/32	10 27/32	10 1/16	9 31/32	10 1/16	10 1/16

APPENDIX D

EXAMPLE SIMPLIFIED EQUATION CALCULATION

Beam C2A:

Input Properties -

$f_c' = 11281\,psi$
Concrete compressive strength

$E_c = 5156\,ksi$
Initial concrete modulus of elasticity

$b = 4\,in.$
Width of cross-section

$L = 31.4\,ft.$
Span of beam

$d = 35.5\,in.$
Depth of mild steel reinforcing

$d_t = 1.5\,in.$
Depth of mild steel reinforcing at top of cross-section

$d_p = 20\,in.$
Depth of prestressing strands

$A_s = 3.16\,in^2$
Area of mild steel reinforcing at the bottom of cross-section

$A_t = 0.79\,in^2$
Area of mild steel reinforcing at the top of cross-section

$A_{ps} = 0.328\,in^2$
Area of prestressing steel

$f_y = 70.3\,ksi$
Yield stress of the mild steel reinforcement

411

$f_{psi} = 158.3 \, ksi$ Initial stress in prestressing strands after losses

$C_1 = 4.23$ Factor for concentrated load at midspan

$C_2 = 1.00$ Factor for simply-supported end conditions

Calculations -

$\varepsilon_c = 0.001555$ Concrete strain at extreme compression fiber (iterated)

$$x = \frac{\varepsilon_c}{\varepsilon_0} = 0.416$$

Ratio of extreme compression strain to strain at maximum stress from Thorenfeldt et al. (1987)

$$f_c = \frac{1.8 f_c' x}{1 + x^2} = 7.196 \, ksi$$

Concrete stress in extreme compression fiber from Thorenfeldt et al. (1987)

$$\beta_1 = \max\left(\frac{\ln\left(1 + x^2\right)}{x}, 0.5\right) = 0.5$$

Average stress under the stress block from Thorenfeldt et al. (1987)

$$k_2 = \left[1 - \frac{2\left(x - \tan^{-1} x\right)}{x^2 \beta_1} \; if \; \beta_1 > 0.5, \; else \; \frac{1}{3}\right] = \frac{1}{3}$$

Center of gravity of compression zone from Thorenfeldt et al. (1987)

$c = 14.678 \, in.$ Compression zone depth (iterated)

$$\varepsilon_{su} = \varepsilon_{se} + \varepsilon_c \frac{d_p - c}{c} = 6.016 \times 10^{-3}$$

Strain in prestressing strands

$f_{ps} = 174.45 \, ksi$ Stress in prestressing strands from stress-strain curve in Figure A.16

$$\varepsilon_s = \varepsilon_c \frac{d-c}{c} = 2.03 \times 10^{-3}$$ Strain in mild steel reinforcing

$$\varepsilon_{st} = \varepsilon_c \frac{d_t - c}{c} = -1.396 \times 10^{-3}$$ Strain in mild steel reinforcing at top of cross-section

$$f_s = \min(\varepsilon_s E_s, f_y) = 58.86 \, ksi$$ Stress in mild steel reinforcing

$$f_{st} = \min(\varepsilon_{st} E_s, f_y) = -40.49 \, ksi$$ Stress in mild steel reinforcing at top of cross-section

$$T = A_s f_s + A_{ps} f_{ps} = 243.23 \, kip$$ Tension in cross-section

$$C = \beta_1 f_c' bc + A_{st} f_{st} = 243.23 \, kip$$ Compression in cross-section

Check if C = T: If equivalent – continue, else – iterate compression zone depth

$$M_a = A_s f_s (d - k_2 c) + A_{ps} f_{ps} (d_p - k_2 c) + A_t f_{st} (k_2 c - d_t) = 6667 \, kip \cdot in$$

Internal moment in cross-section

$$E_{sec} = \frac{f_c}{\varepsilon_c} = 2.03 \times 10^{-3}$$ Concrete secant modulus of elasticity

$$B = E_{sec} \left[\left(\frac{hb^3}{12} \right) \left(\frac{M_R}{M_a} \right)^2 + \left(\frac{cb^3}{12} \right) \left(1 - \left(\frac{M_R}{M_a} \right)^2 \right) \right] = 3.824 \times 10^5 \, kip \cdot in^2$$

Weak-axis flexural stiffness (no effect of reinforcement because it is located at centroid)

$$C = \frac{E_{sec}}{2(1+\nu)} \left\{ \begin{array}{l} \left[\left(\frac{hb^3}{3} \right) \left(1 - 0.35 \frac{b}{h} \right)^2 - \left(\frac{cb^3}{3} \right) \left(1 - 0.35 \frac{b}{c} \right)^2 \right] \left[\left(\frac{M_R}{M_a} \right)^3 - 3 \left(\frac{M_R}{M_a} \right)^2 + 3 \left(\frac{M_R}{M_a} \right) \right] \\ + \left(\frac{cb^3}{3} \right) \left(1 - 0.35 \frac{b}{c} \right)^2 \end{array} \right\}$$

$$= 9.665 \times 10^5 \, kip \cdot in^2$$

Torsional stiffness

$$A = 1 - 1.74 \frac{\alpha}{L} \sqrt{\frac{B}{C}} = 0.976$$

Effect of load application height

$$M_{cr} = \frac{C_1}{C_2 L} A \sqrt{BC} = 6659 \, kip \cdot in$$

Buckling moment for case of zero imperfections

Check if $M_{cr} = M_a$: If equivalent – continue, else – iterate extreme compression strain

$$u_i = 0.313 \, in.$$

Initial lateral displacement at midspan

$$\theta_i = 0.0043 + 0.012217 = 0.01652 \, rad$$

Initial rotation at midspan
(includes applied load angle error)

$$B_r = B \left(1 - \frac{1}{3} \tan^{-1} \left(\frac{I_{gx} \theta_i}{I_{gy}} \right) \left(\frac{2}{\pi} \right) \right) = 2.991 \times 10^5 \, kip \cdot in^2$$

Reduced weak-axis stiffness

$$\Delta_r = 1 - \left(\frac{u_i}{L} \right)^{0.31} = 0.889$$

Reduction for initial lateral displacement

$$\Theta_r = e^{-36.5 \theta_i} = 0.646$$

Reduction for initial rotation

$$M_b = \frac{C_1}{C_2 L} A\sqrt{B_r C}\, \Delta_r \Theta_r = 3380\, kip \cdot in \qquad \text{Buckling moment including imperfections}$$

$$P_b = \left(M_b - \frac{1.35}{1.13} M_{sw} \right)\frac{4}{L} = 32.8\, kip \qquad \text{Buckling load including imperfections}$$

(1.35/1.13 ratio corrects for difference in moment gradient between applied point load and self-weight uniform load)

APPENDIX E

ADDITIONAL DATA & PHOTOGRAPHS FOR BT-54

EXPERIMENT
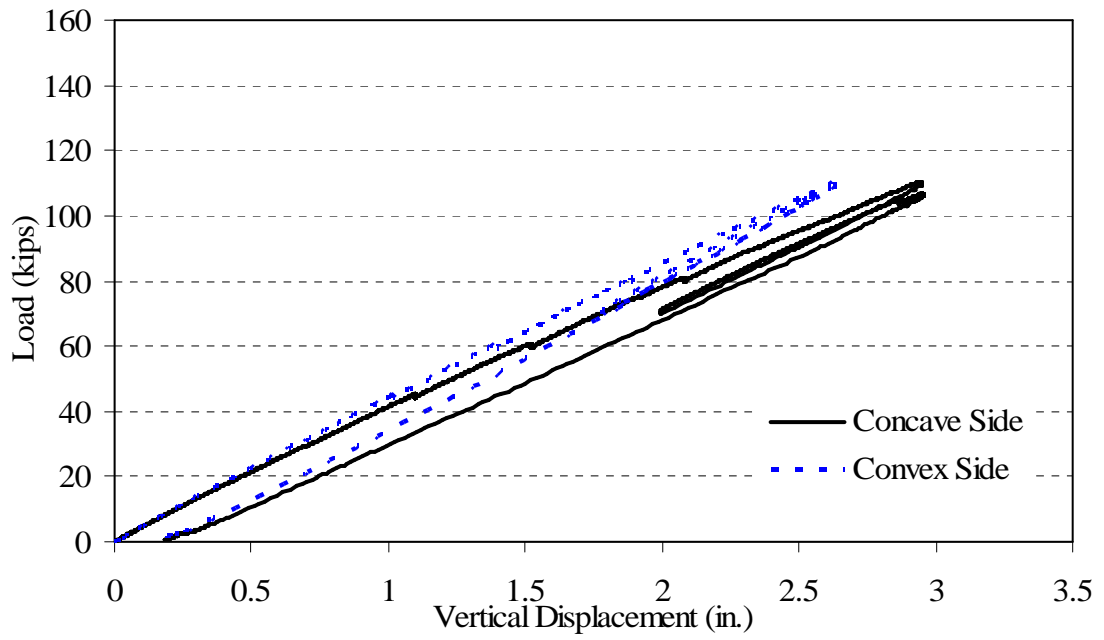
Figure E.1 – BT-54 load vs. vertical displacement
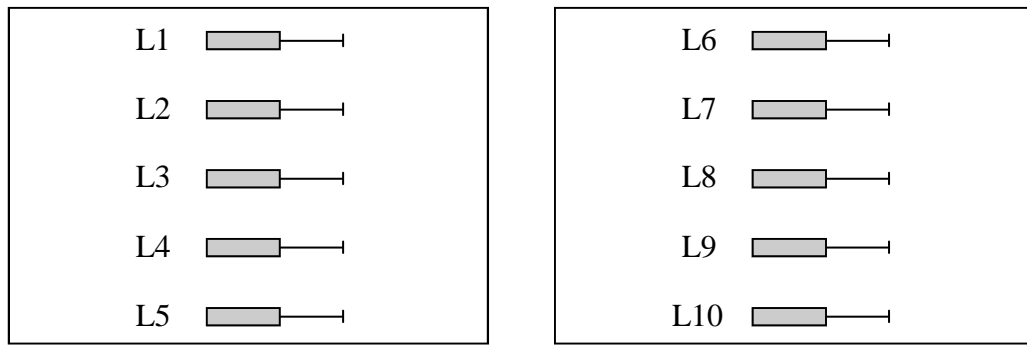
(a) South Side   (b) North Side

Figure E.2 – LVDT nomenclature for BT-54

Table E.1 - Actual LVDT gage lengths for BT-54 (inches)

LVDT #	BT-54
L1	9 31/32
L2	10 1/32
L3	10
L4	10
L5	10
L6	10
L7	10 1/32
L8	10 1/16
L9	10
L10	10 1/16
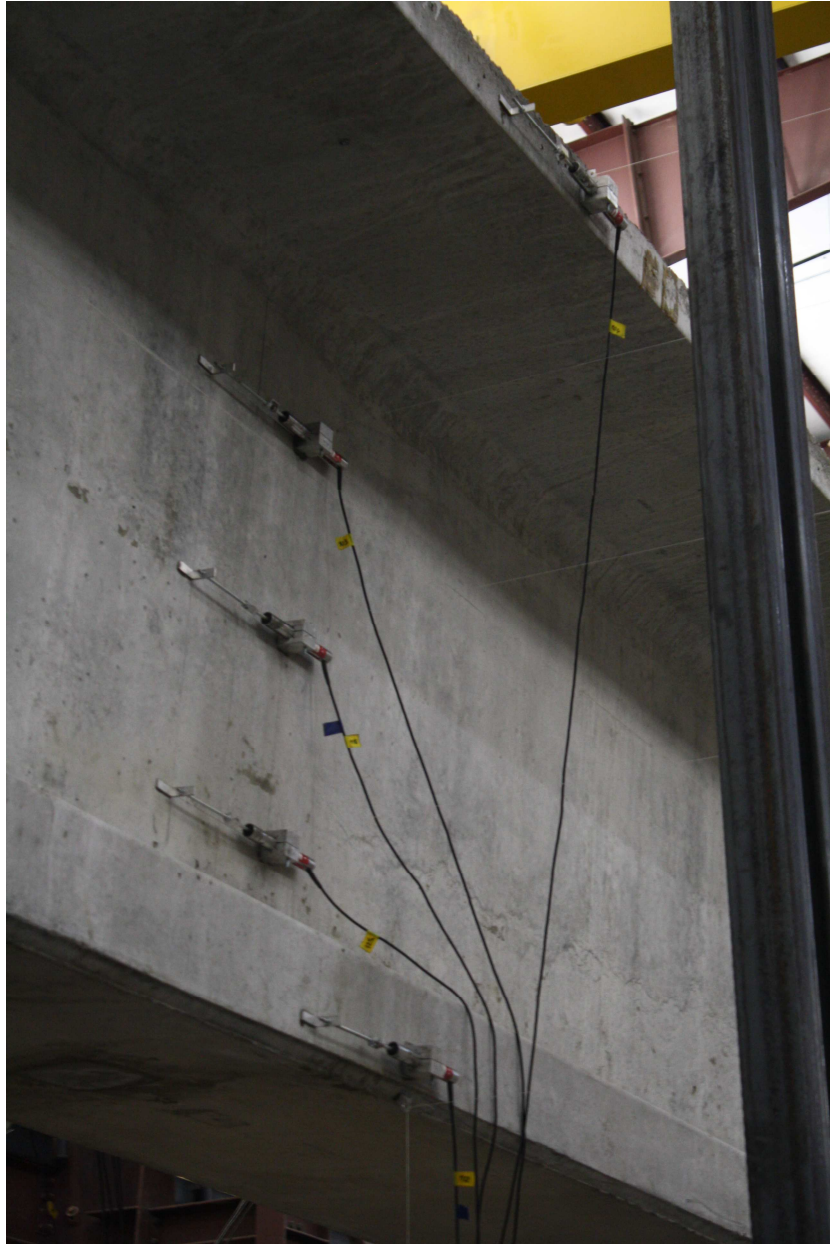
Figure E.3 – Photograph of BT-54 LVDTs
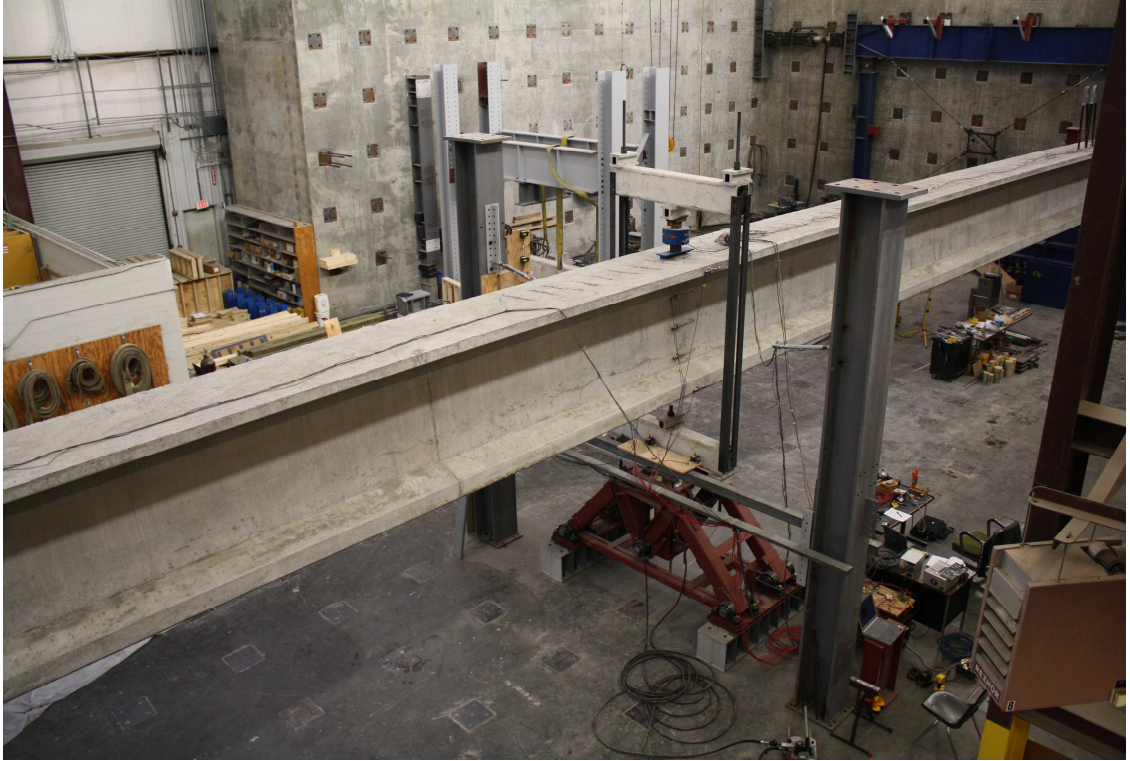
Figure E.4 – Aerial view of BT-54 experimental setup

Figure E.5 – BT-54 end view showing initial rotation

Figure E.6 – Extent of uplift of BT-54, Test #1

APPENDIX F

BEARING PAD VERTICAL DISPLACEMENT CORRECTION

PROCEDURE

The string potentiometers measuring the vertical displacement of the bearing pads required a correction to the raw data. The correction was necessary because the string potentiometers were located a distance of 2-in. (51 mm) from the front edge of the bearing pad, and, therefore, approximately 8-in. (203 mm) from the center of rotation of the bearing pad as shown in Figure F.1.

Figure F.1 – Bearing pad vertical displacement locations

When the girder was loaded, strong-axis flexural behavior caused rotation about the ideally pinned ends thus additional vertical displacement was measured by the string potentiometers. The vertical displacement due to the rotation about the strong-axis must be removed from the raw data to accurately interpret the uplift behavior of the girder on the bearing pad. The vertical displacement due to the strong-axis rotation was calculated using Equation F.1.

$$\delta_{cor} = \frac{PL^2}{16 E_c I_x} x \qquad (\text{F.1})$$

In Equation F.1, "x" is the distance the string potentiometers were from the center of rotation along the longitudinal axis and δ_{cor} is the vertical displacement correction that must be subtracted from the measured data by the string potentiometers. The distance "x" was taken as 8-in. (203 mm); however, the value is approximate because the center of rotation should vary during loading and the initial stress distribution in the bearing pad was unknown. The uncorrected raw data compared with the analytical results from Chapter 7 are shown in Figure F.2.
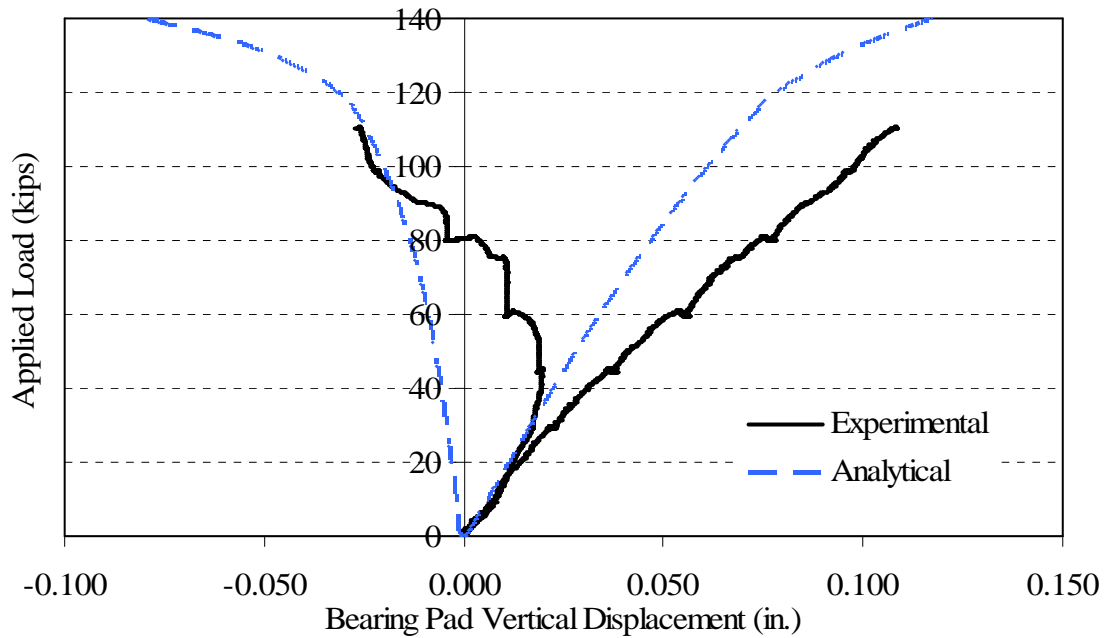
Figure F.2 – Uncorrected bearing pad vertical displacements at edges

Figure F.2 would make it appear that during the experiment, both sides of the bearing pad compressed at approximately the same rate with no end rotation. Then at some critical level, once side of the bearing pad reversed displacement direction inevitably leading to uplift. On the other hand, the analytical results show that after the self-weight was applied, one edge of the girder bottom flange immediately was displacing in the uplift direction.

APPENDIX G

NONLINEAR ANALYSIS FLOWCHARTS

Start

$\theta_{(1)}$ = Initial rotation at midspan
$u_{(1)}$ = Initial sweep at midspan
$\theta_{end(0)}$ = Initial end rotation
L = Span of beam
f_c' = Concrete compressive strength
E_c = Concrete initial modulus of elasticity
E_s = Steel modulus of elasticity
E_{ps} = Prestressing steel modulus of elasticity
ν = Concrete Poisson's ratio
elements = # of segments
Geometric dimensions

j = 1

$u_{(1, j)} = u_{(i)} \sin(\pi \, x_{(j)}/L)$

$\theta_{(1, j)} = \theta_{(i)} \sin(\pi \, x_{(j)}/L)$

j = elements + 1 → No → j = j + 1

Yes

$M_{(1)} = M_{sw}$

Formulate global stiffness matrix, [K]
for the appropriate boundary conditions
using symmetry

i = 2

Calculate moment and torque at each node
or cross-sectional location

Formulate incremental load vector, {ΔP}.
For a concentrated load & symmetry, half the
incremental concentrated load is applied at the
midspan node with dPcos(θ_i) in the vertical direction
and dPcos(θ_i) in the horizontal direction. A constant
torque is applied at midspan with increments of
additional torque along the length to compensate for
deformed configuation of beam.

$dU = [K]^{-1}\{\Delta P\}$

$U_{(i)} = dU + U_{(i-1)}$

j = 1

$c_{d(i,j)}$, $\varphi_{(i,j)}$, $E_{c(i,j)}$, $I_{x(i,j)}$, $I_{y(i,j)}$, $curve_{(i,j)}$
From fiber element subroutine

$c_{(i,j)} = \min(h, c_{d(i,j)} - b/2 \tan(\varphi_{(i,j)}))$

$b_{z(i,j)} = \min(b, c_{d(i,j)} / \tan(\varphi_{(i,j)}))$

$G_{c(i,j)} = E_{c(i,j)} / (2(1 + v))$

$J_{(i,j)}$
From torsion constant subroutine

j = elements + 1   No → j = j + 1

Yes

$\alpha_{(i)} = y_{top} + camber - v_{(i,5)}$

$T_{BP(i)} = P_{(i)}/2(u_{(i,5)} + \alpha_{(i)}(\theta_{(i,5)} + \theta_{BP(i-1)})) + y_{bot}\sin(\theta_{BP(i-1)}) + 0.7854w_{sw}Lu_{(i,5)}$

$\theta_{BP(i)}$, $d_{edge(i)}$
From bearing pad stiffness subroutine

$ShearDisp_{(i)} = (P_{(i)} + w_{sw}L)/2 \sin(\theta_{BP(i)}) / K_{BPshear}$

Formulate global stiffness matrix, [K]
for the appropriate boundary conditions
using symmetry

$u_{(i,5)} > Limit$ No → i = i + 1

Yes

U = Beam displacements and rotations at each node
Section properties at each node - I_x, I_y, J
c = Depth of neutral axis at each node
E = Average element tangent modulus of elasticity at each node
φ = Neutral axis at each node
d_{edge} = Bearing pad axial shortening at compressed edge
θ_{BP} = Bearing pad rotation

End

Figure G.1 – Nonlinear incremental analysis flowchart

```
                              ┌──────────┐
                              │  Start   │
                              └──────────┘
                                   │
                                   ▼
   ╱─────────────────────────────────────────────────────────────╲
  ╱   θ = Rotation of cross-section                                 ╲
 ╱    M =  Applied moment at cross-section                           ╲
╱     φ(k-1) = Neutral axis angle from previous load increment        ╲
╲     curve(i-1) = Curvature from previous load increment             ╱
 ╲    Input element properties - x(z), y(z), Ac(z), Aps(z), As(z)    ╱
  ╲───────────────────────────────────────────────────────────────╱
                                   │
                                   ▼
                              ┌──────────┐
                              │  i = 1   │
                              └──────────┘
                                   │
                                   ▼
                       ┌──────────────────────────────┐
                       │ curve(i) = curve(i-1) + δcurve │◄───
                       │   (δcurve= small incr.)        │
                       └──────────────────────────────┘
                                   │
                                   ▼
                       ┌──────────────────────────────┐
                       │ elements = # of elements       │
                       │ z = 1                          │
                       └──────────────────────────────┘
```

$$E_i = \sum_{z=1}^{elements} E_{cut\,(i,z)}$$

$$P_{c(i)} = \sum_{z=1}^{elements} A_{c(z)} f_{c\,(i,z)}$$

$$P_{ps(i)} = \sum_{z=1}^{elements} A_{ps(z)} f_{ps\,(i,z)}$$

$$P_{s(i)} = \sum_{z=1}^{elements} A_{s(z)} f_{s\,(i,z)}$$

$$\bar{x} = \sum_{z=1}^{elements} \frac{\left(A_{c(z)} + n_{ps}A_{ps(z)} + n_s A_{s(z)}\right) x_{(z)}}{A_c + n_{ps}\left(A_{ps}\right) + n_s\left(A_s\right)}$$

$$\bar{y} = \sum_{z=1}^{elements} \frac{\left(A_{c(z)} + n_{ps}A_{ps(z)} + n_s A_{s(z)}\right) y_{(z)}}{A_c + n_{ps}\left(A_{ps}\right) + n_s\left(A_s\right)}$$

$$I_{x(i)} = \sum_{z=1}^{elements} A_{c(z)}\left(y_{(z)} - \bar{y}\right)^2 + n_{ps}A_{ps(z)}\left(y_{(z)} - \bar{y}\right)^2 + n_s A_{s(z)}\left(y_{(z)} - \bar{y}\right)^2$$

$$I_{y(i)} = \sum_{z=1}^{elements} A_{c(z)}\left(x_{(z)} - \bar{x}\right)^2 + n_{ps}A_{ps(z)}\left(x_{(z)} - \bar{x}\right)^2 + n_s A_{s(z)}\left(x_{(z)} - \bar{x}\right)^2$$

$$f_{p\,(i)} = P_c + P_{ps} + P_s$$

428

Figure G.2 – Fiber analysis subroutine flowchart

Start

θ_BP(i-1) = Bearing pad rotation from previous load increment
P_BP = Axial load on bearing pad
T_BP = Torque on bearing pad about center of bearing pad

$\theta_{BP(i)} = \theta_{BP(i-1)} + \delta\theta_{BP}$
($\delta\theta_{BP}$ = small incr.)

$d_{edge(i)} = d_{edge(i-1)} + \delta d_{edge}$
(δd_{edge} = small incr.)

$d_{(i,j)} = d_{edge(i)} + x\theta_{BP(i)}$
(x = distance of strip "j" from edge of bearing pad)

$F_{strip(j)} = f(d_{(i,j)})$
(f(d(i,j)) = strip force as function of depth from assumed material model)

$F_{total} = \sum_{j=1}^{n} F_{strip\,(j)}$
(n = number of strips)

$F_{total} = P_{BP} +$ — Yes

No

$M_{strip(j)} = F_{strip(j)}(w/2 - x)$
(w = bearing pad width)

$M_{total} = \sum_{j=1}^{n} M_{strip\,(j)}$
(n = number of strips)

$M_{total} = T_{BP} +$ — Yes

No

θ_BP = Bearing pad rotation
d_edge = Bearing pad axial shortening at compressed edge

End

Figure G.3 – Bearing pad model subroutine flowchart

Start

φ = Neutral axis angle
b = Width of cross-section
h = Height of cross-section
b_z = width of compression zone
(equals b if trapezoidal compression zone)
c_d = maximum edge compression zone depth
δt = Perimeter strip thickness (user determined)

$\alpha = \pi/2 - \varphi$

n = 1

$b_z < b$ — Yes

No

n = 1 — No → $c_{2(n)} = \min\left(c_{2(1)} - \left((n-1)\delta t + (n-1)\delta t \cos\alpha\right)\tan\phi, h\right)$

Yes

$c_{1(n)} = c_{1(1)} - (n-1)\delta t$

$b_{z(n)} = b_z$
(width of perimeter strip "n")

$b_{z(n)} = c_{1(1)} - 2(n-1)\delta t$

$c_{2(n)} = \min(b_z \tan(\varphi), h)$
(height of perimeter strip "n"
triangular portion)

$b_{z(n)} < 0$ — No

Yes

$c_{1(n)} = c_d - c_{2(n)}$
(height of perimeter strip "n"
rectangular portion)

$A_{(n)} = (b_{z(n)} c_{2(n)})/2 + b_{z(n)} c_{1(n)}$
(enclosed area of strip "n")

r = 1

$p_{(n)} = b_z + h + (b_z^2 + h^2)^{1/2} + 2c_{1(n)}$
(perimeter of strip "n")

$J = J + \left(dJ_{(r)} + dJ_{(r+1)}\right)\dfrac{\delta t}{2}$

$dJ_{(n)} = 4A_{(n)}^2 / p_{(n)}$
(perimeter of strip "n")

r = z - 1 — No → r = r + 1

Yes

z = n
(used for trap. rule)

J = Torsion constant

n = n + 1

End

Figure G.4 – Torsion constant subroutine flowchart

432

APPENDIX H

NONLINEAR ANALYSIS MATRIX & SECTION PROPERTY

FORMULATION

For each load increment of the nonlinear analysis, the global stiffness matrix of the system had to be reformulated based on the new material and section properties for each segment. The node and segment numbering is shown in Figure H.1. In Figure H.1 the boxed in number represent the segment numbering. Furthermore, details of the symmetric boundary conditions are presented in Section 6.2.2 and in Figure 6.2
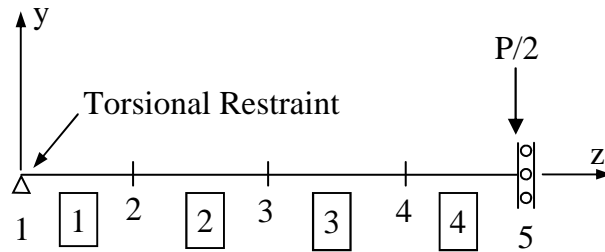
(a) Elevation View

Figure H.1 – Node and segment numbering

The following process was repeated for each load increment. Note that the axial degree of freedom was neglected leaving only five degrees of freedom for each node. First the stiffness matrix of each segment formulated as follows:

$$[k]_i = E_{tan}
\begin{bmatrix}
\dfrac{12I_y}{L_{seg}^3} & 0 & 0 & 0 & \dfrac{6I_y}{L_{seg}^2} & \dfrac{-12I_y}{L_{seg}^3} & 0 & 0 & 0 & \dfrac{6I_y}{L_{seg}^2} \\[2ex]
0 & \dfrac{12I_x}{L_{seg}^3} & 0 & \dfrac{-6I_x}{L_{seg}^2} & 0 & 0 & \dfrac{-12I_x}{L_{seg}^3} & 0 & \dfrac{-6I_x}{L_{seg}^2} & 0 \\[2ex]
0 & 0 & \dfrac{J}{2(1+v)L_{seg}} & 0 & 0 & 0 & 0 & \dfrac{-J}{2(1+v)L_{seg}} & 0 & 0 \\[2ex]
0 & \dfrac{-6I_x}{L_{seg}^2} & 0 & \dfrac{4I_x}{L_{seg}} & 0 & 0 & \dfrac{6I_x}{L_{seg}^2} & 0 & \dfrac{2I_x}{L_{seg}} & 0 \\[2ex]
\dfrac{6I_y}{L_{seg}^2} & 0 & 0 & 0 & \dfrac{4I_y}{L_{seg}} & \dfrac{-6I_y}{L_{seg}^2} & 0 & 0 & 0 & \dfrac{2I_y}{L_{seg}} \\[2ex]
\dfrac{-12I_y}{L_{seg}^3} & 0 & 0 & 0 & \dfrac{-6I_y}{L_{seg}^2} & \dfrac{12I_y}{L_{seg}^3} & 0 & 0 & 0 & \dfrac{-6I_y}{L_{seg}^2} \\[2ex]
0 & \dfrac{-12I_x}{L_{seg}^3} & 0 & \dfrac{6I_x}{L^2} & 0 & 0 & \dfrac{12I_x}{L_{seg}^3} & 0 & \dfrac{6I_x}{L_{seg}^2} & 0 \\[2ex]
0 & 0 & \dfrac{-J}{2(1+v)L_{seg}} & 0 & 0 & 0 & 0 & \dfrac{J}{2(1+v)L_{seg}} & 0 & 0 \\[2ex]
0 & \dfrac{-6I_x}{L_{seg}^2} & 0 & \dfrac{2I_x}{L_{seg}} & 0 & 0 & \dfrac{6I_x}{L_{seg}^2} & 0 & \dfrac{4I_x}{L_{seg}} & 0 \\[2ex]
\dfrac{6I_y}{L_{seg}^2} & 0 & 0 & 0 & \dfrac{2I_y}{L_{seg}} & \dfrac{-6I_y}{L_{seg}^2} & 0 & 0 & 0 & \dfrac{4I_y}{L_{seg}}
\end{bmatrix}$$

The associated displacement vector was as follows:

$$\{u\}_i = \begin{bmatrix} u_j \\ v_j \\ \theta_{zj} \\ \theta_{xj} \\ \theta_{yj} \\ u_{j+1} \\ v_{j+1} \\ \theta_{zj} \\ \theta_{xj+1} \\ \theta_{yj+1} \end{bmatrix}$$

Once all four of the stiffness matrices for each of the segments were formulated, they were combined to form the global stiffness matrix of the system using common degrees of freedom. Furthermore, the restrained degrees of freedom at the support and at the point of symmetry were removed from the global stiffness matrix.

Within the fiber model, the location of the local neutral axis for the local x-axis and y-axis had to be determined to compute the section properties. To determine the local x-axis and local y-axis at a specific node location, the first moment of area was taken about a reference x-axis and y-axis where the cracked area of concrete was not considered. Once the local x-axis and local y-axis were determined, the moments of

inertia, I_x and I_y could be determined from Equations H.1 and H.2. The torsion constant was based on the method by Dooley (1979) and is discussed in Chapter 6.

$$I_x = \sum_{i=1}^{z} \left(A_{ci} \, y^2 + A_{si} \, n \, y^2 \right) \tag{H.1}$$

$$I_y = \sum_{i=1}^{z} \left(A_{ci} \, x^2 + A_{si} \, n \, x^2 \right) \tag{H.2}$$

Once all four of the stiffness matrices for each of the segments were formulated, they were combined to form the global stiffness matrix of the system using common degrees of freedom. Furthermore, the restrained degrees of freedom at the support and at the point of symmetry were removed from the global stiffness matrix.

Geometric nonlinear was taken into consideration by updating the incremental load vector for each load increment. As the lateral displacement and rotation of the cross-section became greater with load increments, so did the applied torque on the system. Furthermore, as the rotation increased at midspan, a larger component of the global vertical load acted about the local weak-axis of the beam as shown in Figure H.2.
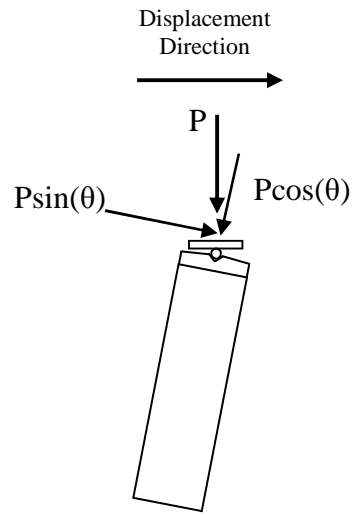
Figure H.2 – Local components of vertically applied load

REFERENCES

AASHTO LRFD Bridge Construction Specifications (2004), 2nd ed. with 2006 and 2007 Interim Revisions, American Association of State Highway and Transportation Officials, Washington, DC.

AASHTO LRFD Bridge Design Specifications (1996), 1st ed., American Association of State Highway and Transportation Officials, Washington, DC.

AASHTO LRFD Bridge Design Specifications (2004), 3rd ed., American Association of State Highway and Transportation Officials, Washington, DC.

AASHTO LRFD Bridge Design Specifications (2007), 4th ed., American Association of State Highway and Transportation Officials, Washington, DC.

ACI 318-83, Building Code Requirements for Structural Concrete (ACI 318-83), American Concrete Institute, Farmington Hills, MI, Section 10.4.

ACI 318-05, Building Code Requirements for Structural Concrete (ACI 318-05), American Concrete Institute, Farmington Hills, MI.

ASTM C31-06, Standard Practice for Making and Curing Concrete Test Specimens in the Field.

ASTM C39-05, Standard Test Method for Compressive Strength of Cylindrical Concrete Specimens.

ASTM C469-02, Standard Test Method for Static Modulus of Elasticity and Poisson's Ratio of Concrete in Compression.

Batdorf, S. B. (1949), "Theories of Plastic Buckling," *Journal of the Aeronautical Sciences*, V. 16, No. 7, July, pp. 405-408.

Beck, H., and Schack, T. (1972), *Bauen mit Beton- und Stahlbetonfertigteilen. Beitrag im Beton-Kalender 1972*, II. Teil, Berlin, München, Düsseldorf, Verlag von Wilhelm Ernst & Son.

Beer, F. P., Johnston, E. R., and DeWolf, J. T. (2001), *Mechanics of Materials*, 3rd Ed., McGraw-Hill, New York, pp. 270-275.

Billig, K. (1953), *Prestressed Concrete*, D. Van Nostrand Company, Inc., New York, pp. 221-222.

Bleich, F. (1952), *Buckling Strength of Metal Structures*, McGraw-Hill, New York.

Burgoyne, C. J., and Stratford, T. J. (2001), "Lateral Instability of Long-Span Prestressed Concrete Beams on Flexible Bearings," *Structural Engineer*, V. 79, No. 6, Mar, pp. 23-26.

Chen, W. F., and Lui, E. M. (1987), *Structural Stability: Theory and Implementation*, Prentice Hall, New Jersey.

Clark, M. J., and Hancock, G. J. (1990), "A Study of Incremental-Iterative Strategies for Non-Linear Analyses," *International Journal for Numerical Methods in Engineering*, V. 29, No. 7, May, pp. 1365-1391.

Code of Practice CP 110: The Structural Use of Concrete, Part 1 (1972), British Standards Institution, Section 3.1.3.

Consolazio, G. R., Hamilton H. R., Bui, L., and Chung, C. (2007), "Lateral Bracing of Long-Span Florida Bulb-Tee Girders" (Final Report), University of Florida, Gainesville, FL, Submitted to Florida Department of Transportation.

Cowan, H. J. (1953), "The Theory of Torsion Applied to Reinforced Concrete Design – Part 2," *Civil Engineering and Public Works Review* (London), V. 48, No. 568, Oct, pp. 950-952.

Crisfield, M. A. (1980), "A Fast Incremental/Iterative Solution Procedure that Handles "Snap-Through,"" *Computers & Structures*, V. 13, No. 1-3, pp. 55-62.

Deneke, O., Holz, K., and Litzner H. (1985), "Übersicht über praktische Verfahren zum Nachweis der Kippsicherheit schlanker Stahlbeton- und Spannbetonträger," *Beton- und Stahlbetonbau*, V. 80, No. 9, Sept, pp. 238-243.

Deneke, O., Holz, K., and Litzner H. (1985), "Übersicht über praktische Verfahren zum Nachweis der Kippsicherheit schlanker Stahlbeton- und Spannbetonträger," *Beton- und Stahlbetonbau*, V. 80, No. 10, Oct, pp. 274-280.

Deneke, O., Holz, K., and Litzner H. (1985), "Übersicht über praktische Verfahren zum Nachweis der Kippsicherheit schlanker Stahlbeton- und Spannbetonträger," *Beton- und Stahlbetonbau*, V. 80, No. 11, Nov, pp. 299-304.

D'Errico, J. (2005), "Surface Fitting using gridfit" (http://www.mathworks.com/matlabcentral/fileexchange/loadFile.do?objectId=8998), MATLAB Central File Exchange, Retrieved April 9, 2009.

Dilger, W. (1966), *Veränderlichkeit der Beige- und Schubsteifigkeit bei Stahlbetontragwerken und ihr Einfluß auf Schnittkraftverteilung und Traglast bei Statisch unbestimmter Lagerung*, Heft 179 des Deutschen Ausschusses für Stahlbeton, Verlag von Wilhelm Ernst & Sohn, Berlin.

Dooley, J. F. (1979), "A Simplified General Method of Analysis of the Elastic Torsion of Non-Circular Solid Sections," *Journal of Strain Analysis*, V. 14, No. 1, pp. 7-10.

Foster, S. (1992), "An Application of the Arc Length Method Involving Concrete Cracking," *International Journal for Numerical Methods in Engineering*, V. 33, No. 2, Jan, pp. 269-285.

Godden, D. I. (1960), "The Effect of Lateral Instability on Post-tensioned Concrete Beams," M. Eng. Thesis, University of Sheffield, UK.

Goodier, J. N. (1941), *Cornell Univ. Eng. Expt. Sta. Bull.*, 27, Dec.

Goodier, J. N. (1942), *Cornell Univ. Eng. Expt. Sta. Bull.*, 28, Jan.

Hansell, W. (1959), "Lateral Stability of Reinforced Concrete Beams," MS Thesis, Cornell University.

Hansell, W., and Winter, G. (1959), "Lateral Stability of Reinforced Concrete Beams," *ACI Journal*, V. 31, No. 3, Sept, pp. 193-213.

Hellweg, H. B., and Crisfield, M. A. (1998), "A New Arc-Length Method for Handling Sharp Snap-Backs," *Computers & Structures*, V. 66, No. 5, Mar, pp. 705-709.

Hognestad, E., Hanson, N. W., and McHenry, D. (1955), "Concrete Stress Distribution in Ultimate Strength Design," *ACI Journal*, V. 27, No. 4, Dec, pp. 455-479.

Hsu, T. T. C. (1984), *Torsion of Reinforced Concrete*, Van Nostrand Reinhold Company Inc., New York.

Imper, R. R., and Laszlo, G. (1987), "Handling and Shipping of Long Span Bridge Beams," *PCI Journal*, V. 32, No. 6, Nov-Dec, pp. 86-101.

Jeltsch, W. (1971), "Ein einfaches Näherungsverfahren zum Nachweis der Kippsicherheit von Stahl-, Stahlbeton- und Spannbetonträgern," Dissertation Technische Hochschule Graz.

Kalkan, I. (2009), "Lateral Torsional Buckling of Rectangular Reinforced Concrete Beams," Ph.D. Dissertation, School of Civil and Environmental Engineering, Georgia Institute of Technology, Atlanta, GA.

Kasparek, K., and Hailer, W. (1973), *Nachweis- und Bemessungsverfahren zum Stabilitätsnachweis nach DIN 1045*, Werner-Verlag, Düsseldorf.

Keim, D. A., and Herrmann, A. (1998), "Gridfit Algorithm: An Efficient and Effective Approach to Visualizing Large Amounts of Spatial Data," *Proceedings of the IEEE Visualization Conference*, pp. 181-187.

Kelly, P. J. (2006), "Bearing Zone Cracking of Precast Prestressed Concrete Bridge Girders," M.S. Thesis, School of Civil and Environmental Engineering, Georgia Institute of Technology, Atlanta, GA.

Kirby, P. A., and Nethercot, D. A. (1979), *Design for Structural Stability (Constrado Monographs)*, Granada Publishing, UK.

König, G., and Pauli, W. (1990), "Ergebnisse von sechs Kippversuchen an schlanken Fertigteilträgern aus Stahlbeton und Spannbeton," *Beton- und Stahlbetonbau*, V. 85, No. 10, Oct, pp. 253-258.

Kraus, D., and Kreuzinger, H. (1983), "Beitrag zur Kippuntersuchung und zur Theorie 2. Ordnung von Trägern mit Berücksichtigung der Vorspannung," Mitteilungen aus dem Institut für Bauingenieurwesen I, Technische Universität München, No. 14, München.

Lam, W. F., and Morley, C. T. (1992), "Arc-Length Method for Passing Limit Points in Structural Calculations," *ASCE Journal of Structural Engineering*, V. 118, No. 1, Jan, pp. 169-185.

Lebelle, P. (1959), "Stabilité Élastique des Poutres en Béton Précontraint a L'Égard du Déversement Latéral," *Institute Technique du Batiment et des Travaux Publics – Annales*, V. 12, No. 141, Sept., pp. 779-831.

Lee, J. H. (2010), "Experimental and Analytical Investigation of the Thermal Behavior of Prestressed Concrete Bridge Girders Including Imperfections," Ph.D. Dissertation, School of Civil and Environmental Engineering, Georgia Institute of Technology, Atlanta, GA.

Leonhardt, F. (1955), *Spannbeton für die Praxis*, Verlag Von Wilhelm Ernst & Sohn, London, pp. 373-376.

Liang, Q. Q. (2008), "Nonlinear analysis of short concrete-filled steel tubular beam-columns under axial load and biaxial bending," *Journal of Constructional Steel Research*, V. 64, pp. 295-304.

Magnel, G. (1944), "Le flambage en béton préconstraint," *Science et Technique*, No. 10, pp. 1-4.

Magnel, G. (1950), *Prestressed Concrete*, Concrete Publications Limited, London, pp. 185-191.

Malangone, P. (1977), "Stabilita Torsinale e Flesso-Torsionale di Travi Precompresse in Parete Sottile," *Giornale del Genio Civile*, V. 115, No. 1, pp. 41-60.

Mann, W. (1976), "Kippnachweis und Kippaussteifung von schlanken Stahlbeton- und Spannbetonträgern," *Beton- und Stahlbetonbau*, V. 71, No. 2, pp. 37-42.

Mann, W. (1985), "Anwendung des vereinfachten Kippnachweises auf T-Profile aus Stahlbeton," *Beton- und Stahlbetonbau*, V. 80, No. 9, pp. 235-237.

Massey, C. (1967), "Lateral Instability of Reinforced Concrete Beams Under Uniform Bending Moments," *ACI Journal*, Proceedings V. 64, No. 3, Mar, pp. 164-172.

Mast, R. F. (1989), "Lateral Stability of Long Prestressed Concrete Beams, Part 1," *PCI Journal*, V. 34, No. 1, Jan-Feb, pp. 34-53.

Mast, R. F. (1993), "Lateral Stability of Long Prestressed Concrete Beams, Part 2," *PCI Journal*, V. 38, No. 1, Jan-Feb, pp. 70-88.

MATLAB® R2006a (2006), The Mathworks, Natick, Massachusetts.

MATLAB® R2009a (2009), The Mathworks, Natick, Massachusetts

Mehlhorn, G. (1974), "Näherunsverfahren zur Abschätzung der Kippstabilität vorgespannter Träger," *Beton- und Stahlbetonbau*, V. 69, No. 1, pp. 7-12.

Molke, E. C. (1956), "Auditorium Framed with Prestressed Roof Girders," *ACI Journal*, Proceedings V. 28, No. 4, Oct, pp. 363-373.

Muller, J. (1962), "Lateral Stability of Precast Members During Handling and Placing," *PCI Journal*, V. 7, No. 1, Feb, pp. 20-31.

Nawy, E. G. (2006), *Prestressed Concrete: A Fundamental Approach*, Pearson Prentice Hall, New Jersey.

Nowak, B. (1971), "Beitrag zur Stabilität eindimensionaler Tragwerke aus Stahlbeton unter allgemeiner Beanspruchung," Dissertation Ruhr-Universität Bochum.

Oesterle, R. G., Sheehan, M.J., Lotfi, H. R., Corley, W. G., and Roller, J. J. (2007), "Investigation of Red Mountain Freeway Bridge Girder Collapse," Final Report, CTLGROUP Project No. 262291, Arizona Department of Transportation, Bridge Group, Nov.

PCI Bridge Design Manual (2003), 2nd ed., Prestressed Concrete Institute, Chicago, IL.

PCI Tolerance Manual for Precast and Prestressed Concrete Construction (2000), 1st ed., Prestressed Concrete Institute, Chicago, IL.

Pettersson, O. (1960), "Vippningsproblem vid hissning och montering av slanka balkar," *Nordisk Betong*, V. 4, pp. 231-270.

Pillai, S. U., and Menon, D. (2002), *Design of Reinforced Concrete Structures*, Tata McGraw Hill, New Delhi, 366 pp.

Plunkett, R. (1965), "Torsion of Inhomogeneous Elastic Prismatic Bars," *Transaction of the American Society of Mechanical Engineers*, 87B, Aug, pp. 391-392.

Rafla, K. (1969), "Näherungsweise Berechnung der kritischen Kipplasten von Stahlbetonbalken," *Beton- und Stahlbetonbau*, V. 64, No. 8, pp. 183-187.

Rafla, K. (1973), "Hilfsdiagramme zur Vereinfachung der Kippuntersuchung von Stahlbetonbalken," *Beton- und Stahlbetonbau*, V. 68, No. 2, pp. 43-47.

Rafla, K. (1973), "Vereinfachter Kippnachweis profilierter Stahlbetonbinder,"*Die Bautechnik*, V. 50, No. 5, pp. 150-156.

Revathi, P., and Menon, D. (2006), "Estimation of Critical Buckling Moments in Slender Reinforced Concrete Beams," *ACI Structural Journal*, V. 103, No. 2, Mar-April, pp. 296-303.

Riks, E. (1979), "An Incremental Approach to the Problem of Snapping and Buckling Problems," *International Journal of Solids and Structures*, V. 15, No. 7, pp. 529-551.

Röder, F. K. (1982), "Berechnung von Stahlbeton- und Spannbetonträgern nach Theorie II. Ordnung.," Dissertation Technische Hochschule Darmstadt, D17.

Röder, F. K., and Mehlhorn, G. (1981), "Kippstabilität ausgewählter Spannbeton- und Stahlbetonträger," Abschlußbericht des vom Hauptverband der Deutschen Bauindustrie geförderten Forschungsvorhabens, Bericht des Instituts für Massivbau der TH Darmstadt.

Saber, A (1998), "High Performance Concrete: Behavior, Design, and Materials in Pretensioned AASHTO and NU Girders," Ph.D. Dissertation, School of Civil and Environmental Engineering, Georgia Institute of Technology, Atlanta, GA.

Sant, J. K., and Bletzacker R. W. (1961), "Experimental Study of Lateral Stability of Reinforced Concrete Beams," *ACI Journal*, Proceedings V. 58, No. 12, Dec, pp. 713-736.

Steit, W., and Mang, R. (1984), "Überschlägiger Kippsicherheitsnachweis für Stahlbeton- und Spannbetonbinder (mit in Längsrichtung konstantem Querschnitt)," *Bauingenieur*, V. 59, pp. 433-439.

Stiglat, K. (1971), "Näherungsberechnung der kritischen Kipplasten von Stahlbetonbaclken," *Die Bautechnik*, V. 48, No. 5, pp. 98-100.

Stoddard, W. P. (1997), "Lateral-Torsional Buckling Behavior of Polymer Composite I-Shaped Members," Ph.D. Dissertation, School of Civil and Environmental Engineering, Georgia Institute of Technology, Atlanta, GA.

Stratford, T. J., and Burgoyne, C. J. (1999), "Lateral Stability of Long Precast Concrete Beams," *Proceedings of the Institution of Civil Engineers*, Structures and Buildings, V. 134, No. 2, May, pp. 169-180.

Stratford, T. J., and Burgoyne, C. J. (2000), "The Toppling of Hanging Beams," *International Journal of Solids and Structures*, V. 37, No. 26, Mar, pp. 3569-3589.

Stratford, T. J., Burgoyne, C. J., and Taylor, H. J. (1999), "Stability Design of Long Precast Concrete Beams," *Proceedings of the Institution of Civil Engineers*, Structures and Buildings, V. 134, No. 2, May, pp. 159-168.

Tavio, and Teng, S. (2004), "Effective Torsional Rigidity of Reinforced Concrete Members," *ACI Structural Journal*, V. 101, No. 2, Mar.-Apr., pp. 252-260.

Thorenfeldt, E., Tomaszewicz, A., and Jensen, J. J. (1987), "Mechanical Properties of High Strength Concrete and Application to Design," *Proceedings of the Symposium: Utilization of High-Strength Concrete*," Stavanger, Norway, June, Tapir Trondheim, pp. 149-159.

Timoshenko, S. (1905), *Bull. Polytech. Inst.,* St. Petersburg.

Timoshenko, S., and Gere, J. (1988), *Theory of Elastic Stability*, McGraw Hill, New York.

Timoshenko, S., and Goodier, J. N. (1951), *Theory of Elasticity*, 2nd ed., McGraw Hill, New York, p. 277.

Timoshenko, S., and Goodier, J. N. (1970), *Theory of Elasticity*, 3rd ed., McGraw Hill, New York.

Trahair, N. S. (1993), *Flexural-Torsional Buckling of Structures*, CRC Press, Florida.

Trahair, N. S. (2000), "Second Order Moments in Torsion Members," Research Report No. R800, Department of Civil Engineering, The University of Sydney, April, Sydney, Australia.

Trahair, N. S., Bradford, M. A., and Nethercot, D. A. (2001), *The Behavior and Design of Steel Structuresto BS5950*, 3rd ed., Spon Press, London.

Turvey, G. J. (1995), "Lateral Buckling Tests on Rectangular Cross-Section Pultruded GRP Cantilever Beams," *Composites: Part B*, V. 27B, pp. 35-42.

Turvey, G. J. and Brooks, R. J. (1996), "Lateral Buckling Tests on Pultruded GRP I-Section Beams with Simply Supported – Simply Supported and Clamped – Simply Supported End Conditions," *Proceedings 1st International Conference on Composites in Infrastructure (ICCI 1996)*, Tuscon, AZ, January 15-17, 1996.

Wilby, C. B. (1963), *Elastic Stability of Post-tensioned Prestressed Concrete Members*, American Elsevier Publishing Company, Inc., New York.

Yarimci, E., Yura, J. A., and Lu, L. W. (1967), "Techniques for Testing Structures Permitted to Sway," *Experimental Mechanics*, V. 7, No. 8, Aug., pp. 321-331.

Yazdini, N., Eddy, S., and Cai, C. S. (2000), "Effect of Bearing Pads on Precast Prestressed Concrete Bridges," *ASCE Journal of Bridge Engineering*, V. 5, No. 3, Aug., pp. 224-232.

Yura, J.A., and Phillips, B.A. (1992), "Bracing Requirements for Elastic Steel Beams," *Research Report 1239-1*, Center for Transportation Research, The University of Texas, Austin, TX.

Zureick, A. H., Kahn L. F., and Will, K. M. (2005), "Stability of Precast Prestressed Concrete Bridge Girders Considering Sweep and Thermal Effects" (Proposal), Submitted to Georgia Department of Transportation.

VITA

JONATHAN B. HURFF

Jonathan Hurff was born on November 12, 1983 in Voorhees, New Jersey. He graduated from West Deptford High School in West Deptford, New Jersey in 2002. In 2006 he graduated with a B.S. in Civil Engineering from Virginia Polytechnic Institute and State University in Blacksburg, Virginia. In 2006 he began working on research at Georgia Institute of Technology and obtained a M.S. in Civil Engineering in 2008 and a Ph.D. in Civil Engineering with an emphasis on structural engineering and mechanics in 2010.